Topics in Applied Physics 133

Tae-Yeon Seong
Jung Han
Hiroshi Amano
Hadis Morkoç *Editors*

III-Nitride Based Light Emitting Diodes and Applications

Second Edition

Topics in Applied Physics

Volume 133

Series editors

Mildred S. Dresselhaus, Physics and Electrical Engineering, Massachusetts Institute of Technology, Cambridge, MA, USA
Young Pak Lee, Radiology, Hanyang University Hospital, Seoul, Republic of Korea
Paolo M. Ossi, NEMAS - WIBIDI Lab, Politecnico di Milano, Milano, Italy

Topics in Applied Physics is a well-established series of review books, each of which presents a comprehensive survey of a selected topic within the broad area of applied physics. Edited and written by leading research scientists in the field concerned, each volume contains review contributions covering the various aspects of the topic. Together these provide an overview of the state of the art in the respective field, extending from an introduction to the subject right up to the frontiers of contemporary research.

Topics in Applied Physics is addressed to all scientists at universities and in industry who wish to obtain an overview and to keep abreast of advances in applied physics. The series also provides easy but comprehensive access to the fields for newcomers starting research.

Contributions are specially commissioned. The Managing Editors are open to any suggestions for topics coming from the community of applied physicists no matter what the field and encourage prospective editors to approach them with ideas.

More information about this series at http://www.springer.com/series/560

Tae-Yeon Seong · Jung Han
Hiroshi Amano · Hadis Morkoç
Editors

III-Nitride Based Light Emitting Diodes and Applications

Second Edition

Editors
Tae-Yeon Seong
Department of Materials Science
and Engineering
Korea University
Seoul
Korea (Republic of)

Hiroshi Amano
Department of Electrical Engineering
and Computer Science
Nagoya University
Nagoya, Aichi
Japan

Jung Han
Department of Electrical Engineering
Yale University
New Haven, CT
USA

Hadis Morkoç
Department of Electrical and Computer
Engineering
Virginia Commonwealth University
Richmond, VA
USA

ISSN 0303-4216 ISSN 1437-0859 (electronic)
Topics in Applied Physics
ISBN 978-981-10-3754-2 ISBN 978-981-10-3755-9 (eBook)
DOI 10.1007/978-981-10-3755-9

Library of Congress Control Number: 2017932011

1st edition: © Springer Science+Business Media Dordrecht 2013
2nd edition: © Springer Nature Singapore Pte Ltd. 2017
This work is subject to copyright. All rights are reserved by the Publisher, whether the whole or part of the material is concerned, specifically the rights of translation, reprinting, reuse of illustrations, recitation, broadcasting, reproduction on microfilms or in any other physical way, and transmission or information storage and retrieval, electronic adaptation, computer software, or by similar or dissimilar methodology now known or hereafter developed.
The use of general descriptive names, registered names, trademarks, service marks, etc. in this publication does not imply, even in the absence of a specific statement, that such names are exempt from the relevant protective laws and regulations and therefore free for general use.
The publisher, the authors and the editors are safe to assume that the advice and information in this book are believed to be true and accurate at the date of publication. Neither the publisher nor the authors or the editors give a warranty, express or implied, with respect to the material contained herein or for any errors or omissions that may have been made. The publisher remains neutral with regard to jurisdictional claims in published maps and institutional affiliations.

Printed on acid-free paper

This Springer imprint is published by Springer Nature
The registered company is Springer Nature Singapore Pte Ltd.
The registered company address is: 152 Beach Road, #21-01/04 Gateway East, Singapore 189721, Singapore

Contents

1 **Progress and Prospect of Growth of Wide-Band-Gap Group III Nitrides** 1
Hiroshi Amano

2 **Ultra-Efficient Solid-State Lighting: Likely Characteristics, Economic Benefits, Technological Approaches** 11
Jeff Y. Tsao, Jonathan J. Wierer Jr., Lauren E.S. Rohwer, Michael E. Coltrin, Mary H. Crawford, Jerry A. Simmons, Po-Chieh Hung, Harry Saunders, Dmitry S. Sizov, Raj Bhat and Chung-En Zah

3 **LEDs Based on Heteroepitaxial GaN on Si Substrates** 29
Takashi Egawa and Osamu Oda

4 **Epitaxial Growth of GaN on Patterned Sapphire Substrates** 69
Kazuyuki Tadatomo

5 **Growth and Optical Properties of GaN-Based Non- and Semipolar LEDs** 93
Michael Kneissl, Jens Raß, Lukas Schade and Ulrich T. Schwarz

6 **Internal Quantum Efficiency in Light-Emitting Diodes** 129
Elison Matioli and Claude Weisbuch

7 **Internal Quantum Efficiency** 163
Jong-In Shim

8 **III-Nitride Tunnel Junctions and Their Applications** 209
S. Rajan and T. Takeuchi

9 **Green, Yellow, and Red LEDs** 239
Jongil Hwang, Rei Hashimoto and Shinji Saito

10 **AlGaN-Based Deep-Ultraviolet Light-Emitting Diodes** 267
Hideki Hirayama, Norihiko Kamata and Kenji Tsubaki

11 Ray Tracing for Light Extraction Efficiency (LEE) Modeling in Nitride LEDs 301
C. Lalau Keraly, L. Kuritzky, M. Cochet and Claude Weisbuch

12 Light Extraction of High-Efficient Light-Emitting Diodes 341
Ja-Yeon Kim, Tak Jeong, Sang Hern Lee, Hwa Sub Oh, Hyung Jo Park, Sang-Mook Kim and Jong Hyeob Baek

13 Electrical Properties, Reliability Issues, and ESD Robustness of InGaN-Based LEDs 363
M. Meneghini, G. Meneghesso and E. Zanoni

14 Phosphors and White LED Packaging 397
Rong-Jun Xie and Naoto Hirosaki

15 High-Voltage LEDs 433
Wen-Yung Yeh, Hsi-Hsuan Yen, Kuang-Yu Tai and Pei-Ting Chou

16 Color Quality of White LEDs 457
Yoshi Ohno

17 Emerging System Level Applications for LED Technology 481
Robert F. Karlicek Jr.

Index 493

Contributors

Hiroshi Amano Institute of Materials and Systems for Sustainability (IMaSS), Nagoya University, Nagoya, Japan

Jong Hyeob Baek Korea Photonics Technology Institute, Gwangju, Republic of Korea

Raj Bhat Corning Incorporated, One Science Center Drive, Corning, NY, USA

Pei-Ting Chou Industrial Technology Research Institute, Hsinchu, Taiwan, ROC

M. Cochet Materials Department, University of California, Santa Barbara, USA

Michael E. Coltrin Sandia National Laboratories, Physical Chemical and Nano Sciences Center, Albuquerque, NM, USA

Mary H. Crawford Sandia National Laboratories, Physical Chemical and Nano Sciences Center, Albuquerque, NM, USA

Takashi Egawa Research Center for Nano-Device and System, Nagoya Institute of Technology, Nagoya, Japan

Rei Hashimoto Corporate Manufacturing Engineering Center, Toshiba Corporation, Isogo-ku, Yokohama, Japan

Hideki Hirayama RIKEN, Wako, Saitama, Japan

Naoto Hirosaki National Institute for Materials Science (NIMS), Tsukuba, Japan

Po-Chieh Hung Technology Strategy Division, Corporate R&D Headquarters Konica Minolta, Inc., Hachioji-shi, Tokyo, Japan

Jongil Hwang Corporate Research and Development Center, Toshiba Corporation, Saiwai-ku, Kawasaki, Japan

Tak Jeong Korea Photonics Technology Institute, Gwangju, Republic of Korea

Norihiko Kamata Saitama University, Sakura-ku, Saitama, Japan

Robert F. Karlicek Jr. Rensselaer Polytechnic Institute, New York, USA

Ja-Yeon Kim Korea Photonics Technology Institute, Gwangju, Republic of Korea

Sang-Mook Kim Korea Photonics Technology Institute, Gwangju, Republic of Korea

Michael Kneissl Institute of Solid State Physics, Technische Universität Berlin, Berlin, Germany; Ferdinand-Braun-Institut, Leibniz Institut für Höchstfrequenztechnik, Berlin, Germany

L. Kuritzky Materials Department, University of California, Santa Barbara, USA

C. Lalau Keraly Materials Department, University of California, Santa Barbara, USA; Department of Electrical Engineering, University of California at Berkeley, Berkeley, USA

Sang Hern Lee Korea Photonics Technology Institute, Gwangju, Republic of Korea

Elison Matioli Institute of Electrical Engineering, École Polytechnique Fédérale de Lausanne, EPFL STI IEL POWERlab, Switzerland

G. Meneghesso University of Padova, Padua, Italy

M. Meneghini University of Padova, Padua, Italy

Osamu Oda Research Center for Nano-Device and System, Nagoya Institute of Technology, Nagoya, Japan

Hwa Sub Oh Korea Photonics Technology Institute, Gwangju, Republic of Korea

Yoshi Ohno National Institute of Standards and Technology, Gaithersburg, USA

Hyung Jo Park Korea Photonics Technology Institute, Gwangju, Republic of Korea

Jens Raß Institute of Solid State Physics, Technische Universität Berlin, Berlin, Germany

S. Rajan The Ohio State University, Columbus, USA

Lauren E.S. Rohwer Physical Chemical and Nano Sciences Center, Sandia National Laboratories, Albuquerque, NM, USA

Shinji Saito Corporate Manufacturing Engineering Center, Toshiba Corporation, Isogo-ku, Yokohama, Japan

Harry Saunders Decision Processes Incorporated, Danville, CA, USA

Lukas Schade Department of Microsystems Engineering, University of Freiburg, Freiburg, Germany

Ulrich T. Schwarz Faculty of Natural Sciences, Chemnitz University of Technology, Chemnitz, Germany

Jong-In Shim Hanyang University, Seoul, Korea

Jerry A. Simmons Sandia National Laboratories, Physical Chemical and Nano Sciences Center, Albuquerque, NM, USA

Dmitry S. Sizov Corning Incorporated, One Science Center Drive, Corning, NY, USA

Kazuyuki Tadatomo Graduate School of Science and Engineering, Yamaguchi University, Ube, Yamaguchi, Japan

Kuang-Yu Tai Industrial Technology Research Institute, Hsinchu, Taiwan, ROC

T. Takeuchi Meijo University, Nagoya, Japan

Jeff Y. Tsao Sandia National Laboratories, Physical Chemical and Nano Sciences Center, Albuquerque, NM, USA

Kenji Tsubaki Panasonic, Kadoma, Oaska, Japan

Claude Weisbuch Materials Department, University of California, Santa Barbara, CA, USA; Laboratoire de Physique de la Matière Condensée, CNRS, Ecole Polytechnique, Palaiseau, France

Jonathan J. Wierer Jr. Sandia National Laboratories, Physical Chemical and Nano Sciences Center, Albuquerque, NM, USA

Rong-Jun Xie National Institute for Materials Science (NIMS), Tsukuba, Japan

Wen-Yung Yeh Industrial Technology Research Institute, Hsinchu, Taiwan, ROC

Hsi-Hsuan Yen Industrial Technology Research Institute, Hsinchu, Taiwan, ROC

Chung-En Zah Corning Incorporated, One Science Center Drive, Corning, NY, USA

E. Zanoni University of Padova, Padua, Italy

Chapter 1
Progress and Prospect of Growth of Wide-Band-Gap Group III Nitrides

Hiroshi Amano

GaAs, InP, and their related compound semiconductors can be grown on native substrates, whereas such growth was not possible for group III nitride semiconductors in the 1970s and 1980s. Despite this drawback, researchers were able to use novel functions of group III nitride semiconductors by growing their thin films on nonnative substrates such as sapphire, SiC and Si. Today, white light-emitting diodes (LEDs) based on nitrides on sapphire substrates are some of the most important key devices for energy savings given their use in general lighting. Also, LEDs and HFETs on Si are considered to be the next-generation high-performance and low-cost energy-saving devices. In this chapter, the author reviews the history of the growth of GaN by metalorganic vapor phase epitaxy using a buffer layer on nonnative substrates. The history of the low-temperature-deposited buffer layer and its impact on nitride research and the subsequent development of devices are explained.

1.1 History of III–V Research (1950s–1970s)

Group III nitride semiconductors (nitrides) belong to group III–V compound semiconductors (III–Vs) such as GaAs and InP. One of the most specific differences between nitrides and other III–Vs is their stable crystal structure. The stable structure of nitrides at room temperature at atmospheric pressure is hexagonal wurtzite, while that of other III–Vs is cubic zinc-blende. The history of nitride research started earlier than those of As- and P-based III–V compounds. AlN and InN were first reported in 1907 [1] and 1910 [2], respectively. GaN has a shorter

H. Amano (✉)
Institute of Materials and Systems for Sustainability (IMaSS), Nagoya University, Nagoya 464-8603, Japan
e-mail: amano@nuee.nagoya-u.ac.jp

© Springer Nature Singapore Pte Ltd. 2017

T.-Y. Seong et al. (eds.), *III-Nitride Based Light Emitting Diodes and Applications*, Topics in Applied Physics 133, DOI 10.1007/978-981-10-3755-9_1

history and was first reported in 1932 [3]. The author would like to focus on GaN in this chapter.

As- and P-based III–Vs were first reported by Welker in 1952, which was 20 years after the first report on GaN [4]. However, the progress of the research on III–Vs was very fast. Ten years later, in 1962, Holonyak and Bevacqua realized a visible red GaAsP laser diode (LD) [5], which triggered the remarkable progress in the development of technologies ranging from crystal growth to device fabrication, and the term “Alloy Road” was coined [6]. Thanks to this progress, various devices have been practically realized and are enriching our lives today, including red and green light-emitting diodes (LEDs), infrared LDs for high-speed optical communications, infrared and visible red LDs for optical recording, photovoltaic cells, high-electron-mobility transistors, and heterojunction bipolar transistors. In the 1960s, many scientists attempted or considered attempting to grow nitride crystals, which belong to the III–Vs, as mentioned above, with the aim of realizing the blue LED, because at that time only the blue LED among the three primary colors remained to be achieved. In June 1968, RCA announced flat-panel liquid crystal displays. At that time, the radio system was changed from vacuum-tube-based circuits to transistor-based electronic circuits. Thus, many researchers felt that even the TV system should be changed from the Braun tube to the solid-state display system. Therefore, flat-panel TVs were considered a very important piece of equipment for the development of future electronics systems. Accordingly, the remaining solid-state blue light source was highly desired. It was not until 1969, seven years after the first red LD was developed, that Maruska and Tietjen first reported the successful growth of GaN single crystals, which are currently used for blue LEDs [7]. The first blue LED using GaN was reported in 1971, 2 years after the growth of its crystals was reported [8]. Nevertheless, the development of the GaN-based blue LED was not straightforward. The serious obstacles that prevented the development of GaN-based blue LEDs were the difficulty in growing high-quality and low-defect-density crystals and the difficulty in controlling conductivity, particularly realization of p-type GaN.

The largest difference between III–Vs and nitrides is whether bulk single crystals with a low-defect density can be practically grown. For example, the melting point of GaAs is 1238 °C at which the dissociation pressure of As is approximately 1 atm [9]. In contrast, the theoretical melting point of GaN is 2500 °C [10] at which the dissociation pressure of N is estimated to be as high as 45000 atm [11]. This means that bulk GaN single crystals cannot be easily realized. The first reported GaN single crystal was also grown on a sapphire substrate by the halogen transport vapor phase epitaxy (HVPE) method, which uses the chemical reaction between GaCl and NH_3 and is also called the hydride vapor phase epitaxy method [7]. Naturally, many research teams shifted their research target from group III–V compound semiconductors to other materials, such as SiC- and ZnSe-based group II–VI compound semiconductors, or adopted wavelength conversion or second-harmonic generation with the aim of realizing blue LEDs. Some research teams, however, continued to study group III nitride semiconductors and methods of growing their thin films on nonnative substrates.

Eventually, blue LEDs were practically applied using group III nitride semiconductors grown on nonnative substrates, i.e., sapphire substrates. The blue-violet LDs used for Blu-ray Discs were also realized on thick-film GaN substrates grown from seed sapphire or GaAs crystals. High-power high-frequency high-electron-mobility transistors (HEMTs) on SiC substrates are already in widespread use in base stations for cell phones. AlGaN/GaN heterojunction field-effect transistors (HFETs) on Si substrates will shortly become available for use as mid-voltage switching devices. These devices can markedly reduce energy consumption. For example, LED lamps may be used in 55% of households worldwide by 2025, and the worldwide reduction in power consumption is estimated to be 1,100 TWh per year, assuming a luminous efficacy of 150 lm/W [12]. This value sufficiently exceeds the total power consumption in Japan in fiscal 2006 of 960 TWh. High expectations are also being placed on scanning laser displays including head-mounted displays in terms of reducing power consumption, because they require neither polarizers nor In-containing transparent electrodes, both of which are currently used in liquid crystal displays. Moreover, the power consumption of motors accounts for approximately 60% of the total power consumption. It is highly expected that inverters with GaN-based switching devices will reduce the power consumption of motors by half or even two-thirds compared with motors without inverters. The rate of inverter employment is high in Japan, in contrast to not only developing countries but also Europe and the US. In the future, switching devices using group III nitride semiconductors are expected to be a key strategic tool for reducing power consumption along with Si-based insulated gate bipolar transistors and SiC switching devices. In addition, InGaN alloys, which cover almost the entire range of the solar light spectrum, are expected to be used to realize photovoltaic cells with an efficiency of over 60% by utilizing multijunction structures, light collection, and multiphoton absorption.

It is astonishing to know that such tremendous impacts to human society have been and will be brought about by the nonperfect crystals grown on nonnative substrates. This was mainly due to the physical properties of group III nitride semiconductors; that is, the diffusion length of excited (injected) carriers for group III nitride semiconductors is shorter than that for As- and P-based compound semiconductors, and group III nitride semiconductors are less affected by crystal defects [13].

Nevertheless, it may be meaningful to explain how researchers tackled the growth of GaN on nonnative substrates. In the next section, the history of the development of the low-temperature-deposited buffer layer for the growth of GaN on a sapphire substrate.

1.2 Dawn of GaN Research (1970s to Mid-1980s)

In Japan, Osamura et al. reported in 1972 the absorption edge of polycrystalline GaN, InN, and their alloys [14]. Isamu Akasaki, Matsushita Research Institute, Tokyo, started ammonia MBE of GaN from 1974 and succeeded in the thin-film

growth of GaN that emitted blue luminescence by cathodoluminescence. Then, the former Ministry of International Trade and Industry, MITI, decided to embark on three-year national projects on the solid-state blue light emitter. One was the second-harmonic generator-based technology proposed by Dr. Izuo Hayashi, NEC, who was famous for the room-temperature CW operation of the AlGaAs-based laser diode, and the other one was the GaN-based technology proposed by Isamu Akasaki. At that time, the quality of the ammonia MBE system was not so good compared with today's system. According to claim, the GaN film grown by ammonia MBE always showed highly conductive n-type behavior. In addition, the growth rate was very low. Therefore, Akasaki's group also started HVPE in addition to ammonia MBE.

In the 1970s, several research groups around the world were pursuing the GaN growth by HVPE, and some groups such as RCA [8], Stanford University [15], Oki Electric [16], and Philips [17] demonstrated the mis-type LEDs based on GaN. However, no group had succeeded in the commercialization of the blue LEDs. The research group of Matsushita Research Institute, Tokyo, concentrated on the commercialization of GaN-based LEDs and developed several important technologies such as selective area growth using a SiO_2 mask and flip-chip bonding for high light extraction [18]. Finally, they succeeded in the sample shipping of the mis-type GaN-based LEDs in 1981. However, the company stopped the development of GaN-based LEDs. Thus, Isamu Akasaki moved to Nagoya University in 1981.

At that time, many researchers had abandoned the "III–V alloy road" for blue light emitters and moved to other materials such as SiC [19] or II–VIs [20]. Only a few groups carried out GaN research [21–23].

1.3 Low-Temperature-Deposited Buffer Layer, p-Type GaN and Highly Luminescent InGaN (Late 1980s)

The author joined Professor Akasaki's group in 1982. In 1985, Yasuo Koide and I developed the vertical-type MOVPE reactor as shown in Fig. 1.1.

First, we coped with the flow dynamic issue. At that time, the maximum hydrogen flow rate of our purifier was very low for growing GaN at a reasonable rate. Therefore, the author used a very tiny and narrow quartz tube and gathered all the gases including hydrogen, metalorganics, and ammonia to realize a high flow rate of about 5 m/s. Figure 1.2 schematically shows the concept of gas injection tube.

Next, the author tackled the problem of large lattice mismatch of about 16% between GaN and a sapphire substrate. In general, it is quite difficult to proceed with epitaxial growth if the lattice mismatch is larger than 1%. Therefore, the grown crystal is mainly composed of tiny grains aligned to the c-axis but the in-plane crystal direction is largely misaligned with each other. The author could not grow

Fig. 1.1 Laboratory-made vertical-type MOVPE reactor for InN, GaN, AlN, InGaN, and AlGaN growth

GaN with an atomically flat surface for a long time. A c-plane sapphire with an offset angle larger than 1° was found to be effective for growing GaN having a relatively flat surface as shown in Fig. 1.3. However, the surface morphology was far from perfect, even worse than that of GaN grown by HVPE. The surface flatness of AlN and AlGaN grown by a colleague was better than that of GaN grown by the author. Thus, the author tried to use thin AlN as a buffer layer between GaN and the sapphire substrate in the autumn of 1985. He knew that single-crystal AlN should be grown at a much higher temperature than that of GaN. However, unfortunately, when he started to grow GaN, he found that the power oscillator did not work properly. Then, he remembered the comment of the associate professor who sometimes said that the substrate surface should be as clean as possible for epitaxial growth. However, if it is impossible to realize an atomically clean surface, it may be effective to deposit a not so high-quality layer that acts as a nucleation layer. Thus, he deposited AlN at a low temperature of approximately 450 °C. In the meantime, the power oscillator recovered to work again. Then, he continued the growth of GaN at the normal temperature of 1,000 °C. When he removed the sample from the reactor after the growth, he first thought that he had forgotten to supply metalorganics because the surface was almost the same as that of the bare sapphire. However, when he observed the surface using a Nomarski microscope, he found that he had overcome the problem of surface roughness. Now, this process is called the low-temperature-deposited buffer layer and becomes the de-fact-standard

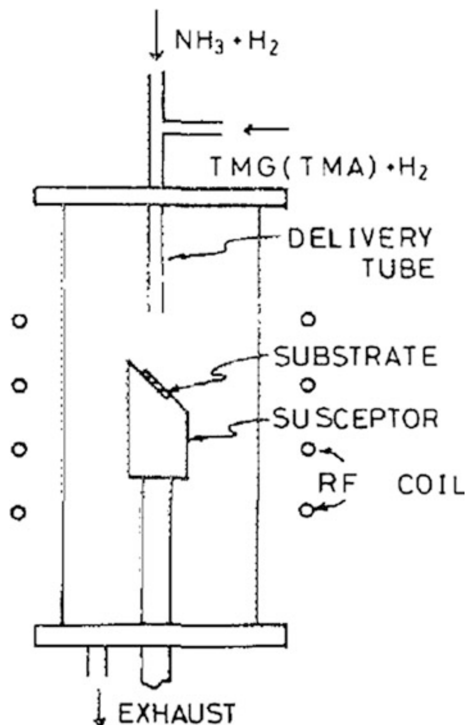

Fig. 1.2 High speed gas injection type MOVPE reactor

technology of the growth of GaN by MOVPE on a sapphire substrate. Figure 1.4 shows the effect of the low-temperature buffer layer on the growth of GaN on a sapphire substrate [24].

Before publishing this remarkable result to the academic journal, the author thought he should submit a patent. At that time, he knew similar results had been already published. For example, M. Akiyama et al. reported that low-temperature-deposited GaAs buffer layer was effective for the improvement of the quality of GaAs on Si by MOVPE [25]. S. Yoshida et al. reported an increase of electron mobility and improvement of the cathodoluminescence property of GaN on a sapphire substrate grown by ammonia MBE by coating with single crystalline AlN [22]. The author knew that low-temperature-deposited GaN buffer layer was also effective to improve the surface morphology of GaN. He also knew that high-temperature-deposited thin AlN also showed some effect to improve the surface morphology of GaN. However, he was afraid that people might think that it was only the imitation of GaAs on Si. Therefore, he wrote a draft of the patent in which the buffer layer was limited to only low-temperature-deposited AlN buffer layer [26]. Later, one company claimed in the patent in 1991 that not only AlN, but also GaN and AlGaN were effective as a low-temperature buffer layer [27].

Third, the author coped with the realization of p-type GaN. At that time, Zn was commonly used as an acceptor dopant because Zn-doped GaN shows a relatively bright blue luminescence. In 1988, the author found that the blue luminescence

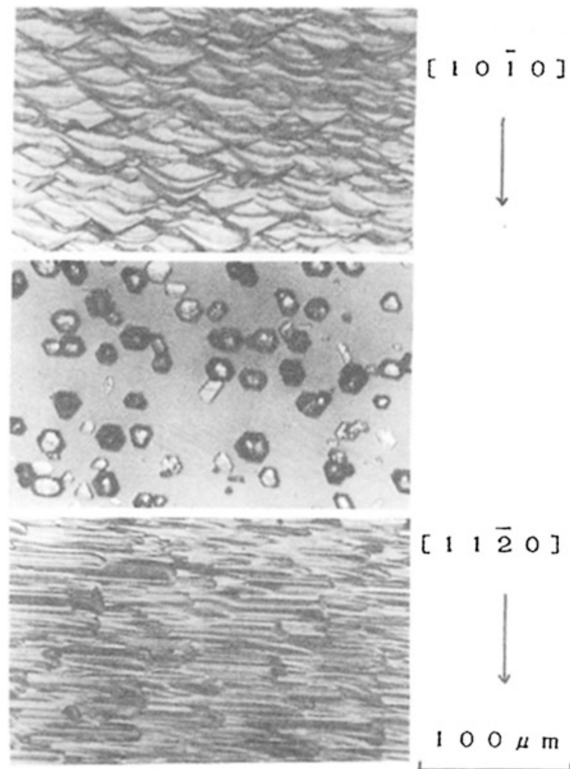

Fig. 1.3 Optical microscopic images of GaN directly grown on sapphire. (From *top* to *bottom*, 3° off toward <11–20> of sapphire, just cut, 3° off toward <10−10> of sapphire)

intensity monotonically increases during low-energy electron beam irradiation [28]. This phenomenon was already published and reported by Saparin et al. in 1983 [29] and 1984 [30]. When he read the textbook written by Phillips and Lucovsky [31], he found that Mg or Be should be better than Zn as an acceptor dopant because of the lower activation energy. Unfortunately, he could not use Be because of safety issues. Thus, he changed the acceptor dopant from Zn to Mg and tried to grow Mg-doped GaN. The as-grown GaN:Mg did not show p-type behavior. However, when it was treated with low-energy electron beam irradiation, he found that the p-type GaN had been successfully realized for the first time. This process was called LEEBI treatment [32]. At that time, he thought he should clarify the mechanism. First, he thought that the mechanism was caused by the heating during electron beam irradiation, which was unexciting to him. Therefore, he investigated another possible mechanism. But, he could not find a good explanation of LEEI effect. Then, in 1991, Nichia Chemicals submitted a patent of thermal annealing. [33].

Anyway, the author presented this result to the International Symposium on GaAs and Related Compounds in 1989, which was held at Karuizawa, Japan. The author attended the program committee meeting on behalf of Professor Isamu Akasaki and found that his paper was just below the borderline, that is, close to being accepted as a poster presentation, but it was rejected during the first

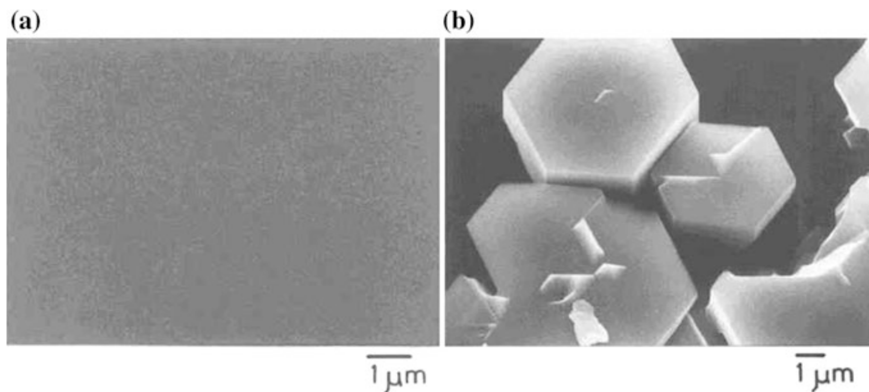

Fig. 1.4 SEM images of GaN grown on a sapphire (0001) substrate **a** with and **b** without low-temperature deposited AlN buffer layer

screening. However, when the sessions were finally arranged, one slot became vacant. Then, he recommended himself of his paper and it was very fortunate that his abstract was allowed to be presented as a poster [34]. At the same symposium, Dr. Takashi Matsuoka of NTT at that time presented the growth of InGaN for the first time [35]. But, a very few people were interested in his presentation.

1.4 Summary

The history of the initial stage of the development of GaN, especially MOVPE growth of GaN on a nonnative sapphire substrate using a low-temperature-deposited buffer layer, and the realization of p-type GaN in the 1980s and 1990s were reviewed. In 2011, more than 3,400 academic papers on GaN and related compounds academic journal papers were published. Also, the number of attendees of the International Workshop on Nitride Semiconductors 2012, which was held in Sapporo, Japan was more than 1000. In addition, the market size of LED displays and lighting will exceed one billion US dollars in 2012. No one probably expected such a vast expansion of the research field in the 1980s. The potential of nitrides should not be limited to LEDs, but should also expand to other fields such as high-frequency and high-power electron devices, laser diodes and photovoltaic devices. Another breakthrough will surely lead to the second expansion of the research field and market of these material systems in the very near future.

Acknowledgements I wish to express my gratitude to M. Yamaguchi and Y. Honda, Nagoya University, and M. Iwaya, T. Takeuchi, S. Kamiyama and I. Akasaki of Meijo University for daily discussions.

References

1. F. Fichter, Z. Anorg. Chem. **54**, 322 (1907)
2. F. Fischer, F. Schroter, Ber. Dtsch. Chem. Ges. **43**, 1465 (1910)
3. W.C. Johnson, J.B. Parsons, M.C. Crew, J. Phys. Chem. **36**, 2588 (1932)
4. H. Welker, Zeitschrift fuer Naturforschung, 7a, 744 (1952)
5. N. Holonyak, S.F. Bevacqua, Appl. Phys. Lett. **1**, 82 (1962)
6. E.E. Loebner, IEEE Trans. Elec. Dev. Electron Devices **23**, 675 (1976)
7. H.P. Maruska, J.J. Tietjen, Appl. Phys. Lett. **15**, 327 (1969)
8. J.I. Pankove, E.A. Miller, D. Richman, J.E. Berkeyheiser, J. Lumin. **4**, 63 (1971)
9. D. Richman, J. Phys. Chem. Sol. **24**, 1131 (1963)
10. J.A. Van Vechten, Phys. Rev. B **7**, 1479 (1973)
11. J. Karpinski, J. Jun, S. Porowski, J. Cryst. Growth **66**, 1 (1984)
12. R. Haitz, J.Y. Tsao, Phys. Status Solidi (A) **208**, 17 (2011)
13. A. Kaneta, M. Funato, Y. Narukawa, T. Mukai, Y. Kawakami, Phys. Status Solidi (C) **3**, 1897 (2006)
14. K. Osamura, K. Nakajima, Y. Murakami, P.H. Shingu, A. Ohtsuki, Solid State Comm. **11**, 617 (1972)
15. H.P. Maruska, W.C. Rhines, D.A. Stevenson, Mater. Res. Bull. **7**, 777 (1972)
16. Y. Matsumoto, Jpn. J. Appl. Phys. **13**, 1307 (1974)
17. M. Boulou, M. Furtado, G. Jacob, Philips Tech. Rev. **37**, 237 (1977)
18. Y. Ohki, Y. Toyoda, H. Kobayashi, I. Akasaki, Inst. Phys. Conf. Ser. **63**, 479 (1982)
19. L. Hoffman, G. Ziegler, D. Theis, C. Weyrich, J. Appl. Phys. **53**, 6962 (1982)
20. N.B. Lukyanchkova, T.M. Pavelko, G.S. Pekar, N.N. Tkachenko, M.K. Sheinkman, Phys. Status Solidi (A), **64**, 697 (1981)
21. T. Kawabata, T. Matsuda, S. Koike, J. Appl. Phys. **56**, 2367 (1984)
22. S. Yoshida, S. Misawa, S. Gonda, Appl. Phys. Lett. **42**, 427 (1983)
23. M.A. Khan, R.A. Skogman, R.G. Schulze, M. Gershenzon, Appl. Phys. Lett. **42**, 430 (1983)
24. H. Amano, N. Sawaki, I. Akasaki, Y. Toyoda, Appl. Phys. Lett. **48**, 353 (1986)
25. M. Akiyama, Y. Kawarada, K. Kaminishi, Jpn. J. Appl. Phys. **23**, L843 (1984)
26. Japan Patent, S60-256806 (1985)
27. Japan Patent, H3-89840 (1991)
28. H. Amano, I. Akasaki, T. Kozawa, K. Hiramatsu, N. Sawaki, K. Ikeda, Y. Ishii, J. Lumin. **40&41**, 121 (1988)
29. G.V. Saparin, S.K. Obyden, I.F. Chetverkova, M.V. Chukichev, S.I. Popov, Vestnik Moskovskogo Universiteta Seriya 3 Fisika Astronomiya **24**, 56 (1983)
30. G.V. Saparin, S.K. Obyden, M.V. Chukichev, S.I. Popov, J. Lumin. **31**, 684 (1984)
31. J.C. Philips, G. Lucovsky, *Bonds and Bands in Semiconductors*, 1st edn. (Momentum Press, 1973), p. 239
32. H. Amano, M. Kito, K. Hiramatsu, I. Akasaki, Jpn. J. Appl. Phys. **28**, L2112 (1989)
33. Japan Patent, H3-321353 (1991)
34. H. Amano, M. Kitoh, K. Hiramatsu, I. Akasaki, Inst. Phys. Conf. Ser. **106**, 725 (1990)
35. T. Matsuoka, H. Tanaka, T. Sasaki, A. Katsui, Inst. Phys. Conf. Ser. **106**, 141 (1990)

Chapter 2
Ultra-Efficient Solid-State Lighting: Likely Characteristics, Economic Benefits, Technological Approaches

Jeff Y. Tsao, Jonathan J. Wierer Jr., Lauren E.S. Rohwer, Michael E. Coltrin, Mary H. Crawford, Jerry A. Simmons, Po-Chieh Hung, Harry Saunders, Dmitry S. Sizov, Raj Bhat and Chung-En Zah

Abstract Technologies for artificial lighting, as illustrated on the left side of Fig. 2.1, have made tremendous progress over the centuries: from fire, with an efficiency of about a tenth of a percent; to incandescent lamps, with an efficiency of about 4%; to gas discharge lamps, with an efficiency of about 20%; and soon to solid-state lighting (SSL), with efficiencies that in principle could approach 100%. At this point in time, there is virtually no question that SSL will eventually displace its predecessor technologies. A remaining question, however, is what the final efficiency of SSL will be. Will it be, as illustrated on the right side of Fig. 2.1, 50%, which is what the community (Haitz and Tsao, Optik Photonik 6:26–30, 2011 [11], Haitz and Tsao, Phys Status Solidi A 208:17–29, 2011 [10]) has long targeted as its "efficient" lighting goal? Will it be 70% or higher, which is what some (Phillips et al, Tsao Laser Photonics Rev 307–333, 2007 [28]) have called the "ultra-efficient" lighting goal? Or will it be even beyond an effective efficiency of 100%, something that might be enabled by smart lighting (Kim and Schubert, Science 308:1274–1278, 2005 [14]), in which one does not just engineer the efficiency with which light is *produced*, but the efficiency with which light is *used*? In

J.Y. Tsao (✉) · J.J. Wierer Jr. · L.E.S. Rohwer · M.E. Coltrin · M.H. Crawford · J.A. Simmons
Physical Chemical and Nano Sciences Center, Sandia National Laboratories, P.O. Box 5800, Albuquerque, NM 87185-0601, USA
e-mail: jytsao@sandia.gov

P.-C. Hung
Technology Strategy Division, Corporate R&D Headquarters Konica Minolta, Inc., 2970 Ishikawa-machi, Hachioji-shi, Tokyo 192-8505, Japan
e-mail: po-chieh.hung@konicaminolta.com

H. Saunders
Decision Processes Incorporated, 2308 Saddleback Drive, Danville, CA 94506, USA

D.S. Sizov · R. Bhat · C.-E. Zah
Corning Incorporated, One Science Center Drive, Corning, NY 14831, USA

© Springer Nature Singapore Pte Ltd. 2017

T.-Y. Seong et al. (eds.), *III-Nitride Based Light Emitting Diodes and Applications*, Topics in Applied Physics 133, DOI 10.1007/978-981-10-3755-9_2

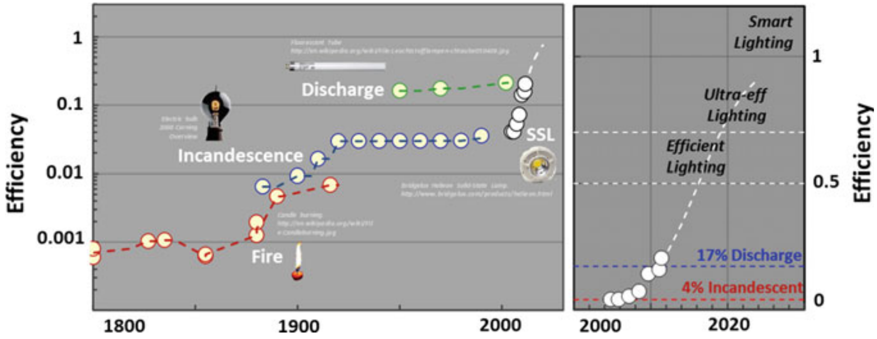

Fig. 2.1 200-year evolution of the efficiency of various lighting technologies. Adapted and updated from [2, 10, 22, 30, 31]

this chapter, we give a perspective on the future of SSL, with a focus on ultra-high efficiencies. We ask, and sketch answers to, three questions. First, what are some of the likely characteristics of ultra-efficient SSL? Second, what are some of the economic benefits of ultra-efficient SSL? And, third, what are some of the challenges associated with the various technological approaches that could be explored for ultra-efficient SSL?

2.1 Some Likely Characteristics of Ultra-efficient (>70%) SSL

We first ask the question: what are some of the likely characteristics of ultra-efficient SSL? We believe there are at least two likely characteristics, both mutually compatible and complementary.

The first likely characteristic of ultra-efficient (>70%) SSL is that, unlike in the current dominant paradigm, it not make use of the wavelength downconversion that is acceptable for (>50%) efficient SSL. Because about 80% of white light power is green or red, and because the Stokes deficit on converting from blue to green and red is about 25%, SSL in which wavelength downconversion is used to produce green and red is automatically at most $1 - 0.8 \times 0.25 = 80\%$ efficient [31], and likely even less because of other loss factors. So the first likely characteristic of ultra-efficient SSL is that it make use of efficient electroluminescence, not wavelength downconversion, across the visible spectrum. Of course, as illustrated in Fig. 2.2, this will be challenging due to the well-known green-yellow gap in the electroluminescence efficiency of compound semiconductors [4]. However, it will be necessary for ultra-efficient SSL.

The second likely characteristic of ultra-efficient SSL is that, also unlike the current dominant paradigm in SSL technology, its white light spectrum not be broadband and continuous, but rather narrowband and “spiky.” To see this, Fig. 2.2

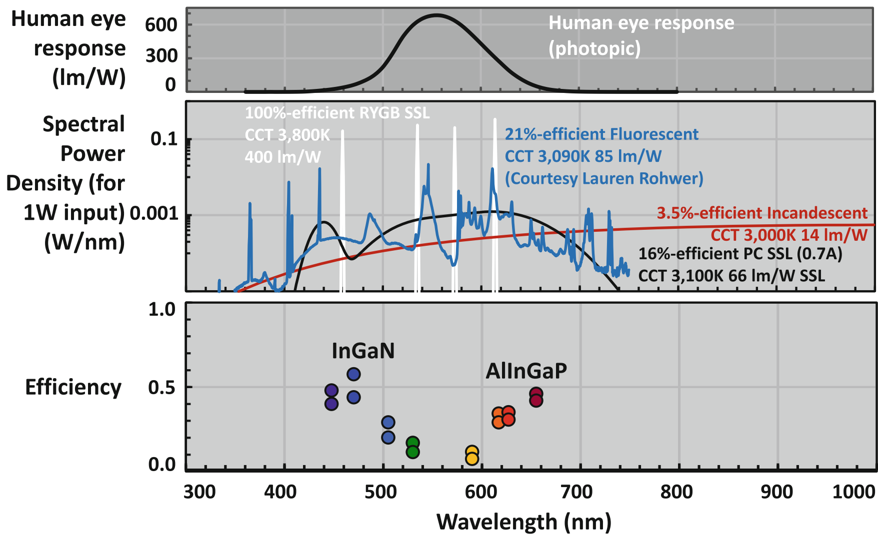

Fig. 2.2 *Top* Photopic (daytime) human eye response. *Middle* Spectral power densities of the output power of various sources for 1 W input electrical power to the source. For the fluorescent lamp, the *red* phosphor is $Y_2O_3:Eu^{3+}$, the *blue* phosphor is $BaMgAl_{10}O_{17}:Eu^{2+}$ (BAM), while the *green* phosphor is either $LaPO_4:Ce^{3+},Tb^{3+}$ or $CeMgAl_{11}O_{19}:Tb^{3+}$. *Bottom* Power conversion efficiencies of state-of-the-art commercial monochromatic light-emitting diodes (LEDs) driven at 350–750 mA/mm^2 [27]

shows the spectral power densities of the output optical power from various white light sources.

Incandescence. The least efficient source is the incandescent lamp, with the continuous spectral power density of black-body radiation shown in red, extending extremely far out into the infrared where the human eye does not see at all. All the light produced in the infrared is wasted, and the spectral efficiency of the light is very poor.

PC-LED. The second least efficient source is the phosphor-converted white LED shown in black, which has very broad green and red phosphor emission extending into the deep red which the human eye can see but not very efficiently. Just as with the incandescent lamp, though not as severely, that wasted power in the deep red means that the spectral efficiency of the white light is poor.

Discharge. Compared to the two lamps just discussed, the discharge-based fluorescent lamp is a much more efficient source. It does not have much wasted light in the deep red, with a spike in its spectral power density near the ideal shallow-red wavelength of 615 nm. But its efficiency is still limited, for the following reasons: the gas discharge is itself only 65% efficient; the Stokes loss from the UV mercury lines at 254 nm into the visible around 555 nm adds an additional 50% inefficiency; and the quantum yield of the phosphor blend is only about 85% efficient. So, despite its spiky and efficient spectral power density [34, 24], its ultimate maximum efficiency is only about 25%.

100%-efficiency. In fact, the best lamp of all would be one that produces the four spikes of light shown in white. There are just enough spikes, spaced widely enough apart, to fill the visible spectrum and render quite well the colors of objects typical in the environment around us [32]. Additionally, the spikes are concentrated within the visible spectrum, without spillover of light into wavelengths at which the human eye is insensitive, resulting in the highest spectral efficiency possible.

2.2 The Ultimate SSL Source is Spiky

One might now ask: how is it that the spiky source illustrated in white in the middle panel of Fig. 2.2 could be a good white light illuminant? First, how could such a spiky four-color spectrum really render the colors of objects in the environment around us well, and be a visually pleasing white light illumination source, even while it is missing so much spectra in between the spikes? And, second, does such a spiky four-color spectrum also maximize luminous efficacy of radiation? In this section, we discuss these two questions in turn.

2.2.1 Spiky Spectra Give Good CRI

Let us start with how it is that spiky spectra can give good color-rendering quality.

In fact, spiky sources are not only predicted to be a visually pleasing white light illuminant by color science [23], but have been shown to be so in a recent experiment [21]. In that experiment, an *extremely* spiky illumination source was created using four visible lasers: blue, green, yellow, and red. The relative powers of the lasers were tuned to maximize color rendering quality and to match color temperature and overall lumen output of a number of reference sources, including the output of an incandescent lamp. Then, two side-by-side scenes were illuminated, one with the four-color laser illuminant and the other with the various reference sources.

One of the results is illustrated in Fig. 2.3. Although the similarity of the side-by-side photos does not automatically imply similarity in human visual experience (because the image sensor in the camera is not the human eye), the human visual experiences of the two scenes were in fact quite similar. As might be expected, when any one of the four colors is removed, the scene looks visually displeasing. But, when that color is put back in, the scene looks visually quite pleasing. In fact, the four-color laser illuminant was, in double-blind tests, on average preferred over the phosphor-converted neutral-white and cool-white LED lamps, and on average neither preferred nor dispreferred over phosphor-converted warm-white LED and incandescent lamps.

Why is this? The reason is that most objects in the world have relatively broad reflectance spectra. It is a rare object, like a diffraction grating, that has a narrow

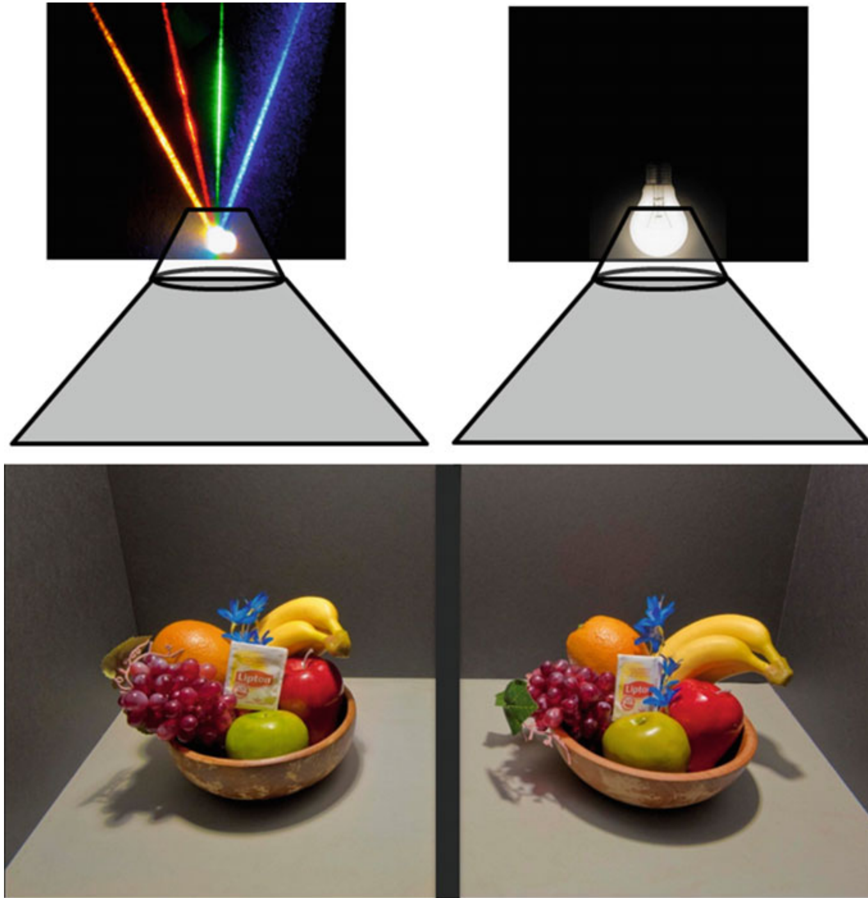

Fig. 2.3 Schematic of side-by-side test of the color rendering quality of a four-color "spiky" laser illuminant and a number of reference sources (including the incandescent lamp depicted). To give a sense for the color rendering quality of the laser illuminant, the photos of the *left* and *right* bowls of fruit were illuminated, respectively, by the four-color laser illuminant and by an incandescent lamp. Although the image sensor in the camera is not the human eye, so the similarity of the photos does not automatically imply similarity in human visual experience, in fact the human visual experience was quite similar

reflectance spectrum that would enable the human eye to distinguish between spiky and nonspiky illuminants.[1]

So the striking conclusion of theory and experiment is that spiky sources do indeed give excellent color rendering quality.

[1]Rare, but not nonexistent. Any iridescent object which supports optical interference phenomena (e.g., opals, soap bubbles, some butterfly wings) would distinguish between spiky and nonspiky illuminants.

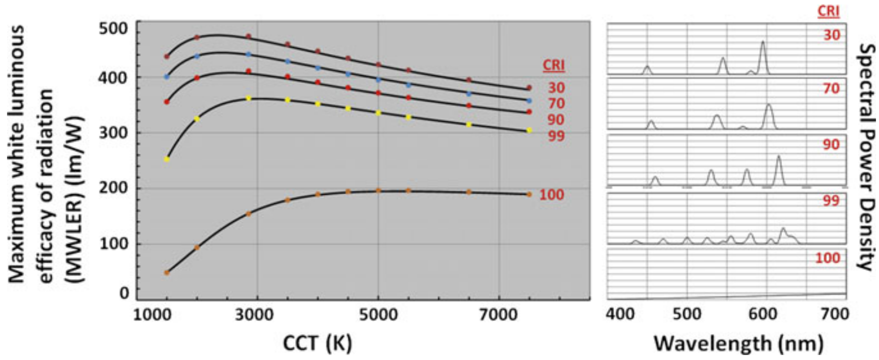

Fig. 2.4 *Left* Maximum white luminous efficacy of radiation versus correlated color temperature (CCT) for various standard color rendering indices (CRIs). *Right* Relative spectral power densities for various CRIs for a CCT of 2856 K. After [13]

2.2.2 Spiky Spectra Give the Highest MWLERs

Let us now consider whether spiky spectra also give good luminous efficacies of radiation.

To answer this question, the right side of Fig. 2.4 shows recent simulations of spectral power densities, unconstrained by whether the spectra are continuos or spiky, which maximize white luminous efficacy of radiation (MWLER) given particular values of standard color rendering index[2] (CRI) and correlated color temperature (CCT) [13]. In fact, the spectral power densities that maximize the white luminous efficacies of radiation are, except for the very highest CRI (of 100), all spiky. Of course, for a very high CRI, as in the panel with CRI of 99, there may be more spikes, but nevertheless the spectral power densities are all spiky. We can conclude that spikiness is in fact a general feature of spectral power densities that maximize luminous efficacy or radiation.

Now, *given* a spiky spectral power density, the maximum white luminous efficacy of radiation does of course depend on CCT and CRI. One can see from the family of curves illustrated in the left half of Fig. 2.4, that, for all CRI values, the MWLER peaks at a particular CCT and drops off at higher or lower color temperatures on either side. The physical reason for this is that, starting from a very high CCT, as CCT decreases, spectra shifts first from the blue to the green and then from the green to the red. Because luminous efficacy of radiation is highest in the green, the MWLER first increases and then decreases.

One can also see from the family of curves illustrated in the left half of Fig. 2.4 that, as CRI increases, all luminous efficacies of radiation decrease. The physical reason for this is that the higher the CRI becomes, the more “spread out” the white

[2]In our treatment here, we mean the standard color rendering index R_a [3].

light spectrum (even if it is spiky) becomes. The more spread out the white light spectrum becomes, the further the spectrum penetrates into the wings of the human eye response (hence further from the peak of the human eye response at 555 nm), and the lower the luminous efficacy of radiation.[3]

We can conclude that spiky spectra are preferred over nonspiky (continuous) spectra: they not only give good color rendering quality, but also maximize white luminous efficacy of radiation.

2.3 Economic Benefits of Ultra-Efficient SSL

Up to this point, we have discussed the characteristics of ultra-efficient SSL: it must not make use of wavelength downconversion, and its spectrum should be spiky. But what are the economic consequences of ultra-efficient SSL? The benefits (i.e., profits) of efficient lighting to the SSL industry will have already manifested themselves by the time SSL has achieved 50% efficiency. At that point, SSL will have beaten both incandescent and gas discharge lamps and will have begun to replace them. Are there additional economy-wide benefits (beyond profit to the SSL industry) that would make it worthwhile to pursue ultra-high efficiencies of 70% and beyond?

To understand the possible answers to this question, in Fig. 2.5 we sketch two possible scenarios for the energy economics of light. Using world gross domestic product (GDP) and world consumption of light and energy in 2011 as a baseline, we ask what the consequences of changes in the efficiency of lighting would be, *all other factors in the economy held constant*. We assume throughout that the impacts of a change in efficiency are twofold: first, less energy is consumed for a given amount of light consumed; and second, the effective cost of light (typically dominated by the energy used to produce the light) decreases.

2.3.1 Scenario 1: Light Is not *a Factor of Production*

The first scenario is sketched in the left panels of Fig. 2.5. This is a scenario in which light is *not* a factor of production in the global economy. Thus, if the efficiency with which light is produced were to increase, world GDP would not change, but would stay constant at its value in 2011 (about 60.5 trillion US dollars). This is also a scenario in which, if light were to become more efficient and hence

---

[3]Note that the higher the CRI, the higher the CCT at which the MWLER maximizes, as discussed in Hung [13].

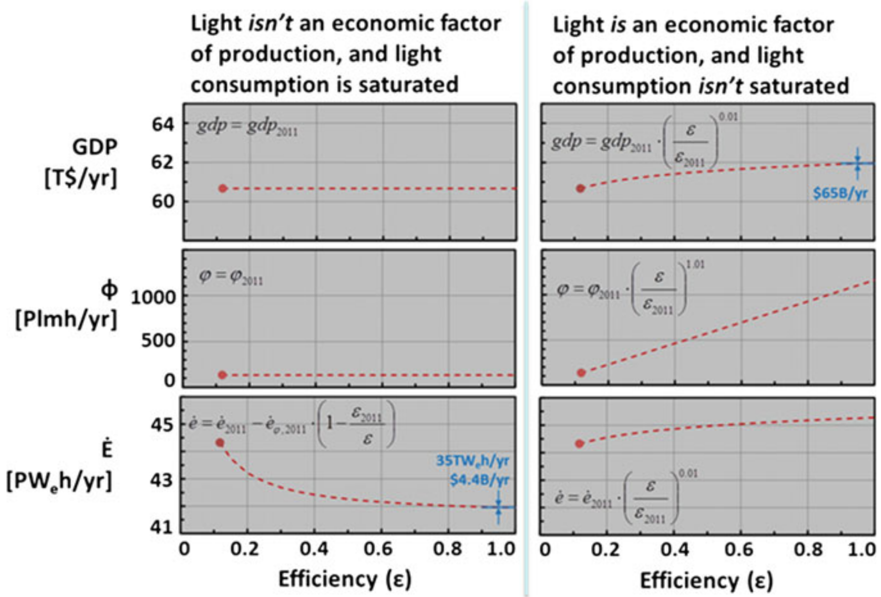

Fig. 2.5 Economic scenarios for world gross domestic product (GDP), world consumption of light (Φ), and world consumption of energy (Ė). The scenario on the *right* is one in which light *is* considered to be a factor of production in the economy; the scenario on the *left* is one in which light is *not* considered to be a factor of production in the economy

cheaper, we would have no tendency to consume more (i.e., consumption of light is saturated).

Hence, in this scenario, the main benefit to increased efficiency is that the consumption of energy associated with the production of light decreases. Since the consumption of energy associated with the production of light is about 1/15 of all consumption of energy, as efficiency of lighting increases, consumption of energy could in principle decrease by nearly 1/15—from about 44.5 PWh/yr to about 42 PWh/yr.

But one can also see that the biggest decreases in energy consumption occur when efficiency is low. As efficiency increases there is a diminishing return or diminishing benefit to continuing to increase efficiency. For example, when efficiency has reached 0.9, increasing efficiency further from 0.9 to 1.0 only decreases energy consumption by 35 TWh/yr, which represents only about $4.3B/yr.[4] This is not a small benefit, but it is *relatively* small, and it is not obvious that an efficiency of 1.0 would be worth the required R&D effort.

[4]Assuming a light-usage-weighted average world electricity price of $120/MWh [33].

2.3.2 Scenario 2: Light is a Factor of Production

The second scenario is sketched in the right panels of Fig. 2.5. This is a scenario in which light *is* a factor of production in the global economy. So, if the efficiency with which light is produced were to increase, the cost of light would decrease, more light would be consumed, and world GDP *would* increase (above where it otherwise would be, again all other things in the world of 2011 held constant). This scenario has been analyzed in some detail using a simple Cobb-Douglas model which treats light as a factor of production in the global economy [34].

The result of that analysis is that there is no direct energy (or environmental) benefit to increased efficiency. Since the consumption of light increases as efficiency increases, energy consumption does not decrease. Indeed, because GDP increases as light consumption increases, there is even a slight increase in energy consumption. So, in this scenario, the main benefit to increased efficiency is an increase in global GDP. In fact, this benefit is huge. Although there is a diminishing return to the increase in GDP, if efficiency were even as high as 0.9, and were increased to 1.0, global GDP would increase by $65B/yr. This economic benefit is huge, nearly 15x larger than in the first scenario, despite the diminishing returns.

Moreover, although in this scenario there is no direct energy (and environmental) benefit to increased efficiency, some of the huge increase in GDP could presumably be harnessed to improve technologies *with* direct energy (and environmental) benefit, including those for renewable energy or for adaptation to the deleterious environmental effects of carbon-emitting energy technologies.

Thus, if this is indeed the scenario that best describes reality, there is a large direct economic benefit and hence large potential indirect energy and environmental benefits to continuing to improve efficiency.

2.3.3 A Qualified Nod to Scenario 2: More Light = More Productivity

Which of the above two scenarios best describes reality? We cannot know for sure, but if the past is any indication, then it is the second scenario.

The reason is illustrated in the plot on the left of Fig. 2.6. The vertical axis of this plot is consumption of light, in Plmh/year. The horizontal axis of the plot is a fixed constant, β, times the ratio between gross domestic product (GDP) and cost of light (CoL). If we use as our units for GDP billions of dollars per year, and for cost of light $/Mlmh, we see that this ratio has the same units, Plmh/year, as the units of the vertical axis. And if we choose the fixed constant, β, to be 0.0072, we see that the empirical data fall very closely along a line of slope unity and zero offset [33].

The ability of this simple formula to predict consumption of light across several centuries and a wide range of countries and groups of countries has two implications. The first implication is that, as GDP has increased, consumption of light has

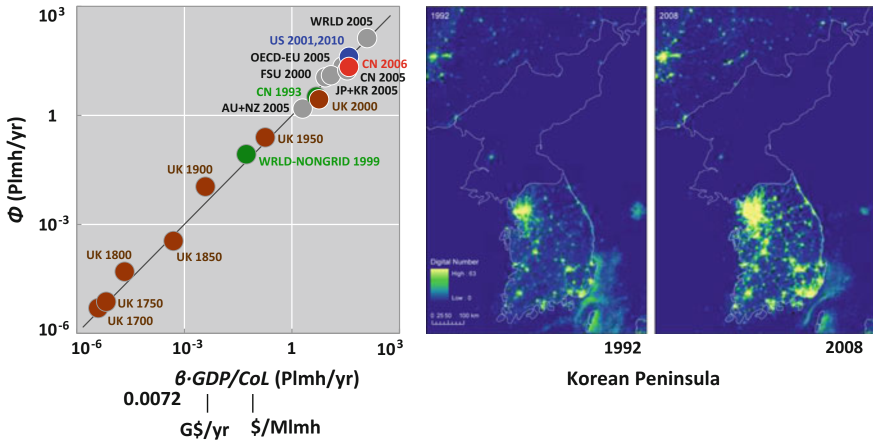

Fig. 2.6 *Left* Consumption of light versus ratio between gross domestic product (GDP) and cost of light (CoL) for various countries at various times in history, after [32]. *Right* Satellite images of the Korean peninsula taken in 1992 and 2008, showing the dramatic increase in consumption of light, correlated with the increase in national GDP during that same time period. After [12]

increased. That is, the wealthier we are, the more light we consume.[5] One can see this graphically for the case of South Korea, where the consumption of light, as seen from outer space, has increased markedly from 1992 to 2008. The second implication is that, as cost of light has decreased, consumption of light has increased as well. That is, the cheaper light is, the more we have consumed.

In fact, these results are exactly what one would predict from the second scenario, the one in which light *is* a factor of production in the economy, so that the more efficiently light is produced, the more we consume and the more productive we are. Now, we do not know whether the future will be like the past, but if it is, then this analysis shows that it *is* worth the effort to continue to improve SSL efficiency, even to ultra-high efficiencies and beyond.

2.4 Two Competing Approaches: Low- and High-Power Densities

We have just discussed the potential economic benefit of achieving the highest possible efficiencies. In fact, there are two approaches, discussed below, that could be pursued to achieve this: one in which the emitters are run at low-power densities and the emission is spontaneous; and one in which the emitters are run at

[5]Indeed, this correlation between GDP and light consumption is being explored as a means to "measure" GDP. See, e.g., Henderson [2].

high-power densities and the emission is stimulated. Both have potential, but both also face challenges.

To illustrate these challenges, let us focus on just the blue light emitter. Eventually, as discussed above, it will be important to find green, yellow, and shallow-red light emitters for ultra-efficient SSL. For our purpose here, however, let us assume the paradigm of white light based on blue light emitters and wavelength downconversion. Then, in Fig. 2.7, we show the implications of input power density into the blue light emitter on the efficiency and cost constraints of the blue light emitter, and also on the resulting heat-sink-limited area and white light flux producible from that area.

The key panel in Fig. 2.7 is the bottom one: the power conversion efficiency of the InGaN-based blue light emitter versus the input power density into the emitter. On the one hand, spontaneous-emission-based blue LEDs (red line) cannot be driven at an input power density more than a few W/cm^2 before efficiency decreases —the so-called "efficiency droop" problem [4, 15, 29]. On the other hand, stimulated emission-based blue lasers (blue line), because of the finite lasing thresholds, must be driven at an input power density more than about a few thousand W/cm^2 before they "turn on" and begin to achieve appreciable efficiency. There is a "valley of death" in input power density within which InGaN-based blue light emitters are not very efficient and, thus, there is currently a tremendous amount of research aimed at circumventing this valley of death by improving the efficiency droop. If it cannot be circumvented, the valley of death motivates two very different approaches [30] to ultra-efficient SSL.

2.4.1 Low-Power-Density Approach (LEDs)

The first approach is to drive a blue LED at a low input power density, near peak efficiency. The red curve in Fig. 2.7d shows efficiency calculated using "ABC" coefficients [5] based on a state-of-the-art Philips Lumileds LED [27]. Peak efficiency is at a power density of roughly 5 W/cm^2 or at about a 15–20 mA drive current into a 1 mm^2 chip [36].

The problem with this approach is that, if the chip is not driven very hard, not much light is output from the chip per unit area. Large integrated chip areas would be required to produce an appreciable light output, so the chip cost per unit area must be low. To see how low, consider the two costs associated with light [31].

First there is the capital cost of light, which can be written as

$$CoL_{cap} = \frac{\alpha \cdot c_{chip} \cdot A_{chip}}{MWLER \cdot \varepsilon_B \cdot \varepsilon_{PP} \cdot P_{in} \cdot L}, \tag{2.1}$$

where α is the ratio between retail lamp price to the consumer and chip cost, c_{chip} is the areal cost of the chip (in \$/cm^2), A_{chip} is the area of the chip (in cm^2), $MWLER$ is

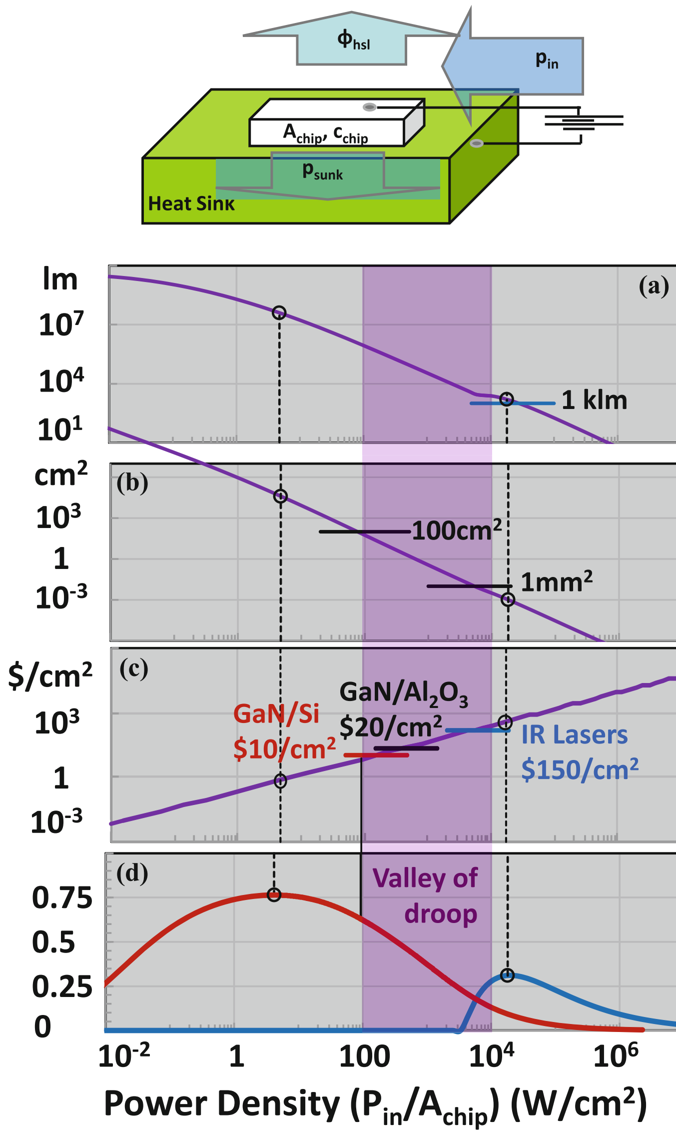

Fig. 2.7 Economics of low-power-density and high-power-density approaches to SSL

the maximum white luminous efficacy of radiation (in lm/W), ε_B and ε_{PP} are the blue emitter and phosphor + package efficiencies, respectively, P_{in} is the electrical power input into the chip (in W), and L is the lifetime of the lamp (in Mh).

Second, there is the operating cost of light, which can be written as

$$CoL_{ope} = \frac{CoE}{MWLER \cdot \varepsilon_B \cdot \varepsilon_{PP}}, \tag{2.2}$$

where CoE is the cost of electricity (in \$/MWh).

For traditional (nonSSL) lighting, the capital cost of light is small relative to (and about 1/6 of) the operating cost of light, and one can anticipate a similarly low ratio between the two costs for SSL in its steady-state future. If so, we would have $CoL_{cap} = CoL_{ope}/6$, and could then deduce that the areal cost of the chip must be roughly

$$c_{chip} = \frac{L \cdot CoE}{6 \cdot \alpha} \cdot \left(P_{in}/A_{chip}\right). \tag{2.3}$$

In other words, the higher the power density (P_{in}/A_{chip}) input into the chip, the higher the areal chip cost can be while still satisfying a low capital-to-operating cost ratio of 1/6. Note that the absolute efficiencies of the blue emitter or of the phosphor + package do not enter in, as these affect both the capital and operating costs in the same manner and cancel out.

If we now assume an input power density-dependent lifetime that decreases smoothly[6] from 0.03 Mh (at a typical LED input power density of 225 W/cm^2) to 0.01 Mh (at a typical laser input power density of 240 kW/cm^2), a retail cost of electricity of roughly 120 \$/MWh, and a retail-lamp-to-chip cost ratio[7] of roughly $\alpha \sim 10$, then we get the diagonal purple line plotted in Fig. 2.7c. If one would like to drive the chip at 5 W/cm^2 power density, where efficiency is maximum for current state-of-the-art blue LEDs, one finds that chip cost per unit area must be lower than \$1/cm^2.[8]

There is thus a strong motivation for developing extremely inexpensive chip technologies, like GaN/Si or GaN nanowires. However, future scenarios [37] for GaN/Si chip technologies predict roughly 2x reductions from GaN/sapphire, not the

[6]We use a simple logarithmic dependence of lifetime on input power density: $\log(L/0.03\text{Mh}) = 0.235 \cdot \log[(P_{in}/A_{chip})/(225\ \text{W/cm}^2)]$, where L is lifetime in Mh and P_{in}/A_{chip} is input power density in W/cm^2.

[7]This multiplier between the cost of a retail lamp to the cost of the chip within the lamp includes various sub-multipliers that connect the chip to the package, the package to the wholesale lamp, and finally the wholesale lamp to the retail lamp [7, 8]. Note that this multiplier is surprisingly similar to those for higher power-density chips such as high-power IR lasers [16, 18] inserted into retail laser modules and for low-power-density chips such as solar cells inserted into residential retail panels [1, 6, 17]. Hence, we use the same multiplier across the range of input power densities considered here.

[8]To put this in perspective, current chip cost per unit area for state-of-the-art GaN/sapphire chips is much higher (about 20 \$/cm^2), while for single-crystal Si solar cells is much lower (about \$0.02/cm^2).

20x reductions that appear to be necessary. Thus, areal chip cost will be a key but difficult challenge for the low-power-density approach to ultra-efficient SSL.

A related challenge is to increase the power density at which ultra-high-efficiencies may be obtained, so that more expensive chips can be used.

2.4.2 High-Power-Density Approach

The second approach is to drive a blue laser at a high input power density where, due to stimulated emission, efficiency can again be higher. The blue curve in Fig. 2.7d shows a threshold-and-slope-efficiency calculation of efficiency based on a state-of-the-art Osram blue laser, showing that efficiency peaks at a power density of roughly 20 kW/cm^2, or at about a 70 A drive current into a 1 mm^2 chip [36].

In this approach, because the chip is being driven very hard, with a lot of light out per unit area, the chip cost per unit area can be high. In fact, if we apply the same economic constraints we applied before, that the cost to buy the lamp should be about 1/6 the lifetime cost to run the lamp, we find that, at the power density at peak efficiency for this blue laser, chip cost per unit area must be less than \$400/cm^2. In fact, high-efficiency [25] high-power IR laser chips, at \$150/cm^2 [16], are already much cheaper than this, with the possibility that they could become much cheaper still [16]. This provides an existence proof that such costs might someday also be achievable with laser chips in the visible.

What is less obvious is whether one can get a reasonable amount of light out of a high input power density light emitter. A limit to the amount of light will be imposed by heat sinking. To determine roughly what that limit might be, we use the usual scaling relationship [9, 19, 30] for the thermal resistance of a conduction-cooled (and hence relatively inexpensive) chip:

$$R_T = \frac{1}{2\kappa_T \cdot \sqrt{4A_{chip}/\pi}}, \tag{2.4}$$

where κ_T is the thermal conductivity of the heat sink, and A_{chip} is the area of the chip.[9] If the power sunk by the heat sink is $P_{sunk} = P_{in} - P_{out} = P_{in} \cdot (1\text{-}\varepsilon_B \varepsilon_{PP})$, then the thermal resistance that enables the temperature increase of the chip due to this sunk power to be less than a maximum allowable ΔT_{max} is:

$$R_T = \frac{\Delta T_{\max}}{P_{in} \cdot (1 - \varepsilon_B \varepsilon_{PP})}. \tag{2.5}$$

[9]Note that this is an underestimate of the thermal resistance for a laser chip, as such chips may be nonsquare with a large aspect ratio.

Equating the two expressions for the thermal resistance allows us to solve for the "heat-sink-limited" maximal area[10] of the chip for a given input power density:

$$A_{hsl} = \left[\frac{2\kappa_T \cdot \sqrt{4/\pi} \cdot \Delta T_{\max}}{(1 - \varepsilon_B \varepsilon_{PP}) \cdot \left(P_{in}/A_{chip}\right)} \right]^2 . \tag{2.6}$$

The "heat-sink-limited" maximal light output of the chip, also for a given input power density, is proportional to this heat-sink-limited maximal area, and can thus be written as:

$$\Phi_{hsl} = MWLER \cdot \varepsilon_B \varepsilon_{PP} \cdot \left(\frac{P_{in}}{A_{chip}} \right) \cdot A_{hsl} = \frac{MWLER \cdot \varepsilon_B \varepsilon_{PP}}{\left(P_{in}/A_{chip}\right)} \left[\frac{2\kappa_T \cdot \sqrt{4/\pi} \cdot \Delta T_{\max}}{(1 - \varepsilon_B \varepsilon_{PP})} \right]^2 . \tag{2.7}$$

Both of these heat-sink-limited quantities, chip area, and chip white light output are plotted in Fig. 2.7a, b for a *MWLER* of 400 lm/W, blue light emitter efficiencies given by those in Fig. 2.7d, a phosphor + package efficiency of $\varepsilon_{PP} \sim 0.7$, a maximum allowable temperature rise of $T_{max} \sim 100$ K, and a thermal conductivity of $\kappa_T \sim 2$ W cm^{-1} K^{-1} (between those of copper and silicon).[11]

One can see that, at the input power density of 20 kW/cm^2, at which the efficiency of a state-of-the-art blue laser maximizes, the chip must be less than a tenth of a mm^2 in area, but the heat-sink-limited light flux out of such a chip would still be over 1,000 lm (the rough equivalent of the light flux from a 75 W incandescent lamp). In other words, single high-power-density and heat-sink-limited chips should have no difficulty generating useful amounts of light.

Instead, for this approach, the main issue will be getting to ultra-high efficiencies. Although peak efficiencies for a laser are not limited by either the *A* or *C* coefficients in the *ABC* model for efficiency, they are limited by other losses such as injection efficiency, optical absorption, and series resistance. So an important challenge will be to understand the origin of those losses and to design ways of reducing them.

[10] In other words, for a given input power density, efficiency and heat-sink properties, there is a maximum chip size that enables the temperature rise of the chip to remain manageable. This maximum chip size depends strongly on (inversely as the square of) input power density because the chip size that gives a particular thermal resistance depends strongly on (inversely as the square of) that thermal resistance.

[11] Note that this thermal conductivity implies, through Eq. (4), a thermal resistance of 2.5 K/W for 1 mm^2 chip size, in the range of (but slightly lower) than that, 5.5 K/W, for a Philips Lumileds Luxeon K2 package [26].

2.5 Summary

First, solid-state lighting is the latest in a series of technologies of ever-increasing efficiencies for producing white light.

Second, getting to the highest possible efficiencies will ultimately require both efficient electroluminescence across the visible as well as spiky spectra. Indeed, the ultimate spiky source, a 4-color laser illuminant, has been shown to provide very good color rendering quality and to maximize white luminous efficacy of radiation, and hence can be thought of as the "gold standard" for white lighting.

Third, getting to the highest possible efficiencies has potentially huge economic benefit, and is likely worth pursuing.

Fourth, and finally, the two different routes for ultra-efficient SSL that could be pursued, low- and high-power density chips, are both promising but face different challenges. The challenge for the low-power-density approach is not so much to improve efficiency, as this is already very high, but to reduce cost while maintaining such high efficiency (or to increase the power density at which such high efficiency can be obtained). The challenge for the high-power-density approach is not so much to reduce cost (as there is an existence proof that this can be low enough), but to increase efficiency.

Acknowledgements We thank Emma Johnson, Justin Sanchez, Emily Stirrup, and Jack Wampler for careful reviews of this chapter and of other manuscripts on which this chapter is based, and thank Edward Stephens for helpful consultations. Work at Sandia National Laboratories was supported by Sandia's Solid-State Lighting Science Energy Frontier Research Center, funded by the U.S. Department of Energy, Office of Basic Energy Sciences. Sandia National Laboratories is a multi-program laboratory managed and operated by Sandia Corporation, a wholly owned subsidiary of Lockheed Martin Corporation, for the U.S. Department of Energy's National Nuclear Security Administration under contract DE-AC04-94AL85000.

References

1. G. Barbose, N. Darghouth, R. Wiser, Tracking the Sun III: the Installed cost of Photovoltaics in the USA from 1998–2009, Lawrence Berkeley National Laboratory Report (2010)
2. A. Bergh, M.G. Craford, A. Duggal, R. Haitz, The promise and challenge of solid-state lighting. Phys. Today **54**, 42–47 (2001)
3. Commission Internationale de l'Eclairage, Method of Measuring and Specifying Colour Rendering Properties of Light Sources, Technical Report 13.3-1995 (1995)
4. M.H. Crawford, LEDs for solid-state lighting: performance challenges and recent advances. IEEE J. Sel. Top. Quantum Electron **15**, 1028–1040 (2009)
5. A. David, M.J. Grundmann, Droop in InGaN light-emitting diodes: a differential carrier lifetime analysis. Appl. Phys. Lett. **96**, 103504 (2010)
6. U.S. Department of Energy Office of Energy Efficiency and Renewable Energy, 2008 Solar Technologies Market Report (January, 2010)
7. U.S. Department of Energy Office of Energy Efficiency and Renewable Energy, Solid-State Lighting Research and Development Manufacturing Roadmap (July, 2011)

8. U.S. Department of Energy Office of Energy Efficiency and Renewable Energy, Solid-State Lighting Research and Development Multi-Year Program Plan (April, 2012)
9. M. Grabherr, M. Miller, R. Jager, R. Michalzik, U. Martin, H.J. Unold, K.J. Ebeling, High-power vcsel's: single devices and densely packed 2-D-arrays, ieee. J. Sel. Top. Quantum Electron. **5**, 495–502 (1999)
10. R. Haitz, J.Y. Tsao, Solid-state lighting: 'The case' 10 years after and future prospects. Phys. Status Solidi A **208**, 17–29 (2011)
11. R. Haitz, J.Y. Tsao, Solid-state lighting: why it will succeed, and why it won't be overtaken. Optik Photonik **6**, 26–30 (2011)
12. J.V. Henderson, A. Storeygard, D.N. Weil, Measuring economic growth from outer space. Am. Econ. Rev. **102**, 994–1028 (2012)
13. P.C. Hung, J.Y. Tsao, Maximum white luminous efficacy of radiation versus color temperature and color rendering index: exact results and a useful semi-empirical expression. Manuscript in preparation (2013)
14. J.K. Kim, E.F. Schubert, Solid-state light sources getting smart. Science **308**, 1274–1278 (2005)
15. M.R. Krames, O.B. Shchekin, R. Mueller-Mach, G.O. Mueller, L. Zhou, G. Harbers, M.G. Craford, Status and future of high-power light-emitting diodes for solid-state lighting. J. Disp. Technol. **3**, 160 (2007)
16. A.L. Ladran, E.R. Ault, R.J. Beach, J.H. Campbell, A.C. Erlandson, A.J. Felker, B.L. Freitas, W.R. Meier, S. Telford, C.A. Ebbers, J.A. Caird, C.P.J. Barty, Inertial Fusion Energy's Role in Developing the Market for High Power Laser Diodes, Lawrence Livermore National Laboratory Report UCRL-CONF-237006 (5 Dec 2007)
17. J. Lushetsky, The Prospect for $1/Watt Electricity from Solar, DOE presentation at the $1/W Workshop (August 10, 2010)
18. R. Martinsen, Industrial markets beckon for high-power diode lasers. Opt. Laser Europe Mag. 26–27, (2007)
19. W. Nakwaski, M. Osinski, Thermal resistance of top-surface emitting vertical-cavity semiconductor lasers and monolithic two-dimensional arrays. Electron. Lett. **28**, 572–574 (1992)
20. Y. Narukawa, M. Ichikawa, D. Sanga, M. Sano, T. Mukai, White light emitting diodes with super-high luminous efficacy. J. Phys. **D43**, 354002 (2010)
21. A. Neumann, J.J. Wierer, Jr., W. Davis, Y. Ohno, S.R.J. Brueck, J.Y. Tsao, Four-color laser white illuminant demonstrating high color rendering quality. Opt. Express **19**, A982–990 (2011)
22. W.D. Nordhaus, in *Do Real-Output and Real-Wage Measures Capture Reality*? *The History of Lighting Suggests Not*, ed by T.F. Breshnahan, R.J. Gordon, The Economics of New Goods, (The University of Chicago Press, Chicago, 1997), pp. 29–70
23. Y. Ohno, Spectral design considerations for color rendering of white LED light sources. Opt. Eng. **44**, 111302 (2005)
24. J.J. Opstelten, D. Radielovic, J.M.P.J. Verstegen, Optimum spectra for light sources. Philips Tech. Rev. **35**, 361–370 (1975)
25. M. Peters, V. Rossin, M. Everett, E. Zucker, in *High Power*, *High Efficiency Laser Diodes at JDSU*, *High-Power Diode Laser Technology and Applications V*, ed. by Zediker. Proceedings of SPIE 6456, 64560G (2007)
26. Philips Lumileds, Luxeon K2 with TFFC Technical Datasheet DS60 (April, 2009)
27. Philips Lumileds, Luxeon Rebel and Luxeon Rebel ES Color Portfolio Datasheet DS68 (December, 2011)
28. J.M. Phillips, M.E. Coltrin, M.H. Crawford, A.J. Fischer, M.R. Krames, R. Mueller-Mach, G. O. Mueller, Y. Ohno, L.E.S. Rohwer, J.A. Simmons, J.Y. Tsao, Research challenges to ultra-efficient inorganic solid-state lighting. Laser Photonics Rev. 1 307–333 (2007)
29. J. Piprek, Efficiency droop in nitride-based light-emitting diodes. Phys. Status Solidi A **207**, 2217–2225 (2010)

30. J.Y. Tsao, Solid-state lighting: lamps, chips, and materials for tomorrow. IEEE Circuits Devices **20**, 28–37 (2004)
31. J.Y. Tsao, M.E. Coltrin, M.H. Crawford, J.A. Simmons, Solid-state lighting: an integrated human factors, technology and economic perspective. Proc. IEEE **98**(7), 1162–1179 (2010)
32. J.Y. Tsao, P. Waide, The world's appetite for light: a simple empirical expression spanning three centuries and six continents. LEUKOS **6**, 259–281 (2010)
33. J.Y. Tsao, H.D. Saunders, J.R. Creighton, M.E. Coltrin, J.A. Simmons, Solid-state lighting: an energy economics perspective. J. Phys. D **43**, 354001 (2010)
34. J.M.P.J. Verstegen, D. Radielovic, L.E. Vrenken, A new generation of deluxe fluorescent lamps, combining an efficacy of 80 lumens/W or more with a color rendering index of approximately 85. J. Electrochem. Soc. **121**, 1627–1631 (1974)
35. C. Vierheilig, C. Eichler, S. Tautz, A. Lell, J. Muller, F. Kopp, B. Stojetz, T. Hager, G. Bruderl, A. Avramescu, T. Lermer, J. Ristic, U. Strauss, Beyond blue pico laser: development of high power blue and low power direct green. Proc. SPIE **8277**, 82770K (2012)
36. J.J. Wierer et al., Blue Lasers for Solid-State Lighting: Potential and Challenges. Manuscript in preparation (2013)
37. Silicon substrates contend for LED opportunity, iLED Issue No. 3, 16–19 (2012)

Chapter 3
LEDs Based on Heteroepitaxial GaN on Si Substrates

Takashi Egawa and Osamu Oda

Recently, LEDs based on heteroepitaxial GaN on Si substrates (GaN/Si) are attracting a great attention and are industrially developed by many companies in order to compete with LEDs based on GaN/sappire and GaN/SiC which are commercially marketed advancing GaN/Si LEDs, though GaN/Si LEDs have been realized early in 2002. The recent attention on GaN/Si is due to the availability of low cost and large wafer size availability (up to 300 mm diameter) of Si substrates. In this article, we review the development of the GaN epitaxial growth on Si and summarize the development made in our laboratory including the device structures achieving the GaN/Si LEDs with higher emission efficiency. We describe on GaN/Si using (i) high-temperature (HT) AlN/AlGaN intermediate layers, (ii) HT intermediate layers (ILs) and multilayers (MLs), and (iii) strained-layer superlattices (SLS) interlayers and their LED performances, respectively. We believe that GaN/Si LEDs with low prices will become important LEDs for general lighting in the near future.

3.1 Introduction

Since there were no low-cost and high-quality bulk substrates available for the epitaxial growth of group-III nitride materials, InGaN-based light emitting diodes (LEDs) have been fabricated on expensive sapphire [1–13] or SiC substrates [14–21]

T. Egawa (✉) · O. Oda
Research Center for Nano-Device and System, Nagoya Institute of Technology, Gokiso-cho, Showa-ku, Nagoya 466-8555, Japan
e-mail: egawa.takashi@nitech.ac.jp

© Springer Nature Singapore Pte Ltd. 2017

T.-Y. Seong et al. (eds.), *III-Nitride Based Light Emitting Diodes and Applications*, Topics in Applied Physics 133, DOI 10.1007/978-981-10-3755-9_3

and these LEDs are commercially fabricated worldwide, not only for blue LEDs but also for white LEDs, which are very promising for the reduction of energy consumption replacing incandescent and fluorescent bulbs. This replacement is expected to contribute to the reduction of CO_2 emission with the level of several percent [22]. In order to achieve the replacement of general lighting, we still need the improvement of LEDs from the view point of cost-effectiveness and high output power.

The present widely produced InGaN-based LEDs on sapphire substrates have disadvantages that the output power is limited because of its low thermal conductivity of sapphire substrates and the cost is high because both electrodes has to be deposited only on one side of the LED chip since sapphire is insulating. The tip area is almost doubled compared with the case when the electrode can be made on the back side of the chip. On the other hand, SiC have advantages such as its high thermal and electrical conductivity that make the above mentioned disadvantage solved using SiC substrates. SiC, however, is costly because commercial substrates are produced by the physical vapor transport method [23]. SiC substrates from 2 in. up to 150 mm diameter have been developed [24–29] and now even 150 mm diameter substrates are commercially available [30]. The future perspective of larger diameter substrates up to 300 mm is, however, not yet well forseen. SiC has therefore a disadvantage from the viewpoint of the substrate cost, though it is improved year by year.

Compared with these disadvantages of sapphire and SiC substrates, GaN/Si is recently taking attention from the viewpoint of its high thermal and electrical conductivity and low substrate cost, for reducing the LED fabrication cost, especially for applying LEDs for general lighting which actually has a huge market counting several hundred M$ [22]. The advantage of GaN/Si-based LEDs is its low material cost since Si substrates are obtainable even to the 300 mm diameter with a reasonable price. Moreover, the fabrication process of LEDs on Si substrates becomes easier than that of LEDs on sapphire because one of the Ohmic contacts can be made from the backside through a conductive Si substrates. The other advantage of GaN/Si LEDs is the possibility of the integration with other devices on Si substrate. It is also pointed out that at high output power, GaN/Si is more advantageous than GaN on sapphire since Si is thermally conductive and higher current can be flowed to obtain higher output power. Nevertheless, GaN/Si-based LEDs have less developed compared with LEDs based on sapphire and SiC substrates because of the following obstacles.

In order to realize high-quality GaN/Si LEDs, we need to overcome the problems caused by large mismatch in lattice constants (16.9%) and difference in thermal expansion coefficients (57%) as shown in Fig. 3.1. These factors attribute to large wafer bending, epitaxial layers with high threading dislocation density ($\sim 10^{10}$ cm^{-2}), deep pits, and cracks to relax the large tensile stress induced by the substrate [31]. The heteroepitaixal growth of GaAs on Si has been already

extensively studied [32–35] and the heteroepitaxial growth of GaN on Si has been developed based on these precedent GaAs epitaxial growth works. The problem as mentioned above has been solved by applying various intermediate layers (they are also called buffer layers). Since it is known that GaN grown on Si has very low device performances compared with GaN on sapphire, it is important to improve the crystal quality. The growth of GaN on Si has been performed initially by molecular beam epitaxy (MBE) [36–40] and later by metal-organic chemical vapor deposition (MOCVD). The various works have been performed using intermediate layers (ILs) or buffer layers (BLs) such as 3C-SiC [41], AlN [2, 38, 42–72], GaN [73, 74], AlN/AlGaN [57, 75–90], AlAs [91], oxidized AlAs [92–94], Al_2O_3 [95], Si_xN_y [59, 60, 96, 97], ZrB_2 [98–103], and silicon delta-doping [104]. AlGaN [105] is also inserted between ILs and GaN grown on that in order to relax the stress formation due to the lattice mismatching. The insertion of AlN/GaN super-lattice structures (SLSs) [106–109] and AlGaN/GaN SLSs [110–112] were effective to improve the luminosity. The effect of Si_xN_y interlayers has also been studied [113, 114]. The reduction of dislocation densities and the prevention of cracking have been performed by various technologies such as epitaxial lateral over growth (ELO) [115–121], patterned Si [122–131], selective area growth (SAG) [58, 61, 132–154], nanohetero epitaxy (NHE) technologies [155–162], and growth on compliant substrates [55, 163–166]. Using some of these technologies, GaN/Si epitaxial layers up to 100 mm [86] and 150 mm [167, 168] have been achieved. In fact, based on the above technologies, the strain in the GaN/Si was relieved as discussed in various references [169–172].

The other obstacle of GaN/Si is in that the half of emitted light from InGaN-based multi-quantum wells (MQWs) is absorbed by Si substrates [173, 174] which has small band gap of 1.12 eV. In order to solve this light absorption, distributed Bragg reflector (DBR) structures [174, 175], wafer bonding [176],

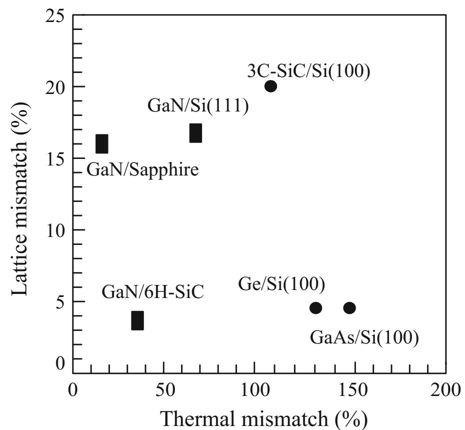

Fig. 3.1 Thermal and lattice mismatches in the growth of heteroepitaxy

laser lift-off [112, 177], and light reflecting interlayer [176] technologies have been developed. In fact, various LEDs such as ultraviolet LED (UV-LED) and violet LED [45, 46], blue LEDs [48, 54, 80, 82, 83, 103, 107, 126, 128, 129, 134, 141, 148, 150, 176–180], green LEDs [78, 79, 82, 106, 111, 181] using these GaN/Si epitaxial layers have been reported since 1998. Various device structures in order to reduce the series resistance of the vertical LEDs, such as wafer bonding [176], laser lift-off [112], and through-holes [181] have also been studied. Some of these developments have been reviewed in [35, 112, 167, 182, 183].

By solving these above mentioned problems, GaN/Si LEDs have already been commercialized by Sanken Electric Co. early in 2002 that collaborated with us [184] though at that time GaN/Si LEDs were believed to be very inferior to GaN/sapphire or GaN/SiC LEDs and to be difficult to make business. GaN/Si LEDs are now, however, becoming very promising for general lighting applications. Various companies hereafter are looking for the commercialization based on 100–200 mm diameter Si substrates [186–191], aiming at the cost reduction of 75–80% by reducing reject rates, minimizing batch time and utilizing automated semiconductor processing equipments, compared with the present LEDs based on sapphire and SiC substrates [192]. Even high bright (HB) LEDs have been achieved with 100–200 lm at 350–1000 mA [188, 191, 196, 197] for applications to domestic, architectural, medical, and automobile lighting. GaN/Si LEDs have therefore the possibility to become the main LEDs in the near future for general lighting.

In this article, we review GaN/Si epitaxial growth and LED fabrication developments (as summarized in Table 3.1), mainly focusing on our laboratory's work performed since 1998.

3.2 Epitaxial Growth and Characterization

In order to reduce dislocations due to lattice mismatching and cracks due to the difference of thermal expansion coefficients, various epitaxial structures have been studies.

3.2.1 GaN Growth on Sapphire

Blue LEDs were first developed using ZnSe and SiC substrates [23, 197]. Blue LEDs based on GaN were then reported as metal-insulating-semiconductor (MIS) structure GaN-based LEDs [198] but their emission efficiency was too weak for industrialization. The crystal quality of GaN on sapphire substrates was improved by MBE growth [199], hydride vapor phase epitaxy (HVPE) growth [200] and then greatly by MOCVD [2, 6]. The p-type GaN was first realized by

Table 3.1 GaN/Si epitaxial growth and LED fabrication

Growth method	Content	Author	Year	References
LPCVD +MOCVD	GaN on Si(111) through 200 nm 3C-SiC IL	Takeuchi et al.	1991	[41]
MOCVD	GaN on Si(111) through LT GaN IL	Ohkoshi et al.	1991	[73]
MOCVD	100–200 nm AlN IL, effect of growth temperature	Watanabe et al.	1993	[42]
RF Sputtering	Growth of GaN on AlN-buffered Si(111)	Meng et al.	1994	[43]
GS-MBE	GaN through AlN/GaN SLS on SiC/SOI substrate	Yang et al.	1995	[163]
CVD +MOCVD	GaN on SOI substrate carbonized by rapid thermal CVD	Steckle et al.	1996	[164]
HVPE	Thick GaN on Si(111) through HT-AlN IL	Hashimoto et al.	1996	[91]
MOCVD	AlO_x IL by oxidation of AlAs layer	Kobayashi et al.	1997, 1998	[92, 93]
MOCVD	GaN on SOI substrate, effect of Si overlayer	Cao et al.	1997	[165, 166]
MOCVD	Initial stage of nitridation of Si	Hashimoto et al.	1997	[209]
PA-MBE	First LEDs using GaN/Si	Guha et al.	1998	[44, 45]
PA-MBE	GaN on Si(111) through amorphous like SiN_x IL	Nakada et al.	1998	[36]
LPCVD +MOCVD	GaN through γ-Al_2O_3 IL on Si(111) and orientation relationship	Wang et al.	1998	[95]
MOCVD	Difficulty of LT-GaN growth on Si	Ishikawa et el.	1998	[76]
PA-MBE	High quality of AlN BL with the thickness of 3 nm	Sanchez-Garcia et al.	1998	[46]
MOCVD	First InGaN/GaN MQW blue LED using GaN/Si	Tran et al.	1999	[48]
MOCVD	GaN on Si(111) through AlAs/AlN IL	Strittmatter et al.	1999	[94]
MOCVD	SAG on dot- and stripe-patterned Si(111) using AlGaN IL	Kawaguchi et al.	1998, 2000	[132–134]
PA-MBE	Two-step growth of GaN on Si through AlN IL	Calleja et al.	1999	[38]
GS-MBE	AlN IL with short period GaN/AlGaN SLS	Nikishin et al.	1999	[37]
MOCVD	AlN IL and the origin of cracks	Follstedt et al.	1999	[50]
MOCVD	Effect of HT-AlN to prevent melt-back etching and LED fabrication	Egawa et al.	1999–2002	[75–79]
MOCVD	GaN on N^+ ion-implanted Si(111) through AlN or GaN/AlN IL	Koh et al.	2000	[55]

(continued)

Table 3.1 (continued)

Growth method	Content	Author	Year	References
GS-MBE +MOCVD	Blue LED using SAG GaN/Si (300 × 300 mm) through MBE grown AlN IL	Yang et al.	2000	[54]
MOCVD	NEH growth on patterned SOI and theoretical consideration	Zubia et al.	2000	[155, 156]
MOCVD	Appropriate condition for AlN IL growth	Lahreche et al.	2000	[51]
MOCVD	Maskless ELO on AlN IL	Lahreche et al.	2000	[115]
GS-MBE	SAG on patterned Si(111) through AlN IL or AlGaN/GaN SLS	Seon et al.	2000	[135]
MOCVD	AlGaN/GaN structure though AlN IL	Schremer et al.	2000	[53]
MOCVD	Crack-free growth of GaN by LT AlN IL	Dadger et al.	2000	[52]
LPCVD +MOCVD	Interface interaction of Si and GaN	Graupner et al.	2000	[210]
MOCVD	Layer by layer growth by Si dosing	Munkholm et al.	2000	[211]
MOCVD	Residual stress in GaN on Si(111) with the V/III molar flow ratio	Fu et al.	2000	[169]
MOCVD	EL from InGaN/GaN QW on AlAs IL	Dadgar et al.	2000	[178]
MOCVD	Effect of AlN BL growth temperature and duration on GaN growth	Zamir et al.	2000	[56]
MOCVD	HT-AlN IL on Si(111) by rapid thermal process MOCVD	Chen et al.	2001	[61]
MOCVD	Crack-free growth of GaN by AlN IL or AlN/GaN ML	Lahreche et al.	2001	[58]
MOCVD	Crack-free GaN using AlN/GaN SLS, strain measurement and green LED fabrication	Feltin et al.	2001	[106, 170]
MOCVD	Growth of InGaN QW and LT AlN + GaN/AlGaN ML on grid patterned Si (111) (100 × 100 μm)	Dadgar et al.	2001	[179]
MOCVD	Blue EL emission from InGaN QW on LT AlN IL + GaN/AlGaN ML	Dadgar et al.	2001	[80]
APCVD +MOCVD	Pendeo-epitaixial growth on 3C-SiC/Si CVD template	Davis et al.	2001	[118]
MOCVD	GaN thorough HT AlGaN IL on periodically grooved Si	Detchprohm	2001	[117]
MOCVD	Mask less ELO of GaN on parallel-grooved Si(111)	Strittmatter et al.	2001	[116]
GS-MBE	Crack-free growth of GaN up to 3 mm on Si(111) through AlN IL	Semond et al.	2001	[39, 40]

(continued)

Table 3.1 (continued)

Growth method	Content	Author	Year	References
MOCVD	SAG of GaN on dot and stripe-patterned Si(111) and (001)	Honda et al.	2001	[136, 137]
MOCVD	HT-AlN IL and graded IL from AlN to GaN	Marchand et al.	2001	[57]
UHVCVD	Step-graded AlGaN IL between GaN and AlN IL	Kim et al.	2001	[81]
MOCVD	Si_xN_y IL between AlN BL and GaN	Hageman et al.	2001	[60]
MOCVD	Effect of AlN BL growth temperature on the electrical and optical properties of GaN	Liaw et al.	2001	[59]
MOCVD	Reduction of cracks by GaN grown on patterned Si	Zamir et al.	2001, 2002	[122–124]
MOCVD	Dislocation density reduction and crack-free epitaxial growth up to 100 mm diameter using HT AlN/AlGaN + AlN/GaN ML, GaN/Si LEDs comparable with LEDs on sapphire	Egawa et al.	2002–2005	[35, 82–89]
MOCVD	Coating of the reactor wall by AlN for HT-AlN IL growth	Lee et al.	2002	[213]
MOCVD	Growth of 100 mm diameter GaN/Si	Brown et al.	2002	[63]
MOCVD	Concept of NHE and growth of GaN on Si	Hersee et al.	2002	[157]
MOCVD	Dislocation annihilation by Si d-doping	Contreas et al.	2002	[104]
MOCVD	Cantilever epitaxy with AlN IL on patterned Si	Katona et al.	2002	[119]
MOCVD	Crack-free 2 in. using two LT AlN ILs with Si_xN_x mask insertion	Dadger et al.	2002	[128, 129]
MOCVD	Review of GaN/Si	Krost et al.	2002	[182]
MOCVD	Growth of GaN/AlGaN and QW on (1-101) GaN side facets of truncated triangular GaN grown on Si(111)	Kato et al.	2002	[120]
MOCVD	SAG of (1-101) GaN on off-angled Si (001)	Honda et al.	2002	[138]
MOCVD	SAG of crack-free GaN on grid mask patterned Si(111)	Honda et al.	2002	[139, 140]
MOCVD	Effect of AlN IL on stress reduction	Krost et al.	2003	[183]
MOCVD	Appropriate growth temperatures for LT AlN+HT GaN+LT AlN IL structure	Dikme et al.	2003	[65]
MBE	NHE on nanopore array Si	Liang et al.	2003	[158]

(continued)

Table 3.1 (continued)

Growth method	Content	Author	Year	References
PA-MBE	Growth of AlGaN on Si through ZrB_2 IL	Tolle et al.	2003, 2004	[98, 99]
MOCVD	Influence of AlN BL thickness on the GaN crystal quality	Zhang et al.	2003	[67]
MOCVD	Growth of InGaN/GaN MQWs on GaN/Si with AlGaN/AlN CBL	Lee et al.	2003	[66]
MOCVD	Blue LED on AlN/AlGaN IL and AlGaN/GaN SLS structure	Lee et al.	2004	[107]
MOCVD	Reduction of dislocation density by Si_xN_x layer insertion	Lee et al.	2004	[96]
MBE	Growth of GaN on nonporous array Si surface	Sun et al.	2004	[159]
MOCVD	Improvement of light extraction by DBR structure	Ishikawa et al.	2004	[174, 175]
MOCVD	Influence of growth temperature of HT-AlN BL on the properties of GaN/Si (111)	Lu et al.	2004	[68]
MOCVD	Effect of V/III ratio of AlN BL growth on the GaN crystal quality	Wu et al.	2004	[69]
MOCVD	Crack-free MQW LEDs by metal bonding and selective lift-off	B. Zhang et al.	2005	[90]
MBE	Growth of GaN on Si through ZrB_2 IL	Yamada-Takamura et al.	2005	[101]
MOCVD	NHE overgrowth of GaN on nanopatterned SiO_2 mask deposited on GaN/AlN/Si	Zang et al.	2005	[160]
MOCVD	Lateral epitaxy on patterned Si substrate	Kim et al.	2005	[121]
HVPE	Thick GaN on AlN templated Si (111) substrate	Honda et al.	2005	[70]
MOCVD	InGaN/GaN DH structure on stripe-patterned Si(111)	Narita et al.	2005	[141]
MOCVD	Crack-free 5.4 mm thick GaN on 150 μm diameter Si	Dadger et al.	2006	[167]
MOCVD	NHE on nonporous Si surface prepared by anodized Al_2O_3 template as a mask	Zang et al.	2006	[161]
MOCVD	NHE on patterned SiO_2/GaN/Si substrate	Wang et al.	2006	[162]
MOCVD	Mechanical properties of GaN grown on patterned Si	Z. Yang et al.	2006	[125]
PA-MBE	Nitridation of ZrB_2 on Si	Wang et al.	2006	[102]
MOCVD	Precise conditions for SiN IL growth	Rieman et al.	2006	[97]

(continued)

Table 3.1 (continued)

Growth method	Content	Author	Year	References
MOCVD	Blue LEDs on patterned Si through AlN and SiN_x ILs	Zhang et al.	2007	[126]
MOCVD	Crack-free Growth of GaN on 150 mm Si wafers	Ubukata et al.	2007	[168]
MOCVD	Blue LEDs with photonic crystals using Si mold substrates	Orita et al.	2008	[295]
MOCVD	Crack-free GaN on patterned Si through HT-AlN IL	Lee et al.	2008	[127]
MOCVD	Semipolar (1-101) and (11-22) GaN on patterned Si(001) and Si(113) and InGaN/GaN SQW LEDs	Tanikawa et al.	2008, 2009	[143–145]
MOCVD	Effect of SixNy interlayers on the growth of GaN on AlGaN/AlN BLs on Si(111)	Cheng et al.	2008	[113]
MOCVD	Nonpolar (11-20) GaN on pattered Si(110)	Tanikawa et al.	2008	[142]
MOCVD	LED structure on Si(110) substrate	Reiher et al.	2009	[180]
MOCVD	Growth of (11-22) GaN on patterned Si(311) with and without SiO_2 mask	Yang et al.	2009	[146, 147]
MOCVD	Effect of AlGaN IL on the structural properties of GaN/AlN BL/Si(111)	Wu et al.	2009	[105]
MOCVD, Magnetron Suppe-tering	Influence of AlN BL thickness on GaN epitaxial growth	Yang et al.	2009	[71]
MOCVD	AlGaN/GaN SLS on AlN IL + AlN/GaN ML, improvement of crystal quality and fabrication of LEDs	Shuhaimi et al.	2009, 2010	[110–112]
MOCVD	Vertical LED with through-hole structure, reduction of the series resistance	Wei et al.	2010	[181]
MOCVD	Semi polar (11-22) GaN stripe crystal on Si by dual selective MOCVD	Murase et al.	2011	[151]
AP-MOCVD	Semi polar (1-101) InGaN/GaN MQW LEDs on pattered Si	Chie et al.	2011	[149, 150]
MOCVD	Growth of InGaN/GaN MQW on nonpolar and semipolar GaN on patterned Si	Tanikawa et al.	2011	[152]

(continued)

Table 3.1 (continued)

Growth method	Content	Author	Year	References
MOCVD	High bright vertical LEDs on Si using wafer bonding	Lee et al.	2011	[176]
MOCVD	Insertion of several AlN interlayers	Drechsel et al.	2011	[62]
MOCVD	Regrowth on patterned mesa structure for the reduction of TDDs	Lee et al.	2011	[130]
GSMBE +MOCVD	InGaN/GaN LEDs on Si hrough ZrB_2 BL	Blake et al.	2012	[103]
MOCVD +HVPE	In situ void formation using a AlN shell structure on GaN stripes on Si	Mitsunari et al.	2012	[153]
MOCVD	Effect of SixNy interlayres on the growth of GaN on AlGaN/AlN BLs on Si(111)	Zhu et al.	2012	[114]
RF-MBE	Growth of GaN on AlN BL/Si(110)	Shen et al.	2012	[72]
MOCVD	Growth of low TDD GaN on 8 in. Si(111) substrate via SiNx interlayers	Nunoue et al.	2013, 2014	[217, 218]
MOCVD	Growth of 200 mm GaN/Si for HEMT devices	Lenci et al.	2013	[192]
MOCVD	Growth of AlGaN/GaN on 200 mm Si substrates using SLSs and AlGaN/AlN BLs	Chisty et al.	2013	[216]
RF-MBE	Effect of (GaN/AlN) alternating-source-feeding (ASF) BLs	Yamaguchi et al.	2013	[245]
MOCVD	Stress distribution of 12 μm thick GaN on patterned SI(110)	Hossain et al.	2013	[131]
MOCVD	LEDs using 6 in. GaN/Si wafers with 150 ml/W at 350 mA	Sun et al.	2013, 2016	[188, 191]
MOCVD	Growth of 200 mm GaN/Si for HEMT devices	Kyaw et al.	2014	[193]
Sputtering +MOCVD	AlN IL growth with reactive sputtering	Yamada et al.	2014	[282]
MOCVD	Optimization of AlN/GaN SL buffers	Ni et al.	2015	[108]
MOCVD	Stress analysis after the transferring GaN films to a flexible layer	Bin-Bin et al.	2015	[244]
MOCVD	Low TDD 150 mm GaN/Si using a SiNx interlayer	Zhang et al.	2015	[221]
Sputtering +MOCVD	Growth of (10-1-3) GaN on Si(100) using sputtered AlN as the buffer layer	Mitsunari et al.	2015	[276]

(continued)

Table 3.1 (continued)

Growth method	Content	Author	Year	References
MOCVD	Effect of V/III ratio and the number of LT-AlN on the surface morphology of AlGaN/GaN/Si(111)	Wosko et al.	2015	[222]
RF Sputtering	Growth of GaN on Si substrates by RF sputtering as a function of RF power	Lee et al.	2015	[292]
MOCVD	Selective area growth GaN on Si(111) by confined lateral guided growth	Song et al.	2015	[154]
RP-ALD	Growth of GaN on (100) Si substrate at 200–500 °C	Shih et al.	2015	[275]
MOCVD	Vertica LEDs on rigid and flexible substrates using GaN/Si with Au-free bonding	Zou et al.	2016	[296]
MOCVD	Origin of hillock defects n GaN/Si(111)	Han et al.	2016	[243]

MOCVD Metal-Organic Chemical Vapor Deposition, *MBE* Molecular Beam Epitaxy, *GS-MBE* Gas Source MBE. *PA-MBE* Plasma Assisted MBE, *HVPE* Halide or Hydride Vapor Phase Epitaxy, *CVD* Chemical Vapor Deposition, *LPCVD* Low Pressure CVD, *UHVCVD* Ultra High Vacuum CVD, *APCVD* Atmospheric Pressure CVD, *SOI* Silicon-On-Insulator, *SAG* Selective Area Growth, *ELO* Epitaxial Lateral Overgrowth, *NHE* Nano-Hetero-Epitaxy, *DBR* Distributed Bragg Reflector, *BL* Buffer Layer, *IL* Intermediate Layer, *ML* Multiple Layer, *SLS* Super-Lattice Structure, *QW* Quantum Well, *MQW* Multiple Quantum Well, *HT* High Temperature, *LT* Low Temperature, *LED* Light Emitting Diode; *DH* Double Hetero, *CBL* Composite Buffer Layer; *RP-ALD* Remote Plasma Atomic Layer Deposition

electron beam irradiation [4] followed by thermal annealing [8] and pn junction GaN-based LEDs have been realized using InGaN as the emission layer grown on sapphire substrates [9–13]. These developments are reviewed in [173, 201]. These blue LEDs showed a significant emission efficiency and this was attributed to the carrier confinement into In islands formed due to the segregation of In in InGaN [202–204]. Since the In island density is about 10^{20} cm^{-2} which is much higher than the dislocation density 10^{9} cm^{-2} and the carrier diffusion length is very short with this In-content, it seems apparent that dislocations do not affect the emission efficiency. It is, however, known that when the carrier injection rate is very high and carriers overflow the band barrier of In islands, overflowed carriers recombine at dislocations, and then the dislocation density affects the emission efficiency. It is therefore necessary to reduce dislocation densities in order to increase the emission efficiency of high power LEDs. Egawa et al. [205] have shown that using AlN/sapphire templates, higher current can flow and higher luminosity can be obtained.

3.2.2 GaN Growth on SiC

SiC was predicted as a promising substrate for GaN epitaxial growth because of its good lattice matching with GaN [206, 207]. 6H-SiC has a lattice constant which is closer to that of GaN than that of sapphire and the lattice mismatching is only 3.4% and was expected to be good substrates for GaN-based LED fabrication. The quality of epitaxial growth on C-face and Si-face of SiC substrates [207] and the growth of (GaN/AlN) multi-layers on 6H-SiC are also studied [208].

GaN-based LEDs on SiC substrates has been then developed [15] and blue LEDs which compete with GaN-based LEDs have been achieved [16], especially applying a structure for better light extraction [17]. These GaN/SiC LEDs have been industrially developed and commercially produced [14, 18–21]. The advantage of GaN/SiC LEDs against GaN/sapphire LEDs is that better emission uniformity could be achieved. Since both electrodes can be formed on top and back surfaces and SiC has a high thermal conductivity, higher current densities can be achieved. The disadvantage of SiC is, however, the substrate cost as already mentioned.

3.2.3 GaN/Si Using Low Temperature (LT) Intermediate Layers

Previously reported GaN-based LEDs on Si have been grown with a low-temperature thick AlN intermediate layer (~750 °C, 8–30 nm) and AlGaN/GaN active layers [45, 48, 80, 106]. The LT grown intermediate layer technique itself was developed for the growth of epitaxial GaAs and GaP on Si [32–35]. It has been called as the two-step growth technique and widely used in the highly mismatched system such as the growth of GaN on sapphire. It was also proven that the SLS is very effective in improving the crystal quality of GaAs on Si. However, the LEDs on Si with a thick LT-AlN intermediate layer suffer from both high operating voltage and high series resistance, which result from the insulating AlN layer and the large band offset at the AlN/Si interface. In fact, the disadvantage of LT intermediate layers has been shown by Ishikawa et al. [74]. This disadvantage which comes from the meltback of Si due to the interaction of Ga with Si has also been studied precisely by many researchers [31, 61, 209–213].

3.2.4 GaN/Si Using High-Temperature (HT) AlN/AlGaN Intermediate Layers

In our laboratory, we have developed several epitaxial growth technologies for GaAs and GaP such as high-temperature growth of the intermediate layers and the

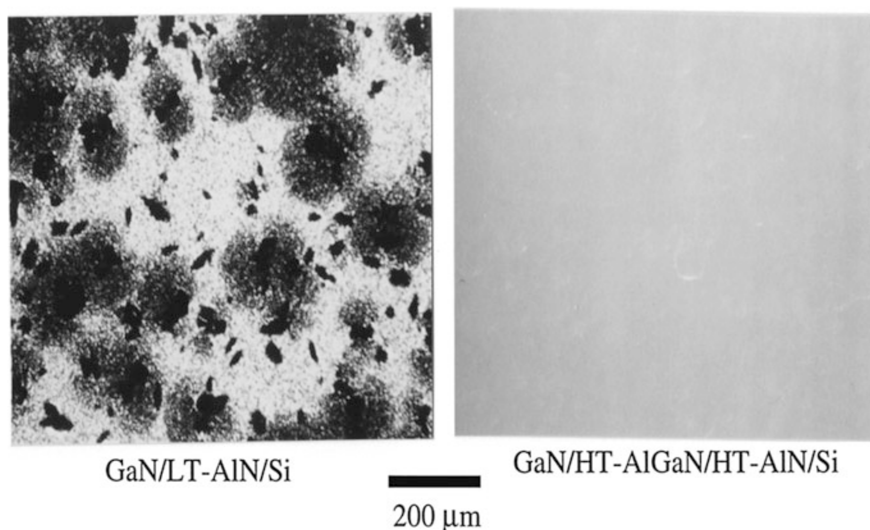

Fig. 3.2 Comparison of surface morphology of GaN on Si using a LT-AlN intermediate layer and a HT-AlN/AlGaN intermediate layer

insertion of SLSs [33] in order to solve the problem of lattice mismatching and cracking. For GaN/Si, we therefore applied these previously developed technologies in order to achieve crack-free large diameter GaN/Si epitaxial growth.

Instead of growing LT intermediate layers, we have grown thin AlN and AlGaN intermediate layers at high temperatures [75–79] on Si substrates with the maximum diameter of 50 mm. This HT growth of intermediate layers is very critical to achieve high-quality GaN growth since these HT layers prevent the interaction of Ga with Si (so called meltback phenomenon [31, 61, 209–213]). This is because at high temperatures nitride layers can be grown layer by layer while at low temperatures, the growth takes place with the three dimensional (3D) mode. This 3D mode growth which makes the interaction of Ga with Si and makes it difficult to obtain mirror-like surface and only cloudy surface is obtained.

Figure 3.2 shows the comparison of the surface morphology of the 1-μm-thick GaN layers on Si using the conventional LT-AlN intermediate layer (two-step growth technique) and the HT-AlN/AlGaN intermediate layer. The GaN on Si grown by the LT-AlN intermediate layer showed a cloudy surface morphology. However, the surface morphology was improved using the HT-AlN/AlGaN intermediate layer, because the Si substrate was protected from melt-back etching by the HT-AlN/AlGaN intermediate layers [76]. The full width at half maximum (FWHM) values of X-ray rocking curve (XRC) symmetric (0004) and asymmetric (20–24) reflections were 670 and 1535 arcsec, respectively.

Figure 3.3 shows the cross-section of the AlGaN/AlN intermediate layer. No hollows were observed at the interface of between the AlN and the Si substrate

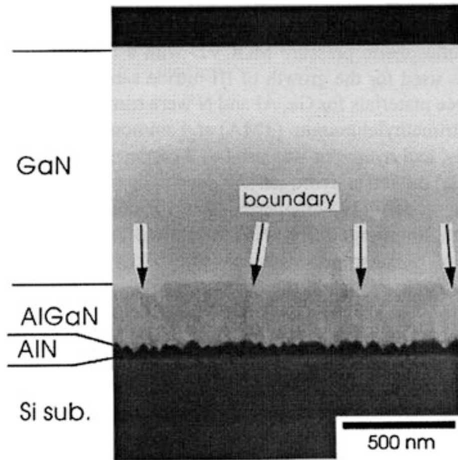

Fig. 3.3 Cross-sectional SEM image of GaN on Si with an AlGaN/AlN intermediate layer (reprinted from [62] with permission, copyright 1999 Japan Society of Applied Physics)

Fig. 3.4 Schematic cross-sectional structure of InGaN MQW LED on Si (reprinted from [72] with permission, copyright 2003 The Institute of Electronics, Information and Communication Engineers)

Layer
p-GaN, 0.2 μm
p-$Al_{0.15}Ga_{0.85}N$, 20 nm
InGaN MQW
n-GaN, 0.2 μm
AlN/GaN (5 nm/20 nm) multilayers (20 pairs)
n-$Al_{0.27}Ga_{0.73}N$, 20 nm
AlN, 3 nm and 120 nm
n-Si (111) substrate

which shows the AlGaN/AlN intermediate layer is effective in preventing the melt-back etching of the Si substrate.

3.2.5 GaN/Si Using HT Intermediate Layers (ILs) and Multilayers (MLs)

In order to improve the luminosity, AlN/GaN MLs have been grown on high-temperature grown AlN/AlGaN intermediate layers (HT-AlN/AlGaN ILs) on n^+-Si(111) substrates with the maximum diameter of 100 mm.

Figure 3.4 shows the typical cross-sectional view of this structure. After thermal cleaning at 1130 °C in H_2 ambient to remove the oxide from the Si surface, AlN layers have been grown with 3 and 120-nm thickness to study the effect of the

thickness of AlN layers. Above these HT intermediate layers, a 20-nm-thick n-$Al_{0.27}Ga_{0.73}N$ layer, 20-pair of AlN (5 nm)/GaN (20 nm) multilayers at 1080 °C, a 0.2-μm-thick n-GaN layer, an InGaN MQW structure, a 20-nm-thick p-$Al_{0.15}Ga_{0.85}N$ layer, and a 0.2 μm-thick p-GaN layer were deposited subsequently. The active layer consists of 3-nm-thick $In_xGa_{1-x}N$ wells and 5-nm-thick $In_{0.01}Ga_{0.99}N$ barrier layers. The typical In-content of the wells were 17% and 23% for the blue and green LEDs, respectively. For comparison, the same structure has been grown on sapphire substrates.

The dark spot densities were measured using a cathodoluminescence technique and were found to be 5×10^8 and $4 \times 10^9\ cm^{-2}$ for the n-GaN layers on sapphire and Si, respectively. Transmission electron microscopy (TEM) analysis was carried out to examine the microscopic structure. Figure 3.5a shows a cross-sectional TEM image for the overall LED structure and Fig. 3.5b is an enlarged picture near the active layer. As shown in Fig. 3.5, the V-defects were initiated at the threading dislocations during MQW growth. The V-defect has been observed in the InGaN MQW structure on sapphire [88, 214]. It is noteworthy that the pyramid-shaped structures are formed during the growth of last few QWs and no threading dislocation was observed in these pyramid-shaped structures. The QWs near the top of pyramid-shaped structures become the quantum-dot-like structure. The dots are ~10 nm in diameter and ~3.8 nm in height. Moreover, the valleys between pyramid-shaped structures are filled with p-AlGaN and p-GaN layers during growth at high temperature due to the enhanced surface migration of reactants. Because the resistivities of both p-GaN and p-AlGaN layers are relatively high, the holes could be effectively injected into the QWs near the top of pyramid-shaped structure through the shortest current passage from the p-electrode.

3.2.6 GaN/Si Using SLS Interlayers

The InGaN-based blue LED structure grown with a DBR was reported by Ishikawa et al. to reduce the light absorption in the Si substrate by the Si(111) substrate [174, 175]. We have recently found that the insertion of $Al_{0.06}Ga_{0.94}N$/GaN SLS interlayers to the InGaN-based MQW structures grown on Si(111) substrates with the HT-AlN/GaN intermediate layer is very effective to reduce the light absorption by the Si substrate. We adopted the SLS interlayer instead of the DBR layer for its superiority in vertical carrier propagation by tunneling effect while simultaneously maintaining good reflectivity. Reflectivity can also be improved either by increasing the Al composition or by increasing the pair numbers of the SLS stacks. The SLS structure is also less prone to cracking compared to the DBR structure.

For the SLS sample, a 20-nm-thick AlN layer was grown at 1100 °C on the Si (111) substrates as the intermediate layer, followed by 40 pairs of AlN/GaN ML with respective thickness of 5 and 20 nm. Subsequently, a 400-nm-thick interlayer was grown which consist of 80 pairs of $Al_{0.06}Ga_{0.94}N$/GaN strained-layer superlatives (SLSs) with respective thickness of 2.5 nm for each layer.

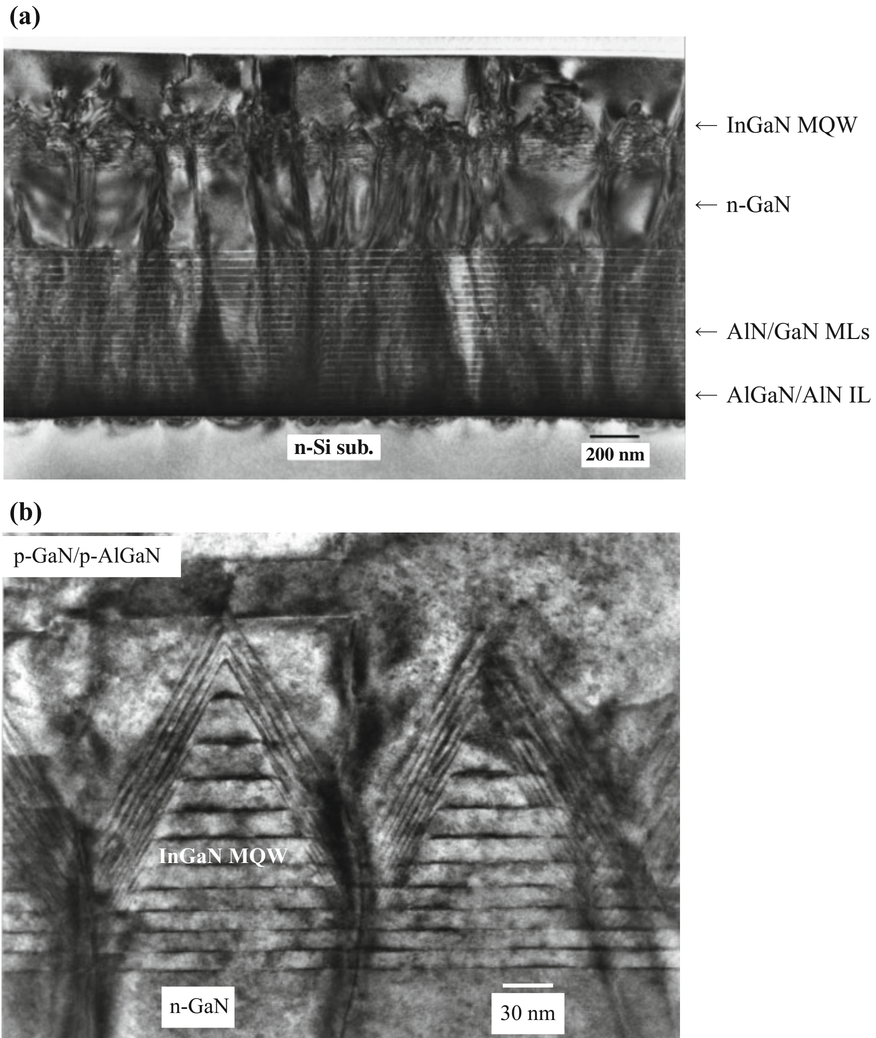

Fig. 3.5 Cross-sectional TEM images for **a** the overall structure and **b** the near active layer of InGaN MQW LED on Si with the thin AlN layer (reprinted from [75], copyright 2005 The Institute of Electrical and Electronics Engineers, Inc. and from [96] with permission, copyright 2010 IOP Publ.)

The $Al_{0.06}Ga_{0.94}N$ portion of the SLS pair was doped with Si (~1 × 10^{18} cm^{-3}) to produce a modulation-doped (MD) structure. For comparison, the SLS interlayer was substituted by a Si-doped (~1 × 10^{18} cm^{-3}) GaN layer conventionally used for the LED growth. Subsequent layers were kept identical for both samples with a 60 nm n-GaN waveguide layer, 10 pairs of 1.5 nm $In_{0.16}Ga_{0.84}N$ well and 9 nm

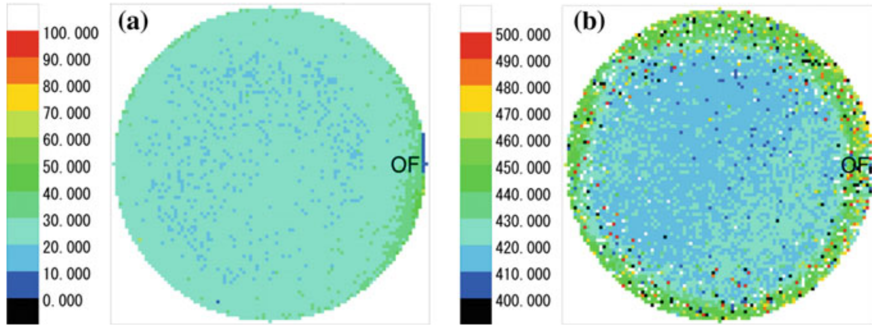

Fig. 3.6 PL surface mapping showing the emission peak wavelength FWHM distribution for wafers with **a** an $Al_{0.06}Ga_{0.94}N$/GaN SLS interlayer and with **b** a GaN interlayer (reprinted from [95] with permission, copyright 2010 Japan Society of Applied Physics)

$In_{0.08}Ga_{0.92}N$:Si barrier in the active layer, and a 10 nm GaN cap layer. Reactor temperature was decreased to 800 °C during the active layer growth.

All samples grown were crack-free and showed no melt-back etching. Samples with the $Al_{0.06}Ga_{0.94}N$/GaN SLS interlayer showed a specular surface for the whole wafer. However, the sample with the GaN interlayer was cloudy at the wafer edge due to the thick GaN layer.

The PL spectrum has been studied and we found several features of the effect of the insertion of SLS structures.

(i) The uniformity of the MQW emission was improved compared with that without SLS structures from 11.1% to 2.5% (Fig. 3.6).
(ii) It shows the main peak at 3.05 eV (S1) while without SLS, 3.02 eV (S2) is the main peak at low temperature as shown in Fig. 3.7. The sample with SLS always demonstrates a higher intensity than that without SLS because the 1.5 nm thin MQW layer gives minimal effect to electron-hole separation in the MQW.
(iii) With the temperature increase, the sample with SLS layers shows a smaller emission peak shift than that without SLS layers.
(iv) The activation energy is 151.1 meV for the sample with SLS which suggests that thermal quenching in that sample is attributed by the thermal escape of electrons and/or holes from the InGaN wells into the InGaN barriers [215].
(v) Internal quantum efficiency (IQE) η_{int} was estimated from integrated photoluminescence (PL) intensity ratio of 300–10 K $(I_{300\text{K}}/I_{10\text{K}})$, assuming that η_{int} at 10 K is 100%. The estimated η_{int} in the sample with SLS and the sample only with the GaN layer was 29.4 and 20.6%, respectively. The higher IQE agrees well with the mechanism of thermal quenching in InGaN MQW [110].

All these features are due to the crystal quality improvement by the insertion of SLS layers. In fact, we have evaluated the crystal quality by TEM observation and

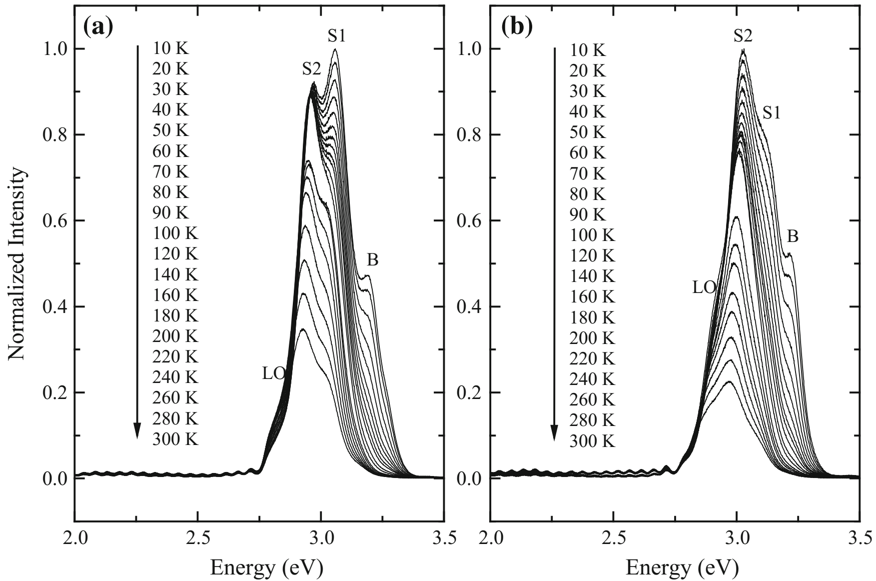

Fig. 3.7 PL spectra of **a** a sample with an $Al_{0.06}Ga_{0.94}N$/GaN SLS interlayer and **b** a sample with a GaN interlayer recorded in 10–300 K temperature range (reprinted from [95] with permission, copyright 2010 Japan Society of Applied Physics)

reciprocal space mapping (RSM) measurement and found that SLS layers have an effect to bend threading dislocations from AlN/GaN MLs and to block screw dislocations at the ML/SLS interface. The dislocation density was thus reduced to the level of 3–6 $\times$ 10^9 cm^{-2} at the upper edge of SLS layers (Fig. 3.8).

Recently, the growth of AlGaN/GaN epitaxial growth with SLS and AlGaN/AlN interlayers on Si substrates with the diameter of 200 mm has been achieved [216].

3.2.7 Recent Progress of the Growth of GaN/Si

As mentioned so far, high-quality GaN/Si epiwafers could be obtained mainly using SLSs. However, it is important to establish much simpler structures for reducing the production cost. From this point of view, several progresses have been reported.

Nunoue et al. [217] and Hikosaka et al. [218, 219] have used SiN_x interlayers above AlGaN/GaN buffer layers (BLs) and could have obtained the threading dislocation densities (TDDs) less than several 10^8 cm^{-2}. Leung et al. [220] have developed step-graded five AlGaN BLs for reducing the dislocation density and the bowing and has achieved XRD FWHM of 476 arcsec. Zhang et al. [221] have also used thin SiN_x interlayers above AlGaN/AlN BLs and obtained XRD FWHM of

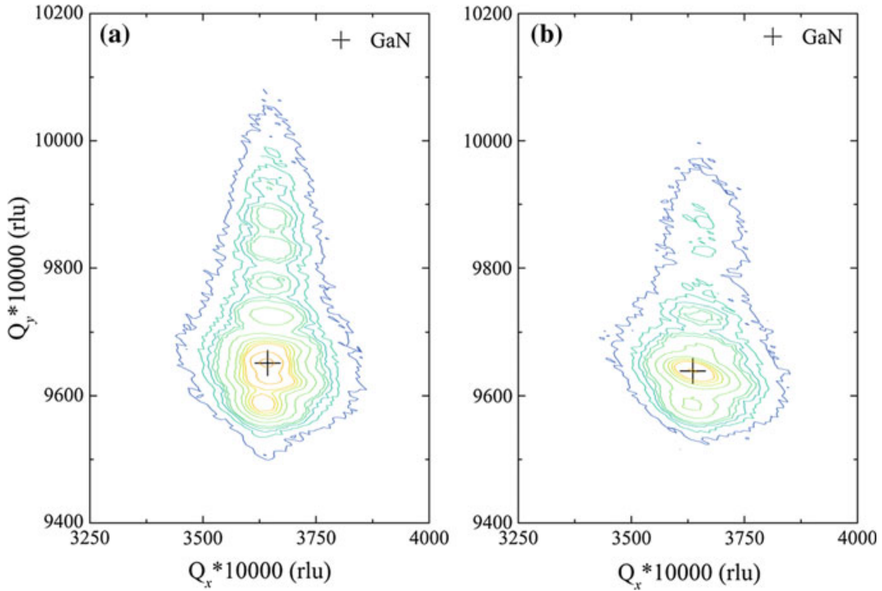

Fig. 3.8 RSM around $(10\bar{1}5)$ diffraction plane of **a** a sample with an $Al_{0.06}Ga_{0.94}N$/GaN interlayer and **b** a sample with a GaN interlayer. The GaN position is marked in each figure (reprinted from [95] with permission, copyright 2010 Japan Society of Applied Physics)

380 arcsec. Wosko et al. [222] have studied the effect of V/III ratio and the number of LT-AlN on the surface morphology of AlGaN/GaN/Si(111).

It is also pointed out that the mechanism of the growth of AlN intermediate layer is important and the precise mechanism is now extensively studied [223]. The physics and chemistry of AlN/Si(111) interface have been in fact extensively studied [37, 44, 224–242] but is not yet well understood. It was long believed that SiN_x layers on Si substrates are not good for the epitaxial growth of nitrides, but there is an argument that the control of atomic structure of SiN_x one monolayer is important for the successive growth of nitrides.

Regarding the origin of hillock defects on GaN/Si [243], it is found that it is due to the formation of Ga-rich secondary phase precipitates in the AlGaN BL which is strongly related with the AlN BL underneath. This insight of defects is important to improve the quality of GaN/Si epitaxial layers.

Another interesting works are the transferring technology of the grown GaN-based LED structure epilayers to other substrate such as Si [244] and (GaN/AlN) alternating-source-feeding (ASF) BLs by Yamaguchi et al. [245] to achieve 2D growth.

3.2.8 Other Epitaxial Growth Methods

The nitride crystal growth has been developed mainly by the MOCVD method. This method has several disadvantages:

(1) high-temperature growth (higher than 1050 °C) which is necessary to activate neutral ammonia to be reactive with metal-organic (MO) gas. High temperature is, however, unfavorable from the viewpoint of wafer bending and cracking due to the larger thermal expansion coefficients between substrates and epitaxially grown layers. It is also unfavorable from the viewpoint of high In containing nitride growth since InN is not stable at higher temperatures.
(2) Since the activation of ammonia gas is too low so that a large amount of ammonia gas has to be flowed with the V/III ratio as high as 2000–3000. This large amount of consumption of ammonia gas prevails about 1/4–1/2 of the production cost of the nitride epitaxial growth.
(3) GaN decomposes at temperatures higher than 800 °C so that when GaN is grown at 1050 °C, growth proceeds with the decomposition of GaN. Therefore, a large amount of TMG is consumed and it is costly and is not environment friendly.

In order to solve these disadvantages of the MOCVD method, several attempts have been made such as the development of high density radical source for MBE to increase the growth rate as the MOCVD [246–251]. Laser deposition [252–254], plasma-assisted MOCVD [255–274], atomic layer deposition [275], and sputtering methods [276–292] are also being developed. In these methods, nitrides can be grown at lower temperatures without costly ammonia gas. They are, however, under development and the MOCVD itself is also scaled up to 200 mm in order to decrease the production cost [216].

3.3 Fabrication of LEDs and Their Performances

3.3.1 Device Characteristics of LED Structures with HT-AlN/AlGaN Intermediate Layers [75–79]

Since we first could grow specular mirror-like surface using HT-AlN/AlGaN intermediate layers as described in Sect. 3.2.4, we have fabricated LEDs with MQW structures on them and evaluated their device performances. Ni/Au thin transparent metals and Ni/Au (12/100 nm) p-type Ohmic metals were fabricated on top of the GaN/Si LED structures and the n-type Ohmic contact was made from the backside through Si substrate using AuSb/Au (18/100 nm) (Fig. 3.9a). In the case of LEDs on sapphire substrates fabricated for comparison, both Ohmic contacts were made on the top side with a mesa structure formed by reactive ion etching (Fig. 3.9b). The operating voltage of 7.0 V and the series resistance of 100 Ω were

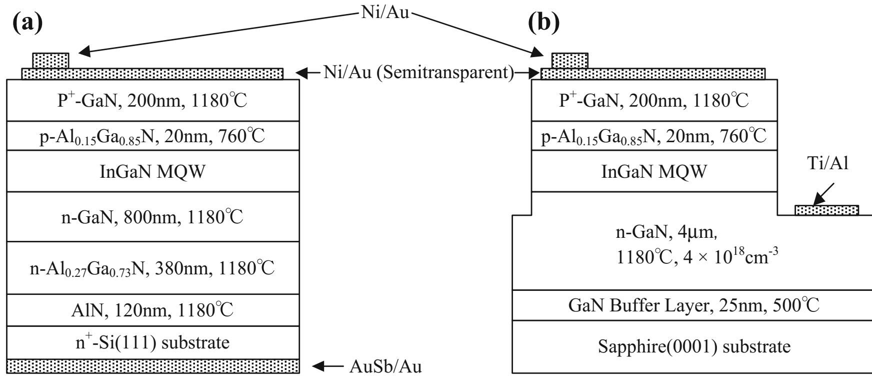

Fig. 3.9 **a** MQW LED structure on sapphire and **b** MQW LED structure on Si (reprinted from [64] with permission, copyright 2002 The Institute of Electronics, Information and Communication Engineers)

obtained for GaN/Si LEDs with the optical output power of 20 μW (The detector was set 10 mm above the surface of LED chip of $10 \times 10\ \mathrm{mm}^2$ size for the measurement. The value is more than two orders magnitude lower that the value measured for a molded LED using an integral sphere detector) at the forward current of 20 mA, with a peak emission wavelength of 505 nm, with a full width at half maximum of 33 nm. The LED also exhibited a stable operation over 500 h under the automatic current control (20 mA) condition at 27 °C. However, the optical output power was still half compared with LEDs on sapphire substrates and the operating voltage and the series resistance were higher compared with GaN/sapphire LEDs with 4.5 V and 40 Ω, respectively. This may be due to the higher resistance at the AlN/Si interface.

3.3.2 Effect of Thin AlN Intermediate Layers and AlN/GaN MLs [35, 82–89]

In order to reduce the operating voltage and the series resistance to the level of LEDs on sapphire substrates, we have developed a structure with a thin AlN intermediate layer with AlN/GaN MLs, as the crystal growth and the characterization of the grown crystal described in Sect. 3.2.5. We have fabricated LEDs with MQW structures on them and LEDs with the same active layer structure on c-plane sapphire substrates. Ni/Au thin transparent metals and Ni/Au (12/100 nm) p-type Ohmic metals were fabricated on top of the GaN/Si LED structures and the n-type Ohmic contact was made from the backside through Si substrate using AuSb/Au (18/100 nm). In the case of LEDs on sapphire substrates, both Ohmic contacts were made on the top side with a mesa structure formed by RIE.

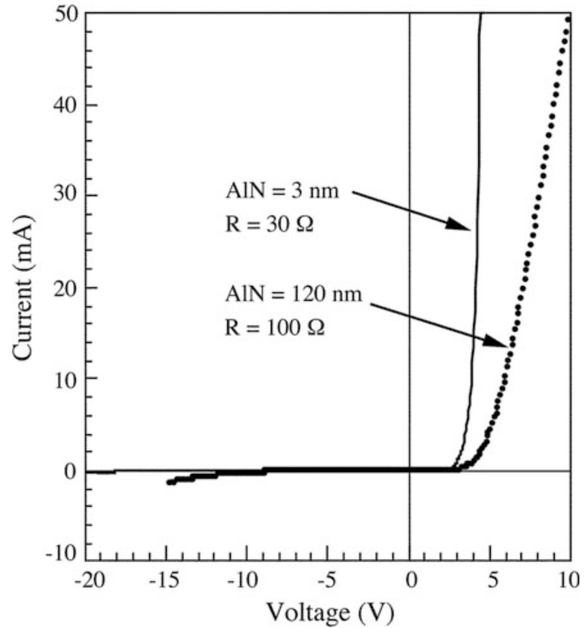

Fig. 3.10 Comparison of I–V characteristics of LEDs on Si with the different thickness of AlN layer (reprinted from [96] with permission, copyright 2010 IOP Publ.)

Figure 3.10 shows the I–V characteristics of blue LEDs grown on Si. Compared with the operating voltage of 7.0 V and the series resistance of 100 Ω at the forward current of 20 mA for LEDs described in Sect. 3.3.1, the operating voltage and the series resistance were reduced to 3.8–4.1 V and 30 Ω, respectively, when the thin AlN layer of 2.5–3 nm together with AlN/GaN MLs was applied. The same active layer structure LED grown on sapphire substrates showed an operating voltage of 3.8 V and a series resistance of 25 Ω at the forward current of 20 mA. GaN/Si LEDs thus showed the similar results as in the case of LEDs on sapphire.

The band diagram at the AlN/Si interface was evaluated using the X-ray photoelectron spectroscopy (XPS) measurement. As shown in the Fig. 3.11, the valence and conduction band discontinuities at the AlN/Si interface were evaluated to be 2.8 ± 0.4 and 2.3 ± 0.4 eV, respectively [293]. Moreover, the AlN layer is an insulator with a band gap of 6.2 eV. When an n-contact is made on the backside of n-Si substrate, electrons are injected into the active layer from the n-Si substrate side through the AlN layer. There is a large barrier to the electron injection due to the presence of thick AlN layer. On the contrary, when the AlN layer is thin below a critical value, the operating voltage of the LED can be largely reduced as mentioned above probably because of the formation of the tunnel junction between the n-AlGaN layer and the n-Si substrate.

Figure 3.12 shows the comparison of L–I characteristics of the LEDs on sapphire and Si substrates under the highly injected current. The wavelengths at 20 mA were 470 and 475 nm for the LEDs on sapphire and Si substrates, respectively. The output power from the LED on sapphire increased with the injected current density

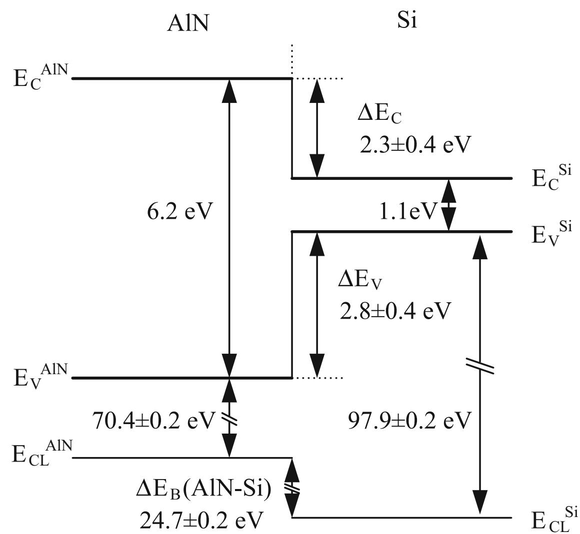

Fig. 3.11 Schematic energy band diagram at the AlN/Si interface (reprinted from [198] with permission, copyright 2003 Japan Society of Applied Physics)

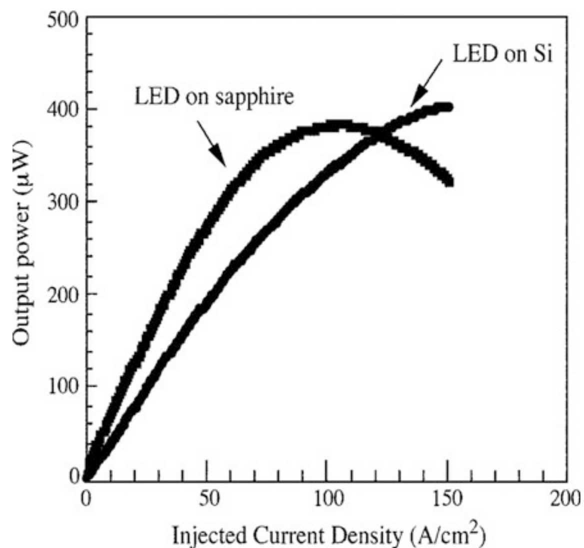

Fig. 3.12 Comparison of L–I characteristics of LEDs on sapphire and Si substrates under highly injected current. The detector was set 10 mm above the surface of LED chip (reprinted from [72] with permission, copyright 2003 The Institute of Electronics, Information and Communication Engineers)

up to 100 A/cm^2 and then decreased with increasing the injected current density. Since the thermal conductivity of sapphire is as low as 0.35 W/cm K, the output power of the LED on sapphire is saturated due to the heating effect. The output power from the LED on Si was lower than that on sapphire below the 120 A/cm^2 because of the absorption of emission by Si substrate. However, the output power from the LED on Si did not saturate till the injected current density of 150 A/cm^2

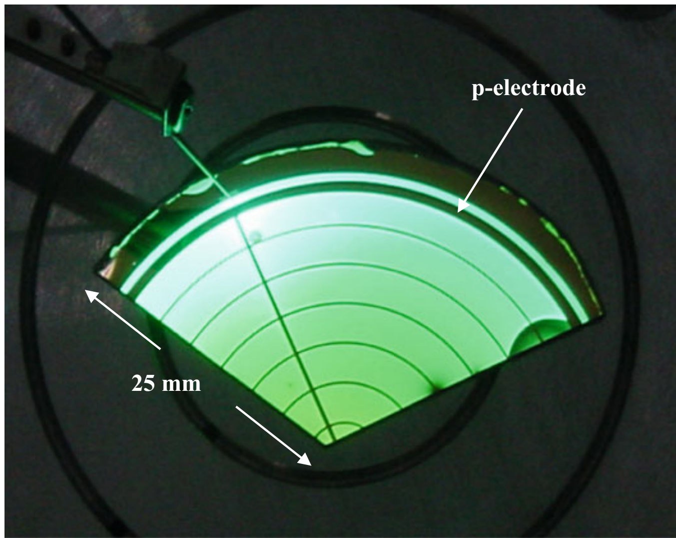

Fig. 3.13 Demonstration of the light emission from a large area green LED on Si with a thin AlN layer under injected current of 800 mA, corresponding to the current density as low as 120 mA/cm^2 (reprinted from [96] with permission, copyright 2010 IOP Publ.)

because of higher thermal conductivity of Si substrate (1.5 W/cm K). Thus, the LED on Si exhibited the better characteristic than that on sapphire under highly injected current. Some LED chips were molded by epoxy resin. The optical output power of the molded blue LEDs on Si were as high as 1.5–2 mW at 20 mA. Based on this technology, very luminous LEDs up to 200 mcd have been commercialized [294]. Taking into account of the absorption of partial emission by Si substrate, it can be concluded that the high-quality active layer is grown on Si substrate in spite of its highly mismatched system. Figure 3.13 shows the emission morphology of a large area green (505 nm) LED on Si with a thin AlN layer under the injected current of 800 mA (120 mA/cm^2). Although the injected current density was as low as 120 mA/cm^2, a uniform emission has been observed for the large area. The onset of emission was observed at 12 mA, corresponding to the injected current density as low as 1.8 mA/cm^2. In Fig. 3.14, blue and green LEDs thus fabricated are shown.

In order to study the reliability of the LED on Si, the aging tests were performed at 27 and 80 °C under automatic current control (ACC). Figure 3.15 shows the reliability results of the blue LED on Si with the thin AlN layer. The output power was constant during the 1000 h aging at 27 °C. At 80 °C, there was a decrease in the output power at the initial stage, which was as low as 6%, but after this small decrease the output power of LED almost remained constant.

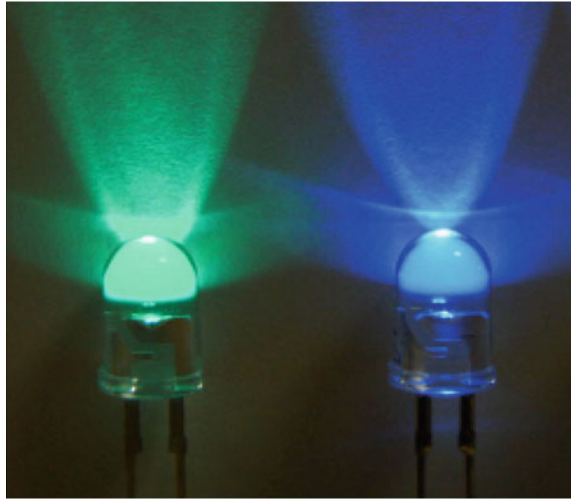

Fig. 3.14 Photographs of the blue and green LEDs on Si emitting at 478 and 505 nm (reprinted from [69] with permission, copyright 2002 Japan Society of Applied Physics)

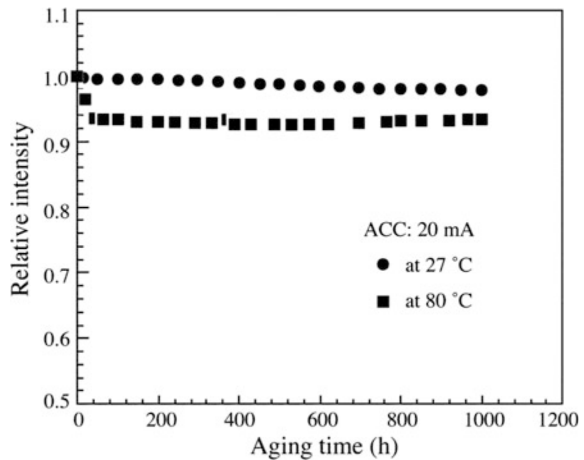

Fig. 3.15 Variation of the optical output power as a function of aging time measured at 27 and 80 °C (reprinted from [96] with permission, copyright 2010 IOP Publ.)

3.3.3 Wafer Bonding and Lift-Off [90]

The problem of GaN/Si LEDs is the partial absorption of the emission by Si substrate. However, the combination of the selective etching of Si and the metal-to-metal bonding was effective in improving the LED characteristics, such as 49% increase in the optical output power and the reduction of the operating voltage to 3.6 V [90].

In this technology, a 10 nm Ni was deposited and annealed on the top surface of the epitaxially grown structure. The LED structure is the same as described in Sect. 3.3.2. In order to reflect the light emitting from the copper carrier side,

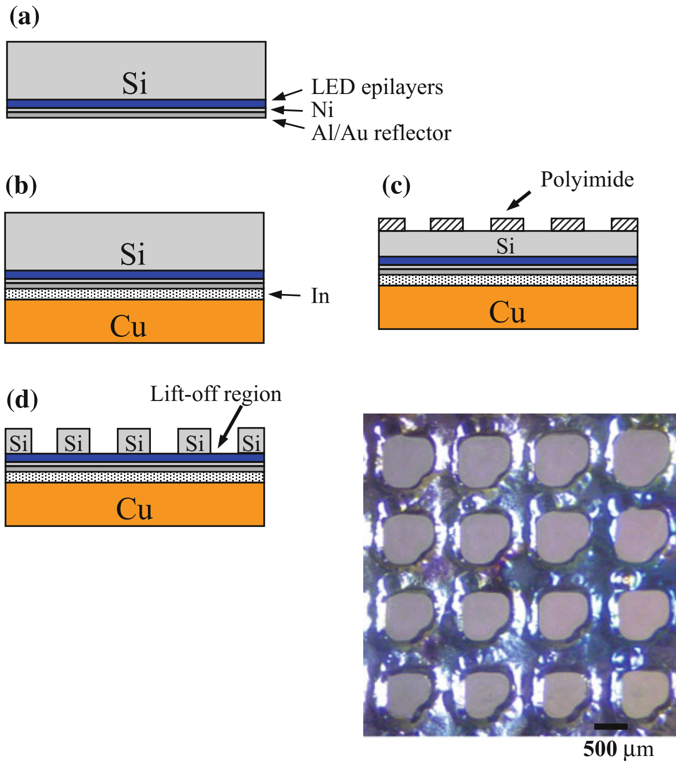

Fig. 3.16 Selective lift-off process flow: **a** formation of the p-type Ohmic contact and the deposition of a high-reflectivity metal reflector (Al/Au) onto the epitaxial surface of the LED epitaxial wafer, **b** bonding of a metal/InGaN MQW LED/Si wafer onto the copper carrier, **c** thin Si substrate by mechanical polishing, and **d** selective removal of the Si substrate by wet-chemical etching. The inset shows the image of the SLO process (reprinted from [77] with permission, copyright 2005 American Institute of Physics)

a highly reflective Al/Au metal reflector was deposited on the thin annealed Ni layer. The InGaN MQW LED epitaxial wafer with the metal reflector was then bonded onto an Au plated copper carrier heated at 200 °C using indium as an adhesive. After the substrate was thinned down to about 60 μm by mechanical polishing, the Si substrate was selectively removed by wet-chemical etching in HNA solution ($HF:HNO_3:CH_3COOH$ = 1:1:1) using a polyimide mask. This selective lift-off (SLO) process flow is shown in Fig. 3.16. Fabrication of LEDs on the substrate removed areas was carried out as follows. First, the AlN/AlGaN buffer layers and AlN/GaN multilayer on the substrate removed areas were removed by RIE in order to further reduce the operating voltage and the series resistance. Then, the exposed n-GaN layer was partially etched to the p-GaN by RIE. Subsequently, thin Ti/Au (5/5 nm) metal patterns were deposited on the exposed n-GaN as a

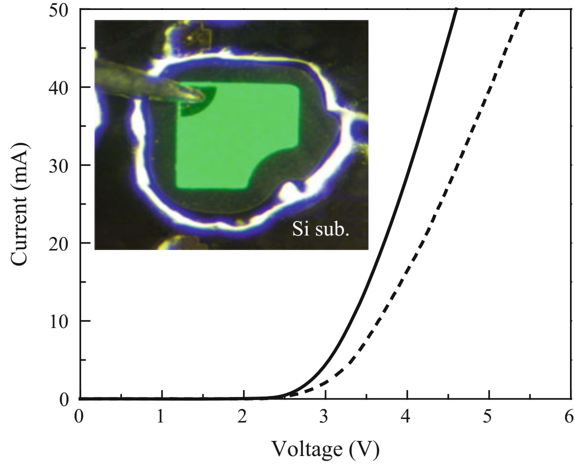

Fig. 3.17 I–V characteristics of the LEDs before (*dashed line*) and after (*solid line*) substrate removal. The inset shows an emission image of the LED fabricated on the substrate removal region. The image was taken at 0.5 mA under room light and microscope light conditions. The emission wavelength is about 518 nm (reprinted from [77] with permission, copyright 2005 American Institute of Physics)

transparent electrode for the n-GaN side up LED. Finally, n-type contact metal Al/Au (45/60 nm) patterns were formed.

Figure 3.17 shows the I–V characteristics of the LED before and after substrate removal. In order to avoid the strain relaxation in the thin nitride epilayer at a high temperature, the n-type contact of the LED after substrate removal was formed without any heat treatment. In spite of this, the operating voltage at 20 mA decreases from 4.2 to 3.6 V, and the series resistance decreases from 42 to 27 Ω for the LED after substrate removal. These results are comparable with that of the LEDs on sapphire substrate. The significant improvement is due to the elimination of the large band offset between the AlN buffer layer and Si substrate after substrate removal. The removal of the AlN intermediate layer and AlN/GaN multilayer was also helpful to decrease the operating voltage and the series resistance. An emission image of the LED fabricated on the substrate removal region is shown in the inset. The image was taken at 0.5 mA under room light and microscope light conditions. The emission wavelength was about 518 nm. It showed crack-free, high-brightness, and uniform emission.

Figure 3.18 illustrates the light output power versus injection current (L–I) characteristics of the LED before and after substrate removal. Since the LED fabricated on the substrate removal region is n-GaN layer side up, the 0.2 μm-thick n-GaN layer is too thin to spread the current. A transparent conducting metal is needed for this kind of LED. However, unlike the conventional p-GaN side up LED, there is no suitable metal which can form Ohmic contact with n-GaN layer and also has a high transmittance. We therefore employed Ti/Au (5/5 nm) as a transparent metal for the LED after substrate removal. The transmittance of the Ti/Au layers is only 52% at the wavelength of 518 nm. In spite of this, the optical power at 20 mA increased from 21 to 31.3 μW (The detector was set 10 mm above the surface of LED chip of 10×10 mm^2 size for the measurement. The value is more than two orders magnitude lower that the value measured for a molded LED

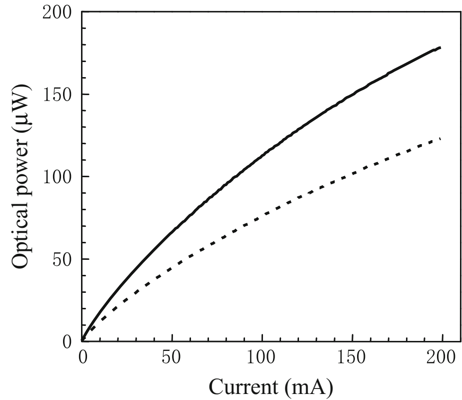

Fig. 3.18 L–I characteristics of the LEDs before (*dashed line*) and after (*solid line*) substrate removal using an on-wafer testing configuration. The detector was set 10 mm above the surface of LED chip of 10×10 mm^2 size (reprinted from [77] with permission, copyright 2005 American Institute of Physics)

using an integral sphere detector) for the LED after substrate removal, corresponding to a 49% increase in optical power compared to the LED before substrate removal. The increase in the output power is attributed to the removal of the absorptive substrate and the Al/Au metal reflector. The light emitting to copper carrier side was reflected to the top side by the metal reflector. The improved I–V characteristics as shown in Fig. 3.17 and the better thermal conductivity of copper carrier were another reason for the output power enhancement.

3.3.4 Effect of the Insertion of SLS Layers [110–112]

The optimized LED structure with the insertion of the $Al_{0.06}Ga_{0.94}N$/GaN SLS interlayer was grown using the MOCVD method as mentioned in Sect. 3.2.5. LED fabrication was performed on the epitaxially grown structure with and without SLS, without substrate removal process. Ni/Au thin transparent metals and Ni/Au (12/100 nm) p-type Ohmic metals deposited on the top p-GaN contact layer. The n-type Ohmic contact was fabricated both from top on mesa-etched n-GaN contact layer using Ti/Al/Ni/Au (15/60/12/60 nm) and from the backside on the Si substrate using AuSb/Au (18/100 nm).

For these samples, current–voltage (I–V), light output power and electroluminescence (EL) spectra were measured. Optical characteristics were measured at room temperature inside an integrated sphere. MQW light emission characteristics were evaluated by temperature-dependent PL.

Figure 3.19a shows the light output power versus the injected current density for the optimized LED structures, with and without the $Al_{0.06}Ga_{0.94}N$/GaN SLS interlayer. TT indicates the current injection from the p-GaN top layer to the n-GaN contact layer, while TB indicates the current injection from the p-GaN top layer to the backside of the n-type Si substrate. The results clearly shows that the LED structure with the $Al_{0.06}Ga_{0.94}N$/GaN SLS interlayer yields a higher intensity and a

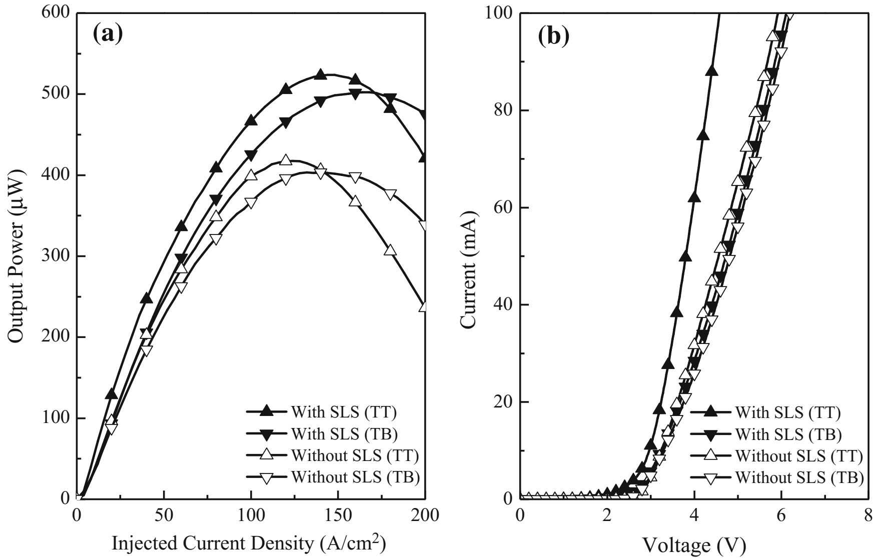

Fig. 3.19 Comparison of **a** light output power versus injected current density and **b** injected current versus voltage, each for optimized LED structure with/without $Al_{0.06}Ga_{0.94}N$/GaN SLS interlayer. The measurement was performed in an integrated sphere for 10×10 mm^2 size area (reprinted from [96] with permission, copyright 2010 IOP Publ.)

higher saturation current in comparison to the conventional LED structure without the SLS interlayer. At 20 A/cm^2 current injection, the light intensity from the LED structure with the $Al_{0.06}Ga_{0.94}N$/GaN SLS interlayer was 34% higher than that of the conventional structure. It was shown that a better current spreading yielded an improved heat distribution in the LED chip at a higher saturation current when the current is injected from the backside of the n-type Si substrate (TB). Figure 3.19b shows a great improvement of the current–voltage characteristics in LED with the $Al_{0.06}Ga_{0.94}N$/GaN SLS interlayer structure than that of conventional structure. The operating voltage measured from the p-GaN top layer to the n-GaN contact layer at 20 mA for LED with the $Al_{0.06}Ga_{0.94}N$/GaN SLS interlayer and the conventional structure was 3.2 and 3.6 V, respectively, with series resistance of 16 and 29 Ω, in each respective structure. The reduction of threading dislocations by the $Al_{0.06}Ga_{0.94}N$/GaN SLS interlayer in the LED structure contributes to significant improvement in lateral carrier spreading, thus greatly improved the electrical characteristics in this LED structure. Typical EL characteristics for respective samples are shown in Fig. 3.20, for each 20 A/cm^2 increment of the injected current. LED structure with the $Al_{0.06}Ga_{0.94}N$/GaN SLS interlayer shows a narrower FWHM spectrum peak of 27 nm, compared to that of 35 nm in the conventional structure. The result agrees well with the improved InGaN emission uniformity that can be achieved by the insertion of the $Al_{0.06}Ga_{0.94}N$/GaN SLS interlayer [111].

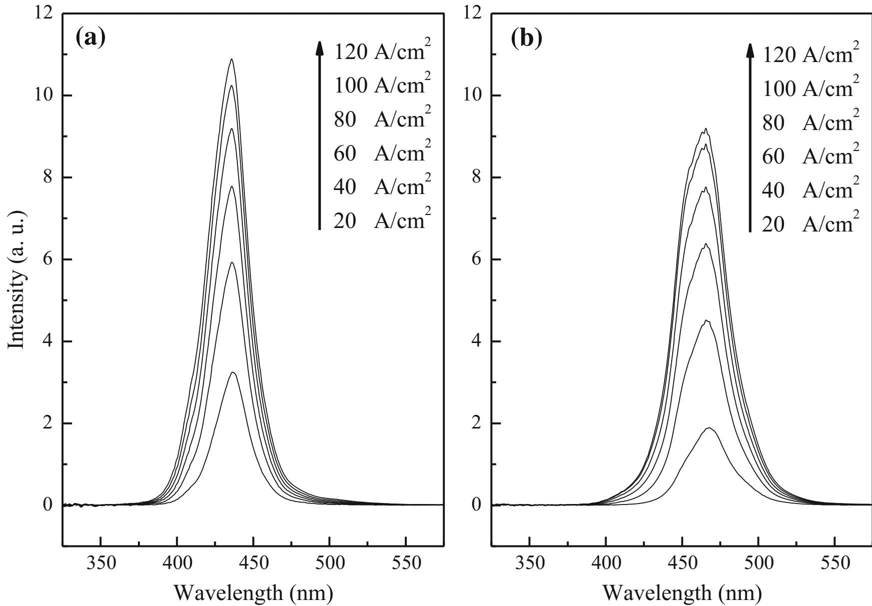

Fig. 3.20 EL characteristics for optimized LED structure **a** with an $Al_{0.06}Ga_{0.94}N$/GaN SLS interlayer and **b** without an $Al_{0.06}Ga_{0.94}N$/GaN SLS interlayer (reprinted from [96] with permission, copyright 2010 IOP Publ.)

3.3.5 Other Structures

In order to solve the problem of the light absorption by Si substrates, we have developed other technologies such as DBR reflectors, through-holes, and photonic crystals (PhCs).

We have first developed a DBR structure [174, 175] in order to increase the reflectivity. The various stack DBR layers were grown on AlN/AlGaN intermediate layer and AlN/GaN multilayers (Sect. 3.2.5) and found that the output power is increased with the number of DBR stacks. It was found that at three stacks, the output power was doubled because of the reflection of the emission light by the DBR layer. The disadvantage is in that the cracking occurs when the DBR number is increased. The other disadvantage is that the series resistance is increased as a function of the stack number, which is disadvantageous for vertical structure LEDs.

We also have developed vertical LEDs using the LED structure of AlN/AlGaN intermediate layer and AlN/GaN multilayers (Sect. 3.2.5), via a through-hole device process as shown in Fig. 3.21. The through-hole has been fabricated via selective Inductively Coupled Plasma-RIE (ICP-RIE) up to the Si substrate. Cr (20 nm)/Pd(20 nm)/Au(200 nm) metals were used to connect the n-GaN and Si substrate. The conventional structure without thorough holes was also fabricated for comparison. AuSb(20 nm)/Au(200 nm) metals were deposited on the back side of

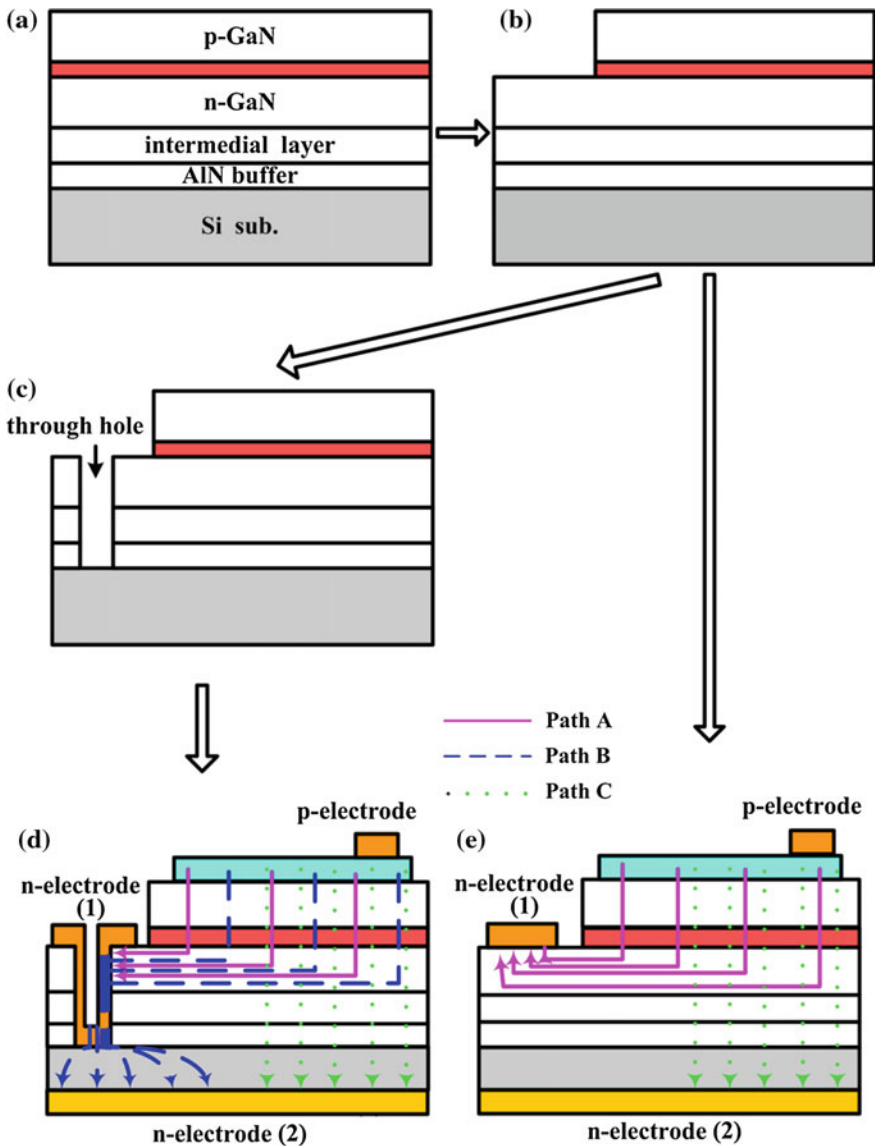

Fig. 3.21 Fabrication process of a novel LED structure with through-holes and a conventional LED structure: **a** epitaxial layer grown on silicon substrate, **b** dry etching to expose the n-GaN layer, **c** formation of through-holes, **d** and **e** deposition of metals as electrodes for the LED structure with through-holes and for the conventional LED structure (reprinted from [162] with permission, copyright 2010 Japan Society of Applied Physics)

the Si substrate after lapping and polishing the substrate down to 150 μm to compare the horizontal and vertical structure. It was found that the series resistance and the operating voltage at 20 mA were reduced from 26 to 22.5 Ω and from 4.4 to

4.0 V, respectively, for the vertical configuration using the through-holes. This is due to the current pass via the through-hole electrode biasing the high resistive AlN layers.

We also have developed LEDs with photonic crystals (PhCs) [298] by using a Si substrate as a mold for forming the PhCs. GaN-based epitaxial layers were grown on 2-D grooved Si substrates and they were bonded onto a highly reflective substrate and the Si substrate was removed. The resultant LEDs with PhC showed the 80% higher optical output power due to the light extraction effect by PhCs. It is also noteworthy that the lateral epitaxial growth using grooved Si substrates decreased the dislocation densities and also affected the increase of the internal quantum efficiency.

Zou et al. [296] have developed vertical LEDs on Si substrates and flexible substrates such as papers by bonding 6 in. GaN/Si epilayers with Au-free Cu/Sn/Cu bonding in order to achieve low-cost LEDs and VLEDs with the light output power of 13.4 mW at 20 mA has been reported. Li et al. [297] has achieved the IQE of 62.9% comparable to that of GaN LED on sapphire by the suppression of band tilting by the quantum-confined Stark effect (QCSE) with reducing the thickness of the thin-film GaN LEDs transferred to Si substrates. Sun et al. [188, 191] have reported the production of LEDs using 6 in. epitaxial layers as shown in Fig. 3.22.

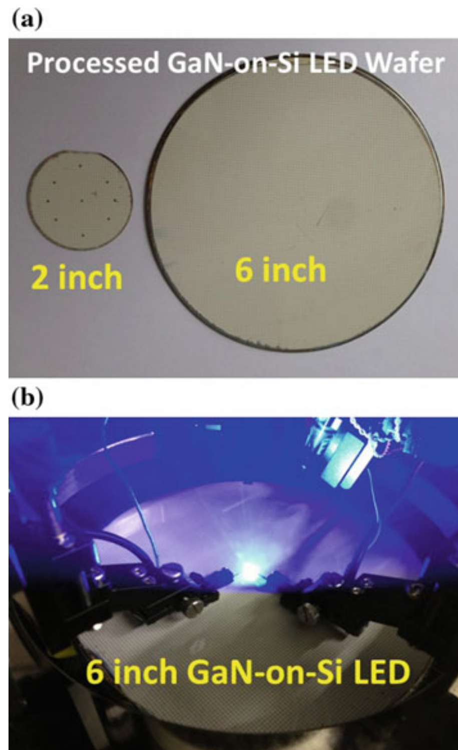

Fig. 3.22 **a** Processed 6-in. GaN-on-Si LED wafer and **b** its lit-top photo (reprinted from [191] with permission, copyright 2016 J. Semiconductors)

They also developed even lasers based on GaN/Si epitaxial wafers [298]. Some development of LEDs with various structures together with epitaxial growth for LEDs is also summarized by Zhu et al. [299] and Dadger [300].

3.4 Conclusion

We have developed high-temperature AlN/AlGaN intermediate layers, AlN/GaN multilayers, and AlGaN/AlN SLSs in order to prevent the cracking and to improve the surface morphology of GaN materials on Si substrates and could succeed in preparing high-quality nitride layers on large diameter Si substrates. We could grow mirrored surface epitaxial layers to the diameter up to 100 mm. We also found that LEDs fabricated on these high-quality epitaxial wafers showed the LED performances similar to LEDs on sapphire substrates. This is mainly due to the reduction of the series resistance by the formation of tunnel junction between the n-AlGaN layer and n-Si substrate with decreasing the high-temperature AlN layer thickness to 3 nm, and also due to the dislocation density reduction by the pyramid-shaped (quantum-dot-like) structure of MQW layers on AlN/GaN multilayers. We also showed the advantage of GaN/Si LEDs compared with LEDs on sapphire is that the optical output power can be increased much higher compared with LEDs on sapphire because of a better thermal conductivity of Si than sapphire. The LEDs also exhibited the good reliability and a uniform emission for a large size wafer. GaN/Si LEDs are thus very promising for future general lighting because it is clear that the fabrication cost will be highly reduced, up to 75–80% of conventional LEDs based on sapphire and SiC substrates. There also have many kinds of structure modifications to improve the disadvantage of GaN/Si so that GaN/Si LEDs have a promising perspective to become the main LEDs in the near future.

Acknowledgements This work was partially supported by a Special Coordination Funds for Promoting Science and Technology.

References

1. I. Akasaki et al., Jpn. Ann. Rev. Electron. Comput. Telecommun. **19**, 295 (1986)
2. H. Amano et al., Appl. Phys. Lett. **48**, 353 (1986)
3. H. Amano et al., Thin Solid Films **163**, 415 (1988)
4. H. Amano et al., Jpn. J. Appl. Phys. **28**, L2112 (1989)
5. S. Nakamura et al., Jpn. J. Appl. Phys. **31**, 1258 (1992)
6. S. Nakamura, Jpn. J. Appl. Phys. **30**, L1705 (1991)
7. S. Nakamura et al., Jpn. J. Appl. Phys. **30**, L1708 (1991)
8. S. Nakamura et al., Jpn. J. Appl. Phys. **31**, L139 (1992)
9. S. Nakamura et al., Jpn. J. Appl. Phys. **30**, L1998 (1991)
10. S. Nakamura et al., Appl. Phys. Lett. **64**, 1687 (1994)
11. S. Nakamura et al., Jpn. J. Appl. Phys. **34**, L797 (1995)

12. S. Nakamura et al., Jpn. J. Appl. Phys. **34**, L1332 (1995)
13. T. Mukai et al., Jpn. J. Appl. Phys. **37**, L839 (1998)
14. C.H. Carter Jr. et al., Mater. Sci. Eng. B **61–62**, 1 (1999)
15. Compound Semiconductor **6**, 11 (2000)
16. V. Harle et al., Phys. Status Solidi (A) **180**, 5 (2000)
17. Compound Semiconductor **7**, 7 (2001)
18. D. Eisert et al., *Proceedings of the International Workshop on Nitride Semiconductors (IWN 2000), IPAP Conference Series 1* (2000), p. 841
19. U. Zehnder et al., J. Crystal Growth **230**, 497 (2001)
20. J. Baur et al., Phys. Status Solidi (A) **194**, 399 (2002)
21. U. Strauss et al., Phys. Status Solidi (C) **0**, 276 (2002)
22. See Chap. 1 Part A in this book
23. See a review in O. Oda, *Compound Semiconductor Materials and Characterization*, vol. 2 (World Scientific Publ., 2012), p. 205
24. D. Hobgood et al., Mater. Sci. Forum **338–342**, 3 (2000)
25. N. Ohtani et al., Mater. Sci. Forum **389–393**, 29 (2002)
26. A.R. Powell et al., Mater Sci. Forum **457–460**, 41 (2004)
27. J.J. Sumaeris et al., MRS Bull. **30**, 280 (2005)
28. R.T. Leonard et al., Mater. Sci. Forum **600–603**, 7 (2009)
29. Cree Research Inc., *Industrial Session at the 8th European Conference on SiC Related Materials* (ECSCRM2010, Norway, Oslo)
30. http://www.cree.com/~/media/Files/Cree/Chips-and-Material/Data-Sheets-Material/MATCATALOG.pdf
31. A. Krost, A. Dadgar, Mater. Sci. Eng. B **93**, 77 (2002)
32. M. Akiyama et al., Jpn. J. Appl. Phys. **23**, L843 (1984)
33. T. Egawa, Doctor thesis, Nagoya Institute of Technology (1991)
34. T. Egawa et al., Jpn. J. Appl. Phys. **37**, 1552 (1998)
35. M. Umeno et al., Oyo Butsuri. Mon. Publ. Jpn. Soc. Appl. Phys. **72**, 273 (2003)
36. Y. Nakada et al., Appl. Phys. Lett. **73**, 827 (1998)
37. S.A. Nikishin et al., Appl. Phys. Lett. **75**, 2073 (1999)
38. E. Calleja et al., J. Crystal Growth **201–202**, 296 (1999)
39. F. Semond et al., Phys. Status Solidi (A) **188**, 501 (2001)
40. F. Semond et al., Appl. Phys. Lett. **78**, 335 (2001)
41. T. Takeuchi et al., J. Crystal Growth **115**, 634 (1991)
42. A. Watanabe et al., J. Crystal Growth **128**, 391 (1993)
43. W.J. Meng et al., J. Appl. Phys. **76**, 7824 (1994)
44. S. Guha et al., Appl. Phys. Lett. **72**, 415 (1998)
45. S. Guha et al., Appl. Phys. Lett. **723**, 1487 (1998)
46. M.A. Sanchez-Garcia et al., J. Electron. Mater. **27**, 276 (1998)
47. U. Kaiser et al., J. Mater. Res. **14**, 2036 (1999)
48. C.A. Tran et al., Appl. Phys. Lett. **75**, 1494 (1999)
49. D.D. Koleske et al., Appl. Phys. Lett. **75**, 3141 (1999)
50. D.M. Follstaedt et al., MRS Internet J. Nitride Semicond. Res. **4S1**, G3.72 (1999)
51. H. Lahreche et al., J. Crystal Growth **217**, 13 (2000)
52. A. Dadger et al., Jpn. J. Appl. Phys. **39**, L1183 (2000)
53. A.T. Schremer et al., Appl. Phys. Lett. **76**, 736 (2000)
54. J.W. Yang et al., Appl. Phys. Lett. **76**, 273 (2000)
55. E.K. Koh et al., J. Crystal Growth **218**, 214 (2000)
56. S. Zamir et al., J. Crystal Growth **218**, 181 (2000)
57. H. Machand et al., J. Appl. Phys. **89**, 7846 (2001)
58. H. Lahreche et al., J. Crystal Growth **231**, 329 (2001)
59. H.M. Liaw et al., Solid State Electron. **45**, 417 (2001)
60. P.R. Hageman et al., Phys. Status Solidi (A) **188**, 523 (2001)
61. P. Chen et al., J. Crystal Growth **225**, 150 (2001)

62. P. Drechsel et al., J. Crystal Growth **315**, 211 (2001)
63. J.D. Brown et al., Solid State Electron. **46**, 1535 (2002)
64. F. Reihner et al., J. Crystal Growth **248**, 563 (2003)
65. Y. Dikme et al., J. Crystal Growth **248**, 578 (2003)
66. S. Lee et al., J. Crystal Growth **249**, 65 (2003)
67. B.S. Zhang et al., J. Crystal Growth **258**, 34 (2003)
68. Y. Lu et al., J. Crystal Growth **263**, 4 (2004)
69. M. Wu et al., J. Crystal Growth **260**, 331 (2004)
70. Y. Honda et al., Phys. Status Solidi (C) **2**, 2125 (2005)
71. J.H. Yang et al., J. Crystal Growth **517**, 5057 (2009)
72. X.Q. Shen et al., Phys. Status Solidi (C) **9**, 503 (2012)
73. S. Ohkoshi et al., *Tenth Record of Alloy Semiconductor Physics and Electronics Symposium*, Nagoya (1991), p. 172
74. H. Ishikawa et al., J. Crystal Growth **189–190**, 178 (1998)
75. H. Ishikawa et al., Phys. Status Solidi (A) **176**, 599 (1999)
76. H. Ishikawa et al., Jpn. J. Appl. Phys. **336708**, 39 (1999)
77. B.J. Hikosaka et al., Phys. Status Solidi (A) **188**, 151 (2001)
78. N. Nishikawa et al., Technical Report IEICE, LQE 2001-142(2002-2), p. 37
79. T. Egawa et al., J. Appl. Phys. **91**, 528 (2002)
80. A. Dadgar et al., Appl. Phys. Lett. **78**, 2211 (2001)
81. M.H. Kim et al., Appl. Phys. Lett. **79**, 2713 (2001)
82. T. Egawa et al., Jpn. J. Appl. Phys. **41**, L663 (2002)
83. T. Egawa, ICN-5, Th-A8.1 (2003), p. 263
84. B. Zhang et al., Jpn. J. Appl. Phys. **42**, L226 (2003)
85. T. Egawa et al., Technical Report IEICE, OPE-2003-202 (2003), p. 177
86. H. Ishikawa et al., Technical Report IEICE, ED2003-149 (2003), p. 291
87. T. Egawa, Taiyo-Nissan Technical Report, 23 (2004), p. 2
88. T. Egawa et al., IEEE Electron Device Lett. **26**, 169 (2005)
89. T. Egawa, *Wide Bandgap Semiconductors*, ed. by K. Takahashi, A. Yoshikawa, A. Sandhu (Springer, 2007), p. 370
90. B. Zhang et al., Appl. Phys. Lett. **86**, 071113 (2005)
91. N.R. Hashimoto et al., Mater. Res. Soc. Symp. **395**, 243 (1996)
92. N.P. Kobayashi et al., Appl. Phys. Lett. **71**, 3569 (1997)
93. N.P. Kobayashi et al., J. Crystal Growth **189–190**, 172 (1998)
94. A. Strittmatter et al., Phys. Status Solidi (A) **176**, 611 (1999)
95. L.S. Wang et al., Appl. Phys. Lett. **72**, 109 (1998)
96. K.J. Lee et al., Appl. Phys. Lett. **85**, 1502 (2004)
97. T. Riemann et al., J. Appl. Phys. **99**, 123518 (2006)
98. J. Tolle et al., Appl. Phys. Lett. **82**, 2398 (2003)
99. J. Tolle et al., Appl. Phys. Lett. **84**, 3510 (2004)
100. C.-W. Hu et al., J. Crystal Growth **267**, 554 (2004)
101. Y. Yamada-Takamura et al., Phys. Rev. Lett. **95**, 266105 (2005)
102. T. Wang et al., J. Appl. Phys. **100**, 033506 (2006)
103. A.H. Blake et al., J. Appl. Phys. **111**, 033107 (2012)
104. O. Contreas et al., Appl. Phys. Lett. **81**, 4712 (2002)
105. Y.X. Wu et al., Chin. Phys. B **18**, 4413 (2009)
106. E. Feltin et al., Jpn. J. Appl. Phys. **40**, L738 (2001)
107. S. Lee et al., J. Korean Phys. Soc. **46**, 1356 (2004)
108. Y. Ni et al., Superlattices Microstruct. **83**, 811 (2015)
109. X.Q. Shen et al., Phys. Status Solidi **11**, 473 (2014)
110. B.A.B.A. Shunaimi et al., Mat. Res. Soc. Symp. Proc. **1167**, O04-01 (2009)
111. B.A.B.A. Shunaimi et al., Jpn. J. Appl. Phys. **49**, 021002 (2019)
112. T. Egawa et al., J. Phys. D Appl. Phys. **43**, 354008 (2010)
113. K. Cheng et al., Appl. Phys. Lett. **92**, 192111 (2008)

114. D. Zhu et al., Phys. Status Solidi (A) **209**, 13 (2012)
115. H. Lahreche et al., Mater. Sci. Forum **338–342**, 1487 (2000)
116. A. Strittmatter et al., Appl. Phys. Lett. **78**, 727 (2001)
117. T. Decchprohm et al., Jpn. J. Appl. Phys. **40**, L16 (2001)
118. R.F. Davis et al., J. Crystal Growth **231**, 335 (2001)
119. T.M. Katona et al., Phys. Status Solidi (A) **194**, 550 (2002)
120. T. Kato et al., J. Crystal Growth **237–239**, 1099 (2002)
121. K.J. Kim et al., J. Korean Phys. Soc. **47**, S500 (2005)
122. S. Zamir et al., Appl. Phys. Lett. **78**, 288 (2001)
123. S. Zamir et al., J. Crystal Growth **230**, 341 (2001)
124. S. Zamir et al., J. Appl. Phys. **81**, 1191 (2001)
125. Z. Yang et al., Appl. Phys. Lett. **88**, 041913 (2006)
126. B. Zhang et al., J. Crystal Growth **298**, 725 (2007)
127. S.-J. Lee et al., Jpn. J. Appl. Phys. **47**, 3070 (2008)
128. A. Dadgar et al., Phys. Status Solidi (A) **192**, 308 (2002)
129. A. Dadger et al., Appl. Phys. Lett. **80**, 3670 (2002)
130. J. Lee et al., J. Crystal Growth **315**, 263 (2011)
131. T. Hossain et al., Phys. Status Solidi (C) **10**, 425 (2013)
132. Y. Kawaguchi et al., Jpn. J. Appl. Phys. **37**, L966 (1998)
133. Y. Kawaguchi et al., Phys. Status Solidi (A) **176**, 553 (1999)
134. S. Tanaka et al., Appl. Phys. Lett. **76**, 2701 (2000)
135. M. Seon et al., Appl. Phys. Lett. **76**, 1842 (2000)
136. Y. Honda et al., J. Crystal Growth **230**, 346 (2001)
137. S. Tanaka et al., Appl. Phys. Lett. **79**, 955 (2001)
138. Y. Honda et al., J. Crystal Growth **242**, 82 (2002)
139. Y. Honda et al., Appl. Phys. Lett. **80**, 222 (2002)
140. Y. Honda et al., J. Crystal Growth **242**, 77 (2002)
141. T. Narita et al., Phys. Status Solidi (C) **2**, 2349 (2005)
142. T. Tanikawa et al., J. Crystal Growth **310**, 4999 (2008)
143. T. Hikosaka et al., Phys. Status Solidi (C) **5**, 2234 (2008)
144. T. Tanikawa et al., Phys. Status Solidi (C) **5**, 2966 (2008)
145. T. Tanikawa et al., J. Crystal Growth **311**, 2879 (2009)
146. M. Yang et al., J. Korean Phys. Soc. **54**, 2363 (2009)
147. M. Yang et al., J. Crystal Growth **311**, 2914 (2009)
148. N. Sawaki et al., J. Crystal Growth **311**, 2867 (2009)
149. C.-H. Chiu et al., J. Crystal Growth **318**, 500 (2011)
150. C.-H. Chiu et al., Appl. Phys. Exp. **4**, 012105 (2011)
151. T. Murase et al., Jpn. J. Appl. Phys. **50**, 01AD04 (2011)
152. T. Tanikkawa et al., Phys. Status Solidi (A) **208**, 1175 (2011)
153. T. Mitsunarit et al., Phys. Status Solidi (C) **9**, 480 (2012)
154. J. Song et al., Adv. Mater. Interfaces **2**, 1500014 (2015)
155. D. Zubia et al., Appl. Phys. Lett. **76**, 858 (2000)
156. D. Zubia et al., J. Vac. Sci. Technol. B **18**, 3514 (2000)
157. S.D. Harsee et al., IEEE JQE **38**, 1017 (2002)
158. J. Liang et al., Appl. Phys. Lett. **83**, 1752 (2003)
159. X.Y. Sun et al., J. Appl. Phys. **95**, 1450 (2004)
160. N.H. Zang et al., Appl. Phys. Lett. **87**, 193106 (2005)
161. K.Y. Zang et al., Appl. Phys. Lett. **88**, 141925 (2006)
162. L.S. Wang et al., Appl. Phys. Lett. **89**, 011901 (2006)
163. Z. Yang et al., J. Vac. Sci. Technol. B **13**, 789 (1995)
164. A.J. Steckl et al., Appl. Phys. Lett. **69**, 2264 (1996)
165. J. Cao et al., Appl. Phys. Lett. **71**, 3880 (1997)
166. J. Cao et al., J. Appl. Phys. **83**, 3829 (1998)
167. A. Dadgar et al., Proc. SPIE **6355**, 63550R (2006)

168. A. Ubukata et al., J. Crystal Growth **298**, 198 (2007)
169. Y. Fu et al., J. Vac. Sci. Technol. A **18**, 965 (2000)
170. E. Feltin et al., Appl. Phys. Lett. **79**, 3230 (2001)
171. E. Feltin et al., Phys. Status Solidi (A) **188**, 531 (2001)
172. J.A. Floro et al., MRS Bull. **27**, 19 (2002)
173. E.F. Schubert, *Light Emitting Diodes* (Cambridge University Press, Cambridge, U.K., 2002)
174. H. Ishikawa et al., Phys. Status Solidi (A) **201**, 2653 (2004)
175. H. Ishikawa et al., J. Crystal Growth **272**, 322 (2004)
176. S.J. Lee et al., Appl. Phys. Exp. **4**, 066501 (2011)
177. W.S. Wong et al., Appl. Phys. Lett. **77**, 2822 (2000)
178. A. Dadger et al., IPAP Conf. Ser. **1**, 845 (2000)
179. A. Dadgar et al., Phys. Status Solidi (A) **188**, 155 (2001)
180. F. Reiner et al., J. Phys. D **42**, 055107 (2009)
181. J. Wei et al., Jpn. J. Appl. Phys. **49**, 072104 (2010)
182. A. Krost et al., Phys. Status Solidi (A) **194**, 361 (2002)
183. A. Krost et al., Phys. Status Solidi (A) **200**, 26 (2003)
184. Nikkei, Nov. 22 (2001)
185. http://www.bridgelux.com/
186. http://www.latticepower.com/
187. http://ledsmagazine.com/news/8/7/2
188. http://www.electroiq.com/articles/sst/2012/03/siltronic-scales-down-150mm-silicon-wafer-production-in-us-and-germany.html
189. http://www.electroiq.com/articles/sst/2012/06/lattice-power-ramps-high-power-gan-on-si-led-production.html
190. Q. Sun et al., IEEE ChinaSSL, 174 (2013)
191. Q. Sun, J. Semiconductors **37**, 044006 (2016)
192. S. Lenci et al., IEEE Electron Dev. Lett. **34**, 10.35.417 (2013)
193. L.M. Kyaw et al., ECS Solid State Lett. **3**, Q5 (2014)
194. http://www.widepr.com/36402
195. http://www.eetindia.co.in/ART_8800644758_1800010_NP_0f814454.HTM
196. http://www.electroiq.com/articles/sst/2011/06/gan-on-si-hb-led-demo.html
197. See a review in O. Oda, *Compound Semiconductor Materials and Characterization* (World Scientific Publ., 2007), p. 27
198. J.I. Pankove, E.A. Miler, J.E. Berkeyheiser, RCA Rev. **32**, 383 (1971)
199. S. Yoshida, S. Misawa, S. Gonda, Appl. Phys. Lett. **42**, 427 (1983)
200. H.P. Maryska, J.J. Tietjen, Appl. Phys. Lett. **15**, 327 (1969)
201. S. Nakamura, S.F. Chichibu, *Introduction to Nitride Semiconductor Blue Lasers and Light Emitting Diodes* (Taylor and Francis, London, 2000)
202. S.D. Lester et al., Appl. Phys. Lett. **66**, 1249 (1995)
203. Y. Narukawa et al., Appl. Phys. Lett. **70**, 981 (1997)
204. L. Sugiura, Appl. Phys. Lett. **70**, 1317 (1997)
205. T. Egawa et al., Appl. Phys. Lett. **81**, 292 (2002)
206. T. Sasaki et al., Appl. Surf. Sci. **41**, 504 (1989)
207. S.Y. Ren, J.D. Dow, Appl. Phys. Lett. **69**, 251 (1996)
208. M. Horie et al., Phys. Status Solidi (A) **192**, 151 (2002)
209. A. Hashimoto et al., J. Crystal Growth **175–176**, 129 (1997)
210. R. Graupner et al., J. Crystal Growth **217**, 55 (2000)
211. A. Munkholm et al., Appl. Phys. Lett. **77**, 1626 (2000)
212. M.K. Sankara et al., Appl. Phys. Lett. **79**, 1546 (2001)
213. I.-H. Lee et al., J. Crystal Growth **235**, 73 (2002)
214. X.H. Wu et al., Appl. Phys. Lett. **72**, 692 (1998)
215. Y. Sun et al., Appl. Phys. Lett. **87**, 093115 (2005)
216. D. Chisty et al., Appl. Phys. Express **6**, 026501 (2013)
217. S. Nunoue et al., IEDM2013-349, 13.2.1 (2013)

218. T. Hikosaka et al., Phys. Status Solidi (C) **11**, 617 (2014)
219. T. Hikosaka et al., J. Appl. Phys. **101**, 103513 (2007)
220. B. Leung et al., Phys. Status Solidi (C) **11**, 437 (2014)
221. L. Zhang et al., J. Electron. Dev. Soc. **3**, 457 (2015)
222. M. Wosko et al., J. Crystal Growth **414**, 248 (2015)
223. F. Semond, MRS Bull. **40**, 412 (2015)
224. Y. Chubachi et al., Thin Solid Films **122**, 259 (1984)
225. W.J. Meng et al., **59**, 2097 (1991)
226. K.S. Stevens et al., Appl. Phys. Lett. **65**, 321 (1994)
227. P. Kung et al., Appl. Phys. Lett. **66**, 2958 (1995)
228. H.J. Wen et al., J. Vac. Sci. Technol. A **13**, 2399 (1995)
229. E. Calleja et al., J. Appl. Phys. **82**, 4681 (1997)
230. A. Bourret et al., J. Appl. Phys. **83**, 2003 (1998)
231. H.P.D. Schnek et al., J. Crystal Growth **201/202**, 359 (1999)
232. M.H. Kim et al., Appl. Phys. Lett. **78**, 2858 (2001)
233. D. Xi et al., Phys. Status Solidi (A) **191**, 137 (2002)
234. R. Liu et al., Appl. Phys. Lett. **83**, 860 (2003)
235. K.Y. Zang et al., Phys. Status Solidi (C) **0**, 2067 (2003)
236. K.Y. Zang et al., J. Crystal Growth **268**, 515 (2004)
237. F. Schulze et al., J. Crystal Growth **272**, 496 (2004)
238. G.P. Dimitrakopulos et al., Phys. Status Solidi (B) **242**, 1617 (2005)
239. G. Radtke et al., Appl. Phys. Lett. **97**, 251901 (2010)
240. G. Radtke et al., Appl. Phys. Lett. **100**, 011910 (2012)
241. Y. Dai et al., J. Crystal Growth **435**, 76 (2016)
242. S. Kaiser et al., J. Vac. Sci. Technol. B **18**, 733 (2000)
243. Y. Han et al., J. Crystal Growth **434**, 123 (2016)
244. H. Bin-Bin et al., Acta Phys. Sin. **64**, 177804 (2015)
245. T. Yamaguchi et al., Phys. Stat. Sol. (c) **1–4** (2013)
246. Y. Kawai et al., ISPlasma2013 (Nagoya Univ., March), Tup-B06OB
247. S. Chen et al., Jpn. J. Appl. Phys. **52**, 021001 (2013)
248. Y. Tsutsumi et al., ISPlasma 2014 (Nagoya Univ., March) 06aP46
249. H. Kondo et al., *Proceedings of 7th International Symposium on Advanced Plasma Science and Its Applications for Nitrides and Nanomaterials/8th International Conference on Plasma˙ Nanotechnology and Science*, (Nagoya University, Aichi, Japan, 2015), B1-I-01
250. Y. Cordier et al., *Proceedings of 18th European Molecular Beam Epitaxy Workshop* (Canazei, Italy, 2015) Tu1.4
251. O. Oda et al., *Proceedings 3rd International Conference on Advanced Electronic Materials* (ICAE2015) (ICC JeJu, Korea, 2015)
252. K.-C. Shen et al., Opt. Express **21**, 26468 (2013)
253. S. Bakalova et al., Vacuum **84**, 155 (2010)
254. H. Takahashi et al., Thin Solid Films **457**, 114 (2004)
255. S. Zembutsu, T. Sasaki, Appl. Phys. Lett. **48**, 870 (1986)
256. S.W. Choi et al., J. Mater. Res. **8**, 847 (1993)
257. M. Sato, J. Appl. Phys. **78**, 2123 (1995)
258. M. Sato, Appl. Phys. Lett. **68**, 935 (1996)
259. C. Sone et al., Mater. Res. Soc. Symp. Proc. **449**, 95 (1997)
260. J. Wang et al., J. Crystal Growth **177**, 181 (1997)
261. T. Tokuda et al., J. Crystal Growth **173**, 237 (1997)
262. T. Tokuda et al., J. Crystal Growth **183**, 62 (1998)
263. C. Sone et al., J. Crystal Growth **189**(190), 321 (1998)
264. W-C. Lai et al., Jpn. J. Appl. Phys. Part 1 **37**, 5465 (1998)
265. M. Losurdo et al., Phys. Status Solidi A **176**, 733 (1999)
266. Y-K. Pu et al., Surf. Coat. Technol. **131**, 470 (2000)
267. A. Wakahara et al., J. Crystal Growth **221**, 305 (2000)

268. R.A. Sugianto et al., J. Crystal Growth **221**, 311 (2000)
269. A. Subagio et al., Proc. ITB **33**, 1 (2001)
270. R. P. Campion et al., Phys. Status Solidi A **188**, 663 (2001)
271. C. Martin et al., Proc. SPIE **6894**, 689407 (2008)
272. S. Fu et al., J. Crystal Growth **311**, 3325 (2009)
273. S. Fu et al., Vacuum **86**, 1517 (2012)
274. Y. Lu et al., J. Crystal Growth **391**, 97 (2014)
275. H-Y. Shih et al., Nanotechnology **26**, 014002 (2015)
276. T. Mitsunari et al., J. Crystal Growth **431**, 60 (2015)
277. J.W. Shon et al., Sci. Rep. **4**, 5325 (2014)
278. C.-C. Li, D.-H. Kou, J. Mater. Sci. **25**, 1404 (2014)
279. Z.X. Zang et al., J. Alloys Comp. **467**, 61 (2009)
280. H.W. Kim, N.H. Kim, Appl. Surf. Sci. **236**, 192 (2004)
281. C.-C. Li, D.-H. Kou, J. Mater. Sci. **25**, 1942 (2014)
282. T. Yamada et al., Jpn. J. Appl. Phys. **52**, 08JB16 (2013)
283. D.M.G. Leite et al., Braz. J. Phys. **36**, 978 (2006)
284. T. Kumada et al., Phys. Status Solidi **3–4**, 515 (2012)
285. K. Sato et al., Appl. Phys. Exp. **2**, 011003 (2009)
286. C.G. Zhang et al., J. Crystal Growth **299**, 268 (2007)
287. E.C. Knox-Davies et al., J. Appl. Phys. **99**, 073503 (2006)
288. T. Miyazaki et al., J. Appl. Phys. **97**, 093516 (2005)
289. Y. Daigo, N. Mutsukura, Thin Solid Films **483**, 38 (2005)
290. E.C. Knox-Davies et al., Diam. Rel. Mater. **12**, 1417 (2003)
291. T. Kikuma et al., Vacuum **66**, 233 (2002)
292. J. Lee et al., J. Korean Phys. Soc. **67**, 1838 (2015)
293. H. Ishikawa et al., Jpn. J. Appl. Phys. **42**, 6413 (2003)
294. http://www.sanken-ele.co.jp/prod/semicon/led/led_f/gan.htm
295. K. Orita et al., IEEE J. Quant. Electron. **44**, 151 (2008)
296. X. Zou et al., IEEE Trans. Electron Dev. **63**, 1587 (2016)
297. H. Li et al., Appl. Phys. Express **9**, 042101 (2016)
298. Y. Sun et al., Nat. Photonics (2016). doi:10.1038/nphoton.2016.158
299. D. Zhu et al., Rep. Prog. Phys. **76**, 106501 (2013)
300. A. Dadger, Phys. Status Solidi (B) **252**, 1063 (2015)

Chapter 4
Epitaxial Growth of GaN on Patterned Sapphire Substrates

Kazuyuki Tadatomo

Abstract This chapter describes the Patterned Sapphire Substrate (PSS). First, the properties and the fabrication process of the PSS are described. Then, the mechanism to decrease the dislocation density in the crystal growth of GaN layer on the PSS is elaborated. Third, the principle of the improvement in the LEE of the GaN-LEDs fabricated on the PSS is explained. Finally, the novel application of the PSS to grow nonpolar and semipolar GaN layers is introduced.

4.1 Introduction

Low-carbon society and sustainable development of society are becoming the most important issue for survival of human beings. In this meaning, high-efficiency solid state lighting technology is one of the significant energy saving technologies. Recently, white light-emitting diodes (LEDs) with high luminous efficacy (η_L) of 249 lm/W and high luminous flux (Φ_V) of 14.4 lm at a forward-bias current of 20 mA were developed by using yellow phosphors $\{(Y_{1\text{-}a}Gd_a)_3(Al_{1\text{-}b}Ga_b)_5O_{12}$: Ce^{3+} (YAG)} and blue GaN-based LEDs (GaN-LEDs) dies fabricated on the break-though technique of “patterned sapphire substrate (PSS)” [1]. The highest luminous efficacy of commercialized white LEDs is 170 lm/W, which is the highest luminous efficacy among all kinds of white light sources.

Briefly, the PSS is the sapphire substrate with micrometer-sized or sub-micrometer-sized artificial structures on its surface, which contributes to improve the internal quantum efficiency (IQE) and the light extraction efficiency (LEE) of the GaN-based LEDs (GaN-LEDs) [2]. On the one hand, the IQE is improved by the reduction of threading dislocation density by selective-area growth (SAG) and by epitaxial lateral overgrowth (ELO) of GaN layers on the PSS. On the

K. Tadatomo (✉)
Graduate School of Science and Engineering, Yamaguchi University,
2-16-1 Tokiwadai, Ube, Yamaguchi 755-8611, Japan
e-mail: tadatomo@yamaguchi-u.ac.jp

© Springer Nature Singapore Pte Ltd. 2017

T.-Y. Seong et al. (eds.), *III-Nitride Based Light Emitting Diodes and Applications*,
Topics in Applied Physics 133, DOI 10.1007/978-981-10-3755-9_4

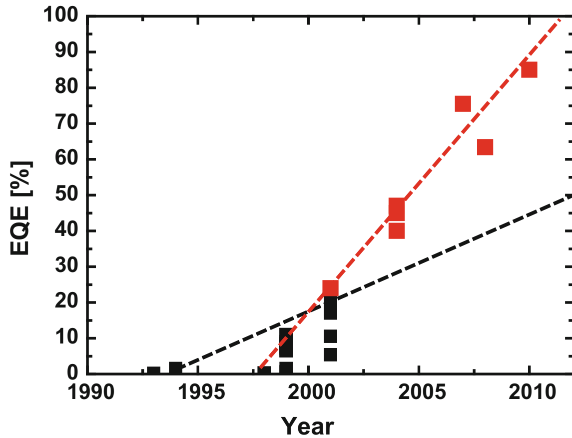

Fig. 4.1 History of the improvement of EQE of GaN-LEDs

other hand, the LEE is improved by the photon scattering at the uneven GaN/sapphire interface.

Figure 4.1 shows the history of the external-quantum efficiency (EQE) of the GaN-LEDs [1–12]. The improvement rate of the EQE after 2001 is larger than that of the years before, because almost all GaN-LEDs are fabricated on the PSS after the year when the PSS was published [2].

In this chapter, the properties and the fabrication process of the PSS are described firstly in Sect. 4.2. Then, the mechanism to decrease the dislocation density in the crystal growth of GaN layer on the PSS is elaborated in Sect. 4.3. Third, the principle of the improvement in the LEE of the GaN-LEDs fabricated on the PSS is explained in Sect. 4.4. Finally, the novel application of the PSS to grow nonpolar and semipolar GaN layers is introduced in Sect. 4.5.

4.2 Properties and Fabrication of PSSs

The PSS technique was derived from the ELO technique, which leads to grow the GaN with lower dislocation density on the PSS. Furthermore, the PSS improves the LEE of GaN-LEDs. The advantages of the GaN layer and the GaN-LEDs on PSS are summarized in Table 4.1 in comparison with the GaN layer (GaN-LEDs) by ELO techniques. The substantial advantage of the PSS technique is that the device structure is grown with a single metal-organic vapor phase epitaxy (MOVPE) growth process without any mask, which cannot be avoided in the conventional ELO process. Therefore, the PSS technique is contamination-free from the mask material such as SiO_2. Additionally, a single growth process gives economical advantage because of shorter growth time. The ELO technique itself has no positive effect to improve the LEE of the GaN-LEDs.

Table 4.1 Advantages of GaN layer and GaN-LEDs on PSS in comparison with those by ELO technique

Item	PSS technique	ELO technique
Growth	• A single growth process of MOVPE • Without any mask	• More than two times growth process of MOVPE • Mask is vital
Production cost	• Shorter growth time	• Longer occupation time of MOVPE • Masking process and machines
Impurity	• No mask material contamination	• Possible contamination from mask material
Dislocation density	• Dislocation density: on average 1×10^{8} cm^{-2}	• Dislocation density: partially 10^{4}–10^{5} cm^{-2}
Availability	• Applied to almost all GaN-LEDs	• Applied to GaN substrate for laser diodes

The PSS is usually fabricated through standard photolithography, inductively coupled plasma reactive ion etching system (ICP-RIE), and water cleaning process. Figure 4.2 shows the sequence of the process thereof. Majority of lithography exposure equipment in manufacturing process is projection stepper or high resolution mask aligner. The photoresist pattern is transferred to the surface structure of the sapphire substrate by ICP-RIE as shown in Fig. 4.2d. The etching gases, such as BCl_3 and/or Cl_2, and inert gas, such as Ar, are used. The typical etching rate is about 100 nm/min, but the rate depends on the etching conditions and type of etchers. The shape of the structure on the PSS is controlled by the sapphire-etching rate and the selective ratio (etching rate of photoresist/etching rate of sapphire substrate) depending on the kind of photoresist, baking conditions, and etching conditions.

The residual photoresist and foreign materials deposited during etching process are removed using water cleaner. Water cleaning process is of following steps; first step: to immerse the PSS in Piranha solution ($H_2SO_4 + H_2O_2$) at 120 °C for 10 min, second step: to immerse the same in SC2 solution ($HCl + H_2O_2$) at 40 °C

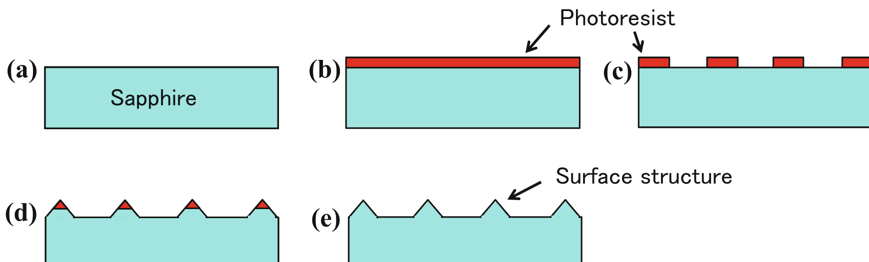

Fig. 4.2 PSS-manufacturing process. **a** Sapphire substrate preparation. **b** Photoresist coating by spinner. **c** Photolithography by stepper and developer. **d** Dry etching by ICP-RIE. **e** Rinse and drying

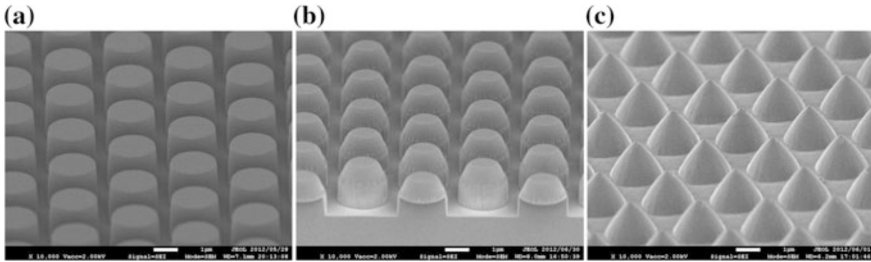

Fig. 4.3 Bird's eye view SEM images of every manufacturing stage of the PSS. **a** The sapphire substrate with columnar-shaped photoresist arranged hexagonal lattice pattern, **b** that of the cone-shaped PSS during ICP-RIE, and **c** that of the PSS after water cleaning

for 10 min, final step: to rinse with deionized water and drying with 2-propanol steam.

Figure 4.3 shows the bird's eye view scanning electron microscope (SEM) images of every manufacturing stage of the cone-shaped PSS. Typical height and diameter of the cones, and distance between the cones are 1.2 μm, 2.0 μm, and 3.0 μm, respectively. The typical PSS surface coverage by the cones is approximately 90%. The LEE of the GaN-LEDs increases in accordance with the increase in the surface coverage up to 90%. However, it is difficult to grow the high-quality GaN layer when the surface coverage exceeds 95%, because etched-flat *c*-plane surface is very important to supply the nucleation sites for the initial SAG and to allow subsequent overgrowth of the GaN layer on the PSS. Therefore, the surface coverage of around 90% is estimated to give the highest LEE.

4.3 Growth of GaN on PSS, and Properties of GaN-LEDs on PSS

4.3.1 SAG and ELO

The PSS technique has been derived from the SAG technique and the ELO technique as mentioned before. In this section, SAG and ELO techniques, which are the origins of the PSS, are reviewed.

The SAG is the technique which fabricates the controlled-structures of GaN such as lines and hexagonal pyramids [13, 14]. Kitamura et al. fabricated the hexagonal pyramids with six {10-11} facets grown on the *c*-plane GaN/sapphire template covered with the dot-patterned SiO_2 mask.

The original idea of the ELO was proposed by Nishinaga et al. to reduce the threading dislocation density of the GaAs layer grown on GaAs substrate and Si

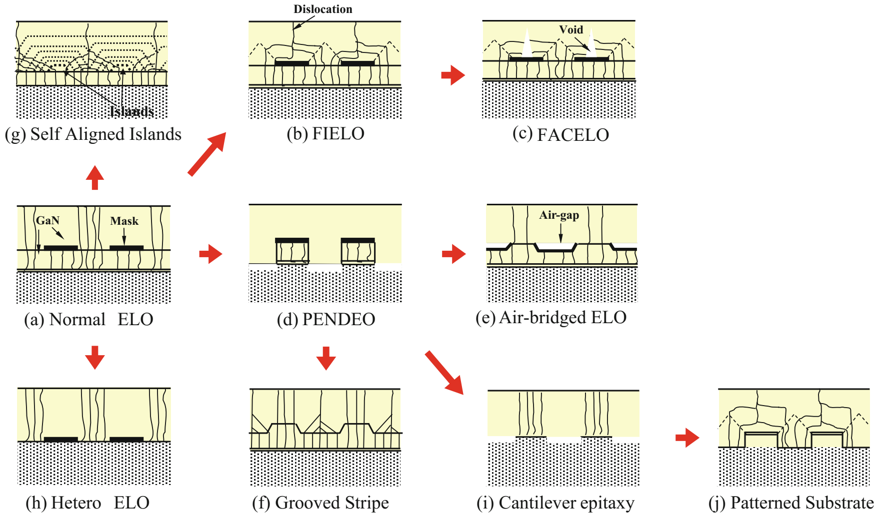

Fig. 4.4 Schematic diagram of various ELO techniques [17]

substrate using liquid phase epitaxy (LPE) [15, 16]. The ELO based on the SAG has attracted considerable attentions, because the ELO is a useful technique to reduce the threading dislocation density of the GaN layer grown on foreign substrate such as sapphire substrate. The various ELO techniques of the GaN layer developed by various researchers are summarized in Fig. 4.4 [17] and Table 4.2.

Here, two representative examples of the ELO techniques are introduced. First, Usui et al. applied the ELO technique to the GaN epitaxial growth on sapphire substrate (Fig. 4.4b) [18, 19]. They developed the break-through technique named facet initiated ELO (FIELO) by hydride vapor phase epitaxy (HVPE). It was revealed that the inclined facet structure formed during FIELO bent the propagation direction of dislocations, resulting in reducing the threading dislocation density. They obtained the GaN layer on SiO_2 mask with a low-dislocation density of the order of 10^7 cm^{-2}. Second, the ELO using grooved substrate was developed by Detchprohm et al. [20–22] (Fig. 4.4i). In the ELO techniques using grooved substrate, GaN layer only grew on the terrace of the grooved substrate and extended the wing on the trench. The dislocation density of the wing area of the GaN was less than 4×10^6 cm^{-2} [21].

Tadatomo et al. developed basic technique of the standard PSS as shown in Fig. 4.4j. They made the stripe-trench-patterned PSS with the depth of more than 1 μm by ICP-RIE using the photoresist mask. Furthermore, they grew the GaN layer not only on the terrace but also on the bottom of the trench. Then, they have succeeded in fabricating high-efficiency GaN-LEDs on the PSS due to the photon scattering at the uneven GaN/sapphire interface.

Table 4.2 Representative ELO techniques

Figure no.	Name/Affiliation/National	Characteristics	References
(a)	Nishinaga et al. Nagoya University, Japan	• Normal ELO, GaAs on GaAs (Si) substrate, LPE	[15, 16]
(a)	Nam et al. North Carolina State University The United State of America	• Normal ELO, SiC substrate, MOVPE	[68]
(b)	Usui et al. NEC Japan	• FIELO (Facet Initiated ELO) • HVPE (Hydride Vapor Phase Epitaxy) • Inclined facet structure during FIELO bent the propagation direction of dislocations • Reduced threading dislocation density	[18, 19]
(c)	Hiramatsu et al. Mie University Japan	• FACELO (Facet Controlled ELO) technique • FACELO is based on the control of GaN facet by growth conditions • Void decreases dislocation density because void terminates the laterally bent dislocations	[69–71]
(d)	Linthicum et al. North Carolina State University The United State of America	• PENDEO (from the Latin: pendeo—to hang, or to be suspended)	[72, 73]
(e)	Kidoguchi et al. Panasonic Corporation, Japan	• Air-bridged ELO (ABLEG) • Laser diodes were achieved	[74, 75]
(f)	Ishida et al. Panasonic Corporation, Japan	• GaN on sapphire substrate template with grooved stripe • Ultraviolet laser diodes were achieved	[76, 77]
(g)	Lahreche et al. (representative) CNRS, France	• Self-organized ELO • Dislocation density was reduced • GaN buffer layer grown at low-temperature technique is included in this group [78]	[78–80]
(h)	Sakai et al. (representative) Tokushima University, Japan	• Direct ELO using the sapphire substrate with SiO_2 mask	[81, 82]
(i)	Detchprohm et al. Nagoya University, Japan	• Cantilever epitaxy using grooved substrate • GaN growth only on the terrace of the grooved substrate • Dislocation density of the wing area $< 4 \times 10^6$ cm^{-2}	[20–22]
(j)	Mitsubishi Cable Industries, Japan Tadatomo et al.	• Basic patterned sapphire substrate (PSS)	[2]

4.3.2 GaN Growth on PSS and the Mechanism of Decreasing Dislocation Density by ELO

The commercially available high-efficiency GaN-LEDs is fabricated on the PSS by MOVPE. The growth conditions of the GaN layer on the PSS are almost the same as those of growth on the flat sapphire substrate (FSS). Figure 4.5 depicts a schematic structure of the standard GaN-LEDs on the PSS fabricated. The detailed GaN-LED structure is shown in Table 4.3.

The p-type GaN layer is partially etched until the n-type GaN layer is exposed. A 100-nm-thick transparent indium–tin oxide (ITO) is used as electrode and current-spreading layer to p-type GaN layer. The transmittance of the ITO is more than 95% at the wavelength range from 400 to 800 nm. A Cr/Au (20/200 nm) layer is deposited on exposed n-type GaN layer and on the partial ITO contact as a pad electrodes. Finally, SiO_2 passivation layer is deposited by plasma-enhanced chemical vapor deposition (PE-CVD) in order to reduce the surface leakage current.

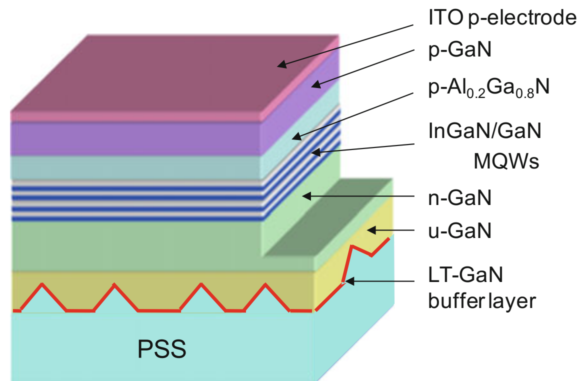

Fig. 4.5 Schematic structure of the GaN-LED on the PSS

Table 4.3 Detailed LED structure

Layer	Growth temperature (°C)	Thickness	Doping
p-type contact layer	1050	80 nm	Mg: 2×10^{19} cm^{-3}
p-type $Al_{0.2}Ga_{0.8}N$ electron blocking layer	1050	20 nm	Mg: 5×10^{19} cm^{-3}
InGaN/GaN multiple quantum well (MQW)	780–820	InGaN/GaN: 2-nm-thick/12-nm-thick	Si in GaN barrier: 1×10^{18} cm^{-3}
n-type GaN layer	1150	4 μm	Si: 2×10^{18} cm^{-3}
Unintentionally doped GaN layer	1150	3 μm	–
GaN buffer layer grown at low-temperature	480°	20 nm	–
Sapphire substrate	–	430 μm	–

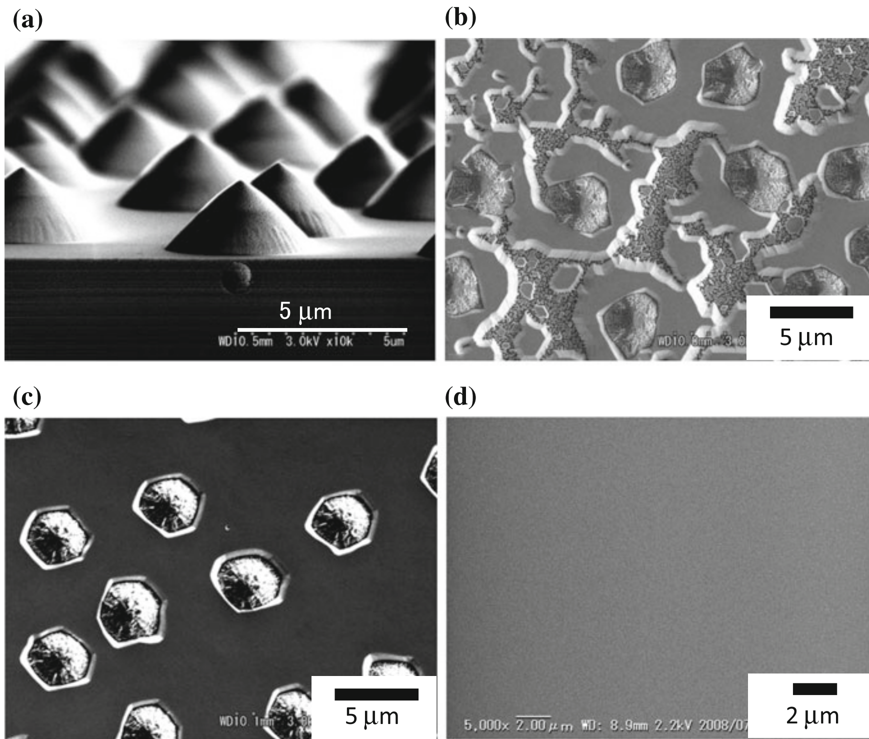

Fig. 4.6 The bird's eye-view or the plan-view SEM images of GaN layer on the RC-PSS at various growth times: **a** before growth, **b** 12 min growth, **c** 24 min growth, and **d** 36 min growth [23]

Figure 4.6 shows the plane-view SEM images of the GaN layer grown on the PSS with randomly arranged-cone (RC-PSS) at the various growth times [23]. Figure 4.6a shows the plane-view SEM image of the RC-PSS before the MOVPE growth of GaN layer. Figure 4.6b, c show the SEM images of the GaN layer grown on the RC-PSS at the growth time of 12 min and 24 min, respectively. Figure 4.6b shows that the GaN grows from the etched-flat *c*-plane surface. Although the GaN deposited at low-temperature (LT-GaN) buffer layer is deposited not only on the etched-flat *c*-plane surface but also on the sidewall of the cones, the LT-GaN buffer on the sidewall evaporated or transported to the etched-flat surface during ramping to the high temperature for the growth of GaN, because *c*-plane GaN on the etched *c*-plane sapphire is more stable than that on the sidewall. Therefore, there is no nuclear GaN layer from LT-GaN buffer layer on the sidewall and the growth of GaN on the sidewall at high temperature does not occur. Figure 4.6c shows that the cones are embedded by the overgrowth of the GaN layer. Finally, the GaN layer with flat surface is obtained by embedding as shown in Fig. 4.6d. Figure 4.7 shows the magnified plane-view SEM image of the GaN layer shown in Fig. 4.6b. Slight growth of the GaN with sixfold symmetry on the sidewall is observed. Although the sidewall has no specific plane to grow the GaN, the GaN may grow on partially

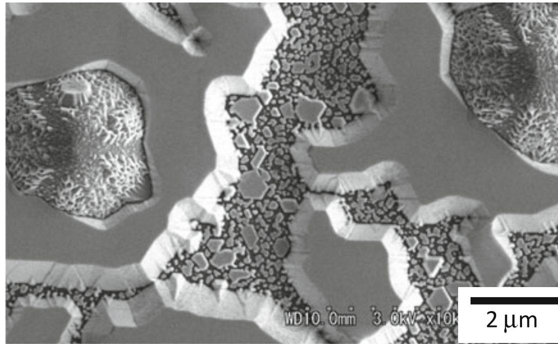

Fig. 4.7 The magnified plan-view SEM image of Fig. 3.3b [23]

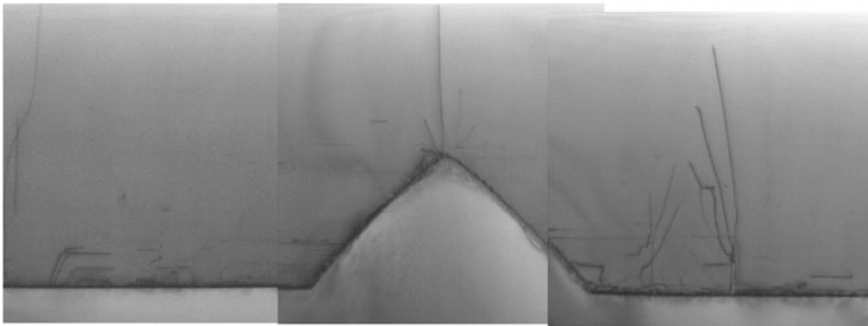

Fig. 4.8 Cross-sectional TEM image of GaN layer grown on the RC-PSS [23]

exposed planes such as *n*-plane. The growth rate of the GaN around the cone is higher than that away from the cone. It is estimated that the migration of the ad-atoms such as Ga atoms from the cones contributes to the growth of GaN layer.

Figure 4.8 shows a cross-sectional transmission electron microscope (TEM) image of the GaN layer grown on the RC-PSS. This TEM image reveals the dislocation behavior during the growth of the GaN layer on the PSS. Some dislocations generated at the GaN/sapphire interface are bent laterally and terminated at the inclined sidewall of the cone. No dislocation is generated from the inclined sidewalls because GaN does not grow on the sidewall. Dislocations generated at the top of the cone are observed because the laterally overgrown GaN layer coalesced on the top of the cone.

The growth of GaN layer initiates from the etched-flat and narrow area, which is a kind of the SAG. In conclusion, when considering the dislocation behaviors and the growth modes, the decrease of the dislocation density of the GaN layer on the PSS is due to the combination of SAG and ELO. On the other hand, in the etched-flat region away from the cones, the dislocation density of the GaN layer is same as that on the FSS. Therefore, the average dislocation density of the GaN layer on the PSS is lower than that on the FSS.

4.3.3 Characteristics of LEDs Grown on PSS

The output power of the GaN-LEDs fabricated on the PSS is usually 30–50% larger than that of GaN-LEDs on the FSS. For example, the output power of the packaged GaN-LEDs on the RC-PSS with the wavelength of the approximate 420 nm is 1.34 times larger than that on the FSS with the same LED structure at a forward-bias current of 20 mA. The output power and the EQE of the packaged GaN-LEDs measured by an integrating sphere systems are 29.6 mW and 49.5% at forward-bias current of 20 mA, respectively. The EQE decreases markedly with increasing injection current, which is well known as "efficiency droop phenomena." The maximum EQE of 75% is observed at a forward-bias current of 0.5 mA.

The EQE is a product of the IQE and the LEE as described in the following formula (4.1).

$$EQE = LEE \times IQE \tag{4.1}$$

Although, it is not easy to measure the LEE and the IQE directly, the IQE can be estimated by the relationship between excitation power density and temperature-dependent photoluminescence (PL) [24]. The GaN-LEDs on the RC-PSS is characterized under selective excitation conditions using a dye laser with a peak wavelength of 385 nm [23]. As a result, the IQE is estimated to be approximately 57%, which is the maximum PL quantum efficiency at room temperature, assuming that the PL quantum efficiency at a cryogenic temperature of 7 K is 100% [24]. At this excitation condition, the photo-excited carrier density is estimated to be nearly equal to the injected-carrier density at 20 mA [24]. The LEE is estimated to be 86.8%, which is EQE (49.5%) divided by IQE (57%), due to the formula (4.1).

4.4 The Principle of Light Extraction Efficiency Improvement of GaN-Based LEDs by Patterned Sapphire Substrate

4.4.1 Impact of Surface Structure of LEDs on Light Extraction Efficiency Improvement

It has been well known that there is a significant gap between the IQE and the EQE of the LEDs since the research and development of GaAs-based LEDs (GaAs-LEDs) have started [25]. For example, the IQE of the GaAs-LEDs with double hetero-structures exceeds 99%, but the EQE is only a few percent. The reason for this gap is the narrow escape cone for photons emitted in the LEDs due to high-refractive index of the semiconductor. The escape cone is defined by the critical angle (ϕ_c) of the total internal reflection at the semiconductor/surrounding

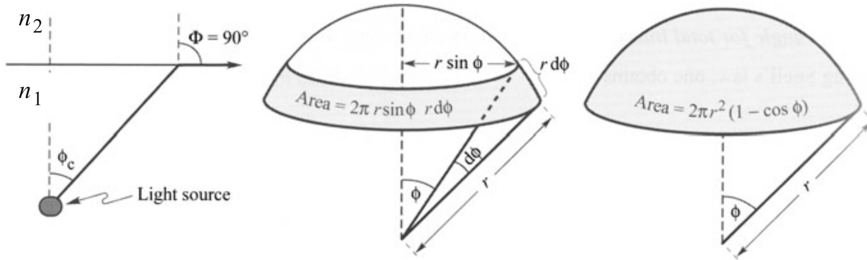

Fig. 4.9 Schematic drawings of escape cone [26]: **a** Definition of the critical angle ϕc of the total internal reflection phenomena. **b** Area element dA. **c** Area of dome-shaped section of the sphere defined by radius r and angle ϕ

material interface. The critical angle of the total internal reflection is described in formula (4.2) by Snell's Law, where n_1: the refractive index of the semiconductor, and n_2: that of surrounding material.

$$\phi_c = \sin^{-1}\left(\frac{n_2}{n_1}\right) \tag{4.2}$$

Because the area of escape cone, where photons can escape from a semiconductor, is

$$2\pi r^2(1 - \cos\phi_c)$$

as shown in Fig. 4.9 [26], the ratio of the escaped photons to all the generated photons at the surface, i.e., the escape ratio (η_c), is described as following formula (4.3).

$$\eta_c = \frac{(1 - \cos\phi_c)}{2} \tag{4.3}$$

For example, in the case of the GaAs ($n_1 = 3.5$) in the air ($n_2 = 1.0$), the critical angle (φ_c) of the total internal reflection and the escape ratio (η_c) at the surface are 16° and 0.02, respectively.

Due to the small escape ratio, many photons are trapped in the planar semiconductor layer as shown in Fig. 4.10a. When the semiconductor layer has textured surface, the photons emitted out of the escape cone originally scatter at the textured surface to get the opportunities to enter into the escape cone as shown in Fig. 4.10b. Thus, the surface structure enhances the LEE of the semiconductor layer. It is essential to destruct the cavity structure trapping photons and to give photons multiple chances to escape from the layer. Therefore, a lot of studies such as the surface-textured LEDs [25, 27], the hemispherical-domed LEDs [28], truncated-inverted-pyramid LEDs [29], etc., have been carried out.

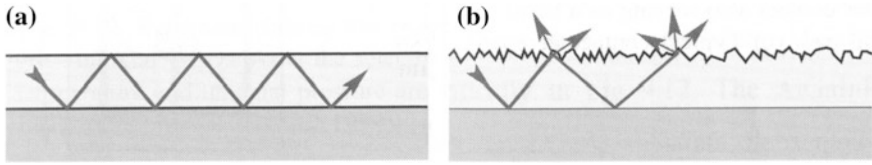

Fig. 4.10 Illustrated photon trajectories: **a** in the planar layer and **b** in the layer with surface structure [25, 26]

4.4.2 The Principle of Light Extraction Efficiency Improvement of GaN-Based LEDs by Patterned Sapphire Substrate

In the case of GaN-LEDs fabricated on a FSS, the critical angle (ϕ_c) and the escape ratio (η_c) at air (n_2 = 1.0)/GaN layer (n_1 = 2.5) interface by formulae (4.2) and (4.3) are 24° and 0.042, respectively. On the other hand, the critical angle and the escape ratio at the GaN layer (n_1 = 2.5)/sapphire (n_2 = 1.7) are 43° and 0.13, respectively. Because the GaN-LEDs have five air/GaN layer interfaces with escape ratio of 0.042 and one GaN layer/sapphire interface with escape ratio of 0.13, the LEE is estimated to be 0.34 by simple calculation. Although the critical angles and the escape ratios at air/GaN layer interface and GaN layer/sapphire interface are larger than those at GaAs/air interface, more than 60% of the emitted photons in the InGaN wells are still trapped in the GaN layer as shown in Fig. 4.11a [1].

The surface structure of the PSS, such as cone-shaped, plays the same role of the surface structure described in the preceding section. To put it more concrete, the structure on the PSS effectively scatters photons emitted out of escape cone and gives them multiple chances to enter the escape cone, and the surface structure with inclined sidewall facilitates the penetration of photon at the interface as shown in Fig. 4.11b. Due to the low-refractive index of a sapphire substrate, photons escape from the sapphire easily. Thus, the PSS improves the LEE of the GaN-LEDs.

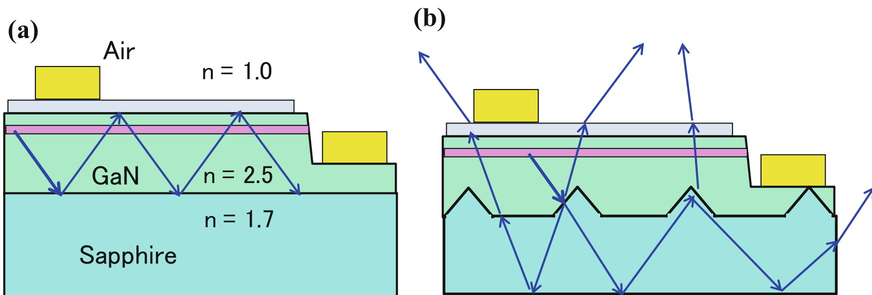

Fig. 4.11 The schematic cross-sectional LED structure and photon trajectories: **a** LED fabricated on a FSS. **b** LED fabricated on a PSS

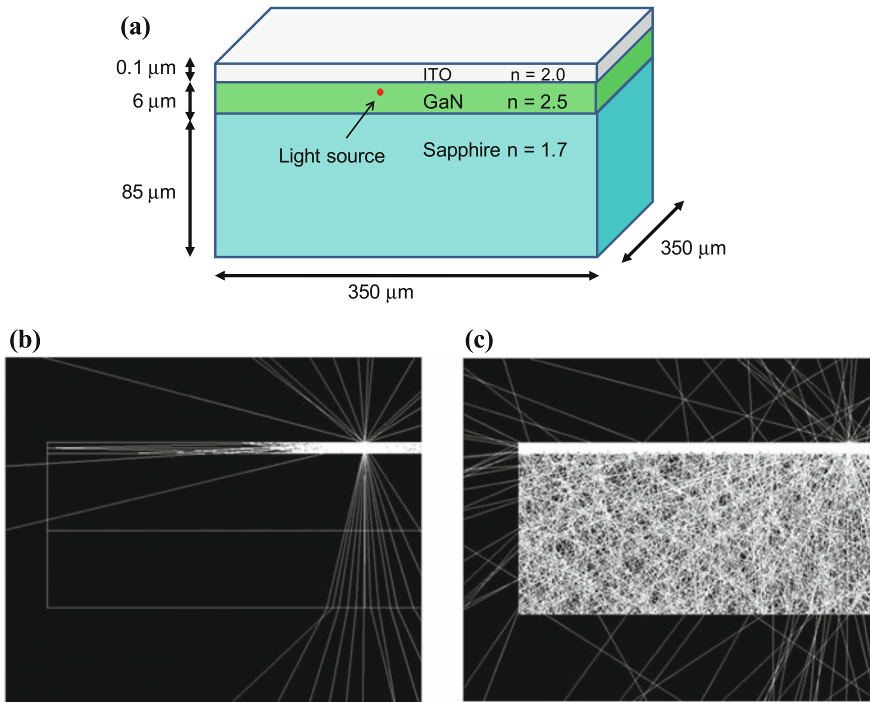

Fig. 4.12 The ray-tracing simulation: **a** Schematic sample structure for simulation. **b** Result of GaN layer on a FSS. **c** Results of GaN layer on the stripe-trench-patterned PSS

Figure 4.12 shows the schematic sample structure for ray-tracing simulation and the results of simulation. The layer structure and the size of the samples are same as GaN-LED chip. One sample is designed on a FSS and the other on the stripe-trench-patterned PSS. The light source is set in the center of MQW only and the sample is set in the air in order to simplify as shown in Fig. 4.12a. Many of photons emitted from MQW are trapped in the GaN layer grown on the FSS and only the photons emitted within the escape cone escape from the sample as shown in Fig. 4.12b, c shows many of photons escape through the PSS into the air, resulting in the improvement of the LEE.

4.4.3 Development of PSS with Micrometer-Sized Structures

The PSS was first reported by Tadatomo et al. in 2001 as mentioned before [2]. The reported GaN-LEDs were fabricated on the stripe-trench-patterned PSS, which direction was along *m*-axis of sapphire. The EQE of the GaN-LEDs, which were

mounted on flip chip package, was 24% at the peak wavelength of 382 nm [2, 30] and 43% at 403 nm [31, 32] at forward-bias current of 20 mA. The dislocation density of the GaN layer grown on the PSS estimated by counting dark spots in the cathodeluminescence (CL) is approximately 1.5×10^8 cm^{-2}, which is approximately one third of that on the FSS.

After 2001, there has been paid great attention in the PSS technique, and the EQE has been improved drastically. Yamada et al. developed hexagonal-patterned PSS [33]. The EQE of the blue GaN-LEDs with the wavelength of 460 nm fabricated on the hexagonal PSS was 35.5% at forward-bias current of 20 mA. The investigation of surface structures with holes, semi-spheres, pyramidal structures, cone array, random-cone, etc., followed by others [34–36]. New lithography technique using polystyrene microspheres instead of photolithography, so-called natural lithography, was also reported to fabricate random-cone-shaped PSS [23]. Wet etching process instead of ICP-RIE was reported as well to fabricate the PSSs [35–39]. Figure 4.13 shows the typical PSSs with micrometer-sized-structures investigated in this trend. The method and properties of the representative PSSs are also summarized in Table 4.4.

4.4.4 Development of PSS with Sub-micrometer-Sized Structures

As mentioned in the preceedings, the PSS with micrometer-sized surface structure improves the LEE of the GaN-LEDs due to extensive scattering of the photons trapped in the GaN layer by the total internal reflection phenomena. When the size and period of the lattice array structure on the sapphire substrate decreases to smaller level of the sub-micrometer, so-called nano-structure, the LEE will be expected to increase more due to diffraction or photonic crystal (PhC) effect instead of photon scattering effect.

Generally, a PhC is fabricated by the artificial periodic structure with a different refractive index from that of the surrounding material. In the PhC, a band structure of photon energy, which is called “photonic bandgap”, is formed due to the artificial periodic structure. In two-dimensional PhC (2D-PhC), the photons having the energy within the photonic bandgap do not propagate along the 2D-PhC. Therefore, if the 2D-PhC is fabricated in the LEDs, the photons which propagate only perpendicular to the 2D-PhC are emitted by the electron-hole radiative recombination, because photons cannot propagate along the 2D-PhC. To put it simple, the photons originally emit in the escape cone, then the LEE of the GaN-LEDs with 2D-PhC is expected to be improved.

To realize the 2D-PhC and/or to improve the LEE, several researches of the GaN-LEDs with sub-micrometer-sized structure PSS have been carried out.

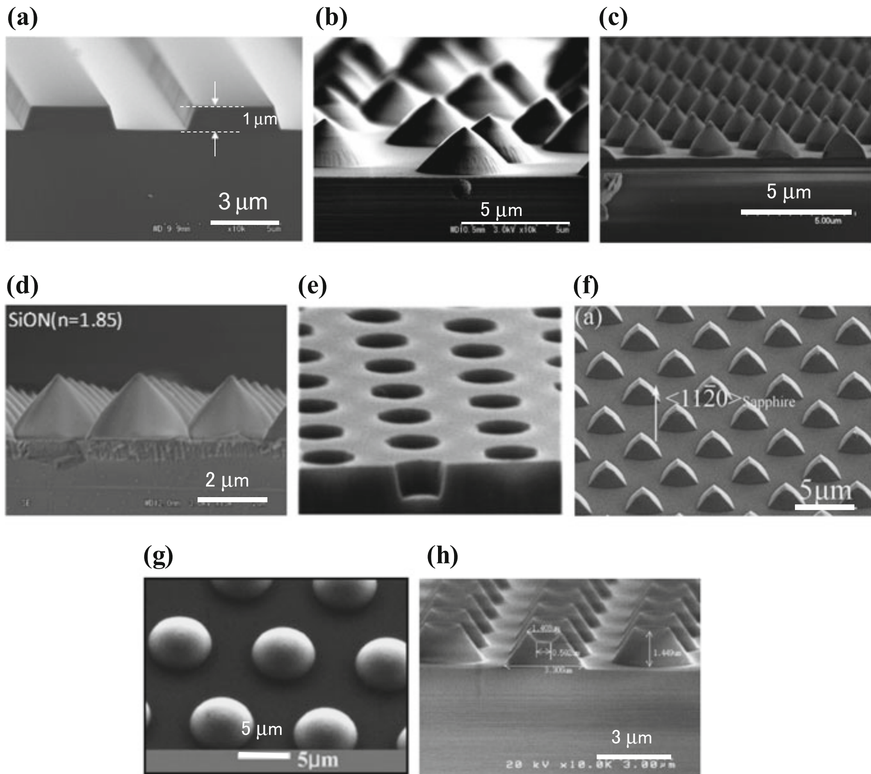

Fig. 4.13 Bird's eye-view SEM images of representative PSSs: **a** stripe-trench-patterned PSS, **b** random-shaped-cone PSS, **c** standard cone PSS, **d** refractive index-controlled PSS, **e** hole-arrayed PSS [66], **f** pyramidal PSS by wet etching [38], **g** hemispherical PSS [36], and volcano type PSS [67]. The SEM images from (**a**) to (**d**) are provided by courtiers of Yamaguchi University

Table 4.5 summarizes the typical results of the application of the sub-micrometer-sized structure PSS to the GaN-LEDs. The majority of the researches incorporate with the surface structures on the chips, such as p-type GaN layer or transparent ITO contact, which were fabricated by electron beam lithography and RIE [40–42]. Some researches have achieved sub-micrometer-sized structure PSS using laser holography [43] or nano-imprint lithography (NIL) [44, 45] and ICP-RIE, and have tried to apply the PhC-LEDs. But, PhC-PSS is currently still under investigation.

Figure 4.14a shows the bird's eye view of SEM image of nano-PSS. The sub-micrometer-sized structure PSS, which has the hexagonally arranged pillars with the diameter of 200 nm, was fabricated by NIL and ICP-RIE. The period, the diameter, and the height of the arranged pillar structure are 400 nm, 200 nm, 200 nm, respectively. The far field pattern of the GaN-LEDs fabricated on the

Table 4.4 Representative sub-micrometer-sized PSSs. (Methods and properties of the PSS are summarized from papers published by those affiliations)

Year	Affiliation	Name	Methods and properties	References
2001	Mitsubishi Cable Industries, Japan	K. Tadatomo et al.	Photolithography and ICP-RIE	[2, 30]
			Stripe-trench-patterned PSS	
			Improvement of EQE = 24% at 382 nm	
2002	Nichia Corporation, Japan	M. Yamada et al.	Photolithography and ICP-RIE	[33]
			Hexagonal-patterned PSS	
			EQE = 35.5% (at 20 mA, 460 nm)	
2003	Mitsubishi Cable Industries, Japan	H. Kudo et al.	Photolithography and ICP-RIE	[31]
			Stripe-trench-patterned PSS	
			EQE > 43% (at 20 mA, 405 nm)	
2003	Mitsubishi Cable Industries, Japan	K. Tadatomo et al.	Stripe-trench-patterned PSS	[32]
			Improved LEE	
2003	National Cheng Kung Univ. Taiwan	S.J. Chang	Stripe-PSS	[83]
			Reduced dislocation density	
2005	National Chung Hsing Univ. Taiwan	W.K. Wang et al.	Photolithography and ICP-RIE	[66]
			Stripe-trench-patterned PSS	
2005	National Chiao Tung Univ. Taiwan	Y.J. Lee et al.	Photolithography and ICP-RIE	[34]
			Hole-arrayed PSS	
2006	Nichia Corporation, Japan	Y. Narukawa et al.	Photolithography and ICP-RIE	[10]
			PSS and ITO, EQE > 63% (at 20 mA, blue)	
2008	Yamaguchi Univ. Japan	K. Hoshino et al.	Photolithography and ICP-RIE	[84]
			Stripe-trench-patterned PSS, thick SiO_2 mask	
			Low-dislocation density	
2008	Chinese Academy of Science, China	H. Gao et al.	Photolithography (Self-assembled Ni mask) and wet etching, Pyramidal PSS	[38, 39]
			EQE of the LED on nano-PSS larger than that on micro-PSS	
2009	Yamaguchi Univ. Japan	N. Okada et al.	Natural lithography (Polystyrene sphere)	[23]
			Random-cone PSS	
			EQE = 50% (at 420 nm, 20 mA)	
2010	National Chung Hsing Univ. Taiwan	J.H. Cheng et al.	Photolithography and wet etching	[35]
			Triangle pyramidal array PSS	
2010	National Central Univ. Taiwan	Y.J. Chen et al.	Mask free wet etching	[37]
			Pyramidal PSS	
2010	Chonbuk National Univ. Korea	S.M. Jeong et al.	Photolithography and ICP-RIE	[36]
			Lens-PSS	
			Improved LEE	
2010	Korea Photonics Tech. Inst. Korea	J.B. Kim et al.	Photolithography and ICP-RIE	[67]
			Volcano-PSS	
2010	Nichia Corporation, Japan	Y. Narukawa et al.	Photolithography and ICP-RIE	[1]
			PSS and ITO, EQE > 84% (at 20 mA, blue)	

Table 4.5 Representative sub-micrometer-sized structure PSSs. (Fabrication methods and properties of PSS summarized from papers published by those affiliations.)

Year	Affiliation	Name	Method and property	References
2004	Panasonic Corporation, Japan	K. Orita et al.	Electron Beam Lithography and RIE	[40]
			PhC patterned on p-GaN Surface for Blue LED	
2006	Univ. California Santa Barbara, USA	A. David et al.	Electron Beam Lithography and RIE	[41, 42]
			Surface Patterning	
2008	National Cheng Kung Univ. Taiwan	Y.K. Su et al.	Polystyrene nano-sphere, followed by Ni evaporation, lift-off, and ICP-RIE	[85]
2009	National Central Univ. Taiwan	C.H. Chan et al.	SiO_2Nano-sphere and Wet Etching	[86]
2009	Seoul National Univ. Korea	J. Lee et al.	Laser Holography	[43, 87]
			2D PhC-PSS Lattice constant/diameter/height = 500 nm/230 nm/125 nm	
2010	National Cheng Kung Univ. Taiwan	C.C. Kao et al.	Nano-imprint Lithography	[44]
			Nano-PSS	
			Lattice constant/diameter/height (typical) = 500 nm/200 nm/200 nm	
2011	Rensselaer Polytechnic Inst. USA	Y. Li et al.	Nano-imprint Lithography	[45]
			Nano-PSS	
			Triple output power	

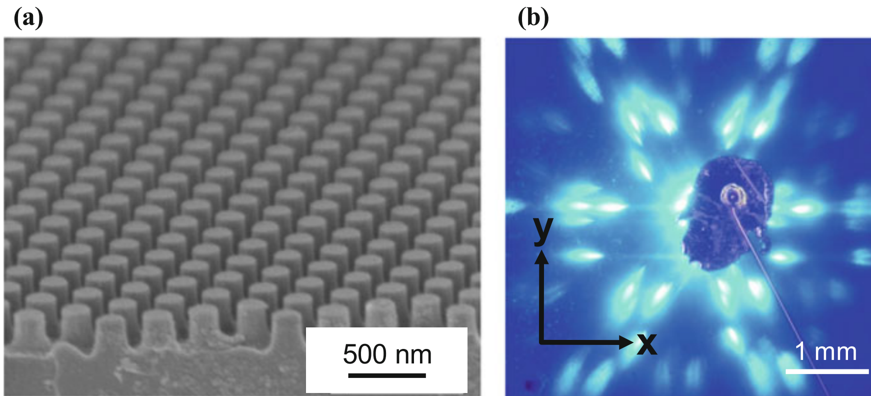

Fig. 4.14 **a** Bird's eye-view SEM image of nano-PSS. **b** Far field pattern of electroluminescence from GaN-LED on sub-micrometer-sized PSS. (Provided by courtiers of Yamaguchi University)

sub-micrometer-sized structure PSS at a forward-bias current of 20 mA before chip dicing is the sixfold symmetric diffraction pattern as shown in Fig. 4.14.

The output power towards the upper side of the GaN-LEDs fabricated on the sub-micrometer-sized PSS measured by probing system is two times larger than that of the GaN-LEDs on the micrometer-sized PSS. But the total radiant flux of the GaN-LED dies fabricated on the sub-micrometer-sized PSS structure measured by integral sphere system is nearly equal to that on micrometer-sized PSS. It is eagerly expected to optimize the sub-micrometer-sized structure PSS and to develop the PSS with 2D-PhC.

4.5 Novel Application of PSS to Growth of Nonpolar or Semipolar GaN

The commercialized GaN-LEDs fabricated on a polar *c*-plane GaN layer are under the quantum-confined Stark effect (QCSE) due to the polarization-induced large electric field such as piezoelectric field. The QCSE causes band bending in InGaN quantum well (QW) in multiple quantum wells (MQWs) and results in the electron-hole spatial separation. The QCSE is one of the reasons to decrease the IQE especially at long wavelength region and to cause so-called green-gap problem [46]. Usually, thin-InGaN-QW, around 3-nm-thick, is fabricated in the GaN-LEDs in order to enhance the overlap of the electron and hole wave-functions. This thin-InGaN-QW may be one of the possible suspected origins of "efficiency droop phenomenon" at the high injection current density [47, 48].

To overcome these problems, the GaN-LEDs fabricated on nonpolar GaN layer, such as *m*-plane, or semipolar GaN layer, such as {11-22} plane, have been investigated. The nonpolar and/or semipolar GaN have possibility to resolve the green-gap problem due to reduced QCSE in InGaN-QW [49]. Furthermore, thick-InGaN-QWs are available due to the reduced QCSE, which will result in reducing the efficiency droop due to lowered the carrier density in the thick-InGaN-QWs [50–52].

The high-quality *c*-plane GaN bulk crystal is fabricated by hydride vapor phase epitaxy (HVPE) [53]. The Na-flux solution method [54] and ammonothermal growth [55, 56] have been studied intensively to obtain the GaN bulk crystal. On the other hand, semipolar or nonpolar GaN substrates are usually obtained by slicing these GaN bulk crystals. Thus, these GaN substrates are small in size and expensive.

Nonpolar and semipolar GaN layers grown on the patterned Si substrates have been developed by SAG from the Si sidewall [57, 58]. However, there are many problems, such as the low transmittance of Si for the visible light. Thus, the development of large diameter, low-cost, transparent, and high-quality nonpolar and semipolar GaN substrate has been eagerly awaited.

The novel growth technique of nonpolar or semipolar GaN layers with large diameter and high quality on transparent PSS has been investigated. The nonpolar or semipolar GaN layer is grown from the sapphire sidewall of the PSS using SAG and ELO [59–65].

Figure 4.15 schematically shows the growth principle of nonpolar or semipolar GaN layer on the PSS. As an example, the growth of semipolar {11-22} GaN layer on the stripe-trench-patterned *r*-plane PSS is described in Fig. 4.15. The stripe-trench-pattern is formed perpendicular to the *c*-axis of the *r*-plane sapphire by conventional photolithography and the ICP-RIE. The exposed sidewall of the trench is *c*-plane-like, because the etched-sapphire-sidewall is not the exact *c*-plane. Because the angle of 57.61° between *r*-plane and the *c*-plane of a sapphire is similar to that of 58.41° between {11-22} plane and *c*-plane of GaN, *c*-plane GaN with {11-22} facets grows from *c*-plane-like sidewall of *r*-plane PSS, resulting in the growth of semipolar {11-22} GaN on *r*-plane PSS as shown in Fig. 4.15. The significant point of this technique is that *c*-plane GaN layer grows on *c*-plane-like sapphire sidewall and both *c*-axes are exactly parallel.

Furthermore, the {11-22} GaN with perfect flat surface grows on the 0.8°-off-angle *r*-plane PSS, because the {11-22} plane of the GaN layer is exactly parallel to the surface of 0.8°-off-angle *r*-plane sapphire substrate. The typical trench depth, the width, and the period are 1 μm, 3 μm, and 6 μm, respectively. In the case of {11-22} GaN growth on *r*-plane PSS, SiO_2 mask is not necessary on the terrace region of the PSS, because the growth rate of *c*-plane GaN on *c*-plane-like sapphire sidewall is larger than that of *a*-plane GaN on *r*-plane terrace region of *r*-plane PSS. The SiO_2 mask may be used to prevent the GaN growth on the terrace region of the PSS, when *n*-plane PSS on which c-GaN grows is used.

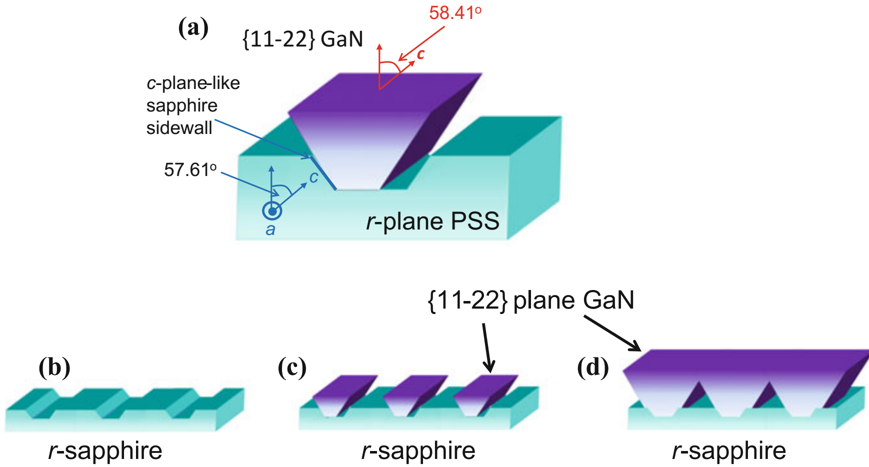

Fig. 4.15 Principle of the growth of semipolar {11-22} GaN on *r*-plane PSS: **a** Relationship between crystal orientations of GaN layer and sapphire substrate. **b** Stripe-trench-patterned *r*-plane PSS. **c** Initial stage of semipolar {11-22} GaN growth on the *r*-plane PSS. **d** Semipolar {11-22} GaN layer grown on the *r*-plane PSS

The cross-sectional SEM image of semipolar {11-22} GaN layer grown on *r*-plane PSS is shown in Fig. 4.16. The GaN layer is selectively and laterally grown from the *c*-plane-like-sapphire sidewall only, and forms a facet structure with {11-22} and -*c* (000-1) plane [60]. As seen in this Fig. 4.16, the GaN layer coalesced perfectly. Okada et al. report that the average threading dislocation density of {11-22} GaN layer is estimated to be approximately 2×10^8 cm^{-2} by counting dark spots in the cathodeluminescence (CL) images.

Fig. 4.16 Cross-sectional SEM image of {11-22} GaN layer grown on *r*-plane PSS

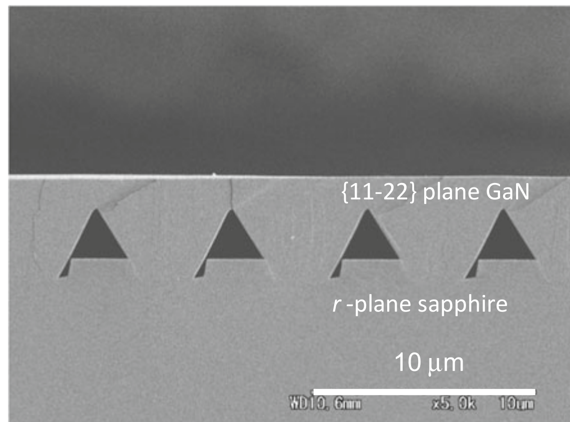

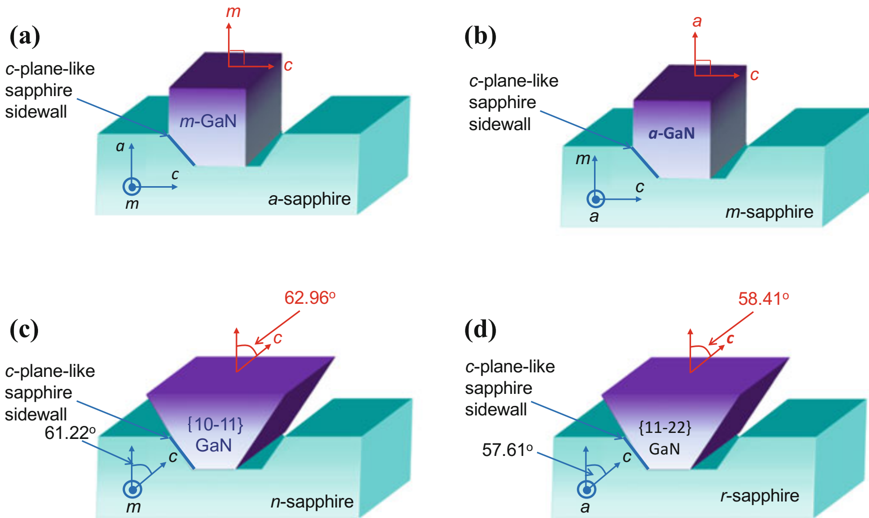

Fig. 4.17 Relationship between crystal orientations of the GaN layer and sapphire substrate. **a** *m*-plane GaN is grown on *a*-plane PSS. **b** *a*-plane GaN is grown on *m*-plane PSS. **c** {10-11} plane GaN is grown on *n*-plane PSS. **d** {11-22} plane GaN is grown on *r*-plane PSS

Using this principle, *m*-plane, *a*-plane, {1-101} plane, and {11-22} plane GaN layers are grown on the *a*-plane, *m*-plane, *n*-plane, *r*-plane PSSs, respectively [59–61, 88], as shown in Fig. 4.17. and {20-21} plane GaN is grown on {11-23} plane PSS [89]. Each PSS has a small off-angle to obtain the GaN layer with the lattice plane, such as {11-22}, parallel to the surface of sapphire substrate. In principle, the GaN layer with any lattice plane is able to grown on the PSS by this procedure.

4.6 Summary

In this chapter, the fabrication technique, the history, future technique "nano-PSS," principle of decreasing the dislocation, principle of increasing light extraction efficiency of GaN-based LED, and novel application to nonpolar and/or semipolar GaN of the Patterned Sapphire Substrate (PSS) are elaborated. Advanced PSS enables us to obtain high-efficiency GaN-LEDs due to both increasing the Internal Quantum Efficiency (IQE) and increasing the light extraction efficiency (LEE) of the GaN-LEDs.

References

1. Y. Narukawa, M. Ichikawa, D. Sanga, M. Sano, T. Mukai, J. Phys. D Appl. Phys. **43**, 354002 (2010)
2. K. Tadatomo, H. Okagawa, Y. Ohuchi, T. Tsunekawa, Y. Imada, M. Kato, T. Taguchi, Jpn. J. Appl. Phys. **40**, L583 (2001)
3. H. Amano, M. Kitoh, K. Hiramatsu, I. Akasaki, Jpn. J. Appl. Phys. **28**, L2112 (1989)
4. S. Nakamura, T. Mukai, M. Senoh, Jpn. J. Appl. Phys. **30**, L1998 (1991)
5. S. Nakamura, M. Senoh, T. Mukai, Appl. Phys. Lett. **62**, 2390 (1993)
6. S. Nakamura, Microelectron. J. **25**, 651 (1994)
7. T. Mukai, S. Nakamura, Jpn. J. Appl. Phys. **38**, 5735 (1999)
8. S. Nagahama, N. Iwasa, M. Senoh, T. Matsushita, Y. Sugimoto, H. Kiyoku, T. Kozaki, M. Sano, H. Matsumura, H. Umemoto, K. Chocho, T. Yanamoto, T. Mukai, Phys. Status Solidi A **188**, 1 (2001)
9. D. Morita, M. Yamamoto, K. Akashi, K. Matoba, K. Yasutomo, Y. Kasai, M. Sano, S. Nagahama, T. Mukai, Jpn. J. Appl. Phys. **43**, 5945 (2004)
10. Y. Narukawa, J. Narita, T. Sakamoto, K. Deguchi, T. Yamada, T. Mukai, Jpn. J. Appl. Phys. **45**, L1084 (2006)
11. Y. Narukawa, M. Sano, M. Ichikawa, S. Minato, T. Sakamoto, T. Yamada, T. Mukai, Jpn. J. Appl. Phys. **46**, L963 (2007)
12. Y. Narukawa, M. Sano, T. Sakamoto, T. Yamada, T. Mukai, Phys. Status Solidi A **205**, 1081 (2008)
13. Y. Kato, S. Kitamura, K. Haramatsu, N. Sawaki, J. Cryst. Growth **144**, 133 (1994)
14. S. Kitamura, K. Haramatsu, N. Sawaki, Jpn. J. Appl. Phys. **34**, L1184 (1995)
15. Y. Ujiie, T. Nishinaga, Jpn. J. Appl. Phys. **28**, L337 (1989)
16. T. Nishinaga, T. Nkano, S. Zhang, Jpn. J. Appl. Phys. **27**, L964 (1988)
17. K. Hiramatsu, Inst. Phys. Conf. Ser. No. 170: Chapter 9, 693 (2002)
18. A. Usui, H. Sunagawa, A. Sakai, A. Yamaguchi, Jpn. J. Appl. Phys. **36**, L899 (1997)
19. A. Sakai, H. Sunagawa, A. Usui, Appl. Phys. Lett. **71**, 2259 (1997)
20. C.I.H. Ashby, C.C. Mitchell, J. Han, N.A. Missert, P.P. Provencio, D.M. Follstaedt, G.M. Peake, L. Griego, Appl. Phys. Lett. **77**, 3233 (2000)
21. T. Detprohm, M. Yano, S. Sano, R. Nakamura, S. Mochiduki, T. Nakamura, H. Amano, I. Akasaki, Jpn. J. Appl. Phys. **40**, L16 (2001)
22. A. Strittmatter, S. Rodt, L. Reissmann, D. Bimberg, H. Schroder, E. Obermeier, T. Riemann, J. Christen, A. Krost, Appl. Phys. Lett. **78**, 727 (2001)
23. N. Okada, T. Murata, K. Tadatomo, H.C. Chang, K. Watanabe, Jpn. J. Appl. Phys. **48**, 122103 (2009)
24. S. Watanabe, N. Yamada, M. Nagashima, Y. Ueki, C. Sasaki, Y. Yamada, T. Taguchi, K. Tadatomo, H. Okagawa, H. Kudo, Appl. Phys. Lett. **83**, 4906 (2003)
25. I. Schnitzer, E. Yablonovitch, C. Caneau, T.J. Gmitter, A. Scherer, Appl. Phys. Lett. **63**, 2174 (1993)
26. E.F. Shubert, *Light Emitting Diodes*, 2nd edn. (Cambridge)
27. R. Windisch, P. Heremans, A. Knobloch, P. Kiesel, G.H. Döhler, B. Dutta, G. Borghs, Appl. Phys. Lett. **74**, 2256 (1999)
28. W.N. Carr, G.E. Pittman, Appl. Phys. Lett. **3**, 173 (1963)
29. M.R. Krames, M.O. Holcomb, G.E. Höfler, C.C. Coman, E.I. Chen, I.H. Tan, P. Grillot, N.F. Gardner, H.C. Chui, J.W. Huang, S.A. Stockman, F.A. Kish, M.G. Craford, T.S. Tan, C. P. Kocot, M. Hueschen, J. Posselt, B. Loh, G. Sasser, D. Collins, Appl. Phys. Lett. **75**, 2365 (1999)
30. K. Tadatomo, H. Okagawa, Y. Ohuchi, T. Tsunekawa, T. Jyouichi, Y. Imada, M. Kato, H. Kudo, T. Taguchi, Phys. Status Solidi A **188**, 121 (2001)
31. H. Kudo, Y. Ohuchi, T. Jyouichi, T. Tsunekawa, H. Okagawa, K. Tadatomo, Y. Sudo, M. Kato, T. Taguchi, Phys. Status Solidi A **200**, 95 (2003)

32. K. Tadatomo, H. Okagawa, Y. Ohuchi, T. Tsunekawa, H. Kudo, Y. Sudo, M. Kato, T. Taguchi, J. Light Vis. Environ. **27**, 10 (2003)
33. M. Yamada, T. Mitani, Y. Narukawa, S. Shioji, I. Niki, S. Sonobe, K. Deguchi, M. Sano, T. Mukai, Jpn. J. Appl. Phys. **41**, L1431 (2002)
34. Y.J. Lee, T.C. Hsu, H.C. Kuo, S.C. Wang, Y.L. Yang, S.N. Yen, Y.T. Chu, Y.J. Shen, M.H. Hsieh, M.J. Jou, B.J. Lee, Mater. Sci. Eng. B **122**, 184 (2005)
35. J.H. Cheng, Y.C.S. Wu, W.C. Liao, B.W. Lin, Appl. Phys. Lett. **96**, 051109 (2010)
36. S.M. Jeong, S. Kissinger, Y.H. Ra, S.H. Yun, D.W. Kim, S.J. Lee, H.K. Ahn, J.S. Kim, C.R. Lee, Jpn. J. Appl. Phys. **49**, 04DH02 (2010)
37. Y.J. Chen, C.H. Kuo, C.J. Tun, S.C. Hsu, Y.J. Cheng, C.Y. Liu, Jpn. J. Appl. Phys. **49**, 020201 (2010)
38. H. Gao, F. Yan, Y. Zhang, J. Li, Y. Zeng, G. Wang, J. Appl. Phys. **103**, 014314 (2008)
39. H. Gao, F. Yan, Y. Zhang, J. Li, Y. Zeng, G. Wang, Solid-State Electron. **52**, 962 (2008)
40. K. Orita, S. Tamura, T. Takizawa, T. Ueda, M. Yuri, S. Takigawa, D. Ueda, Jpn. J. Appl. Phys. **43**, 5809 (2004)
41. A. David, T. Fujii, R. Sharma, K. McGroddy, S. Nakamura1, S.P. DenBaars, E.L. Hu, C. Weisbuch, H. Benisty, Appl. Phys. Lett. **88**, 061124 (2006)
42. A. David, T. Fujii, B. Moran, S. Nakamura, S.P. DenBaars, C. Weisbuch, H. Benisty, Appl. Phys. Lett. **88**, 133514 (2006)
43. J. Lee, S. Ahn, S. Kim, D.U. Kim, H. Jeon, S.J. Lee, J.H. Baek, Curr. Appl. Phys. **9**, 633 (2009)
44. C.C. Kao, Y.K. Su, C.L. Lin, J.J. Chen, Appl. Phys. Lett. **97**, 023111 (2010)
45. Y. Li, S. You, M. Zhu, L. Zhao, W. Hou, T. Detchprom, Y. Taniguchi, N. Tamura, S. Tanaka, C. Wetzel, Appl. Phys. Lett. **98**, 151102 (2011)
46. M. Funato, M. Ueda, Y. Kawakami, Y. Nakamura, T. Kosugi, M. Takahashi, T. Mukai, Jpn. J. Appl. Phys. **45**, L659 (2006)
47. A. David, M.J. Grundmann, Appl. Phys. Lett. **96**, 103504 (2010)
48. K.S. Kim, J.H. Kim, Y.M. Park, S.J. Jung, Y.J. Park, S.N. Cho, Appl. Phys. Lett. **97**, 031113 (2010)
49. R. Sharma, P.M. Pattisson, H. Masui, R.M. Farrell, T.J. Baker, B.A. Haskell, F. Wu, S.P. DenBaars, J.S. Speck, S. Nakamura, Appl. Phys. Lett. **87**, 231110 (2005)
50. C.H. Chiu, D.W. Lin, C.C. Lin, Z.Y. Li, W.T. Chang, H.W. Hsu, H.C. Kuo, T.C. Lu, S.C. Wang, W.T. Liao, T. Tanikawa, Y. Honda, M. Yamaguchi, N. Sawaki, Appl. Phys. Express **4**, 012105 (2011)
51. S.C. Ling, T.C. Lu, S.P. Chang, J.R. Chen, H.C. Kuo, S.C. Wang, Appl. Phys. Lett. **96**, 231101 (2010)
52. Y. Zhao, S. Tanaka, C. Pan, K. Fujito, D. Feezell, J.S. Speck, S.P. DenBaars, S. Nakamura, Appl. Phys. Express **4**, 082104 (2011)
53. K. Motoki, T. Okahisa, R. Hirota, S. Nakahata, K. Uematsu, N. Matsumoto, J. Cryst. Growth **305**, 377 (2007)
54. F. Kawamura, M. Tanpo, N. Miyoshi, M. Imade, M. Yoshimura, Y. Mori, Y. Kitaoka, T. Sasaki, J. Cryst. Growth **311**, 3019 (2009)
55. R. Dwilinski, R. Doradzinski, J. Garczynski, L.P. Sierzputowski, A. Puchalski, Y. Kanbara, K. Yagi, H. Minakuchi, H. Hayashi, J. Cryst. Growth **310**, 3911 (2008)
56. R. Dwilinski, R. Doradzinski, J. Garczynski, L.P. Sierzputowski, M. Zajac, M. Rudzinski, J. Cryst. Growth **311**, 3058 (2009)
57. Y. Honda, N. Kameshiro, M. Yamaguchi, N. Sawaki, J. Cryst. Growth **242**, 82 (2002)
58. T. Tanikawa, D. Rudlph, T. Hikosaka, Y. Honda, M. Yamaguchi, N. Sawaki, J. Cryst. Growth **310**, 4999 (2008)
59. N. Okada, Y. Kawashima, K. Tadatomo, Appl. Phys. Express **1**, 111101 (2008)
60. N. Okada, H. Kurisu, K. Tadatomo, Appl. Phys. Express **2**, 091001 (2009)
61. N. Okada, K. Tadatomo, Semicond. Sci. Technol. **27**, 024003 (2012)
62. S. Schwaiger, I. Argut, T. Wunderer, R. Rösch, F. Lipski, J. Biskupek, U. Kaiser, F. Scholz, Appl. Phys. Lett. **96**, 231905 (2010)

63. P. de Mierry, N. Kriouche, M. Nemoz, S. Chenot, G. Nataf, Appl. Phys. Lett. **96**, 231918 (2010)
64. S. Schwaiger, S. Metzner, T. Wunderer, I. Argut, J. Thalmair, F. Lipski, M. Wieneke, J. Blasing, F. Bertram, J. Zweck, A. Krost, J. Christen, F. Scholz, Phys. Status Solidi B **248**, 588 (2011)
65. K. Okuno, Y. Saito, S. Boyama, N. Nakada, S. Nitta, R.G. Tohmon, Y. Ushida, N. Shibata, Appl. Phys. Express **2**, 031002 (2009)
66. W.K. Wang, D.S. Wuu, W.C. Shih, J.S. Fang, C.E. Lee, W.Y. Lin, P. Han, R.H. Horng, T.C. Hsu, T.C. Huo, M.J. Jou, A. Lin, Y.H. Yu, Jpn. J. Appl. Phys. **44**, 2512 (2005)
67. J.B. Kim, S.M. Kim, Y.W. Kim, S.K. Kang, S.R. Jeon, N. Hwang, Y.J. Choi, C.S. Chung, Jpn. J. Appl. Phys. **49**, 042102 (2010)
68. O.-H. Nam, M.D. Dremser, T.S. Zheleva, R.F. Davis, Appl. Phys. Lett. **71**, 2638 (1997)
69. K. Hiramatsu, K. Nishiyama, A. Motogaito, H. Miyake, Y. Iyechika, T. Maeda, Phys. Status Solidi A **176**, 535 (1999)
70. K. Hiramatsu, K. Nishiyama, M. Onishi, H. Mizutani, M. Narukawa, A. Motogaito, H. Miyake, Y. Iyechika, T. Maeda, J. Cryst. Growth **221**, 316 (2000)
71. Y. Honda, Y. Iyechika, T. Maeda, H. Miyake, K. Hiramatsu, Jpn. J. Appl. Phys. **40**, L309 (2001)
72. K. Linthicum, T. Gehrke, D. Thomson, E. Carlson, P. Rajagopal, T. Smith, D. Batchelor, R.F. Davis, Appl. Phys. Lett. **75**, 196 (1999)
73. T.S. Zheleva, S.A. Smith, D.B. Thomson, T. Gehrke, K.J. Linthicum, P. Rajagopal, E. Carlson, W.M. Ashmawi, R.F. Davis, in *Proceedings of Material Research Society Symposium*, vol. 537 (1999), pp. G3.38
74. I. Kidoguchi, A. Ishibashi, G. Sugahara, A. Tsujimura, Y. Ban, Jpn. J. Appl. Phys. **39**, L453 (2000)
75. I. Kidoguchi, A. Ishibashi, G. Sugahara, Y. Ban, Appl. Phys. Lett. **76**, 3768 (2000)
76. M. Ishida, M. Ogawa, K. Orita, O. Imafuji, M. Yuri, T. Sugino, K. Itoh, J. Cryst. Growth **221**, 345 (2000)
77. K. Iida, T. Kawashima, A. Miyazaki, H. Kasugai, S. Mishima, A. Honshio, Y. Miyake, M. Iwaya, S. Kamiyama, H. Amano, I. Akasaki, Jpn. J. Appl. Phys. **43**, L499 (2004)
78. H. Lahreche, P. VenneHgues, B. Beaumont, P. Gibart, J. Cryst. Growth **205**, 245 (1999)
79. S. Tanaka, S. Iwai, Y. Aoyagi, Appl. Phys. Lett. **69**, 4096 (1996)
80. K. Hoshino, N. Yanagita, M. Araki, K. Tadatomo, J. Cryst. Growth **298**, 232 (2007)
81. S. Sakai, T. Wang, Y. Morishima, Y. Naoi, J. Cryst. Growth **221**, 334 (2000)
82. X. Zhang, R.R. Li, P.D. Dapkus, D.H. Rich, Appl. Phys. Lett. **77**, 2213 (2000)
83. S.J. Chang, Y.C. Lin, Y.K. Su, C.S. Chang, T.C. Wen, S.C. Shei, J.C. Ke, C.W. Kuo, S.C. Chen, C.H. Liu, Solid-State Electron. **47**, 1539 (2003)
84. K. Hoshino, T. Murata, M. Araki, K. Tadatomo, Phys. Status Solidi C **5**, 3060 (2008)
85. Y.K. Su, J.J. Chen, C.L. Lin, S.M. Chen, W.L. Li, C.C. Kao, Jpn. J. Appl. Phys. **47**, 6706 (2008)
86. C.H. Chan, C.H. Hou, S.Z. Tseng, T.J. Chen, H.T. Chien, F.L. Hsiao, C.C. Lee, Y.L. Tsai, C. C. Chen, Appl. Phys. Lett. **95**, 011110 (2009)
87. J. Lee, S. Ahn, S. Kim, D.U. Kim, H. Jeon, S.J. Lee, J.H. Baek, Appl. Phys. Lett. **94**, 101105 (2009)
88. M. Takami, A. Kurisu, Y. Abe, N. Okada, K. Tadatomo, Phys. Status Solidi C **8**, 2101 (2011)
89. N. Okada, H. Oshita, K. Yamane, K. Tadatomo, Appl. Phys. Lett. **99**, 242103 (2011)

Chapter 5
Growth and Optical Properties of GaN-Based Non- and Semipolar LEDs

Michael Kneissl, Jens Raß, Lukas Schade and Ulrich T. Schwarz

5.1 Introduction

The development of smooth (0001) GaN films on c-plane sapphire [1] and the activation of p-dopants in GaN [2] led very quickly to the realization of high brightness InGaN LEDs on c-plane sapphire substrates [3, 4]. Already at the end of the last century blue and green LEDs with tens and hundreds of milli-Watt output power levels were demonstrated. Today, blue InGaN LEDs boast record external quantum efficiencies exceeding 80% and the emission wavelength of c-plane InGaN QW LEDs has been pushed into the yellow and even red spectral range. Although the performance characteristics of c-plane LEDs seem excellent, the strong polarization fields at InGaN/GaN heterointerfaces can lead to a significant deterioration of the device performance. This polarization field is suppressed or reduced in LEDs with InGaN/GaN heterointerfaces of nonpolar or semipolar orientation, respectively. Triggered by the first demonstration of nonpolar GaN quantum wells grown on $LiAlO_2$ by Waltereit and colleagues in 2000 [5], impressive advancements in the field of non- and semipolar nitride semiconductors and devices have been achieved. Today, a large variety of heterostructures free of polarization fields exhibiting exceptional optical properties have been demonstrated, and the fundamental understanding of polar,

M. Kneissl (✉) · J. Raß
Institute of Solid State Physics, Technische Universität Berlin, 10623 Berlin, Germany
e-mail: kneissl@physik.tu-berlin.de

M. Kneissl
Ferdinand-Braun-Institut, Leibniz Institut für Höchstfrequenztechnik, 12489 Berlin, Germany

L. Schade
Department of Microsystems Engineering, University of Freiburg, 79108 Freiburg, Germany

U.T. Schwarz
Faculty of Natural Sciences, Chemnitz University of Technology, 09126 Chemnitz, Germany

© Springer Nature Singapore Pte Ltd. 2017

T.-Y. Seong et al. (eds.), *III-Nitride Based Light Emitting Diodes and Applications*, Topics in Applied Physics 133, DOI 10.1007/978-981-10-3755-9_5

semipolar, and nonpolar nitrides has made significant leaps forward. This chapter is intended to provide an overview on the epitaxial growth and optical properties of group-III-nitride LEDs on non- and semipolar surface orientations [6]. After introducing the physical origins of piezoelectric and spontaneous polarization effects in group-III nitrides, different approaches for the heteroepitaxial growth of low defect density non- and semipolar (Al, In)GaN layers and (Al, In)GaN/GaN heterointerfaces are presented, followed by a discussion of the effect of surface orientation on the indium incorporation efficiency in InGaN layers and quantum wells. In the third section, the polarized light emission characteristics and the optical properties of non- and semipolar InGaN QWs are discussed and finally the performance characteristics of non- and semipolar LEDs are presented including the effects on droop, wavelength shift, and external quantum efficiencies of state-of-the-art devices.

5.2 Piezoelectric and Spontaneous Polarization in Group-III Nitrides

The stable crystal structure of the group-III nitrides AlN, GaN, and InN and their ternary compounds AlGaN, InGaN, and AlInN is the hexagonal Wurtzite structure. The high electronegativity of the nitrogen atom creates a strong dipole in the metal–nitrogen bond which is the origin of the strong polar character of the group-III nitrides. In their real crystal structure, the bond lengths and bond angles deviate slightly from the ideal tetrahedral configuration of the Wurtzite structure, without loosing the hexagonal crystal symmetry C_{6V}. This is the point group of highest symmetry without a center of inversion [7]. Because of this distinction between “up” and “down,” the crystal has two polar surfaces, one terminated with metal atoms Al, Ga, or In, the other N-face. By convention, the [0001] direction points from a metal atom to the nearest neighbor nitrogen atom in the direction of highest symmetry, which is also the optical axis of the uniaxial crystal, or the c-axis.

Because of the missing inversion symmetry, the material is pyroelectric and consequently exhibits spontaneous and piezoelectric polarization [8]. This leads to sheet charge layers at surfaces and interfaces. Surface charges screen most of the fields in thick layers or bulk material. However, at internal interfaces the spontaneous and piezoelectric polarization causes strong band bending and can induce two-dimensional electron gases (2DEG) of high charge carrier density. These are the basic mechanisms enabling GaN-based high electron mobility transistors (HEMT) [9]. In InGaN quantum wells (QW) of optoelectronic devices, the piezoelectric field has a strong influence on radiative recombination. In standard c-plane LEDs or laser structures, the active region consists of several few nanometer thick InGaN QWs between GaN or InGaN barriers. Because of the increasing in-plane lattice constants of InGaN with indium content, the QW experiences biaxial compressive strain. The thickness of the QWs must remain below the critical thickness to suppress the formation of new dislocations. In this regime of pseudomorphic growth, the in-plane

strain ε_{xx} for the QW is given by the difference of the a-lattice constant a of the QW and a_0 of the barrier:

$$\varepsilon_{xx} = \frac{a - a_0}{a_0} \tag{5.1}$$

Stress and strain are related through the elastic tensor with elastic constants c_{ij}. For the polar QW with biaxial strain the stress component σ_1 in the basal plane can be calculated by

$$\sigma_1 = \varepsilon_{xx} \left(c_{11} + c_{12} - 2\frac{c_{13}^2}{c_{33}} \right). \tag{5.2}$$

Strain and piezoelectric polarization are related through the piezoelectric coefficients d_{ij}. For the hexagonal crystal of C_{6V} symmetry the piezoelectric polarization P_i in i direction is given by

$$P_i = \sum_j d_{ij} \sigma_j \qquad i = 1, 2, 3 \quad j = 1, \ldots, 6. \tag{5.3}$$

For the polar QW the piezoelectric polarization in the direction z perpendicular to the QW resulting from biaxial in-plane strain ε_{xx} is then given by [8]

$$P_z = 2d_{31}\varepsilon_{xx} \left(c_{11} + c_{12} - 2\frac{c_{13}^2}{c_{33}} \right). \tag{5.4}$$

The resulting internal field in an InGaN QW is of the order of 0.5 MV/cm to 3 MV/cm for a standard LED structure. This large internal field causes a strong bending of the band edge in the active region. It severely affects recombination rates, wavelength of emission, and transport.

Radiative recombination is proportional to the absolute square of the overlap integral of electron and hole wave functions. The field inside the QW causes a spatial separation of the electron and hole wave function, resulting in a spatial indirect transition which reduces the radiative recombination rate. This shifts the balance from radiative to nonradiative recombination, which is less affected by the internal field, and therefore reduces the internal quantum efficiency of the LED.

The wavelength of emission is shifted due to the so-called Quantum Confined Stark Effect (QCSE): Band bending in the active region shifts the transition between bound states of the QW to longer wavelengths. Because the internal fields are partially screened with increasing carrier density, the wavelength of a polar InGaN LED is shifting toward shorter wavelength with increasing current density. This effect is most pronounced for LEDs emitting in the green spectral region where the strain and consequently the field inside the QW is largest. Carrier transport is affected because the piezoelectric field causes additional barriers in the active region which affect forward voltage and current injection efficiency [10, 11].

A way to avoid these limitations is to use different lattice orientations than the polar c-plane. For planes perpendicular to the c-plane the spontaneous and piezoelectric

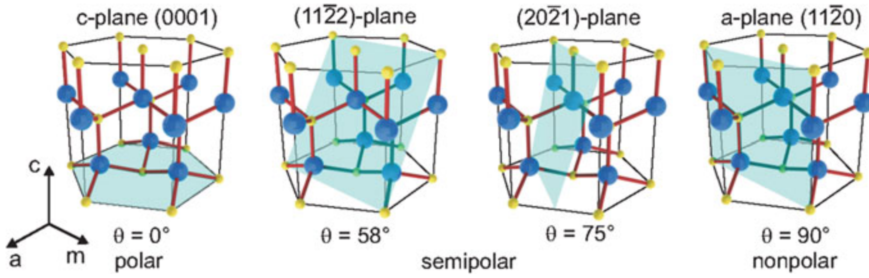

Fig. 5.1 Orientations of c-plane, semipolar (11$\bar{2}$2)- and (20$\bar{2}$1)-planes and nonpolar (10$\bar{1}$0)-plane (*shaded blue polygons*) with inclination angle θ to the c-plane [12]

field perpendicular to the QW is zero because of crystal symmetry. These planes are therefore called nonpolar planes. In other planes with an inclination between polar and nonpolar plane the polarization fields can be expected to be reduced. Prominent polar, semipolar, and nonpolar planes which are being used for LED growth are shown in Fig. 5.1. Each plane is associated with a specific angle θ between the axis perpendicular to the QW and the c-axis of GaN. This angle ranges from $\theta = 0°$ for the polar QW to $\theta = 90°$ for the nonpolar case.

A simple projection of the piezoelectric field pointing in c-direction as described by (5.3) on the respective plane will not give correct results for the internal field. Instead, one has to first calculate the strain for the QW under the assumption of pseudomorphic growth in the respective orientation. From the strain components, the piezoelectric polarization is then calculated with the piezoelectric coefficients. A semipolar QW has nonvanishing strain components ε_{xx}, ε_{yy}, ε_{zz}, and ε_{xz}. In a strain model developed by Park and Chuang, the strain components as function of the inclination θ are given by

$$\varepsilon_{xx} = \varepsilon_{xx}^{(0)} + \varepsilon_{xz} \tan\theta, \tag{5.5}$$

$$\varepsilon_{yy} = \varepsilon_{xx}^{(0)}, \tag{5.6}$$

$$\varepsilon_{zz} = \varepsilon_{zz}^{(0)} + \varepsilon_{xz} \cot\theta, \tag{5.7}$$

$$\varepsilon_{xz} = -\frac{\left((c_{11} + c_{12} + c_{13}\frac{\varepsilon_{zz}^{(0)}}{\varepsilon_{xx}^{(0)}}) \sin^2\theta + (2c_{13} + c_{33}\frac{\varepsilon_{zz}^{(0)}}{\varepsilon_{xx}^{(0)}}) \cos^2\theta\right)\epsilon_{xx}^{(0)} \cos\theta \sin\theta}{c_{11} \sin^4\theta + 2(c_{13} + 2c_{44}) \sin^2\theta \cos^2\theta + c_{33} \cos^4\theta}, \tag{5.8}$$

where $\epsilon_{xx}^{(0)} = (a_s - a_e)/a_e$ and $\epsilon_{zz}^{(0)} = (c_s - c_e)/c_e$ of the substrate and epiaxial layer, respectively [13]. Remark: a_s, c_s: substrate a_e, c_e: epitaxial layer. The fact that the shear strain ε_{xz} is nonvanishing in a semipolar QW has major consequences for the band structure and polarization of the optical emission, as will be discussed in Sect. 5.4. The dependency of the different components of the strain tensor on θ is shown in Fig. 5.2.

The polarization discontinuity $\Delta P_{z'}$ between QW and barrier is then given through the strain tensor and piezoelectric coefficients d_{ij}:

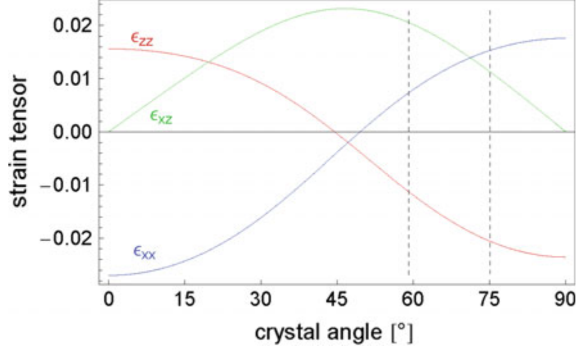

Fig. 5.2 Strain tensor components as function of crystal angle for a fully strained $In_{0.25}Ga_{0.75}N$ layer grown on free-standing GaN substrate. The *dashed lines* mark the semipolar $(11\bar{2}2)$- and the $(20\bar{2}1)$-planes [12]

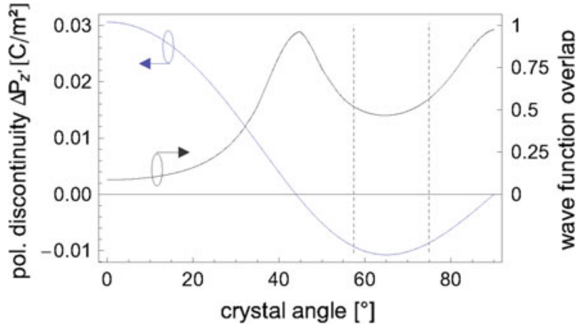

Fig. 5.3 Polarization discontinuity along growth direction (*blue*) and wave function overlap (*black*) as function of crystal angle for a 3 nm wide $In_{0.25}Ga_{0.75}N$ quantum well. The *dashed lines* mark the semipolar $(11\bar{2}2)$- and the $(20\bar{2}1)$-planes [12]

$$\Delta P_{z'} = \Big([d_{31}(c_{11} + c_{12}) + d_{33}c_{13}]\,(\varepsilon_{xx} + \varepsilon_{yy}) + (2d_{31}c_{13} + d_{33}c_{33})\varepsilon_{zz} \Big) \cos\theta$$
$$+ (2d_{15}c_{44}\varepsilon_{xz}) \sin\theta + \Big(P_{\mathrm{sp}}^{(\mathrm{QW})} - P_{\mathrm{sp}}^{(\mathrm{b})} \Big) \cos\theta. \tag{5.9}$$

Here, z' points in growth direction and perpendicular to the QW. $P_{sp}^{(QW/b)}$ is the spontaneous polarization in the quantum well and barrier. The (5.9) holds for all angles θ. The resulting polarization discontinuity is plotted in Fig. 5.3 together with the wave function overlap for a 3 nm wide $In_{0.25}Ga_{0.75}N$ QW. The polarization discontinuity can be implemented as sheet charge layers at the interfaces between QWs and barriers in a drift-diffusion model. This allows the calculation of the internal field as well as carrier transport as function of external applied bias voltage within the accuracy of the drift-diffusion model. An estimation for the internal field can be given by assuming appropriate boundary conditions and employing Gauss' law $\nabla \cdot (\varepsilon\varepsilon_0 \mathbf{E} + \mathbf{P}) = 0$, resulting in [12]:

$$\varepsilon^{(\mathrm{QW})} E_z^{(\mathrm{QW})} - \varepsilon^{(\mathrm{b})} E_z^{(\mathrm{b})} = -\frac{\Delta P_{z'}}{\varepsilon_0}. \tag{5.10}$$

Here, ε_0 is the permittivity of vacuum, $\varepsilon^{(b)}$ and $\varepsilon^{(QW)}$ are the static dielectric constants for the barrier layers and the quantum well, respectively.

For an inclination of about $\theta = 50°$, the different components of the piezoelectric field compensate each other, resulting in a zero polarization discontinuity. For some time, the existence of this zero transition of the polarization field was heavily discussed, as it depends critically on the parameters used in the strain model on the theoretical side and on the strain in a real QW when the internal field is determined experimentally [14–16]. However, currently the parameters determining strain and piezoelectric field are converging and there is a general agreement on the existence of the zero crossing for the internal field. Because this zero crossing is close to the angle corresponding to the $(11\bar{2}2)$ lattice plane, this plane, which also shows stable growth, is preferred for semipolar LEDs. However, considering also optical properties and transport, other planes may be better candidates for semipolar LEDs and laser diodes. We will later see that the effect of polarization switching is most prominent for the $(11\bar{2}2)$ orientation, which is relevant for semipolar optoelectronic devices emitting in the green spectral region.

5.3 Growth of GaN and InGaN on Different Non- and Semipolar Surface Orientations

The synthesis of GaN layers with non- or semipolar surface orientations can be achieved by different means. The most straightforward approach is the growth of single crystal GaN boules, from which GaN wafer slabs can be cut out at basically any angle and therefore crystal orientation of choice. Another advantage of this approach is that the defect densities in the semi- and nonpolar bulk GaN substrates are similar to the defect densities of the original GaN boule. Since GaN boules can be realized with very low defect densities, the resulting semi- and nonpolar bulk GaN provide an excellent growth substrate with very low defect densities. This type of approach has already been successfully demonstrated by a number of research groups [17–21]. In most cases, the bulk GaN crystal boules have been grown by hydride vapor phase epitaxy (HVPE) or ammonothermal growth along the (0001) direction. In order to obtain GaN wafers with non- or semipolar surface orientations, the GaN boules have to be cut perpendicular to the c-plane surface for nonpolar orientations or at the appropriate off-axis angle corresponding to the respective semipolar surface plane. The challenge with this approach is that in order to obtain larger non- and semipolar substrate sizes the c-plane GaN boules have to be large in height as well as in diameter. This is still a significant challenge, since the GaN growth rates, even with HVPE, are relatively low and the built-up of strain and parasitic deposits during growth limits the maximum heights that can be achieved without fracturing the boule. In addition, the fabrication costs for bulk GaN boules are relatively high, which also translates into high costs for the semi- and nonpolar bulk GaN substrates. Therefore, the heteroepitaxial growth of non- and semipolar GaN layers on readily available sapphire, silicon, SiC, and other substrates is still of great interest and importance. All of the heteroepitaxial substrates are available with large diameters (e.g., 6″ is already

standard for sapphire substrates and 8″ and 12″ sapphire are under development), and the cost of these substrate are low to moderate. In the past decade, a large number of substrate materials and surface orientations have been explored in order to realize heteroepitaxial GaN layers with different non- and semipolar surface orientations. A detailed discussion of the different approaches is given in the following paragraph.

5.3.1 Heteroepitaxial Growth of Non- and Semipolar GaN on Sapphire, Silicon, Spinel, and $LiAlO_2$ Substrates

Growth of non- and semipolar GaN layers has been demonstrated on sapphire, silicon, SiC, spinel, as well as $LiAlO_2$ substrates and on a number of different substrate orientations. Initially most of the experiments have focused on heteroepitaxial growth on planar substrates [5, 22–27]. In these instances, the orientation of the grown GaN layers is strongly correlated with the crystal orientation of the host substrate, although in some cases several semipolar orientations can be obtained for the same growth substrates (e.g., growth on m-plane sapphire can yield $(11\bar{2}2)$ and $(10\bar{1}3)$ GaN layers). An overview of the different heteroepitaxial substrates and the orientations of the resulting non- and semipolar GaN layers is provided in Fig. 5.4.Although the

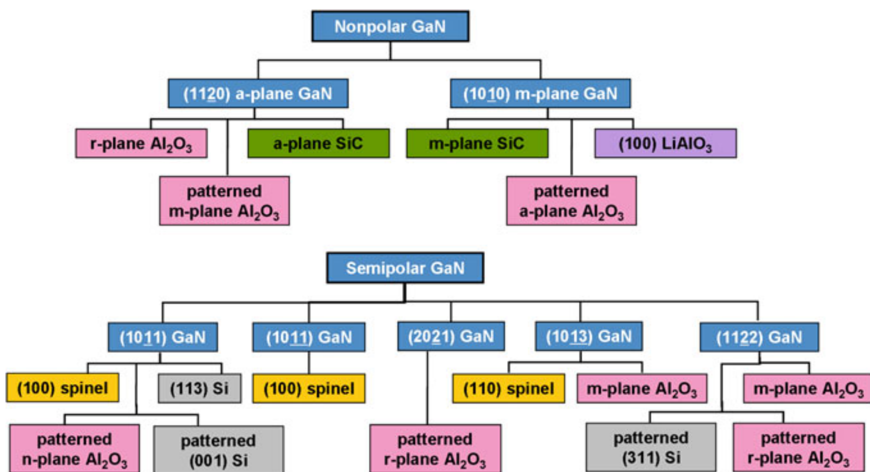

Fig. 5.4 Overview showing the relationship between different substrate orientations and materials and the orientation of the resulting GaN layer. The examples include heteroepitaxial growth of GaN layers on planar substrates as well as growth of non- and semipolar GaN on patterned sapphire and silicon substrates

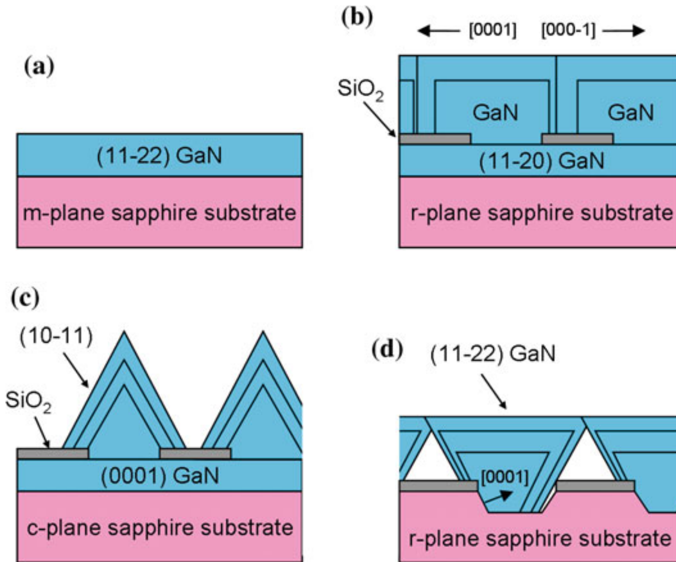

Fig. 5.5 Schematic illustration of **a** heteroepitaxial growth of semipolar $(11\bar{2}2)$ GaN on planar $(10\bar{1}0)$ m-plane sapphire substrate, **b** defect reduction by epitaxial lateral overgrowth (ELO) for $(11\bar{2}0)$ GaN layers on r-plane sapphire, **c** $(10\bar{1}1)$ GaN facet on 3-dimensional stripes on c-plane sapphire and **d** heteroepitaxial growth of semipolar $(11\bar{2}2)$ GaN on a stripe-patterned $(10\bar{1}2)$ r-plane sapphire substrate

figure does not attempt to provide a complete list, all of the main approaches are included. In addition, the heteroepitaxial growth of non- and semipolar GaN has also been demonstrated on patterned host substrates. Growth of GaN on stripe-patterned substrates allows access to different surface orientations depending on the angle of the exposed growth facet and simultaneously is a method to reduce the defect density in the overgrown GaN layers. Figure 5.5 shows schematically the heteroepitaxial growth on planar host substrate and on a stripe-patterned sapphire substrate. In order to prepare the stripe pattern, several micron wide mesa stripes oriented along the a-direction are dry-etched into the r-plane sapphire substrate. To prevent GaN growth on the n-plane mesa terraces a 100 nm thin SiO_2 layer is deposited on top of the mesa. The subsequent GaN growth is nucleated at the inclined etched mesa facet, which is close to parallel to the sapphire and GaN c-planes. The GaN growth from these facets continues along the c-direction and a planar $(10\bar{1}1)$ GaN surface is formed when the adjacent GaN growth stripes coalesce. This method has been pioneered by K. Tadatomo et al. [28, 29] and Sawaki et al. [30, 31] and has since been demonstrated for a number of different patterned sapphire as well as silicon substrates can be seen from the genealogy displayed in Fig. 5.4. The patterned substrate approach provides access to a number of GaN surface orientation, e.g., by adjusting the angle of the mesa facets or by utilizing different crystal orientations. Using the patterned sapphire substrate approach m-plane GaN layers on patterned a-plane sapphire, a-plane GaN

on m-plane or c-plane sapphire, $(10\bar{1}1)$ GaN on $(11\bar{2}3)$ sapphire, and $(20\bar{2}1)$ and $(10\bar{1}3)$ GaN on $(10\bar{1}2)$ sapphire have been demonstrated. Similarly $(10\bar{1}1)$, GaN layers have been realized on patterned (001) silicon substrates and $(11\bar{2}2)$ GaN on patterned (311) silicon substrates. Most recently the group of A. Krost et al. have shown the growth of $(1\bar{1}06)$ oriented GaN films on (112) Si as well as $(1\bar{1}05)$ and $(1\bar{1}04)$ GaN layers on (113) Si substrates [32]. Again, this list is certainly not complete and the number of possible orientations is expected to grow as more and more substrate materials, stripe patterns, and orientations are being explored.

5.3.2 Surface Morphologies and Strutural Defects of Non- and Semipolar GaN Films

The control of the surface morphology and defect densities of heteroepitaxially grown semipolar and nonpolar GaN layers on planar substrates is very challenging. Wernicke et al. have investigated $(11\bar{2}0)$ GaN on r-plane sapphire, $(10\bar{1}0)$ GaN on $LiAlO_2$, and $(11\bar{2}2)$ GaN on $(10\bar{1}0)$ sapphire substrates [33] and found strongly varying surface morphologies. For example, one problem with the growth of a-plane GaN was the creation of surface pits that are formed by $(10\bar{1}0)$, $(10\bar{1}1)$ and $(000\bar{1})$ facets, whereas semipolar $(11\bar{2}2)$ GaN layers exhibited a strong tendency to roughen and show arrowhead like features as depicted in Fig. 5.6 [34, 35].

Distinct surface morphologies develop even for non- and semipolar GaN layers grown on low defect density bulk GaN substrates as shown in Fig. 5.6b. The SWLI images of homoepitaxially grown m-plane, $(10\bar{1}1)$, $(10\bar{1}2)$, and $(11\bar{2}2)$ GaN layers show very distinct short range surface features for each surface orientation. While the $(11\bar{2}2)$ surface seems relatively smooth, the m-plane and the $(10\bar{1}1)$ exhibit very distinct microscopic features, which are partly due to faceting. The surface

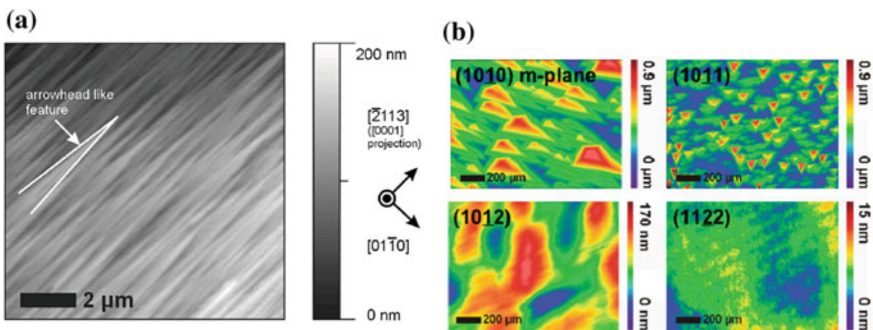

Fig. 5.6 **a** Atomic force microscopy (AFM) image of a $(11\bar{2}2)$ GaN layer grown on an m-plane sapphire substrate [34]. Clearly visible are arrowhead like features on the surface, which are oriented along the c' $[11\bar{2}\bar{3}]$ direction. **b** Scanning white light interferometry (SWLI) images of m-plane GaN, $(10\bar{1}1)$, $(10\bar{1}2)$, and $(11\bar{2}2)$ GaN layers homoepitaxially grown on bulk GaN substrates [33]

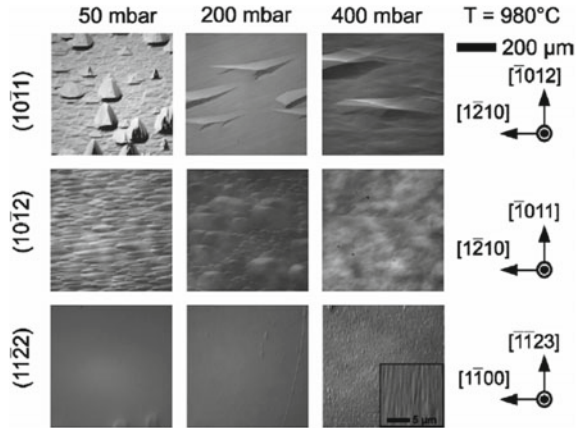

Fig. 5.7 Normarski contrast microscope images of semipolar $(10\bar{1}1)$, $(10\bar{1}2)$, and $(11\bar{2}2)$ GaN layers grown homoepitaxially with different reactor pressures on bulk GaN [33]. The growth temperature was kept constant at 980 °C

morphologies are affected by the growth conditions, in particular growth temperature and reactor pressure. Figure 5.7 shows a series of Normarski contrast microscope images of semipolar $(10\bar{1}1)$, $(10\bar{1}2)$, and $(11\bar{2}2)$ GaN layers grown homoepitaxially with different (metal organic vapour phase epitaxy) reactor pressures on bulk GaN substrates. While under optimized growth conditions the $(10\bar{1}2)$ and $(11\bar{2}2)$, GaN layers showed a relatively smooth surface morphology, the $(10\bar{1}0)$ and $(10\bar{1}1)$, GaN surfaces exhibited macroscopic pyramids, which originated from screw dislocations [36].

Even though the surface morphologies of non- and semipolar GaN layers can be significantly improved by optimization of the growth parameters, the reduction of the defect densities, especially for heteroepitaxially grown layers is much more challenging. Despite refined growth processes, the edge dislocation densities of heteroepitaxially grown non- and semipolar GaN layers range typically from 10^9 to 10^{10} cm^{-2} and the basal plane stacking faults (BSF) density is about 10^6 cm^{-1}. This poses serious limitations to the device performance, since extended defects act as nonradiative recombination centers and are thus detrimental to the internal quantum efficiencies of light emitting diodes. In order to reduce the dislocation densities, a number of different techniques have been explored. The most intensively explored is lateral epitaxial overgrowth (ELOG) [37]. Originally, the ELOG method has been applied to reduce the defect density in planar semi- and nonpolar GaN layers. For example, thin silicon dioxide stripes were patterned on nonpolar $(11\bar{2}0)$ GaN layers on sapphire which enabled a selective re-growth of a-plane GaN in the mask openings [38]. By aligning the 100 nm thick SiO_2 stripe mask parallel to the $[10\bar{1}0]$ direction, TEM investigations and other studies have shown that the BSF and threading dislocation densities can be reduced by several orders of magnitudes in the laterally overgrown GaN areas [39–41]. The improved structural quality also translates into much improved optical properties of the nonpolar GaN films. For example, cathodoluminescence (CL) investigations of ELOG GaN films show sharp donor bound excitonic emission from the defect-reduced laterally overgrown areas whereas without defect

Table 5.1 Cathodoluminescence (CL) dark spot density of different semipolar GaN layers grown on patterned sapphire substrates [28, 29, 42]

GaN orientation	Patterned sapphire orientation	Dark spot density [cm^{-2}]	References
$(11\bar{2}2)$	$(10\bar{1}2)$	2×10^8	[28]
$(10\bar{1}1)$	$(11\bar{2}3)$	1.2×10^8	[28]
$(20\bar{2}1)$	$(22\bar{4}3)$	5.6×10^6	[29]
$(10\bar{1}0)$	$(11\bar{2}0)$	Not specified	[42]

reduction the CL is dominated by BSF luminescence [40]. An alternative approach to defect reduction is the growth on patterned substrates, as already described in Sect. 5.3.1. Since the semi- and nonpolar layers are selectively nucleated on c-plane like facets very few basal plane stacking faults are generated in the grown GaN layers and the threading dislocations are mostly concentrated in the coalesced regions [28, 29]. Depending on the semipolar orientation of the overgrown GaN layer and the patterned sapphire substrate, the threading dislocation densities and BSF densities can vary significantly. Table 5.1 summarizes some of the recent results. As can be seen from Table 5.1, very low CL dark spot densities in the $10^6\,cm^{-2}$ range can be achieved. These values are close to numbers obtained from growth of non- and semipolar layers on bulk GaN substrates, indicating that heteroepitaxial growth has the potential to provide low defect density templates for high efficiency non- and semipolar light emitters.

Recently Ravash et al. have shown that high silicon doping [32] can lead to a significant reduction of threading dislocation density and BSF in $(1\bar{1}06)$ and $(1\bar{1}04)$ GaN layers grown on (112) and (113) Si substrates, respectively. Similarly the insertion of low-temperature (LT) AlN interlayers [43] has also led to a significant reduction of threading dislocation and BSF density in $(1\bar{1}06)$ and $(1\bar{1}04)$ GaN. In both cases, the reduction of BSFs is most likely due to the generation of a- and c-type misfit dislocations at the LT-AlN/GaN interface, which are preferential to the generation of new stacking faults, especially for semipolar GaN with a low-inclination angle.

A third approach to realize InGaN light emitters on semipolar GaN surfaces is the selective growth of three-dimensional (3D) triangular-shaped GaN structures on stripe-patterned c-plane GaN/sapphire substrates [44]. A schematic of this approach is shown in Fig. 5.5. Depending on the growth conditions, the resulting triangular-shaped GaN stripes can either exhibit $\{1\bar{1}01\}$ or $\{11\bar{2}2\}$ facets. One advantage of this approach is that it can be realized on large area and low-cost (0001) sapphire substrates. Since the growth originates from the c-plane, the semipolar surfaces are mostly free of stacking faults and exhibit fairly low threading dislocation densities. The downside is that the 3-dimensional growth makes the device fabrication and electrical contacting more difficult. In addition, indium incorporation efficiency depends strongly on the position on the pyramid leading to large scale fluctuations of the emission wavelength.

5.3.3 *Indium Incorporation in InGaN Layers and Quantum Wells on Different Semipolar and Nonpolar Surfaces*

For the realization of high efficiency blue, green, and yellow LEDs indium incorporation efficiency in InGaN layers and quantum wells is very critical. Theoretical studies based on first principles calculations by Northrup et al. [45] have already shown that the indium incorporation efficiency on $(11\bar{2}2)$ surfaces is expected to be higher than for $(10\bar{1}0)$ surfaces. For the $(11\bar{2}2)$ and $(10\bar{1}0)$ surfaces this was explained by the strain-induced repulsive interaction between the relatively large indium atoms at the surface. Recently, a systematic experimental study by Wernicke et al. [46] has shown that the indium incorporation in InGaN multiple quantum well structures varies indeed significantly for the different semi- and nonpolar surfaces. A fundamental aspect of these experiments was to compare the growth of InGaN QWs on low defect density bulk GaN substrates with different surface orientations, in particular $(10\bar{1}0)$, $(10\bar{1}1)$, $(10\bar{1}2)$, $(11\bar{2}2)$, and $(20\bar{2}1)$ GaN surfaces for a series of growth temperatures. The experiments showed that the indium incorporation efficiency in InGaN QWs was consistently highest on the $(10\bar{1}1)$ surfaces and very similar to (0001) GaN surfaces for growth on $(11\bar{2}2)$ and $(20\bar{2}1)$ oriented surfaces. In contrast, InGaN QWs grown on the $(10\bar{1}2)$ and $(10\bar{1}0)$ surfaces showed much lower indium mole fractions than QWs grown on the conventional (0001) GaN surfaces. Figure 5.8 summarizes these results for a number of different non- and semipolar orientations as well as different growth temperatures. These results indicate that growth on $(11\bar{2}2)$ and $(20\bar{2}1)$ oriented GaN may be preferable, especially for long-wavelength light emitters that require high In mole fraction InGaN QWs. Overall these investigations demonstrates that the growth on semipolar GaN constitutes a very interesting approach for high efficiency green, yellow, and even longer wavelength light emitting diodes.

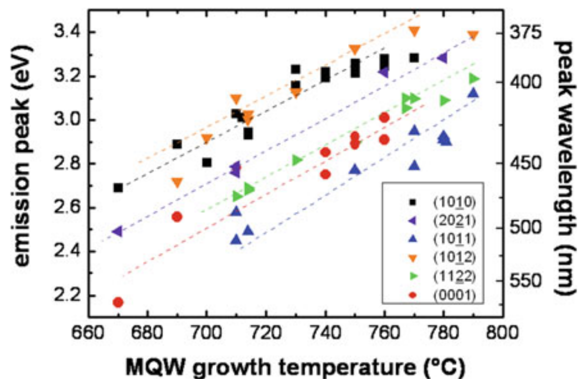

Fig. 5.8 Emission wavelength and indium incorporation efficiency of InGaN multiple quantum well structures grown on c-plane and different semipolar and nonpolar GaN substrates [46]

5.4 Polarization of the Light Emission from Non- and Semipolar InGaN QWs

In contrast to LEDs with c-plane QWs which emit unpolarized light in the direction perpendicular to the surface, a planar LED structure with QWs of semipolar and nonpolar growth direction emits light which is partially polarized. This polarization is a direct consequence of the lower symmetry of the system. While a polar QW is symmetric within the QW plane, a semipolar or nonpolar QW has two distinct directions, parallel and perpendicular to the projection of the c-axis of the crystal onto the plane of the QW. Standard notation is to introduce a Cartesian coordinate system (x', y', z') with z' perpendicular to the QW, x' and y' within the QW plane; x' and y' are parallel and perpendicular to the projection of the c-axis onto the QW plane, respectively. The degree of polarization is then defined as

$$P = \frac{I_{y'} - I_{x'}}{I_{y'} + I_{x'}} \tag{5.11}$$

and determined from intensities $I_{y'}$ and $I_{x'}$ measured using linear polarizers oriented in y' and x' direction. $P = \pm 1$ corresponds to fully linear polarized light, $P = 0$ to unpolarized light. Positive and negative P stands for a dominant polarization perpendicular (y') and parallel (x') to the projection of the c-axis onto the QW plane, respectively. One has to be aware that this definition of the degree of polarization does not distinguish between partially linear polarized light and elliptically or circular polarized light. The latter may arise in InGaN LEDs due to birefringence or reflection from tilted surfaces. The full state of polarization in that case can be described with Stokes parameters.

Emission of polarized light was observed in electroluminescence [47, 48] and photoluminescence [49]. For nonpolar QWs in m-direction polarization ratios as high as 0.91 [48–50] have been observed by electroluminescence at room temperature. Light emitted from nonpolar QWs is linearly polarized, perpendicular to the c-axis. Semipolar QWs generally emit light with a lower degree of polarization. Ueda et al. observed that the direction of the predominant polarization changes from perpendicular to the c-axis to parallel to the c-axis with increasing indium content for QWs of $(11\overline{2}2)$ orientation [51]. This phenomenon was termed “polarization switching” and was reproduced in semipolar InGaN QWs of different lattice orientations [49].

Generally, the degree of polarization and the dominant direction of the linearly polarized light depend both on the structure of the LED, which is determined during growth, and on measurement conditions. During growth, QW inclination, composition (In or Al content), thickness, and strain are fixed. Upon observation, temperature and excitation density are free parameters. The first set of parameters determines the band structure. The symmetry of the band structure and consequently the selection rules for intraband transitions are the physical origin of the emission of polarized light. The second set of parameters determines the occupation of the subbands, such selecting those states which contribute to light emission. The situation is compli-

cated by the inhomogeneities of the ternary InGaN or AlGaN QWs. Composition, thickness, and strain vary within the QW plane. As discussed in the previous section, semipolar QWs tend to form micro-facets of different lattice orientations with different physical properties. Dislocations—in particular stacking faults intersecting nonpolar QWs—modify strain and are a competing source of polarized light. Last but not least, a precise measurement of the degree of polarization is complex. The experimental setup may either scramble polarization (e.g., with a microscope objective of high numerical aperture), leading to the observation of a lower degree of polarization, or artificially polarize the emitted light by reflection from a tilted surface of an optical component (e.g., a beam splitter). Still, the main effect causing polarized light emission is the band structure. Therefore in the following the band structure of polar, nonpolar and semipolar InGaN QWs will be discussed, proceeding from the simplest to the most complex situation.

The crystal and band structure of bulk GaN at the Γ-point ($k_{x'} = k_{y'} = k_{z'} = 0$) is shown in Fig. 5.9. The spin degenerate heavy-hole (HH), light-hole (LH), and crystal-field split-off (CH) bands form the valence band. They are composed from wave functions of p-character with angular momentum $l = 1$. The angular momentum eigenfunctions of heavy-hole and light-hole bands are $\frac{1}{\sqrt{2}}|X + iY\rangle$ and $-\frac{1}{\sqrt{2}}|X - iY\rangle$ at the Γ-point. For the crystal-field split-off band the eigenfunction is $|Z\rangle$. Here, we neglect the spin degree of freedom. A full description of the 6×6 Hamiltonian in $k \cdot p$ approximation can be found, e.g., in [13, 52, 53]. The eigenfunction of the conduction band has s-character with angular momentum $l = 0$ and is spherical symmetric. The angular momentum eigenfunction for all bands is shown as insets in Fig. 5.9. As the intensity of an optical transition is proportional to the transition

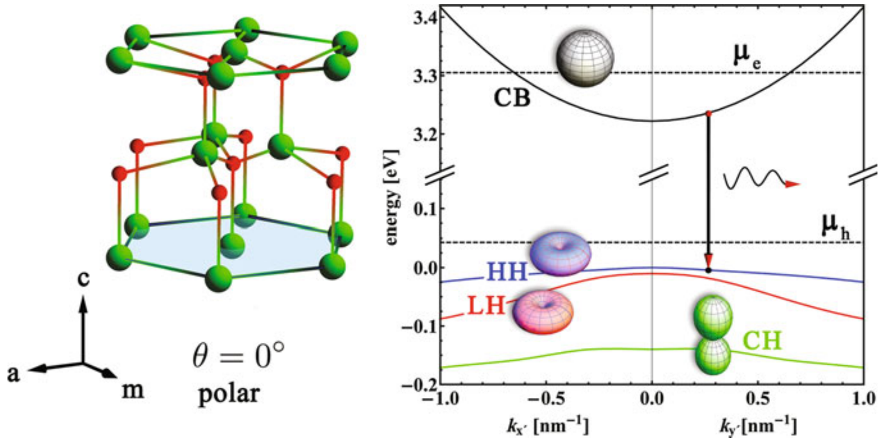

Fig. 5.9 *Left* Orientation of the polar (0001) lattice plane with respect to the GaN lattice structure. *Right* Band structure of a 3 nm $In_{0.1}Ga_{0.9}N$ QW. The insets show the angular momentum eigenfunctions of the individual bands. The dashed lines show the quasi-Fermi levels for electrons (*black*) and holes (*blue*) at a charge carrier density of 8×10^{12} cm^{-2} and room temperature. The *arrow* marks one possible optical transition. Higher order confinement states appearing between LH and CH band are omitted here for clarity [12]

matrix element, the degree of polarization for an individual subband m can be written in the following way [54]:

$$P_m = \frac{|M_{y'}^m|^2 - |M_{x'}^m|^2}{|M_{y'}^m|^2 + |M_{x'}^m|^2} \tag{5.12}$$

The transitions matrix elements $M_{x'}^m$ and $M_{y'}^m$ between conduction and valence band states are calculated in dipole approximation from the wavefunctions of the individual subband as calculated in $k \cdot p$ approximation. Technical details of these calculations are discussed, e.g., in [53–55].

For light emitted in c-direction, the polarization vector is perpendicular to the c-axis of the crystal. The transition matrix element is large and independent of the in-plane direction for transitions between conduction band and both heavy-hole and light-hole bands. Therefore, light emitted from both bands in c-direction is unpolarized. This can be seen from the shape of the angular momentum eigenfunctions as shown in Fig. 5.9. The crystal-field split-off band does not contribute to emission in c-direction, because its angular momentum eigenfunction has neither $|X\rangle$ nor $|Y\rangle$ component. The situation changes for light emitted in a direction perpendicular to the c-axis. From the orientation of the angular momentum eigenfunctions, it follows that photons stemming from the transition between conduction band and heavy-hole or light-hole bands are polarized perpendicular to the c-axis, while the transition from conduction band to crystal-field split-off band is polarized parallel to the c-axis. The energy splitting between heavy-hole and light-hole band is smaller than $k_B T$ at room temperature, therefore the thermal occupation of both states is similar. However, the crystal-field split-off band is separated by about 100 meV from the band edge, therefore contributing to a much lesser extend to light emission. Therefore, light emitted perpendicular to the c-axis in a bulk GaN crystal is linearly polarized. This is also the reason for the higher gain of the TE mode when compared to the TM mode in an in-plane (Al, In)GaN laser diode.

The bound states in an InGaN QW result in subbands of the band structure. Anti-crossing between these bands results in a modification of the transition matrix elements. For a c-plane QW, however, the in-plane symmetry is conserved. Therefore the polarization characteristics are those of the bulk GaN crystal, i.e., unpolarized light is emitted perpendicular to the QW. Light propagating along the QW plane remains linearly polarized, resulting in a larger TE gain.

5.4.1 Light Emission from Nonpolar InGaN QWs

This symmetry is broken in a nonpolar QW. Even in an unstrained thick InGaN or GaN layer, light emitted in a-direction perpendicular to the c-axis is polarized because of the symmetry of the crystal structure, as discussed above. In addition to this effect, the band structure is strongly modified in a nonpolar QW by anisotropic strain. This anisotropic strain is a consequence of the different lattice constants in the direction parallel and perpendicular to the c-axis. It modifies the band structure

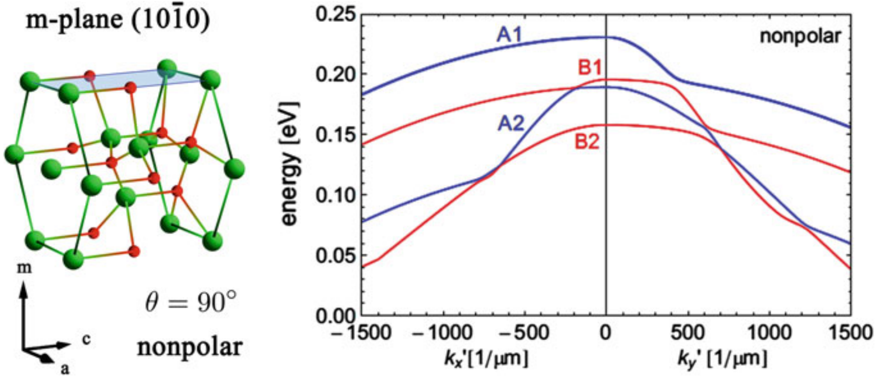

Fig. 5.10 Topmost valence bands of a 3 nm thick nonpolar $In_{0.2}Ga_{0.8}N$ QW at a sheet carrier density of $1 \times 10^{18}\,cm^{-3}$ [53]

through the deformation potential, which is described in $k \cdot p$ approximation by six parameters D_1 to D_6. The resulting band structure for a 3 nm thick nonpolar $In_{0.2}Ga_{0.8}N$ QW at a sheet carrier density of $7 \times 10^{12}\,cm^{-2}$ is shown in Fig. 5.10. The bands are labeled with capital letters A_m, B_m, and C_m for the valence bands and a number m for the respective subband corresponding to the bound states of the QW. For the nonpolar QW the eigenstates are fully polarized at the Γ-point. For the A_m, B_m, and C_m bands the angular momentum eigenfunctions are approximately $|Y\rangle$, $|X\rangle$, and $|Z\rangle$, respectively.

In contrast to the polar case (cf. Fig. 5.9), the band structure in a nonpolar QW is different in k_x' and k_y' directions, resulting in an anisotropy of the effective mass and density of states [56]. The energy distance between A_1 and B_1 band in a nonpolar QW is considerably larger than the splitting between heavy-hole and light-hole band in a polar QW. The band structure in Fig. 5.10 was calculated with standard parameters and strain model, resulting in an A_1–B_1 splitting of approximately $k_B T$. Experiments usually report a wider splitting, which is probably caused by a higher strain in the QW. The large energy difference results in a small occupation of the B_1 band and consequently to a high degree of polarization even at room temperature.

For a typical QW thickness of a few nanometer, the confinement energy is similar to the splitting between A and B subbands. This results in anti-crossing of the B_1 and A_2 bands close to the Γ-point, as shown in Fig. 5.10. Transitions from conduction band to the A_2 band are forbidden by symmetry in the nonpolar QW. However, the A_2 band contributes to the density of states. Also, the subbands exchange their dominant polarization at these anti-crossings. This means that transitions from the conduction band to the B_1 band are x'-polarized at the Γ-point. However, for $k_x' > 200\,cm^{-1}$ and for $k_y' > 600\,cm^{-1}$ the emitted photon will be y'-polarized.

The strain model used in the $k \cdot p$, Hamiltonian is symmetric with respect to a tilt of the QW toward m- or a-direction. So from the theoretical point of view no difference between a-plane and m-plane nonpolar QWs would be expected. However,

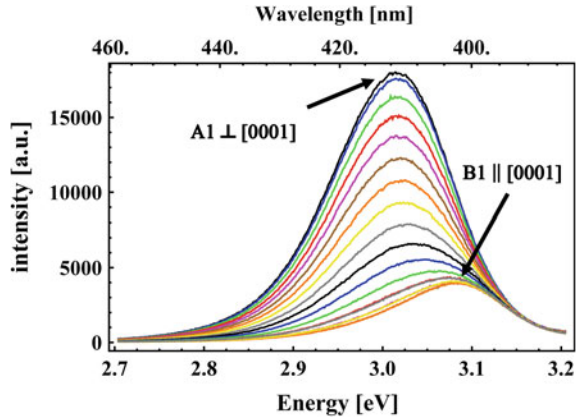

Fig. 5.11 Polarization dependent spectra measured for a nonpolar $(10\bar{1}0)$ QW sample at room temperature. The spectra were measured with a linear polarizer as analyzer which was rotated in 5° steps between each spectrum

the microscopic growth conditions are different on the individual lattice plane, as was discussed above. Therefore a-plane and m-plane QWs grown in a single growth run may be different not only in terms of indium incorporation and thickness but also with respect to their microstructure and anisotropic strain within the QW, modifying both band structure and optical properties.

The measured photoluminescence spectra of a nonpolar $(10\bar{1}0)$ QW sample are shown in Fig. 5.11. The spectra were taken with a linear polarizer, rotated by 5° between each spectrum. The emitted light is strongly polarized in y'-direction, i.e., perpendicular to the c-axis. This is the emission from the transition from conduction band to the A_1 valence band. With the polarizer rotated by 90°, the emission of the B_1 band can be measured. It is much weaker and blue shifted by 78 meV. The spectrally integrated degree of polarization is $P = 0.68$. This high value at room temperature is in quantitative agreement with the large energetic spacing of the A_1 and B_1 band [57].

5.4.2 *Light Emission from Semipolar InGaN QWs*

For semipolar orientation, the eigenstates of the valence bands are composed of all three angular momentum eigenfunctions $|Y\rangle$, $|X\rangle$, and $|Z\rangle$ even at the Γ-point. Therefore, partially polarized light is emitted from the transition of the conduction band to the uppermost valence band already at low temperature. Still, one of the angular momentum eigenfunctions dominates at the Γ-point. This predominant component of the hole wave function is indicated for the semipolar planes $(11\bar{2}2)$ and $(20\bar{2}1)$ in Fig. 5.12. In the example of 3 nm thick $In_{0.35}Ga_{0.65}N$ QWs, the polarization of the transition to the uppermost valence band changes from parallel to the projection of the c-axis for the $(11\bar{2}2)$ plane to perpendicular polarization for the $(20\bar{2}1)$ plane. The band ordering depends on the inclination of the lattice plane, and a crossing of

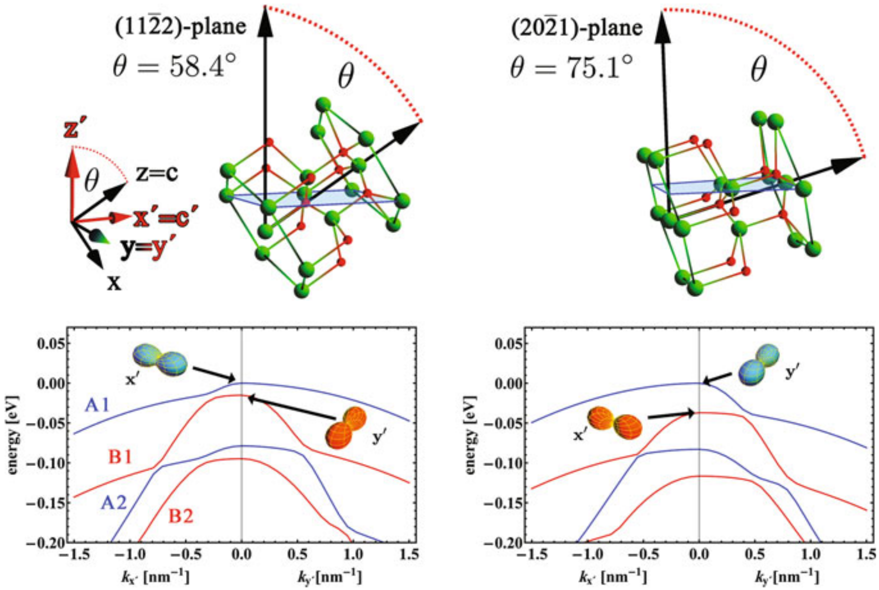

Fig. 5.12 *Top left* Orientation of the (11$\bar{2}$2) lattice plane (*light blue rectangle*) with respect to the GaN lattice structure. Indicated are the crystal coordinate system x, y, z, and the growth coordinate system x', y', z'. The angle between the surface normal and the crystal c-axis is $\theta = 58°$. *Top right* Orientation of the (20$\bar{2}$1) crystal plane; this image has to be adapted to the one on the *top left*. Below are the valence band structures for a 3 nm $In_{0.35}Ga_{0.65}N$ QW of the respective orientation. The angular momentum of the in-plane component of the hole wave function at the Γ-point is indicated for the two topmost valence bands [12]

the A_1 and B_1 bands occurs between $\theta = 58°$ and $\theta = 75°$. It is worth noting that the band structure of the (20$\bar{2}$1) plane is very similar to that of the nonpolar plane, indicating little change of the band structure between $\theta = 75°$ and $\theta = 90°$.

For the (11$\bar{2}$2) band structure, the energy spacing of the uppermost bands A_1 and B_1 is relatively small, and anti-crossing occurs close to the Γ-point. Both effects reduce the degree of polarization. The small energy shift results in a similar thermal occupation of both bands. The anti-crossing indicates a strong mixing of the angular momentum eigenfunctions.

Ueda et al. first observed a dependency of the polarization on the indium content of the semipolar (11$\bar{2}$2) $In_xGa_{1-x}N$ QW [51]. For an indium content $x < 0.3$, the polarization degree was positive, for $x > 0.3$ it was negative (see Fig. 5.13). Also the energy difference between the two uppermost valence bands changed accordingly. They termed this behavior “polarization switching” and interpreted it in terms of band ordering. This behavior was confirmed by electroluminescence measurements for (11$\bar{2}$2) LEDs [58] as well as for other lattice planes [49].

The mechanism causing polarization switching is illustrated by the band structure for (11$\bar{2}$2) $In_xGa_{1-x}N$ QW with increasing indium content $x = 0.15$, 0.25 and 0.35

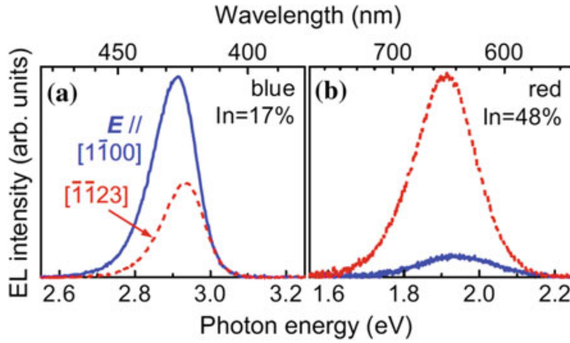

Fig. 5.13 Polarization resolved electroluminescence spectra of a $(11\bar{2}2)$ *blue* and *red* LED with indium content of 17% and 48%, respectively. The *solid blue* and *broken red line* correspond to y' and x' polarization, respectively. The LED was driven at 0.5 mA [51]

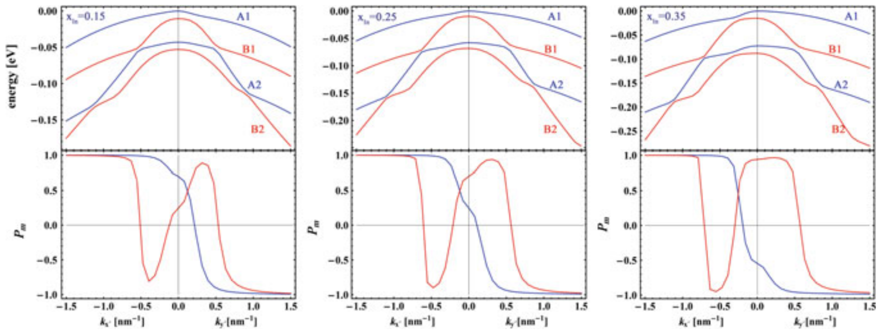

Fig. 5.14 Band structure and polarization of the two topmost valence bands A_1 (*blue*) and B_1 (*red*) for an $(11\bar{2}2)$ QW. The indium content is 15, 25, and 35%, as indicated. The polarization P_m corresponding to the A_1 and B_1 subbands is plotted below the respective band structure plots. Higher order valence bands are drawn for reasons of clarity

in Fig. 5.14. As the indium mole fraction increases, the point of anti-crossing moves from $k_{y'}$ direction to $k_{x'}$ direction, changing the symmetry at the Γ-point and shifting the dominant contribution to the hole wave function changes from $|Y'\rangle$ to $|X'\rangle$ [59]. The polarization P_m of the A_1 and B_1 subbands is plotted in Fig. 5.14 below the respective band structure. Going from $k_{x'}$ to $k_{y'}$, the polarization of the A_1 subband changes from $P_m = +1$ to $P_m = -1$. The k-value where polarization becomes zero is a function of indium content. For an indium content of about 30%, polarization P_m is zero at the Γ-point. This corresponds to the situation where polarization switches from y' to x'. Looking at Fig. 5.14 it becomes obvious that this is a smooth transition, which also depends on the occupation of states in k-space and therefore on carrier density. Quantum confinement has only slight effect on ordering and cannot explain the observed polarization switching [60].

The main cause for the switching of the uppermost valence bands is the anisotropic strain in the semipolar InGaN QW. Ueda et al. pointed out that a high value of the deformation potential D_6 for InN is necessary to explain the observed polarization switching. From his measurements, he derived a value $D_6 = -8.8\,\text{eV}$ [51]. To calculate the band structure shown in Fig. 5.14, we used the value $D_6 = -7.1\,\text{eV}$ [59] and the strain model as proposed by Park and Chuang [13]. Other models for the strain in semipolar InGaN QWs have been developed [61, 62], but leads to similar results regarding strain and band structure. The large value of D_6 is however in contradiction to first-principles calculations which predict $D_6 = -3.95\,\text{eV}$ for GaN and $D_6 = -3.02\,\text{eV}$ for InN [63]. Using the standard strain models, these lower values of D_6 would not be able to explain the observed polarization switching. Yan et al. proposed that a partial strain relaxation would cause polarization switching of a semipolar InGaN QW even for these low values of D_6. The morphology of semipolar InGaN QWs supports this idea of an anisotropic strain relaxation [58]. Yet, XRD, and TEM measurements demonstrate pseudomorphic growth of an $(11\bar{2}2)$ InGaN QW between GaN barriers [62].

Polarization switching is not a phenomenon of the individual $(11\bar{2}2)$ lattice plane, but rather a general property of InGaN QWs which can be explained for all lattice orientations and indium compositions in a unified picture [49]. This can be seen from the plot of polarization for transitions to the two uppermost valence bands, as shown in Fig. 5.15. For this figure, the band structures for 3.5 nm wide QWs with indium contents between $x = 0.05$ and $x = 0.35$ have been calculated in $k \cdot p$ approximation. The blue family of curves shows the degree of polarization for the A_1 subband. For semipolar QW orientation $\theta < 30°$, the polarization is negative, i.e., the polarization is parallel to the projection of the c-axis on the QW, the x' direction. For large angles $\theta > 70°$ up to nonpolar case $\theta = 90°$ the emission is y' polarized, perpendicular to the c-axis. For intermediate planes, the direction of polarization

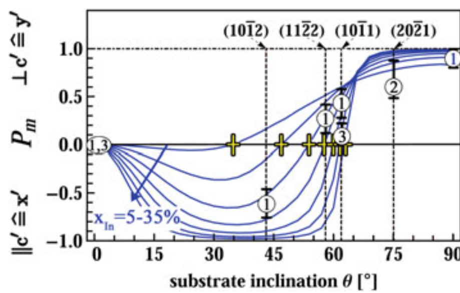

Fig. 5.15 Degree of polarization P_m for transitions from the conduction band to the A_1 band at the Γ-point. The indium content was varied between 5 and 35% in steps of 5%. QW thickness was 3.5 nm and carrier density was $n = 10^{18}\,\text{cm}^{-3}$. The numbered markers (*1*) to (*3*) represent measured polarizations at $T = 10\,\text{K}$. (*1*) photoluminescence from *violet* light emitting QW structures; (*2*) electroluminescence from *violet* $(20\bar{2}1)$ LED; (*3*) photoluminescence from *blue–green* light emitting QW structures. The nonpolar values were obtained at room temperature. The *yellow* crosses mark the critical angle θ_c for the different indium contents [49]

switches from negative to positive. The switching point therefore depends on the indium content. The yellow crosses mark the critical angle θ_c where polarization switching occurs for a given indium concentration. The maximum critical angle is $\theta_{c,max} = 69.4°$ for InN and the chosen set of parameters [49]. For angles smaller than $\theta_{c,max}$ the degree of polarization P_m decreases with increasing indium content, for angles larger than $\theta_{c,max}$ it increases.

Electroluminescence and photoluminescence measurements of LED structures on different polar, semipolar and nonpolar orientations are indicated as markers in Fig. 5.15. Also the polarization switching as observed by Ueda et al. [51] and the decreasing P_m with increasing indium content observed by Masui et al. for $(11\bar{2}2)$ LEDs [58] are in agreement with this unified picture of polarization switching. However, the values measured for the $(20\bar{2}1)$ orientation by several groups [49, 58, 64] are consistently lower than predicted by Fig. 5.15. Still, the increase of the polarization ratio with increasing indium content was confirmed by experiments for the $(11\bar{2}2)$ plane [58].

Zhao et al. studied the polarization ratio of semipolar LEDs in the blue and green wavelength region grown on the $(20\bar{2}1)$- and $(20\bar{2}\bar{1})$-facet. Both of these planes are tilted by ±15° from the m-plane and differ in their surface configuration [65]. The experimental work showed that the LEDs on $(20\bar{2}\bar{1})$ have a higher degree of polarization and a larger band splitting than the $(20\bar{2}1)$-devices. This was attributed to indium interdiffusion in $(20\bar{2}1)$ QWs and consequently a modification of the valence sub band structure.

As pointed out above, the polarization is not only important at the Γ-point, but has to be considered in k-space, as band mixing occurs in semipolar QWs in the valence band close to the Γ-point. Therefore the degree of polarization is plotted in Fig. 5.16 for the A_1 and B_1 band of a 3.5 nm thick $In_{0.3}Ga_{0.7}N$ QW as function of substrate inclination θ and hole momentum $k_{x'}$ and $k_{y'}$. Red and blue shading indicates the sign of P_m. In the red shaded area the polarization is perpendicular to the c-axis. For nonpolar orientation ($\theta = 90°$), the range of positive P_m extends from the Γ-point both in $k_{x'}$ and $k_{y'}$ direction. The dotted line and white shading indicates the unpolarized case $P_m = 0$. The polar QW with $\theta = 0°$ is unpolarized. The dotted line crosses the k = 0 axis again between the black vertical lines marking the lattice planes of $(11\bar{2}2)$ and $(10\bar{1}1)$ orientation. This is the signature of polarization switching of the $(11\bar{2}2)$ QW at the indium composition of about $x = 0.30$. The polarization map of the B_1 band is complementary to that of the A_1 band in the center of the Brillouin zone. At higher k-values mixing with higher bands modifies the polarization of the B_1 band.

The map of P_m shows clearly that polarization switching is not an abrupt phenomenon, but rather a transition of a QW through a range of low degree of polarization as function of either inclination θ or indium content. The map also tells that high degrees of polarization can only be expected far from regions of polarization switching. This explains why large values of P_m are observed for nonpolar QWs. The experimental fact that $(20\bar{2}1)$ QWs up to now do not show the expected high polarization ratios may either suggest some strain relaxation mechanisms or faceting during the growth of these QWs, or that the deformation potential parameters are still not correct.

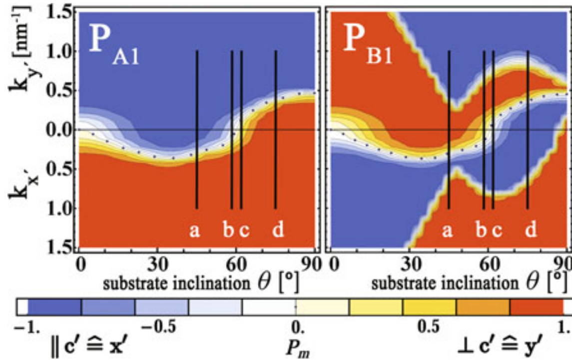

Fig. 5.16 Degree of polarization P_m for transitions from the conduction band to the A_1 (*left*) and B_1 (*right*) valence bands as function of substrate inclination θ in k'_x–k'_y space for a 3.5 nm wide $In_{0.3}Ga_{0.7}N$ QW. The *dotted line* represents unpolarized emission ($P_m = 0$). The *vertical lines a* to *d* mark the lattice planes $(10\bar{1}2)$, $(11\bar{2}2)$, $(10\bar{1}1)$, and $(20\bar{2}1)$ [49]

Masui et al. observed a decrease of polarization with current injection in a nonpolar LED [66]. They suggested that the filling of states according to Fermi statistics is responsible for this reduction of P_m. With increasing carrier density the quasi-Fermi level comes close to the top of the valence band, resulting in a similar occupation probability of the A_1 and B_1 bands. Because of the complementary polarization of both bands, the ratio of polarization decreases. Another effect is that states further away from the Γ-point are occupied, which also decreases the overall polarization ratio (see Fig. 5.16). It should be noted that Kyono et al. did not observe a decreasing polarization ratio with increasing current for a semipolar QW [64]. However, for a nonpolar LED structure the decrease of the polarization ratio with increasing carrier density was confirmed by Schade et al. [57] and could be explained quantitatively by state filling using the Fermi-Dirac distribution.

5.5 Performance Characteristics of Non- and Semipolar InGaN QW Light Emitting Diodes

5.5.1 Wavelength Shift

Light emitting diodes based on the (Al, In, Ga)N material system show a strong dependency of the emission wavelength λ on the carrier concentration n in the quantum well (QW) active region and hence on the injected current I. This behavior is undesired since this means a dependency of spectral characteristic on the light output power, which is unacceptable for many applications such as lighting, sensing, and

consumer electronics systems. There are four main effects that influence the emission wavelength.

- Due to ohmic heating at high operation currents, the bandgap E_g decreases and hence the wavelength is red-shifted to longer values. This effect is present in all semiconductor materials and cannot be avoided completely. Thermal management, heat sinking and the reduction of the current density by increasing the device area can reduce the effect. The dependency of the bandgap on the temperature T is phenomenologically described by the Varshni model:

$$E_g(T) = E_g(T = 0) - \frac{\alpha T^2}{T + \beta} \quad (5.13)$$

  where α and β are the Varshni parameters (e.g., [67]).
- At high injection currents I the increased carrier density n leads to the so-called band filling where lower energy states are filled and the emission moves to higher excited states in the quantum well. The consequence is a blueshift in emission wavelength. In order to avoid this the volume of the active region can be increased, thus reducing the carrier density n. This can be done either by an increase in the number of quantum wells or by an increase of the thickness and volume of each quantum well. The reduction of the carrier density also reduces the droop (see Sect. 5.5.2).
- If the active region exhibits fluctuations in the thickness of the quantum well or the indium content, the emission spectra broaden. Especially the indium fluctuations are an important technological challenge and the strength of the fluctuation increases with the total amount of indium in the active region, making the growth of green and yellow emitters more challenging. Upon carrier injection the high-indium states are filled first since they have the lowest band gap energy. When the injection current increases, emission from material regions with lower indium content and hence shorter emission wavelength occurs, shifting the emission wavelength to the blue.
- If polarization fields are present in the active region, the emission wavelength is originally red-shifted by the QCSE (see Sect. 5.2). This effect is reduced in semipolar emitters and vanishes for nonpolar emitters. If carriers are injected into the active region then the polarization charges at the interfaces of the quantum well are partially screened by the free carriers, compensating the initial red-shift. The consequence is a strong blueshift of the emission wavelength which is stronger in c-plane devices than in semipolar or nonpolar devices. This effect therefore dominates the emission characteristics in c-plane devices while it is not present in nonpolar devices and reduced in semipolar devices.

All of the above-mentioned effects occur at the same time. The design of the active region, the crystal orientation and the material quality determine which effect is the dominating part. If the crystal quality is low and the indium fluctuations are large, the filling of higher indium states dominates.

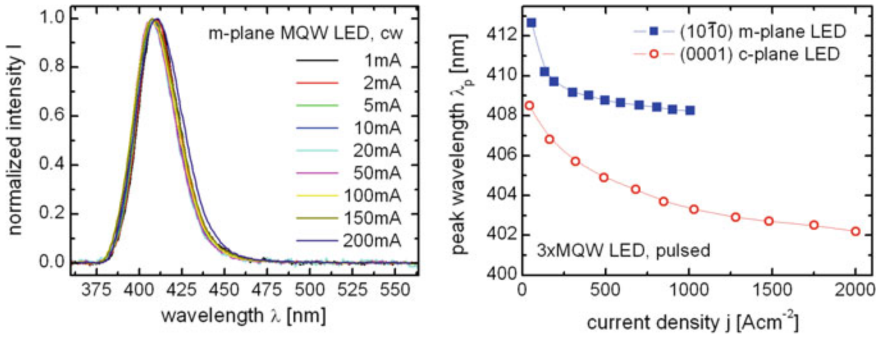

Fig. 5.17 The comparison of current dependent emission wavelength in nonpolar and polar MQW-LEDs shows a strongly reduced blue shift in nonpolar LEDs due to the absence of polarization fields

In Fig. 5.17 a spectrum of an m-plane MQW-LED in cw-mode is shown and only a very small shift is observed. The blueshift in pulsed mode is compared to an LED with the same epitaxial structure on (0001) c-plane. At low current densities j the initial shift of the m-plane LED is stronger than for the c-plane LED which is attributed to filling of states caused by indium fluctuations. When j is increased, the shift of the m-plane LED is smaller than that of the c-plane LED, since here no polarization fields occur and hence the only cause is band filling, while strong polarization fields in the c-plane LED are partially screened, causing a stronger blueshift.

Similar results have been found by Kuokstis et al. [68]. Schmidt et al. reported a very small wavelength shift of less than 1 nm for a 407 nm m-plane LED on bulk GaN in the range of 1–20 mA [69]. LEDs on (20$\bar{2}\bar{1}$) GaN that have been reported by Zhao et al. also show a very small wavelength shift, caused by the strongly reduced polarization fields [70].

5.5.2 Droop

The term "droop" describes the fact that the external quantum efficiency EQE which is defined as the ratio of extracted photons divided by the injected carriers is not a constant, but is influenced by the carrier concentration n in the active region and therefore the injected current I. The easiest way to describe this phenomenon is to treat the recombination mechanism by a third order polynomial model, the ABC-model. Since the different contributions to the overall recombination rate are proportional to n (nonradiative Shockley Read Hall SRH recombination, e.g., at defects), to n^2 ("radiative recombination") and to n^3 (Auger-like recombination), the overall efficiency can be described as

$$EQE = \frac{r_{rad}}{r_{nrad} + r_{rad} + r_{Aug}} = \frac{Bn^2}{An + Bn^2 + Cn^3}. \tag{5.14}$$

A, B, and C are the corresponding recombination parameters. The consequence of this droop model is that the maximum EQE is found at a carrier concentration $n_{max} = \sqrt{A/C}$. Beyond this density, the efficiency decreases, making it favorable to drive the LED at low currents. There has been a strong debate regarding the actual cause for the droop [71], since theory predicts a C-coefficient that is so low for nitrides, that droop should not occur at normal carrier concentrations. The fact that many groups observed strong droop was explained by higher than expected C-coefficients [72], electron leakage [73], nonconstant ABC-coefficients [74], density-activated defect recombination (DADR) [75] or indirect Auger recombination which was mediated by electron–phonon coupling and alloy scattering [76].

In order to reduce the unfavorable droop, the carrier concentration in the active region of the LED should be small, and as close as possible to n_{max}. This however contradicts the demand for high-power devices and requires an increase in the device area, which in turn increases the device costs. In semipolar and nonpolar LEDs, the droop in principle should be smaller than in c-plane devices due to the absence of polarization fields. Since the QCSE is reduced or eliminated, the radiative recombination rate and the B-coefficient are much larger, increasing the device efficiency.

In c-plane devices, the quantum wells are very thin in order to limit the effect of spatial separation of the electron- and hole wavefunctions and thus the reduction in oscillator strength. This limitation in the design of the active region is lifted for non- and semipolar LEDs and hence the quantum wells can be made much thicker, thus reducing the carrier concentration n at a given injection current I.

Pan and Zhao et al. studied the droop in blue LEDs on $(20\overline{2}\overline{1})$ GaN for multiple 3 nm thin quantum wells (MQW) [70] and one 12 nm thick single quantum well (SQW) [77]. The EQE reduced from 52.6% at 35 Acm^{-2} current density to 45.3% at 200 Acm^{-2} for the MQW LED which is very low compared to c-plane devices [78, 79]. Similar results were found for the SQW-LEDs.

5.5.3 *Polarization and Light Extraction*

It is important to note that the optical polarization of the emitted light is a crucial factor for the light extraction. Only photons which are emitted within a narrow angle ϑ with respect to the surface normal can escape due to total internal reflection. The refractive index n_r of the GaN and the surrounding air together define the escape cone. Only photons with a **k**-vector within this cone can escape. Since $\mathbf{E} \perp \mathbf{k}$, this means that mostly TE-polarized light is emitted. A change in the optical polarization for semipolar and nonpolar emitters, as discussed in Sect. 5.4, therefore strongly affects the light extraction efficiency.

There has been much work on the increase in light extraction efficiency by surface roughening techniques and attempts to increase the angle ϑ of the escape cone. The mechanisms behind this is the random and multiple reflection of photons at the rough surface which changes the propagation direction and hence allows the photons to escape from the semiconductor. The drawback of this method is that the linear

polarization, which is desirable for many applications such as liquid crystal display (LCD) back lighting, is lost during the scattering process.

In order to increase the extraction rate and maintain the polarization, Matioli et al. employed photonic crystals (PhC) tailored to the wavelength and dominant polarization direction of m-plane oriented blue LEDs [80]. By using one-dimensional air-gap PhCs, the extraction rate was significantly increased compared to planar devices.

Regarding optical properties, one should also be aware that InN, GaN, and AlN are birefringent. This is of particular importance to semipolar (Al, In)GaN laser diodes, where waveguide modes have to be categorized as TE/TM or ordinary/extraordinary, depending on the waveguide orientation [53, 81–84]. In an LED the effect of birefringence is of lesser importance, as light usually passes only through a thin layer of semiconductor. Still, one has to be aware that the thickness if a $\lambda/4$ plate for 470 nm made of a-plane GaN would be of about 4.5 μm which is of the order of the n-GaN layer of a typical thin-film LED. For a standard planar nonpolar LED the polarization is perpendicular to the c-axis which is the optical axis of the crystal. Therefore the layer does not convert the emitted linearly polarized light to circular polarized light. However, in any structure with out-of-plane geometry or photonic structures, one needs to consider birefringence also in GaN-based LEDs.

5.5.4 3D-semipolar LEDs on C-plane Sapphire

One of the main obstacles in the realization of nonpolar and semipolar LEDs is the challenge of supplying large area and cheap substrates of high quality. While many groups experimented with heteroepitaxial growth on various crystal planes on sapphire, spinel or silicon (see Sect. 5.3.1), another approach is to use high quality semipolar surfaces on conventional planar c-plane GaN-on-sapphire substrates. Selective area growth of stripes along the $[11\bar{2}0]$-direction results in triangular pyramidal stripes with $\{10\bar{1}1\}$ side facets. The quality of these samples exceeds the one known from other methods since the growth starts from a high quality c-plane GaN template [44]. Although the surface of the overgrown wafer is not planar anymore, devices have been processed using this technique. First LEDs with continuous wave emission at 425 nm with 0.7 mW at 20 mA have been shown in 2008 by Wunderer et al. [85]. In 2010 Scholz et al. demonstrated 495 nm LEDs on these stripes with an output power of 0.24 mW at 20 mA driving current [86] (Fig. 5.18).

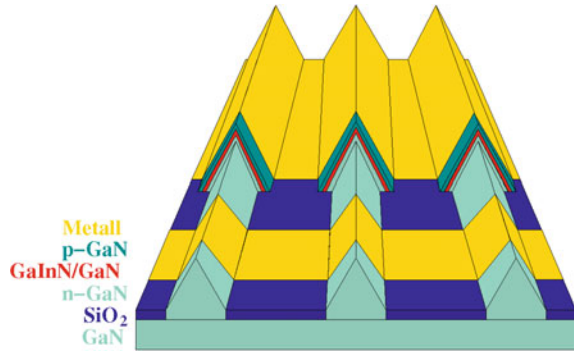

Fig. 5.18 The selective growth of *triangular stripes* with semipolar side facets allows the realization of semipolar LEDs on high quality (0001) GaN templates [87]

5.5.5 State of the Art of Non- and Semipolar Blue, Green, and White LEDs

During the past 10 years, several groups worldwide have investigated the properties of nonpolar and semipolar LEDs, and tremendous progress has been achieved. In the beginning, the limiting factor was the availability of large area and high quality substrates, and hence most LEDs were grown heteroepitaxially on foreign substrates with a high density of threading dislocations (TDD) and basal plane stacking faults (BSF). Among the most favored substrates were sapphire overgrown by HVPE-GaN, and in 2012 Jung et al. demonstrated a violet LED on $(11\bar{2}0)$-GaN with 0.24 mW output power at a dc current of 20 mA [88]. By using epitaxial lateral overgrowth (ELO or LEO) for defect reduction, Chakraborty et al. realized a blue nonpolar LED on a sapphire substrate with 7.5 mW emission power [89]. Furthermore, LEDs with 439 nm emission wavelength were demonstrated on semipolar $(10\bar{1}\bar{3})$- and $(10\bar{1}\bar{1})$-GaN orientations grown on (100) and (110) spinel $MgAl_2O_4$ substrates [90]. Due to its large available size, low cost, and the compatibility to existing processing procedures, silicon has attracted high interest. In 2008 Hikosaka et al. realized LEDs with blue-violet emission on patterned Si on the semipolar $(11\bar{2}2)$ and $(10\bar{1}1)$ orientation [91].

Due to the large defect densities present in all heteroepitaxially grown LEDs, many groups focussed on homoepitaxial growth on quasi-bulk substrates cut from HVPE-grown boules. Although the size and price of these substrates is a limiting factor, LEDs with emission from the violet, blue, and green up the yellow wavelength region have been demonstrated. For a long time, the most commonly used orientations were the nonpolar a- and m-planes and the semipolar $(11\bar{2}2)$-plane. In 2009, impressive progress was shown based on the newly studied $(20\bar{2}1)$-plane [102, 103], and many groups have explored LEDs on this plane since then [46, 49, 65, 104–108]. Other planes such as the $(30\bar{3}1)$-plane have also been investigated for the use in LEDs and laser diodes [109].

In the blue region external quantum efficiencies (EQE) of more than 50% have been reported on the $(10\bar{1}\bar{1})$-plane [95] and on the $(20\bar{2}\bar{1})$-plane by Zhao et al. [70].

Green emitters with high EQE-values were realized on the semipolar $(20\bar{2}1)$-plane with 516 and 552 nm wavelength and 19.1 and 11.6% external quantum efficiency, respectively [97]. Furthermore, on the $(11\bar{2}2)$-plane a 562.7 nm LED was shown with 13.4% EQE under pulsed conditions [94].

Figure 5.19 shows the emission power P and the external quantum efficiency (EQE) of semipolar and nonpolar LEDs. For blue and green emitters EQE-values of more than 50% and 20% have been achieved, respectively.

5.5.6 *Toward Yellow LEDs and Beyond*

The initial driving force behind the increase in wavelength of nitride-based light emitting diodes was the aim to close the "green gap," thus making the realization of emitters for the green wavelength region the most profitable and also most challenging goal. Since the InGaN-system covers the whole visible spectrum from UV to IR, even longer wavelength such as yellow and orange seem possible. This is even more challenging due to the higher indium content of the longer wavelength active region resulting in problems such as material decomposition, indium inhomogeneities and strain due to the increased lattice mismatch. The increased strain also increases the polarization fields, making semipolar and nonpolar crystal orientations the natural choice for this application.

The interest for the realization of GaN-based yellow light emitters is not as strong as for green, though, the AlInGaP-system covers this wavelength range and the wavelength is on the long-wavelength edge of the "green gap." In 2008 Sato et al. reported on yellow semipolar $(11\bar{2}2)$ LEDs and compared them to AlInGaP-based devices [94]. They showed that for nitride-based LEDs the dependency of output power and EQE onto the ambient temperature was lower than for the phosphide-

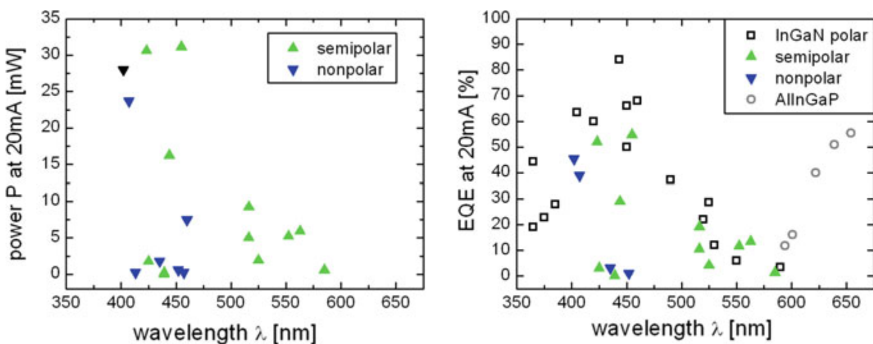

Fig. 5.19 Emission power P (*left*) and external quantum efficiency EQE (*right*) of polar, nonpolar and semipolar InGaN-based LEDs and AlInGaP showing the "green gap." For reference see Table 5.2 and [78, 110–117]

Table 5.2 Overview over performance of nonpolar and semipolar LEDs at 20 mA dc current

Growth plane	Substrate	Wavelength [nm]	Power [mW]	EQE [%]	References
$(11\bar{2}2)$	GaN	425	1.76	3.0	[92]
$(11\bar{2}2)$	GaN	525	1.91	4.1	[92]
$(11\bar{2}2)$	GaN	585	0.54	1.3	[92]
$(11\bar{2}2)$	GaN	516	5.0	10.5	[93]
$(11\bar{2}2)$	GaN	562.7	5.9 (pulsed)	13.4	[94]
$(11\bar{2}2)$	Patterned Si	439			[91]
$(10\bar{1}1)$	Patterned Si	419			[91]
$(10\overline{11})$	GaN	455	31.1	54.7	[95]
$(10\overline{11})$	GaN	444	16.21 (pulsed)	29	[96]
$(20\bar{2}1)$	GaN	516.3	9.2	19.1	[97]
$(20\bar{2}1)$	GaN	552.3	5.2	11.6	[97]
$(11\bar{2}0)$	PLOG-sapphire	460	7.5		[88]
$(11\bar{2}0)$	HVPE-LEO	413	0.24		[89]
$(10\bar{1}0)$	GaN	435	1.79	3.1	[98]
$(10\bar{1}0)$	GaN	407	23.7	38.9	[69]
$(10\bar{1}0)$	GaN	457	0.24		[99]
$(10\bar{1}0)$	GaN	452	0.6	1.09	[100]
$(10\bar{1}0)$	GaN	402	28 (pulsed)	45.4	[101]
$(10\overline{13})$	$MgAl_2O_4$	439	0.19	0.35	[90]
$(10\overline{11})$	$MgAl_2O_4$	439	0.01	0.02	[90]
$(20\overline{21})$	GaN	423	30.6	52	[70]

based devices. This behavior was attributed to carrier overflow due to the smaller energy offset between quantum well and barriers in the AlInGaP-LEDs.

5.6 Summary and Outlook

Despite the short-time period in which the growth of light emitters on non- and semipolar surfaces has been explored, non- and semipolar InGaN QW LEDs already show great promise. This is impressively demonstrated by a number of performance indicators. For example, external quantum efficiencies of blue, green and yellow non- and semipolar light emitters are close or already exceeding those of conventional c-plane InGaN LEDs. Other important parameters like droop and wavelength stability with drive current are also showing great advances compared to LEDs grown on polar surfaces. However, many of these improvements and records have been realized on the relatively costly bulk GaN substrates. Therefore the questions remains whether

non- and semipolar InGaN QW LEDs can also be produced cost-effectively, e.g., on sapphire or silicon substrates. Some of the possible approaches have been outlined in the previous chapter and indicate a number of pathways to realize low-cost and large volume production of high efficiency non- and semipolar LEDs. Young start-up companies, like Soraa Inc. (Fremont, USA) are already trying to seize these opportunities and have introduced the first LED lamps based on non- and semipolar technology that generate more than 2300 candela of white light with only 12 W of electric input power [118]. Of course this is just the start. Only time will tell whether non- and semipolar LEDs will have a lasting impact on future lighting technology. Considering the short-time span in which non- and semipolar light emitters have been explored and the astonishing advances that have already been demonstrated, non- and semipolar LEDs are certainly serious contenders.

Acknowledgements This work was partially supported by the Deutsche Forschungsgemeinschaft (DFG) within the Collaborative Research Center (SFB 787) “Semiconductor Nanophotonics” and the Research Group (FOR 957) “PolarCon.”

References

1. I. Akasaki, H. Amano, Y. Koide, K. Hiramatsu, N. Sawaki, Effects of AlN buffer layer on crystallographic structure and on electrical and optical properties of GaN and $Ga_{1-x}Al_xN$ $(0<x\leq 0.4)$ films grown on sapphire substrate by MOVPE. J. Cryst. Growth **98**, 209–219 (1989)
2. I. Akasaki, H. Amano, Breakthroughs in improving crystal quality of GaN and invention of the p-n junction blue-light-emitting diode. Jpn. J. Appl. Phys. **45**, 9001–9010 (2006)
3. S. Nakamura, T. Mukai, M. Senoh, Candela-class high-brightness InGaN/AlGaN double-heterostructure blue-light-emitting diodes. Appl. Phys. Lett. **64**(13), 1687 (1994)
4. S. Nakamura, M. Senoh, N. Iwasa, S.-I. Nagahama, High-brightness InGaN blue, green and yellow light-emitting diodes with quantum well structures. Jpn. J. Appl. Phys. **34**, L797–L799 (1995)
5. P. Waltereit, O. Brandt, A. Trampert, H.T. Grahn, J. Menniger, M. Ramsteiner, M. Reiche, K.H. Ploog, Nitride semiconductors free of electrostatic fields for efficient white light-emitting diodes. Nature **406**, 865 (2000)
6. J. Han, M. Kneissl, Non-polar and semipolar nitride semiconductors. Semicond. Sci. Technol. **27**, 020301 (2012)
7. F. Bernardini, V. Fiorentini, D. Vanderbilt, Spontaneous polarization and piezoelectric constants of III-V nitrides. Phys. Rev. B **56**(16), 10024–10027 (1997)
8. O. Ambacher, J. Majewski, C. Miskys, A. Link, M. Hermann, M. Eickhoff, M. Stutzmann, F. Bernardini, V. Fiorentini, V. Tilak, B. Schaff, L. Eastman, Pyroelectric properties of Al(In)GaN/GaN hetero- and quantum well structures. J. Phys.: Condens. Matter **14**, 3399–3434 (2002)
9. O. Ambacher, J. Smart, J.R. Shealy, N.G. Weimann, K. Chu, M. Murphy, W.J. Schaff, L.F. Eastman, R. Dimitrov, L. Wittmer, M. Stutzmann, W. Rieger, J. Hilsenbeck, Two-dimensional electron gases induced by spontaneous and piezoelectric polarization charges in N- and Ga-face AlGaN/GaN heterostructures. J. Appl. Phys. **85**(6), 3222 (1999)
10. D.S. Sizov, R. Bhat, A. Zakharian, J. Napierala, K. Song, D. Allen, C.-E. Zah, Impact of carrier transport on aquamarine-green laser performance. Appl. Phys. Express **3**, 122101 (2010)

11. D.S. Sizov, R. Bhat, A. Zakharian, K. Song, D.E. Allen, S. Coleman, C.-E. Zah, Carrier transport in InGaN MQWs of aquamarine- and green-laser diodes. IEEE J. Sel. Top. Quantum Electron. **17**, 1390–1401 (2011)
12. W.G. Scheibenzuber, *GaN-Baser Laser Diodes-Towards Longer Wavelengths and Short Pulses* (Springer, Heidelberg, 2012)
13. S. Park, S. Chuang, Crystal-orientation effects on the piezoelectric field and electronic properties of strained wurtzite semiconductors. Phys. Rev. B **59**(7), 4725–4737 (1999)
14. M. Feneberg, F. Lipski, R. Sauer, K. Thonke, T. Wunderer, B. Neubert, P. Brückner, F. Scholz, Piezoelectric fields in GaInN/GaN quantum wells on different crystal facets. Appl. Phys. Lett. **89**(24), 242112 (2006)
15. M. Feneberg, K. Thonke, T. Wunderer, F. Lipski, F. Scholz, Piezoelectric polarization of semipolar and polar GaInN quantum wells grown on strained GaN templates. J. Appl. Phys. **107**(10), 103517 (2010)
16. M. Funato, M. Ueda, D. Inoue, Y. Kawakami, Y. Narukawa, T. Mukai, Experimental and theoretical considerations of polarization field direction in semipolar InGaN/GaN quantum wells. Appl. Phys. Express **3**, 071001 (2010)
17. T. Paskova, K. Evans, GaN substrates–progress, status, and prospects. IEEE J. Sel. Top. Quantum Electron. **15**, 1041–1052 (2009)
18. K. Fujito, S. Kubo, I. Fujimura, Development of bulk GaN crystals and nonpolar/semipolar substrates by HVPE. MRS Bull. **34**, 313–317 (2009)
19. K. Motoki, T. Okahisa, N. Matsumoto, M. Matsushima, H. Kimura, H. Kasai, K. Takemoto, K. Uematsu, T. Hirano, M. Nakayama, S. Nakahata, M. Ueno, D. Hara, Y. Kumagai, A. Koukitu, H. Seki, Preparation of large freestanding GaN substrates by hydride vapor phase epitaxy using GaAs as a starting substrate. Jpn. J. Appl. Phys. **40**(Part 2, No. 2B), L140–L143 (2001)
20. K. Motoki, T. Okahisa, S. Nakahata, N. Matsumoto, H. Kimura, H. Kasai, K. Takemoto, K. Uematsu, M. Ueno, Y. Kumagai, A. Koukitu, H. Seki, Growth and characterization of freestanding GaN substrates. J. Cryst. Growth **237–239**, Part 2(0), 912–921 (2002). The Thirteenth International Conference on Crystal Growth in Conjunction with the Eleventh International Conference on Vapor Growth and Epitaxy
21. R. Kucharski, M. Zajac, R. Doradzinski, M. Rudzinski, R. Kudrawiec, R. Dwilinski, Nonpolar and semi-polar ammonothermal GaN substrates. Semicond. Sci. Technol. **27**(2), 024007 (2012)
22. M.D. Craven, S.H. Lim, F. Wu, J.S. Speck, S.P. DenBaars, Structural characterization of nonpolar $(11\bar{2}0)$ a-plane GaN thin films grown on $(1\bar{1}02)$ r-plane sapphire. Appl. Phys. Lett. **81**(3), 469–471 (2002)
23. M.D. Craven, F. Wu, A. Chakraborty, B. Imer, U.K. Mishra, S.P. DenBaars, J.S. Speck, Microstructural evolution of a-plane GaN grown on a-plane SiC by metalorganic chemical vapor deposition. Appl. Phys. Lett. **84**(8), 1281–1283 (2004)
24. T.J. Baker, B.A. Haskell, F. Wu, P.T. Fini, J.S. Speck, S. Nakamura, Characterization of planar semipolar gallium nitride films on spinel substrates. Jpn. J. Appl. Phys. **44**(29), L920–L922 (2005)
25. T.J. Baker, B.A. Haskell, F. Wu, J.S. Speck, S. Nakamura, Characterization of planar semipolar gallium nitride films on sapphire substrates. Jpn. J. Appl. Phys. **45**(6), L154–L157 (2006)
26. S. Ploch, M. Frentrup, T. Wernicke, M. Pristovsek, M. Weyers, M. Kneissl, Orientation control of GaN $\{11\bar{2}2\}$ and $\{10\bar{1}3\}$ grown on $(10\bar{1}0)$ sapphire by metal-organic vapor phase epitaxy. J. Cryst. Growth **312**(15), 2171–2174 (2010)
27. S. Ploch, J.B. Park, J. Stellmach, T. Schwaner, M. Frentrup, T. Niermann, T. Wernicke, M. Pristovsek, M. Lehmann, M. Kneissl, Single phase $\{11\bar{2}2\}$ GaN on $(10\bar{1}0)$ sapphire grown by metal-organic vapor phase epitaxy. J. Cryst. Growth **331**(1), 25–28 (2011)
28. N. Okada, K. Tadatomo, Characterization and growth mechanism of nonpolar and semipolar GaN layers grown on patterned sapphire substrates. Semicond. Sci. Technol. **27**(2), 024003 (2012)
29. N. Okada, H. Oshita, K. Yamane, K. Tadatomo, High-quality $\{20\bar{2}1\}$ GaN layers on patterned sapphire substrate with wide-terrace. Appl. Phys. Lett. **99**(24), 242103 (2011)

30. T. Kato, Y. Honda, M. Yamaguchi, N. Sawaki, Fabrication of GaN/AlGaN heterostructures on a (111) Si substrate by selective MOVPE. J. Cryst. Growth **237–239**, Part 2(0), 1099–1103 (2002). The Thirteenth International Conference on Crystal Growth in Conjunction with the Eleventh International Conference on Vapor Growth and Epitaxy
31. N. Sawaki, T. Hikosaka, N. Koide, S. Tanaka, Y. Honda, M. Yamaguchi, Growth and properties of semi-polar GaN on a patterned silicon substrate. J. Cryst. Growth **311**(10), 2867–2874 (2009)
32. R. Ravash, P. Veit, M. Müller, G. Schmidt, A. Dempewolf, T. Hempel, J. Bläsing, F. Bertram, A. Dadgar, J. Christen, A. Krost, Growth and stacking fault reduction in semi-polar GaN films on planar Si(112) and Si(113). Phys. Status Solidi (C) **9**(3–4), 507–510 (2012)
33. T. Wernicke, S. Ploch, V. Hoffmann, A. Knauer, M. Weyers, M. Kneissl, Surface morphology of homoepitaxial GaN grown on non- and semipolar GaN substrates. Phys. Status Solidi (B) **248**(3), 574–577 (2011)
34. T. Wernicke, *Wachstum von nicht- und semipolaren InAlGaN-Heterostrukturen für hocheffiziente Lichtemitter/Growth of GaN-based Non- and Semipolar Heterostructures for High Efficiency Light Emitters*. Dissertation, Technische Universität Berlin (2010)
35. S. Ploch, T. Wernicke, D.V. Dinh, M. Pristovsek, M. Kneissl, Surface diffusion and layer morphology of $(11\bar{2}2)$ GaN grown by metal-organic vapor phase epitaxy. J. Appl. Phys. **111**(3), 033526 (2012)
36. R.M. Farrell, E.C. Young, F. Wu, S.P. DenBaars, J.S. Speck, Materials and growth issues for high-performance nonpolar and semipolar light-emitting devices. Semicond. Sci. Technol. **27**(2), 024001 (2012)
37. T.S. Zheleva, O.-H. Nam, M.D. Bremser, R.F. Davis, Dislocation density reduction via lateral epitaxy in selectively grown GaN structures. Appl. Phys. Lett. **71**(17), 2472–2474 (1997)
38. T. Wernicke, U. Zeimer, C. Netzel, F. Brunner, A. Knauer, M. Weyers, M. Kneissl, Epitaxial lateral overgrowth on $(2\bar{1}\bar{1}0)$ a-plane GaN with $[0\bar{1}11]$-oriented stripes. J. Cryst. Growth **311**(10), 2895–2898 (2009). Proceedings of the 2nd International Symposium on Growth of III Nitrides
39. C. Netzel, T. Wernicke, U. Zeimer, F. Brunner, M. Weyers, M. Kneissl, Near band edge and defect emissions from epitaxial lateral overgrown a-plane GaN with different stripe orientations. J. Cryst. Growth **310**(1), 8–12 (2008)
40. B. Bastek, F. Bertram, J. Christen, T. Wernicke, M. Weyers, M. Kneissl, A-plane GaN epitaxial lateral overgrowth structures: growth domains, morphological defects, and impurity incorporation directly imaged by cathodoluminescence microscopy. Appl. Phys. Lett. **92**(21), 212111 (2008)
41. Z.H. Wu, A.M. Fischer, F.A. Ponce, B. Bastek, J. Christen, T. Wernicke, M. Weyers, M. Kneissl, Structural and optical properties of nonpolar GaN thin films. Appl. Phys. Lett. **92**(17), 171904 (2008)
42. Y. Kawashima, K. Murakami, Y. Abe, N. Okada, K. Tadatomo, Growth mechanism of nonpolar m-plane GaN on maskless patterned a-plane sapphire substrate. Phys. Status Solidi (C) **7**(7–8), 2066–2068 (2010)
43. A. Dadgar, R. Ravash, P. Veit, G. Schmidt, M. Müller, A. Dempewolf, F. Bertram, M. Wieneke, J. Christen, A. Krost, Eliminating stacking faults in semi-polar GaN by AlN interlayers. Appl. Phys. Lett. **99**(2), 021905 (2011)
44. F. Scholz, Semipolar GaN grown on foreign substrates: a review. Semicond. Sci. Technol. **27**(2), 024002 (2012)
45. J.E. Northrup, GaN and InGaN $(11\bar{2}2)$ surfaces: group-III adlayers and indium incorporation. Appl. Phys. Lett. **95**(13), 133107 (2009)
46. T. Wernicke, L. Schade, C. Netzel, J. Rass, V. Hoffmann, S. Ploch, A. Knauer, M. Weyers, U. Schwarz, M. Kneissl, Indium incorporation and emission wavelength of polar, nonpolar and semipolar InGaN quantum wells. Semicond. Sci. Technol. **27**(2), 024014 (2012)
47. N.F. Gardner, J.C. Kim, J.J. Wierer, Y.C. Shen, M.R. Krames, Polarization anisotropy in the electroluminescence of m-plane InGaN-GaN multiple-quantum-well light-emitting diodes. Appl. Phys. Lett. 3–5 (2005)

48. H. Masui, H. Yamada, K. Iso, S. Nakamura, S.P. DenBaars, Optical polarization characteristics of InGaN/GaN light-emitting diodes fabricated on GaN substrates oriented between $(10\overline{1}0)$ and $(10\overline{1}\overline{1})$ planes. Appl. Phys. Lett. **92**(9), 091105 (2008)
49. L. Schade, U.T. Schwarz, T. Wernicke, J. Rass, S. Ploch, M. Weyers, M. Kneissl, On the optical polarization properties of semipolar InGaN quantum wells. Appl. Phys. Lett. **99**(5), 051103 (2011)
50. H. Jönen, H. Bremers, T. Langer, U. Rossow, A. Hangleiter, Large optical polarization anisotropy due to anisotropic in-plane strain in m-plane GaInN quantum well structures grown on m-plane 6H-SiC. Appl. Phys. Lett. **100**(15), 151905 (2012)
51. M. Ueda, M. Funato, K. Kojima, Y. Kawakami, Y. Narukawa, T. Mukai, Polarization switching phenomena in semipolar $In_xGa_{1-x}N$/GaN quantum well active layers. Phys. Rev. B **78**, 2–5 (2008)
52. S. Chuang, C. Chang, $k \cdot p$ method for strained wurtzite semiconductors. Phys. Rev. B **54**, 2491–2504 (1996)
53. W. Scheibenzuber, U. Schwarz, R. Veprek, B. Witzigmann, A. Hangleiter, Calculation of optical eigenmodes and gain in semipolar and nonpolar InGaN/GaN laser diodes. Phys. Rev. B **80**, 115320 (2009)
54. K. Kojima, H. Kamon, M. Funato, Y. Kawakami, Theoretical investigations on anisotropic optical properties in semipolar and nonpolar InGaN quantum wells. Phys. Status Solidi (C) **5**, 3038–3041 (2008)
55. L. Schade, U.T. Schwarz, T. Wernicke, M. Weyers, M. Kneissl, Impact of band structure and transition matrix elements on polarization properties of the photoluminescence of semipolar and nonpolar InGaN quantum wells. Phys. Status Solidi (B) **248**, 638–646 (2011)
56. T. Ohtoshi, A. Niwa, T. Kuroda, Crystal orientation effect on valence-subband structures in wurtzite-GaN strained quantum wells. Jpn. J. Appl. Phys. Part 2 Lett. **35**, 1566–1568 (1996)
57. L. Schade, U.T. Schwarz, T. Wernicke, J. Rass, S. Ploch, M. Weyers, M. Kneissl, Auger effect in nonpolar quantum wells. Proc. SPIE **8262**(0), 82620K–82620K–9 (2012)
58. H. Masui, H. Asamizu, A. Tyagi, N.F. DeMille, S. Nakamura, S.P. DenBaars, Correlation between optical polarization and luminescence morphology of $(11\overline{2}2)$-oriented InGaN/GaN quantum-well structures. Appl. Phys. Express **2**, 071002 (2009)
59. W.G. Scheibenzuber, U.T. Schwarz, Polarization switching of the optical gain in semipolar InGaN quantum wells. Phys. Status Solidi (B) **248**, 647–651 (2011)
60. C. Roberts, Q. Yan, M.-S. Miao, C.G. Van de Walle, Confinement effects on valence-subband character and polarization anisotropy in $(11\overline{2}2)$ semipolar InGaN/GaN quantum wells. J. Appl. Phys. **111**(7), 073113 (2012)
61. A.E. Romanov, T.J. Baker, S. Nakamura, J.S. Speck, Strain-induced polarization in wurtzite III-nitride semipolar layers. J. Appl. Phys. **100**(2), 023522 (2006)
62. M. Funato, D. Inoue, M. Ueda, Y. Kawakami, Y. Narukawa, T. Mukai, Strain states in semipolar III-nitride semiconductor quantum wells. J. Appl. Phys. **107**(12), 123501 (2010)
63. Q. Yan, P. Rinke, M. Scheffler, C.G. Van de Walle, Role of strain in polarization switching in semipolar InGaN/GaN quantum wells. Appl. Phys. Lett. **97**(18), 181102 (2010)
64. T. Kyono, Y. Yoshizumi, Y. Enya, M. Adachi, S. Tokuyama, M. Ueno, K. Katayama, T. Nakamura, Optical polarization characteristics of InGaN quantum wells for green laser diodes on semi-polar $\{20\overline{2}1\}$ GaN substrates. Appl. Phys. Express **3**(1), 011003 (2010)
65. Y. Zhao, S. Tanaka, Q. Yan, C.-Y. Huang, R.B. Chung, C.-C. Pan, K. Fujito, D. Feezell, C.G.V. de Walle, J.S. Speck, S.P. DenBaars, S. Nakamura, High optical polarization ratio from semipolar $(20\overline{2}\overline{1})$ blue-green InGaN/GaN light-emitting diodes. Appl. Phys. Lett. **99**(5), 051109 (2011)
66. H. Masui, H. Yamada, K. Iso, S. Nakamura, S.P. DenBaars, Optical polarization characteristics of m-oriented InGaN/GaN light-emitting diodes with various indium compositions in single-quantum-well structure. J. Phys. D: Appl. Phys. **41**, 225104 (2008)
67. I. Vurgaftman, J.R. Meyer, Band parameters for nitrogen-containing semiconductors. J. Appl. Phys. **94**, 3675 (2003)

68. E. Kuokstis, J.W. Yang, G. Simin, M.A. Khan, R. Gaska, M.S. Shur, Two mechanisms of blueshift of edge emission in InGaN-based epilayers and multiple quantum wells. Appl. Phys. Lett. **80**(6), 977–979 (2002)
69. M.C. Schmidt, K.-C. Kim, H. Sato, N. Fellows, H. Masui, S. Nakamura, S.P. DenBaars, J.S. Speck, High power and high external efficiency m-plane InGaN light emitting diodes. Jpn. J. Appl. Phys. **46**(7), L126–L128 (2007)
70. Y. Zhao, S. Tanaka, C.-C. Pan, K. Fujito, D. Feezell, J.S. Speck, S.P. DenBaars, S. Nakamura, High-power blue-violet semipolar $(20\overline{2}\overline{1})$ InGaN/GaN light-emitting diodes with low efficiency droop at 200 a/cm^2. Appl. Phys. Express **4**(8), 082104 (2011)
71. J. Piprek, Efficiency droop in nitride-based light-emitting diodes. Phys. Status Solidi (A) **207**(10), 2217–2225 (2010)
72. Y.C. Shen, G.O. Mueller, S. Watanabe, N.F. Gardner, A. Munkholm, M.R. Krames, Auger recombination in InGaN measured by photoluminescence. Appl. Phys. Lett. **91**(14), 141101 (2007)
73. M.-H. Kim, M.F. Schubert, Q. Dai, J.K. Kim, E.F. Schubert, J. Piprek, Y. Park, Origin of efficiency droop in GaN-based light-emitting diodes. Appl. Phys. Lett. **91**(18), 183507 (2007)
74. A. David, M.J. Grundmann, Droop in InGaN light-emitting diodes: a differential carrier lifetime analysis. Appl. Phys. Lett. **96**(10), 103504 (2010)
75. J. Hader, J.V. Moloney, S.W. Koch, Density-activated defect recombination as a possible explanation for the efficiency droop in GaN-based diodes. Appl. Phys. Lett. **96**(22), 221106 (2010)
76. E. Kioupakis, P. Rinke, K.T. Delaney, C.G.V. de Walle, Indirect auger recombination as a cause of efficiency droop in nitride light-emitting diodes. Appl. Phys. Lett. **98**(16), 161107 (2011)
77. C.-C. Pan, S. Tanaka, F. Wu, Y. Zhao, J.S. Speck, S. Nakamura, S.P. DenBaars, D. Feezell, High-power, low-efficiency-droop semipolar $(20\overline{2}\overline{1})$ single-quantum-well blue light-emitting diodes. Appl. Phys. Express **5**(6), 062103 (2012)
78. M. Krames, O. Shchekin, R. Mueller-Mach, G. Mueller, L. Zhou, G. Harbers, M. Craford, Status and future of high-power light-emitting diodes for solid-state lighting. J. Disp. Technol. **3**, 160–175 (2007)
79. A. Laubsch, M. Sabathil, J. Baur, M. Peter, B. Hahn, High-power and high-efficiency InGaN-based light emitters. IEEE Trans. Electron Devices **57**, 79–87 (2010)
80. E. Matioli, S. Brinkley, K.M. Kelchner, S. Nakamura, S. DenBaars, J. Speck, C. Weisbuch, Polarized light extraction in m-plane GaN light-emitting diodes by embedded photonic-crystals. Appl. Phys. Lett. **98**(25), 251112 (2011)
81. J. Rass, T. Wernicke, W.G. Scheibenzuber, U.T. Schwarz, J. Kupec, B. Witzigmann, P. Vogt, S. Einfeldt, M. Weyers, M. Kneissl, Polarization of eigenmodes in laser diode waveguides on semipolar and nonpolar GaN. Phys. Status Solidi (RRL)—Rapid Res. Lett. **4**, 1–3 (2010)
82. J. Rass, T. Wernicke, S. Ploch, M. Brendel, A. Kruse, A. Hangleiter, W. Scheibenzuber, U.T. Schwarz, M. Weyers, M. Kneissl, Polarization dependent study of gain anisotropy in semipolar InGaN lasers. Appl. Phys. Lett. **99**(17), 171105 (2011)
83. J.C. Raß, *Charakterisierung von InGaN-basierten Lichtemittern auf semipolaren und nichtpolaren Halbleiteroberflächen/Characterization of InGaN-based light emitters on semipolar and nonpolar semiconductor orientations*. Dissertation, Technische Universität Berlin (2012)
84. C.-Y. Huang, A. Tyagi, Y.-D. Lin, M.T. Hardy, P.S. Hsu, K. Fujito, J.-S. Ha, H. Ohta, J.S. Speck, S.P. DenBaars, S. Nakamura, Propagation of spontaneous emission in birefringent m-axis oriented semipolar $(11\overline{2}2)$ (Al, In, Ga)N waveguide structures. Jpn. J. Appl. Phys. **49**, 010207 (2010)
85. T. Wunderer, P. Bruckner, B. Neubert, F. Scholz, M. Feneberg, F. Lipski, M. Schirra, K. Thonke, Bright semipolar GaInN/GaN blue light emitting diode on side facets of selectively grown GaN stripes. Appl. Phys. Lett. **89**(4), 041121 (2006)
86. F. Scholz, T. Wunderer, M. Feneberg, K. Thonke, A. Chuvilin, U. Kaiser, S. Metzner, F. Bertram, J. Christen, GaInN-based LED structures on selectively grown semi-polar crystal facets. Phys. Status Solidi (A) **207**(6), 1407–1413 (2010)

87. T. Wunderer, M. Feneberg, F. Lipski, J. Wang, R.A.R. Leute, S. Schwaiger, K. Thonke, A. Chuvilin, U. Kaiser, S. Metzner, F. Bertram, J. Christen, G.J. Beirne, M. Jetter, P. Michler, L. Schade, C. Vierheilig, U.T. Schwarz, A.D. Dräger, A. Hangleiter, F. Scholz, Three-dimensional GaN for semipolar light emitters. Phys. Status Solidi (B) **248**(3), 549–560 (2011)
88. S. Jung, Y. Chang, K.-H. Bang, H.-G. Kim, Y.-H. Choi, S.-M. Hwang, K.H. Baik, High brightness nonpolar a-plane (11-20) GaN light-emitting diodes. Semicond. Sci. Technol. **27**(2), 024017 (2012)
89. A. Chakraborty, B.A. Haskell, S. Keller, J.S. Speck, S.P. DenBaars, S. Nakamura, U.K. Mishra, Nonpolar InGaN/GaN emitters on reduced-defect lateral epitaxially overgrown a-plane GaN with drive-current-independent electroluminescence emission peak. Appl. Phys. Lett. **85**(22), 5143–5145 (2004)
90. A. Chakraborty, T.J. Baker, B.A. Haskell, F. Wu, J.S. Speck, S.P. Denbaars, S. Nakamura, U.K. Mishra, Milliwatt power blue InGaN/GaN light-emitting diodes on semipolar GaN templates. Jpn. J. Appl. Phys. **44**, L945–L947 (2005)
91. T. Hikosaka, T. Tanikawa, Y. Honda, M. Yamaguchi, N. Sawaki, Fabrication and properties of semi-polar $(1\bar{1}01)$ and $(11\bar{2}2)$ InGaN/GaN light emitting diodes on patterned Si substrates. Phys. Status Solidi (c) **5**(6), 2234–2237 (2008)
92. M. Funato, M. Ueda, Y. Kawakami, Y. Narukawa, T. Kosugi, M. Takahashi, T. Mukai, Blue, green, and amber InGaN/GaN light-emitting diodes on semipolar $11\bar{2}2$ GaN bulk substrates. Jpn. J. Appl. Phys. **45**(26), L659–L662 (2006)
93. H. Sato, A. Tyagi, H. Zhong, N. Fellows, R.B. Chung, M. Saito, K. Fujito, J.S. Speck, S.P. DenBaars, S. Nakamura, High power and high efficiency green light emitting diode on free-standing semipolar $(11\bar{2}2)$ bulk GaN substrate. Phys. Status Solidi (RRL)—Rapid Res. Lett. **1**(4), 162–164 (2007)
94. H. Sato, R.B. Chung, H. Hirasawa, N. Fellows, H. Masui, F. Wu, M. Saito, K. Fujito, J.S. Speck, S.P. DenBaars, S. Nakamura, Optical properties of yellow light-emitting diodes grown on semipolar $(11\bar{2}2)$ bulk GaN substrates. Appl. Phys. Lett. **92**(22), 221110 (2008)
95. Y. Zhao, J. Sonoda, C.-C. Pan, S. Brinkley, I. Koslow, K. Fujito, H. Ohta, S.P. DenBaars, S. Nakamura, 30-mw-class high-power and high-efficiency blue semipolar $(10\bar{1}\bar{1})$ InGaN/GaN light-emitting diodes obtained by backside roughening technique. Appl. Phys. Express **3**(10), 102101 (2010)
96. H. Zhong, A. Tyagi, N.N. Fellows, F. Wu, R.B. Chung, M. Saito, K. Fujito, J.S. Speck, S.P. DenBaars, S. Nakamura, High power and high efficiency blue light emitting diode on freestanding semipolar $(10\bar{1}\bar{1})$ bulk GaN substrate. Appl. Phys. Lett. **90**(23), 233504 (2007)
97. S. Yamamoto, Y. Zhao, C.-C. Pan, R.B. Chung, K. Fujito, J. Sonoda, S.P. DenBaars, S. Nakamura, High-efficiency single-quantum-well green and yellow-green light-emitting diodes on semipolar $(20\bar{2}1)$ GaN substrates. Appl. Phys. Express **3**(12), 122102 (2010)
98. K. Okamoto, H. Ohta, D. Nakagawa, M. Sonobe, J. Ichihara, H. Takasu, Dislocation-free m-plane InGaN/GaN light-emitting diodes on m-plane gan single crystals. Jpn. J. Appl. Phys. **45**(45), L1197–L1199 (2006)
99. A. Chakraborty, B.A. Haskell, S. Keller, J.S. Speck, S.P. Denbaars, S. Nakamura, U.K. Mishra, Demonstration of nonpolar *m*-plane InGaN/GaN light-emitting diodes on free-standing *m*-plane GaN substrates. Jpn. J. Appl. Phys. **44**(5), L173–L175 (2005)
100. A. Chakraborty, B.A. Haskell, H. Masui, S. Keller, J.S. Speck, S.P. DenBaars, S. Nakamura, U.K. Mishra, Nonpolar *m*-plane blue-light-emitting diode lamps with output power of 23.5 mW under pulsed operation. Jpn. J. Appl. Phys. **45**(2A), 739–741 (2006)
101. K.-C. Kim, M.C. Schmidt, H. Sato, F. Wu, N. Fellows, M. Saito, K. Fujito, J.S. Speck, S. Nakamura, S.P. DenBaars, Improved electroluminescence on nonpolar m-plane InGaN/GaN quantum wells LEDs. Phys. Status Solidi (RRL)—Rapid Res. Lett. **1**(3), 125–127 (2007)
102. Y. Yoshizumi, M. Adachi, Y. Enya, T. Kyono, S. Tokuyama, T. Sumitomo, K. Akita, T. Ikegami, M. Ueno, K. Katayama, T. Nakamura, Continuous-wave operation of 520 nm green InGaN-based laser diodes on semi-polar $\{20\bar{2}1\}$ GaN substrates. Appl. Phys. Express **2**(9), 092101 (2009)

103. Y. Enya, Y. Yoshizumi, T. Kyono, K. Akita, M. Ueno, M. Adachi, T. Sumitomo, S. Tokuyama, T. Ikegami, K. Katayama, T. Nakamura, 531 nm green lasing of InGaN based laser diodes on semi-polar $\{20\bar{2}1\}$ free-standing GaN substrates. Appl. Phys. Express **2**, 082101 (2009)
104. T. Yamashita, T. Akiyama, K. Nakamura, T. Ito, Surface reconstructions on GaN and InN semipolar $(20\bar{2}1)$ surfaces. Jpn. J. Appl. Phys. **49**, 018001 (2010)
105. Y.S. Kim, A. Kaneta, M. Funato, Y. Kawakami, T. Kyono, M. Ueno, T. Nakamura, Optical gain spectroscopy of a semipolar $(20\bar{2}1)$-oriented green InGaN laser diode. Appl. Phys. Express **4**, 052103 (2011)
106. Y. Zhao, S. Tanaka, C.-C. Pan, K. Fujito, D. Feezell, J.S. Speck, S.P. DenBaars, S. Nakamura, High-power blue-violet semipolar $(20\bar{2}\bar{1})$ InGaN/GaN light-emitting diodes with low efficiency droop at 200 A/cm^2. Appl. Phys. Express **4**, 082104 (2011)
107. Y. Kawaguchi, C.-Y. Huang, Y.-R. Wu, Q. Yan, C.-C. Pan, Y. Zhao, S. Tanaka, K. Fujito, D. Feezell, C.G. Van de Walle, S.P. DenBaars, S. Nakamura, Influence of polarity on carrier transport in semipolar $(20\bar{2}1)$ and $(20\bar{2}\bar{1})$ multiple-quantum-well light-emitting diodes. Appl. Phys. Lett. **100**(23), 231110 (2012)
108. Y. Zhao, Q. Yan, C.-Y. Huang, S.-C. Huang, P. Shan, Hsu, S. Tanaka, C.-C. Pan, Y. Kawaguchi, K. Fujito, C G. Van de Walle, J.S. Speck, S.P. DenBaars, S. Nakamura, D. Feezell, Indium incorporation and emission properties of nonpolar and semipolar InGaN quantum wells. Appl. Phys. Lett. **100**(20), 201108 (2012)
109. P.S. Hsu, K.M. Kelchner, A. Tyagi, R.M. Farrell, D.A. Haeger, K. Fujito, H. Ohta, S.P. DenBaars, J.S. Speck, S. Nakamura, InGaN/GaN blue laser diode grown on semipolar $(30\bar{3}1)$ free-standing GaN substrates. Appl. Phys. Express **3**(5), 052702 (2010)
110. D. Morita, M. Yamamoto, K. Akaishi, K. Matoba, K. Yasutomo, Y. Kasai, M. Sano, S. Ichi, Nagahama, T. Mukai, Watt-class high-output-power 365 nm ultraviolet light-emitting diodes. Jpn. J. Appl. Phys. **43**(9A), 5945–5950 (2004)
111. Y. Narukawa, M. Ichikawa, D. Sanga, M. Sano, T. Mukai, White light emitting diodes with super-high luminous efficacy. J. Phys. D: Appl. Phys. **43**(35), 354002 (2010)
112. T. Mukai, M. Yamada, S. Nakamura, Characteristics of InGaN-based UV/blue/green/amber/red light-emitting diodes. Jpn. J. Appl. Phys. **38**(Part 1, No. 7A), 3976–3981 (1999)
113. Y. Narakawa, Nichia Corporation, Recent developments of high efficiency white light emitting diodes. Presentation at the ICNS-7, Las Vegas, USA (2007)
114. Nichia Corporation Oral presentation at the ICNS-8, Jeju, Korea (2009)
115. W. Goetz, Philips-Lumileds Lighting, High power III-nitride based light emitting diodes: progress and challenges. Presentation at the ICNS-7, Las Vegas, USA (2007)
116. W. Goetz, Philips-Lumileds Lighting Presentation at the rump session on the "Future of Solid State Lighting" at the ICNS-8, Jeju, Korea (2009)
117. Nichia Corporartion, 2012 Nichia LED Catalogue. Website (2012), http://www.nichia.co.jp
118. Soraa, Soraa premium MR 16 LED lamp, product# MR16-50-B01-12-830-25. Website (2012), http://www.soraa.com

Chapter 6
Internal Quantum Efficiency in Light-Emitting Diodes

Elison Matioli and Claude Weisbuch

In this chapter, we present different techniques used to assess the internal quantum efficiency (IQE) in light-emitting diodes (LEDs). The commonly used technique based on temperature-dependent photoluminescence relies in strong assumptions which are discussed in this chapter. We introduce an alternative method to determine IQE based on electroluminescence, in which the external quantum efficiency (EQE) is measured from a single facet of the LED, where the light emission can be calculated with good accuracy. The IQE is ultimately obtained from the ratio of the EQE and the calculated light extraction efficiency. We develop an optical model of the light emission in a multilayered LED structure, from which we derive and validate an approximate model to easily calculate the extraction efficiency through the top facet of any LED structure. We address the various assumptions made to calculate the direct emission model through a single facet and evaluate the effect of photon recycling in the quantum wells. We also calculate the sensitivity of the model to the LED parameters and surface roughness. Finally, we apply this technique to calculate the IQE of both a state-of-the-art and a low-performance GaN-based LEDs, highlighting the particular features in each structure.

E. Matioli (✉)
Institute of Electrical Engineering, École Polytechnique Fédérale de Lausanne,
EPFL STI IEL POWERlab, Building ELD, Station 11 CH1015, Switzerland
e-mail: elison.matioli@epfl.ch

C. Weisbuch (✉)
Materials Department, University of California, Santa Barbara, CA 93106-5050, USA
e-mail: weisbuch@engineering.ucsb.edu; claude.weisbuch@polytechnique.fr

C. Weisbuch
Laboratoire de Physique de la Matière Condensée, Ecole Polytechnique,
91128 Palaiseau Cedex, France

© Springer Nature Singapore Pte Ltd. 2017

T.-Y. Seong et al. (eds.), *III-Nitride Based Light Emitting Diodes and Applications*,
Topics in Applied Physics 133, DOI 10.1007/978-981-10-3755-9_6

6.1 Introduction

The development of the next generation of high efficiency light-emitting diodes (LEDs) for solid-state lighting requires a quantitative determination of intrinsic device parameters to further performance. A common metric of optoelectronic devices is their output power emitted externally to the device (P_{out}) measured in an integrating sphere. From there, two quantities define the efficiency of the LEDs: the wall-plug efficiency (WPE) η_{wp}, i.e., the ratio of electrical input power to optical output power, and the external quantum efficiency (EQE) η_{EQE}, ratio between the number of electrically injected carriers and externally observed photons. The WPE is related to EQE by the voltage drop V at the device due to the diode forward voltage and series resistance, as $\eta_{wp} = P_{out}/VI$, where I is the injected current. To optimize it for a given EQE, one requires structures with low contact resistance and high conductivity materials, as well as efficient heat sink to maintain high performance under all operating conditions [1]. η_{EQE} is easily assessed by $\eta_{EQE} = P_{out}/(\hbar\omega)(I/q)$ but it only reveals the combination of non-easily separable key parameters, such as carrier injection efficiency η_{inj}, internal quantum efficiency (IQE) η_{IQE}, and light extraction efficiency (LEE) η_{extr} of the LED structure, ratio between the externally emitted photons and the internally generated photons in the active region.

What determines these efficiencies rely on intrinsic and extrinsic properties of materials and architecture of the LEDs. η_{extr} is mainly determined by the LED architecture (such as chip shaping [2], use of patterned substrates [3], photonic crystals [4], surface roughening [5, 6], etc.) with however some dependence on materials parameters (materials absorption, reflection, etc.) (see the chapter by Lalau Keraly et al. in this book); η_{IQE} is mainly connected to the quality of the active layer which is determined by growth conditions such as growth temperature, pressure, quality and flow of precursors, impurity incorporation, as well as growth technique and reactor used, and by the choice of substrate, which affect the crystalline quality, doping profile, defect density of the material, uniformity, and surface morphology. It is therefore of great importance to have a precise evaluation of the materials quality as given by η_{IQE} to assess growth quality. This quantity also serves to separately evaluate η_{extr} from η_{EQE} and compare on an absolute scale the various techniques to enhance light extraction.

In addition, the IQE defined by the ratio between the electrically injected carriers and the internally emitted photons is itself the product of the electron injection efficiency η_{inj}, ratio of carriers injected in the device to those reaching the light-emitting regions (usually quantum wells (QWs)) and of the radiative efficiency, η_{rad}, ratio of injected electron–hole (e–h) pairs that recombine radiatively to generate photons and the total number of injected e–h pairs. η_{inj} is mostly determined by the LED heterostructure design, with carrier overflow and QWs uniform injection being examples of phenomena to be controlled.

Equations (6.1) and (6.2) express the relations between these various quantities.

$$P_{out} = \frac{\hbar\omega}{q} I \eta_{inj} \eta_{rad} \eta_{extr} \tag{6.1}$$

$$\eta_{IQE} = \eta_{inj} \eta_{rad}, \tag{6.2}$$

where $\hbar\omega$ is the photon energy and q is the electron charge.

The variations in the measured IQE are expected to be mainly due to η_{rad}, which is directly linked to materials quality, allowing to assess growth quality in a routine fashion, to optimize epitaxial design and to check run-to-run reproducibility. From (6.1), the IQE in an LED structure can be written as

$$\eta_{IQE} = \frac{P_{out}}{\frac{\hbar\omega}{q} I \eta_{extr}} = \frac{\eta_{EQE}}{\eta_{extr}}. \tag{6.3}$$

In the following sections, we present two methods to determine IQE, the first based on photoluminescence (PL) and the second on electroluminescence (EL). To obtain η_{IQE} from the η_{EQE} measurement using (6.3) requires a good knowledge of η_{extr}, which is not known in a complex LED structure usually containing light extraction features which complicates the precise determination of η_{extr}. The PL-based method circumvents this issue by considering a reference point at low temperature (LT) where η_{IQE} is assumed to be unity, and assuming that η_{extr} is the same at room temperature (RT), any variation between LT and RT is due to the change in η_{IQE}. Thus the η_{IQE} at RT is just the ratio of the η_{EQE} measurements at RT and LT. The EL-based method considers a LED structure with a well-defined geometry and without light extractors, such that η_{extr} is known a priori. Then the η_{IQE} is determined from η_{EQE} as η_{EQE}/η_{extr}.

6.2 Assessment of IQE from Photoluminescence Measurements

The IQE is widely estimated by temperature-dependent photoluminescence (PL), in which the intensity of the emitted light at a certain range of PL excitation is measured at low temperature (LT), usually below ~10 K and at room temperature (RT). The IQE is then estimated from the ratio of the peak PL intensities I_{RT} at RT and I_{LT} at LT, which relies on the assumption that the IQE at LT is 100% and that η_{extr} does not change with T:

$$\eta_{IQE} = \frac{I_{RT}}{I_{LT}}. \tag{6.4}$$

The assumption that IQE is unity at low temperatures is often made regardless the excitation power density. However, the IQE and the PL intensities are themselves dependent on excitation power density [7, 8] at all temperatures, being dominated

by Shockley–Read–Hall (SRH), or non-radiative recombination mechanisms at low excitation density and by Auger recombinations at high excitations [9] (see Fig. 1 from [7]).

A careful procedure is therefore required for estimating the IQE using the temperature-dependent PL method. A large range of excitation power densities, over several orders of magnitude, is needed to correctly determine the peak IQE at low temperature; otherwise, the base level that normalizes the low-temperature PL intensity at 100% IQE is incorrect. This procedure is often times overseen in the literature [10].

The assumption of unity IQE considers that non-radiative recombination mechanisms are eliminated at low temperatures, which would be justified if only thermally activated defect-induced recombinations were the dominant non-radiative recombination mechanism. However, Fig. 6.1 shows that non-radiative mechanisms are still present at low excitation density even at low temperatures. The assumption that the peak PL at LT corresponds to 100% IQE lacks fundamental support.

Another issue is that the peak PL emission occurs at different excitation power densities at LT and RT, and hence to different carrier densities in the active region, which makes it difficult to compare these quantities since the competition between SRH, radiative and auger recombinations depends on carrier density.

The IQE determined from PL-based methods also assumes similar carrier injection to the active region compared to electroluminescence. It neglects the effects of applied bias in the internal electric field in the QWs, and also neglects the different carrier injections in individual wells of a MQW structure under PL and EL excitation. In a MQW structure under PL excitation, electron–hole pairs are generated in all QWs, whereas under EL excitation, the carrier distribution in the MQW is, in general, inhomogeneous and dependent on temperature and current density [11, 12]. Laubsch et al. demonstrated a similar behavior of the emission under PL and EL excitation for a single QW structure [8]; however, the majority of the LEDs fabricated today are based on MQW structures.

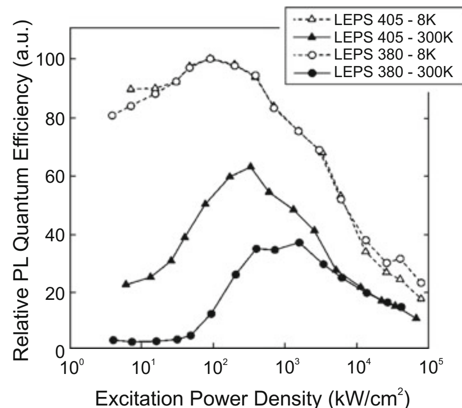

Fig. 6.1 [After Watanabe et al. [7]] Relative PL emission normalized by the peak intensity at LT as a function of excitation power density for two different devices at 8 and 300 K. Note that the PL emission is largely dependent on excitation density and the peak of PL emission occurs at different excitation power densities at LT and RT

These strong assumptions used in the temperature-dependent PL method justify the search for other techniques based on similar operation condition and injection mechanisms as the operating LED.

6.3 Principle of IQE Assessment from Electroluminescence Measurements

As given by (6.3), P_{out}, or equivalently η_{EQE}, can be measured at a given current, and as for a simple enough LED geometry the η_{extr} can be precisely calculated. This section is divided in two parts, the first covering the results of calculations of the η_{extr} in a simple LED geometry, with details to be found in [13] or in Appendix A of this chapter, and the second covering the fabrication details of a simple LED structure adapted for this method [14], and experimental results.

The small extraction efficiency of planar LED structures originates from the fact that only a small fraction of the photons generated within the active region is directly emitted out of the device at their encounter with interfaces, which corresponds to the fraction of light emitted with its wavevector within the air cone. The majority of the light is emitted outside the air cone and is reflected back in the device. A fraction of such photons is dissipated by material defects, free carriers in doped regions, and absorbing materials (such as metal contacts). Another fraction is absorbed by the active material in the device which can be re-emitted and may re-attempt to escape the LED structure. This mechanism, called photon recycling, is an efficient way to significantly increase extraction efficiency in the LED when both η_{IQE} and the fraction of light recycled (F_{rec}, ratio of light reabsorbed by the active region QWs to the light remaining in the LED) are large. F_{rec} is determined from the competition between the various dissipation mechanisms with the re-absorption by the QWs. This is treated in more detail in Sect. 6.5 of this chapter. Photons can also escape the LED through the light cone of any exposed facets after a few bounces within the structure. This mechanism can be very efficient when dissipation mechanisms, including QW re-absorption, are very small along the sometimes long trajectories required to bounce back in the escape angle: suffices to remark that in GaAs LEDs with 2% direct extraction, tens of bounces are required to extract most of the light [1]. It is the variety of fates for emitted photons that makes the extraction efficiency difficult to quantify, and highly dependent on the LED chip architecture. The light extraction efficiency based on the use of extracting features such as truncated pyramids, roughened surfaces, patterned sapphire substrates, and surface photonic crystals is in a way difficult to quantify, as it will depend on the exact description of the LED geometry, including its sidewalls, and on the loss mechanisms within the LED for the various materials and regions. Detailed simulations rely on ray-tracing techniques to explore the different trajectories (see the chapter by Lalau Keraly et al. in this book) or on solving full Maxwell's equations by finite-difference time-domain (FDTD) or plane wave expansion [15].

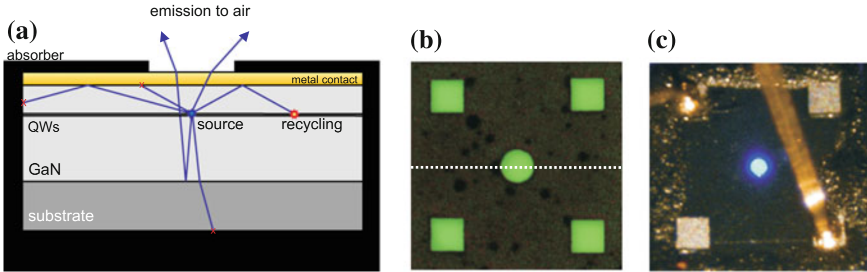

Fig. 6.2 **a** Schematic of a simple geometry LED (contact pads are not shown) surrounded by light-absorbing material, along with possible trajectories of the light emitted by the QWs. This view corresponds to the cross-sectional view at the *dashed line* in part **b**. A small circular aperture allows directly emitted light from the QWs to escape as well as the small fraction reflected off the substrate hetero-interface. Light attempting to escape from sidewalls and backside of the device is dissipated and therefore eliminated from the collected light through the aperture (indicated by *red crosses*). **b** Picture of the absorbing material covering the LED. The *squares* are openings for electric contacts and the *circle* is the aperture for light emission. **c** Picture of the LED covered with absorbing material under bias. Only light emitted through the aperture is observed in air [After [14]]

The way to circumvent the difficult analysis of η_{extr} in commonly used LED structures is to rely on a simple LED geometry, with a computable direct light extraction, where all other extraction paths are suppressed. This is achieved by covering the LED with a perfectly absorbing material and leaving only a small well-defined aperture of area a on the LED top surface. This is illustrated in Fig. 6.2a, where all trajectories originating from sidewalls, backside of the device, contact pads (not shown), etc., are dissipated by this surrounding material and therefore eliminated from the collected light. Only photons emitted directly from the QW region, plus a small fraction reflected off the substrate hetero-interface (in the case of hetero-structures, for example GaN on sapphire) go through the aperture, and thus reliable estimates of the extraction efficiency η_{extr} can be made. Some care is required when defining the aperture in the absorber material, such as a large spatial separation from the sidewalls and contacts, and a much larger aperture size compared to the GaN thickness L (both roughly larger than 10 L).

The η_{EQE} is measured using an integrating sphere and subsequently corrected by the ratio between the aperture surface a and the total LED top surface A, corresponding to the surface of current injection, as $\eta_{\mathrm{EQE}} = \eta_{\mathrm{EQE}}^{\mathrm{meas}} A/a$, where $\eta_{\mathrm{EQE}}^{\mathrm{meas}}$ is the measured EQE in the integrating sphere. Bringing this technique into practice requires effort in two separate areas. First, we must calculate with good accuracy the light extraction for this device and evaluate the precision of such model. Second, a device with only direct light extraction as described above must be fabricated.

One possible difficulty is that the distribution of light emission from multi-QWs is somewhat involved. QWs in LEDs, usually more than one, are distributed over a finite thickness within the device and are each few nanometers wide, spaced apart by barrier layers tens of nanometers thick. One might assume that each well is equally excited and thus emits an equal number of photons in a spherically symmetric

pattern. However, it is just as plausible to assume that under EL conditions, either the first well that carriers encounter, the last well (perhaps immediately preceding an electron barrier layer) or one of the center wells (being most equally accessible to both electrons and holes) would have a disproportionately larger share of the emission. David et al. [12] examined this question with regard to GaN/InGaN LEDs, and reported that nearly all of the emission from an LED comes from the QW nearest to the p-doped side of the device. The predominant emission from the top QW was attributed to the poor hole transfer between QWs, and occurs regardless of the number of quantum wells, often requiring some special design such as a double heterostructure to modify the carrier distribution [12]. That determination was made possible due to the fact that the various QWs have different emission patterns due to their different distances to the interface with an Ag mirror. In our structures comprising materials with only low index contrast, the exact position of emitting QWs will not make any difference as long as they are sufficiently away from the device interfaces with non-nitride materials (see discussion in Appendix B).

For the sake of completeness, Kivisaari et al. [16] proposed an alternative EL-based method to measure the IQE based on extracting the radiative part as the quadratic term of the A-B-C model [17] from the measurements of EQE. The ABC model uses as parameter the carrier density in the active region. However, in practice, it is not possible to assess this parameter from the current density injected in the device, especially in the case of multiple quantum wells: this method assumed that all QWs were equally injected with an injection efficiency of 100% which has been demonstrated to be inaccurate in the nitride system [12]. Their attempt to correct for the uneven injection in each QW, which directly influences the carrier density in each well, was to deliberately consider a thinner active region, replacing the nominal 25 nm by 10 nm without clear theoretical or experimental support. As a consequence, the estimated A, B, and C coefficients, representing the Shockley–Read–Hall (SRH), radiative, and Auger coefficients, do not match the values in the literature, which in turn might lead to an inaccurate estimation of the absolute IQE. Another issue is to assign the quadratic term to radiative recombination only. This is a critical point to the method and this assumption might fail in cases where the injection efficiency is not unity or varies with applied current density. This technique however could have some merits as a relative measurement between batches of similar chips, to assess variations on growth and fabrication quality.

A simple LED geometry on a sapphire substrate can be described from an optical point of view as consisting of three distinct homogeneous layers: the LED active layer (L), substrate (s), and a thin metal contact (m) in the top surface, as shown in Fig. 6.3. The outer medium is air (a). The structure is surrounded by light-absorbing material (abs) which removes all contributions to E_{out} other than the direct propagation of the $E_{\mathrm{source}}^{(\gamma,\rho)}$ upward and its reflection at the LED/substrate interface. Here γ indicates the dipole orientation and ρ the polarization TE and TM. In the analysis presented in [13] and in Appendix A, we derive a general expression of the electric field in a structure without metal contacts and separately calculate a transmission function corresponding to the absorbing metal, the reason being that the electric field is much

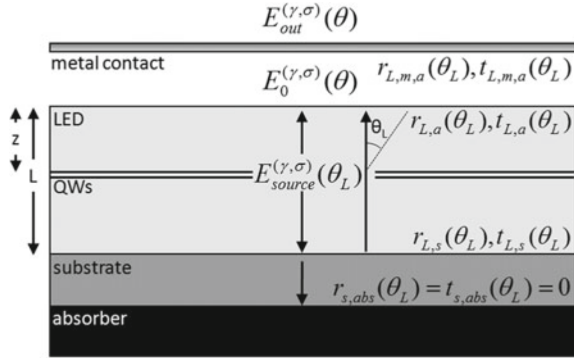

Fig. 6.3 Schematics of the simple LED geometry consisting of three distinct homogeneous layers: the LED (*L*), substrate (*s*), and a thin metal contact (*m*) in the top surface

more sensitive to the metal parameters, such as thickness and refractive index, than to the LED structure parameters—this is actually the core of our analysis.

The external electric field $E_{\text{out}}^{(\gamma,\rho)}$ is then calculated from the metal transmission function $\mathcal{T}_m^{\rho}$ and the external electric field of a structure without metal contact $E_0^{(\gamma,\rho)}$, benefiting from a general property of light propagating in stratified planar media [18, 19], described by a matrix formalism, which allows us to separate the effect of the metal contact from the LED as [13] $|E_{\text{out}}^{(\gamma,\rho)}|^2 = \mathcal{T}_m^{\rho}|E_0^{(\gamma,\rho)}|^2$. From the expression of the electric field emitted to air, we calculate the external power per solid angle $dP_{\text{out}}^{(\gamma,\rho)}(\theta,\lambda)/d\Omega dS$ and the exact extraction efficiency. The complete derivation of these expressions is described in Appendix A and [13]. The extraction efficiency was then simplified by the following approximations (see Appendix A):

Variable-Incidence (VI) approximation:

$$\eta_{\text{extr}} \simeq \left\langle \mathcal{T}_m^{\text{TE}} \right\rangle_{(\lambda,\theta)} \eta_{\text{extr}}^{0,\text{TE}} + \left\langle \mathcal{T}_m^{\text{TM}} \right\rangle_{(\lambda,\theta)} \eta_{\text{extr}}^{0,\text{TM}} \tag{6.5}$$

or the **Normal-Incidence (NI) approximation**:

$$\eta_{\text{extr}} \simeq \langle \mathcal{T}_m(0°) \rangle_{\lambda}\, \eta_{\text{extr}}^{0} \tag{6.6}$$

where $\left\langle \mathcal{T}_m^{\rho} \right\rangle_{(\lambda,\theta)}$ is the metal transmission function averaged in both λ and θ, $\langle \mathcal{T}_m(0°) \rangle_{\lambda}$ is the metal transmission function averaged over the LED emission wavelengths, and η_{extr}^{0} is the extraction efficiency of the LED with metal contacts.

6.3.1 *Calculation of Light Extraction Efficiency in a Simple GaN-Based LED*

The LED structure considered here is the same used in the experimental section of this chapter. The LED material is GaN on a sapphire substrate. The LED thickness is

$L = 4869$ nm, and the distance z of the top surface to the QW is 140 nm. The central emission wavelength from the QW is 445 nm and the measured refractive indexes of the materials at this wavelength are $n_L = 2.475$ and $n_s = 1.779$ for the LED and substrate, respectively. The lineshape of the QW was approximated by a symmetric Gaussian function centered at 445 nm with variance $\sigma^2 = 25$ nm, which is typical for InGaN/GaN QWs. We calculated the extraction efficiency versus metal thickness for the common metals: Au, Ag, and Al, whose optical constants are $n_{\text{Au}} = 1.544 + i1.896$, $n_{\text{Ag}} = 0.155 + i2.421$, and $n_{\text{Al}} = 0.616 + i5.394$ at $\lambda = 445$ nm were obtained from the literature [20]. We calculated the exact extraction efficiency from this structure considering both mono- and polychromatic radiation from the QWs and compared these results to the VI and NI approximative models, shown in Fig. 6.4a. The approximative models show an excellent agreement to the analytical and polychromatic results for these three different metals presenting very different optical constants, which further validates our approximate models. The details on the evaluation of the approximative model given by (6.5) and (6.6) and validation with the exact calculation of the extraction efficiency for a monochromatic and polychromatic light emission are presented in Appendix A.

Figure 6.4b shows the effect of the LED thickness and position of the QWs relative to the top surface of the LED on the calculated extraction efficiency without metal η^0_{extr}. The extraction efficiency oscillates significantly for an LED structure thinner than 1 μm and tends to a fixed value for thicker structures ($L/\lambda > 5$) and for the QWs located far from the bottom interface with the sapphire substrate (this is the case for most of the GaN-on-sapphire LEDs). In practical LEDs, the fast oscillating behavior shown in Fig. 6.13a is averaged due to thickness fluctuations and polychromatic emission from the source which yields a much smoother function almost independent on LED thickness. Suffice to notice that the half period of such oscillations is

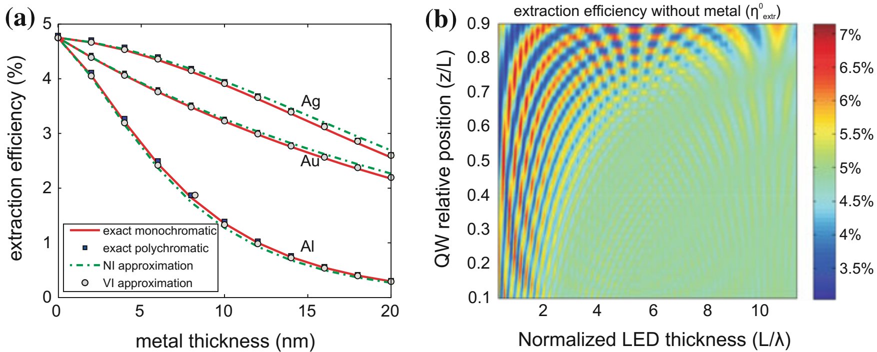

Fig. 6.4 **a** Extraction efficiency of a GaN-based LED on sapphire substrate versus metal thickness for Au, Ag, and Al, using the analytical expressions for monochromatic (*solid*) and polychromatic (*squares*) emission, VI (*circle*), and NI (*dashdotted*) approximations. The center wavelength was $\lambda = 445$ nm and for the polychromatic emission $\sigma^2 = 25$ nm. **b** Extraction efficiency to air as a function of LED thickness and QW position in the LED (z is relative to the LED top surface)

$\sim$50 nm for a fixed $\lambda = 445$ nm, which is much shorter than the thickness variations present in real devices where the GaN thickness is a few microns.

Therefore, the extraction efficiency results shown in Fig. 6.4a can be generally used to assess the IQE for a large range of LED structures other than the one considered in this section. In fact, the calculation of the extraction efficiency is mostly, if not solely, affected by the metal contact properties. The slope of the curves in Fig. 6.4 reflects the sensitivity of these results to thickness variations of the metal contact, where Au and Ag seem to be a better choice than Al. A more detailed investigation of the sensitivity of our model to different metal contacts, presented in Appendix B, shows that the appropriate choice of metal contacts, such as Au for example (see Fig. 6.13 in Appendix B), reduces significantly the dependence of the modeling results on the LED parameters.

6.3.2 Application to LEDs Grown on Bulk GaN Substrates, Complex LED Structures, and Lasers

Let us calculate here the extraction efficiency to air η^0_{extr} for bulk GaN LEDs, which can then be applied to determine the IQE in such structures using the VI or NI approximations. The external electric field in this case is written in a simple expression, due to the absence of the interface with the substrate, $|E_0^{(\gamma,\rho)}| = |E_{\text{source}}^{(\gamma,\rho)}||t^{\rho}_{L,a}|$, which also eliminates the oscillations due to the LED cavity on the extraction efficiency. Figure 6.5a shows the η^0_{extr} for a bulk GaN LED (solid-red) for QWs placed at 140 nm from the top surface. In this case, the absence of the reflection from the substrate reduces slightly the extraction efficiency through the top surface, considering that the bottom interface is covered with absorbing material.

The $\eta^0_{\text{extr}}(\lambda)$ can be easily calculated for bulk LED from a quadratic fit of this curve:

$$\eta^0_{\text{extr}}(\lambda) = -1.493 \times 10^{11}\lambda^2 + 1.860 \times 10^5\lambda - 5.817 \times 10^{-3}. \tag{6.7}$$

For an easy comparison, we plot in the same figure the η^0_{extr} for a GaN LED on sapphire (dashed-blue), previously calculated.

The extraction efficiency through a simple facet is often approximated by the fraction of solid angle of the air cone, given by $\left[1 - \cos\left(\theta_c(\lambda)\right)\right]/2$, where $\theta_c(\lambda)$ is the critical angle of total internal reflection inside GaN. For comparison to the exact results, we plot the solid angle approximation (dashdotted-green) in Fig. 6.5a, which shows that this simple approximation has a significant error of at least 10%, which is due to a non-isotropic radiation from the dipole source.

Turning to the impact of various additional structures commonly found in LEDs, we investigate the two most important: superlattices, often grown above the nucleation layer at the substrate interface to improve growth quality, and the confining layers, needed in most laser structures. We leave aside the thin electron blocking layers, commonly used in LEDs, as it would have a smaller optical effect than these

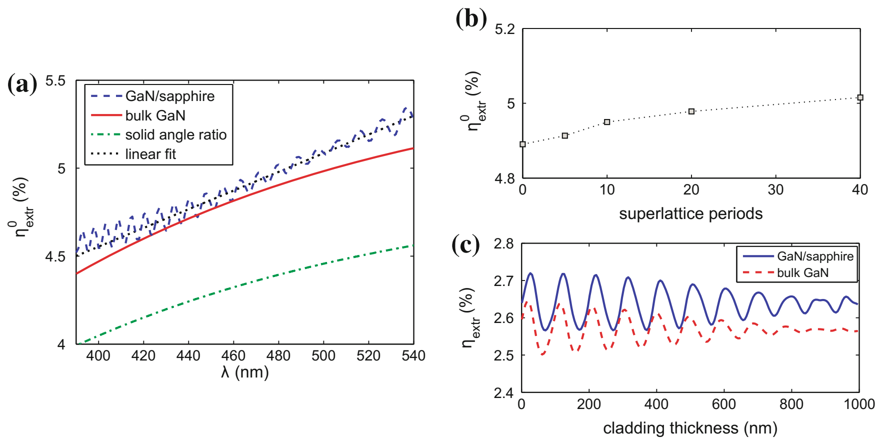

Fig. 6.5 **a** Extraction efficiency η^0_{extr} for bulk GaN LED (*solid-red*) and for the GaN LED on sapphire previously calculated (*dashed-blue*), for QWs placed at 140 nm from the top surface, along with the solid angle ratio approximation for the extraction efficiency (*dashdotted-green*). **b** Effect of embedded superlattices on the light extraction efficiency to air. We considered a 2-nm-InGaN/2-nm-GaN superlattice below the active region with 0, 5, 10, 20, and 40 periods. **c** Impact of AlGaN cladding layers thickness on the light extraction efficiency using a 15.4-nm-thick Ni–Au contact and Al content of 15% in the cladding layer. We considered an active layer (quantum wells, barriers, guiding layers) of fixed 240 nm thickness, sandwiched by two equal cladding layers, for a GaN structure grown on a sapphire substrate (*solid-blue*) or on a bulk GaN (*dashed-red*)

two dominant structures. Figure 6.5b shows the effect of the superlattices: even for 40 period superlattices, the relative modification to light extraction remains below 2%. Figure 6.5c shows the impact of adding $Al_{0.15}Ga_{0.85}N$ cladding layers of variable thicknesses to an active layer (quantum wells, barriers, guiding layers) of fixed 240 nm thickness over a 4-μm-thick GaN slab on a sapphire substrate (solid-blue) or on a bulk GaN (dashed-red). The extraction efficiency remains fairly constant in both cases. The rigid downwards shift of 3% observed when compared to heterostructure is due to the absence of reflection at a substrate interface.

Therefore, the results presented in Fig. 6.4 can be extended to more complex nitride-based LED structures as well as lasers. In the following section we present the combination of this theoretical result with experiments to determine the internal quantum efficiency of LEDs.

6.4 Experimental Assessment of IQE

In the present technique, the LED must be coated with a perfectly light-absorbing material containing only a small well-defined aperture on the LED top surface [14] (illustrated in Fig. 6.2a). The aperture diameters varied from 5 to 300 μm to assess

the dependence of the total collected light on the aperture size, which is used to feed the theoretical model. The P_{out} from each aperture, for a given current, was measured using an integrating sphere and subsequently corrected by the ratio between the aperture surface a and the total LED top surface A, corresponding to the surface of current injection. Current was injected by a semitransparent thin metal layer on the top surface of the LED, through large metallic pads placed far (tens to hundreds of microns) from the circular aperture where the light is collected, to isolate the light measured from optical features with uncertain properties. The IQE was then determined from the following expression:

$$\eta_{IQE} = \frac{\eta_{EQE}}{\eta_{extr}} = \frac{qP_{out}}{\hbar\omega I \eta_{extr}} \frac{A}{a}, \tag{6.8}$$

where $\hbar\omega$ is the photon energy, q is the electron charge, and η_{extr} is the extraction efficiency for a single facet of the LED as calculated in the previous section.

Next sections show the application of such method to a state-of-the-art GaN-based LED as well as to a relatively poor performance device [14].

6.4.1 IQE Measurement of a State-of-the-Art LED

The LED investigated was a state-of-the-art device from Seoul semiconductors, grown by metal organic chemical vapor deposition (MOCVD) on a sapphire substrate. The LED structure consisted of a ~4670-nm-thick n-GaN followed by 60-nm-thick layer of QWs emitting at $\lambda = 445$ nm and a 140-nm-thick p-GaN layer. The LED top surface was extremely smooth (RMS roughness ~0.247 nm for a $5 \times 5\,\mu m^2$ scan measured by atomic force microscope (AFM)), which is an important requirement of the technique. Homogeneous current injection was assured by an annealed semitransparent Ni–Au contact (5-/10-nm-thick) of area $A = 484.5 \times 484.5\,\mu m^2$ over the LED top surface. The complex refractive index of the Ni–Au alloy ($n_{alloy} = 1.4649 + 1.6485i$) was measured from co-deposited and co-annealed films on a sapphire substrate, using variable angle spectroscopic ellipsometry (VASE) [21].

The light-absorbing material used was an equal volume mixture of AZ4210 photoresist (PR) and PureBlack carbon black particles (Superior Graphite Corp.). Apertures of 50, 100, 200, and 300 μm diameters were patterned into the absorber by liftoff, where a bilayer of PMGI SF 15 PR followed by AZ4210 was spun onto the surface of the processed LED structure [21, 22]. The deposited absorber presented optical transmissivity of 0.04% and reflectivity of 0.8% at normal incidence. The light-absorbing material for the backside and sidewalls of the device was flat black paint (Rustoleum). The measured specular reflection at normal incidence for this material was less than 1.5%, and the total scattered reflection was less than 3% of incident light from an absorber–air interface, which are suitable for the application

envisaged in this work. After coating with absorber, samples were diced, mounted to headers, and wire-bonded for integrating sphere measurements.

As shown in the previous section, the theoretical η_{extr} is readily available for the common metals, such as Ag, Au, and Al (Fig. 6.4). The calculation for other metal contacts requires the accurate knowledge of the refractive index of the semitransparent contact $n_{alloy} = 1.4649 + 1.6485i$, which in this case was done by VASE. The calculated η_{extr} for this device, using the model described in Appendix A, was 2.7%. This low value is justified by the rather thick Ni–Au current spreading layer that considerably absorbs the light going to air. As shown in Fig. 6.4, the calculated η_{extr} is fairly constant for a GaN layer thicker than 1.5 μm and does not depend on the QW position in the present structure. For the nominal GaN thickness and QW relative position of our structure, the maximum variation in η_{extr} is at most 1.6% (Appendix B).

As a confirmation of the theoretical predictions, we compared the angular pattern of the light emitted to air from the theoretical model (6.27) to the experimental results (Fig. 6.6). The angular emission from the LED was assessed using an angle-resolved setup, where the far-field spectrum was collected at all angles θ from –90° to 90°. The oscillations observed correspond to Fabry–Perot interferences from the GaN interfaces with the substrate and the metal. The excellent match between the experimental and theoretical curves in Fig. 6.6a is an indication of the correct theoretical model used to predict the LED light emission. As explained in Appendix C, a small damping corresponding to an isotropic emission of 1% of the total output power emitted from the LED ($F_{rough} = 1\%$) was considered in the theoretical curve. While this improved the agreement between the experimental and theoretical curves, it accounted for light scattering from any small roughness present in the metal contact. In the following section, we show that the damping included in LEDs with much rougher surfaces (rms roughness of ~10 nm for a $5 \times 5\ \mu m^2$ scan measured by AFM) is as high as 70%, which corroborates the smoothness of the interfaces in the present samples.

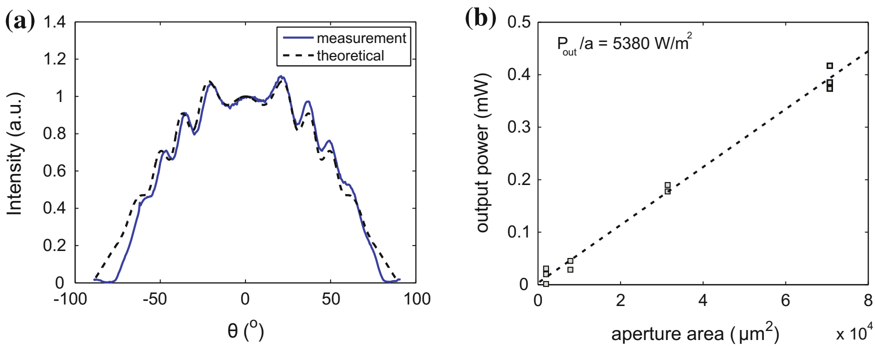

Fig. 6.6 **a** Theoretical (*dashed*) and experimental (*solid*) angle-resolved pattern of the light emission from the LED. **b** Output power emitted from aperture versus aperture area

The output power of the light emitted from the aperture on the LEDs was measured in an integrating sphere under pulsed excitation, with duty cycle of 0.1%, to eliminate the degrading effect of heating on the IQE. The measured output power for 50, 100, 200, and 300 μm diameter apertures varied linearly with the aperture area as presented in Fig. 6.6b. The linear variation of the output power versus aperture size validates one of the key assumptions of the theoretical model which allowed the use of a homogeneously distributed set of dipoles replacing the QWs. The power per unit area P_{out}/a deduced from its slope at a nominal input current density of 8.52 A/cm^2, averaged for several devices, was 5380 ± 380 W/m^2. This current density corresponds to the peak IQE, which was first determined by measuring the P_{out} versus current density. Using this value in (6.8) combined to the theoretical η_{extr} of 2.7% resulted in

$$\eta_{\mathrm{IQE}} = 83.8\%.$$

6.4.2 EL-Based IQE Measurement of a Poor-Performing LED: Effect of Surface Roughness

We also applied the present technique in a poor-performing LED. The GaN-based LED used in this study was grown by MOCVD on a sapphire substrate, with 5x-InGaN QWs emitting at 445 nm. The LED was processed with a semitransparent Ni–Au contact to the p-GaN layer. The LED structure was composed of a 4570-nm-thick GaN over a sapphire substrate. The QWs, emitting at $\lambda = 445$ nm, were below a 295-nm-thick p-GaN layer. The index of refraction and effective thickness of the Ni/Au alloy, measured by ellipsometry, was n_{alloy}=1.544 + i1.016 at $\lambda =$ 445 nm and 18.4 nm, respectively. The sapphire substrate was considered infinitely thick because of the assumption that the light going downwards in the sapphire substrate is completely absorbed at the interface of the absorbing material and sapphire. The calculated η_{extr} for this device was 3.03%, which was different than the previous sample due to differences on the index of refraction and thickness of the Ni/Au alloy. This result also considered a device with a smooth material-to-air interface. The output power varied linearly with aperture area indicating uniform emission across the device surface. The slope of the curve in Fig. 6.7a yields a power per unit area of 2900 W/m^2 at an injection current density of 7.9 A/cm^2, where the peak EQE occurred. Using (6.8), the peak IQE of these devices was estimated to be 43% at a current density of 7.9 A/cm^2. The IQE value obtained must be carefully considered at this point.

The theoretical model assumes a perfectly flat and smooth surface, however, the device material used had a RMS surface roughness of 10 nm measured by AFM, due to the low-temperature growth conditions used for the p-type GaN. This rough surface destroys the constructive interferences in the LED interfaces and enhances the extraction efficiency of the device compared to the calculated value. The ratio between guided light and directly extracted light is not maintained which partially

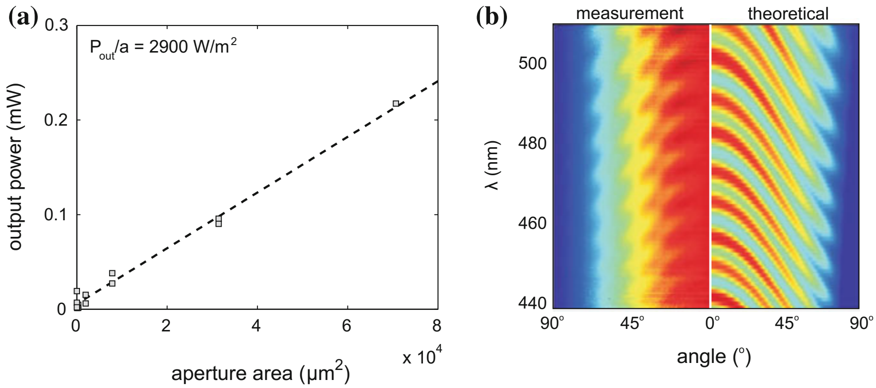

Fig. 6.7 **a** Measured output power versus aperture surface. **b** Angle-resolved measurement on the sample with rough surface (*left*) compared to the calculated emission using the dipole model (*right*). Notice the blurry Fabry Perot fringes from the current sample indicating a pronounced effect of the roughened surface

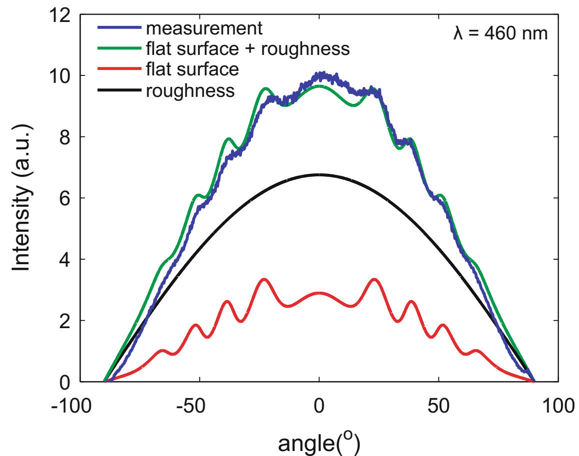

Fig. 6.8 Cross section of the angle-resolved measurement at $\lambda = 460$ nm (*blue curve*). The *red curve* represents the calculated emission of the dipoles inside the structure with a perfectly flat surface for the same wavelength. The *black curve* is the Lambertian emission due to the rough surface and the *green curve* shows the Lambertian emission added to the theoretical Fabry–Perot oscillations which matches the experimental curve

invalidates the results from the theoretical model. Figure 6.7b shows the angle-resolved measurement in this rough LED and the calculated radiation from a similar LED with flat surfaces. The Fabry–Perot fringes are much less pronounced when the LED surface is rough.

To account for this effect, we modeled the effect of the surface roughness as a Lambertian light source emitting simultaneously with the dipoles inside the flat structure, as described in details in Appendix C. This is justified by considering that the light impinging the rough surface is randomly scattered, corresponding to an isotropic source inside the structure (see Appendix C). Let us use this model to account for the surface roughness in our sample. The comparison of the angle-resolved emission between the measurements and dipole model is shown in Fig. 6.8.

The blue curve corresponds to the angle-resolved measurement of the LED at $\lambda = 460$ nm, which is simply a cross section of the measurement shown in Fig. 6.7b. The red curve corresponds to the calculated emission of the dipoles inside the structure with a perfectly flat surface for the same wavelength, which is far from matching the experimental result shown in blue. However, when the Lambertian emission due to the rough surface, represented by the black curve in Fig. 6.8, is added to the theoretical Fabry–Perot oscillations, it results in the green curve which matches very well the experimental curve. The addition of an amount of Lambertian emission related to the surface roughness to the calculated angular pattern resulted in a excellent agreement to the measurements, validating the dipole model used.

The angle-resolved measurement is therefore a very useful technique to assess the contribution of light randomly scattered to the measured EQE which ultimately can be used to validate the model requirements of flat interfaces. The pronounced oscillations in such measurements fade away proportionally to the presence of light scatterers in the LED and the accuracy of this model is largely reduced with the presence of such scatterers. The intensity of the Lambertian emission here corresponds to 70% of the intensity from the measurement. To roughly estimate the IQE, we consider that only the remainder 30% of the measured P_{out} is due to the emission from dipoles in a flat surface, for which our theoretical extraction efficiency is valid, which results in an estimated IQE of 13%. However, this should be considered just a rough estimation to account for the effect of surface roughness on the present model, a precise determination of the IQE requires flat smooth interfaces.

6.5 Model for Photon Recycling

In this section, we present a simple model to estimate the effect of photon recycling on the extraction efficiency of an LED [1, 13, 23]. This mechanism consists of a sequence of re-absorption of the guided light in the LED structure and re-emission by the QWs, which ultimately can play an important role in extracting photons that have not been directly emitted in the air cone in the first pass. The schematic in Fig. 6.9a illustrates the infinite iterations of this mechanism. The η_{EQE} can be written as $\eta_{\text{EQE}} = \eta_{\text{IQE}}\eta_{\text{extr}} + \eta_{\text{IQE}}^2(1-\eta_{\text{extr}})F_{\text{rec}}\eta_{\text{extr}} + \cdots$; therefore, the extraction efficiency with photon recycling is

$$\eta_{\text{extr}}^{\text{PR}} = \eta_{\text{extr}}\left[1 + \frac{\eta_{\text{IQE}}(1-\eta_{\text{extr}})F_{\text{rec}}}{1-\eta_{\text{IQE}}(1-\eta_{\text{extr}})F_{\text{rec}}}\right] \tag{6.9}$$

where $F_{\text{rec}} = \dfrac{F_{\text{QW}}}{F_{\text{QW}} + F_{\text{diss}}}$ is the ratio of the LED guided light absorbed by the QWs (F_{QW}) to the total dissipated light ($F_{\text{diss}} + F_{\text{QW}}$).

In the case of nitride-based LEDs, the absorption by QW is spectrally shifted (large Stokes shift) from its emission edge, and only the tail of the absorption

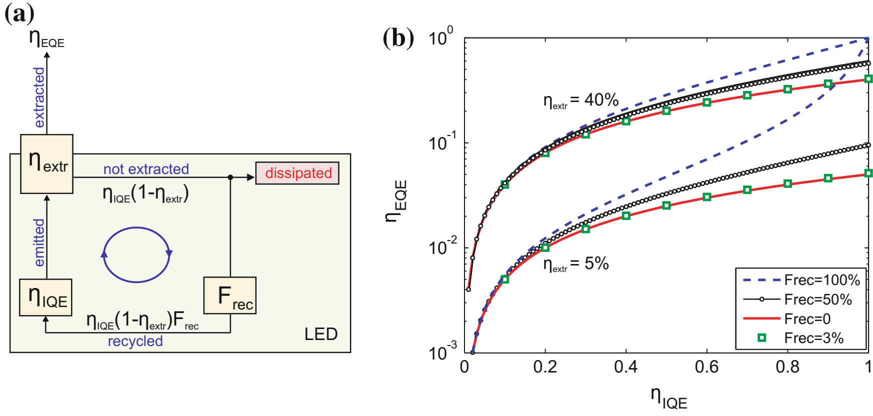

Fig. 6.9 **a** Schematic of the light emitted within the LED structure. **b** Calculated $\eta_{\text{extr}}^{\text{PR}}$ versus η_{IQE} for $F_{\text{rec}} = 0$, 3%, 50%, and 100% and for $\eta_{\text{extr}} = 5\%$ and 40%

curve overlaps the emission spectrum, thus the absorption coefficient is quite small (experimentally estimated in [24] as 10^3 cm^{-1}). The volume ratio of the QWs to the LED is approximatively 1.5%. The absorption coefficient of the metal layer, which is the most significant absorption mechanism in the LED, is approximatively $\alpha_m = (4\pi/\lambda)k_m = 5 \times 10^5$ cm^{-1} and the volume fraction penetrated by the guided modes in the metal layer is about 0.2%. Thus, as a rough estimation, $F_{\text{rec}} \approx 3\%$.

Figure 6.9 shows the plot of $\eta_{\text{extr}}^{\text{PR}}$ versus η_{IQE} for the cases without, with 50% and 100% photon recycling, as well as the estimated $F_{\text{rec}} = 3\%$ for a nitride-based LED. Two different extraction efficiencies are considered which illustrated both the case of a simple LED geometry ($\eta_{\text{extr}} = 5\%$) as well as a extreme case of an ultra thin microcavity LED ($\eta_{\text{extr}} = 40\%$). In neither of these cases was $\eta_{\text{extr}}^{\text{PR}}$ modified by the photon recycling for nitride-based LEDs, due to the very small F_{rec}.

In other material systems, where there is a larger overlap between the absorption and emission energy edges of the QWs, F_{rec} is much higher and can be close to 100% [1]. In this case, photon recycling is very efficient in increasing the effective extraction efficiency of the LED [25]. This effect is more pronounced when the direct extraction efficiency (without photon recycling) is small. Equation (6.9) provides a corrective factor for the extraction efficiency for material systems such as GaAs where photon recycling is an effective mechanism.

6.6 Conclusions

In this chapter, we presented an overview of a few techniques to assess the internal quantum efficiency in LEDs. The IQE is widely estimated by temperature-dependent photoluminescence which relies on strong assumptions, such as that non-radiative

mechanisms are totally eliminated at low temperatures; the peak emission from PL excitation occurs at different excitation power densities at LT and RT, and hence to different carrier densities in the active region; and also similar carrier injection to the active region compared to electroluminescence, neglecting effects of applied bias on the internal electric field in the QWs and different carrier injections in individual wells of a MQW structure under PL and EL excitations.

We presented a technique based on electroluminescence to measure IQE in GaN-based LEDs, which relies on similar operation conditions and injection mechanisms as the operating LED. We derived a model to determine light extraction efficiency, LEE, through a single facet of simple LED structures. The model relies on covering the LED with light-absorbing material, which eliminates the difficult to model indirectly extracted light. Thus, the output power, or η_{EQE}, measured in an absolute manner by integrated sphere is only due to directly extracted light, an easily calculated quantity. Applied to GaN structures, the model predicts that the LEE is a product of a bare GaN LED LEE times the transmission function of the top metal contact. General values of the bare LED LEE as $\eta^0_{extr}(\lambda) = 5.31 \times 10^4 \lambda + 2.43 \times 10^{-2}$ were given, which were quite independent on the details of the LED structure such as exact value of GaN thickness, presence of superlattices or confinement layers, etc. The same is true for LEDs grown over GaN substrate, with a small modification of $\eta^0_{extr}(\lambda)$ as one misses the power reflected from the GaN/sapphire interface into the escape cone. The effect of different contact metals on the LEE was investigated, leading to a conclusion that Au-based metal contacts are the best choice, among commonly used metals, for the application of the present technique in terms of LEE robustness to LED parameters.

This model was extended to predict the angular light emission in LEDs, which can be used to compare the theoretical and experimental results as well as to identify the presence of surface roughness which could be detrimental to this model. Photon recycling was evaluated and shown to be negligible in nitride structures, mainly because of the large Stokes shift between emission and absorption.

We also presented the experimental details to fabricate a suitable structure for the application of the present method, consisting of patterning a well-defined aperture in a light-absorbing material that surrounds the device. The application of this method to a state-of-the-art GaN LED yielded a peak IQE of 83.8%. The angle-resolved prediction of the light emitted in the LED from the theoretical model was validated with experimental data and the excellent match between theory and experiments corroborates the model developed.

Acknowledgements The authors would like to thank James Speck for triggering this work, for his continuous interest and many enlightened discussions and Amorette Getty for the contribution with the experimental part in this work. This material is based upon work partially supported as part of the 'Center for Energy Efficient Materials' at UCSB, an Energy Frontier Research Center funded by the U.S. Department of Energy, Office of Science, Office of Basic Energy Sciences under Award Number DE-SC0001009 and by the Department of Energy (DOE) under project No. DE-FC26-06NT42857 and by the Solid State Lighting and Energy Center (SSLEC) at the University of California, Santa Barbara (UCSB).

Appendix A: Theoretical Model of Light Emission in LEDs: QW Emission Described by Classical Dipoles

QWs in LEDs are usually more than one, distributed over a finite thickness within the device, as each is a few nanometers wide and spaced apart by barrier layers of tens of nanometers thick. One might assume that each well is equally excited and thus emits an equal number of photons in a spherically symmetric pattern. However, it is just as plausible to assume that under EL excitation, either the first well that carriers encounter, the last well (perhaps immediately preceding an electron barrier layer), or one of the center wells (being most equally accessible to both electrons and holes) would have a disproportionately larger share of the emission. David et al. [12] examined this question with regard to GaN/InGaN LEDs, and reported that nearly all of the emission from an LED comes from the QW nearest to the p-doped side of the device. The predominant emission from the top QW was attributed to the poor hole transfer between QWs and occurs regardless of the number of quantum wells, often requiring some special design such as a double heterostructure to modify the carrier distribution [12]. That determination was made possible due to the fact that the various QWs have different emission patterns due to their different distances to the strongly reflecting Ag/GaN interface.

To address the question of calculating light emission per QW, we refer to Benisty et al. [26], who used dipole emitters as a photon source term in LED emission models. Benisty et al. model the emission from the dipoles as a discontinuity in the scattering matrix propagation technique [27], as we describe below. The use of dipole emitters is justified by the similarity between the normalized expressions of the rate of spontaneous emission in QWs and the power emitted by classic electric dipoles. The rate of spontaneous transitions of e–h pairs between the conduction and valence bands in a QW, given by Fermi's golden rule, is proportional to $\mathcal{M}_{c-v} = |\langle\psi_c \mid \hat{e}\hat{p} \mid \psi_v\rangle|^2$, where $\hat{e}$ is the light polarization, $\hat{p}$ is the momentum operator, and ψ_c and ψ_v are the conduction and valence band wavefunctions, respectively [28, 29]. The angular dependence of $\mathcal{M}_{c-v}$ is well described by combinations of horizontal and vertical dipole-like terms [30]. The normalized radiation patterns, given by the power per unit of solid angle, of vertical (v) and horizontal (h) dipoles, for both TE and TM polarizations are given by [26]

$$\frac{dP_{\text{source}}^{(v,TM)}}{d\Omega}(\theta_L) = \frac{3}{8\pi}\sin^2\theta_L \tag{6.10a}$$

$$\frac{dP_{\text{source}}^{(h,TE)}}{d\Omega}(\theta_L) = \frac{3}{16\pi} \tag{6.10b}$$

$$\frac{dP_{\text{source}}^{(h,TM)}}{d\Omega}(\theta_L) = \frac{3}{16\pi}\cos^2\theta_L, \tag{6.10c}$$

where θ_L is the angle with respect to the vertical direction.

The replacement of the electron–hole excitons by a uniform distribution of dipoles, whose emission is propagated through the multilayered structure by transfer matrix formalism, allows the calculation of the electric field in any layer of the structure by propagating the electric field from the dipole layer, which are determined from (6.10) as

$$E_{\text{source}}^{(\gamma,\rho)}(\theta_L) = \sqrt{\frac{dP_{\text{source}}^{(\gamma,\rho)}}{d\Omega}(\theta_L)} \tag{6.11}$$

for a γ dipole orientation and a ρ polarization.

Analytical Model for Light Extraction Efficiency

The theoretical assessment of the light extraction efficiency η_{extr} in an LED structure is based on the fraction of the integrated emitted power that exits the LED structure and propagates to air. This is determined from the calculation of the electric field radiated from the QWs, based on the propagation of the dipole electric field throughout the structure. The external power per solid angle $dP_{\text{out}}^{(\gamma,\rho)}/d\Omega dS(\theta)$, in the external direction θ, is given by the flux of the Poynting vector emitted from the dipoles, transmitted through the structure and corrected by the change in solid angle when the medium is changed [26]:

$$\frac{dP_{\text{out}}^{(\gamma,\rho)}}{d\Omega dS}(\theta) = \underbrace{\left(|E_{\text{out}}^{(\gamma,\rho)}(\theta)|^2 \frac{n_{\text{out}}\cos(\theta)}{n_L\cos(\theta_L)}\right)}_{\text{transmitted power from dipoles}} \underbrace{\left(\frac{n_{\text{out}}^2\cos(\theta)}{n_L^2\cos(\theta_L)}\right)}_{\text{change in solid angle}}, \tag{6.12}$$

where $E_{\text{out}}^{(\gamma,\rho)}$ is the external electric field for a γ dipole orientation and a ρ polarization, and n_{out} and n_L are the refractive indexes of the external and LED media, respectively. θ and θ_L are respectively the external and internal angles with respect to the vertical direction. The angles in each medium θ_i, between the vertical and the propagation direction of emitted light, are determined from Snell's law $n_i\cos(\theta_i) = n_j\cos(\theta_j)$. The first term in (6.12) corresponds to the transmitted power from the dipole source to the external medium, given by the Fresnel transmission coefficient and the second term corresponds to the changes in solid angle from different media, obtained from the derivative of Snell's law.

The light extraction efficiency of the LED through a single facet is given by the ratio of the total output power, calculated from the integration of (6.12) for θ from 0 to $\pi/2$, to the total emitted power. The total emitted power by the normalized dipole source is unity for dipoles in bulk material. However, the total radiation by the dipole source inside an LED heterostructure is modified by the Purcell factor, which corresponds to the relative change in spontaneous emission from a source within an optical cavity compared to the same source in a bulk material [31]. The

Purcell factor depends largely on the position of the QWs relative to the interface between the metallic contact and GaN, as well as on the choice of metal (or more specifically, on the metal reflectivity), which is treated in more details in Appendix B. Figure 6.13 in Appendix B shows the deviation from unity of the total emitted power by the dipoles for different metals (Al, Au, and Ag) versus the distance of the QW to their interface with GaN. A judicious choice of contact metal, such as Au, can largely reduce this dependence and for most of the practical cases as well as for the simple geometry structure treated here, the Purcell factor is close to one and the total emitted power by the dipoles can be approximated to unity (deviation from unity of 2.8% at most). Figure 6.13 of Appendix B also offers a correction factor in case a different metal is used as contacts.

Therefore, the light extraction efficiency of the LED through its top facet is given by

$$\eta_{\mathrm{extr}} = \int_0^{\frac{\pi}{2}} 2\pi \frac{dP_{\mathrm{out}}^{(\gamma,\rho)}(\theta)}{d\Omega dS} \sin(\theta)\, d\theta \tag{6.13}$$

summed for $\rho = \mathrm{TE}$ and TM, and $\gamma = v$ and h. The e-HH recombinations in the QWs, in both TE and TM polarizations, can be well described by horizontal electric dipoles. The e-LH recombinations can only be partially described by the combination of horizontal and vertical dipoles and will be neglected at low current injections due to the nondegeneracy of the light hole band at the minimum of energy and to the lower density of states of this energy band [30]. Thus $\gamma = h$. Therefore, the only requirement to determine η_{extr} is to calculate the external electric field $E_{\mathrm{out}}^{(\gamma,\rho)}$, which is treated in the following section.

Exact Calculation of the Electric Field in a Multilayer Structure

The calculation of the electric field in a multilayer structure is based on the transfer matrix formalism, where a wave $E_{\uparrow} e^{+ik_z z} + E_{\downarrow} e^{-ik_z z}$ is represented by $\begin{pmatrix} E_{\uparrow} \\ E_{\downarrow} \end{pmatrix}$, which is the electric field of the upward and downward plane waves, respectively, and $k_z^i = n_i k_0 cos(\theta_i)$ in the medium i.

In a multilayer structure, the source electric field is propagated through the structure by multiplying it to propagation M_{prop} matrices in the homogeneous layers and interface M_{interf} matrices in the interface between two different media. A convenient property of this method is that an equivalent matrix $\mathcal{M}$ for the entire structure can be simply obtained by multiplying all the interface and propagation matrices corresponding to the structure (Fig. 6.10), as

$$\mathcal{M} = \dots M_{\mathrm{interf}}^{i+1,i} M_{\mathrm{prop}}^{i} M_{\mathrm{interf}}^{i,i-1} \dots \tag{6.14}$$

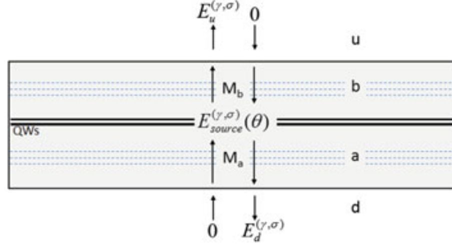

Fig. 6.10 Schematic of a propagation of the electric fields in a multilayer structure. The external electric fields E_u and E_d, from the *top* and *bottom* media, are propagated to the source, where the discontinuity from the source electric field is applied. The matrices M_a and M_b correspond to the transfer matrix of the *bottom* (a) and *top* (b) halves of the LED structure

The propagation matrix from z_1 to z_2 in a homogeneous medium is

$$M_{\text{prop}} = \begin{bmatrix} e^{i(k_z(z_2-z_1))} & 0 \\ 0 & e^{-i(k_z(z_2-z_1))} \end{bmatrix}. \tag{6.15}$$

The interface matrices for TE and TM polarizations are given by

$$M_{\text{interf}}^{\text{TE}} = \begin{bmatrix} \dfrac{k_z^{(2)}+k_z^{(1)}}{2k_z^{(2)}} & \dfrac{k_z^{(2)}-k_z^{(1)}}{2k_z^{(2)}} \\ \dfrac{k_z^{(2)}-k_z^{(1)}}{2k_z^{(2)}} & \dfrac{k_z^{(2)}+k_z^{(1)}}{2k_z^{(2)}} \end{bmatrix}, \; M_{\text{interf}}^{\text{TM}} = \begin{bmatrix} \dfrac{n_2^2k_z^{(1)}+n_1^2k_z^{(2)}}{2n_1n_2k_z^{(2)}} & \dfrac{-n_2^2k_z^{(1)}+n_1^2k_z^{(2)}}{2n_1n_2k_z^{(2)}} \\ \dfrac{-n_2^2k_z^{(1)}+n_1^2k_z^{(2)}}{2n_1n_2k_z^{(2)}} & \dfrac{n_2^2k_z^{(1)}+n_1^2k_z^{(2)}}{2n_1n_2k_z^{(2)}} \end{bmatrix}. \tag{6.16}$$

To obtain analytical expressions for the electric field in the outer media, we impose, as boundary condition of this problem, that the electric field of the incoming waves in the outer media is zero (Fig. 6.10). The external electric fields, from the top and bottom media, are then propagated to the source, where the discontinuity from the source is applied as

$$\mathcal{M}_b \begin{pmatrix} E_u^{(\gamma,\rho)} \\ 0 \end{pmatrix} - \mathcal{M}_a \begin{pmatrix} 0 \\ E_d^{(\gamma,\rho)} \end{pmatrix} = \begin{pmatrix} E_{\text{source}}^{(\gamma,\rho)}(\theta) \\ E_{\text{source}}^{(\gamma,\rho)}(\theta) \end{pmatrix} \tag{6.17}$$

where

$$\mathcal{M}_a = \begin{bmatrix} a_{11} & a_{12} \\ a_{21} & a_{22} \end{bmatrix} \text{ and } \mathcal{M}_b = \begin{bmatrix} b_{11} & b_{12} \\ b_{21} & b_{22} \end{bmatrix} \tag{6.18}$$

are calculated from (6.14) for the bottom (a) and top (b) halves of the LED structure (Fig. 6.10). The electric fields in the top (u) and bottom (d) outer media are

$$E_u^{(\gamma,\rho)}(\theta) = E_{\text{source}}^{(\gamma,\rho)} \frac{\frac{1}{b_{11}}(1 + \frac{a_{12}}{a_{22}})}{1 - \frac{b_{21}}{b_{11}}\frac{a_{12}}{a_{22}}} \text{ and } E_d^{(\gamma,\rho)}(\theta) = E_{\text{source}}^{(\gamma,\rho)} \frac{\frac{1}{a_{22}}(1 + \frac{b_{21}}{b_{11}})}{1 - \frac{b_{21}}{b_{11}}\frac{a_{12}}{a_{22}}}. \tag{6.19}$$

In the case of the simple geometry considered in this chapter, the matrix terms are

$$\frac{1}{b_{11}} = \frac{2k_z^b}{k_z^b + k_z^u} e^{ik_z^b L_b} \text{ and } \frac{1}{a_{22}} = \frac{2k_z^a}{k_z^a + k_z^d} e^{ik_z^a L_a}, \tag{6.20}$$

which correspond to transmission coefficients and

$$\frac{b_{21}}{b_{11}} = \frac{k_z^b - k_z^u}{k_z^b + k_z^u} e^{2ik_z^b L_b} \text{ and } \frac{a_{12}}{a_{22}} = \frac{k_z^a - k_z^d}{k_z^a + k_z^d} e^{2ik_z^a L_a}, \tag{6.21}$$

corresponding to reflection coefficients.

The electric field after the metal layer can be written as

$$E_{\text{out}}^{(\gamma,\rho)} = \frac{E_{\text{source}}^{(\gamma,\rho)} t_{L,m,a}^{\rho} e^{i\phi'}(1 + r_{L,s}^{\rho} e^{i2(\phi-\phi')})}{1 - r_{m,L,a}^{\rho} r_{L,s}^{\rho} e^{i2\phi}} = \frac{E_{\text{source}}^{(\gamma,\rho)} t_{L,a}^{\rho} e^{i\phi'}(1 + r_{L,s}^{\rho} e^{i2(\phi-\phi')})}{1 - r_{L,a}^{\rho} r_{L,s}^{\rho} e^{i2\phi}} \frac{1 - r_{L,a}^{\rho} r_{L,s}^{\rho} e^{i2\phi} t_{L,m,a}^{\rho}}{1 - r_{m,L,a}^{\rho} r_{L,s}^{\rho} e^{i2\phi} t_{L,a}^{\rho}}. \tag{6.22}$$

The first term is the external electric field without metal contacts and the second is the metal transmission function. Using the general property: $x, y \in \mathbb{C}$, $|xy|^2 = |x|^2|y|^2$, we obtain [13]

$$|E_{\text{out}}^{(\gamma,\rho)}|^2 = \mathcal{T}_m^{\rho} |E_0^{(\gamma,\rho)}|^2. \tag{6.23}$$

Let us first calculate the external electric field $E_0^{(\gamma,\rho)}$ in a structure without metal contact. Let the total LED thickness be L and the position of the dipole source within the LED be z. The corresponding phase shifts in the LED are $\phi(\theta_L) = n_L k_0 L \cos(\theta_L)$ and $\phi'(\theta_L) = n_L k_0 z \cos(\theta_L)$, where $k_0 = 2\pi/\lambda$, λ is the wavelength of the emitted light, n_L and θ_L are the refractive index and angle in the LED layer, respectively. The transmission and reflection coefficients for a polarization ρ, at each interface from a medium i to j, are given respectively by $t_{i,j}^{\rho}$ and $r_{i,j}^{\rho}$.

The external electric field can be determined from the propagation of the dipole electric field $E_{\text{source}}^{(\gamma,\rho)}$ [18]:

$$E_0^{(\gamma,\rho)}(\theta) = E_{\text{source}}^{(\gamma,\rho)} e^{i\phi'} t_{L,a}^{\rho}(1 + r_{L,a}^{\rho} r_{L,s}^{\rho} e^{2i\phi} + \cdots) + E_{\text{source}}^{(\gamma,\rho)} e^{i(2\phi-\phi')} r_{L,s}^{\rho} t_{L,a}^{\rho}(1 + r_{L,a}^{\rho} r_{L,s}^{\rho} e^{2i\phi} + \cdots)$$

$$E_0^{(\gamma,\rho)}(\theta) = \frac{E_{\text{source}}^{(\gamma,\rho)} t_{L,a}^{\rho} e^{i\phi'}(1 + r_{L,s}^{\rho} e^{i2(\phi-\phi')})}{1 - r_{L,a}^{\rho} r_{L,s}^{\rho} e^{i2\phi}}. \tag{6.24}$$

We recall the transmission and reflection expressions for both TE and TM polarizations for a plane wave going from a medium i to j:

$$r_{i,j}^{\mathrm{TE}} = \frac{n_i\cos(\theta_i) - n_j\cos(\theta_j)}{n_i\cos(\theta_i) + n_j\cos(\theta_j)}, r_{i,j}^{\mathrm{TM}} = \frac{n_i\cos(\theta_j) - n_j\cos(\theta_i)}{n_i\cos(\theta_j) + n_j\cos(\theta_i)}$$
$$t_{i,j}^{\mathrm{TE}} = \frac{2n_i\cos(\theta_i)}{n_i\cos(\theta_i) + n_j\cos(\theta_j)}, t_{i,j}^{\mathrm{TM}} = \frac{2n_i\cos(\theta_i)}{n_j\cos(\theta_i) + n_i\cos(\theta_j)}.$$

The transmission function $\mathcal{T}_m^{\rho}$ for the metal contact is a simple replacement of the transmission and reflection coefficients of a simple LED/air interface (L, a) with those of an LED/metal/air interface (L, m, a). It contains all the metal parameters separated from the more general expression of $E_0^{(\gamma,\rho)}(\theta)$ and it is written as

$$\mathcal{T}_m^{\rho} = |\frac{1 - r_{L,a}^{\rho} r_{L,s}^{\rho} e^{i2\phi}}{1 - r_{m,L,a}^{\rho} r_{L,s}^{\rho} e^{i2\phi}} \frac{t_{L,m,a}^{\rho}}{t_{L,a}^{\rho}}|^2, \tag{6.25}$$

where now $r_{L,m,a}^{\rho}$ and $t_{L,m,a}^{\rho}$ accounts for the complex refractive index $\tilde{n}_m = n_m + ik_m$ and thickness t_m of the metal layer as in a homogeneous film [18]:

$$r_{L,m,a}^{\rho} = \frac{r_{L,m}^{\rho} + r_{m,a}^{\rho} e^{i\beta}}{1 + r_{L,m}^{\rho} r_{m,a}^{\rho} e^{i2\beta}}, \quad t_{L,m,a}^{\rho} = \frac{t_{L,m}^{\rho} t_{m,a}^{\rho} e^{i\beta}}{1 + r_{L,m}^{\rho} r_{m,a}^{\rho} e^{i2\beta}} \tag{6.26}$$

where $\beta = k_0 \tilde{n}_m t_m \cos(\theta_m)$. Therefore, the external field after the metal contact is calculated using (6.24) and (6.25) in (6.23).

The angular dependence of the external power per solid angle can be directly calculated as

$$\frac{dP_{\mathrm{out}}^{(\gamma,\rho)}}{d\Omega dS}(\theta) = \mathcal{T}_m^{\rho}(\theta)|E_0^{(\gamma,\rho)}(\theta)|^2 \frac{n_{\mathrm{out}}^3 \cos(\theta)^2}{n_L^3 \cos(\theta_L)^2}. \tag{6.27}$$

This equation predicts the angular emission of the LED which is used to corroborate the theoretical and experimental results, as shown in later sections. The light extraction efficiency from the top surface in such structure is then calculated using (6.13), which can be easily done numerically.

Model for Light Extraction in a Simple LED Geometry

The analytical model presented in the previous section considered a monochromatic emission from the dipoles, but the QW emission in practical LEDs has a broad spectrum (typically 5–10% of the central wavelength). In this section, the spectral

broadening of the source is considered and, while the results are not much different from the monochromatic model, it allows us to simplify the analytical model for η_{extr}.

The effect of the QW lineshape is included in the previous model by averaging the extraction efficiency at different wavelengths with the normalized spectral emission $s(\lambda)$ from the QWs as $\eta_{\text{extr}}^{poly} = \int_0^\infty s(\lambda)\eta_{\text{extr}}(\lambda)\,d\lambda$.

The QW spectral emission can be approximated by a Gaussian function $s(\lambda) = \frac{1}{\sqrt{2\pi\sigma^2}} e^{-\frac{(\lambda-\lambda_c)^2}{2\sigma^2}}$ and the asymmetry of its lineshape can be taken into account by combining two Gaussian functions, with different variances σ^2, at their central wavelength. The polychromatic extraction efficiency is thus explicitly written as

$$\eta_{\text{extr}}^{poly} = \sum_{\rho=\text{TE,TM}} \int_0^\infty s(\lambda) \int_0^{\frac{\pi}{2}} 2\pi \mathcal{T}_m^\rho(\theta,\lambda) \frac{dP_0^{(\gamma,\rho)}(\theta,\lambda)}{d\Omega dS} sin(\theta)\,d\theta\,d\lambda, \tag{6.28}$$

where $dP_0^{(\gamma,\rho)}(\theta,\lambda)/d\Omega dS$ is the external power per unit of solid angle of a structure without metal contacts and its dependence with λ is due to Fabry–Perot interferences on the interfaces of the LED layer, which is generally not very pronounced in most of LED structures (thick LED structures), allowing us to make the following approximation [13]:

$$\eta_{\text{extr}}^{poly} \simeq \sum_{\rho=\text{TE,TM}} \int_0^{\frac{\pi}{2}} \underbrace{\left[\int_0^\infty s(\lambda)\mathcal{T}_m^\rho(\theta,\lambda)d\lambda\right]}_{\langle \mathcal{T}_m^\rho(\theta)\rangle_\lambda} 2\pi \frac{dP_0^{(\gamma,\rho)}(\theta,\overline{\lambda})}{d\Omega dS} sin(\theta)\,d\theta \tag{6.29}$$

for a fixed $\overline{\lambda}$ and only the metal transmission function is averaged with respect to λ. The averaged function $\langle \mathcal{T}_m^\rho(\theta)\rangle_\lambda$ varies very slowly with θ for both TE and TM polarizations (an example is shown in Fig. 6.11). This is because the reflection and transmission coefficients do not vary much for θ_L inside the air cone, which is small in the case of high refractive index semiconductors, such as GaN and GaAs. Thus we can approximate (6.29) by a **Variable-Incidence (VI) approximation**:

$$\eta_{\text{extr}} \simeq \langle \mathcal{T}_m^{\text{TE}}\rangle_{(\lambda,\theta)}\, \eta_{\text{extr}}^{0,\text{TE}} + \langle \mathcal{T}_m^{\text{TM}}\rangle_{(\lambda,\theta)}\, \eta_{\text{extr}}^{0,\text{TM}}, \tag{6.30}$$

where $\langle \mathcal{T}_m^\rho\rangle_{(\lambda,\theta)}$ is the metal transmission function averaged in both λ and θ.

A simpler expression can be obtained by noticing that the averaged function $\langle \mathcal{T}_m^\rho(\theta)\rangle_\lambda$ is nearly constant inside the air cone for both TE and TM polarizations (Fig. 6.11). Moreover, its value at $\theta = 0°$ is the same for both polarizations $\langle \mathcal{T}_m^{\text{TE}}(0°)\rangle_\lambda = \langle \mathcal{T}_m^{\text{TM}}(0°)\rangle_\lambda = \langle \mathcal{T}_m(0°)\rangle_\lambda$ (reflection and transmission coefficients are equal for both polarizations at normal incidence), thus we obtain the **Normal-Incidence (NI) approximation**:

$$\eta_{\text{extr}} \simeq \langle \mathcal{T}_m(0°)\rangle_\lambda\, \eta_{\text{extr}}^0. \tag{6.31}$$

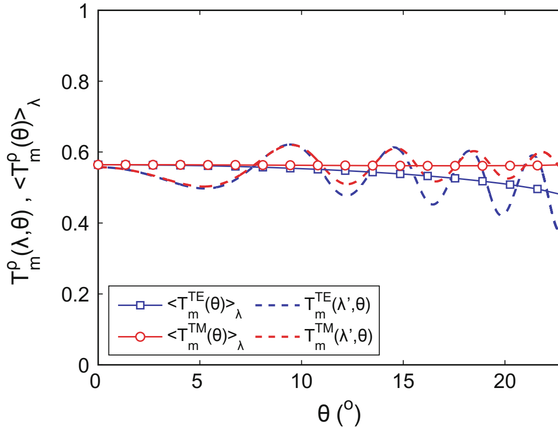

Fig. 6.11 Plot of $\mathcal{T}_m^{\rho}(\theta)$ for θ within the air cone ($\theta < \theta_c$) and $\lambda' = 445$ nm for TE (*dashdotted*) and TM (*dotted*), along with the plot of the averaged $\left\langle \mathcal{T}_m^{\rho}(\theta) \right\rangle_\lambda$ for TE (*squares*) and TM (*circles*) polarizations. The structure is composed of a 4869-nm-thick GaN-based LED over a sapphire substrate, and the QWs are 140 nm below the top surface. The 15.4-nm-thick metal contact is Ni–Au alloy with experimentally determined optical properties [14]

Notice that we started calculating the polychromatic extraction efficiency but ended with expressions for the monochromatic extraction efficiency. The spectrally averaged transmission function $\langle \mathcal{T}_m(0°) \rangle_\lambda$ is numerically calculated as

$$\langle \mathcal{T}_m(0°) \rangle_\lambda = \sum_{\lambda=\lambda_1}^{\lambda_2} \mathcal{T}_m(0°, \lambda) \frac{1}{\sqrt{2\pi\sigma^2}} e^{-\frac{(\lambda-\lambda_c)^2}{2\sigma^2}} \Delta\lambda, \tag{6.32}$$

where $\Delta\lambda = \frac{(\lambda_2 - \lambda_1)}{n-1}$, n is the number of discrete values of λ, and the interval $[\lambda_1, \lambda_2]$ needs to be at least a few times larger than σ^2.

The determination of the extraction efficiency of any LED structure is very simple using one of the two approximative models above. The monochromatic extraction efficiency for the LED structure with metal contacts for any wavelength is simply obtained from the multiplication of the averaged transmission function of the metal, averaged also in the air cone or at $\theta = 0°$, and the monochromatic extraction efficiency of the LED without metal contact (η^0_{extr}).

η^0_{extr} is not very sensitive to the LED parameters in this simple LED geometry (treated in Appendix B), which can be generally calculated for any LED structure for a given material. The most sensitive parameters in these models are those from the metal, which are contained solely in the metal transmission function $\mathcal{T}_m^{\rho}$ and can be separately calculated using (6.25). In the following section, we apply these models to the case of a GaN-based LED.

Determination of the extraction efficiency: evaluation of η_{extr}, η^0_{extr}, $\mathcal{T}^{\rho}_m(\theta, \lambda)$ ***and*** $\langle \mathcal{T}_m(0°)\rangle_\lambda$

Let us evaluate the terms $\mathcal{T}^{\rho}_m(\theta, \lambda)$, $\langle \mathcal{T}_m(0°)\rangle_\lambda$ and η^0_{extr} and compare the results of the extraction efficiency η_{extr} from the approximative models (6.30) and (6.31) with the analytical model (6.27) to validate our approximations.

The transmission function $\mathcal{T}_m(\theta, \lambda)$ was averaged using (6.32) to obtain the approximative models (6.30) and (6.31), for which the main assumption was that $\left\langle \mathcal{T}^{\rho}_m(\theta)\right\rangle_\lambda$ varied slowly with θ for both TE and TM polarizations. The evaluation of such function for the case of the GaN LED, for both polarizations, is presented in Fig. 6.11, which shows the plot of $\mathcal{T}^{\rho}_m(\theta)$ for a fixed $\lambda' = 445$ nm for TE (dashdotted) and TM (dotted), as well as the averaged $\left\langle \mathcal{T}^{\rho}_m(\theta)\right\rangle_\lambda$ for TE (squares) and TM (circles) polarizations, for θ within the air cone. The oscillations with respect to λ observed in $\mathcal{T}^{\rho}_m(\theta)$ are completely eliminated when this function is averaged with the lineshape of the QWs. As a matter of fact, the averaged function is nearly constant for both polarizations, within the air cone, which supports both approximations made to obtain (6.30) and (6.31). This is due to the weak variation of the reflection and transmission coefficients inside the air cone which, in its turn, is small in the case of high refractive index semiconductors, such as GaN and GaAs. Let us now calculate the extraction efficiency to air η^0_{extr} (without metal contact) for the GaN LED treated here, which is shown in Fig. 6.12a (dashed line). The small oscillations in extraction efficiency to air with λ for a monochromatic emission average out in real devices with polychromatic (poly) emission—note that the oscillation period in this

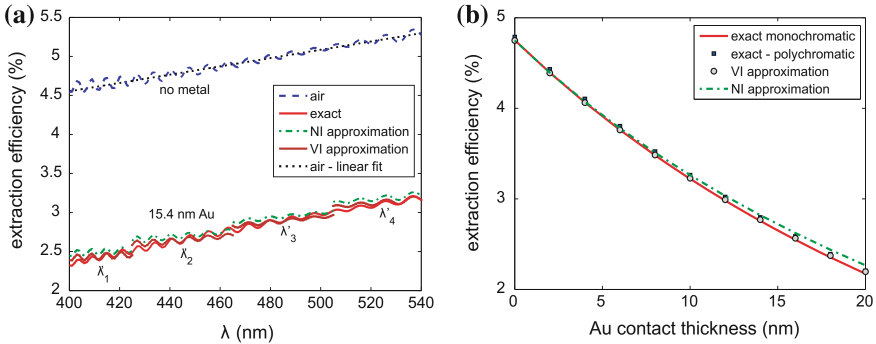

Fig. 6.12 **a** Extraction efficiency of the GaN LED structure versus wavelength using the analytical (*solid-red*), variable-incidence (VI) (*cross-brown*) and normal-incidence (NI) (*dashdotted-green*) approximations along with the extraction efficiency to air (*dotted-blue*) and its linear fit (*dashed-black*). The structure is composed of a 4869-nm-thick GaN-based LED over a sapphire substrate, and the QWs are 140 nm below the top surface. The 15.4-nm-thick metal contact is Ni–Au alloy with optical properties determined experimentally. Four different emission wavelengths were considered, $\lambda'_1 = 405$ nm, $\lambda'_2 = 445$ nm, $\lambda'_3 = 485$ nm, and $\lambda'_4 = 525$ nm in the function $s(\lambda)$ to evaluate the approximative models. **b** Extraction efficiency of the GaN LED structure versus metal thickness using the analytical with a monochromatic (*solid*) and polychromatic (*squares*) emission, VI (*circle*), and NI (*dashdotted*) approximations

example is around 7 nm, which is substantially less than the typical 25 nm EL linewidth for blue GaN-based LEDs. As shown later, the extraction efficiency to air, through the top surface of the LED, depends weakly on the LED 'fine' structure (for a simple LED geometry), and therefore we can determine a general extraction efficiency to air for GaN LEDs grown in sapphire substrates by a linear fit of η^0_{extr}, which is represented by the dashed line in Fig. 6.12a:

$$\eta^0_{\mathrm{extr}}(\lambda) = 5.31 \times 10^4 \lambda + 2.43 \times 10^{-2}. \tag{6.33}$$

To validate the models, we calculate the extraction efficiency of the GaN LED structure using the analytical model (6.27) and compare the results to the ones from the approximative models.

The extraction efficiency of the GaN LED structure after the metal contact (η_{extr}) versus wavelength calculated using the analytical model is shown in the solid-red curve in Fig. 6.12a, along with the results of the VI (cross-brown) and the NI (dashdotted-green) approximations. Four different emission wavelengths were considered in this plot, $\lambda' = 405, 445, 485$, and 525 nm, which were used in the function $s(\lambda)$ to evaluate the approximative models.

The application of both models for same structure when the metal thickness is varied is shown in Fig. 6.12b, where the circles correspond to the VI and the dashdotted line corresponds to the NI approximations. Again, there is a very good agreement with the analytical results (solid line).

These results were compared to the polychromatic extraction efficiency ($\eta^{\mathrm{poly}}_{\mathrm{extr}}$) taking into account the lineshape of the QWs, which was calculated analytically from (6.28) and represented in Fig. 6.12b by the full squares. The polychromatic $\eta^{\mathrm{poly}}_{\mathrm{extr}}$ is very similar to the monochromatic results which is due to the peaked QW emission at the center wavelength (variance σ^2 is small compared to the center wavelength). The polychromatic extraction efficiency to air $\eta^{\mathrm{poly},0}_{\mathrm{extr}}$ (corresponding to 0 nm of metal contact) agrees well with the monochromatic η^0_{extr} calculated at the center wavelength of the QW linewidth.

Appendix B: Sensitivity of Model to LED Parameters

We present in this section, the investigation of the sensitivity of the calculated extraction efficiency to LED parameters, revealing that for large range of LED thicknesses and QW positions within the LED, the extraction efficiency through the top facet does not change significantly. Indeed the estimation of the extraction efficiency is mostly, if not solely, affected by the metal contact properties. Moreover, the sensitivity of our model to different metal contacts is presented, which shows that the appropriate choice of metal contacts reduces significantly the dependence of the modeling results on the LED parameters.

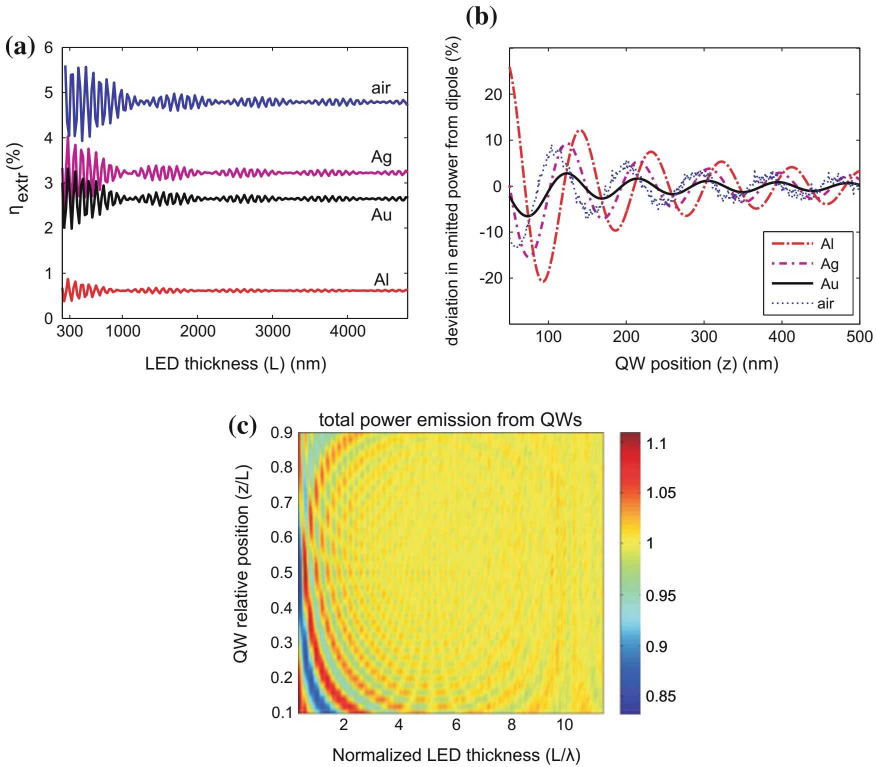

Fig. 6.13 **a** Extraction efficiency as a function of LED thickness for a QW positioned at a fixed 140 nm from the top surface for four cases of metal contacts: no metal, Au, Ag, and Al and all metals are 15.4-nm-thick. **b** Deviation from unity of total radiated power by the source within the LED as a function of the QW position for the same metals. **c** Total radiated power by the dipole source inside the LED as a function of LED thickness and QW position

Let us first present the effect of the LED thickness on the calculated extraction efficiency η_{extr}. Figure 6.13a shows the η_{extr} of a GaN LED on sapphire substrate for $\lambda = 445$ nm, where the QW is positioned at a fixed 140 nm distance from the top surface. Four cases of metal contacts are considered: no metal, Au, Ag, and Al, where the metal thickness is 15.4 nm. In all cases, the extraction efficiency oscillates significantly for an LED structure thinner than 1 μm and tends to a fixed value for thicker structures. In practical LEDs, the fast oscillating behavior shown in Fig. 6.13a is averaged due to thickness fluctuations and polychromatic emission from the source which yields a much smoother function almost independent on LED thickness. Suffice to notice that the half period of such oscillations is ~50 nm for a fixed $\lambda = 445$ nm, which is much shorter than the thickness fluctuations present in real devices. A more general map of the extraction efficiency is shown in Fig. 6.4b, where an LED structure without metal contacts was considered, showing that the extraction efficiency η^0_{extr} is fairly constant for thick LED structures.

Let us investigate the effect of the LED parameters on the total power emitted from the source inside the LED cavity. In the models presented in this chapter, the dipole terms were normalized to yield a unity emitted power in a homogeneous medium. When these dipoles are placed inside the LED heterogeneous medium, or in an optical cavity, the total power emitted from the dipole source may vary because its amplitude is kept constant but the optical medium is modified. This effect is related to a change in radiative emission rate from a source within an optical cavity, or Purcell effect [31]. One assumption made in our models was that the total emitted power from the dipole sources inside the LED would be considered unity due to a negligible Purcell effect in common LED structures.

Here, we test this assumption by calculating the deviation from unity of the total emitted power by the dipole sources inside the LED cavity. Let us consider the effect of the most sensitive LED parameter which is the distance of the QWs to the top surface. The deviation of the total emitted power from unity by the dipole sources inside the LED structure calculated as a function of the QW distance to the top surface z for a total LED thickness of 4729 nm is shown in Fig. 6.13b. The same four cases of metal contacts are considered: no metal, Au, Ag, and Al, where the metal thickness is 15.4 nm and it is interesting to notice that the metal contact plays a significant role in this case.

The deviation from unity in total emitted power due to a cavity effect can be significantly reduced by judiciously choosing the metal contacts, for example, in the case of Au, it is at most 2% for realistic LED structures (z > 150 nm). In case other metals such as Al or Ag are used as contacts, the deviation given in this plot can be used as a corrective factor for the theoretical extraction efficiency. The total emitted power tends to unity as the QW is placed farther from the LED top surface. While the oscillations observed in Fig. 6.13b are only slightly averaged to the polychromatic emission from the source, the use of several QWs or thick active regions, as well as thickness fluctuations of the LED structure, averages these oscillations resulting in a smaller deviation of the emitted power from unity.

A more general map of the deviation from unity of the power emitted from the dipole sources inside the LED is shown in Fig. 6.13c, where an LED structure without metal contacts was considered. As can be seen, the total emission from the dipole source is fairly constant for a thick LED structure ($(L/\lambda) > 5$).

Therefore, under appropriate choice of metal contacts, the technique presented in this chapter is robust to LED parameters and the results presented in Sect. 6.3.1, or more specifically shown in Fig. 6.4 can be generally applied to a large range of LED configurations.

Appendix C: Modeling the Angle-Resolved Emission from LEDs: Accounting for Surface Roughness

The model presented in this chapter (details in Appendix A) can be used to predict the angular emission of an LED structure, as shown in Fig. 6.6. In particular,

it is useful to check whether light emission occurs according to theoretical predictions. The power per solid angle of an LED can be experimentally measured using an angle-resolved setup [32] and compared to the theoretical angle-resolved emission, as demonstrated in [14]. The light radiated to air from the LED structure corresponds to $dP_{\text{out}}^{(h,\text{total})}/d\Omega dS(\theta) = dP_{\text{out}}^{(h,\text{TE})}/d\Omega dS + dP_{\text{out}}^{(h,\text{TM})}/d\Omega dS$. To compare this angular power flow to the corresponding angle-resolved measurement, a correction term $\cos(\theta)$ needs to be used to take into account the projection of the power flow (perpendicular to the LED top surface) into the plane perpendicular to the rotating detector.

Figure 6.14a shows the radiation from the LED (total power per solid angle) versus θ and λ, where the oscillations observed correspond to the Fabry–Perot interferences on the interfaces of the LED structure. While experimental results for LEDs with flat surface match such angular emission (Fig. 6.6a), LEDs with rough surface or pits present diminished oscillations in their angular diagram. The effect of surface roughness can be considered as a damping on the Fabry–Perot oscillations through the assumption that the roughness randomizes the angular distribution of the power flow. Therefore, a fraction F_{rough} of the original power flow is now randomly emitted in all angles, which can be approximated by an isotropic emission normalized by the total power emitted to air η_{extr}, as $R = \eta_{\text{extr}}/2\pi$. A more rigorous investigation of the effect of rough surfaces is presented in [33, 34]. The normalized angular output power flow due to the rough surface is approximated by

$$\frac{F_{\text{rough}}R + (1 - F_{\text{rough}})dP_{\text{out}}^{(h,\text{total})}/d\Omega dS}{\eta_{\text{extr}}}. \tag{6.34}$$

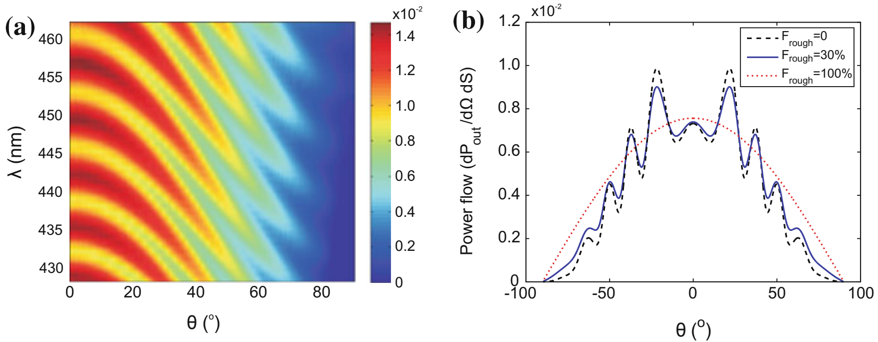

Fig. 6.14 **a** Theoretical angle-resolved radiation ($dP_{\text{out}}^{(h,\text{total})}/d\Omega dS$) versus θ (for θ from 0° to 90°) and λ showing the Fabry–Perot interferences at the interfaces of the LED structure. The LED structure consisted of a 4.87-µm-thick GaN with QW embedded at 140 nm below the top surface. **b** Effect of surface roughness on the angular power flow, normalized by the total power emitted to air, for a smooth LED with $F_{\text{rough}} = 0$ (*dashed line*), for $F_{\text{rough}} = 30\%$ (*solid line*) and for $F_{\text{rough}} = 100\%$ (*dotted line*))

Figure 6.14b illustrates this effect, where the dashed line is the corrected angular power flow, normalized by the total power emitted to air, for a smooth LED with $F_{\mathrm{rough}} = 0$. The solid line corresponds to $F_{\mathrm{rough}} = 30\%$ and the dotted line is for $F_{\mathrm{rough}} = 100\%$. The angle-resolved measurement is a useful technique to assess the contribution of light randomly scattered at rough surfaces to the measured EQE, which ultimately can be used to validate the model requirements of flat interfaces. The pronounced Fabry–Perot oscillations in this measurement fade with increase of F_{rough} which largely reduces the accuracy of this model.

References

1. I. Schnitzer, E. Yablonovitch, C. Caneau, T.J. Gmitter, Appl. Phys. Lett. **62**, 131 (1993)
2. M.R. Krames, M. Ochiai-Holcomb, G.E. Hofler, C. Carter-Coman, E.I. Chen, I.-H. Tan, P. Grillot, N.F. Gardner, H.C. Chui, J.-W. Huang, S.A. Stockman, F.A. Kish, M.G. Craford, T.S. Tan, C.P. Kocot, M. Hueschen, J. Posselt, B. Loh, G. Sasser, D. Collins, Appl. Phys. Lett. **75**, 2365 (1999)
3. M. Yamada, T. Mitani, Y. Narukawa, S. Shioji, I. Niki, S. Sonobe, K. Deguchi, M. Sano, T. Mukai, Jpn. J. Appl. Phys. **41**, L1431 (2002)
4. J.J. Wierer, M.R. Krames, J.E. Epler, N.F. Gardner, M.G. Craford, J.R. Wendt, J.A. Simmons, M.M. Sigalas, Appl. Phys. Lett. **84**, 3885 (2004)
5. I. Schnitzer, E. Yablonovitch, C. Caneau, T.J. Gmitter, A. Scherer, Appl. Phys. Lett. **63**, 2174 (1993)
6. T. Fujii, Y. Gao, R. Sharma, E.L. Hu, S.P. DenBaars, S. Nakamura, Appl. Phys. Lett. **84**, 855 (2004)
7. S. Watanabe, N. Yamada, M. Nagashima, Y. Ueki, C. Sasaki, Y. Yamada, T. Taguchi, K. Tadatomo, H. Okagawa, H. Kudo, Appl. Phys. Lett. **83**, 4906 (2003)
8. A. Laubsch, M. Sabathil, J. Baur, M. Peter, B. Hahn, IEEE Trans. Electron. Devices **57**, 1 (2010)
9. J. Piprek, *Semiconductor Optoelectronic Devices: Introduction to Physics and Simulation* (Academic Press, San Diego, 2003)
10. A. Hangleiter, D. Fuhrmann, M. Grewe, F. Hitzel, G. Klewer, S. Lahmann, C. Netzel, N. Riedel, U. Rossow: Phys. Status Solidi (A) **201**, 2808–2813 (2004)
11. M. Peter, A. Laubsch, P. Stauss, A. Walter, J. Baur, B. Hahn, Phys. Status Solidi (C), **5**(6), 2050 (2008)
12. A. David, M.J. Grundmann, J.F. Kaeding, N.F. Gardner, T.G. Mihopoulos, M.R. Krames, Appl. Phys. Lett. **92**(5), 053502 (2008)
13. E. Matioli, C. Weisbuch, J. Appl. Phys. **109**, 073114 (2011)
14. A. Getty, E. Matioli, M. Iza, C. Weisbuch, J. Speck, Appl. Phys. Lett. **94**(18), 181102 (2009)
15. S.G. Tikhodeev, A.L. Yablonskii, E.A. Muljarov, N.A. Gippius, T. Ishihara, Phys. Rev. B **66**(4), 045102 (2002)
16. P. Kivisaari, L. Riuttanen, J. Oksanen, S. Suihkonen, M. Ali, H. Lipsanen, J. Tulkki, Appl. Phys. Lett. **101**, 021113 (2012)
17. Y.C. Shen, G.O. Mueller, S. Watanabe, N.F. Gardner, A. Munkholm, M.R. Krames, Appl. Phys. Lett. **91**, 141101 (2007)
18. M. Born, E. Wolf (Cambridge University Press, 2000)
19. L.A. Coldren, S.W. Corzine, (Wiley, 1995)
20. E.D. Palik (Academic Press, 1985)
21. A. Getty, Ph.D. thesis, UCSB, 2009

22. The carbon black particles prevent proper exposure of the PR to UV light, hence it is not possible to pattern this layer using standard photolithography techniques. Instead, a lift-off method was applied, where a bilayer of PMGI SF 15 PR followed by AZ4210 was spun onto the sample surface, on which complete LED structures had already been processed. The AZ4210 was then patterned using standard optical lithography, which acted as a mask for the deep-UV exposure of the PMGI SF 15 layer. This exposed layer was then developed, re-exposed, and developed again, creating a deep undercut in the lift-off mask profile. The mixture of PR and carbon black particles was spun over this patterned lift-off mask and then baked at 200 °C for 1 hour. The baking process caused the mixture to adhere strongly to the sample surface and did not affect the PMGI SF 15, which is robust to temperatures up to 250 °C. The lift-off was completed by placing the sample in 1165 PR stripper at 80 °C for 1 hour with strong sonication
23. H. Benisty, H. De Neve, C. Weisbuch, IEEE J. Quantum Electron. **34**, 9 (1998)
24. E. Matioli, B. Fleury, E. Rangel, E. Hu, J.S. Speck, C. Weisbuch, J. Appl. Phys. **107**, 053114 (2010)
25. R. Windisch, P. Altieri, R. Butendeich, S. Illek, P. Stauss, W. Stein, W. Wegleiter, R. Wirth, H. Zull, K. Streubel, Proc. SPIE **5366**, 43 (2004)
26. H. Benisty, R. Stanley, M. Mayer, J. Opt. Soc. Am. A **15**, 1192–1201 (1998)
27. J.P. Weber, S. Wang, IEEE J. Quantum Electron. **27**, 2256 (1991)
28. S.L. Chuang, C.S. Chang, Phys. Rev. B **54**(4), 2491 (1996)
29. S.L. Chuang (Wiley, 2009)
30. D. Ochoa, Ph.D. thesis, EPFL, 2000
31. E.M. Purcell, H.C. Torrey, R.V. Pound, Phys. Rev. **69**, 37–38 (1946)
32. A. David, C. Meier, R. Sharma, F.S. Diana, S.P. DenBaars, E. Hu, S. Nakamura, C. Weisbuch, H. Benisty, Appl. Phys. Lett. **87**(10), 101107 (2005)
33. G. Lerondel, R. Romestain, Appl. Phys. Lett. **74**, 2740 (1999)
34. J.M. Elson, J.P. Rahn, J.M. Bennett, Appl. Opt. **19**, 669 (1980)

Chapter 7
Internal Quantum Efficiency

Jong-In Shim

Abstract In the first part, we have introduced experimental results of the internal quantum efficiency (IQE) droop depending on temperature in both the electroluminescence and the resonant photoluminescence. The IQE droop mechanisms ever reported have been reviewed. An inherent origin of the efficiency droop has been suggested as the saturation of the radiative recombination rate in the InGaN quantum well at low current and subsequent increase in the nonradiative recombination rates at high current. The degree of saturation is determined by operating temperature and effective active volume. Although the saturation of the radiative recombination rate is common origin of the IQE droop, the shapes of the IQE versus current, i.e. the IQE droop curve, vary with the dominant nonradiative recombination process. In the second part, we have reviewed the IQE measurement methods theoretically as well as experimentally. A simple IQE estimation method based on the constant ABC model in the carrier rate equation is introduced in terms of its convenience and application limitation. Other methods have been also reviewed by focusing on all-optical methods such as the temperature-dependent photoluminescence (TDPL) and the temperature-dependent time-resolved photoluminescence (TD-TRPL) methods.

7.1 LED Efficiency

InGaN light-emitting diodes (LEDs) have been of great importance in recent years. Their applications are now in many areas such as traffic lights, mobile phones, automotives, display units, and general lighting. The application expansion capacity depends on both efficiency and reliability improvements, especially for the areas requiring high-brightness LEDs like general lighting.

Usually, an LED is electrically driven by a battery producing the voltage of V and the forward current of I and the total electrical power supplied is VI. The LED

J.-I. Shim (✉)
Hanyang University, ERICA campus, Seoul, Korea
e-mail: jishim@hanyang.ac.kr

© Springer Nature Singapore Pte Ltd. 2017

T.-Y. Seong et al. (eds.), *III-Nitride Based Light Emitting Diodes and Applications*,
Topics in Applied Physics 133, DOI 10.1007/978-981-10-3755-9_7

operation is more clearly understood when we express VI as $(qV)(I/q)$ where q is the unit elementary charge of $1.6 \times 10^{-19}[C]$, I/q is the total number of electrons injected into the active layer per second, and qV is an electrical potential energy of each electron. In the ideal case, each electron energized by a battery emits one photon without any energy loss so that both quantum particles should have the same energy of qV. In a real case, however, there are many sorts of electrical and optical energy loss mechanisms during the electrical-to-optical energy conversion process.

The overall efficiency of an LED is characterized by the wall-plug efficiency ($\eta_{wall\text{-}plug}$), which is defined by the ratio of the optical power emitted into free space from the LED to the electrical power provided to the LED [1]. Then, the wall-plug efficiency can be rewritten in detail by utilizing the voltage efficiency (η_{VTG}), the injection efficiency (η_{INJ}), the radiative efficiency (η_{RAD}), and the light extraction efficiency (η_{LEE}) in terms of energy conversion processes from a battery to a detector in free space as $\eta_{wall-plug} = \eta_{VTG} \times \eta_{INJ} \times \eta_{RAD} \times \eta_{LEE}$. η_{VTG}, η_{INJ}, η_{RAD}, and η_{LEE} are defined as follows:

$$\eta_{VTG} = \frac{\text{Average photon energy emitted from active region}}{\text{Average electron energy supplied by battery}} = \frac{h\bar{\nu}}{qV} \tag{7.1}$$

$$\eta_{INJ} = \frac{\text{\# of electrons injected into active region per second}}{\text{\# of electrons injected into LED per second}} = \frac{I_{active}/q}{I/q} \tag{7.2}$$

$$\eta_{RAD} = \frac{\text{\# of photons emitted from active per second}}{\text{\# of electrons injected into active region per second}} = \frac{P_{active}/(h\bar{\nu})}{I_{active}/q} \tag{7.3}$$

$$\eta_{LEE} = \frac{\text{\# of photons emitted into free space per second}}{\text{\# of photons emitted from active per second}} = \frac{P_{out}/(h\bar{\nu})}{P_{active}/(h\bar{\nu})}, \tag{7.4}$$

where P_{out}, V, I, $h\bar{\nu}$, I_{active}, and P_{active} are the optical power emitted from an LED to the free space, the applied voltage, the forward current, the average energy per photon, the current injected into the active region, and the radiated optical power from the active region, respectively.

The voltage efficiency (η_{VTG}) is a measure for the electrical potential energy loss during electron transport from a battery to the active region of an LED. The average energy of one photon emitted from an LED is almost equal to the bandgap energy of the active region of an LED. The losses in electrical potential energy mainly results from the Ohmic losses occurring at the metal and semiconductor interface, semiconductor heterointerfaces, and semiconductor bulk materials. In addition, the electrical potential loss is inevitable at the quantum well (QW) active region during the carrier capture process from the three-dimensional bulk region to the two-dimensional QW. In order to improve the voltage efficiency, both low forward turn-on voltage and small series resistance are required. The voltage efficiency is

experimentally measurable so that the value can be improved by a sort of feedbacks to fabrication processes and LED chip designs.

The injection efficiency (η_{INJ}) is a measure for how many electrons recombine in the active QW region compared with the total injected electrons into a LED. It depends on the current level as well as the LED structure itself. The efficiency is determined by nonradiative recombination rates occurring outside the active QW regions. Possible leakage currents are semiconductor surface current, defect-related tunneling current, and electron overflow from the QW active region to p-clad region [2–4]. The surface leakage current is initially observed at around zero bias voltage and it shows very symmetric current–voltage curve for forward and reverse biases. Special surface treatment and passivation techniques have been utilized to suppress the surface leakage current. The electron blocking layer in the epitaxial growth has been introduced to reduce the electron overflow from the active region to the p-type clad layer at high-level current injection [5]. Current spreading is important to improve the current injection efficiency in terms of reducing current density over an entire LED surface. The nonuniform current injection increases both the Joule heating and the nonradiative recombination processes and eventually lowers the light wall-plug efficiency [6, 7].

The radiative efficiency (η_{RAD}) is defined as the ratio of the radiative recombination rate to the sum of the total recombination rate, i.e. the sum of the radiative and nonradiative recombination rates, in the active multiple-quantum-well (MQW) layers. In order to improve the radiative efficiency, it is necessary to increase the radiative recombination rate and decrease the nonradiative recombination rate. High-quality epitaxial growth with low defects is essential to reduce the nonradiative recombination rate. The radiative recombination rate is determined basically by the "Fermi's golden rule" and the total number of recombining electron-hole pairs [8]. Elimination of the piezoelectric field is very effective to increase the recombination probability of an electron-hole pair and large active volume is one of the best ways to increase the total number of carriers contributing to the radiative recombination.

The light extraction efficiency (LEE, η_{LEE}) is a measure for the photon losses during the propagation from the active region into free space. In an ideal LED, all photons emitted by the active region should escape from the LED die. However, in a real LED, not all the power emitted from the active region is emitted into free space. This is due to the phenomenon of total internal reflection and several possible optical loss mechanisms. The total internal reflection of GaN-based LEDs results from the large difference in refractive index between a GaN film (n = 2.4) and surrounding air (n = 1.0). The light reaching the surface beyond the critical angle will undergo internal reflection and will continue to be reflected within LEDs until it is absorbed. Thus, much of the light generated by conventional LEDs will continue to be reflected until it is absorbed. The light can be absorbed by the substrate, epitaxial layers, and the metallic layer via free carrier absorption or band-to-band absorption. One method of reducing the percentage of total internal reflection of light is to generate light-scattering centers inside or outside the LED chip. The methods improving the light extraction efficiency are known as angular

randomizations by scattering of photons via random texturing of the LED's surfaces, artificial voids inside the epitaxial layers, micro patterning of the sapphire substrate or epitaxial layers, chip shaping of multiple escape cones, and the coupling of photons to surface plasmons [9, 10].

The internal quantum efficiency (IQE, η_{IQE}) is defined as the product of the injection efficiency and the radiative efficiency and is the ratio of the number of the photons emitted from the active region to the number of electrons injected into a LED. The IQE and the LEE are two principal parameters for improving the efficiency of LEDs, both of which can be improved through the improvement of crystal quality and the modification of the structure of the epitaxial layers. The external quantum efficiency (EQE, η_{EQE}) is defined as the product of the IQE and the LEE and is the ratio of the number of useful photons to the number of injected electrons.

$$\eta_{IQE} = \frac{\text{\# of photons emitted from active per second}}{\text{\# of electrons injected into LED per second}} = \left(\frac{I_{active}/q}{I/q}\right)\left(\frac{P_{active}/h\bar{\nu}}{I_{active}/q}\right) = \left(\frac{P_{active}/h\bar{\nu}}{I/q}\right) = \eta_{INJ} \times \eta_{RAD} \tag{7.5}$$

$$\begin{aligned}\eta_{EQE} &= \frac{\text{\# of photons emitted into free space per second}}{\text{\# of electrons injected into LED per second}} = \left(\frac{I_{active}/q}{I/q}\right)\left(\frac{P_{active}/h\bar{\nu}}{I_{active}/q}\right)\left(\frac{P_{out}/h\bar{\nu}}{P_{active}/h\bar{\nu}}\right) \\ &= \left(\frac{P_{out}/h\bar{\nu}}{I/q}\right) = \eta_{INJ} \times \eta_{RAD} \times \eta_{LEE}.\end{aligned} \tag{7.6}$$

We summarized six types of efficiencies used in the LED society, i.e., the wall-plug efficiency ($\eta_{wall\text{-}plug}$), the voltage efficiency (η_{VTG}), the injection efficiency (η_{ING}), the radiative efficiency (η_{RAD}), the light extraction efficiency (η_{LEE}), the internal quantum efficiency (η_{IQE}), and the external quantum efficiency (η_{EQE}). Among these seven efficiencies, however, only three efficiencies, $\eta_{wall\text{-}plug}$, η_{VTG}, and η_{EQE} are experimentally measurable but others of η_{INJ}, η_{RAD}, η_{IQE}, and η_{LEE} are hardly measurable by experiments. Among these efficiencies, the IQE is the most important because it is directly related to the crystal growth technology. Once we know the IQE value, then the LEE can be known from the measured EQE. In the following sections, we first review the IQE characteristics focusing on the droop and then present the IQE measurement methods.

7.2 Efficiency Droop Mechanisms

7.2.1 Efficiency Droop Overview

A major challenge for III-nitride LEDs is delivering the highest efficiency performance at the current density and temperatures relevant to high-power operation. The EQE efficiency breakthroughs are due to improvements in both the IQE and the LEE. Since the LEE is nearly independent of the operational environments, the

variation of the EQE is attributed to that of the IQE. Typically, the IQE shows a maximum at low injection current and then decreases as current is further increased, the so-called efficiency (or IQE) droop. Experimentally, the IQEs are strong functions of emission wavelength, current density, and temperature as sketched in Fig. 7.1. InGaN-based LEDs operating especially at blue-green wavelengths suffer from very large efficiency droop. The IQE droop is currently a limiting factor to more efficient LEDs under high current. Understanding origins of the IQE droop is an imperative in terms of reducing the droop and finding the IQE measurement method for the future of general lighting.

The following experimental IQE behaviors are commonly observed: The IQE droop of III-nitride LED is observed (1) in both blue and green LEDs [11–13] (2) in both resonant photoluminescence (PL) and electroluminescence (EL) measurements with very similar excitation dependences [12, 14] (3) under pulsed, as well as continuous-wave (CW), current injections [15, 16], (4) in polar, nonpolar, and semi-polar QW structures [17–20], (5) for single QW, MQW, and bulk active layers [13, 17, 21], (6) at all temperatures from 4 to 450 K [11–13, 15–19], and (7) less severe in short wavelengths (near-UV) and more pronounced at longer wavelengths (green-yellow) [22].

The IQE defined in (7.5) can be rewritten by the current ratio of the radiative recombination current I_r in the active region to the total injection current I as shown in (7.7). The total current I consists of the radiative recombination current and the nonradiative recombination current I_{nr}. At room temperature, electrons and holes in the active region can be considered as free carriers and they recombine radiatively according to the Fermi's golden rule. There are three types of the nonradiative recombination currents around the active region as shown in Fig. 7.2: (i) the electron overflow current recombining radiatively and nonradiatively in p-GaN, (ii) the electron tunneling leakage current from the active QW to the p-side, and

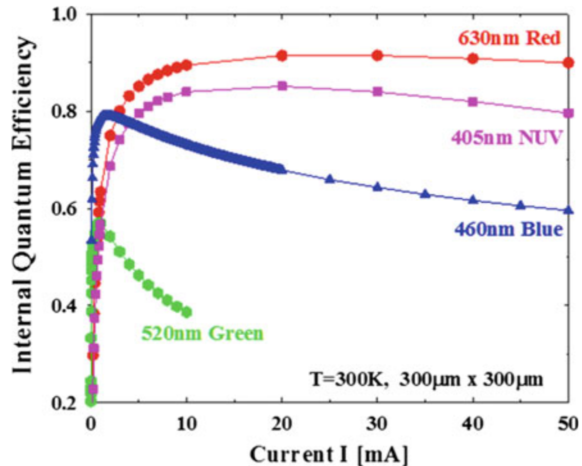

Fig. 7.1 IQEs of red, green, blue, and near-UV LEDs as a function of current at room temperature. All LEDs are nearly the same sizes of 300 × 300 μm^2. IQEs are estimated by an analysis method based on the carrier rate equation

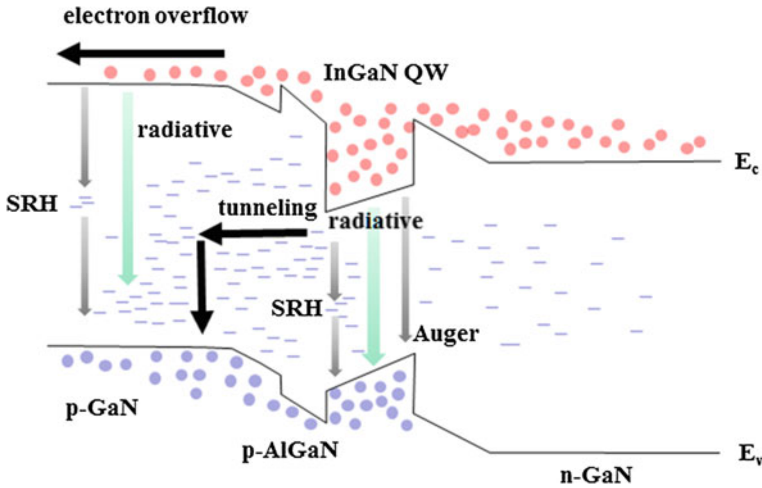

Fig. 7.2 Schematic illustration of current components in an InGaN-based LED. The radiative current in p-GaN stands for the electron recombination current through defects resulting from the Mg impurity doping

(iii) the recombination currents in the active QW via the Shockley-Read-Hall (SRH), the radiative, and the Auger recombination processes.

$$\eta_{IQE} = \eta_{INJ} \times \eta_{RAD} = \frac{I_r}{I} = \frac{I_r}{I_r + I_{nr}} = \frac{1}{1 + I_{nr}/I_r}, \tag{7.7}$$

where $I_{active} = \eta_{INJ} I$ and $I_r = \eta_{RAD} I_{active} = \eta_{RAD}\eta_{INJ} I = \eta_{IQE} I$

In general, the optical power P_{active} from the active QW is a monotonically increasing function of total current I and P_{active} is linearly proportional to the radiative current I_r. Thus, we know from (7.7) that the IQE droop happens only when I_{nr} increases faster than I_r with increasing total current I. This implies that the amount of IQE droop is mainly determined by I_{nr} rather than I_r, which is the reason why the nonradiative recombination processes has been considered as a dominant mechanism of the IQE droop.

Many possible explanations have been proposed to explain the efficiency droop, including local junction heating [15], carrier overflow enhanced by internal polarization field [16], poor hole injection [23, 24], or asymmetric electron and hole distributions in the active region [25], carrier delocalization from indium-rich regions and nonradiative recombination at high defect sites [4, 26], and Auger recombination [10–14, 27, 28]. All previous IQE droop explanations were based on additional increases in the nonradiative recombination rates with increasing current. More recently, saturation of the radiative recombination rate and subsequent increase of the nonradiative recombination rate was proposed by us in order to explain the IQE droop phenomena more comprehensively including their temperature dependences [29, 30]. Nevertheless, a consensus on the mechanism behind the

IQE droop remains elusive [31–34]. Here, we first review the proposed IQE droop mechanisms by comparing experimental IQE behaviors and then explain the importance of the radiative recombination rate on the IQE behaviors depending on current as well as temperature.

7.2.2 Auger Nonradiative Recombination

To find the origin of the EL efficiency droop, the PL efficiency is frequently utilized with different operating temperatures and optical pumping powers. In the resonant PL experiments, the photon energy of the optical pumping source is between the bandgap energy of QWs and that of barriers to selectively excite the carriers only in the QWs. The experimentally observed PL efficiency droop shows the dependences on the carrier density and the operating temperature quite similar to those of the EL efficiency droop [11–13, 16, 35]. This observation is consistent with intrinsic recombination mechanisms in the active QW itself, such as Auger recombination and carrier escape from the QWs, because the carrier transport issue is not involved in the resonant PL experiments.

Nonradiative electron-hole recombination processes transfer the excess electron energy to other particles except photons. In case of direct Auger recombination, these other particles are electrons or holes that are excited into higher energy levels within the same band. The theoretical probability of this Auger process decreases exponentially with increasing bandgap energy E_g and decreasing operating temperature T, i.e., $C \propto \exp\left(-E_g/k_B T\right)$, where C is the Auger coefficient and k_B is the Boltzmann constant [7]. Therefore, the importance of Auger recombination in III-nitride semiconductors has been in doubt for a long time. However, similar efficiency droop curves in the resonant PL and EL experiments invoked Auger process as the dominant nonradiative mechanism leading to efficiency loss at high carrier density. Efforts to verify the Auger recombination have been carried out both theoretically and experimentally.

Several theoretical groups calculated the III-nitride Auger coefficients [14, 27–29]. Hader et al. computed a very small Auger coefficient C of 3.5×10^{-34} cm^6/s using the $8 \times 8\, \vec{k} \cdot \vec{p}$ band model for the direct band-to-band Auger process and concluded that this value is too small to explain the experimentally observed droop [14]. Delaney et al. calculated a peak Auger coefficient of 2×10^{-30} cm^6/s in bulk InGaN with a 2.5 eV bandgap ($\lambda_g = 495$-nm) using first-principle density-functional and many-body-perturbation theory and concluded that an interband Auger may be responsible for droop in InGaN LEDs [27]. But the probability of this interband Auger process decreases rapidly with changing bandgap and it seems to be insufficient to explain the efficiency droop observed across a wide wavelength range. In addition, Pasenow et al. proposed the phonon-assisted Auger recombination as one of the candidates for explaining the droop [28]. But some people still argued that the

Table 7.1 Carrier recombination A, B, and C coefficients of InGaN-based LEDs

Wavelength λ (nm)	A (1/s)	B (cm^3/s)	C (cm^6/s)	References
440	5.4×10^{7}	2.0×10^{-11}	2.0×10^{-30}	Harder et al. [14]
407	1.0×10^{7}	2.0×10^{-11}	1.5×10^{-30}	Zhang et al. [103]
450	2.3×10^{7}	1.0×10^{-11}	1.0×10^{-30}	Meneghini et al. [104]
523	0.47×10^{7}	1.2×10^{-12}	3.5×10^{-31}	Laubsch et al. [13]
444	–	1.0×10^{-10}	8.0×10^{-29}	Dai et al. [37]
445	1.0×10^{7}	1.9×10^{-10}	3.2×10^{-29}	Özgür et al. [42]
440	$(8.13–15.6) \times 10^{7}$	1.0×10^{-10}	–	Schubert et al. [43]

phonon-assisted Auger process is typically not strong enough to generally explain the droop [26, 31].

The influence of Auger recombination is typically estimated by using the constant ABC model in the semiconductor carrier rate equation. The C coefficient in the rate equation stands for the nonradiative recombination rate due to Auger processes. Table 7.1 gives an overview of recombination coefficients for InGaN QWs extracted from measurements using the ABC model [32, 33]. Reported Auger coefficients at room temperature in InGaN-based LEDs range from 3.5×10^{-31} to 3.2×10^{-29} cm^6/s. These experimental values are generally larger compared to theoretical values of about 10^{-34}–10^{-30} cm^6/s. In fact, it is not easy to obtain exact values of these three fit parameters simultaneously by only one fit process. Thus, most of works fit the A and B coefficients in the low current injection regime and the C coefficient in the high current injection regime. It should be noted that all these measurements neglected the influence of carrier leakage, i.e., $\eta_{INJ} = 1$.

Recently, we successfully developed an analysis method of the IQE and each recombination current at arbitrary current based on the constant ABC model [36]. A similar method was also proposed in the reference [37]. We managed to cut the number of fitting parameters from three to one by manipulating the rate equations so that the fitting errors can be minimized. Our method is applied to InGaN-based blue and green LEDs and their IQE curves are relatively well-fitted by the constant ABC model. However, the estimated range of C coefficients is around 10^{-28}–10^{-25} cm^6/s, which is at least 100 times higher than the reported C coefficients of 10^{-30} cm^6/s. To date, there are no theories explaining such large C coefficients. Thus, it is plausible that the carrier loss process with a N^3-dependence, where N is the carrier density, could represent other processes than the Auger processes.

7.2.3 Defect-Related Nonradiative Recombination

The InGaN material system has lots of defects compared to other III–V semiconductors. Since the early stage, attention has been paid to the defect-related recombination mechanisms as another origin of the efficiency droop. They include

carrier delocalization from local in-plane potential minima and nonradiative recombination at high defect sites and defect-assisted tunneling of carriers out of the active region [4, 26, 38–41].

The idea of surprisingly high radiative recombination rate at low current is based on the early observation of a nonuniform indium distribution inside InGaN QWs. Indium-rich clusters are associated with a lower bandgap and therefore lead to carrier localization. At low current and low QW carrier density, indium clusters then keep carriers away from structural defects. With higher current, however, carriers gradually escape from these potential minima of indium-rich clusters due to carrier–carrier screening and increasingly recombine nonradiatively at defects. This IQE droop mechanism can be modeled theoretically by assuming that the SRH recombination coefficient A itself exhibits a superlinear rise with the QW carrier density N [26]. On the other hand, the IQE droop due to the defect-assisted tunneling of carriers out of the active region should be modeled by the injection efficiency varying with the carrier density.

Similar to Auger recombination processes, however, additional increase of nonradiative recombination rate due to defected-related nonradiative recombination mechanisms in the MQW active region cannot fully explain the temperature-dependent characteristics of the IQE droop [11, 17, 29, 30]. As the operating temperature is reduced, the amount of droop in both the resonant PL efficiency and the EL efficiency is observed to increase. But it is expected that the nonradiative recombination at defects working as the nonradiative recombination centers (NRCs) in the MQW active region decrease as temperature decreases. Thus, larger efficiency droop at lower temperature is hard to be explained only by the defect-related droop mechanisms without the aids of other temperature-dependent recombination mechanisms.

7.2.4 Transport-Related Nonradiative Recombination

Unbalanced carrier transport mechanisms have also been suspected as a dominant cause resulting in the poor current injection efficiency and consequently the IQE droop [23–25, 42–46]. It is still controversial whether electron leakage out of the active region or ineffective hole injection into the active region is the cause of eventual electron leakages from the active region to the p-side region. There are two cores in this model. One is a parasitic nonradiative carrier recombination on the p-side of the device. The other is that the carrier capture process from the bulk region to the QW active region is assumed to be insufficient. The piezoelectric field, low hole concentration in the p-side, asymmetry in electron and hole distributions, and quasi-ballistic electron transport are proposed as the background deterioration mechanisms of the carrier injection efficiency defined in (7.2). It was reported that the IQE droops were alleviated by introducing special LED structures such as the electron blocking layer (EBL) [46, 47] and the polarization controlled MQW active

region [44, 45]. Although the carrier-transport-related droop model cannot completely explain all the experimental droop phenomena, it seems evident that the model is useful in improving the IQE droop [24, 44–57].

While there is a difference in the degree of efficiency droop depending on temperature, the EL efficiency droop is observed not only in InGaN-based blue and green LEDs, but also in AlGaInP-based red LEDs grown on GaAs substrates [58]. It is noticeable that the AlGaInP/GaAs material system is quite different from the InGaN-based material system in that (i) the AlGaInP epitaxial system is perfectly lattice-matched to the GaAs substrate, (ii) the active volume of the AlGaInP red LED is more than 10 times larger than that of the InGaN blue or green LED, and (iii) the AlGaInP material is not subject to the internal electric field caused by the spontaneous and piezoelectric polarizations. Moreover, it was reported that InAs/GaAs quantum dot (QD) structures grown on the GaAs substrate show temperature-dependent EL behaviors at 1.3 μm, which are very similar to those of InGaN-based blue and green LEDs [59]: The efficiency droop also increases with decreasing temperature or QD size. From these results, we suspect that the efficiency droop is not a peculiar phenomenon existing only in the InGaN-based material system. Thus, it is plausible that the carrier recombination mechanism governing the efficiency droop is not the unique one that is possible only in a special epitaxial structure or material system. Consequently, it is natural that the increase in nonradiative recombination rate assisted by the piezoelectric field is not a key mechanism of the efficiency droop because there is almost no piezoelectric field in both AlGaInP and InAs/GaAs material systems.

On the other hand, as the operating temperature is reduced, the hole concentration in GaN-based LEDs drastically decreases due to high activation energy of the hole, leading to poor hole transport in the MQWs [25, 58, 60]. Therefore, carriers typically recombine in MQWs near the p-GaN clad. The asymmetric carrier distribution attributed from the poor hole transport may promote the carrier overflow from the MQW region [61–63]. In this sense, the UV LEDs incorporating the p-type AlGaN are expected to show more carrier asymmetry than the p-GaN used in blue and green LEDs. However, the UV LEDs show less efficiency droop than the blue and green LEDs. Moreover, LEDs with single QW or bulk active layer also show the efficiency droop. This implies that all experimental IQE droop results cannot be consistently explained only by one of the transport-related mechanisms.

Up to now, none of the above droop model is generally accepted. Auger and defect-related processes consider additional increase in the nonradiative recombination process inside the QW active region and sufficient carrier capture rates into the QW active region. On the other hand, carrier-transport-related models suspect additional increase in the nonradiative recombination outside the QW active region like in the p-side and insufficient carrier capture rate into the QW active region due to different reasons. However, all these models focus on faster increases in the nonradiative recombination without taking into account the possible mechanisms of slower increase in the radiative recombination rate. In addition, most of these models are trying to explain the IQE droop behavior just at room temperature without encompassing cryogenic temperatures. Actually, the IQE is greatly

dependent on several factors such as the device structure, emission wavelength, current injection level, and operating temperature. Thus, we need to develop an advanced IQE droop model which is able to explain previously reported experimental results not only qualitatively but also quantitatively in a unified manner.

7.2.5 Saturated Radiative Recombination

We know from (7.7) that the IQE droop at certain temperature can happen just in case that the nonradiative recombination rate increases faster than the radiative recombination rate or the radiative recombination rate increases slower than the nonradiative recombination rate. As a concept for an origin of the IQE droop, the former is different from the latter in the following sense; the former emphasizes additional increase in the nonradiative recombination rate without taking into account the increasing speed in the radiative recombination rate seriously. On the other hand, the latter supposes that saturation in the radiative recombination rate at high carrier density is a motive for the IQE droop and subsequently it accelerates additional increases in the nonradiative recombination rate. In the former case, for reducing the IQE droop, we need to find important nonradiative recombination processes and eliminate them in the first place. In the latter case, however, we need to increase the radiative recombination rate without its saturation up to high current level. Thus, it is essential to clarify which concept is more suitable to understand the LED efficiency comprehensively.

Here, we attempt to investigate the saturation characteristics in the radiative recombination rate. In addition, we do not specify a dominant nonradiative recombination process because it can vary with operating conditions as well as the LED device structure. Note that the nonradiative recombination processes can take place both inside and outside the active QW region, but the radiative recombination process occurs only inside the active QW region.

Recently, there have been some reports investigating the saturation characteristics of the radiative recombination rate in the active QW and relating them to the LED efficiency droop although each proposed origin of the LED droop is different [29, 64–67]. Different parameters are utilized as a measure of the saturation in the radiative recombination rate such as the fall time of the temporal response in an electrical–optical pump–probe technique, the depth of the S-shape of the PL peak energy and the PL efficiency as in the temperature-dependent PL excitation, differential carrier lifetime with current, and the temporal decay times in the time-resolved PL techniques. Here, we propose another technique showing the saturation phenomenon in the radiative recombination rate. The method is a comparative study of the PL efficiency, the EL efficiency, and the open-circuit voltage under different temperatures and excitation powers in InGaN-based blue LEDs.

The structure of the LED used in this work was grown on a c-plane (0001) sapphire substrate, followed by a 30-nm-thick buffer layer, and a 2.8-nm-thick n-GaN layer (n-doping = 5×10^{18} cm^{-3}). The active region consisted of six 3-nm-thick

$In_{0.15}Ga_{0.85}N$ QWs sandwiched by 5-nm-thick GaN barriers. On top of the active region were a 40-nm thick p-$Al_{0.18}Ga_{0.12}N$ EBL and a 60-nm thick p-GaN layer (p-doping = 8×10^{17} cm^{-3}). The device geometry was designed into a rectangular shape of 700×270 μm^2. The device had lateral electrodes and was mounted on an SMD-type package.

The PL efficiency was measured under open-circuit configuration from the room temperature to 12 K as a function of excitation laser power. The device was cooled by a helium closed-cycle cryostat by Advanced Research System. A 405-nm semiconductor diode laser was utilized for resonant optical excitation. The excitation power was varied from 3 to 100 mW by controlling the laser diode current. The excitation spot size of the laser on the LED device had a diameter of <80 μm. The PL signal was collected by a spectrometer and the open-circuit voltage was measured simultaneously. Also, the EL signal was collected separately by an optical power meter as a function of injection current.

Figure 7.3 depicts the open-circuit voltage as a function of excitation power from room temperature to cryogenic temperatures. At room temperature, as expected in other photovoltaic devices, the open-circuit voltage increases monotonically from 2.43 to 2.57 V as the excitation power increases. This experimental result comes from the difference in quasi-Fermi energy induced by photogenerated charge carriers in MQWs by the resonant excitation. However, at cryogenic temperatures below 100 K, the open-circuit voltage does not increase any more with the excitation power. For example, at 12 K, it increases and then decreases from 2.79 to 2.69 V with the excitation power. Figure 7.4 shows the PL efficiency as a function of excitation power from room temperature to cryogenic temperatures, in which the PL efficiency is normalized by the maximum PL efficiency at 12 K.

By comparing the open-circuit voltage in Fig. 7.3 with the PL efficiency in Fig. 7.4, we find that there is a very close relationship between their droop behaviors. In other words, the PL efficiency droop and the reduction in open-circuit voltage show a similar trend at the same temperature and become worse with decreasing temperature. We explain these temperature-dependent behaviors as

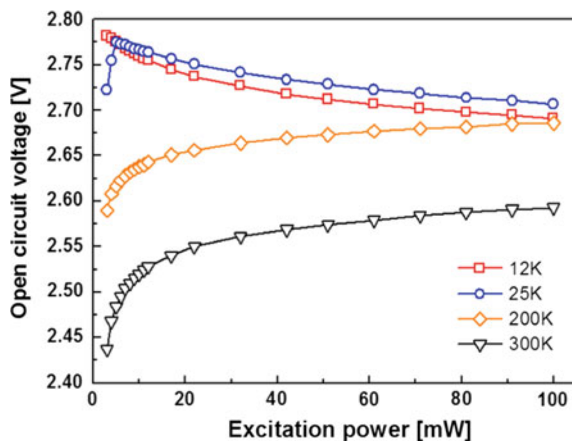

Fig. 7.3 Experimental result of the open-circuit voltage as a function of excitation power from room temperature to cryogenic temperatures

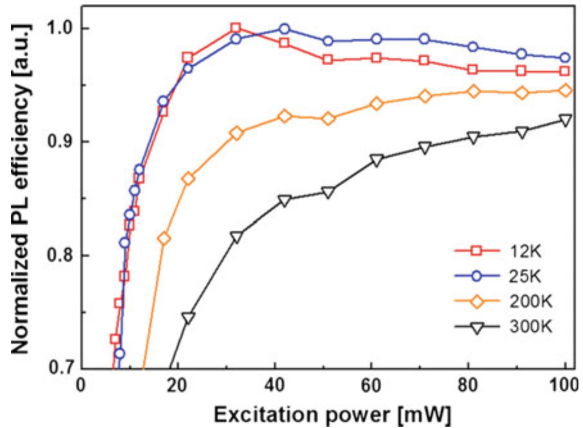

Fig. 7.4 Experimental result of the PL efficiency as a function of excitation power from room temperature to cryogenic temperatures

follows. We first consider the case of room temperature. Electron-hole pairs generated by optical pumping recombine via radiative and nonradiative recombination processes in MQWs. Since some of the generated charge carriers escape outside the MQW region (electrons to the n-side and holes to the p-side) and no net current should flow under open-circuit configuration, the quasi-Fermi levels in MQW region for the electron and the hole separate, playing a role of forward bias that cancels the photogenerated current. This forward bias manifests as the open-circuit voltage. When the excitation power is increased, more carriers are generated, accumulate, and recombine radiatively in MQWs, increasing the PL efficiency and the open-circuit voltage. We next consider the case of cryogenic temperatures. As the laser excitation power initially increases, the open-circuit voltage also increases. This is because rapid carrier accumulation in MQWs occurs due to the elimination of nonradiative recombination channel at NRCs and early saturation of the radiative recombination. With further increase of the laser excitation power, now the carriers in MQWs can start escaping to opposite directions (electrons to the p-side and possibly holes to the n-side), reducing the forward bias for the open-circuit and as a result, the open-circuit voltage.

Figure 7.5 is the EL efficiency normalized by the maximum EL efficiency at 12 K as a function of injection current. As the temperature decreases from room temperature, overall IQE values initially increase with a similar amount of droop. Beyond a critical temperature, the IQE curve starts to show the droop. The initiation of droop depending on the operating temperature is considered to be caused by the increase of carrier overflow due to the temperature dependence of saturation of the radiative recombination rate. When the temperature dependence of the open-circuit voltage and the PL efficiency in Figs. 7.3 and 7.4 are compared with that of the EL efficiency, we can observe very similar tendencies among three experimental results. In the resonant PL experiments, the temperature-dependent droop behaviors of both the PL efficiency and the open-circuit voltage are determined mainly by the carrier escape process rather than the carrier capture process in the QW. Thus, we think that the rapid carrier pileup due to the saturation of

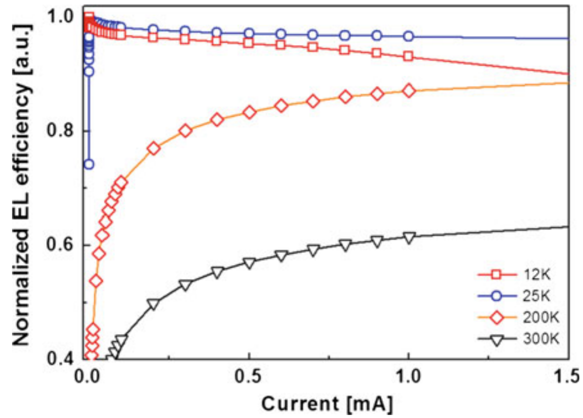

Fig. 7.5 Experimental result of the EL efficiency as a function of injection current from room temperature to cryogenic temperatures

radiative recombination rate and subsequent increase of nonradiative recombination rate due to the carrier leakage of electron overflow from the MQW region to the p-GaN layer is the dominant mechanism behind all these droop phenomena at cryogenic temperatures.

There are three important points to be noted from previous discussions. First, carriers excited by the resonant laser pumping do escape from the QWs, although the photon energy of the pump laser is smaller than the bandgap energy of the semiconductor surrounding the active QWs. The carrier escape may result from the carrier heating process at the early stage of the pumping [65, 68]. There is the same result of carrier escape from the QWs at the resonant optical pumping in reference [69]. Second, the origin of efficiency droops in the PL and EL experiments is the same. Third, carrier overflow from the QW to the p-side is dominated by the carrier escape process rather than the carrier capture process. In other words, carriers injected from the outside QWs are mostly captured into the QWs without passing them as long as the total carrier recombination rate, i.e. the sum of the radiative and nonradiative recombination rates, is so fast that the captured carriers are completely consumed.

In summary, by examining the temperature-dependent PL efficiency, EL efficiency, and open-circuit voltage, comprehensive model of efficiency droop phenomenon has been verified. Through comparative studies, we suggest that the inherent origin of the efficiency droop is the saturation of the radiative recombination rate in the InGaN QW at low current and subsequent increase in the nonradiative recombination rates at high current. The degree of saturation is determined by the operating temperature and the effective active volume.

7.2.6 Comprehensive Efficiency Droop Model

Now we seek to find an efficiency droop model that can comprehensively explain the experimental phenomena depending on both temperature and excitation levels in InGaN-based MQW blue and green LEDs. As the operating temperature is

reduced, the amount of droop in the resonant PL efficiency and the EL efficiency is observed to increase [11, 12, 60]. We believe that this gives an important clue to the origin of the efficiency droop in addition to the saturation characteristics of the radiative recombination rate.

For experiments, InGaN/GaN MQW blue and green LED devices (with indium compositions of ~20% and ~35%, respectively) were used. Both devices had lateral electrodes and the chip sizes for blue and green LEDs were 350 × 430 μm^2 and 400 × 400 μm^2, respectively [30]. First, the IQEs were measured from 300 to 50 K for both samples. From the measured EL intensity at different temperatures, IQEs were obtained. For both blue and green LED samples, the maximum IQEs at 50 K were defined to be 100%. The maximum current was limited to 50 mA (10 mA for the green LED) to avoid any issue related to heat generation caused by increased forward voltage at low temperature.

Figures 7.6 and 7.7 depict the estimated IQEs as a function of current for blue and green LEDs, respectively. For clarification of the IQE behaviors at low currents, the same data are plotted on a log scale as well. As the temperature is lowered from 300 K, it is seen that the IQE curves for blue and green LEDs show two distinct behaviors, which is clearer on a linear scale. As the temperature is lowered from 300 K, the IQE curves initially shift to higher values overall with similar amounts of efficiency droop. This indicates that the number of defects in QWs causing the nonradiative recombination via the SRH process is reduced rather monotonically with decreasing temperature [43, 70]. Beyond certain temperatures (200 K for blue and 250 K for green LEDs), however, the shape of IQE curves changes to show a more pronounced maximum at a lower current level with severer droop. This tendency becomes more distinct as temperature is lowered further. From this characteristics change in the IQE curves beyond certain temperatures, one can guess that the dominant droop mechanism undergoes a qualitative change. Since the nonradiative recombination lifetime in the QW active region becomes longer at lower temperatures [1], the severer droop cannot be dominated by the nonradiative recombination at defects in the QW active region. At the lowest

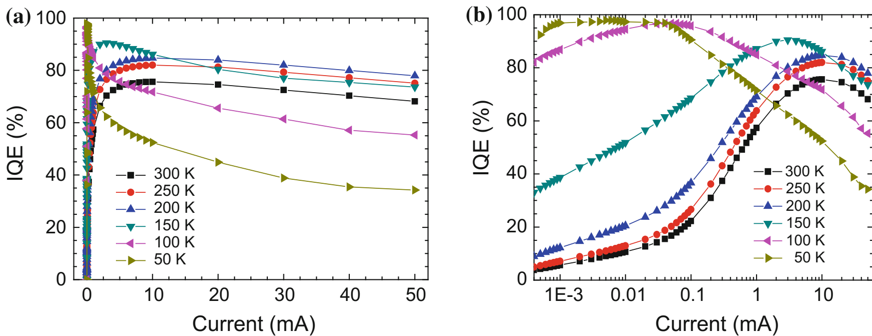

Fig. 7.6 Estimated IQEs for the *blue* LED plotted on **a** linear and **b** log scales for current

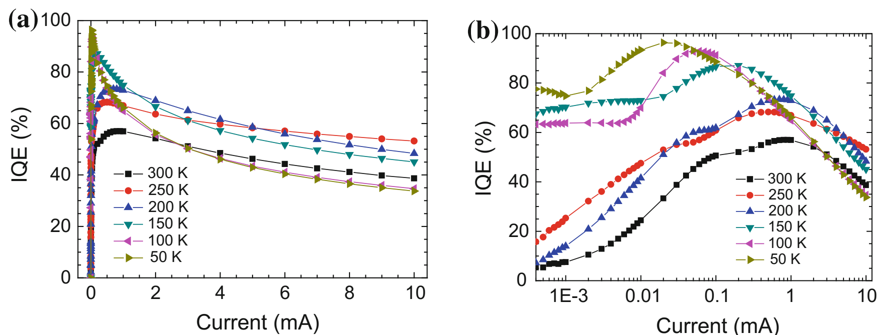

Fig. 7.7 Estimated IQEs for the *green* LED plotted on **a** linear and **b** log scales for current

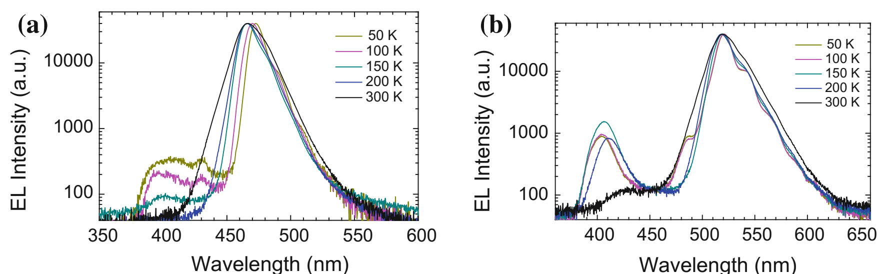

Fig. 7.8 EL spectra at 10 mA for **a** *blue* and **b** *green* LEDs measured at different temperatures. The main peaks are normalized to give the same value

temperature of 50 K, the defects in the QWs causing the nonradiative recombination via the SRH process in the QW active region can almost be ruled out from possible sources of droop. One can also note that the amount of droop at the same current level is much larger for the green LED than for the blue LED.

Figure 7.8a, b show the EL spectra measured at 10 mA under different temperatures for blue and green LEDs, respectively. As the temperature is lowered from 300 K, a side peak is seen to grow at ~400-nm. The side peak is thought to originate from the Mg acceptor level in p-GaN and is caused by the electrons overflowing to the p-GaN cladding layer [71–74]. At the same current level of 10 mA, this side peak at 400-nm is more pronounced for the green LED, indicating severer electron overflow than for the blue LED. Combining these EL spectra with the IQE curves, one can deduce that the severe IQE droop at low temperatures is mostly caused by the overflow of electrons to the p-GaN clad and the nonradiative recombination there.

A question remains as to why the electron overflow becomes severer at lower temperatures. There are two possibilities. One is the carrier-transport-limited droop model in which the electron overflow is originated partly from less carrier capture rate from the bulk region to the QW active region and partly from an increased

carrier asymmetry in electron and hole concentrations in the MQW region. The other is the carrier spillover from the QW active region to the bulk region due to the saturation in the total carrier recombination rate, especially the radiative recombination rate. According to the discussion in the previous section, we think that the growing overflow with decreasing temperature originates from the saturation of the radiative recombination rate at a smaller current and also decreasing nonradiative recombination rate rather than the carrier transport process.

The degree of saturation in the radiative recombination rate increases as the effective active volume or the radiative recombination probability per electron-hole pair becomes small. The effective active volume becomes smaller than the nominal one due to two reasons: First, the QWs in the active region are not fully utilized due to the carrier transport problem caused especially by holes in the conventional LED structure [61–63]. Second, even in a fully utilized QW, the effective volume is smaller than the nominal QW volume as indiums in the QW tend to cluster, making the region with less indium content inefficient in emitting light [29, 38–41, 75].

The fact that the overflow becomes severer at lower temperature can be explained by the first observation. As the hole transport becomes more difficult with lower temperature, combined with a smaller number of activated holes, the number of QWs utilized becomes smaller, reducing the effective active volume. The radiative recombination rate in this reduced effective active volume is eventually saturated at low current (but still high effective current density), and the electrons not recombined in the QW overflow to the p-GaN. As the nonradiative recombination rate becomes smaller at lower temperatures, the tendency of overflow is reinforced. The saturation in the radiative recombination rate is caused fundamentally by the selection rule in *k*-space [8, 29, 76]. In GaN-based LEDs, this saturation can be exacerbated by the piezoelectric field that induces the quantum-confined Stark effect, making the overlap integral of electron and hole wavefunctions smaller.

The fact that the overflow is severer with the green LED than with the blue LED can be explained by the second observation. With higher indium concentration in the green LED, the QW becomes even more inhomogeneous with severer indium clustering, resulting in more reduced effective active volume than in the blue LED. Also, with higher indium concentration in the QW, the piezoelectric field becomes higher, which negatively impacts the radiative recombination rate in the green LED. The hole transport in the green LED can also be negatively affected by deeper potential in the QW and higher hole effective mass with higher indium composition. Consequently, premature saturation in the radiative recombination rate results at a lower current level than with the blue LED. The temperature at which the different IQE behavior starts to appear is also higher with the green LED than with the blue LED. It is important to note here that the overflow becomes severer with decreasing temperature as the radiative recombination rate saturates at lower current due to the reduced effective active volume. In this way, the overflow and the saturation in the radiative recombination rate are interrelated. One can say that the latter dictates the former, especially at low temperature, rather than the other way around. Although the electron overflow is a dominant nonradiative mechanism in this experiment

especially at a low temperature, it should be noted that a dominant nonradiative recombination process can be different with different LED device structures as well as operational conditions.

In summary, by examining the temperature-dependent IQEs and EL spectra of blue and green LEDs, a comprehensive model of efficiency droop phenomena has been explained. As temperature is lowered to the cryogenic region, very severe efficiency droop has been observed in both blue and green LEDs. This severe droop is caused by the saturation of the radiative recombination rate at low current and subsequent increase in the nonradiative recombination rate via the electron overflow as confirmed by the EL spectra. The degree of saturation in the radiative recombination rate increases as the effective carrier density increases due to the decreased effective active volume with the decreasing temperature. It should be noted again that a dominant nonradiative recombination process can vary with operating conditions as well as LED device structure. Figure 7.9 shows a schematic flow chart for the IQE droop model explained so far. We have found from additional works that the shapes of the IQE versus current, i.e. the IQE droop curve, may vary with the dominant nonradiative recombination processes. Table 7.2 explains the relation between them. The concave, linear, and convex shapes in the IQE curves may originate from the electron overflow escaping from the outside QW to the p-side, the electron tunneling from the inside QW to the p-side, and the SRH recombination at the inside QW, respectively. In order to reduce the efficiency droop, one should try to suppress the saturation of the radiative recombination rate and reduce the nonradiative recombination rate. Suppression of the saturation in radiative recombination rate requires increased effective active volume via balanced distribution of electrons and holes in the MQW region, small piezoelectric field, and reduced indium clustering. Insights obtained in this work should shed light on designing a more efficient LED structure with reduced droop.

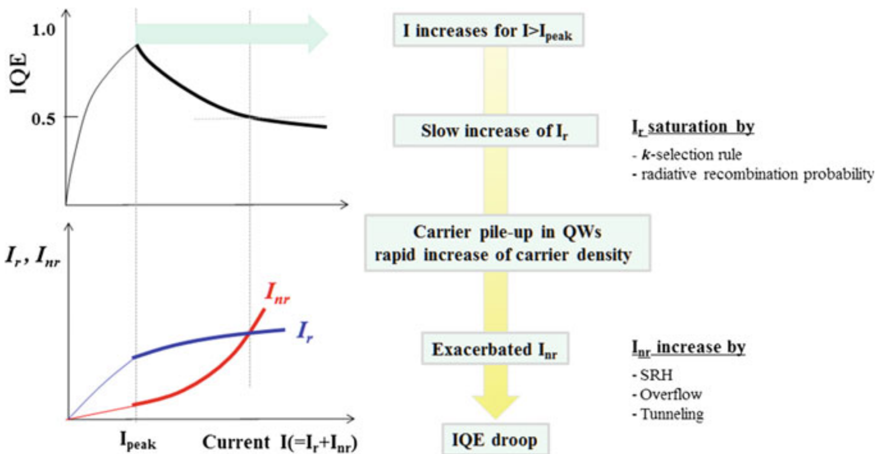

Fig. 7.9 Schematic explanation on the proposed IQE droop model

Table 7.2 Three typical IQE curves of concave, linear, and convex shapes. A dominant nonradiative recombination process may be different for each IQE curve shape as designated below

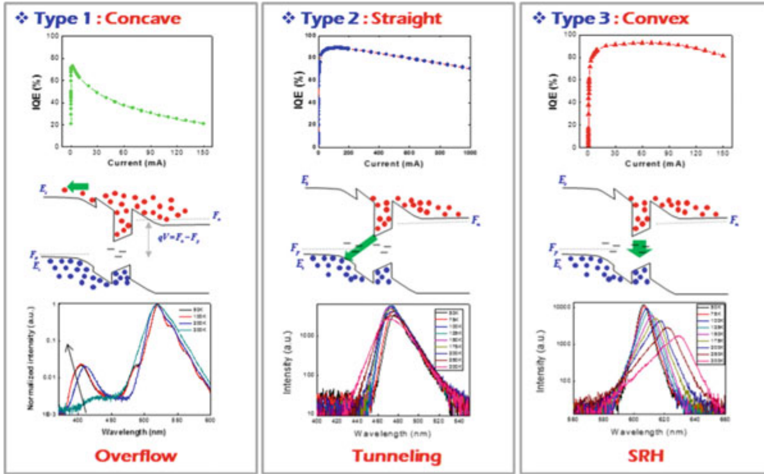

7.3 IQE Measurement Methods

The EQE is one of the fundamental parameters for the LED performance evaluation and is defined by the product of the IQE and the LEE. The EQE can be estimated directly by measuring the optical power emitted from a LED. The EQE depends on the emitting wavelength, and the highest EQE is obtained in the peak wavelength range of 430–460-nm. In recent advanced blue LEDs, EQEs higher than 60% are typically reported and the highest EQE ever reported is 75.5% for a blue LED [77]. Since the EQE can be limited by the IQE or the LEE, it is important to evaluate the IQE and the LEE separately and improve both components individually. The measurement of the LEE is very difficult because the LEE is sensitive to micro- and nanoscale structures embedded in the LED chip itself as well as its package. Different IQE measurement methods have been reported but not fully established yet. The reported IQEs and LEEs have exceeded up to 70–80% in InGaN blue LEDs [77–79].

The discrete and accurate measurement of the IQE in QWs as a function of carrier density is a constant challenge. Different measurement methods of the IQE have been reported in InGaN-based QWs. The IQE measurement methods are typically divided into three categories: (1) absolute intensity measurements by an integrating sphere with theoretically estimated LEEs, (2) analysis of EL characteristics of LEDs or laser diodes (LDs) operating at the steady state or modulated state, and (3) all-optical methods.

Method (1) indirectly measures the IQE by dividing the measured EQE with the known LEE. This method is frequently used due to its simplicity, but some errors can easily occur when estimating the LEE [80–84]. Method (2) is especially suitable for LDs. The IQE above the threshold is easily extracted from a curve of the external differential efficiency versus the cavity length [85]. The IQE below threshold is evaluated by analyzing the light power–current (P-I) curve based on the carrier rate equation where the current injection efficiency and the recombination coefficients are assumed to be certain constants [86]. In LED chips, two types of IQE measurement methods based on the carrier rate equation have been reported. One method is to analyze the P-I curve of a LED chip operating at the steady state, where the radiative recombination coefficient is calculated theoretically by the parabolic band model [15]. Another method is to measure the EL decay time by applying a small current pulse with an extremely fast falling time as a function of bias current level, where both radiative and nonradiative recombination coefficients are thought to be independent of the bias current level [87]. Furthermore, the experimental set-up for measuring decay time in EL requires complicated configurations such as impedance matching, a high-speed pulse generator, and a detector. One of the limitations included in method (2) is that the fundamental physical parameters, such as recombination coefficients, are treated as known or unknown constants with respect to the carrier density in InGaN-based QWs.

Method (3), the all-optical method, is nondestructive and the IQE of the QWs is evaluated on an epitaxial wafer without fabricating actual devices. The most popularly utilized IQE measurement method among these is the continuous-wave (CW) temperature-dependent photoluminescence (TDPL) [88–93]. In this method, the IQE can be directly determined by the ratio of the PL intensity at room temperature to that at a low temperature. An advantage of TDPL is that the IQE can be directly determined experimentally without the aid of any calculations or physical parameter assumptions. However, the TDPL has a bold assumption that the IQE is unity at a low temperature, which has not yet been verified either experimentally or theoretically. Furthermore, we will show that the influence of the optical absorption coefficient on the laser excitation intensity is neglected in the conventional TDPL method. The temperature-dependent time-resolved photoluminescence (TD-TRPL) method is useful because both the temporal and the spectral information are obtained simultaneously [94–100]. The TD-TRPL method can characterize both the IQE and carrier lifetimes at the same time. The conventional TD-TRPL method also has similar assumptions as the TDPL method. Furthermore, it does not have clear definitions of the carrier lifetimes depending on the operational conditions of the steady state and the transient state. Another method for determining the IQEs at room temperature is proposed by fitting the laser pump intensity to powers of the integrated PL intensity [101, 102]. The dependence of the PL intensity on laser pump power is formulated by using photon and carrier rate equations in a semiconductor with the assumption that both the optical absorption coefficient and carrier recombination rate coefficients are independent of the laser pump power. Although this method is useful to the GaAs/AlGaAs system, it has some limitations

in InGaN-based QWs where the aforementioned internal physical coefficients strongly depend on the carrier density in a QW due to the internal electric field.

This section reviews some of the popularly utilized IQE measurement methods such as the constant ABC model, TDPL, and TD-TRPL methods both theoretically and experimentally. A measurement method of the IQE at room temperature based on the intensity-dependent PL, i.e. IDPL method, is presented. The proposed method utilizes the laser excitation power as a varying parameter instead of temperature in the conventional TDPL and the TD-TRPL methods. This new method can evaluate the IQE at any temperature without the aid of any calculated parameters.

7.3.1 Constant ABC Model

Assuming that the electron and hole concentrations in the active QW region are nearly equal to each other, the current, I, and the IQE, η_{IQE}, can be written as

$$I = qV_a\left(AN + BN^2 + CN^3\right) \text{ and } P = \eta_c h\nu V_a\left(BN^2\right) \tag{7.8}$$

$$\eta_{IQE} = \eta_{INJ}\frac{BN^2}{AN + BN^2 + CN^3}, \tag{7.9}$$

where A, B, and C coefficients represent the nonradiative recombination via SRH process, bimolecular radiative recombination, and Auger recombination, respectively. N, I, P, q, $h\nu$, η_{INJ}, η_c, and V_a are carrier density, current, measured optical power, unit elementary charge, photon energy, injection efficiency, and light coupling efficiency between a LED to an optical detector, and the active volume, respectively [36]. With (7.7) and (7.8), it is possible to fit the experimental results of the IQE versus current I using the A, B, and C coefficients as fitting parameters. Generally, people try to fit A and B coefficients in the low current injection regime and C coefficient in high current injection regime. Here, we show an analysis method of the IQE and each recombination current at an arbitrary current. We use the peak point in an experimental IQE versus current curve for analysis of the rate equation. This method requires only one fit parameter among three recombination coefficients, i.e., A, B, and C.

In the relation of the IQE versus the current density in typical LEDs, there exists the maximum value of IQE, η_{max} and the current, I_{max} where η_{max} occurs. η_{max} and $I_{\max}$ can be obtained from the condition, $d\eta/dI = 0$. Then, η_{max} and I_{max} are expressed as follows:

$$\eta_{\max} = \frac{B}{B + 2\sqrt{AC}} \quad I_{\max} = \frac{kA}{C}\left(B + 2\sqrt{AC}\right), \tag{7.10}$$

where $k = qV_a/\eta_{INJ}$. By assuming $\eta_{INJ} = 1$, k is determined directly from the active volume. From (7.10), the A, B, C coefficients are related to each other through η_{max} and I_{max}.

$$B = \frac{4\eta_{\max}k}{I_{\max}(1-\eta_{\max})^2}A^2,\ \ C = \frac{4k^2}{I_{\max}^2(1-\eta_{\max})^2}A^3 \tag{7.11}$$

Therefore, if one of the A, B, C coefficients is known, remaining coefficients can be obtained by using (7.11) with known quantities of η_{max}, I_{max}, and k.

Using (7.7)–(7.9), the IQE, η_{IQE}, at any current I is expressed as

$$\eta_{IQE} = 1 - \frac{(1-\eta_{\max})}{2}\left(1 + \frac{\eta_{IQE}I}{\eta_{\max}I_{\max}}\right)\sqrt{\frac{\eta_{IQE}I_{\max}}{\eta_{\max}I}} \tag{7.12}$$

The IQE versus current relation is determined by solving the above equation. Interestingly, the IQE has no explicit dependence on the A, B, C coefficients, and is unambiguously determined only from the $I_{\max}$ and η_{max} values. Note that $I_{\max}$ is exactly known by the measurement of EQE versus current relation, and η_{max} can be used as a fit parameter and compared with the measurement. Therefore, three fit parameters are reduced to only one in our approach, which makes the fit process much easier and gives accurate results on the IQE analysis of the LED efficiency.

The fitting procedure is as follows: (i) Experimentally measure a relative EQE curve as a function of current I, normalize the experimental EQE curve by the peak EQE value, and find the $I_{\max.}$ (ii) Simulate curves of η_{IQE} versus I for different η_{max} satisfying (7.12). (iii) Select η_{max} that gives the best fit between the experimental and simulated curves from the step (i) and the step (ii), respectively. (iv) Calculate $k = qV_a/\eta_{INJ}$ by assuming η_{INJ} of unity and V_a. Finally, estimate A, B, and C coefficients from (7.4) by assuming one of them, for example A.

From the fitted IQE curve as a function of I, $\eta_{IQE}(I)$, we can calculate each recombination current as

$$\begin{aligned}
I_{SRH} &= \left(\frac{1-\eta_{\max}}{2}\sqrt{\frac{\eta_{IQE}I_{\max}}{\eta_{\max}I}}\right)I = \eta_{SRH}I,\\
I_{SRH} &= \left(\frac{1-\eta_{\max}}{2}\sqrt{\frac{\eta_{IQE}I_{\max}}{\eta_{\max}I}}\right)I = \eta_{SRH}I,\\
I_{Auger} &= \left(\frac{(1-\eta_{\max})}{2}\frac{\eta_{IQE}}{\eta_{\max}}\sqrt{\frac{\eta_{IQE}I}{\eta_{\max}I_{\max}}}\right)I = \eta_{Auger}I.
\end{aligned} \tag{7.13}$$

Again, it is interesting to note that the SRH, radiative, and Auger recombination currents have no explicit dependence on the A, B, C coefficients and that they can be expressed as a function of current from known quantities, $\eta_{\max}$, $I_{\max}$, η_{IQE}, and I. At

sufficiently high current where $I >> I_{max}$, I_{Auger} is much higher than I_{SRH} and the nonradiative current is considered dominated by the Auger recombination current.

However, the fit η_{IQE} from (7.12) often deviates from the experimental IQE curve, η, which is defined as

$$\eta_{IQE} = \eta_{\max} \frac{P/I}{P_{\max}/I_{\max}}, \tag{7.14}$$

where $\eta_{\max}$ is known from the fit of (7.12) and the others, $I_{\max}$, $P_{\max}$, I, and P are experimentally measured. We think that the difference of the experimental IQE, η, in (7.14) and the fitted IQE, η_{IQE}, fitted from (7.12) results from an additional nonradiative recombination current, $I_{leakage}$, for the very high current range. By using (7.13), $I_{leakage}$ is calculated as

$$I_{leakge} = I - \left(\eta_{SRH} + \eta_{IQE} + \eta_{Auger}\right)I \tag{7.15}$$

Now the theoretical analysis of the efficiency droop is compared with experimental efficiency curves. We measured the output power of a commercial-grade LED sample as a function of current at room temperature. The active region of the LED consists of two 2.5-nm thick InGaN QWs with a 10-nm thick GaN barrier. The peak wavelength of the emission spectrum is 460-nm. Figure 7.10 shows an example to estimate the IQE value following the aforementioned procedure. The I_{max} of this sample is 1.66 mA. The theoretical IQE curves obtained by solving (7.12) for different η_{max} are overlaid on the measured result of the EQE curve versus current, and good agreement is observed up to 100 mA when η_{max} is 79%. Using η_{max}, $I_{\max}$, and k of the LED sample, the relation between A and C coefficients can be found from (7.11). Figure 7.10c shows the nonradiative carrier lifetime (τ_{SRH}) that is the inverse of the A coefficient as a function of the C coefficient. Recently reported A coefficient values of InGaN LEDs as shown in Table 7.1 are between 0.5×10^7 and 2×10^8 s^{-1}, which corresponds to τ_{SRH} of 5–100 ns. In Fig. 7.10c, however, when τ_{SRH} lies between 5–200 ns, the corresponding range of the C coefficient is around 10^{-28}–10^{-24} cm^6/s. To date, there are no theories explaining such large C coefficients. Thus, it is plausible that a carrier loss process with the N^3-dependence, which is obvious in InGaN-based QW LEDs, may not represent the Auger processes.

Figure 7.11 shows another example of the normalized EQE curves (solid lines) for different IQE peak values as a parameter and an experimental data (rectangular symbols) from a 460-nm InGaN LED. In this sample, we cannot find a $\eta_{\max}$ value giving a good fit between experimental data and the theoretical line. This result implies that there would be a different nonradiative recombination mechanism at high injection current, which cannot be described by N^3-dependence.

In summary, we have introduced a very simple fitting method based on the constant ABC model in the carrier rate equation. The method utilizes just two parameters of current at the IQE peak and the IQE peak value itself. It is possible to know the IQE and the carrier recombination currents simultaneously without any

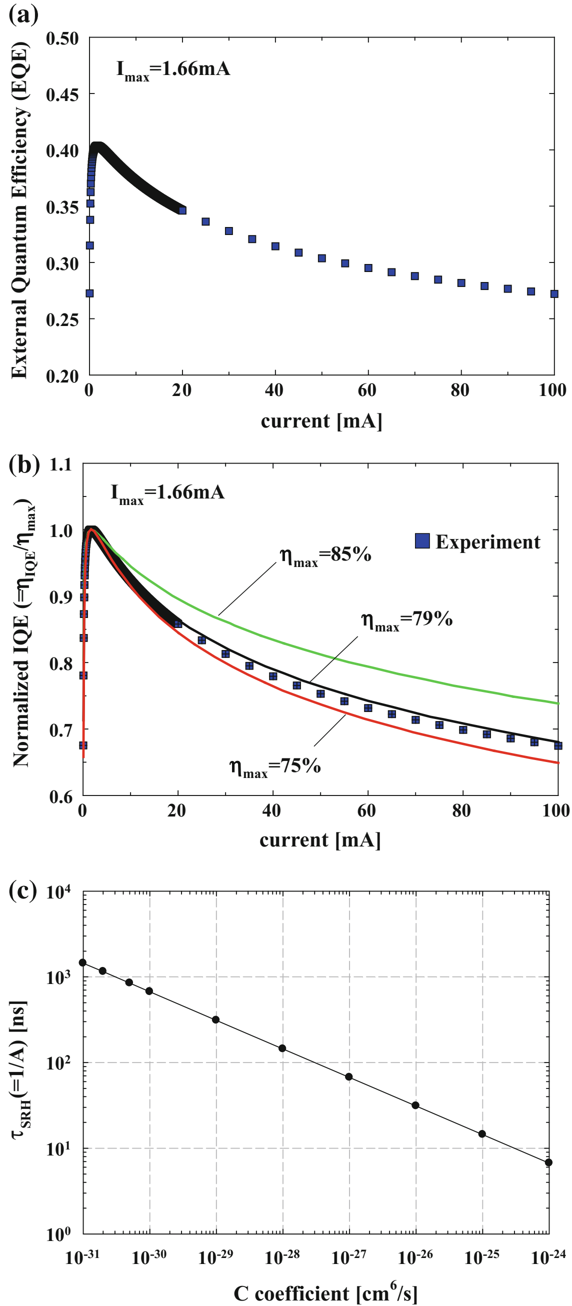

Fig. 7.10 **a** Experimentally measured EQE of a blue LED sample, **b** normalized EQE curves (*solid lines*) for different IQE peak value of η_{max}. Good agreement is found between the theoretical and experimental data at η_{max} = 79%. **c** SRH nonradiative carrier lifetime τ_{SRH} (=1/A) as a function of the C coefficient calculated from (7.11)

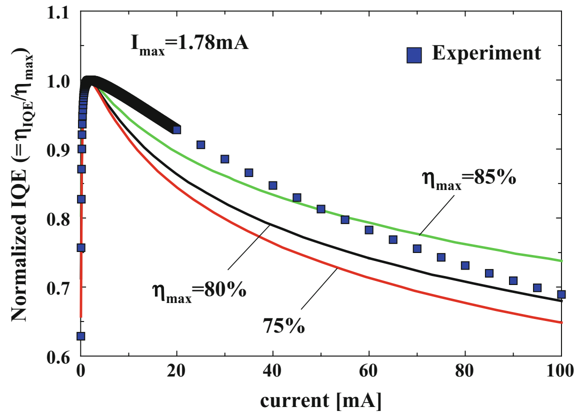

Fig. 7.11 Normalized EQE curves (*solid lines*) and experimental data (*rectangular symbols*) for different IQE peak values as a parameter in an InGaN blue LED emitting at 460-nm

knowledge of A, B, and C recombination coefficients. We applied the method to two different InGaN blue LEDs emitting at 460-nm. In one sample, good agreement was obtained between the experimental and theoretical data. However, the C coefficient was estimated to be a few orders larger than the previously reported Auger coefficients. In the other sample, the experimental data could not be well fitted with the theory. These experimental results imply that the Auger recombination alone could not explain the efficiency droop phenomenon in InGaN LEDs.

7.3.2 *Temperature-Dependent Photoluminescence (TDPL) Method*

Improvements in the luminous efficacy in blue/green LEDs have been hampered by numerous material defects associated with the indium segregation in InGaN QWs. Even though the self-organized small or dot-like indium-rich InGaN regions may improve the radiative efficiency by localizing carriers and preventing carriers from reaching dislocations, those regions may contain many nonradiative defects due to the compositional disorder and strain. The product of the current injection efficiency and the radiative efficiency is the LED IQE. The radiative efficiency is defined as the ratio of the radiative recombination rate to the sum of the radiative and nonradiative recombination rates in the active QWs. PL studies using resonant optical excitation of the active QW are generally used in order to ensure that transport effects can be avoided. Thus, it has been assumed that in the case of resonant excitation, the injection efficiency is perfect as unity and the radiative efficiency in the InGaN active layer is regarded as the IQE. However, as written in Sect. 7.2.5, even in the resonant optical excitation, carrier escape from QWs does take place and shows strong dependence upon the excitation and temperature conditions. Nevertheless, all-optical methods are still useful to investigate physical mechanisms of epitaxial

layers because of their advantages of nondestructive nature and no fitting parameters required between theory and experiment.

One of the popularly utilized methods for determining IQE at room temperature is the continuous-wave TDPL method [88–93]. The integrated PL intensity (I_{PL}) normalized to the excitation laser intensity (I_L), the so-called PL efficiency (η_{PL}), is dependent on both the temperature T and the excitation level I_L. The PL efficiencies are taken for various temperatures and excitation intensity levels. The maximum PL efficiency $\eta_{PL,max}$ is usually found at very low temperature T_l and a certain excitation level $I_{L,max}$. Then, η_{PL} for any temperature T and excitation intensity I_L is normalized by $\eta_{PL,max}$ and the normalized values are considered as the IQE for any T and I_L, i.e.,

$$\eta_{\mathrm{IQE}}(T, I_L)\big|_{TDPL} = \frac{\eta_{PL}(\mathrm{T}, I_L)}{\eta_{\mathrm{PL,\,max}}(T_l, I_{\mathrm{L,\,max}})} \tag{7.16}$$

First, the validity of (7.16) is considered qualitatively. In the conventional TDPL, it is assumed that the IQE is linearly proportional to the PL efficiency so that the maximum PL efficiency denotes the maximum IQE of 100%, i.e., $\eta_{IQE}(T_l, I_{L,max}) = 100\%$. This assumption is usually supported by the following experimental result: The PL efficiency (η_{PL}) for a given excitation laser intensity ($I_{L,c}$) does not change below a certain temperature T_c and drops gradually above it [91, 97, 98]. It is considered that the decrease of the PL intensity for $T > T_c$ results from the increase in density of activated NRCs and that the saturated characteristic of the PL intensity for $T < T_c$ comes from all frozen NRCs. In fact, however, some epitaxial wafers show that the PL efficiency varies with the excitation laser intensity even for $T < T_c$. If the nonradiative recombination processes are zero at a low temperature, then the PL efficiency should be constant regardless of the excitation level. This observation implies that nonradiative recombination processes may not be negligible even at extremely low temperatures and certain excitation powers. Moreover, the conventional TDPL method does not give any clear IQE difference at room temperature between the epitaxial wafers for green and blue LEDs. This is because $\eta_{IQE}(T_l, I_{L,max})$ is assumed as 100% in all material systems. But it is well recognized that the crystal quality of InGaN-based QWs decreases with increasing indium composition (or emission wavelength). Combining the facts quoted above, we need a method to estimate the IQE without the assumption of $\eta_{IQE}(T_l, I_{L,max}) = 100\%$.

Now the conventional TDPL method is reviewed theoretically based on the carrier rate equation. Assuming that the carrier concentration generated by optical pumping is small and that they recombine at the generated layer without escape, the rate equation of the carrier density $N(t)$ in the active QW under weak excitation condition is written as

$$\frac{dN}{dt} = -\left(AN + BN^2\right) + (1 - R)\frac{\alpha I_L}{h\nu_L} \tag{7.17}$$

where A is the nonradiative recombination coefficient through the SRH recombination process and B is the radiative recombination rate coefficient. R, α, $h\nu_L$, and I_L are the reflectivity of the semiconductor surface, the absorption coefficient in the QWs, the photon energy, and the excitation intensity of an excitation laser, respectively [99]. At the steady state $(dN/dt = 0)$, (7.16) can be rewritten as

$$\frac{I_L}{h\nu_L} = \frac{AN + BN^2}{(1 - R)\alpha} \tag{7.18}$$

The integrated PL intensity (I_{PL}) detected by a photodetector over the wavelengths is given by

$$\frac{\mathrm{I_{PL}}}{\mathrm{h}\bar{\nu}} = \left(\eta_{\mathrm{det}}\eta_{\mathrm{LEE}}\frac{V_a}{\mathrm{A_{det}}}\right)\mathrm{BN}^2 = \eta_{\mathrm{c}}\mathrm{BN}^2 \tag{7.19}$$

where η_{det}, η_{LEE}, $h\bar{\nu}$, V_a, and $\mathrm{A_{det}}$ are the detector coupling efficiency, the light extraction efficiency, the average photon energy, the active volume, and the detector area, respectively, and $\eta_{\mathrm{c}} = \eta_{\mathrm{det}}\eta_{\mathrm{LEE}}(V_a/\mathrm{A_{det}})$. The PL efficiency ($\eta_{PL}$) is defined as the ratio of the radiative photon rate to the excitation laser photon rate, i.e.,

$$\eta_{PL} = \frac{\mathrm{I_{PL}}/\mathrm{h}\bar{\nu}}{I_L/h\nu_L} = \eta_{\mathrm{c}}(1 - \mathrm{R})\alpha\frac{\mathrm{BN}^2}{\mathrm{AN} + \mathrm{BN}^2} = K_{PL}\alpha\eta_{\mathrm{IQE}} \tag{7.20}$$

where $K_{PL} = \eta_{\mathrm{c}}(1 - \mathrm{R})$. The PL efficiency expressed by (7.20) is understandable because the spontaneously radiated light power will increase with the number of photons absorbed in the QWs and also with the number of radiatively recombining carriers at a certain excitation intensity.

The IQE can be also represented by using the carrier lifetimes at the steady state as

$$\eta_{\mathrm{IQE}} = \frac{\mathrm{BN}^2}{\mathrm{AN} + \mathrm{BN}^2} = \frac{N/\tau_r}{N/\tau_{nr} + N/\tau_r} \tag{7.21}$$

τ_r and τ_{nr} are the radiative and nonradiative carrier lifetimes, respectively. The carrier lifetimes of τ_r and τ_{nr} are related to the recombination coefficients of A and B by

$$\tau_r = \frac{1}{BN} \text{ and } \tau_{nr} = \frac{1}{A} \quad (7.22)$$

The carrier lifetimes at the steady state are different from those at the transient state, as in TRPL experiments. An explicit relation between the IQE in (7.21) and the IQE based on the conventional TDPL method in (7.16) is expressed as

$$\eta_{IQE}(T_h, I_L) = \left[\eta_{IQE}(T_l, I_{L,\max}) \frac{\alpha(T_l, I_{L,\max})}{\alpha(\mathrm{T}_h, I_L)}\right] \eta_{IQE}(T_h, I_L)\big|_{TDPL} \quad (7.23)$$

Equation (7.23) shows that two conditions should be satisfied simultaneously in order to recognize the IQE measured by the conventional TDPL as a real IQE: (i) IQE at a low temperature and a certain excitation intensity, i.e., $\eta_{IQE}(T_l, I_L)$, is equal to 100%, i.e., $\eta_{IQE}(T_l, I_L) = 100\%$ and (ii) the optical absorption coefficient α is completely independent of the excitation intensity and temperature.

Figure 7.12 shows an example of the relative η_{PL} normalized by the maximum value at 8 K [89]. The sample used in this study was a near-UV InGaN MQW LED emitting at 406-nm grown on a sapphire substrate. The PL efficiency at 8 K or 300 K increases with an increasing excitation intensity at low excitation levels and shows the peak value at a certain excitation intensity denoted by $I_{L,max}$. Then, it decreases with further increasing the excitation intensity at high excitation levels. The reasons for these behaviors have not been clearly known, but it is thought that the dominant nonradiative recombination mechanism in both sides of the excitation levels may be different. At 8 K, the carrier escape from the excited layer via tunneling and spillover mechanisms can be considered as possible dominant non-radiative recombination mechanisms at low and high excitation levels around $I_{L,max}$, respectively. Anyway, it is reasonable to choose the peak efficiency among all investigated conditions of temperature and excitation level as 100% in the TDPL method. However, this bold assumption of the peak PL efficiency as 100% for

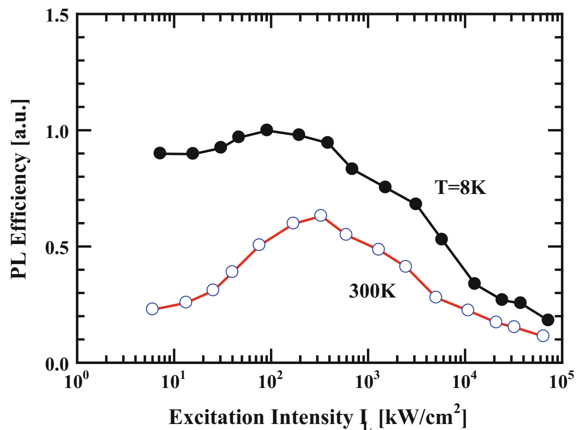

Fig. 7.12 PL efficiencies as a function of excitation intensity, measured at 300 and 8 K

samples without showing the saturation characteristics in low excitation intensity and temperature could result in an overestimated PL efficiency at room temperature. Therefore, we need a method to estimate the PL efficiency just at room temperature without comparing the PL efficiency at low temperature.

7.3.3 Intensity-Dependent Photoluminescence (IDPL) Method

In this section, we propose a method to estimate the PL efficiency at room temperature only by utilizing relative PL efficiency data as a function of excitation power. In InGaN-based QWs grown on a sapphire substrate along the c-axis, there exist strong internal electric fields due to the piezoelectric and spontaneous polarizations even without an external bias. The internal electric field reduces as the carrier density increases due to the carrier screening of polarizations by the increasing excitation intensity I_L. Thus, the PL efficiency is determined by several physical parameters such the absorption coefficient α, the SRH nonradiative recombination coefficient A, the radiative recombination coefficient B, and the carrier density N, and eventually the IQE η_{IQE}. We suppose that there is a weak excitation intensity of $I_{L,o}$. In this situation, carriers in the active layer are nondegenerate and the nonradiative loss due to N^3-dependency is negligible. Moreover, the electron energy band does not vary with the carrier density due to enough carrier screening of the internal electric fields. As a consequence, the coefficients of α, A, and B can be considered as constants of α_o, A_o, and B_o, respectively, for a small change of the excitation intensity around $I_{L,o}$.

Our method starts with finding the $I_{L,o}$ based on the carrier rate equation at a certain temperature. We first measure the PL intensity as a function of excitation intensity (i.e., the IDPL experiment). Then, a specific excitation intensity of $I_{L,o}$ is found by utilizing two successive excitation intensities of $I_{L,n}$ and $I_{L,n+1}$, where n represents the *nth* data point and $I_{L,n} < I_{L,n+1}$. In the excitation range between $I_{L,n}$ and $I_{L,n+1}$ with assumed constants of α_0, B_0, and A_0, the following equations are obtained from (7.19) and (7.20):

$$A_o + s\sqrt{I_{PL,n}} = m\frac{I_{L,n}}{\sqrt{I_{PL,n}}} \text{ and } A_o + s\sqrt{I_{PL,n+1}} = m\frac{I_{L,n+1}}{\sqrt{I_{PL,n+1}}} \tag{7.24}$$

$$B_o N_n = s\sqrt{I_{PL,n}} \text{ and } B_o N_{n+1} = s\sqrt{I_{PL,n+1}} \tag{7.25}$$

$$A_o = \chi s \tag{7.26}$$

$$\chi = \sqrt{I_{PL,n}}\left(\frac{I_{PL,n+1}}{I_{PL,n}} - \frac{I_{L,n+1}}{I_{L,n}}\right) \Big/ \left(\frac{I_{L,n+1}}{I_{L,n}} - \sqrt{\frac{I_{PL,n+1}}{I_{PL,n}}}\right) \tag{7.27}$$

where $s = \sqrt{B_o/h\bar{\nu}\eta_c}$ and $m = (1-R)\alpha_o\sqrt{h\bar{\nu}\eta_c B_o}/h\nu_l$. $N_{o,n}$ and $N_{o,n+1}$ are carrier densities in a QW for $I_{L,n}$ and $I_{L,n+1}$, respectively. Equation (7.27) shows the condition for finding an excitation intensity of $I_{L,n} = I_{L,o}$ where variations of A_0 and s become zero.

$$\left.\frac{\Delta\chi}{\Delta I_L}\right|_{I_{L,n}=I_{L,o}} = 0 \tag{7.28}$$

Equation (7.28) shows that if a laser intensity of I_{Ln} is found where χ shows a peak value as χ_n, then I_{Ln} corresponds to the laser intensity giving minimum variations of the internal physical parameters (α_0, B_0, and A_0) with laser intensity. In general, χ has a concave shape as a function of I_L.

Then, the IQE at I_{Ln} is obtained as

$$\eta_{IQE,n} = \frac{B_o N_n}{A_o + B_o N_n} = \frac{\sqrt{I_{PL,n}}}{\sqrt{I_{PL,n}} + \chi_n} = \frac{1}{1+\gamma_n} \tag{7.29}$$

where

$$\gamma_n = \frac{\chi_n}{\sqrt{I_{PL,n}}} = \left(\frac{I_{PL,n+1}}{I_{PL,n}} - \frac{I_{L,n+1}}{I_{L,n}}\right) / \left(\frac{I_{L,n+1}}{I_{L,n}} - \sqrt{\frac{I_{PL,n+1}}{I_{PL,n}}}\right) \tag{7.30}$$

It is noticeable that the IQE at I_{Ln} is only determined by the ratios of $I_{L,n}/I_{L,n+1}$ and $I_{PL,n}/I_{PL,n+1}$ without using any assumed values of α, B, and A. Thus, this method generates small errors when determining the IQE compared to previous methods.

The IQE $\eta_{IQE,i\neq n}$ at any excitation intensity $I_{L,i(i=1,2,\ldots)}$ can be found by using a known $\eta_{IQE,i=n}$ in (7.29). The IQE $\eta_{IQE,i\neq n}$ at $I_{L,i(i=1,2,\ldots)}$ is expressed from (7.21) as

$$\eta_{IQE,i} = \left.\frac{BN^2}{AN + BN^2}\right|_{I_{L,i}} = \frac{K_\eta}{\alpha_i}\frac{I_{PL,i}}{I_{L,i}}, \text{ where } K_\eta = \frac{h\nu_L}{(1-R)h\bar{\nu}\eta_c} \tag{7.31}$$

In (7.31), i stands for the ith excitation intensity used in the experiment, α_i is the optical absorption coefficient at $I_{L,i}$, and K_η is a constant. We can eliminate K_η by dividing $\eta_{IQE,i}$ by $\eta_{IQE,n}$ and express $\eta_{IQE,i}$ by using experimentally measurable data as follows:

$$\eta_{IQE,i} = \frac{\alpha_n}{\alpha_i}\eta_{PL,i}\eta_{IQE,n}, \text{ where } \eta_{PL,i} = \frac{I_{PL,i}/I_{L,i}}{I_{PL,n}/I_{L,n}} \tag{7.32}$$

At a given temperature, the optical absorption coefficient α is a function of the excitation intensityI_L. Therefore, it is not easy to estimate the ratio of α_n/α_i in

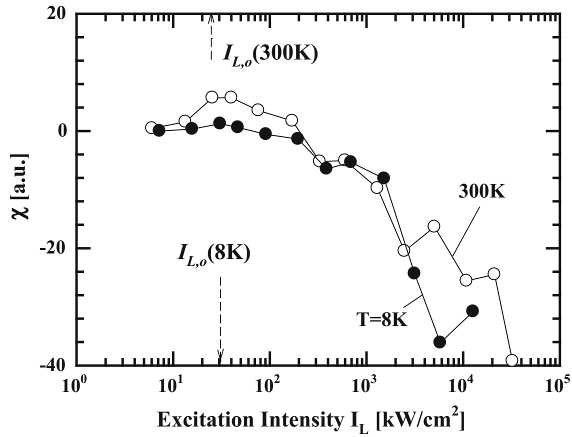

Fig. 7.13 Calculated $\chi's$ as a function of excitation intensity I_L for PL efficiencies in Fig. 7.12. It is assumed that electron energy bands in InGaN QWs become flat at the excitation intensity of $I_{L,o}$ due to the carrier screening of the internal electric field

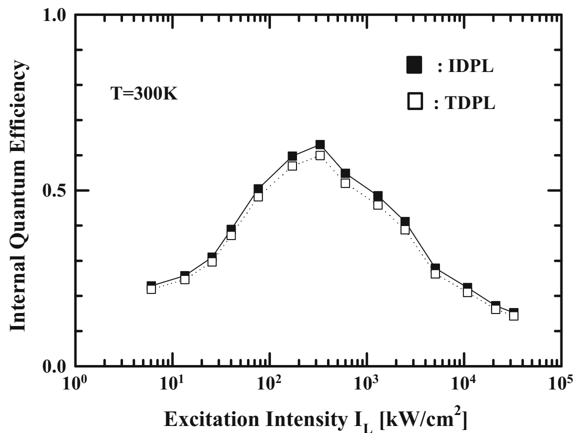

Fig. 7.14 IQEs at room temperature estimated by the conventional TDPL method in Sect. 7.3.2 and the IDPL method in Sect. 7.3.3. Both methods show almost identical IQE values for this sample

(7.32). At this moment, it is assumed that the optical absorption coefficient α_i is the same as α_n.

Figure 7.13 shows the calculated $\chi's$ from (7.27) for the PL efficiency at room temperature plotted in Fig. 7.12. The maximum χ value is obtained at the excitation intensity of 30 kW/cm^2 which corresponds to $I_{L,n}$ at room temperature. In general, χ has a concave shape as shown in Fig. 7.13. From (7.29), the IQEs at $I_{L,n}$ for 300 K and 10 K are found to be 34.4% and 56.6%, respectively. Figure 7.14 shows the IQE values estimated by the proposed IDPL and the conventional TDPL methods at room temperature. Both methods show almost identical IQE values at room temperature. The dependency of the PL efficiency indicates that the measured sample does not have a 100% IQE at 8 K. The maximum IQE at 8 K is estimated as 83% by the IDPL. In addition to the IDPL method being able to measure the absolute IQE at any temperature, it has advantages that can minimize errors

resulting from experimental conditions that the integrated PL intensity as a function of excitation intensity at room temperature and their relative ratios are used.

7.3.4 Temperature-Dependent Time-Resolved Photoluminescence (TD-TRPL) Method

The TD-TRPL method is frequently utilized in order to estimate the IQE and the radiative and nonradiative carrier lifetimes simultaneously [90–96]. The short radiative lifetime and long nonradiative lifetime in LEDs are desirable for a reduced carrier density in QWs, high-power operations, and good reliability. The TD-TRPL method utilizes a sort of short pulse train as a photoexcitation source, whose single pulse width is about a few hundred femtoseconds and the pulse period is long enough to measure the single pulse response safely without intersymbol interferences. It also measures temporal and spectral responses with a monochromator and a high-speed detector such as a streak camera, respectively.

A transient TRPL response integrated over wavelengths is generally well fitted by the sum of two exponential functions with fast and slow decay times as

$$I(t) = I_o(T)\left\{\exp\left(-\frac{t}{\tau_{TRPL}(T)}\right) + C_{slow}\exp\left(-\frac{t}{\tau_{slow}(T)}\right)\right\} \tag{7.33}$$

where C_{slow} is a constant. $\tau_{TRPL}(T)$ and $\tau_{slow}(T)$ are the fast and slow decay times of luminescence at the beginning and ending of the PL decay curve, respectively. They are usually a function of temperature T (in K) as well as the excitation laser intensity I_L (in W/m^2). This two-exponential characteristic is due to the co-existence of different types of carriers, including free carriers, free excitons, and bound excitons. It has been explained that the fast decay time is a result of the free carrier recombination in the blue side of the spectrum and under a higher density of excitons. The slow decay time comes from free excitons in the spectral position and bound excitons localized by impurity, an alloy, or well width fluctuations in the red side of the spectrum [97–101]. Therefore, each carrier lifetime is represented by the sum of different recombination processes depending on temperature and the excitation conditions. In this work, the carrier dynamics are expected in the high carrier density regime, corresponding to the normal LED or LD operation conditions, especially at room temperature. Therefore, we are only concerned with the fast component for our purpose.

With the single exponential approximation of (7.32), the luminescence decay $I(t)$ is expressed as

$$I(t) = I_{o,eff}(T)\exp\left(-\frac{t}{\tau_{TRPL}(T)}\right) \tag{7.34}$$

where $I_{o,eff}(T)$ is an effective PL intensity integrated over entire wavelengths and is obtained by integrating both sides of (7.34) with respect to time.

$$I_{o,eff}(T) = \frac{\int_0^{\infty} I(t)dt}{\tau_{TRPL}(T) + C_{slow}\tau_{slow}(T)} \tag{7.35}$$

One of the most important steps in the TD-TRPL method is to discriminate the radiative and nonradiative decay times at room temperature. The inverse of $\tau_{TRPL}(T)$ is described by the sum of two components,

$$\frac{1}{\tau_{TRPL}(T)} = \frac{1}{\tau_{r,PL}(T)} + \frac{1}{\tau_{nr,PL}(T)} \tag{7.36}$$

where $\tau_{r,PL}(T)$ and $\tau_{nr,PL}(T)$ are the PL decay times due to the radiative and nonradiative carrier recombination processes, respectively. A relationship between the measured temporal TRPL response and the $\tau_{TRPL}(T)$ is obtained by

$$I_n(T) = \int_0^{\infty} \frac{I(t)}{I_{o,eff}} dt = \tau_{TRPL}(T) = \frac{\tau_{r,PL}(T)\tau_{nr,PL}(T)}{\tau_{r,PL}(T) + \tau_{nr,PL}(T)} \tag{7.37}$$

In some experimental cases, the normalized TRPL intensity $I_n(T)$ defined in (7.37) does not change below a certain temperature T_c and drops gradually at temperatures above T_c. Similar to the TDPL method, it is assumed that nonradiative recombination is completely negligible and the IQE is unity in this temperature range, i.e., $T < T_c$. This means that the normalized intensity at low temperature T_l $(T_l < T_c)$ is approximately equal to the radiative lifetime $\tau_{r(d)}(T_l)$, i.e.,

$$I_n(T_l) \approx \tau_{r,PL}(T_l) \tag{7.38}$$

If the radiative lifetime is independent of temperature, the expression of the IQE at a high temperature $T_h(T_h > T_c)$ can be obtained from (7.23), (7.37), and (7.38):

$$\eta_{IQE}(T_h) = \frac{\tau_{nr,PL}(T_h)}{\tau_{r,PL}(T_h) + \tau_{nr,PL}(T_h)} \approx \left[\frac{\tau_{r,PL}(T_h)\tau_{nr,PL}(T_h)}{\tau_{r,PL}(T_h) + \tau_{nr,PL}(T_h)}\right] / \tau_{r,PL}(T_l) = \frac{I_n(T_h)}{I_n(T_l)} \tag{7.39}$$

The radiative and nonradiative lifetimes at room temperature are obtained by

$$\tau_{r,PL}(T_h) = \frac{\tau_{TRPL}(T_h)}{\eta_{IQE}(T_h)} = \tau_{TRPL}(T_h)\frac{I_n(T_l)}{I_n(T_h)} \tag{7.40}$$

$$\tau_{nr,PL}(T_h) = \frac{\tau_{TRPL}(T_h)}{1 - \eta_{IQE}(T_h)} = \tau_{TRPL}(T_h)\frac{I_n(T_l)}{I_n(T_l) - I_n(T_l)} \tag{7.41}$$

Hence, from the measurement of the intensity $I_n(T)$ and lifetime $\tau_{PL}(T_h)$ with respect to T, radiative and nonradiative lifetimes are derived as a function of T.

We have reviewed the conventional TD-TRPL method, which characterizes the IQE and the radiative and nonradiative carrier lifetimes simultaneously. This method uses numerous assumptions: (i) the zero nonradiative recombination rate and 100% IQE at a low enough temperature, (ii) the excitation intensity is not dependent on carrier lifetimes or the IQE, (iii) the radiative lifetime is invariant with temperature, and (iv) there are no clear relationships between the PL decay times and the carrier recombination lifetimes through the radiative and nonradiative carrier recombination processes. Assumptions (i) and (ii) are investigated in Sect. 7.3.2, and the results show that the IQE cannot be considered as unity and is usually dependent on the excitation intensity. Moreover, the dominant radiative recombination process in InGaN-based QWs changes with both excitation condition and temperature. The radiative carrier lifetime calculated from (7.39) usually shows a large dependency on temperature since the IQE depends on temperature [97–99]. Therefore, the internal parameters of the QWs should be carefully estimated in the TD-TRPL experiment.

7.3.5 Room Temperature Time-Resolved Photoluminescence (RT-TRPL) Method

This section proposes a simple method to estimate the IQE and carrier lifetimes at room temperature. The method is based on room temperature TRPL (RT-TRPL) measurement and the analysis of the carrier rate equation depending on the laser excitation intensity. Immediately after the illumination of an extremely short laser pulse of less than a few hundred femtoseconds in a QW structure, electrons and holes are photoexcited on the conduction band and valence band, respectively. These excited carriers quickly relax in the electron momentum and energy spaces through many scattering processes within a few tenths of picoseconds. They are distributed into the mostly stable states known as the quasi-Fermi distributions. Then, redistributed carriers start to recombine with each other in the range of a few nanoseconds to a hundred nanoseconds and lose their energies radiatively and nonradiatively.

A schematic of the TRPL experiment is shown in Fig. 7.15. At the beginning of the temporal response in the TRPL method, $t = 0+$, electrons and holes generated in a QW by a single femtosecond laser pulse will already be in the quasi-equilibrium state. This situation can be considered as a pump light source of a certain laser optical power, i.e., P_{pump}, in the CW PL method as shown in Fig. 7.15a. Also, the density of free carriers in the conduction band can be assumed as initially pumped to the steady state N_0 by P_{pump} and begins its recombination process just after the pulse has been turned off ($t = 0+$) as shown in Fig. 7.15b. Here, P_{pump} is assumed to be sufficiently high so that the recombination of free

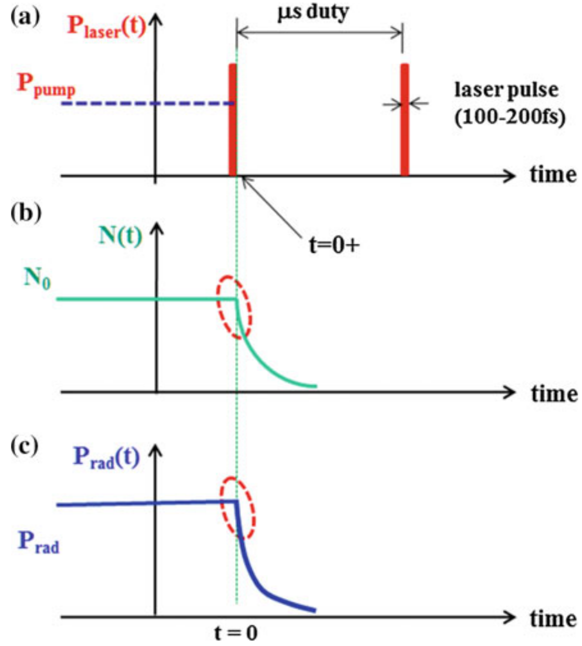

Fig. 7.15 Illustration of the TRPL experiment. **a** Modified optical pump beam power, **b** carrier density generated by modified optical pump beam power P_{pump}, and **c** detected light emission by radiative recombination of free carriers

excitons can be ignored. Since the spontaneous light emission from LEDs shown in Fig. 7.15c is proportional to the radiative recombination, the detected amount of light power $P_{PL}(t)$ is given by

$$P_{\mathrm{TRPL}}(t) = (\mathrm{h}\bar{\nu}\eta_{\mathrm{det}}\eta_{\mathrm{LEE}}V_a)\mathrm{BN}^2(t) \tag{7.42}$$

where $\mathrm{h}\bar{\nu}$, η_{det}, η_{LEE}, and V_a are the averaged photon energy, the detector coupling efficiency, the light extraction efficiency, and the active volume, respectively.

In this model [67, 102], the carrier rate equation at room temperature with a negligible Auger coefficient C in the QW active layer is written as

$$\frac{dN}{dt} = 0 = -\left(AN_o + BN_o^2\right) + (1-R)\frac{\alpha P_{pump}}{h\nu_L A_L} \text{ for } t \le 0 \tag{7.43}$$

$$\frac{dN}{dt} = -\left(AN + BN^2\right) \text{ where } \frac{1}{\tau} = \frac{1}{\tau_{nr}} + \frac{1}{\tau_r} = A + BN \text{ for } t > 0 \tag{7.44}$$

where R, α, P_{pump}, $h\nu_L$, and $A_L$are the reflectivity on the semiconductor surface, the absorption coefficient in QWs, time-averaged power of the excitation source, the photon energy of the excitation source, and the net illuminated area at surface of the LED, respectively. The subscript 'o' represents the steady state. τ is total carrier lifetime which can be separated into nonradiative recombination carrier lifetime (τ_{nr}) and radiative recombination carrier lifetime (τ_r). We consider for all t as an

approximation that the nonradiative recombination coefficient A, the radiative recombination coefficient B, and the optical absorption coefficient α as constants regardless of the carrier density $N(t)$.

For $t > 0$, the carrier rate equation is written as

$$\frac{d(\Delta N)}{dt} = -(AN_0 + BN_0^2) - (A + 2BN_0)\Delta N - B(\Delta N)^2 \text{ with } N(t) = N_0 + \Delta N(t) \tag{7.45}$$

N_0 is the carrier density for t < 0 and $\Delta N(t)$ represents the time-dependent variation of the carrier density for $t > 0$. Then, the temporal responses of the carrier density $N(t)$ in (7.45) is obtained analytically with the boundary conditions of $N(t=0) = N_o$ and $N(t=\infty) = 0$ as

$$N(t) = \frac{A}{B}\frac{\eta_{IQE(0)}e^{-At}}{1-\eta_{IQE(0)}e^{-At}} \text{ where } \eta_{IQE(0)} = \frac{BN_0^2}{AN_0 + BN_0^2} \tag{7.46}$$

The nonradiative lifetime is at the steady state and $\tau_{nr} = 1/A$ as defined in (7.44). Then, the detected light power can be calculated from (7.42) and (7.46). For simplicity, a temporal response of the integrated PL intensity is normalized by the peak intensity at $t = 0$, i.e., $P_{TRPL}(t=0)$, and is given by

$$P_{nor}(t) = \frac{P_{TRPL}(t)}{P_{TRPL}(0)} = \left(\frac{A}{BN_0}\right)^2 \frac{\eta_{IQE(0)}^2 \mathrm{e}^{-2At}}{\left(1-\eta_{IQE(0)}\mathrm{e}^{-At}\right)^2} \tag{7.47}$$

$P_{nor}(t)$ is a more complicated function than the single exponential function with respect to time for constant carrier recombination coefficients. It can be approximated as a single exponential function at the initial and final stages as follows:

$$P_{nor}(t) \approx e^{-t/\tau_{TRPL,\,initial}} \text{ as } t \to 0 \tag{7.48}$$

$$P_{nor}(t) \approx \left(\frac{A}{A + BN_0}\right)^2 e^{-t/\tau_{TRPL,final}} \text{ as } t \to \infty \tag{7.49}$$

In (7.48) and (7.49), each lifetimes are given as follows:

$$\frac{1}{\tau_{TRPL,\,initial}} = 2(A + BN_0) = 2\left(\frac{1}{\tau_{nr}} + \frac{1}{\tau_r}\right) \tag{7.50}$$

$$\frac{1}{\tau_{TRPL,final}} \approx 2A = \frac{2}{\tau_{nr}} \tag{7.51}$$

Note that at $t = 0+$, $\tau_{TRPL,initial}$ is one half of the carrier lifetime τ defined in (7.44). On the other hand, for the case of the final stage of the TRPL response ($t >> \tau_{TRPL,initial}$), $\tau_{TRPL,final}$ can be approximately given in terms of the nonradiative recombination coefficient only. The nonradiative carrier lifetime τ_{nr} is two times of the carrier lifetime of the final stage of the TRPL response ($\tau_{TRPL,final}$). Equations (7.50) and (7.51) mean that both the radiative and nonradiative recombination processes determine the lifetime of the TRPL response at the initial stage, whereas the nonradiative recombination process mainly determines the lifetime at the final stage. This can be understood as both radiative and nonradiative recombination processes competing with each other at the initial stage of the PL decay when the radiated power is high. Then, as time has progressed to the final stage of the PL decay, most of the radiative recombination process has taken place and the PL decay curve is mainly governed by the nonradiative recombination lifetime.

From (7.50) and (7.51), the IQE at t = 0 and the radiative recombination carrier lifetime (τ_r) can be obtained directly from measured $\tau_{TRPL,initial}$ and $\tau_{TRPL,final}$ by

$$\eta_{IQE(0)} = \frac{\tau_{TRPL,final} - \tau_{TRPL,initial}}{\tau_{TRPL,final}} \tag{7.52}$$

$$\frac{1}{\tau_r} = \frac{1}{2}\left(\frac{1}{\tau_{TRPL,initial}} - \frac{1}{\tau_{TRPL,final}}\right) \tag{7.53}$$

$$\tau_{nr} \approx 2\tau_{TRPL,final} \tag{7.54}$$

Thus, one can find the IQE, radiative recombination carrier lifetime (τ_r), and nonradiative recombination carrier lifetime (τ_{nr}) simultaneously by just one measurement of the TRPL response at room temperature.

We applied the proposed method to a vertical blue LED chip with a size of 1 mm × 1 mm. The sample was excited by the Hamamatsu PLP-10, which has an operation pulse width less than 100 ps and a repetition rate up to 100 MHz. The excitation power of the PLP-10 was varied by neutral density filters from 0.04 to 0.16 mW. The value of $P_{TRPL}(t)$ was measured by a Hamamatsu C4780 Picosecond Fluorescence Lifetime Measurement System with a temporal resolution of 5 ps. $P_{TRPL}(t)$ of each excitation power was measured at every 20 ps until the maximum number of photons counted reached 1000 (inset of Fig. 7.16). In our experimental set-up, an averaged noise level was less than 0.3% of the maximum $P_{TRPL}(t)$. After subtracting the background noise, results were normalized to the peak values and they were numerically fitted with a combination of exponential functions and then drawn on a natural logarithmic scale, as shown in Fig. 7.16. In the figure, there is a time range during which $P_{TRPL}(t)$ decays linearly, which means that the response itself can be approximated by a single exponential function with a decay time constant of $\tau_{TRPL,initial}$or $\tau_{TRPL,final}$ on a linear scale. As shown in the figure, generally the fitting range of TRPL lifetimes for $\tau_{TRPL,final}$ is much wider than that of $\tau_{TRPL,initial}$, which indicates a smaller estimating error of τ_{nr} compared to that of τ_r.

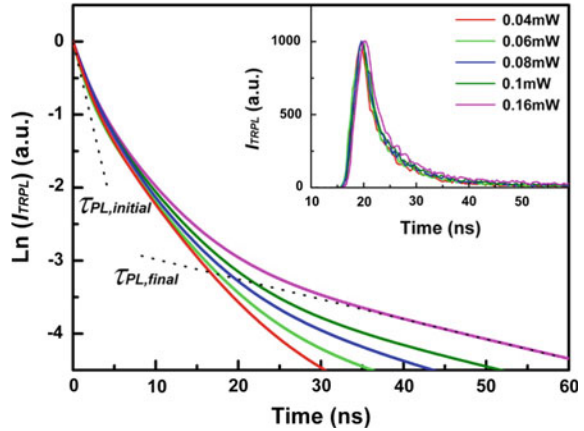

Fig. 7.16 Fitted results of the measured excitation power-dependent TRPL data shown in the inset. Examples of $\tau_{TRPL,final}$ and $\tau_{TRPL,initial}$ are also shown

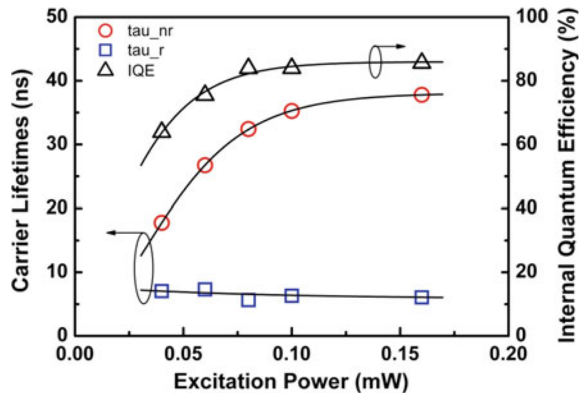

Fig. 7.17 Estimated τ_{nr}, τ_r, and the IQE as a function of excitation power. *Solid lines* are drawn to guide the eyes

The estimated results are summarized in Fig. 7.17. Here, τ_{nr} was calculated by using (7.54). $\tau_{TRPL,final}$ was estimated at the intensity range between −3.5 and −4 in the y-axis of Fig. 7.16 corresponding to 3–1% of the peak intensity. The results show that τ_{nr} gradually increase with increasing the excitation power P_{pump} up to 0.1 mW. It seems clear that τ_{nr} becomes independent for $P_{pump} > 0.1$ mW. This implies that the nonradiative recombination processes may be different for P_{pump} below and above 0.1 mW. We suppose that there are two defect-related nonradiative recombination processes in a LED chip. The first is the carrier loss via the tunneling transport from the QW active to the p-side as shown in Fig. 7.2. This defect-related tunneling process is easily saturated by increasing carrier density, which explains an increasing τ_{nr} for $P_{pump} < 0.1$ mW. The other is carrier loss via the SRH recombination inside the QWs. It is a well-known fact that the nonradiative carrier lifetime via the SRH recombination is hardly changed by the carrier density. This is the case for $P_{pump} > 0.1$ mW were τ_{nr} is almost constant over a wide range of excitation powers. On the other hand, $\tau_{PL,initial}$ was determined from

0 to −0.2, where the TRPL intensity decays to ~80% of its peak intensity. The results show that the measured τ_r slightly decreases with increasing excitation power. This is due to the fact that the carrier density increases with the excitation power and τ_r is inversely proportional to the carrier density.

The TD-TRPL measurement on a commercial LED sample was carried out as the temperature changed from 30 to 300 K using a closed-cycle helium cryostat. It is well known that the PL efficiency is sensitive to the temperature, *T*, because the nonradiative recombination processes are a function of temperature, i.e., τ_{nr} (T). This means that $\tau_{TRPL,final}$ in our model should be dependent on temperature. In Fig. 7.18a, the fitted results of the normalized TD-TRPL measurements are depicted using a natural logarithmic scale. They clearly show that the linear decay in the last stage of $P_{TRPL}(t)$ increases as temperature increases. This indicates that τ_{nr} is decreasing as the temperature increases. $\tau_{TRPL,final}$ is estimated from Fig. 7.18a and τ_{nr} is obtained from (7.54) and plotted in Fig. 7.18b. The largest τ_{nr} is observed at 75 K. Since τ_{nr} is inversely proportional to the PL efficiency, we tried to compare τ_{nr} to the TRPL intensity by integrating the TRPL response from its peak to −4 on the y-axis of Fig. 7.18a. Relatively measured TRPL efficiency as a

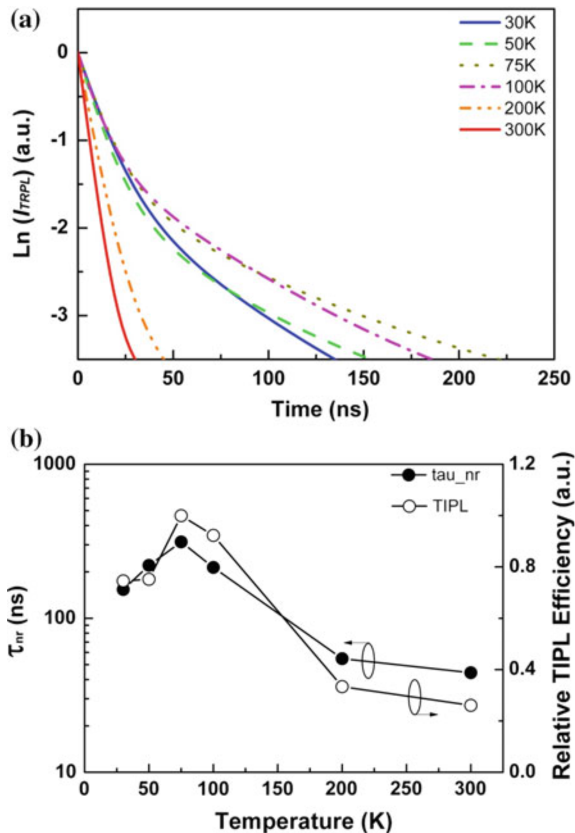

Fig. 7.18 **a** Fitted results of the normalized TRPL responses at different temperatures and **b** comparison of the estimated τ_{nr} from the TRPL (*left* y-axis, *filled circles*) and the time-integrated photoluminescence (TIPL) efficiency (*right* y-axis, *open circles*)

function of temperature is shown as open circles in Fig. 7.18b as well. Both curves in Fig. 7.18b show very similar tendency with temperature, which supports our analysis result that $\tau_{TRPL,final}$ is a measure of τ_{nr}.

Next, we show another application of our model. We also prepared four blue LED chips emitting with slightly different EL efficiencies from the same wafer. Thus, they have the same device size and active layer structure but different defect levels, i.e., the nonradiative recombination rates. Figure 7.19a shows the relative EL efficiency as a function of injected current at room temperature. The current at the peak EL efficiency, $I_{\eta\text{max}}$, is quite different from each chip. This indicates that each sample has a different defect density. It is known that $I_{\eta\text{max}}$ becomes high as the nonradiative recombination rate increases in case of same physical dimensions. The estimated $I_{\eta\text{max}}$ and τ_{nr} for each sample are shown in Fig. 7.19b. The figure indicates that the sample with a smaller τ_{nr} requires larger $I_{\eta\text{max}}$ of the peak EL efficiency peak. This shows quite consistent results between the proposed TRPL and the EL characteristics. The proposed TRPL analysis method can be utilized to understand the carrier dynamics in semiconductors more easily.

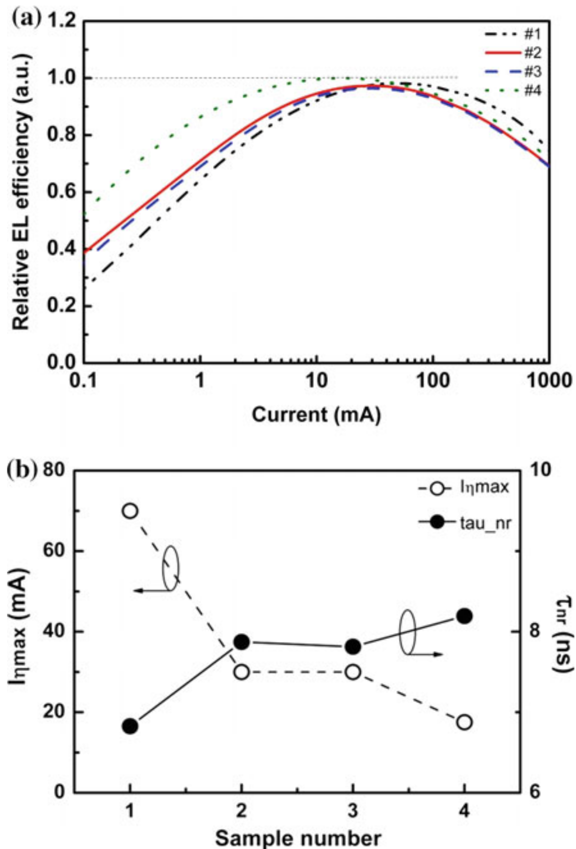

Fig. 7.19 **a** Measured relative EL efficiency curves at room temperature for four different blue LED chips and **b** the correlation between the injected current level to achieve the maximum EL efficiency (*left* y-axis, *open circles*) and the estimated τ_{nr} (*right* y-axis, *filled circles*) from the TRPL measurement for each sample

7.4 Conclusion

We have summarized the definitions of various LED efficiencies, i.e., the wall-plug efficiency ($\eta_{wall\text{-}plug}$), the voltage efficiency (η_{VTG}), the injection efficiency (η_{ING}), the radiative efficiency (η_{RAD}), the light extraction efficiency (η_{LEE}), the internal quantum efficiency (η_{IQE}), and the external quantum efficiency (η_{EQE}). Among these efficiencies, the IQE is the most important but its characteristics as well as measuring methods have not been clearly known yet. We have first introduced experimental results of the IQE droop depending on temperature and current. Then, the IQE droop mechanisms ever reported have been reviewed. Up to now, none of the popular droop model is able to explain all the experimental droop phenomena consistently. Auger and defect-related processes consider additional increase in the nonradiative recombination process inside the QW active region as well as sufficient carrier capture rates into the QW active region. On the other hand, carrier-transport-related models suspect additional increase in the nonradiative recombination outside the QW active region like the p-side and insufficient carrier capture rate into the QW active region. However, all these models focus on faster increases in the nonradiative recombination without taking into account the possible mechanisms of slower increase in the radiative recombination rate.

We have also investigated and compared the temperature dependences of the PL efficiency, the open-circuit voltage, and the EL efficiency as functions of operating temperature and excitation power. Through comparative studies, we have suggested that the inherent origin of the efficiency droop is the saturation of the radiative recombination rate in the InGaN QW at low current and subsequent increase in the nonradiative recombination rates at high current. The degree of saturation is determined by operating temperature and effective active volume. Although the saturation of the radiative recombination rate is common origin of the IQE droop, the shapes of the IQE versus current, i.e. the IQE droop curve, vary with the dominant nonradiative recombination process.

We have reviewed the IQE measurement methods both theoretically and experimentally. We have introduced a very simple fitting method based on the constant ABC model in the carrier rate equation. The method utilizes just two parameters of current at the IQE peak and the IQE peak value itself. It is possible to know the IQE and the carrier recombination current simultaneously without any knowledge of A, B, and C recombination coefficients. This method is very useful to extract the recombination coefficients with very small errors from the measured curve of current versus optical power.

Then, the IQE measurement methods have been reviewed by focusing on all-optical methods such as the temperature-dependent photoluminescence (TDPL) and the temperature-dependent time-resolved photoluminescence (TD-TRPL) methods. The assumptions used in the TDPL and TD-TRPL methods have been theoretically examined by using the carrier rate equation in semiconductors.

Another method based on the intensity-dependent PL, i.e. IDPL, has also been presented and demonstrated experimentally. This method utilizes the laser excitation power as a varying parameter instead of the temperature in the conventional TDPL and TD-TRPL methods and is able to evaluate the IQE at any temperature without the aid of any calculated parameters.

We have also developed a theory of carrier dynamics from the TRPL measurement just at room temperature and found a simple and effective method to obtain the carrier lifetimes and the IQEs. The meanings of the measured TRPL response curves have been verified rigorously by solving the carrier rate equation in the QW active layer. It has been shown that the radiative and nonradiative recombination processes compete with each other at the initial stage of the TRPL and is gradually dominated by the nonradiative recombination at the final stage. The proposed method can be regarded as a very unique and efficient tool for measuring the nonradiative recombination carrier lifetime without the tediously long measurements. The method also avoids the temperature dependencies of carrier lifetimes. We hope that this article is helpful for better understanding of the carrier dynamics in semiconductors and further improvements in optoelectronic device performances.

References

1. E. Fred Schubert, *Light-Emitting Diodes* (Cambridge University Press, New York, 2010)
2. Y. Yang, X.A. Cao, C.H. Yan, Appl. Phys. Lett. **94**, 041117 (2009)
3. X.A. Cao, A. Teetsova, F. Shahedipour-Sandvikb, S.D. Arthura, J. Cryst. Growth **264**, 172 (2004)
4. B. Monemar, B.E. Sernelius, Appl. Phys. Lett. **91**, 181103 (2007)
5. S. Choi, H.J. Kim, S.-S. Kim, J. Liu, J. Kim, J.-H. Ryou, R.D. Dupuis, A.M. Fischer, F.A. Ponce, Appl. Phys. Lett. **96**, 221105 (2010)
6. J. Yun, D.-P. Han, J.-I. Shim, D.-S. Shin, IEEE Trans. Electron. Device **59**, 1799 (2012)
7. S. Hwang and J.-I. Shim: IEEE Trans. Electron. Device 55 (2008) 1123
8. G.P. Agrawal, N.K. Dutta, *Semiconductor Lasers*, 2nd edn. (Van Norstrand Reinhold, New York, 1993)
9. I. Schnitzer, E. Yablonovitch, C. Caneau, T.J. Gmitter, A. Scherer, Appl. Phys. Lett. **63**, 2174 (1993)
10. A.I. Zhmakin, Phys. Rep. **498**, 189 (2011)
11. M. Peter, A. Laubsch, W. Bergbauer, T. Meyer, M. Sabathil, J. Baur, B. Hahn, Phys. Status Solidi A **206**, 1125 (2009)
12. A. Laubsch, M. Sabathil, W. Bergbauer, M. Strassburg, H. Lugauer, M. Peter, S. Lutgen, N. Linder, K. Streubel, J. Hader, J.V. Moloney, B. Pasenow, S.W. Koch, Phys. Status Solidi C **6**, 913 (2009)
13. A. Laubsch, M. Sabathil, J. Baur, M. Peter, B. Hahn, IEEE Trans. Electron. Device **57**, 79 (2010)
14. J. Hader, J.V. Moloney, B. Pasenow, S.W. Koch, M. Sabathil, N. Linder, S. Lutgen, Appl. Phys. Lett. **92**, 261103 (2008)
15. A.A. Efremov, N.I. Bochkareva, R.I. Gorbunov, D.A. Lavrinovich, Y.T. Rebane, D.V. Tarkhin, Y.G. Shreter, Semiconductors **40**, 605 (2006)

16. M.-H. Kim, M.F. Schubert, Q. Dai, J.K. Kim, E.F. Schubert, J. Piprek, Y. Park, Appl. Phys. Lett. **91**, 183507 (2007)
17. K. Fujiwara, H. Jimi, K. Kaneda, Phys. Status Solidi C **6**, 814 (2009)
18. X. Li, X. Ni, J. Lee, M. Wu, U. Özgür, H. Morkoç, T. Paskova, G. Mulholland, K.R. Evans, Appl. Phys. Lett. **95**, 121107 (2009)
19. Y.-D. Lin, A. Chakraborty, S. Brinkley, H.C. Kuo, T. Melo, K. Fujito, J.S. Speck, S. P. DenBaars, S. Nakamura, Appl. Phys. Lett. **94**, 261108 (2009)
20. S.-P. Chang, T.-C. Lu, L.-F. Zhuo, C.-Y. Jang, D.-W. Lin, H.-C. Yang, H.-C. Kuo, S.-C. Wang, J. Electrochem. Soc. **157**, 501 (2010)
21. N.F. Gardner, G.O. Müller, Y.C. Shen, G. Chen, S. Watanabe, W. Götz, M.R. Krames, Appl. Phys. Lett. **91**, 243506 (2007)
22. Y. Yang, X.A. Cao, C.H. Yan, Phys. Status Solidi A **206**, 195 (2009)
23. J. Xie, X. Ni, Q. Fan, R. Shimada, U. Özgür, H. Morkoç, Appl. Phys. Lett. **93**, 121107 (2008)
24. S. Hwang, W. Jin Ha, J. Kyu Kim, J. Xu, J. Cho, E. Fred Schubert, Appl. Phys. Lett. **99**, 181115 (2011)
25. D.S. Meyaard, G.B. Lin, Q. Shan, J. Cho, E. Fred Schubert, H. Shim, M.H. Kim, C. Sone, Appl. Phys. Lett. **99**, 251115 (2011)
26. J. Hader, J.V. Moloney, S.W. Koch, Appl. Phys. Lett. **96**, 221106 (2010)
27. K.T. Delaney, P. Rinke, C.G. Van de Walle, Appl. Phys. Lett. **94**, 191109 (2009)
28. B. Pasenow, S.W. Koch, J. Hader, J.V. Moloney, M. Sabathil, N. Linder, S. Lutgen, Phys. Status Solidi C **6**, 864 (2009)
29. J.-I. Shim, D.-S. Shin, H.-S. Kim, H.-Y. Ryu, J. Korean Phys. Soc. **58**, 503 (2011)
30. D.-S. Shin, D.-P. Han, J.-Y. Oh, J.-I. Shim, Appl. Phys. Lett. **100**, 153506 (2012)
31. F. Bertazzi, M. Goano, E. Bellotti, Appl. Phys. Lett. **97**, 231118 (2010)
32. J. Piprek, Phys. Status Solidi A **207**, 2217 (2010)
33. S.Y. Karpov, Proc. SPIE **7939**, 79391 (2011)
34. M.H. Crawford, IEEE J. Sel. Topics Quantum Electron. **15**, 1028 (2009)
35. D. Saguatti, L. Bidinelli, G. Verzellesi, M. Meneghini, G. Meneghesso, E. Zanoni, R. Butendeich, B. Hahn, IEEE Trans. Electron. Device **59**, 1402 (2012)
36. H.-Y. Ryu, H.-S. Kim, J.-I. Shim, Appl. Phys. Lett. **95**, 081114 (2009)
37. Q. Dai, Q. Shan, J. Wang, S. Chhajed, J. Cho, E.F. Schubert, M.H. Crawford, D.D. Koleske, M.-H. Kim, Y. Park, Appl. Phys. Lett. **97**, 133507 (2010)
38. S.F. Chichibu, A. Uedono, T. Onuma, B.A. Haskell, A. Chakraborty, T. Koyama, P.T. Fini, S. Keller, S.P. DenBaars, J.S. Speck, U.K. Mishra, S. Nakamura, S. Yamaguchi, S. Kamiyama, H. Amano, I. Akasaki, J. Han, T. Sota, Nat. Mater. **5**, 810 (2006)
39. S.F. Chichibu, T. Sota, K. Wada, O. Brandt, K.H. Ploog, S.P. DenBaars, S. Nakamura, Phys. Status Solidi A **183**, 91 (2001)
40. K. Okamoto, A. Scherer, Y. Kawakami, Appl. Phys. Lett. **87**, 161104 (2005)
41. A. Kaneta, K. Okamoto, Y. Kawakami, S. Fujita, G. Marutsuki, Y. Narukawa, T. Mukai, Appl. Phys. Lett. **81**, 4353 (2002)
42. U. Özgur, H. Liu, X. Li, X. Ni, H. Morkoç, Proc. IEEE **98**, 1180 (2010)
43. M.F. Schubert, S. Chhajed, J.K. Kim, E.F. Schubert, D.D. Koleske, M.H. Crawford, S.R. Lee, A.J. Fischer, G. Thaler, M.A. Banas, Appl. Phys. Lett. **91**, 231114 (2007)
44. M.F. Schubert, J. Xu, J.K. Kim, E.F. Schubert, M.H. Kim, S. Yoon, S.M. Lee, C. Sone, T. Sakong, Y. Park, Appl. Phys. Lett. **93**, 041102 (2008)
45. J. Xu, M.F. Schubert, A.N. Noemaun, D. Zhu, J.K. Kim, E.F. Schubert, M.H. Kim, H. J. Chung, S. Yoon, C. Sone, Y. Park, Appl. Phys. Lett. **94**, 011113 (2009)
46. J. Lee, X. Li, X. Ni, U. Özgür, H. Morkoç, T. Paskova, G. Mulholland, K.R. Evans, Appl. Phys. Lett. **95**, 201113 (2009)
47. C.H. Wang, C.C. Ke, C.Y. Lee, S.P. Chang, W.T. Chang, J.C. Li, Z.Y. Li, H.C. Yang, H.C. Kuo, T.C. Lu, S.C. Wang, Appl. Phys. Lett. **97**, 261103 (2010)
48. Y.Y. Kudryk, A.V. Zinovchuk, Semicond. Sci. Technol. **26**, 095007 (2011)

49. Y.-K. Kuo, M.-C. Tsai, S.-H. Yen, Ta.-C. Hsu, Y.-J. Shen, IEEE J. Quantum Electron. **46**, 1214 (2010)
50. R.-M. Lin, M.-J. Lai, L.-B. Chang, C.-H. Huang, Appl. Phys. Lett. **97**, 181108 (2010)
51. C.-L. Chao, R. Xuan, H.-H. Yen, C.-H. Chiu, Y.-H. Fang, Z.-Y. Li, B.-C. Chen, C.-C. Lin, C.-H. Chiu, Y.-D. Guo, H.-C. Kuo, J.-F. Chen, S.-J. Cheng, IEEE Photo. Technol. Lett. **23**, 798 (2011)
52. C.H. Wang, S.P. Chang, W.T. Chang, J.C. Li, Y.S. Lu, Z.Y. Li, H.C. Yang, H.C. Kuo, T.C. Lu, S.C. Wang, Appl. Phys. Lett. **97**, 181101 (2010)
53. S. Tanaka, Y. Zhao, I. Koslow, C.-C. Pan, H.-T. Chen, J. Sonoda, S.P. DenBaars, S. Nakamura, IEE Electron. Lett. **47**, 339 (2011)
54. Y.-J. Lee, C.-H. Chen, C.-J. Lee, IEEE Photon. Technol. Lett. **22**, 1506 (2010)
55. Y.-L. Li, Y.-R. Huang, Y.-H. Lai, IEEE J. Sel. Topics Quantum Electron. **15**, 1128 (2009)
56. X. Ni, X. Li, J. Lee, S. Liu, V. Avrutin, Ü. Özgür, H. Morkoç, A. Matulionis, T. Paskova, G. Mulholland, K.R. Evans, Appl. Phys. Lett. **97**, 031110 (2010)
57. Y.B. Tao, S.Y. Wang, Z.Z. Chen, Z. Gong, E.Y. Xie, Y.J. Chen, Y.F. Zhang, J. McKendry, D. Massoubre, E.D. Gu, B.R. Rae, R.K. Henderson, G.Y. Zhang, Phys. Status Solidi C **9**, 616 (2012)
58. J.-I. Shim, D.-P. Han, H. Kim, D.-S. Shin, G.-B. Lin, D.S. Meyaard, Q. Shan, J. Cho, E. Fred Schubert, H. Shim, C. Sone, Appl. Phys. Lett. **100**, 111106 (2012)
59. D.L. Huffaker, D.G. Deppe, Appl. Phys. Lett. **73**, 520 (1998)
60. A. Hori, D. Yasunaga, A. Satake, K. Fujiwara, J. Appl. Phys. **93**, 3152 (2003)
61. J.P. Liu, J.-H. Ryou, R.D. Dupuis, J. Han, G.D. Shen, Appl. Phys. Lett. **93**, 021102 (2008)
62. K. Ding, Y.P. Zeng, X.C. Wei, Z.C. Li, J.X. Wang, H.X. Lu, P.P. Cong, X.Y. Yi, G.H. Wang, J.M. Li, Appl. Phys. B **97**, 465 (2009)
63. H.-Y. Ryu, J.-I. Shim, C.-H. Kim, J.H. Choi, H.M. Jung, M.-S. Noh, J.-M. Lee, E.-S. Nam. IEEE Photonics Technol. Lett. **23**, 1866 (2011)
64. S. Hammersley, D. Watson-Parris, P. Dawson, M.J. Godfrey, T.J. Badcock, J. Appl. Phys. **111**, 083512 (2012)
65. J.-W. Shi, C.-W. Lin, M.L. Lee, J.-K. Sheu, IEEE Photon. Technol. Lett. **23**, 1585 (2011)
66. A. David, M.J. Grundmann, Appl. Phys. Lett. **96**, 103504 (2010)
67. H. Kim, D.-P. Han, J.-Y. Oh, J.-I. Shim, J. Korean Phys. Soc. **60**, 1934 (2012)
68. G. Tamulaitis, J. Mickevičius, D. Dobrovolskas, E. Kuokštis, M.S. Shur, M. Shatalov, J. Yang, R. Gaska, Phys. Status Solidi C **9**, 1677 (2012)
69. M. F. Schubert, J. Xu, Qi Dai, F.W. Mont, J.K. Kim, E. Fred Schubert, Appl. Phys. Lett. **94**, 081114 (2009)
70. S. Chhajed, J. Cho, E. Fred Schubert, J.K. Kim, D.D. Koleske, M.H. Crawford, Phys. Status Solidi A **208**, 947 (2011)
71. T.S. Jeong, C.J. Youn, M.S. Han, J.W. Yang, K.Y. Lim, J. Cryst. Growth **259**, 267 (2003)
72. M. lIegems, R. Dingle, J. Appl. Phys. **44**, 4234 (1973)
73. I. Akasaki, H. Amano, M. Kito, K. Hiramatsu, J. Lumin. **4**(8, 49), 666 (1991)
74. E. Oh, H. Park, Y. Park, Appl. Phys. Lett. **72**, 70 (1998)
75. G.H. Gu, C.G. Park, K.B. Nam, Phys. Status Solidi RRL **3**, 100 (2009)
76. P.G. Eliseev, M. Osin'ski, H. Li, I.V. Akimova, Appl. Phys. Lett. **75**, 3838 (1999)
77. T. Miyoshi, T. Yanamoto, T. Kozaki, S.-I. Nagahama, Y. Narukawa, M. Sano, T. Yamada, T. Mukai, Proc. SPIE 689414 (2008)
78. G. Chen, M. Craven, A. Kim, A. Munkholm, S. Watanabe, M. Camras, W. Götz, F. Steranka, Phys. Status Solidi A **205**, 1086 (2008)
79. Y. Narukawa, J. Narita, T. Sakamoto, T. Yamada, H. Narimatsu, M. Sano, T. Mukai, Phys. Status Solidi A **204**, 2087 (2007)
80. T. Fleck, M. Schmidt, C. Klingshirn, Phys. Status Solidi A **198**, 248 (2003)
81. H. Gauck, T.H. Gfroerer, M.J. Renn, E.A. Cornell, K.A. Bertness, Appl. Phys. A **64**, 143 (1997)
82. I. Schnitzer, E. Yablonovitch, C. Caneau, T.J. Gmitter, Appl. Phys. Lett. **62**, 131 (1993)

83. V. Zabelin, D.A. Zakheim, S.A. Gurevich, IEEE J. Quantum Electron. **40**, 1675 (2004)
84. R. Windisch, C. Rooman, B. Dutta, A. Knobloch, G. Borghs, G.H. Döhler, P. Heremans, IEEE J. Sel. Topics Quantum Electron. **8**, 248 (2002)
85. S. Nakamura, M. Senoh, S. Nagahama, N. Iwasa, T. Yamada, Appl. Phys. Lett. **69**, 1568 (1996)
86. H.Y. Ryu, K.H. Ha, J.H. Chae, K.S. Kim, J.K. Son, Appl. Phys. Lett. **89**, 171106 (2006)
87. S. Saito, T. Narita, K. Zaima, K. Tachibana, H. Nago, G.-I. Hatakoshi, S. Nunoue, Phys. Status Solidi C **5**, 2195 (2008)
88. J.K. Son, S.N. Lee, H.S. Paek, T. Sakong, K.H. Ha, O.H. Nam, Y. Park, Phys. Status Solidi C **4**, 2780 (2007)
89. S. Watanabe, N. Yamada, M. Nagashima, Y. Ueki, C. Sasaki, Appl. Phys. Lett. **83**, 4906 (2003)
90. C. Netzel, R. Doloca, S. Lahmann, U. Rossow, A. Hangleiter: Phys. Status Solidi C **0**, 324 (2002)
91. C. Netzel, S. Heppel, F. Hitzel, S. Miller, A. Weimar, G. Brüderl, H.J. Lugauer, A. Lell, V. Härle, A. Hangleiter, Status Solidi C **0**, 2304 (2003)
92. M.S. Minsky, S. Watanabe, N. Yamada, J. Appl. Phys. **91**, 5176 (2002)
93. J.S. Hwang, A. Gokarna, Y.-H. Cho, J.K. Son, S.N. Lee, Appl. Phys. Lett. **90**, 131908 (2007)
94. J.S. Hwang, A. Gokarna, Y.-H. Cho, J.K. Son, S.N. Lee, J. Appl. Phys. **102**, 013508 (2007)
95. Y.J. Ding, C.L. Guo, J.B. Khurgin, K.K. Law, J.L. Merz, Appl. Phys. Lett. **60**, 2051 (1992)
96. A. Reale, G. Massari, A.D. Carlo, P. Lugli, A. Vinattieri, J. Appl. Phys. **93**, 400 (2003)
97. C.-K. Sun, S. Keller, T.-L. Chiu, G. Wang, M.S. Minsky, J.E. Bowers, S.P. DenBaars, IEEE J. Sel. Topics Quantum Electron. **3**, 731 (1997)
98. R. Olshansky, C.B. Su, J. Manning, W. Powazinik, IEEE J. Quantum Electron. **20**, 838 (1984)
99. Y. Kawakami, Z.G. Peng, Y. Narukawa, S. Fujita, S. Fujita, Appl. Phys. Lett. **69**, 1414 (1996)
100. M.-Y. Ryu, C.Q. Chen, E. Kuokstis, J.W. Yang, G. Simin, Appl. Phys. Lett. **80**, 3943 (2002)
101. X.A. Cao, E.B. Stokes, P.M. Sandvik, S.F. LeBoeuf, J. Kretchmer, D. Walker, IEEE Electron Device Lett. **23**, 535 (2002)
102. H. Kim, D.-S. Shin, H.-Y. Ryu, J.-I. Shim, Jpn. J. Appl. Phys. **49**, 112402 (2010)
103. M. Zhang, P. Bhattacharya, J. Singh, J. Hinckley, Appl. Phys. Lett. **95**, 201108 (2009)
104. M. Meneghini, N. Trivellin, G. Meneghesso, E. Zanoni, U. Zehnder, B. Hahn, J. Appl. Phys. **106**, 114508 (2009)

Chapter 8
III-Nitride Tunnel Junctions and Their Applications

S. Rajan and T. Takeuchi

Abstract Interband tunneling in semiconductors [1, 2] is one of the clearest manifestations of quantum mechanics in electronic devices. In the case of interband tunneling in a heavily doped PN junction, in reverse bias, electrons tunnel from the filled states in the valence band to the empty states in the conduction band. Under forward bias, tunneling current is observed when electrons tunnel from filled states in the conduction band to empty states in the valence band, as shown in Fig. 8.1. As the conduction band on the n-side becomes biased higher in energy than the valence band, states are not available for electrons to tunnel into. As a result, the current decreases, leading to a characteristic *negative differential resistance* regime.

8.1 Introduction and Motivation

Interband tunneling in semiconductors [1, 2] is one of the clearest manifestations of quantum mechanics in electronic devices. In the case of interband tunneling in a heavily doped PN junction, in reverse bias, electrons tunnel from the filled states in the valence band to the empty states in the conduction band. Under forward bias, tunneling current is observed when electrons tunnel from filled states in the conduction band to empty states in the valence band, as shown in Fig. 8.1. As the conduction band on the n-side becomes biased higher in energy than the valence band, states are not available for electrons to tunnel into. As a result, the current decreases, leading to a characteristic *negative differential resistance* regime.

Tunneling currents in devices are strongly dependent on the energy gap or height of the barrier, and the width of the barrier. For a general tunneling barrier, the tunneling current can be written as

S. Rajan (✉)
The Ohio State University, Columbus, USA
e-mail: rajan.21@osu.edu

T. Takeuchi
Meijo University, Nagoya, Japan
e-mail: take@meijo-u.ac.jp

© Springer Nature Singapore Pte Ltd. 2017

T.-Y. Seong et al. (eds.), *III-Nitride Based Light Emitting Diodes and Applications*,
Topics in Applied Physics 133, DOI 10.1007/978-981-10-3755-9_8

$$J_T = q \int_0^{qV_r} dE_z \int_{-\infty}^{\infty} dE_t \left(f_n^p(E_z+E_t)\rho^p(E_z+E_t) - f_n^n(E_z+E_t)\rho^n(E_z+E_t) \right) \sqrt{\frac{2E_z}{m_z}} T(E_z)$$

where E_z and E_t are the kinetic energy components of the electron on the n-side along and perpendicular to the tunnel direction, $v_z = \sqrt{\frac{2E_z}{m_z}}$ is the tunnel velocity. f_n^p and f_n^n are the Fermi–Dirac distributions of electrons, ρ^p and ρ^n are the density of states (superscripts p and n regions on either side of the TJ). $T(E_z)$ is the tunnel probability calculated by WKB approximation. The interband tunnel barrier is assigned as half-electron barrier and half-hole barrier to account for electron-hole duality during the calculation of interband tunneling probability [3].

The tunneling probability depends strongly on the energy barrier and depletion width, both of which depend on the energy gap. As a result, as a function of band gap, tunneling probability, and tunneling currents are expected to decreases significantly. As the doping density is increased, the depletion barrier decreases, and so tunneling probability is expected to increase as the doping density is increased. Wide band gap GaN and AlGaN have relatively large band gaps compared to conventional semiconductors, such as Si, GaAs, InGaAs, and Ge, and therefore, the tunneling probability is relatively low for PN junctions unless they are doped extremely heavily [4].

However, there are several devices that could benefit greatly from the availability of efficient tunnel junctions. Conventional LEDs today are fabricated using either

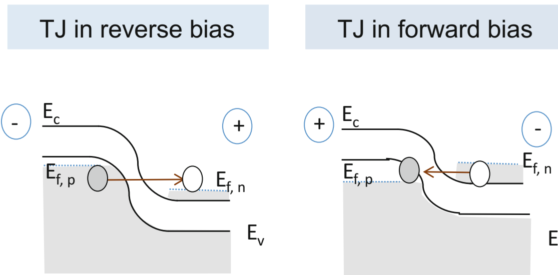

Fig. 8.1 Schematic of tunnel junctions showing transport in the reverse and forward bias

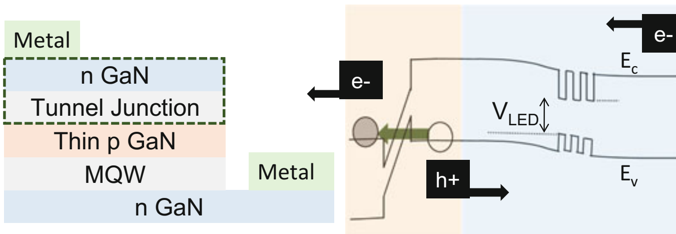

Fig. 8.2 Schematic epitaxial structure and energy band diagram of a TJ-based LED

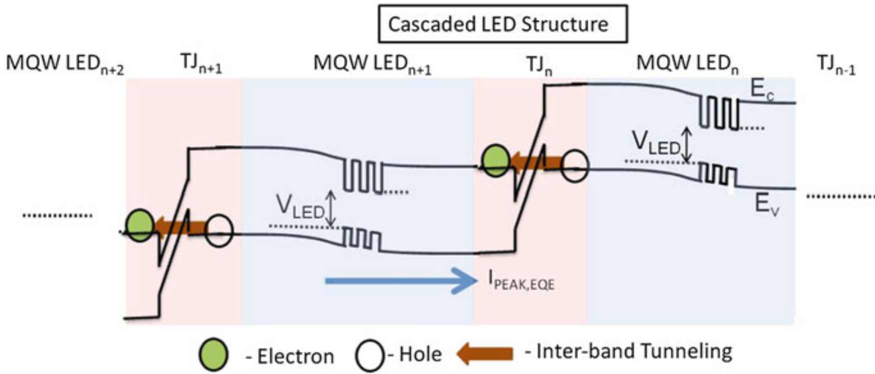

Fig. 8.3 Schematic epitaxial structure and energy band diagram of a multi-junction LED

ITO contacts for the top p-GaN layer, or using a flip-chip process where a reflective contact is used for the top p-GaN layer, and light is extracted from the backside. A tunnel junction could be used to make a top transparent n-type contact to the top p-GaN layer (Fig. 8.2). Since n-GaN has lower absorption than typical ITO contacts, this can enable new LED device and packaging designs that allow for low metal coverage on the top surface for efficient light extraction, as well as a much simpler process flow. Tunnel junctions also enable multiple active region structures with several LEDs connected using tunnel junctions (Fig. 8.3). Such a structure could be used to connect LEDs with different peak emission wavelengths (such as RGB for white luminaires) for additional efficiency and functionality. Tunnel junctions can also be used to create multi-junction LEDs emitting at the same wavelength, as a way of circumventing efficiency droop [5]. The use of multiple LEDs cascaded with tunnel junctions enables high power density through voltage scaling rather than current scaling. Tunnel junctions can also enable new device structures like VCSELs, which are currently limited by absorption losses in the ITO contacts for current confinements. Finally, tunnel junctions for wider band gap materials could enable great efficiency in AlGaN-based ultraviolet LEDs. Currently, UV LEDs use an absorbing p-GaN top layer for hole injection, which greatly reduces extraction efficiency. Efficient tunnel junctions could enable transparent n-AlGaN contact and spreading layers on top of p-AlGaN, enabling significantly higher efficiency. In the UV-B and UV-C wavelength ranges, poor hole availability in the p-AlGaN layer also affects the injection efficiency and leads to poor balancing of electron and hole currents. Efficient tunnel junctions could provide significant advantages by enabling more efficient nonequilibrium injection of holes.

Since a fundamental component of tunnel junctions is a PN junction containing very high donor/acceptor impurity doping levels and their abrupt profiles at the junction interface, MBE is a better choice in principle to grow the tunnel junction structure. On the other hand, MOCVD is well suited to mass production of semiconductor-based devices. Furthermore high-quality GaN films with the low-temperature-deposited buffer layers [6] and high-brightness III-Nitride blue

Table 8.1 A list of published papers demonstrating III-Nitride tunnel junctions and related devices

Year	Affiliation	Device	Tunnel junction	Growth method	References
2001	Chonbuk National University	LED with GaN TJ	GaN	MOCVD	[8]
2001	Agilent	LED with InGaN TJ	InGaN	MOCVD	[9]
2001	Brown University	Two-color LED	InGaN	MOCVD	[15]
2001	Brown University	RCLED	InGaN	MOCVD	[16]
2002	Chonbuk National University	Micro LED with Buried TJ	GaN	MOCVD	[17]
2004	Lumileds Lighting	Photonic crystal LED	InGaN	MOCVD	[18]
2007	UC Santa Barbara	Two-color LED	AlN	MBE	[13, 19]
2010	Ohio State University	InGaN TJ	InGaN	MBE	[14, 20]
2013	Ohio State University	Cascaded/tandem LED	GdN	MBE	[5]
2013	Meijo University	Lateral Mg activation	InGaN	MOCVD	[21]
2013	Meijo University	LED with InGaN TJ	InGaN	MOCVD	[22]
2014	Ohio State University	LED with InGaN TJ	InGaN	Hybrid	[23]
2014	Meijo University	Tandem Solar Cells	InGaN	MOCVD	[24]
2014	University of Tokyo	Photocathode	AlN	MOCVD	[25]
2014	Meijo University	Micro LED Array	InGaN	MOCVD	[26]
2015	Meijo University	LED with InGaN TJ	InGaN	MOCVD	[27]
2015	McGill University	Nanowire Photocathode	InGaN	MBE	[28]
2015	McGill University	Nanowire Cascaded LED	InGaN	MBE	[29]
2015	Ohio State University	Cascaded LED	InGaN	MBE	[30]
2015	UC Santa Barbara	Vertical Cavity Laser	GaN	Hybrid	[31]
2015	NCKU, Taiwan	Cascaded LED	InGaN/AlGaN	MOCVD	[32]
2015	Ohio State University	UV LED	InGaN	MBE	[33]
2015	EPFL	Micro LED with buried TJ	GaN	Hybrid	[4]
2015	Ohio State University	Sub 300 nm UV LED	GaN	MBE	[34, 35]
2015	Meijo University	LED with buried InGaN TJ	InGaN	MOCVD	[36]

(continued)

Table 8.1 (continued)

Year	Affiliation	Device	Tunnel junction	Growth method	References
2016	UC Santa Barbara	Edge-emitting Laser	GaN	Hybrid	[37]
2016	EPFL	GaN TJ	GaN	MBE	[38]
2016	Dalian Univ. of Tech.	Sub 300 nm UV LED	AlGaN	Hybrid	[39]
2016	UC Santa Barbara	LED with GaN TJ	GaN	Hybrid	[40]
2016	Meijo University	LED with InGaN TJ	Graded InGaN	MOCVD	[41]
2016	McGill University	Nanowire LED	Al	MBE	[42]

light-emitting diodes [7] have been obtained by MOCVD. The first III-Nitride tunnel junction was also realized by MOCVD in 2001 [8]. A reverse-biased tunnel junction grown on a standard blue LED was fabricated in order to take advantage of current injection from the top n-layers to the p-layers of the LED. Since then, developments toward low resistive tunnel junctions under reverse bias have been pursued using MBE and MOCVD, and additional challenges for MOCVD-grown tunnel junctions have been recognized. The first InGaN tunnel junction was grown by MOCVD [9], and reported in 2001, the same year as the first GaN tunnel junction was reported. The concept of using the InGaN layer in the tunnel junctions was to leverage a narrower gap [10] with a lower ionized energy of a Mg acceptor [11]. New concepts of the polarization doping were reported in 2000 and 2010 using an AlGaN/GaN structure [12, 13] and a InGaN/GaN structure [14], respectively. Table 8.1 shows a list of the published papers demonstrating III-Nitride tunnel junctions and related optoelectronic devices. In the following sections, we will describe such developments, including polarization engineering, MBE-based and MOCVD-based tunnel junctions, and various optoelectronic devices with the tunnel junctions.

8.2 Polarization Engineering for Enhanced Tunneling

The wide band gap of GaN and AlGaN provides a principal challenge to realizing efficient tunnel junctions. A promising method to overcome the limitations of homojunction PN junctions is to use the spontaneous and piezoelectric polarization sheet charges that are formed at heterointerfaces of the III-Nitride system [12–14]. The basic idea is outlined in Fig. 8.4. In the case of a conventional PN junction, built-in voltage is supported by charges in the N and P depletion regions. The width of the depletion region is limited by the maximum amount of dopant charges that can be put into the semiconductor. III-Nitride heterostructures grown along the

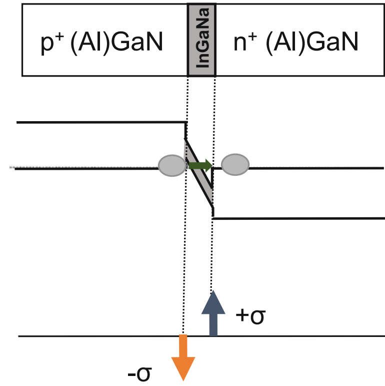

Fig. 8.4 Energy band and charge diagram of a GaN/InGaN/GaN tunnel junction

c-plane exhibit large spontaneous and piezoelectric polarization discontinuities at the barrier. Since significantly high charge densities ($>10^{13}$ electrons/cm^2) can be achieved in such systems (Fig. 8.4), these polarization charges can act in place of the conventional doping charges to reduce the depletion region width significantly. As shown in the charge diagram, the charge sheets from the polarization can enable a high areal sheet density, and enable significantly higher electric fields than would be possible for a homojunction. More significantly, since the acceptor level in GaN is 140 meV, it is challenging to achieve degenerate p-type GaN. For nondegenerate p-GaN, the energy difference between the Fermi level and the valence band implies that the valence band maximum is not aligned with the conduction band minimum at zero bias, and some voltage must be applied before electrons can tunnel from the valence band to the conduction band (or vice versa). Polarization charges can create a degenerate hole population at the heterojunction interface, leading to zero-voltage offset tunneling. It should be noted that in heavily doped materials band tail states [43] induced near the valence and conduction band edges could also enable low voltage offset tunneling and higher tunneling probability.

Grundmann [13], Simon [44], and Schubert [45] discussed in detail the use of AlN as such as heterojunction layer to enhance tunneling in III-Nitride tunnel junctions. The advantage of this method is that the AlN/GaN heterojunction provides a high polarization charge density that reduces the tunneling barrier significantly. This enabled cascaded LEDs with multiple active regions separated by tunnel junctions, as shown in Fig. 8.5. However, GaN/AlN/GaN tunnel junctions are relatively resistive due to the large barrier presented by the AlN, which has a large band gap (6.2 eV).

To surmount the problem of high band gap in AlN, Krishnamoorthy et al. [14] proposed a GaN/InGaN/GaN heterojunction to enhance tunneling. This approach allows for a short depletion width (due to the high piezoelectric polarization in pseudomorphic InGaN layers on GaN) while simultaneously providing a smaller band gap than GaN that can enhance the tunneling probability. At a certain "critical" thickness (not related to the critical thickness for lattice relaxation), the band

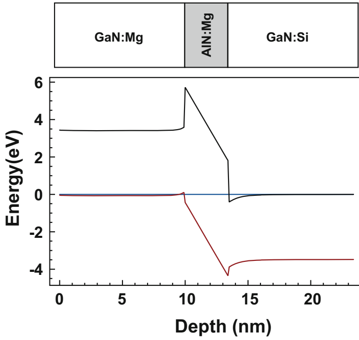

Fig. 1 Current-voltage characteristics of multi-color LED under forward bias.

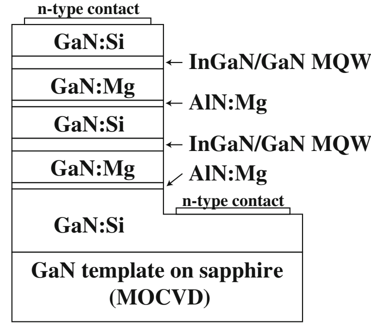

Fig. 2 Schematic diagram of MBE-grown multi-color LED.

Fig. 8.5 Epitaxial structure and energy band diagram of a GaN/AlN/GaN tunnel junction (from [13])

bending in the InGaN becomes sufficient to drop the entire band gap. If the thickness is lower than this, then the potential drop occurs both in the InGaN and in the depletion regions. For thickness greater than this, 2D electron and hole gases are induced on either side of the InGaN. Using the WKB approximation, the maximum tunneling probability across the InGaN layer for a Indium certain composition can be estimated to be

$$p(t_{cr}) = \exp\left(-2\int_{0}^{t_{cr}}\sqrt{\frac{2m^{*}E_{g}t}{\hbar q t_{cr}}}\mathrm{d}t\right)$$

where t_{cr} represents the thickness of the InGaN required to drop the entire band gap, and E_g is the corresponding band gap of InGaN. Note that the tunneling probability across the depletion region is not taken into account here, since it is in most cases much higher than the probability of tunneling across the InGaN itself, and therefore does not impact the tunneling rate significantly.

8.3 MBE-Based GaN Tunnel Junctions

Grundmann et al. [13] showed several early results involving tunnel junctions using polarization engineered GaN/AlN/GaN structures, where ultrathin AlN layers were used to create large electric fields within the tunnel junction. The epitaxial structure and energy band diagram of the GaN/AlN/GaN tunnel junction are shown in Fig. 8.5. These devices showed higher tunneling conductivity than similarly doped PN junctions, demonstrating that the polarization-engineered tunnel junctions are a

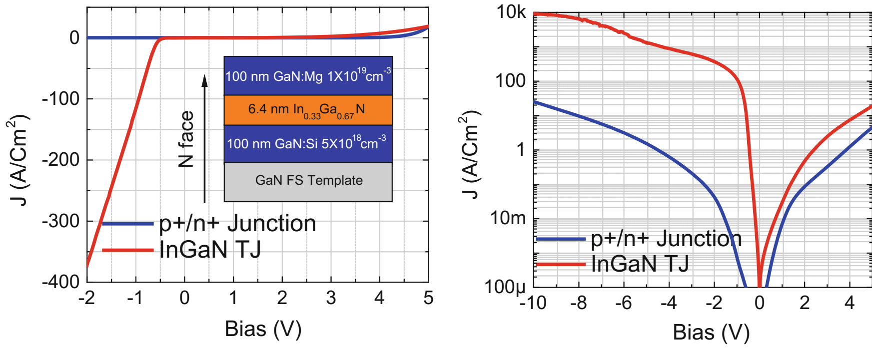

Fig. 8.6 Current–voltage characteristics of a p-GaN/n-GaN, and p-GaN/InGaN/n-GaN tunnel junction

viable route to achieving efficient tunneling. The voltage drop and resistance were, however, relatively high compared with metal-based p-contact.

Using the same polarization engineering concept, but replacing AlN with InGaN can overcomes the issue of the large tunneling barrier [14] and can enable high tunneling probability and low tunneling resistance. To realize this structure, an n-GaN/InGaN/p-GaN structure was grown along the N-polar direction (as shown in Fig. 8.6). Comparison of the current–voltage characteristics of structures with and without the InGaN layer, clearly show that the PN junction with the InGaN layer has significantly higher current. Current density of up to 10 kA/cm^2 was achieved on these devices.

With thicker InGaN (and higher nominal composition), Krishnamoorthy et al. [20] observed for the first time negative differential resistance characteristics in the forward bias direction, a characteristic feature of tunnel junctions. However, when the device was biased beyond the NDR onset voltage, the device showed hysteresis in current with respect to sweep direction as shown in Fig. 8.7. The hysteresis was attributed to trapping effects related to a donor-like hole trap found at positive polarization charge interfaces close to the valence band edge that has also been found previously in III-Nitride heterostructures [46].

In 2013, Krishnamoorthy et al. [47] reported integration of the polarization-engineered GaN/InGaN/GaN structures with a PN junction. The structure enables a tunneling contact to the p-layer. The structure showed low resistance and high current operation, with a series resistance of less than 1.5×10^{-4} Ω-cm^2. This showed that as expected, a tunnel junction can provide an excellent contact to a PN junction and enable low-resistance contacts comparable or better than existing metal p-contact, while enabling visible transparent and conductive n-GaN window layers to the device. This was followed by a report [23] of integration of the MBE tunnel junction with an MOCVD active layer, to realize a p-contact-free LED with low on resistance and transparent GaN top layer. In this case, the regrowth was carried out on the p-layer from the MOCVD LED epitaxial wafer, and interfacial

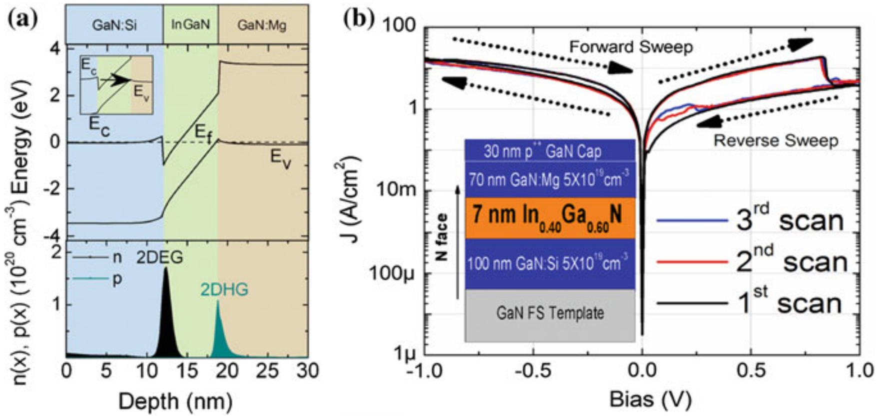

Fig. 8.7 Current–voltage characteristics of a GaN/InGaN/GaN tunnel junction showing negative differential resistance and hysteresis

impurities were found to reduce the tunneling conductivity, presumably due to the formation of a potential barrier for hole transport at the regrowth interface. More efforts to understand interfacial contamination and preparation are needed to overcome these issues.

The successful approaches discussed until now using heterostructure polarization engineering can enable enhanced tunneling probability. However, there are still some advantages of achieving polarization-free tunnel junctions using heavily doped PN junctions. One significant advantage of homojunction PN tunnel junctions is that remove the dependence on polarization charge. While GaN/InGaN/GaN or GaN/AlN/GaN tunnel junctions can only be made on high polarization planes (such as the c-plane), and along a specific orientation (c-plane for n-GaN/InGaN/p-GaN and p-GaN/AlN/n-GaN), the use of homojunctions eliminates such restrictions, and enables tunnel junctions in the opposite polarity (such as n-GaN/p-GaN along the c-direction) or on nonpolar and semi-polar planes where the polarization charge is very low. Furthermore, the use of InGaN in the tunnel junctions, although thin, can cause parasitic absorption within a light emitter structure. In the case of homojunctions, the tunneling resistivity is ultimately limited by the maximum possible doping density which in turn depends on material considerations related to dopant solubility and material quality. As the doping density is increased, band tail effects could further enhance the tunneling probability by providing a low-energy barrier for carrier tunneling.

Malinverni et al. [4] reported the first highly conductive PN homojunction tunnel junction contacts to an LED using a hybrid MOCVD/MBE technology. In this work, they carried out MBE regrowth of an n-type layer on top of MOCVD-grown p-type film. The high density of donor-like impurities formed at the regrowth interface enhances the tunneling probability in these structures. Following Malvinerni's work,

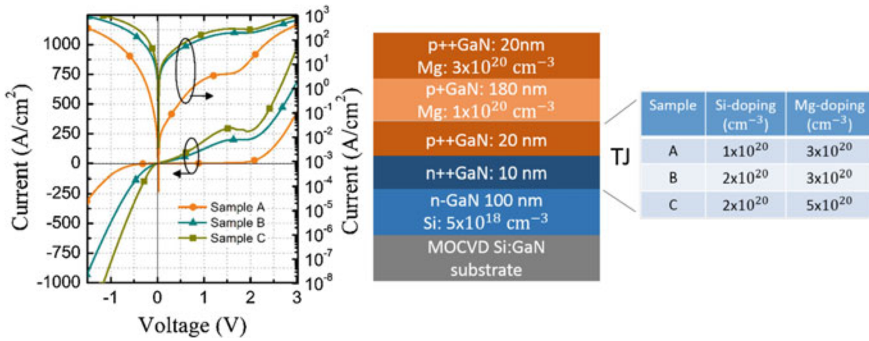

Fig. 8.8 Current–voltage characteristics and epitaxial structure of a p+GaN/n+GaN PN tunnel junction (from [43])

MBE-based homojunction tunnel junctions were reported by other groups using regrowth on an MOCVD wafer [31] and all MBE-growth [48].

The doping density dependence for stand-alone heavily doped PN junctions was investigated [48] and it was shown that as expected, the tunnel junction resistance decreased as the doping on the n and p sides were increased (Fig. 8.8). At the highest doping density (Sample C in the Fig. 8.8, exceeding 2×10^{20} cm^{-3} on both sides), tunnel junctions were found to display zero offset ohmic characteristics, as expected in a degenerately doped PN junction. In addition, the forward tunneling characteristics showed repeatable negative conductance as expected from in heavily doped PN diodes [2]. The forward tunneling behavior also provided insight into the influence of band-tail states in these heavily doped PN junctions. Using the model proposed by Kane [49] for band tail states, it was postulated that the band tail states from heavily doped P and N layers reduce the effective barrier for tunneling across heavily doped PN junction by creating density of states within the band gap of the p-type and n-type layers. For the doping concentrations used calculations using the Kane model showed that the significant density of band tail states could be as deep as 1 eV in the band gap (Fig. 8.9). In addition, band tail states also affect the threshold voltage for tunneling. Due to the deep acceptor activation energy in GaN: Mg, degenerate doping is not ordinarily possible, and therefore, the Fermi level is above the valence band. For lighter doped materials, some voltage needs to be applied before the valence band maximum on the p-type side can be aligned with the conduction band minimum on the n-type side, which is the prerequisite for energy conservation and elastic tunneling. In the case of heavily doped p-GaN, band tail states from acceptors can be created above the Fermi level in the p-layer, and therefore zero-voltage threshold tunneling is feasible. Homojunction PN tunnel junctions have been integrated with PN junctions [48], as well as LED [40] and laser structures [31, 37]. Extremely high current densities up to 150 kA/cm^2 were demonstrated for NPN junction structures, showing the effectiveness of homojunction PN junctions.

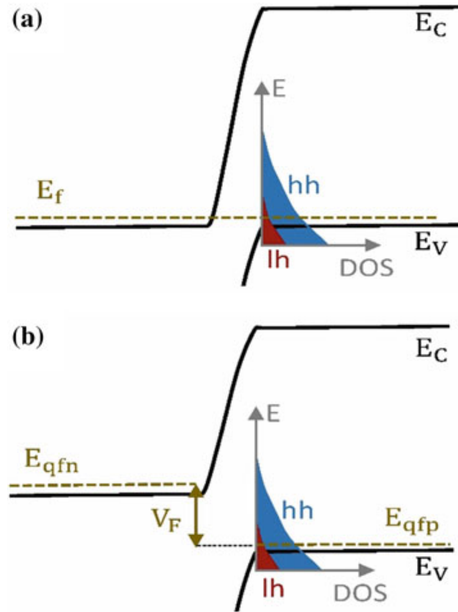

Fig. 8.9 Schematic energy band diagram showing the effect of band tail states on interband tunneling (from [43])

A different approach using Al interlayers to increase tunneling current was also reported to be effective in nanowires [42]. Nanowire light-emitting diodes with low turn-on voltage were reported using this method.

8.4 MOCVD-Grown III-Nitride Tunnel Junctions

The following sections deal with fabrication and characterization of MOCVD-grown III-Nitride tunnel junctions showing low resistance in optoelectronic devices. Some key findings in the MOCVD-grown tunnel junctions are provided here, mainly related to Mg doping.

The first InGaN tunnel junction [9] consisting of 15-nm heavily Si-doped GaN and a 15-nm heavily Mg-doped InGaN layer was grown on a standard blue LED layer structure, corresponding to an n-p-n structure (similar to a structure shown in Fig. 8.10a). A combination of very high Si and Mg doping concentrations (3×10^{20} and 2×10^{20} cm^{-3}) resulted in an operating voltage of 4.1 V at 50 A/cm^2. Since a typical operating voltage of a standard blue LED containing a standard p-contact with a semi-transparent metal electrode was 3.5 V, the voltage drop at the InGaN tunnel junction was estimated to be 0.6 V at that time. On the other hand, recent InGaN tunnel junctions grown by MOCVD have shown to have similar contact resistance to a standard p-contact. The differential device resistivity of the LED with the recent InGaN tunnel junction was 2.3×10^{-4} Ω cm^2 at

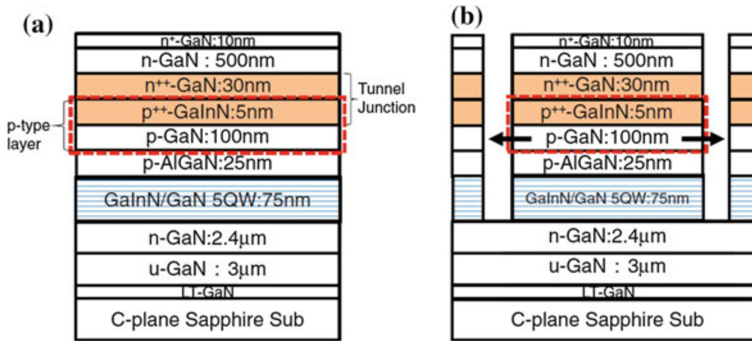

Fig. 8.10 Schematics of **a** a layer structure containing a tunnel junction and a LED structure and, **b** the same layer structure but after the mesa etching. The *arrows* indicate hydrogen diffusion paths during the Mg activation [21]

3 kA/cm^2 [41]. The following three subsections describe design and fabrication criteria to obtain such a low resistive tunnel junction by MOCVD.

8.4.1 Lateral Mg Activation

It is well known that acceptors in semiconductors grown under hydrogen atmosphere are passivated with hydrogen atoms. For instance, Mg in GaN [52] and C in GaAs [50] are passivated with hydrogen. Therefore, it is not until the acceptors are activated by removing the hydrogen atoms that the semiconductors with the acceptors show p-type characteristics. For instance, Mg-doped GaN layers and Mg-doped GaInP layers need to be treated with low-energy electron beam irradiation [51] or thermal annealing [52] in order to remove hydrogen atoms. In such processes, removed hydrogen atoms need to diffuse out from the p-layers. At the same time, an intriguing result that hydrogen can pass through p-layers but not through n-layers has been reported [53, 54]. Note that in typical structures of LEDs with the tunnel junctions, the p-layers are fully covered with the top n-layers as shown in Fig. 8.10a. In such a case, the hydrogen may not be able to efficiently diffuse from the p-layers to the outside of the wafer through the n-layers.

Kuwano et al. proposed a lateral Mg activation method, in which hydrogen diffuses laterally from etched sidewalls of the p-layers to the outside, as shown in Fig. 8.10b [21]. In their standard LED fabrication procedure, a LED wafer was first thermally annealed for the Mg activation so that hydrogen diffused vertically through the surfaces. Then, the wafer was etched to form a device mesa which size was about 300 μm square. On the other hand, in the newly developed procedure for the LEDs with the tunnel junctions, the device mesas with sidewalls were formed first by etching, and then annealed under oxygen atmosphere. In this case all the p-layers (p-AlGaN, p-GaN, and heavily Mg-doped InGaN) located under the top n-layers were partly

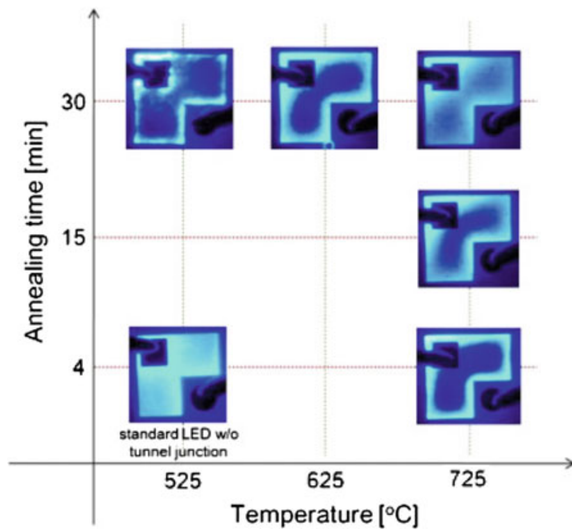

Fig. 8.11 Top-view emission patterns of LEDs with tunnel junctions activated under various thermal annealing conditions. A case of a standard LED without a tunnel junction but with a p-electrode annealed under a standard condition is also shown [21]

exposed to the outside thorough the etched sidewalls during the thermal annealing as indicated with arrows in Fig. 8.10b. Figure 8.11 shows top view emission patterns of the LEDs with the tunnel junctions annealed with the new activation procedure. Various annealing temperatures (525–725 °C) and time (4–30 min) were performed here. The most uniform emission pattern was obtained from the LED with the tunnel junction annealed at 725 °C for 30 min. On the contrary, the LED with the tunnel junction annealed under low temperatures or short time show specific emission patterns which are restricted near the edge of the device mesas. Actually, annealing conditions with lower temperature or shorter time resulted in narrower emission patterns located near the mesa edges. Such specific emission patterns should be caused by nonuniform current injection through the tunnel junctions since the InGaN quantum well active regions are uniform in a scale of the mesa size. Therefore, the result regarding the emission patterns suggests that the Mg activations occurred first at the regions which were close to the sidewall edges, where p-layers were directly exposed to oxygen ambient and then were extended from the edge to the center of the device mesas. Figure 8.12a shows a definition of "Mg activation length" as indicated with arrows, and Fig. 8.12b shows the Mg activation length as a function of a square root of annealing time, clearly showing a linear relationship. This result suggests that the Mg activation length should be governed by some diffusion process. Thus, they concluded that hydrogen atoms diffused only toward the lateral direction through the etched sidewalls but not toward the vertical direction through the sample surface due to the existence of the top n-layers. A typical Mg activation condition is 525 °C for 4 min, and it was found that much higher temperature and much longer time were required. This is because the activation length of the LED with the tunnel junction is much longer (~100 μm: comparable to a mesa size) than that of the standard LED with the p-contact (~100 nm: only the p-layer thickness). They also observed that

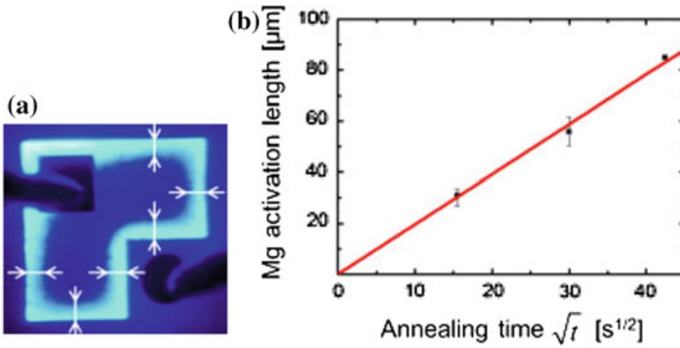

Fig. 8.12 **a** Mg activation length is indicated with *arrows*, and **b** Mg activation length as a function of a square root of annealing time at 725 °C is shown [21]

sufficient lateral Mg activation showing more uniform emission patterns led to lower operating voltages. In brief, the MOCVD-grown LEDs with the tunnel junctions require the lateral Mg activation to obtain sufficient Mg activation. This is an additional requirement for the MOCVD-grown tunnel junctions compared to the MBE-grown ones.

8.4.2 InGaN-Based Tunnel Junctions

As mentioned in the previous sections, there are several reasons to use InGaN layers with high InN mole fractions in the III-Nitride tunnel junctions. The first one is a narrow band gap with a small ionized energy of Mg acceptors, and the second one is large polarization charges generated at the hetero interfaces. Both of these are effective to obtain a thin depletion layer which increase the tunneling probability of electrons from the valence band edge to the conduction band edge. In addition, a third advantage was revealed for the MOCVD-grown tunnel junctions, which was a suppression of Mg segregation into the above n-layers.

Operating voltages of the LEDs with the InGaN tunnel junctions as a function of InN mole fractions have been systematically investigated [22, 27]. The test structure here was the same structure mentioned in the previous section, the n-p-n structure. The lateral Mg activation was also carried out for all the samples, which have the same layer structures but different InN mole fractions and different thicknesses of the InGaN layers in the tunnel junctions. The InN mole fraction was varied from 0 to 0.4, and the thickness was also adjusted to 7.5–2 nm along with the InN mole fractions to minimize surface roughness caused by the lattice-mismatching between InGaN and GaN. Figure 8.13 shows current–voltage characteristics of the blue LEDs with the InGaN tunnel junctions containing various InN mole fractions. For comparison, characteristics of a conventional blue LED with a p-contact are also plotted in the same figures. Clearly, higher InN mole fractions resulted in lower

operating voltages, and voltage drops of the tunnel junctions with 0.35 InN mole fraction and higher were almost the same as that of the standard p-contact in Fig. 8.13b. Such low voltage drops at the InGaN tunnel junctions with higher InN mole fractions are attributed to the narrow band gap and the large polarization charges. At the same time, Mg profiles around the tunnel junctions suggest that smaller Mg segregations with higher InN mole fractions could also play an important role to obtain the low voltage drop at the tunnel junctions. Figure 8.14 shows the Mg profiles around the InGaN tunnel junctions measured by Secondary Ion Mass Spectrometry. In the samples with the InN mole fractions of 0.2 and lower, large Mg segregations into the above n-layers were observed. The residual

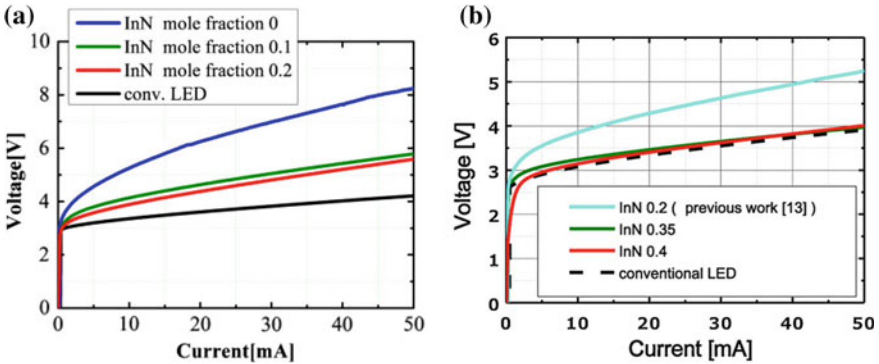

Fig. 8.13 I–V characteristics of *blue* LEDs with InGaN tunnel junctions with the InN mole fractions **a** from 0 to 0.2 [21] and **b** from 0.2 to 0.4 [27]. For comparison, characteristics of a conventional LED with a p-electrode is also plotted

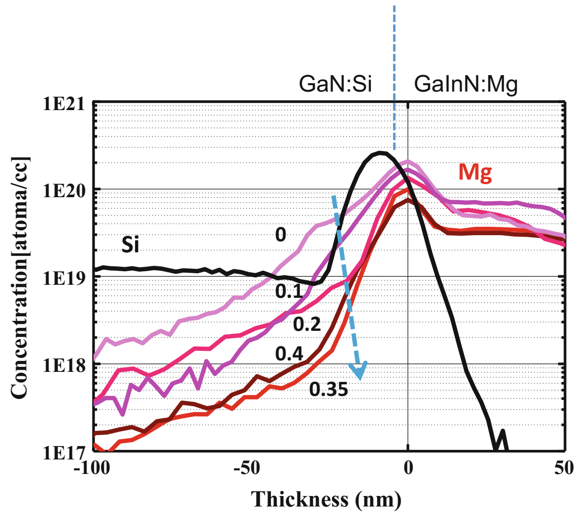

Fig. 8.14 Mg and Si doping profiles measured by SIMS around InGaN tunnel junctions with the InN mole fractions from 0 to 0.4 [22, 27]

Mg concentrations were still around 1 × 10^{19} cm^{-3} at the end of the heavily Si-doped GaN layers, which were comparable to the Si concentrations in the topmost n-GaN. On the other hand, 0.35 and 0.4 InN mole fraction cases showed much lower residual Mg concentrations, about 1 × 10^{18} cm^{-3}, resulting in a sufficient margin with the Si doping. The low residual Mg concentrations should help to form more abrupt tunnel junction interface, resulting in low voltage drop, and seem to be caused by higher amount of In atoms on the surface and low growth temperature coincidentally necessary for higher InN mole fractions [55].

The Mg memory effect mentioned above has an impact on donor and acceptor impurity concentration dependencies. Figure 8.15a and b shows Mg and Si doping dependences in the $In_{0.2}Ga_{0.8}N$ tunnel junctions on operating voltages of the LEDs with the tunnel junctions [22]. As shown in Fig. 8.15b, the operating voltages of the LEDs were greatly influenced by the amount of the Si doping. Actually, lower Si concentration (1 × 10^{20} cm^{-3}) clearly led to much higher operating voltage (7 V at 20 mA), implying that the high amount of residual Mg atoms in the highly Si-doped GaN could compensate some of the Si atoms. Interestingly as shown in Fig. 8.15a, the operating voltages were almost independent of the amount of Mg concentrations. One of the possible explanations is that more Mg doping resulted in not just a high Mg concentration in the Mg-doped InGaN layer but also high residual Mg concentration in the following Si-doped GaN layer. Both influences could be compensated each other, resulting in such a less Mg concentration dependence. Thus, in the case of MOCVD-grown tunnel junctions, a Mg doping profile must be carefully optimized by taking into account not just a Mg concentration in the p-layer of the tunnel junction but also the residual Mg concentration into the upper n-layers.

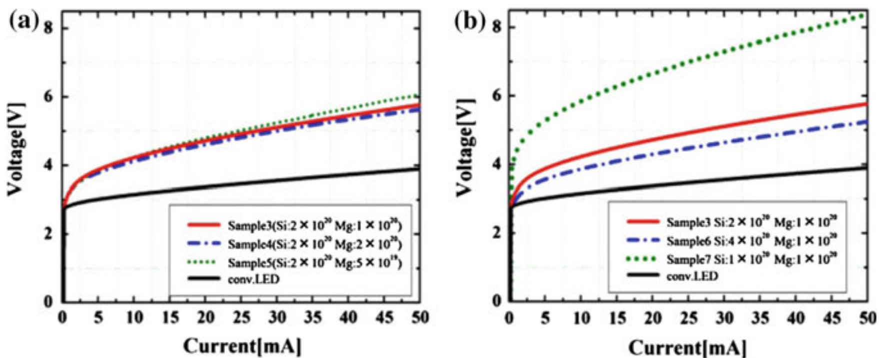

Fig. 8.15 I–V characteristics of **a** Mg and **b** Si doping dependences in LEDs with $In_{0.2}Ga_{0.8}N$ tunnel junctions. For comparison, characteristics of a conventional LED with a p-electrode is also plotted [22]

8.4.3 Band Engineering: Graded Layers

A low voltage drop at the tunnel junction is demanded toward a low operating voltage of any optoelectronic device with the tunnel junction. Most investigations have paid attention to a resistance of the tunnel junction itself, in other words, high tunneling probability through the junction interface. At the same time, the operating voltage of the device depends on not only one part of the device but also other parts. Figure 8.16a shows a calculated band diagram of the tunnel junction consisting of a p-GaN/2 nm heavily Mg-doped $In_{0.4}Ga_{0.6}N$/4 nm heavily Si-doped GaN/n-GaN structure. It seems that the InGaN layer should enhance the tunneling probability due to its narrow band gap. However, the narrow band gap also causes large energy spikes for electrons and holes at the interfaces with the adjacent GaN layers. This means that it could be easier for electron to tunnel through the InGaN layer, but it could be more difficult to pass through the spike and reach the adjacent GaN layer. It has been reported that such large energy spikes at heterointerfaces drastically increase resistances, like at GaAs/AlAs interfaces of semiconductor-based distributed Bragg reflectors. A high doping (over 1×10^{19} cm^{-3}) and a graded interface (~10 nm) were proposed to reduce the energy spikes [56]. Since the tunnel junction is already highly doped, just the graded layer structure should be adopted in the tunnel junction.

Figure 8.16b shows a calculated band diagram of the tunnel junction consisting of a p-GaN/2 nm heavily Mg-doped graded InGaN (from 0 to 0.4)/2 nm heavily Mg-doped graded InGaN (from 0.4 to 0)/4 nm heavily Si-doped GaN/n-GaN structure. In other words, the potential profile of the graded InGaN layers here is a V shape. Note that the total amount of In atoms in the tunnel junction is the same as that of the structure in Fig. 8.16a. Even though the graded layer thickness is very thin (2 nm) compared with a typical graded layer in other structures, the band diagram shows a clear reduction of the energy spikes. Takasuka et al. [41] prepared

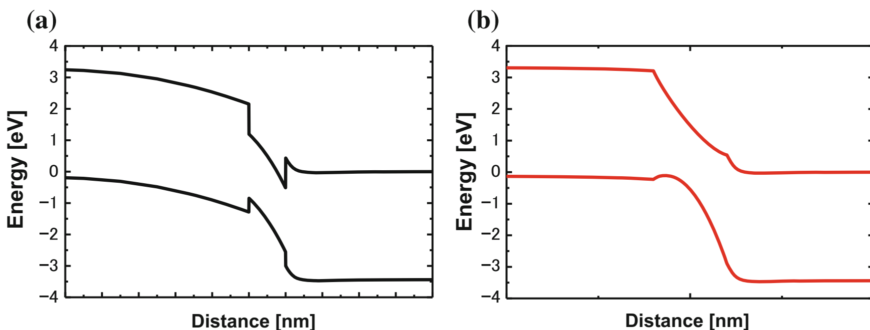

Fig. 8.16 Calculated band diagram of tunnel junctions consisting of **a** a p-GaN/2 nm heavily Mg-doped $In_{0.4}Ga_{0.6}N$/4 nm heavily Si-doped GaN/n-GaN structure and **b** a p-GaN/2 nm heavily Mg-doped graded InGaN (from 0 to 0.4)/2 nm heavily Mg-doped graded InGaN (from 0.4 to 0)/ 4 nm heavily Si-doped GaN/n-GaN structure [41]

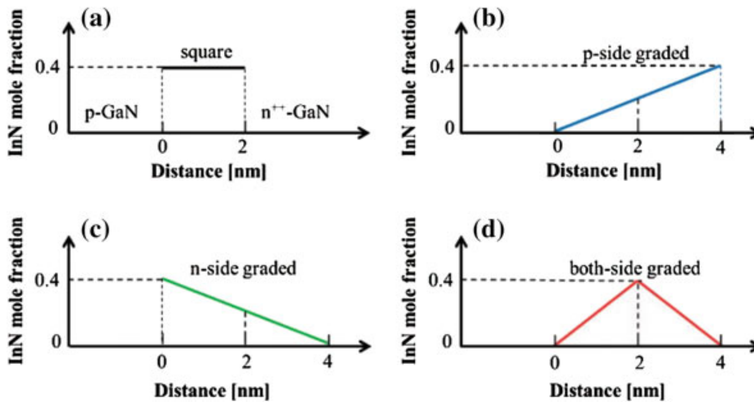

Fig. 8.17 Designed InN mole fraction profiles in the InGaN tunnel junctions: **a** a 2 nm $In_{0.4}Ga_{0.6}N$, **b** a 4 nm p-side graded InGaN, **c** a 4 nm n-side graded InGaN, and **d** a 4 nm both sides graded InGaN [41]

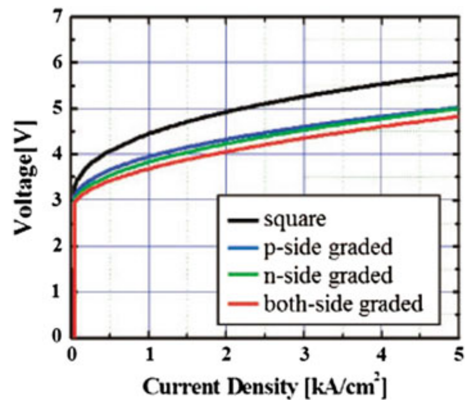

Fig. 8.18 j–V characteristics of the LEDs with the InGaN tunnel junctions containing the 2 nm $In_{0.4}Ga_{0.6}N$, the 4 nm p-side graded InGaN, the 4 nm n-side graded InGaN, or the 4 nm both sides graded InGaN [41]

four different InN mole fraction profiles of the graded InGaN layers in the InGaN tunnel junctions. The structures of the samples were similar to those in Fig. 8.10a. Figures 8.17 show designed InN mole fraction profiles in the tunnel junctions of the four different samples. Sample A has a square InGaN composition profile as shown in Fig. 8.17a, which band diagram is described in Fig. 8.16a. Sample B and C have one-side graded InGaN layers for p-side and n-side as described in Fig. 8.17b and c, respectively. Sample D has InGaN layer compositions graded on both sides as shown in Fig. 8.17d, which band diagram is also described in Fig. 8.16b. Figure 8.18 shows current–voltage characteristics of the four LEDs with the various InN mole fraction profiles. Here, micro LEDs with 35 μm diameter were fabricated in order to measure current–voltage characteristics at high current density regions. Clearly, the samples with the graded InGaN layers showed lower operating voltages than that with the square InGaN layer. This result suggests that not just the

tunneling probability but also the conductivity at the interfaces after the tunneling are important in terms of low device resistance. Note that in principle the tunneling probability and the conductivity at the interface are in a trade-off relationship due to a restriction of the lattice-mismatching, so that the InN mole fraction in the InGaN tunnel junction should be optimized by taking the trade-off into account.

The tunnel junction resistances reported here are comparable to that of the standard p-contact even at high current density regions. The contact resistivity at 3 kA/cm^2 of the tunnel junction estimated from a differential device resistivity of the I–V curve is at most $2.3 \times 10^{-4}\ \Omega\ \mathrm{cm}^2$ and also comparable to the MBE-grown ones [40, 43]. To sum up, the important technologies to obtain low resistive MOCVD-grown III-Nitride tunnel junctions are the lateral Mg activation, the InGaN layer with the high InN mole fraction, and the graded interfaces.

8.5 Device Realization Utilizing Tunnel Junctions

So far, some III-Nitride optoelectronic devices utilizing tunnel junctions have been proposed and demonstrated. A couple of important devices with the tunnel junctions, such as a tandem structure [15] and LEDs with current confinement/spreading structures [16], were already demonstrated in early 2000. At that time, all the device structures were grown by MOCVD, since a single MOCVD growth simply produced the whole structures containing the main optoelectronic device part and the tunnel junction part. Since 2010, when low resistive MBE-grown tunnel junctions were reported, the number of published papers reporting optoelectronic devices with tunnel junctions has drastically increased, containing not just visible LEDs but also ultraviolet LEDs [33–35, 39], a solar cell [24], an edge-emitting laser [37], and a VCSEL [31]. A hybrid approach using MOCVD for the growth of main optoelectronic device structures and MBE for the growth of simple GaN tunnel junction structures has been adapted [4]. The next sections describe some examples of integration of tunnel junctions into optoelectronic devices.

8.5.1 Tandem Structures

A tandem structure is containing two or more p-n junction devices alternately stacked with the tunnel junctions, corresponding to a p-n p-n…p-n cascaded structure. If the devices emitting or receiving different wavelengths are cascaded, multi-color LEDs or high-efficiency solar cells can be obtained. In addition, since the tunnel junctions are composed of semiconductor-based materials, a single epitaxial growth produces such a tandem structure, providing cost-effective devices.

The first III-Nitride cascaded LEDs were reported in 2001, containing a bottom green LED and a top blue LED with the InGaN tunnel junction [15] to produce dual wavelength light emission from one chip. In addition, this device had the third

electrode located just on the tunnel junction, so that the two LEDs could be independently operated with three terminals. The LEDs were operated in a time-sequential mode with nearly 100 MHz speed. Note that operating voltage of the LED including tunnel junction was high because the tunnel junction at that time was not so optimized yet. Later on, a new concept of the cascaded LEDs was proposed by Akyol et al. in 2013 [5]. In the concept, the identical LEDs are cascaded with the tunnel junctions so that the cascaded LEDs can be operated under multiple turn-on voltage and low injected current density. In other words, the cascaded LEDs can convert an electric power configuration from low voltage/high current density typically used in high power LEDs to high voltage/low current density. This is the reason why the cascaded LEDs could overcome the efficiency droop which is one of the biggest issues in the III-Nitride LEDs [57].

Tandem solar cells were also obtained in 2014, which structure is almost the same as the cascaded LEDs with different active regions covering different wavelength regions [24]. The tandem solar cells showed a higher open-circuit voltage, but not high as expected, compared to a single solar cell previously reported. This was probably due to a formation of pits on the wafer surfaces. Actually further investigation by cross-sectional TEM revealed that additional dislocations were generated near the tunnel junction interface, and the dislocations were connected to a formation of the pits. As already mentioned, high InN mole fractions and high Mg/Si concentrations resulted in low resistance of the tunnel junctions, but such conditions certainly increase a possibility of a degradation of material quality. This point must be considered when the tandem structure is fabricated since additional active regions must be located on the tunnel junctions.

8.5.2 Current Confinement Structures

One of the most useful structures using the tunnel junctions is a buried tunnel junction for current confinement. It is necessary for laser diodes to inject high current density for the operations, meaning that the current confinement structures are required. For instance, a typical VCSEL requires a small current aperture, such as 10-μm diameter, and therefore oxide-apertures [58] or the buried tunnel junction apertures [59] are often used in infrared GaAs-based VCSELs. However, the oxide-apertures cannot be formed in AlN-based materials, unlike AlAs-based materials, one must rely on other techniques to form the small aperture in GaN-based VCSELs. In reality, a simple combination of a SiO_2 aperture and an ITO electrode has been used for the GaN-based VCSELs. Unfortunately, ITO has large absorption, leading to a low external differential quantum efficiency. This is why the III-Nitride buried tunnel junctions could be an ideal solution for the GaN-based VCSELs. So far the tunnel junction has already been applied in a GaN-based VCSEL structure [31], showing a pulsed operation with a low threshold current density. In this device, the tunnel junction in the VCSEL was used for

current injection but not for current confinement, and the confinement was done by another method (Al ion implantation).

The first attempt to obtain the III-Nitride buried tunnel junction was reported by Jeon et al. in 2002 [17]. They first grew the layer structure consisting of a 3-μm bottom n-GaN, a GaInN/GaN MQW active region, a 150-nm p-GaN, a GaN tunnel junction (10-nm p^{++}-GaN/10-nm n^{++}-GaN), and a 10-nm top n-GaN. Then, mesas were formed by etching with a 100 nm depth, so that the areas without the mesas no longer contained the tunnel junction. Following the etching, a 330-nm top n-GaN layer was regrown to bury the tunnel junction mesas. Thus, the current injected from the top n-GaN can pass through the buried tunnel junction areas but not in the other areas with (non-tunnel) p-n junctions. Near field patterns showed clear light emission from the LEDs with the various buried tunnel junctions, with sizes ranging from 8 to 20 μm diameter. However, the buried tunnel junction structures did show large leak current under forward bias in the LEDs, and no emission was observed up to a current density of 2 kA/cm^2. The leakage was attributed to the regrowth interface.

More recently, buried tunnel junctions on LEDs were reported in 2015 by a combination of MOCVD and MBE [4]. The bottom LED part was prepared by MOCVD, and the top tunnel junction and a regrown top n-GaN layer were grown by MBE. The MOCVD-grown layer structure consisted of an n-GaN, an InGaN/GaN 2QW active region, and a 20 nm p-AlGaN. Then, a 150 nm p-GaN, and a GaN tunnel junction (25 nm Mg-doped GaN (1×10^{20} cm^{-3})/20 nm n^{++}-GaN (2×10^{20} cm^{-3})) were grown on the MOCVD-grown structure by MBE. Circular mesas for which diameters were 4–16 μm were fabricated by etching with a 150 nm depth. Then, a 200 nm n-GaN was grown again on the wafers with the mesas by MBE. Interestingly, the LEDs with the buried tunnel junctions showed light even at low current density, ~10 A/cm^2, indicating that almost no leakage path existed.

From the above results, it is not possible to conclude if the reduction in leakage was due to the growth method used (MBE versus MOCVD) or due to the difference in the epitaxial structure. Recent work by Ino et al. has led to a better understanding of this issue. In this work, the influence of etching on the leakage current at tunnel junction mesas was investigated [36]. The current density-voltage and output power characteristics of the buried tunnel junction LED fabricated with various etching depths (and therefore varying etching damage) (Fig. 8.19a) was compared. Four different LEDs with the buried tunnel junctions (Sample 1–4) were prepared. All the layer structures were grown by MOCVD including the top regrown n-GaN after forming tunnel junction mesas. Each etching depth (A) and remaining p-layer thickness (B) is listed in Fig. 8.19a. All the samples showed well-defined light emission patterns which corresponded to the tunnel junction mesa sizes as Fig. 8.19b shows an example. On the contrary, clear differences were observed in j–V and j–L characteristics in Fig. 8.20a, b. The samples with thicker etching depths (meaning a thinner remaining p-layer) showed larger leak currents in both j–V and j–L characteristics. The experiment suggest that the remaining p-layer thickness needs to be 130 nm or more to suppress leakage current. These results suggest that the growth method is not responsible for the low leakage current

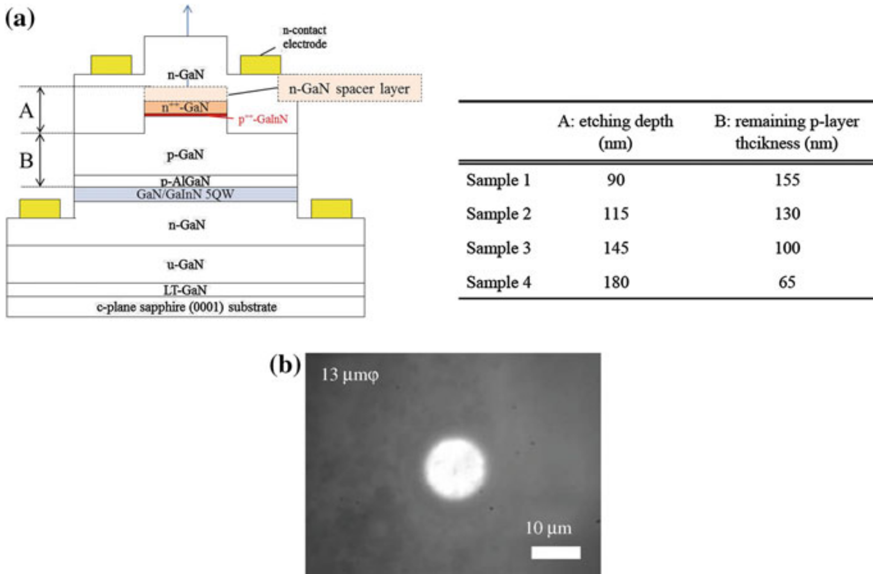

	A: etching depth (nm)	B: remaining p-layer thcikness (nm)
Sample 1	90	155
Sample 2	115	130
Sample 3	145	100
Sample 4	180	65

Fig. 8.19 **a** Schematic of a LED with a buried tunnel junction. “A” indicates etching depth and “B” indicates remaining p-layer thickness. **b** A light emission pattern of the LED with a 13 μm ϕ tunnel junction mesa is shown [36]

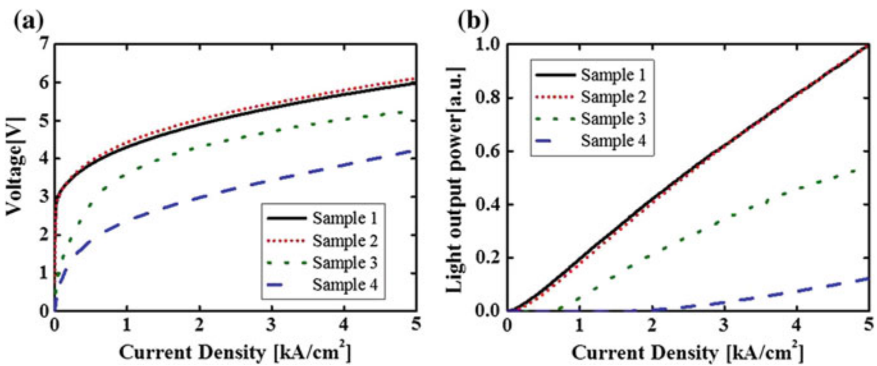

Fig. 8.20 **a** j–V and **b** j–L characteristics of LEDs with the buried tunnel junction mesas as a function of etching depths are plotted [36]

observed in the buried tunnel junction LED, but the buried structure needs to be properly designed to account for etching-related damage.

Figure 8.21 shows an example of the optoelectronic device with the buried tunnel junction, that is a 2-mm-long LED indicator, displaying “Meijo University” with Chinese characters. In the fabrication of the indicator, mesas with Chinese character shape (rather than circular mesas) were formed. The top n-GaN layers

were grown after forming the mesas. The mask set containing specific character shape was required, but the process procedure was the same as the small-aperture buried tunnel junction LED. Such a micro indicator can be used in small projection-type equipment for displaying large areas.

8.5.3 Simple Device Fabrications

Another advantage of tunnel junctions is that they enable simpler device fabrication. Because no p-contact layer is needed, a single deposition of n-electrodes on the top and the bottom n-layers is required. In addition, a low resistive top n-layer, such as n-GaN, will work as a current spreading layer, so a simple combination of the n-electrode and the current spreading top n-layer is sufficient to obtain reasonable light extraction efficiency. Such a simple fabrication becomes more crucial for array devices because a yield of such array devices is typically lower than a single device.

Watanabe et al. demonstrated a 10 × 10 channel matrix-addressable III-Nitride micro LED array and an over 1000 channel micro LED display [26]. They implemented not just the tunnel junctions but also semiconductor-based cathode lines into the micro LED arrays as shown in Fig. 8.22a. In the fabrication process, only four photomasks for two etching processes (device isolation and cathode line formation) and two deposition processes (insulator and n-metal) were just required. In Fig. 8.22b, the semiconductor-based cathode lines are extended laterally and the

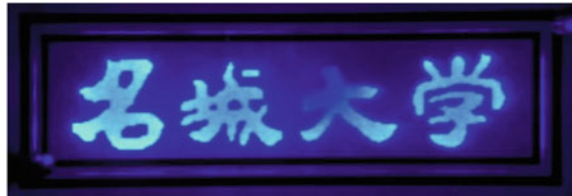

Fig. 8.21 An example of the optoelectronic device with the buried tunnel junction. A 2-mm-long LED indicator, displaying “Meijo University” with Chinese characters

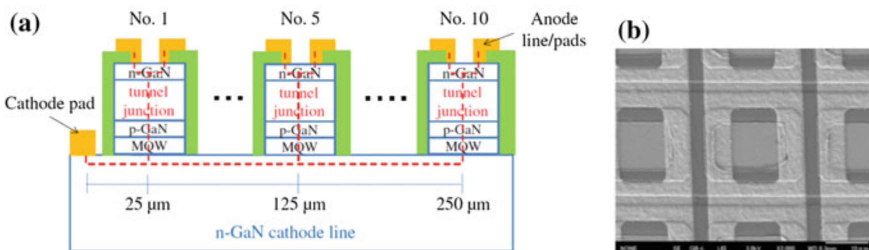

Fig. 8.22 **a** A cross-sectional schematic of an unit consisting of 10 in-line LEDs connected with an n-GaN cathode line in a 10 × 10 channel array with the tunnel junction, and **b** a scanning electron microscopy image of channels in the array [26]

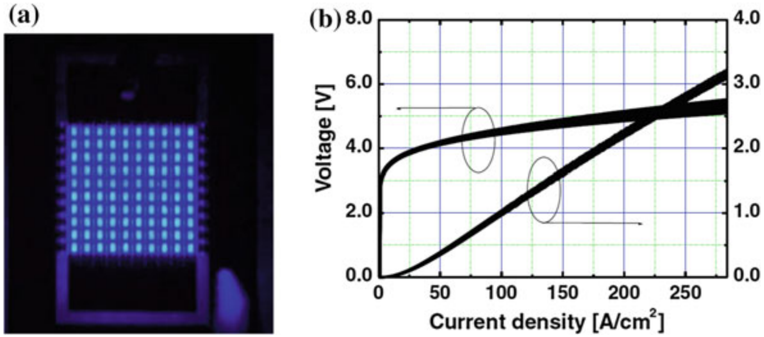

Fig. 8.23 **a** An emission image of the 10 × 10 channel array and **b** voltage and light output power of 10 in-line channels connected with the n-GaN cathode line in the 10 × 10 channel array as a function of current density [26]

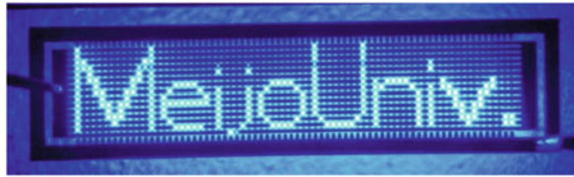

Fig. 8.24 A microscopy image of a 14 × 72 channel microdisplay with tunnel junctions under operation [26]

metal-based anode lines (shown as whitish areas) are extended vertically. Thanks to low resistance of the top n-GaN on the tunnel junction, current can pass laterally in the top n-GaN from the edge of the mesa with the anode aperture frame to the center of the mesa as indicated with dotted lines in Fig. 8.22a. Thus, most of the light was extracted from the center of the mesa and sufficiently high extraction efficiency was obtained even with the simple device structure. Note that if the tunnel junction is not used, three more photomasks which require fine alignments are necessary, leading to poor yield. Figure 8.23a and b show an image of the 10 × 10 channel matrix-addressable III-Nitride micro LED array fabricated by the above-mentioned procedure and I–L–V characteristics of the 10 in-line LEDs connected with the same n-GaN cathode in the array. The size of each LED was 16 × 10 μm^2 with a pitch length of 25 μm. Very uniform I–L–V characteristics were obtained due to the small number of the process step. Finally, Fig. 8.24 shows the over-1000 channel micro LED display with a 2 mm length. Fourteen vertically aligned LEDs were connected with the n-GaN cathode line and 72 horizontally aligned LEDs were connected with the metal anode line. Clear and uniform emission was obtained, proving that the simple fabrication process provides the benefit of high yield in such a large-scale array fabrication.

8.6 AlGaN-Based Tunnel Junctions for UV LEDs

The concept of polarization engineering described earlier is not only useful for GaN tunnel junctions but can be expanded to larger band gaps such as for AlGaN. Since achieving high hole concentrations in AlGaN is even more challenging than for GaN, this can be an important advantage for ultraviolet light emitters. The first demonstration of a tunnel junction for an AlGaN-based UV LED was in 2015 by Zhang et al. [33], who demonstrated efficient tunneling and hole injection for AlGaN with Al composition of 30%, as shown in Fig. 8.25. The tunnel junction was integrated with a UV LED emitting at 320 nm, which showed good output characteristics. A top surface roughened TJ-LED structure was also reported by Zhang et al. [60], to show enhanced light extraction by over 40%. However, further work is necessary in finding device topologies that improve light extraction from UV LEDs, while taking advantage of the transparent conductive window layers.

A detailed analysis of the predicted tunneling current and resistance for shorter wavelength (and higher Al composition) emitters was reported by Zhang et al. [35]. It was found that similar to the previous discussion of graded layers in GaN-based tunnel junctions, grading the layers adjacent to the tunnel junction was also critical to achieving low voltage drop and tunneling resistance in AlGaN-based tunnel junctions. Furthermore, the tunnel junction resistance for non-graded tunnel junctions was significantly higher than that for graded tunnel junctions, especially for higher Al compositions. Reports of tunneling-based hole injection for UV LEDs at shorter wavelengths have also been realized, leading to demonstration of 290 nm LEDs [34, 35, 39], (Fig. 8.26) as well as shorter wavelength emission down to 270 nm [61].

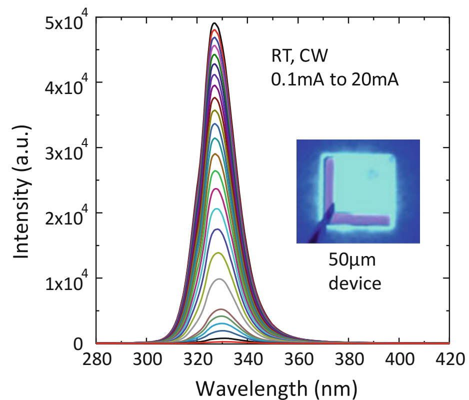

Fig. 8.25 Output characteristics of a tunnel junction injected ultraviolet LED (from [33])

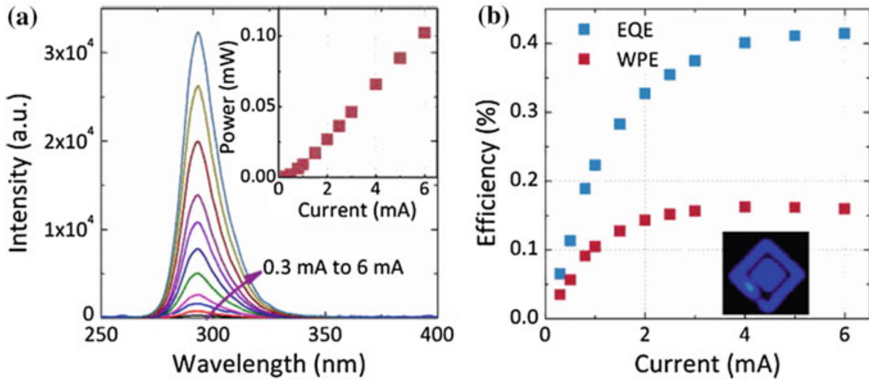

Fig. 8.26 Output characteristics of a tunnel junction injected ultraviolet LED emitting at 292 nm (from [34])

8.7 Summary and Future Directions

In summary, III-Nitride tunnel junctions grown by MBE and MOCVD are now a highly active area of research, driven by the huge potential for improvements in device performance and functionality. Both MBE-grown and the MOCVD-grown tunnel junctions show low resistivity, a few 10^{-4} Ω cm^2, comparable to the standard p-contact. The flexibility of MBE will enable it to be a powerful tool for realizing new and efficient tunneling structures in the future. In addition, while MBE technology may not be suitable for mass production in the visible range, it may be more applicable to lower volume production such as in the deep UV emitter area. MOPVE-grown tunnel junctions showed the specific issues related to Mg doping, but the issues have been recognized and addressed. The lateral Mg activation, high InN mole fraction for small Mg segregation, and graded layer structures have been developed. In addition, various optoelectronic devices utilizing the tunnel junctions have been demonstrated, proving the feasibility of the tunnel junctions.

Regarding the future directions, a couple of challenges for III-Nitride tunnel junctions still remain. At this moment, reliability performance of III-Nitride tunnel junctions is not known. Since III-Nitride tunnel junctions contain very high impurity doping levels, material quality could be impacted, and this can affect device reliability. This issue needs to be addressed prior to practical uses. Further optimization toward lower resistivity compared to the standard p-contact should also be continued. While a surface of the standard p-contact must be exposed to air, the surface of the p-layer in the tunnel junction can be protected with the top n-type layer, which is a more ideal situation, and should ultimately enable lower resistivity p-type contacts. Finally, for MOCVD-tunnel junctions, in situ Mg activation for the p-layers including the tunnel junctions is critical need. The in situ Mg activation

could require lower temperature and shorter time than the current lateral Mg activation and reduce damage to active layers.

As pointed out earlier, multiple active region LEDs using tunnel junctions can provide a direct solution to the problem of efficiency droop at high power density if the absorption and defect generation are understood and controlled. Such tunnel-enabled cascade light emitters could revolutionize lighting and display by providing highly efficient high power sources. With future improvements in longer wavelength emitters based on III-Nitrides, tunnel junctions will also enable multi-wavelength sources that can overcome phosphor efficiency limits, and get solid-state lighting closer to the ultimate quantum limits. Finally, tunnel junctions have now been demonstrated for band gaps beyond GaN, up to 70% AlGaN. Advances in tunneling enabled ultraviolet emitters could enable orders of magnitude improvements in the efficiency and cost of emitters at these wavelength ranges, and enable a new generation of compact, low cost, and sage water purification and air disinfection systems that could have enormous societal benefit.

The recent progress in this field and the surge in activity across the world will continue to enable significant advances towards realizing more efficient, manufacturable III-Nitride tunnel junctions. Through further investigation and understanding, III-Nitride-based tunnel junction will eventually be a standard and integral part of a large majority of III-Nitride-based optoelectronic devices.

Acknowledgements T.T. would like to thank Prof. Akasaki, Prof. Kamiyama, and Prof. Iwaya for their fruitful discussions and continued encouragements. S.R. would like to thank past and present colleagues Dr. Sriram Krishnamoorthy, Dr. Fatih Akyol, and Mr. Yuewei Zhang (The Ohio State University) and Prof. Digbijoy Nath (Indian Institute of Science). S.R. acknowledges financial support from the U.S. National Science Foundation (NSF ECCS-1408416, NSF DMR-1106177, NSF PFI-AIR TT 1640700), and the Office of Naval Research DATE MURI Program (Program Manager: Dr. Paul Maki). T.T. acknowledges financial support from Japan Society for the Promotion of Science Grant-in-Aid for Research Activity Start-up (22860064), Grant-in-Aid for Scientific Research (C) (23560015), Grant-in-Aid for Science Research (B) (26286045), and Grant-in-Aid for Exploratory Research (15K13959).

References

1. C. Zener, A theory of the electrical breakdown of solid dielectrics. Proc. R. Soc. Lond. Ser. A Contain. Pap. Math. Phys. Charact. **145**(855), 523–529 (1934)
2. L. Esaki, New phenomenon in narrow germanium p−n junctions. Phys. Rev. **109**(2), 603 (1958)
3. D. Sarkar, M. Krall, K. Banerjee, Electron-hole duality during band-to-band tunneling process in graphene-nanoribbon tunnel-field-effect-transistors. Appl. Phys. Lett. **97**(26), 263109 (2010)
4. M. Malinverni, D. Martin, N. Grandjean, InGaN based micro light emitting diodes featuring a buried GaN tunnel junction. Appl. Phys. Lett. **107**(5), 051107 (2015)
5. F. Akyol, S. Krishnamoorthy, S. Rajan, Tunneling-based carrier regeneration in cascaded GaN light emitting diodes to overcome efficiency droop. Appl. Phys. Lett. **103**(8), 081107 (2013)

6. H. Amano, N. Sawaki, I. Akasaki, Y. Toyoda, Metalorganic vapor phase epitaxial growth of a high quality GaN film using an AlN buffer layer. Appl. Phys. Lett. **48**(5), 353–355 (1986)
7. S. Nakamura, T. Mukai, M. Senoh, Candela-class high-brightness InGaN/AlGaN double-heterostructure blue-light-emitting diodes. Appl. Phys. Lett. **64**(13), 1687–1689 (1994)
8. S.R. Jeon, Y.H. Song, H.J. Jang, G.M. Yang, S.W. Hwang, S.J. Son, Lateral current spreading in GaN-based light-emitting diodes utilizing tunnel contact junctions. Appl. Phys. Lett. **78** (21), 3265–3267 (2001)
9. T. Takeuchi, G. Hasnain, S. Corzine, M. Hueschen, R.P. Schneider Jr., C. Kocot, …, L.W. Cook, GaN-based light emitting diodes with tunnel junctions. Jpn. J. Appl. Phys. **40**(8B), L861 (2001)
10. N. Yoshimoto, T. Matsuoka, T. Sasaki, A. Katsui, Photoluminescence of InGaN films grown at high temperature by metalorganic vapor phase epitaxy. Appl. Phys. Lett. **59**(18), 2251–2253 (1991)
11. S. Yamasaki, S. Asami, N. Shibata, M. Koike, K. Manabe, T. Tanaka, …, I. Akasaki, p-type conduction in Mg-doped Ga0. 91In0. 09N grown by metalorganic vapor-phase epitaxy. Appl. Phys. Lett. **66**(9), 1112–1113 (1995)
12. M. Singh, Y. Zhang, J. Singh, U. Mishra, Examination of tunnel junctions in the AlGaN/GaN system: consequences of polarization charge. Appl. Phys. Lett. **77**(12), 1867–1869 (2000)
13. M.J. Grundmann, U.K. Mishra, Multi-color light emitting diode using polarization-induced tunnel junctions. Phys. Status Solidi (C) **4**(7), 2830–2833 (2007) (duplicated with 19)
14. S. Krishnamoorthy et al., Polarization-engineered GaN/InGaN/GaN tunnel diodes. Appl. Phys. Lett. **97**(20), 203502 (2010)
15. I. Ozden, E. Makarona, A.V. Nurmikko, T. Takeuchi, M. Krames, A dual-wavelength indium gallium nitride quantum well light emitting diode. Appl. Phys. Lett. **79**(16), 2532–2534 (2001)
16. M. Diagne, Y. He, H. Zhou, E. Makarona, A.V. Nurmikko, J. Han, …, M. Krames, Vertical cavity violet light emitting diode incorporating an aluminum gallium nitride distributed Bragg mirror and a tunnel junction. Appl. Phys. Lett. **79**(22), 3720–3722 (2001)
17. S.R. Jeon, C.S. Oh, J.W. Yang, G.M. Yang, B.S. Yoo, GaN tunnel junction as a current aperture in a blue surface-emitting light-emitting diode. Appl. Phys. Lett. **80**(11), 1933–1935 (2002)
18. J.J. Wierer, M.R. Krames, J.E. Epler, N.F. Gardner, M.G. Craford, J.R. Wendt, …, M.M. Sigalas, InGaN/GaN quantum-well heterostructure light-emitting diodes employing photonic crystal structures. Appl. Phys. Lett. **84**(19), 3885–3887 (2004)
19. M.J. Grundmann, Polarization-induced tunnel junctions in III-nitrides for optoelectronic applications. Ph.D. dissertation (University of California, Santa Barbara, 2007)
20. S. Krishnamoorthy, P.S. Park, S. Rajan, Demonstration of forward inter-band tunneling in GaN by polarization engineering. Appl. Phys. Lett. **99**(23), 233504 (2011)
21. Y. Kuwano, M. Kaga, T. Morita, K. Yamashita, K. Yagi, M. Iwaya, …, I. Akasaki, Lateral hydrogen diffusion at p-GaN layers in nitride-based light emitting diodes with tunnel junctions. Jpn. J. Appl. Phys. **52**(8S), 08JK12 (2013)
22. M. Kaga, T. Morita, Y. Kuwano, K. Yamashita, K. Yagi, M. Iwaya, …, I. Akasaki, GaInN-based tunnel junctions in n–p–n light emitting diodes. Jpn. J. Appl. Phys. **52**(8S), 08JH06 (2013)
23. S. Krishnamoorthy, F. Akyol, S. Rajan, InGaN/GaN tunnel junctions for hole injection in GaN light emitting diodes. Appl. Phys. Lett. **105**(14), 141104 (2014)
24. H. Kurokawa, M. Kaga, T. Goda, M. Iwaya, T. Takeuchi, S. Kamiyama, …, H. Amano, Multijunction GaInN-based solar cells using a tunnel junction. Appl. Phys. Express **7**(3), 034104 (2014)
25. A. Nakamura, K. Fujii, M. Sugiyama, Y. Nakano, A nitride based polarization-engineered photocathode for water splitting without a p-type semiconductor. Phys. Chem. Chem. Phys. **16**(29), 15326–15330 (2014)

26. M. Watanabe, K. Nakajima, M. Kaga, Y. Kuwano, D. Minamikawa, T. Suzuki, …, I. Akasaki, Over 1000 channel nitride-based micro-light-emitting diode arrays with tunnel junctions. Jpn. J. Appl. Phys. **53**(5S1), 05FL06 (2014)
27. D. Minamikawa, M. Ino, S. Kawai, T. Takeuchi, S. Kamiyama, M. Iwaya, I. Akasaki, GaInN-based tunnel junctions with high InN mole fractions grown by MOVPE. Phys. Status Solidi (B) **252**(5), 1127–1131 (2015)
28. S. Fan, B. AlOtaibi, S.Y. Woo, Y. Wang, G.A. Botton, Z. Mi, High efficiency solar-to-hydrogen conversion on a monolithically integrated InGaN/GaN/Si adaptive tunnel junction photocathode. Nano Lett. **15**(4), 2721–2726 (2015)
29. S.M. Sadaf, Y.H. Ra, H.P.T. Nguyen, M. Djavid, Z. Mi, Alternating-current InGaN/GaN tunnel junction nanowire white-light emitting diodes. Nano Lett. **15**(10), 6696–6701 (2015)
30. F. Akyol, S. Krishnamoorthy, Y. Zhang, S. Rajan, GaN-based three-junction cascaded light-emitting diode with low-resistance InGaN tunnel junctions. Appl. Phys. Express **8**(8), 082103 (2015)
31. J.T. Leonard, E.C. Young, B.P. Yonkee, D.A. Cohen, T. Margalith, S.P. DenBaars, …, S. Nakamura, Demonstration of a III-nitride vertical-cavity surface-emitting laser with a III-nitride tunnel junction intracavity contact. Appl. Phys. Lett. **107**(9), 091105 (2015)
32. S.J. Chang, W.H. Lin, C.T. Yu, GaN-based multiquantum well light-emitting diodes with tunnel-junction-cascaded active regions. IEEE Electron Device Lett. **36**(4), 366–368 (2015)
33. Y. Zhang, S. Krishnamoorthy, J.M. Johnson, F. Akyol, A. Allerman, M.W. Moseley, A. Armstrong, J. Hwang, S. Rajan, Interband tunneling for hole injection in III-nitride ultraviolet emitters. Appl. Phys. Lett. **106**(14), 141103 (2015)
34. Y. Zhang, S. Krishnamoorthy, F. Akyol, S. Khandaker, A. Allerman, M.W. Moseley, …, S. Rajan, Sub 300 nm wavelength III-Nitride tunnel-injected ultraviolet LEDs, in *2015 73rd Annual Device Research Conference (DRC)*, June 2015 (IEEE), pp. 69–70
35. Y. Zhang, S. Krishnamoorthy, F. Akyol, A.A. Allerman, M.W. Moseley, A.M. Armstrong, S. Rajan, Design and demonstration of ultra-wide bandgap AlGaN tunnel junctions. Appl. Phys. Lett. **109**(12), 121102 (2016) (duplicated with 39)
36. M. Ino, D. Takasuka, K. Iwase, T. Takeuchi, S. Kamiyama, M. Iwaya, N. Koide, I. Akasaki, *2015 MRS Fall Meeting*, *Symposium RR*, Boston, 29 Nov–4 Dec
37. B.P. Yonkee, E.C. Young, C. Lee, J.T. Leonard, S.P. DenBaars, J.S. Speck, S. Nakamura, Demonstration of a III-nitride edge-emitting laser diode utilizing a GaN tunnel junction contact. Opt. Express **24**(7), 7816–7822 (2016)
38. H. Okumura, D. Martin, M. Malinverni, N. Grandjean, Backward diodes using heavily Mg-doped GaN growth by ammonia molecular-beam epitaxy. Appl. Phys. Lett. **108**(7), 072102 (2016)
39. H. Liang, P. Tao, X. Xia, Y. Chen, K. Zhang, Y. Liu, …, G. Du, Vertically conducting deep-ultraviolet light-emitting diodes with interband tunneling junction grown on 6H-SiC substrate. Jpn. J. Appl. Phys. **55**(3), 031202 (2016)
40. E.C. Young, B.P. Yonkee, F. Wu, S.H. Oh, S.P. DenBaars, S. Nakamura, J.S. Speck, Hybrid tunnel junction contacts to III–nitride light-emitting diodes. Appl. Phys. Express **9**(2), 022102 (2016)
41. D. Takasuka, Y. Akatsuka, M. Ino, N. Koide, T. Takeuchi, M. Iwaya, …, I. Akasaki, GaInN-based tunnel junctions with graded layers. Appl. Phys. Express **9**(8), 081005 (2016)
42. S.M. Sadaf, Y.H. Ra, T. Szkopek, Z. Mi, Monolithically integrated metal/semiconductor tunnel junction nanowire light-emitting diodes. Nano Lett. **16**(2), 1076–1080 (2016)
43. F. Akyol et al., Low-resistance GaN tunnel homojunctions with 150 kA/cm^2 current and repeatable negative differential resistance. Appl. Phys. Lett. **108**(13), 131103 (2016)
44. J. Simon et al., Polarization-induced Zener tunnel junctions in wide-band-gap heterostructures. Phys. Rev. Lett. **103**(2), 026801 (2009)
45. M.F. Schubert, Interband tunnel junctions for wurtzite III-nitride semiconductors based on heterointerface polarization charges. Phys. Rev. B **81**(3) 035303 (2010)
46. S. Rajan, A. Chini, M.H. Wong, J.S. Speck, U.K. Mishra, N-polar GaN/AlGaN/GaN high electron mobility transistors. J. Appl. Phys. **102**(4), 044501 (2007)

47. S. Krishnamoorthy, F. Akyol, P.S. Park, S. Rajan, Low resistance GaN/InGaN/GaN tunnel junctions. Appl. Phys. Lett. **102**(11), 113503 (2013)
48. F. Akyol, S. Krishnamoorthy, Y. Zhang, J. Johnson, J. Hwang, S. Rajan, Low-resistance GaN tunnel homojunctions with 150 kA/cm^2 current and repeatable negative differential resistance. Appl. Phys. Lett. **108**(13), 131103 (2016)
49. E.O. Kane, Band tails in semiconductors. Solid-State Electron. **28**(1–2), 3–10 (1985)
50. D.M. Kozuch, M. Stavola, S.J. Pearton, C.R. Abernathy, W.S. Hobson, Passivation of carbon-doped GaAs layers by hydrogen introduced by annealing and growth ambients. J. Appl. Phys. **73**(8), 3716–3724 (1993)
51. H. Amano, M. Kito, K. Hiramatsu, I. Akasaki, P-type conduction in Mg-doped GaN treated with low-energy electron beam irradiation (LEEBI). Jpn. J. Appl. Phys. **28**(12A), L2112 (1989)
52. S. Nakamura, N. Iwasa, M. Senoh, T. Mukai, Hole compensation mechanism of p-type GaN films. Jpn. J. Appl. Phys. **31**(5R), 1258 (1992)
53. J. Neugebauer, C.G. Van de Walle, Role of hydrogen in doping of GaN. Appl. Phys. Lett. **68**, 1996 (1829)
54. J.I. Pankove, C.W. Magee, R.O. Wance, Hole-mediated chemisorption of atomic hydrogen in silicon. Appl. Phys. Lett. **47**(7), 748–750 (1985)
55. J. Ran, X. Wang, G. Hu, J. Wang, J. Li, C. Wang, …, J. Li, Study on Mg memory effect in npn type AlGaN/GaN HBT structures grown by MOCVD. Microelectron. J. **37**(7), 583–585 (2006)
56. P. Zhou, J. Cheng, C.F. Schaus, S.Z. Sun, K. Zheng, E. Armour, …, G.A. Vawter, Low series resistance high-efficiency GaAs/AlGaAs vertical-cavity surface-emitting lasers with continuously graded mirrors grown by MOCVD. IEEE Photonics Technol. Lett. **3**(7), 591–593 (1991)
57. Y.C. Shen, G.O. Mueller, S. Watanabe, N.F. Gardner, A. Munkholm, M.R. Krames, Auger recombination in InGaN measured by photoluminescence. Appl. Phys. Lett. **91**(14), 1101 (2007)
58. D.L. Huffaker, D.G. Deppe, K. Kumar, T.J. Rogers, Native-oxide defined ring contact for low threshold vertical-cavity lasers. Appl. Phys. Lett. **65**(1), 97–99 (1994)
59. J.J. Wierer, D.A. Kellogg, N. Holonyak Jr., Tunnel contact junction native-oxide aperture and mirror vertical-cavity surface-emitting lasers and resonant-cavity light-emitting diodes. Appl. Phys. Lett. **74**(7), 926–928 (1999)
60. Y. Zhang, A.A. Allerman, S. Krishnamoorthy, F. Akyol, M.W. Moseley, A.M. Armstrong, S. Rajan, Enhanced light extraction in tunnel junction-enabled top emitting UV LEDs. Appl. Phys. Express **9**(5), 052102 (2016)
61. Y. Zhang, S. Krishnamoorthy, J.M. Johnson, F. Akyol, A. Allerman, M.W. Moseley, A. Armstrong, J. Hwang, S. Rajan, *International Workshop for Nitrides 2016* (Orlando FL)

Chapter 9
Green, Yellow, and Red LEDs

Jongil Hwang, Rei Hashimoto and Shinji Saito

Abstract A study to overcome the "green gap" problem is introduced. We show a breakthrough achieved by two-step growth with adopting AlGaN interlayer in this chapter. Bright yellow, amber with red LEDs and an application of phosphor-free white LED are demonstrated.

9.1 Introduction

InGaN-based semiconductor light-emitting diodes (LEDs) have been commercialized for high-efficiency solid-state lighting. The InGaN compounds have a direct band gap of from 0.7 to 3.4 eV corresponding to luminous wavelengths of 365–1900 nm, which include the entire visible spectrum. Recently, high-efficiency blue LEDs have been developed. For example, Narukawa et al. reported a peak wall-plug efficiency (WPE) of blue LEDs of 81.3% [1]. The WPE can be described as the product of three partial efficiencies: internal radiation η_i, light extraction η_{LEE}, and voltage efficiency η_v,

$$WPE = \eta_i \times \eta_{LEE} \times \eta_V.$$

The WPE of 81.3% indicates that the average of these parameters is over 93%. White LEDs can be constructed using a combination of a blue LED with phosphors that convert the blue light into yellow light (Fig. 9.1a). Owing to the high efficiency of the blue LEDs, the peak luminous efficacy of radiation (LER) of these white LEDs exceeds 250 lm/W [1], which is approaching the theoretical limits. However,

J. Hwang
Corporate Research and Development Center, Toshiba Corporation,
1, Komukai-Toshiba-cho, Saiwai-ku, Kawasaki 212-8582, Japan

R. Hashimoto · S. Saito (✉)
Corporate Manufacturing Engineering Center, Toshiba Corporation, 33, Shin-Isogo-Cho,
Isogo-ku, Yokohama 235-0017, Japan
e-mail: sh.saito@toshiba.co.jp

© Springer Nature Singapore Pte Ltd. 2017

T.-Y. Seong et al. (eds.), *III-Nitride Based Light Emitting Diodes and Applications*,
Topics in Applied Physics 133, DOI 10.1007/978-981-10-3755-9_9

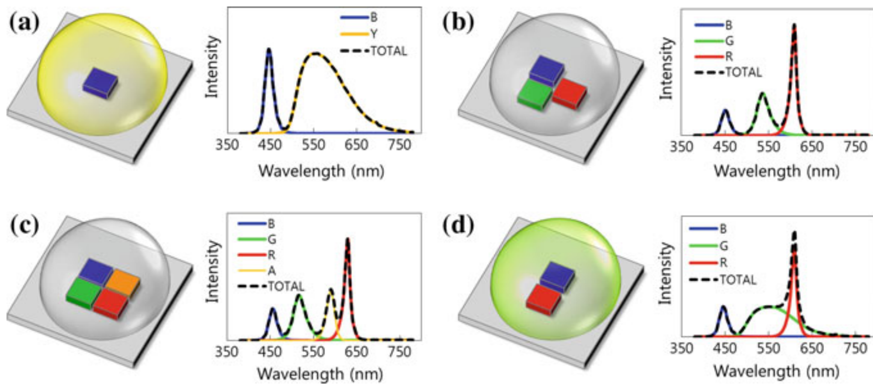

Fig. 9.1 White LED assemblies and spectra. **a** Blue LED with a yellow phosphor, **b** RGB LEDs, **c** RBGA LEDs, and **d** RB LEDs with a green phosphor

this kind of white LED emitting blue and yellow light is limited to a very low color rendering index (CRI) because of lack of spectra in other visible regions. This is increasingly becoming an important issue in terms of prospects for next-generation white LEDs in which a high CRI is desired. LEDs emitting a mixture of red, green, and blue (RGB) without using phosphors have been proposed (Fig. 9.1b) for the next generation of white LEDs. Theoretically, ideal efficacy with high CRI can be achieved in color-mixing LEDs because of the elimination of Stokes loss. The visible region can be fully covered by adding amber to RGB (RGBA), resulting in the most natural illumination (Fig. 9.1c). This color-mixing LED is expected to be an ideal light source in terms of CRI and efficacy. The U.S. Department of Energy has presented a roadmap for the efficacy of high-CRI LED-based solid-state lighting [2], noting that color-mixing LEDs are the most efficient light source under ideal conditions. However, due to the limited WPE of green LEDs in actual use, the report anticipated that RB LEDs with a green phosphor would serve as a practical candidate (Fig. 9.1d). Conversely, this also indicates that color-mixing LEDs have the potential for practical use if the power conversion efficiency of green LEDs can be made to exceed expectations. We have started development using an unconventional approach to realize high-efficiency green and yellow LEDs and to further develop red LEDs by replacing AlInGaP LEDs with nitride-based ones.

9.2 The "Green Gap"

9.2.1 Phosphor-Conversion LEDs and Color-Mixing RGB LEDs

In conventional white LEDs, Stokes loss inevitably occurs due to light conversion from blue to other colors. Numerical simulations have indicated that an LER of

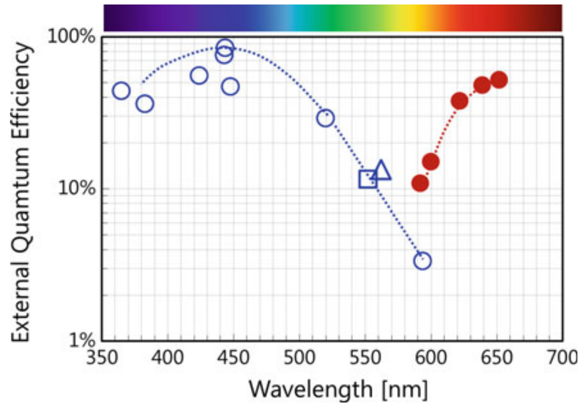

Fig. 9.2 EQE of conventional LEDs in the visible region [2–8]. AlInGaN-based LEDs on c-plane polar surface (*open circles*), on (11–22) surface (*open triangles*), on (2021) surface (*open squares*), and AlGaInP-based LEDs (*filled circles*)

350–450 lm/W is achievable by means of color-mixing LEDs if the power conversion efficiency of each color can be increased to 60% [2]. This is possible by using LED chips that emit primary colors. Color-mixing LEDs such as RGB LEDs and RGBA LEDs are capable of maximal efficacy.

High-efficiency LEDs in the green-to-amber region are required in order to achieve high-performance RGB LEDs. However, the external quantum efficiency (EQE) of conventional LEDs rapidly drops in this spectral range. Figure 9.2 shows the EQEs of LEDs plotted against wavelength [1, 3–8]. The reported EQEs are over 30% in green LEDs, about 10% in yellow LEDs, and a few percent in amber LEDs. Although high-efficiency LEDs have been developed in the amber region and longer wavelengths using AlInGaP-based quaternary LEDs, the low EQE still remains in the green-yellow region. This problem is known as the “green gap” and remains a major obstacle to the development of full-LED white light sources with a high CRI and LER.

To address the green gap problem from the longer wavelength side, the emission wavelength of the AlInGaP system can be shortened by increasing the aluminum content in the quantum well (QW). However, this also decreases the potential barrier height to the QW state, resulting in decreased carrier confinement. The AlInGaP system is therefore limited in terms of band engineering. The band gap is also strongly dependent on temperature, even for AlInGaP in the red spectral region where a high EQE has been obtained [9]. This is an important subject in terms of the thermal stability of the white balance radiated from color-mixing RGB LEDs, even when a high-efficiency AlInGaP LEDs is used as the red source. In contrast, it is possible to design the potential barrier in the InGaN system to be sufficiently higher than the QW across the entire visible wavelength range. In addition, this nitride has superior temperature stability of the band gap, resulting in stable emission wavelength regardless of temperature [10]. From the perspective of fundamental physical properties, InGaN-based LEDs are considered to be a potential candidate for efficient and stable RGB LEDs. To develop an ideal RGB LED entirely based on the InGaN system, it is important to examine the possibility of realizing InGaN-based LEDs with longer wavelengths including the red region.

9.2.2 *Obstacles in InGaN Systems with High Indium Content*

There have been two major challenging issues for growing InGaN with high indium content.

First, degradation of InGaN crystal becomes significant as the indium content is increased. Segregations and excess phases also tend to form due to the miscibility gap in the InGaN crystal phase. Several types of defects such as V-shaped pits (Vpits) that form at crystallographic dislocations also appear with increasing indium content.

The second problem is the quantum-confined Stark effect (QCSE). Because InGaN is a piezoelectric crystal, the stress caused by lattice mismatch induces a piezoelectric field in the InGaN QW. The wave functions of the electrons and holes in the QW are shifted in the opposite direction to each other due to the internal electric field as depicted in Fig. 9.3a, resulting in a decrease in the overlap integral and thereby in radiative recombination rates.

One approach to controlling the QCSE is to use nonpolar or semipolar substrates. The overlap between the electron and hole wave functions can be enhanced by reduced generation of the piezoelectric field in comparison with polar surfaces [11]. An LED in the green gap region has been fabricated using semipolar GaN substrates [7, 8]. However, it is difficult to incorporate indium into a GaN host during growth on nonpolar or semipolar surfaces [12, 13]. Doing so requires careful selection of the surface orientation and the growth conditions. The two issues of crystal degradation and the QCSE thus remain interlinked in the practical growth of InGaN QWs.

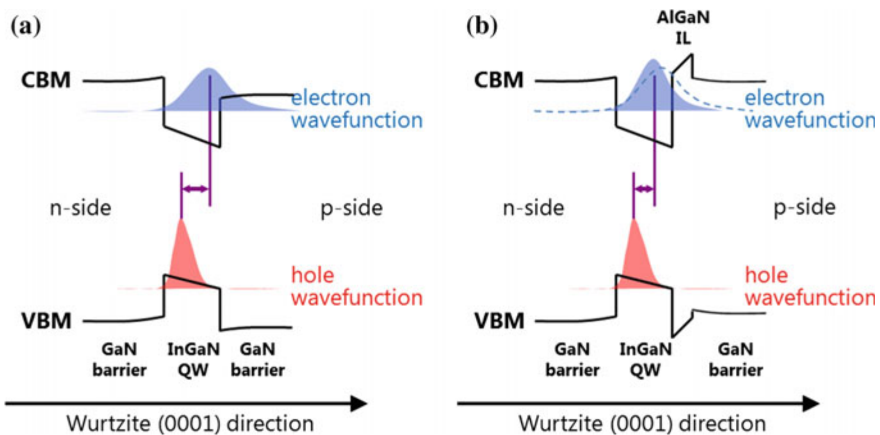

Fig. 9.3 Band diagram of InGaN quantum QW and QB layer **a** grown on a (0001) polar surface, and **b** in the case of AlGaN IL embedded on the (0001) side of a QW

From the viewpoint of productivity and compatibility with conventional LED fabrication processes, it is preferable for the green gap LED technology to use c-face sapphire substrates on which high indium incorporation can be obtained. An approach to controlling the QCSE can be employed together with band engineering utilizing c-face sapphire substrates. We adopted this strategy, namely, designing and optimizing layer structures in multiple-quantum wells (MQWs) grown on a polar surface. To improve carrier confinement, an AlGaN interlayer (IL) was embedded in each InGaN QW (Fig. 9.3b). This IL also plays a role in crystal growth, which is discussed later. By optimizing the layer structure and the InGaN growth conditions, we were able to obtain InGaN-based MQWs of very high quality and thereby able to achieve high-intensity emissions in the longer wavelength region. The remainder of this section discusses a strategy for overcoming these remaining challenges. Sections 9.3 and 9.4 introduce a growth method and layer structure design for obtaining high-quality active layers in LEDs [14–16]. These sections discuss both optimization of InGaN growth and the effects of local layer structures such as AlGaN IL and short-period quantum barrier (QB) on optical properties. Section 9.5 introduces the device properties based on these results [17, 18], and also presents the application of phosphor-free white light sources such as multi-color MQW and stacked LED chip structures.

9.3 Growth of InGaN Films with High Indium Content

9.3.1 Immiscibility of Indium Incorporation into GaN

The crystal growth of InGaN with high indium content has been widely studied, and several issues have been identified. First, compositional phase separation has been predicted to occur because of the immiscibility of indium in GaN. For strained InGaN grown on GaN, theoretical studies have predicted that phase separation occurs around $x = 0.5$ in $In_xGaN_{1-x}N$ [19, 20]. Second, strain relaxation of InGaN occurs according to the critical thickness. This lowers the maximum indium content giving rise to phase separation, observed experimentally at $x = 0.28$ [21, 22]. Third, crystallographic degradation of MQWs occurs in subsequent high-temperature processes such as p-GaN layer formation following MQW growth [23]. This promotes strain relaxation [24, 25]. In the long wavelength region, therefore, strain relaxation and post processing are critical for crystal quality. As shown in Fig. 9.4, PL intensity decreases exponentially with increasing wavelength. Meanwhile the density of Vpits that appear on the surface increases drastically with increasing indium content [26]. Although threading dislocations (TD) trigger the formation of Vpits during InGaN growth [27–29], the Vpits density in sample B exceeded 1×10^{12} cm^{-2}, much higher than the TD density of 1×10^{9} cm^{-2} in the GaN substrate.

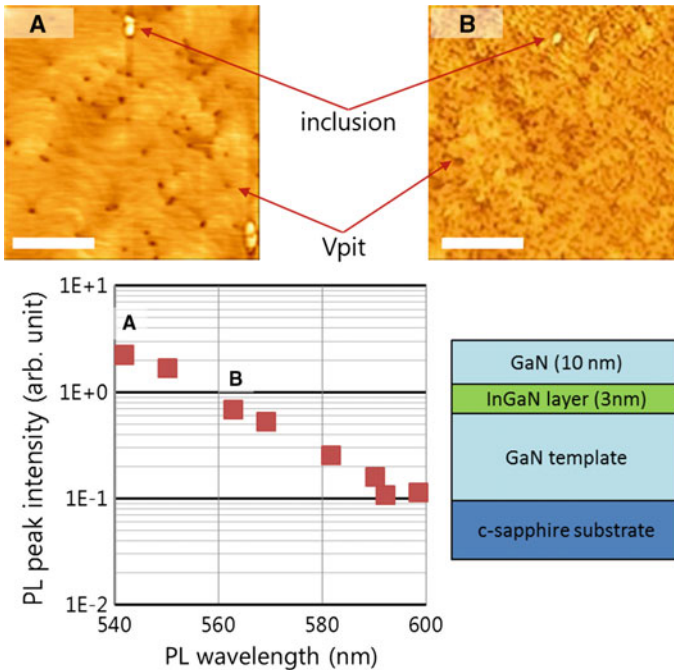

Fig. 9.4 PL peak intensity versus wavelength. AFM image labeled as *A* and *B* is also shown. The scale bar in the AFM image represents 1 μm

It has been suggested that the nonradiative center of the TD density is suppressed by the Vpits that form in the active layer [30]. In the present PL measurements, in contrast, the intensity decreases exponentially with increasing indium content to generate the Vpits (Fig. 9.4). This suggests that most of the observed Vpits suppress radiative recombination in the active layer.

With reference to accumulation of compressive strain in QWs with increasing indium content, Vpits also form through strain relaxation [29, 31]. The strain relaxation occurs by inducing planar defects such as stacking faults (SFs) and misfit dislocations (MDs) around the QW [32], resulting in the formation of emerging vertical defects such as SF boundaries [33] and symmetrical pairs of inclined dislocations [34]. Furthermore, atomic defects and inclusions are often observed on the surface of InGaN with high indium content [35].

Thus, one can see that in the long wavelength region, a variety of defects may be generated accompanying strain relaxation in MQWs. These defects (SFs and MDs resulting in Vpits) dominate the degradation of optical properties [36]. Therefore, InGaN with high indium content primarily requires suppression of such defects while the QCSE still acts in the InGaN layer.

9.3.2 Growth of MQWs at High Temperatures and High Growth Rates

An epitaxial film was grown by MOCVD [15, 17, 18]. Trimethylgallium (TMGa), trimethylindium (TMIn), and trimethylaluminum (TMAl) were used as the group-III source materials and ammonia (NH3) was used as the group-V source material. Hydrogen and nitrogen were used as the carrier gases. A 2-μm-thick undoped GaN layer was grown on a c-plane sapphire substrate. First, we investigated the dependency of indium content of the $In_xGa_{1-x}N$ layer on growth rate and growth temperature (T_g) at 760 Torr. We estimated the indium content by means of X-ray diffraction measurements. For this, 3-nm-thick InGaN was grown on the GaN/sapphire template as the test structure.

Figure 9.5 shows the indium content obtained at several T_g versus growth rate. This shows that the indium content increases with increasing growth rate. Indium content of over $x = 0.35$ was obtained at the lowest T_g of 715 °C. At a T_g of 715 °C, an indium content of $x = 0.23$ was obtained at a growth rate of 0.5 nm/min. The same indium content was obtained even at the higher T_g of 775 °C when the growth rate was set to 5.2 nm/min. We changed the growth rate by changing the molar flux of metal–organic sources at a fixed NH_3 flow rate (changed V/III ratio).

The surface morphologies of InGaN with the same indium content of $x = 0.23$ were compared by means of atomic force microscopy (AFM) between samples grown using different growth condition: (I) 715 °C and 0.5 nm/min; (II) 745 °C and 1.5 nm/min; and (III) 775 °C and 5.2 nm/min (labeled in Fig. 9.5). As seen in Fig. 9.6, the Vpits density decreases exponentially and the atomic step-and-terrace structure becomes observable as the growth rate and the T_g are increased. As a result, the root mean square (RMS) surface roughness was improved (Fig. 9.6e). These results can be attributed to enhanced migration length in the reaction rate of the group III species by increasing the T_g under lowered V/III ratio [37].

Figure 9.7 shows photoluminescence (PL) micrographs of InGaN/GaN MQW samples. The MQW consisted of four periods of GaN barrier layer and 3-nm-thick

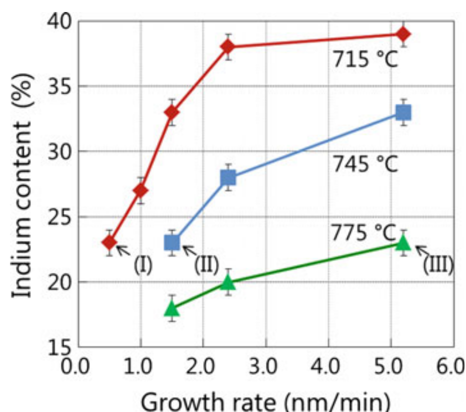

Fig. 9.5 Indium content of InGaN grown at several growth temperatures and growth rates. Reproduced with permission from [14], copyright 2013 Wiley

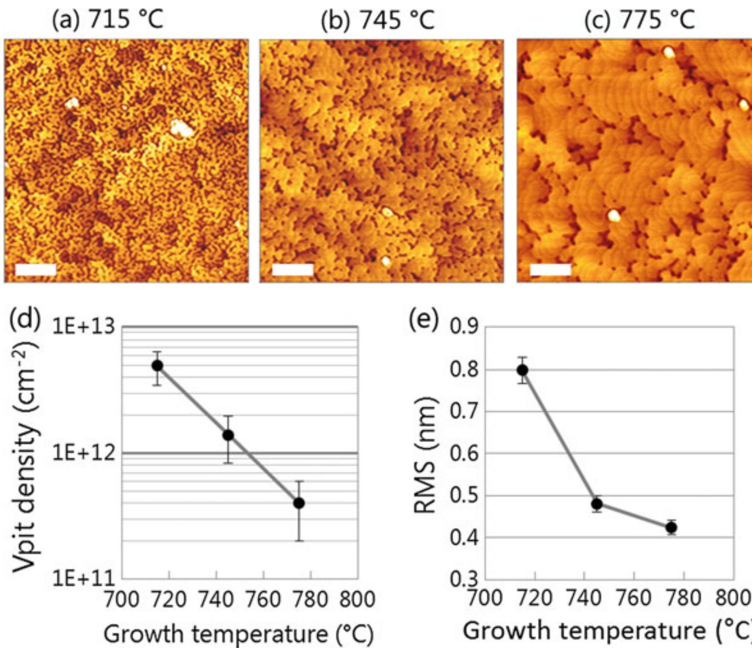

Fig. 9.6 AFM images of InGaN grown using conditions **a** I, **b** II, and **c** III, respectively. The *scale bar* represents 500 nm. The **d** Vpit density and **e** RMS value are also shown. Reproduced with permission from [14], copyright 2013 Wiley

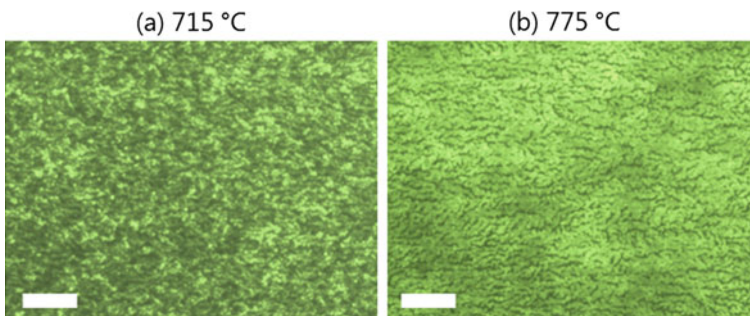

Fig. 9.7 PL micrograph of InGaN/GaN MQW with each set of QW growth conditions **a** I and **b** II, respectively. The *scale bar* represents 10 μm. Reproduced with permission from [14], copyright 2013 Wiley

InGaN QW layer grown under QW growth conditions of (I) 715 °C and 0.5 nm/min and (III) 775 °C and 5.2 nm/min, with a fixed GaN barrier conditions. The bright area is obviously larger in the 775 °C sample compared with the 715 °C sample. This is consistent with the improvements in the surface morphology, as seen in Fig. 9.6. We believe that the improved luminous area relates to the

reduction of surface Vpits. These results indicate that growth conditions of 775 °C and 5.2 nm/min are advantageous for the fabrication of green-yellow LEDs.

In contrast, as seen in the AFM image in Fig. 9.6, indium inclusions still exist even under growth conditions with high growth rate and T_g. It is thought that indium inclusions relate to not only the QW growth but also the subsequent GaN barrier growth process [35, 38].

Next, we investigated the effect of the T_g of the GaN barrier layers on the surface morphology. For this, three samples of MQW structures were fabricated using barrier layer growth conditions of (a) 830 °C, (b) 890 °C, and (c) 920 °C with fixed QW growth conditions.

Figure 9.8 shows an AFM image measured on top of the fourth GaN barrier layer of the MQW structure. From the AFM image of the GaN barrier grown at 830 °C, Vpits and inclusions were observed. However, the inclusions disappeared and the radii of Vpits decreased with increasing T_g.

PL micrographs of the MQW samples are shown in Fig. 9.9. From these, the degradation of the optical morphology was observed at higher T_g. The dark spots became more prominent at 920 °C compared with 830 °C, even when the surface

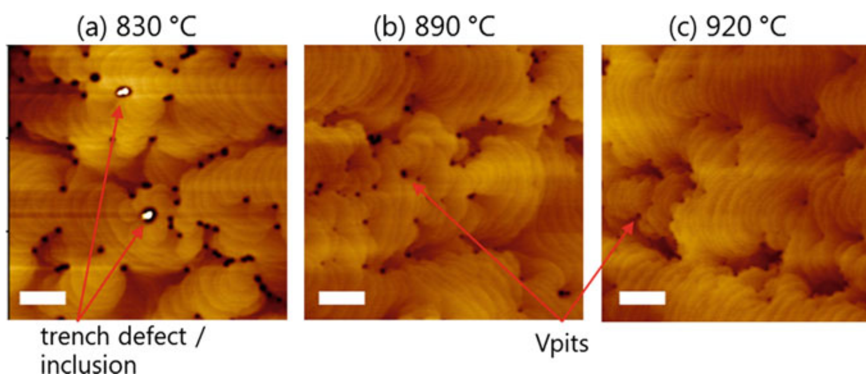

Fig. 9.8 AFM images of the MQW structure with QB grown at **a** 830, **b** 890, and **c** 920 °C, respectively. The *scale bar* represents 500 nm. Reproduced with permission from [15], copyright 2013 Wiley

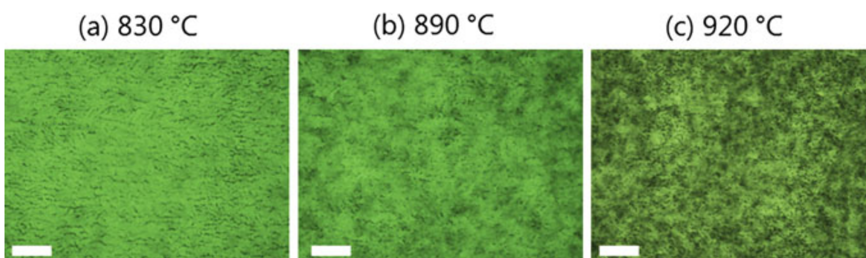

Fig. 9.9 PL micrograph of InGaN/GaN MQW with QB growth conditions of **a** 830, **b** 890, and **c** 890 °C, respectively. The *scale bar* represents 10 μm

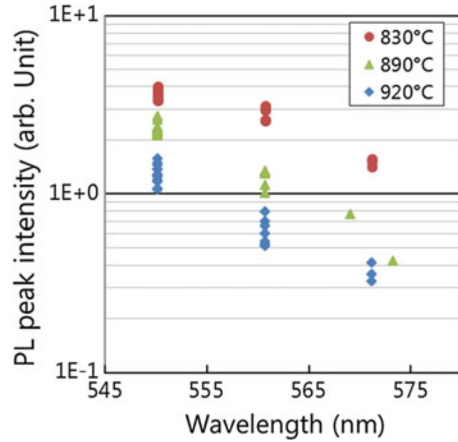

Fig. 9.10 PL intensity versus PL wavelength

morphology was improved as seen in AFM images (Fig. 9.8). As shown in Fig. 9.10, the PL intensity decreased across the entire wavelength range as the T_g of the barrier layer increased. The discrepancy between the surface morphology and optical uniformity depending on the growth conditions suggests that the thermal budget due to the post-growth sequence of InGaN QWs largely affects the optical properties. This leads us to conclude that controlling both the atomic surface and the thermal budget during the growth needs to be carefully optimized to improve optical properties. To suppress inclusions and trench defects without a thermal budget, further methods such as adding hydrogen to QB growth should be considered [35].

9.4 Local Structure in MQWs

9.4.1 Effect of Thin AlGaN Capping IL onto Each QW Layer

As shown in Fig. 9.3, the strain-induced piezoelectric field in InGaN QW shifts the electron and hole wave functions in opposite directions. In the case of a QW with high indium content, the wave function penetrates into adjacent QB regions, especially for electrons. These wave functions tend to couple with defects around the interface, and further tunnel into the potential barriers tilted when forward bias is applied. To confine the wave function adequately into the QW region, we adopted AlGaN IL embedding on each QW layer.

The AlGaN embedded on the (0001) side of the QW confines the electron wave function tightly within the QW region, resulting in enhancement of the overlap integral between electrons and holes. In contrast, the AlGaN IL affects the crystallinity. To clarify the effect of the AlGaN IL, we investigated the surface morphology and the evolution toward stacking layers.

Figure 9.11 shows AFM images observed at corresponding surfaces. On the QW surface (Fig. 9.11a), an atomic step-and-terrace structure was observed. The density of the Vpits was estimated to be 5×10^8 cm^{-2}, which is comparable to the TD density. After the growth of the AlGaN IL, the surface morphology became uniform in case of 30% aluminum content (Fig. 9.11b), while a three-dimensional structure appeared in case of 90% (Fig. 9.11d) because of a large mismatch in the lattice constant between the InGaN QW and the AlGaN IL with much higher aluminum content. After the growth of the barrier layer, however, the surface morphology in case of the 90% aluminum content was markedly improved (Fig. 9.11e). The diameter of the Vpits was smaller than that in the case of 30% aluminum content (Fig. 9.11c). This shows that the surface morphology and the evolution of the layer stacking depend on the aluminum content in the AlGaN IL. No clear lattice relaxation was observed in the reciprocal space mapping even for 100% aluminum content. It is thought that in-plane defects such as MDs and/or SFs are suppressed by inserting the AlGaN IL through strain compensation, resulting in a reduction of Vpits [39] (Fig. 9.12).

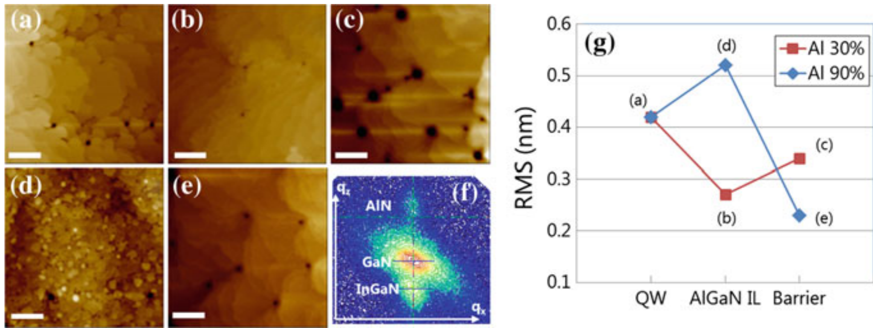

Fig. 9.11 AFM images of each layer surface. **a** InGaN QW, **b**, **d** AlGaN IL and **c**, **e** following GaN barrier, for aluminum content 30% (**b**, **c**) and 90% (**d**, **e**). The *scale bar* represents 200 nm. **f** Reciprocal space mapping in the case of 100% aluminum content in the IL. **g** RMS values extracted from each surface labeled of corresponding AFM. Reproduced with permission from [18], copyright 2014 Japan Society of Applied Physics

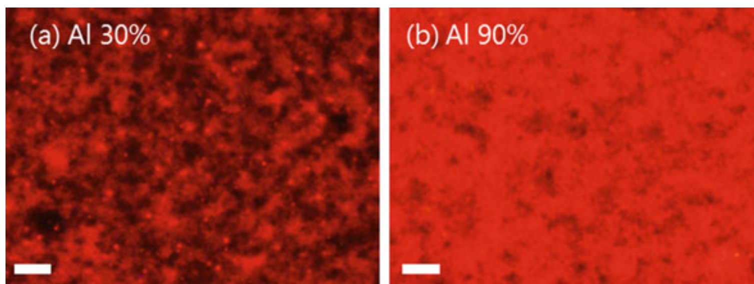

Fig. 9.12 PL micrograph of InGaN/GaN MQW in the *red* region with **a** 30% and **b** 90% aluminum content in AlGaN IL. Reproduced with permission from [18], copyright 2014 Japan Society of Applied Physics

The effect of the AlGaN IL is seen in cases of even higher indium content. Bright emissions in the red spectral region were obtained by increasing the aluminum content up to 90%. This emphasizes that the AlGaN IL plays an important role in the crystal quality.

9.4.2 Effect of Short-Period InGaN/GaN Barrier Layer

As mentioned above, the growth conditions of the barrier layer have an impact on optical properties. As seen in Sect. 9.3.2, the surface morphology can be improved by increasing the T_g of the QB, but this also degrades the optical properties (See Fig. 9.9). We therefore show the effects of the structure on the optical properties in this section instead. In general, it is thought that increasing the average indium content of the entire MQW tends to induce lattice relaxation due to stress accumulation. This behavior is expected by inserting InGaN into the barrier layer. On the other hand, the InGaN barrier layer may contribute to reduce QCSE through strain modulation in the barrier layer. For instance, two pairs of InGaN/GaN with thickness of 1 nm each can be embedded instead of the front part of the GaN barrier. As shown in Fig. 9.13, a short-period superlattice (SL) QB was confirmed by cross-sectional transmission electron microscopy (TEM). In the MQWs, no drastic degradation such as generation of emerging Vpits was observed.

To evaluate the effects of the InGaN/GaN short-period SL QB, we investigated the PL properties of the intensity, the decay time, and the excitation power dependence. The magnitude of the internal electric field in the QW can also be deduced from the excitation-power dependence.

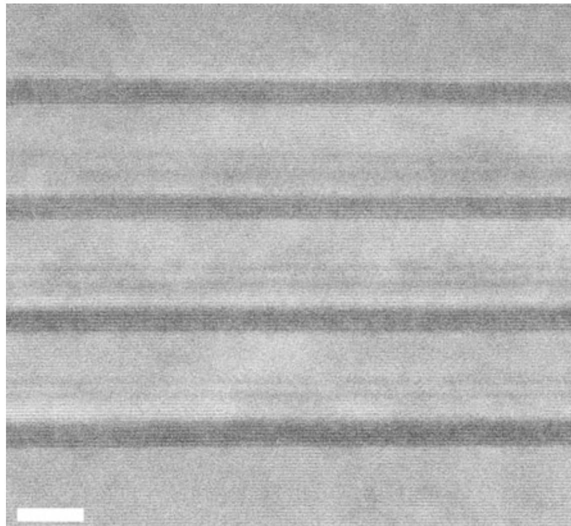

Fig. 9.13 Cross-sectional TEM image of MQW with InGaN/GaN short-period SL QB. The *scale bar* represents 10 nm

For the PL measurements, we prepared samples as references (labeled A to C), each with three different wavelengths and samples with the InGaN/GaN short-period SL QB (labeled D to F). Time-resolved PL spectra were measured using a pulsed dye laser ($\lambda = 390$ nm, selective excitation of the QW layer) excited by nitrogen gas laser. The time width of the pulse and the spot size were 800 ps and 2 mm diameter, respectively. Excitation intensity could be changed from 0.5 to 0.005 MW/cm^2 by using a set of neutral density filters. Time-resolved PL spectra were obtained using a streak camera. The time resolution was sufficient (20 ps) compared with the time width of the excitation pulse. The PL decay curve and the PL spectrum were obtained by integrating the time-resolved spectrum over time and energy (wavelength), respectively. PL decay time was estimated from the tail part of spectra excited at the minimum power (0.005 MW/cm^2). All PL measurements were performed at room temperature.

Figure 9.14 shows the blueshift in the region from 570 to 470 nm depending on the excitation power. The peak shift can be explained by taking into account the band filling and the built-in electric field screening by the photogenerated carriers [35]. To evaluate the magnitude of the internal electric field, we analyzed the peak shift using a simple model in which a triangular potential well is assumed to be produced by the sum of both the built-in electric field and the photogenerated carriers [40, 41]. In this model, it is assumed that the photogenerated carriers accumulate at well/barrier interfaces. The transition energy can then be evaluated as

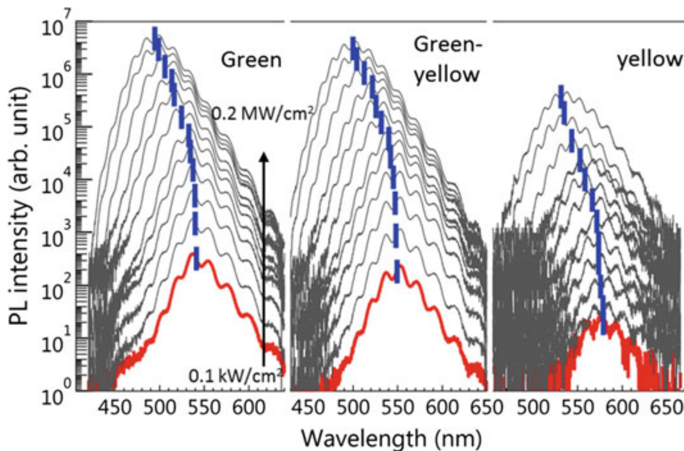

Fig. 9.14 PL spectra and excitation-power dependency. Reproduced with permission from [16], copyright 2013 Society of Photo Optical Instrumentation Engineers

$$
\begin{aligned}
h\nu &= E_g - eF(\sigma)L_w + \left[\frac{9ehF(\sigma)}{16\sqrt{2}}\right]^{2/3}\left[\left(\frac{1}{m_e^*}\right)+\left(\frac{1}{m_h^*}\right)\right]^{1/3} \\
F(\sigma) &= F_0 + \frac{eL_b\sigma}{\varepsilon_0(L_w\varepsilon_b + Lb\varepsilon_w)}.
\end{aligned}
\tag{9.1}
$$

where ε_0, h, and e are the dielectric constant of vacuum, the Planck's constant, and the elementary charge, respectively, E_g and $m^*_{e,h}$ are the bandgap energy and effective masses of electrons and holes, $L_{w,\,b}$ and $\varepsilon_{w,\,b}$ are the width and the relative dielectric constant of the QW and the QB, F_0 is the internal electric field composed of the sum of the piezo and the spontaneous polarization, and σ is the two-dimensional density of the photogenerated carriers which can be expressed by the formula $\sigma = \alpha\tau PL_w/h\nu^{exc}$ using the absorption coefficient α, carrier lifetime τ, excitation power P, and photon energy $h\nu^{exc}$, and L_w. The constants used in the calculation are listed in Table 9.1. The $h\nu$ in formula (9.1) was fitted to the experimental peak position over P with E_g and F_0 as the fitting parameters. As shown by the dashed line in Fig. 9.15a, the best fit to the experimental data was obtained for $F_0 = 2.85$ ($\lambda = 540.8$) and 3.07 (551.8) for the reference samples (sample A to C), and 2.35 (520.2), 2.60 (531.2), and 3.50 (562.8) for the samples with the InGaN/GaN short-period SL QB (sample E to G). The estimated values of the internal electric field were 30% smaller than the theoretical values estimated by the piezoelectric and elastic constants from the binary values [42]. This may be attributable to the approximation used in the calculation [40, 43].

Figure 9.15c shows PL decay curves of the MQW with (sample E) and without (sample A) InGaN/GaN short-period SL QB measured at low-level excitation, with both exhibiting almost the same wavelength of 531 nm (Fig. 9.15b). The time and relative intensity are shown by the vertical and horizontal axes, respectively. The PL decay curves exhibited single-exponential behavior, and the slope of sample E was smaller than that of sample A. The decay time τ was deduced to be 78.7 ns for sample A and 125.1 ns for sample E, and the PL intensity was higher in sample E.

The wavelength dependence of the PL intensity, and F_0 of all samples thus deduced are shown in Fig. 9.16. The magnitude of F_0 monotonically increases with increasing wavelength. This shows that the wavelength dependence is almost the same for the samples with and without the InGaN/GaN short-period SL QB, indicating that however, the τ_{PL} and PL intensity were both enhanced compared with the reference sample in the wavelength range measured here. This is attributable to a reduction in nonradiative recombination. This suggests that the InGaN

Table 9.1 Material parameters used in calculations

Parameter		Parameter	
L_w (nm)	3	m_e^*	0.2 m
L_b (nm)	10	m_h^*	1.0 m
ε_w	10.4	α (cm^{-1})	1×10^5
ε_b	8.9	τ (ns)	100

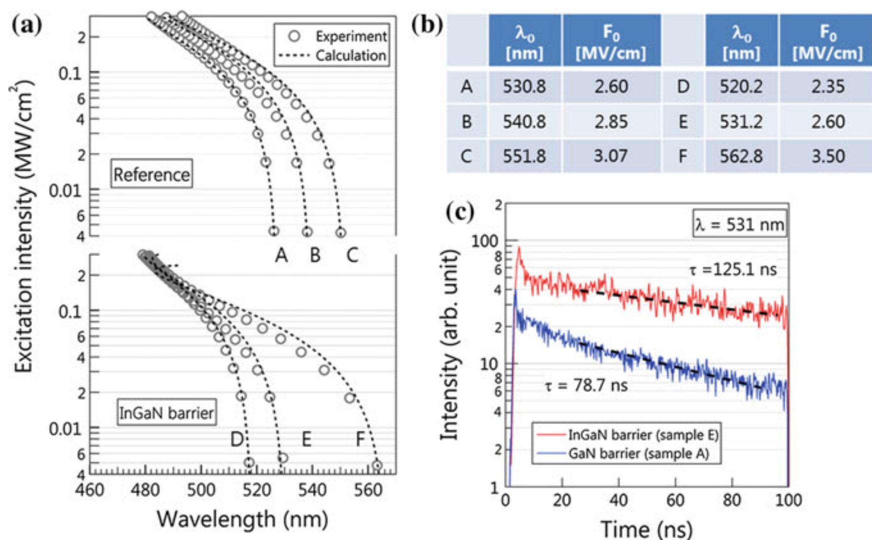

	λ_0 [nm]	F_0 [MV/cm]		λ_0 [nm]	F_0 [MV/cm]
A	530.8	2.60	D	520.2	2.35
B	540.8	2.85	E	531.2	2.60
C	551.8	3.07	F	562.8	3.50

Fig. 9.15 **a** PL peak wavelength versus excitation power dependency. **b** Parameters of the best fit. **c** PL decay curves. Reproduced with permission from [16], copyright 2013 Society of Photo Optical Instrumentation Engineers

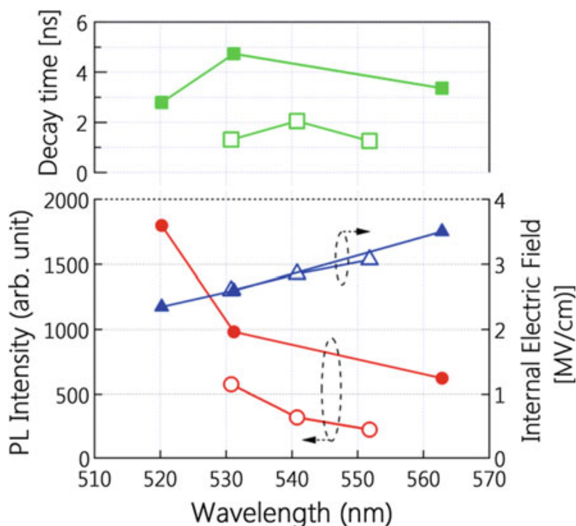

Fig. 9.16 PL decay time, intensity, and estimated internal electric field versus wavelength. Reproduced with permission from [16], copyright 2013 Society of Photo Optical Instrumentation Engineers

short-period SL QB dominantly suppresses the degradation of the crystal quality rather than the QCSE. This scenario suggests that the internal quantum efficiency can be improved through the suppression of the degradation of InGaN QW by optimizing the local structure as well as the growth conditions.

As seen in these sections, we optimized the growth conditions and the local structures of both QW and QB, and then based on the optimization, we fabricated LED devices and investigated their electroluminescence (EL) properties. The device properties are discussed in the next section.

9.5 Device Performance and Characteristics

9.5.1 Device Structure

Figure 9.17 shows a schematic of a longer wavelength LED fabricated on a conventional sapphire (0001) patterned substrate. The active region employs a 4 or 5-period multi-QW structure consisting of a 3-nm-thick InGaN QW layer, a 1-nm-thick AlGaN IL, and a 10-nm-thick barrier with InGaN/GaN short-period SL QB with the growth conditions introduced in Sect. 9.3. Indium content in the InGaN QW and aluminum content in the AlGaN IL are adequately determined based on the emission wavelength. For wavelengths in the range of 540–630 nm, the InGaN QW and AlGaN IL need approximately 20–35% indium and 30–90% aluminum content, respectively. In MQW growth, the growth temperature of the well layer and AlGaN IL was 715–775 °C, and a two-step temperature growth method was used such that the T_g of the barrier layer was about 100 °C higher than that of the well layer and AlGaN IL. We thus tuned the composition and obtained bright LEDs across the entire visible range from blue to red (photographs shown in Fig. 9.18). A p-type GaN layer and a p+-GaN contact layer were grown after the last barrier layer. The simple device structure with a face-up structure was adopted by applying an indium tin oxide p-type transparent contact with Ti/Pt/Au pad metals and Ti/Pt/Au n-type electrodes.

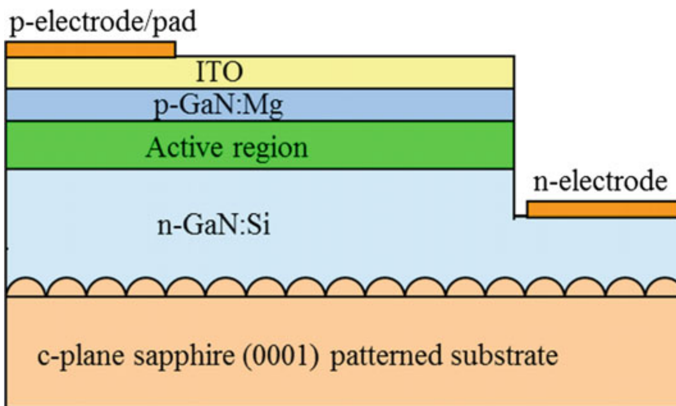

Fig. 9.17 Schematic of the structure of the fabricated LEDs

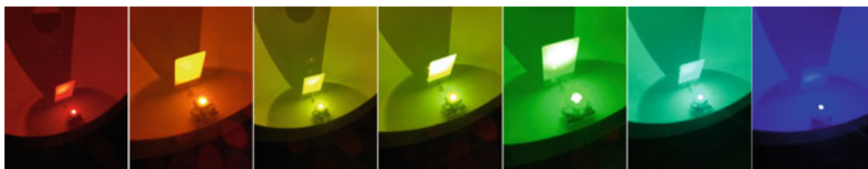

Fig. 9.18 Photograph of fabricated visible wavelength LEDs

The current injection area on the LED chip was 460 × 460 μm. The LED chip were assembled on an Ag-coated package and molded in silicone resin. Optical and electrical measurements were carried out at room temperature under direct current conditions in the range of 1–350 mA using a calibrated integrating sphere. In this section, we discuss the wavelength mainly at an injection current of 20 mA as standard, although a large blueshift in the peak wavelength is observed as discussed in the following subsection.

9.5.2 Dependence of Characteristics on Wavelength

Figure 9.19 shows EL spectra of the green-yellow LED measured at several injection levels. The spectra exhibited a single peak at up to 200 mA, while a shoulder in the shorter wavelength region appeared at 350 mA. The spectral shape scarcely changed with changing wavelength between 559 (LED-1), 569 (LED-2), and 576 nm (LED-3) as shown in Fig. 9.20. The full width at half-maximum (FWHM) for LED-1, LED-2, and LED-3 was 38, 38, and 39 nm, respectively. Compared with the results shown in Fig. 9.21, FWHM of around 38 nm and reduced dependence on wavelength were achieved, which contrasts with the

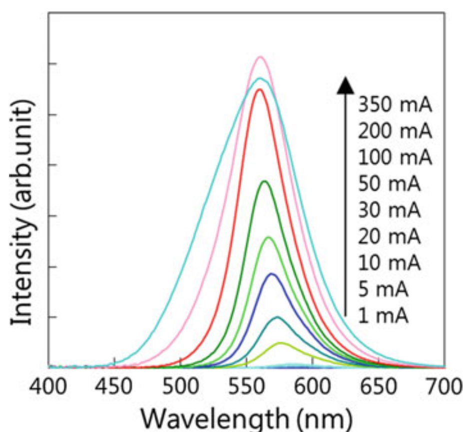

Fig. 9.19 Example of measurement results: EL spectra of fabricated yellow LED. Reproduced with permission from [15], copyright 2013 Wiley

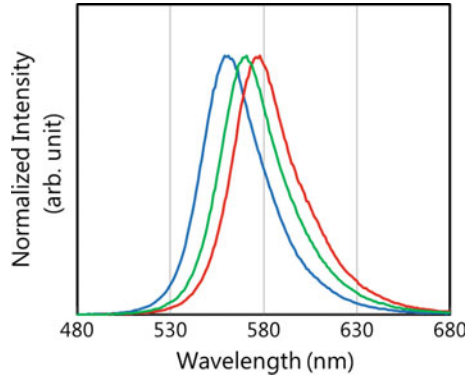

Fig. 9.20 Normalized EL spectral of LED-1(*blue line*), LED-2 (*green line*), and LED-3 (*red line*). Reproduced with permission from [17], copyright 2013 Japan Society of Applied Physics

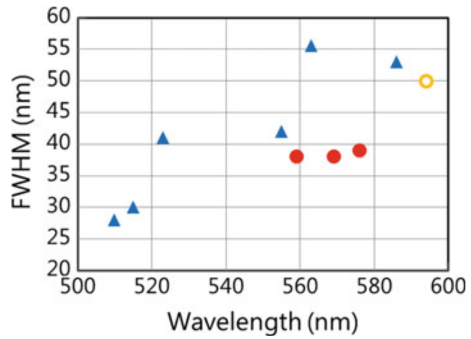

Fig. 9.21 Wavelength dependence of reported FWHMs on c-face sapphire substrate (*open circles*) [6], semipolar GaN substrates (*triangle*) [7, 8, 39, 40] and this work (*filled circles*). Reproduced with permission from [17], copyright 2013 Japan Society of Applied Physics

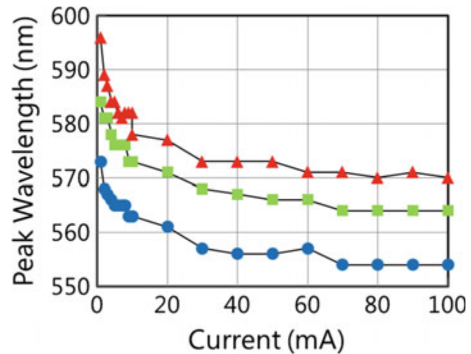

Fig. 9.22 Peak wavelength of LED-1 (*circle*), LED-2 (*square*), and LED-3 (*triangle*) versus DC drive current. Reproduced with permission from [17], copyright 2013 Japan Society of Applied Physics

conventional values previously reported that tend to increase with increasing wavelength [6–8, 44, 45].

Figure 9.22 shows the dependence of the peak EL wavelength on injection current. These blueshift and FWHM results show the potential profile fluctuation of both the band gap and the smooth interface between the QW and QB. These results indicate that a high-quality active layer was obtained in the “green gap” region.

Figure 9.23 shows the light output power (LOP) and EQE of these three LEDs versus injection current. The wavelength, LOP, forward voltage (V_f), and EQE are summarized in Fig. 9.23. This shows that the brightest LED in the yellow region achieved an EQE of over 13%. This significant improvement was achieved by means of two-step high-temperature QW growth, embedding both an AlGaN IL and short-period SL QB.

However, a reduction in the EQE with increasing wavelength can still be seen in these LEDs. This is attributable to increases in the Shockley–Read–Hall-type nonradiative process that predominantly suppresses the quantum efficiency at lower carrier concentrations [46, 47].

In addition to the LEDs in the green gap region, we addressed the development of LEDs in the red region. With increasing indium content in the InGaN QW, a red LED was obtained when the aluminum content of the AlGaN IL was set to 90%. Figure 9.24a shows the EL spectrum of the red LED. The EL intensity increased with increasing injection current. In addition to the main peak, a weak emission was observed at approximately 430 nm as shown in the inset of Fig. 9.24a. An additional emission appeared above the injection current of 5 mA and decreased in intensity above 100 mA. The additional peak can be attributed to emission from the phase-separated component in the InGaN QW [19, 48, 49]. In comparison with the main peak, the intensity of the additional emission is negligibly small. This

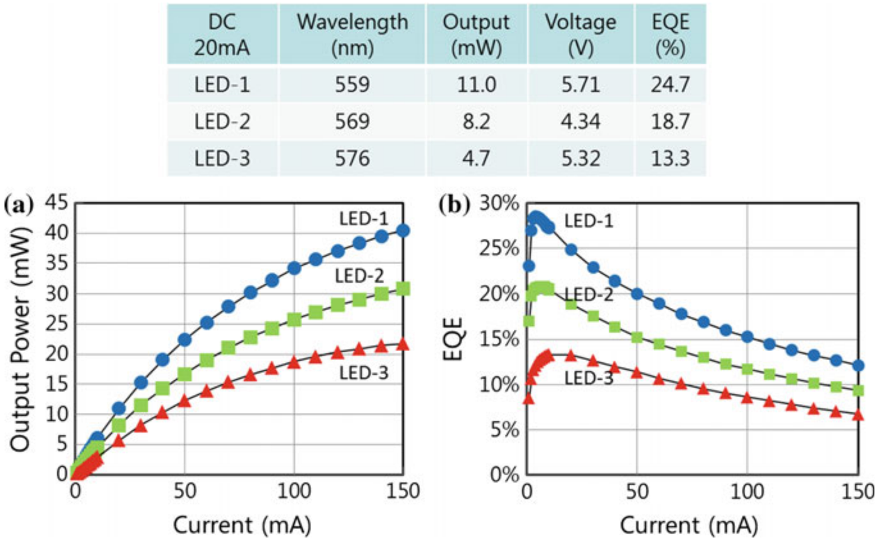

DC 20mA	Wavelength (nm)	Output (mW)	Voltage (V)	EQE (%)
LED-1	559	11.0	5.71	24.7
LED-2	569	8.2	4.34	18.7
LED-3	576	4.7	5.32	13.3

Fig. 9.23 **a** LOP versus DC drive current. At 20 mA, the output powers for LED-1 (*circle*), LED-2 (*square*), and LED-3 (*triangle*) are 11.0 mW, 8.2 mW, and 5.7 mW, respectively. **b** EQE versus DC drive current. At 20 mA, the output power, EQEs for LED-1 (*circle*), LED-2 (*square*), and LED-3 (*triangle*) are 24.7%, 18.7%, and 13.3%, respectively. Reproduced with permission from [17], copyright 2013 Japan Society of Applied Physics

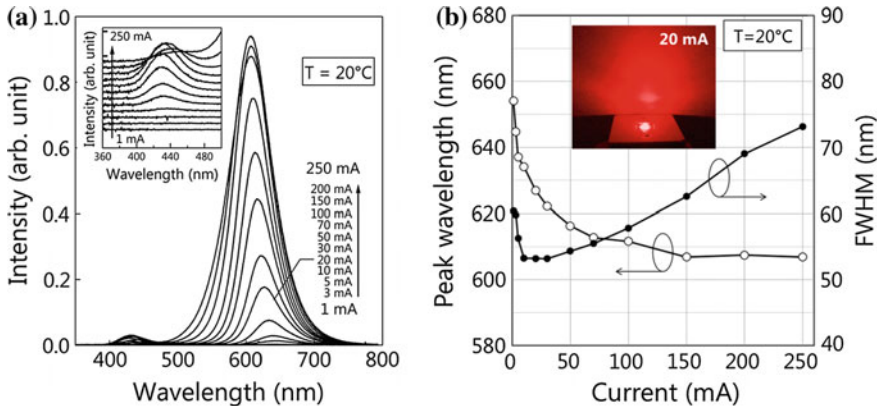

Fig. 9.24 EL properties of red LED. **a** EL spectra measured at each injection current level. **b** Peak wavelength and FWHM of the spectrum (*inset* emission image of red LED measured at 20 mA). Reproduced with permission from [18], copyright 2014 Japan Society of Applied Physics

indicates that the phase separation in the InGaN QW was effectively suppressed in the present red LED.

The peak wavelength and the FWHM are shown in Fig. 9.24b versus injection current. The peak wavelength and the FWHM at the injection current of 20 mA were 629 and 53 nm, respectively. Bright red emissions can be clearly seen as shown in the inset of Fig. 9.24b. The peak wavelength exhibited a blueshift with increasing injection current. A blueshift with narrowing FWHM up to 30 mA is a characteristic of carrier screening of the piezoelectric field in the InGaN QW structure. The magnitude of the blueshift was twice that in the yellow LED (Fig. 9.22), possibly because of the increase in both the potential fluctuation and the piezoelectric field of the InGaN QW due to high indium content.

Figure 9.25 shows LOP, EQE, and V_f versus injection current measured at 20 °C. The LOP and EQE at 20 mA were 1.1 mW and 2.9%, respectively. To our knowledge, this is the first demonstration of a nitride-based red LED with LOP exceeding 1 mW operating at 20 mA. The LOP reached 7.8 mW at a current of 250 mA. The V_f at 20 mA was 4.4 V, whereas that at 0.1 mA was 1.9 V, which is comparable to the emission energy of the red spectral region. In this case, the peak EQE was observed at 30 mA, which is rather high compared with yellow LEDs, indicating an increase of the nonradiative centers as mentioned above.

Thus, EQEs are enhanced by an AlGaN IL with high aluminum content. This trend was maintained without crystal quality degradation due to factors such as indium segregation in the InGaN well layer. In regard to the critical growth conditions such as the high indium content, indium segregation readily occurred in regions with relatively high indium content as a result of indium fluctuations, resulting in nonradiative centers. Moreover, the injection carriers in well layers diffuse to the low energy level regions. The growth conditions for low fluctuations are very important in InGaN when the indium content is high. The two-step

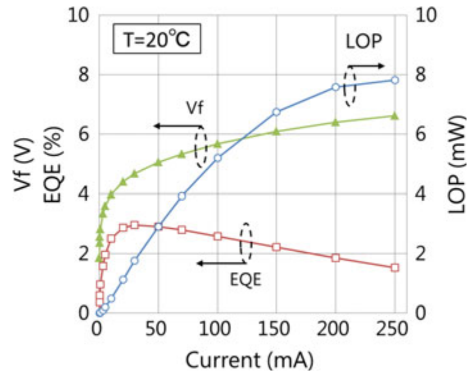

Fig. 9.25 LOP, EQE, and V_f of red LED as functions of injection current measured at 20 °C. Reproduced with permission from [18], copyright 2014 Japan Society of Applied Physics

high-temperature growth and AlGaN IL play important roles in suppressing the fluctuations in the case of high indium content.

In summary, the EL FWHM values are low even when using sapphire substrates. We speculate that this result is attributable to the AlGaN IL with high aluminum content and the optimized growth conditions that ensured low indium fluctuations.

9.5.3 Temperature Dependence

As mentioned in Sect. 9.1, the InGaN system is expected to have superior temperature dependence compared with the AlInGaP system. We performed EL measurements at several temperatures, and Fig. 9.26a shows the relative output power of the fabricated LEDs versus ambient temperature at an injection current of 20 mA. The LOPs exhibited thermal droop, which was particularly large in the red (628 nm) LED. The thermal droop can be characterized by the following phenomenological formula:

$$I = I_0 \exp\left(-\frac{(T - 20\,°\mathrm{C})}{T_0}\right).$$

Here, I is the LOP, I_0 is the LOP at an ambient temperature of 20 °C, T is the ambient temperature, and T_0 is the characteristic temperature. A larger T_0 implies better temperature stability. Figure 9.26b shows the measured T_0 values for each of the fabricated LEDs compared with the AlGaInP LED [9]. The InGaN system LEDs basically exhibited better T_0 compared with the AlGaInP LED. In the present red LED, the EQE and T_0 below 30 mA were suppressed, indicating nonradiative centers still dominate the EQE at lower current levels. Further improvements are expected through the suppression of defect generation in the active layer by optimizing the local structure and the growth conditions (Fig. 9.27).

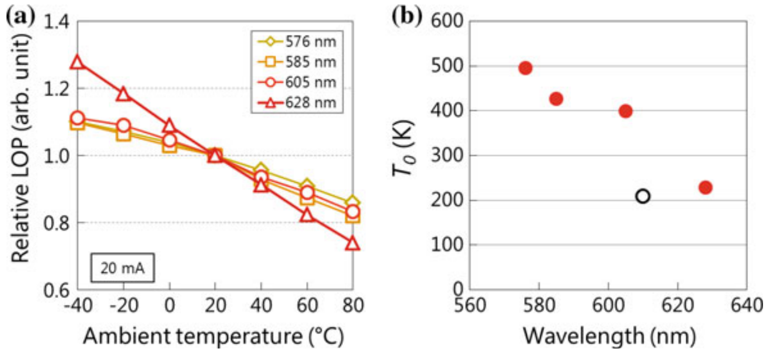

Fig. 9.26 Temperature dependence of longer wavelength LEDs. **a** Temperature dependence of LOP and **b** T_0 of this work (*filled circles*) with a data of AlGaInP (*open circles*) [9]

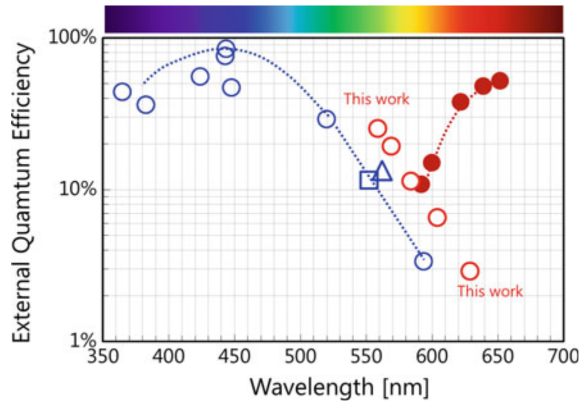

Fig. 9.27 Plots of previously reported EQE values. InGaN system (*blue open marks*), AlGaInP system (*brown filled marks*), and present work (*red open marks*)

As seen in this section, two-step high-temperature MQW growth, AlGaN IL with high aluminum content and InGaN/GaN short-period SL QB were used to fabricate LEDs that had improved EL in the green gap spectral region. At a drive current of 20 mA, the LOP and EQE were 11.0 mW and 24.7% for the yellow-green LED (559 nm), and 4.7 mW and 13.3% for the yellow LED (576 nm), which were the highest values, even in the green gap region. In the red spectral region, an InGaN-based red LED with LOP exceeding 1 mW operating at 20 mA was demonstrated for the first time with a characteristic temperature of 229 K, comparable to that of the AlInGaP system.

These results indicate the possibility of overcoming the green gap problem by means of InGaN-based LEDs grown on a polar surface. These results open the way to wavelength-tunable light emitters, visible light communications based on InGaN LEDs, and phosphor-free high-efficiency white light sources. If a breakthrough in the red spectral region can be achieved in the future in InGaN-based LEDs, a color-mixing monolithic light source system will be possible.

9.5.4 Phosphor-Free Single White LED Using Multi-wavelength MQW

Generating white light basically required use of yellow phosphors in the past due to the lack of good growth conditions for InGaN emitting in the yellow wavelength range. Many kinds of novel device structures have been investigated aiming for phosphor-free single white LEDs [50–53], but the luminous efficiency of these new structures has not been as high as conventional white LEDs employing phosphors. In this section, we introduce an attempt at a phosphor-free single white LED using the multi-wavelength MQW technique since we now have good growth conditions for yellow.

Figure 9.28 shows a schematic of a fabricated phosphor-free single white LED and its active region structure. The basic LED structure consisting of an active region employing a four-period multi-QW structure is the same as the face-up LED introduced in Sect. 9.5.1 except for the indium content of each QW. To generate blue and yellow light at the same time, the first, second, and third QWs was designed as blue emitters with an estimated indium content of 10%, and the fourth QW was designed as a yellow emitter with an estimated indium content of 28%.

Figure 9.29 shows the EL spectra from 20 to 60 mA together with an optical micrograph of the emissions at an injection current of 40 mA. Both blue and yellow peaks were clearly observed in the spectrum, which produced good white light without use of phosphors. At 40 mA, the CIE color chart (Cx, Cy), the color temperature, and the Ra were (0.340, 0.341), 5176 K and approximately 65, respectively.

The results clearly show that we succeeded in fabricating a single phosphor-free white LED chip. To generate stable white light using this system, however, several practical problems still remain. First, the luminous efficiency is still poor. The maximum LER measured was only about 1 lm/W, probably due to the insufficient active volume, particularly for the yellow wavelength range. Second, the EQE curves of the blue QWs and the yellow QW are not the same, resulting in the color

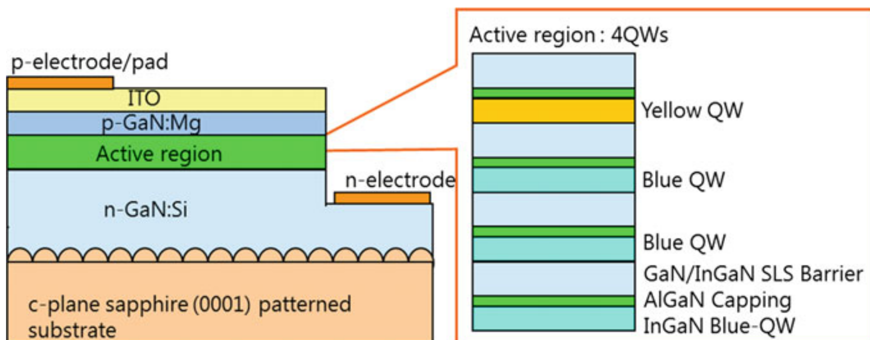

Fig. 9.28 Schematic of the phosphor-free white LED and its active region

temperature and color chart fluctuating with increasing injection current. Thirdly, the peak wavelength blueshifted as the injection current increased, particularly from the yellow QW, which also causes fluctuations. Figure 9.30 shows the CIE color chart plot for injection currents from 20 to 80 mA. The color chart basically shifted towards the blue area because the EQE of the blue QWs is higher than that of the yellow QW.

From these results, we can discuss the distribution of injection current among the first to third blue QWs and the fourth yellow QW. In our work, the EQE of a single-color blue LED (480 nm) is estimated to be approximately fourfold that of a yellow LED (570 nm) at an injection current of 40 mA. As shown in Fig. 9.29, however, the peak intensity of the blue light is only twice that of the yellow light. Despite this, three QWs were used for blue and only one QW was used for yellow. It is thus thought that a large part of the injection current was consumed by the fourth QW compared to the first to third QWs.

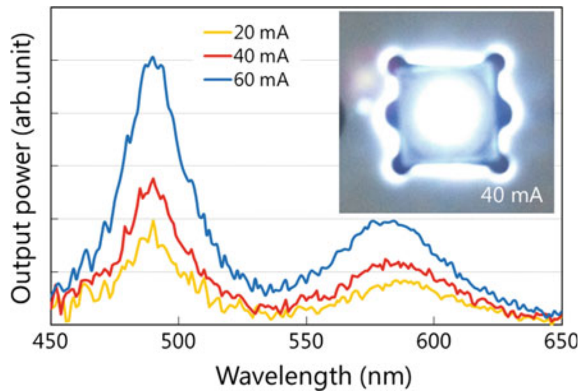

Fig. 9.29 EL spectra and an optical micrograph of fabricated single phosphor-free white LED

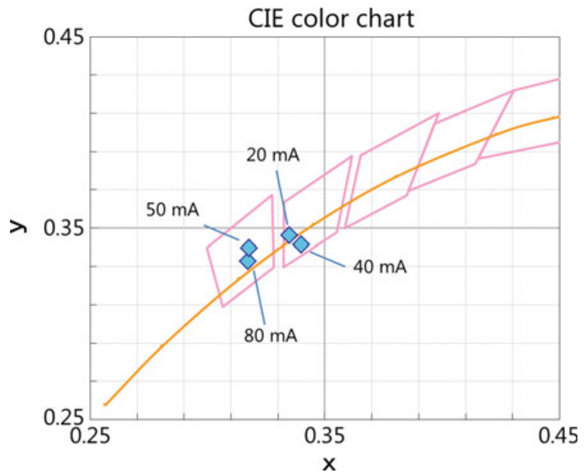

Fig. 9.30 CIE color chart shift of fabricated single phosphor-free white LED

In future work, we intend to consider the parameters for fabricating ideal high-efficiency high-Ra single white phosphor-free LEDs.

9.5.5 *Stacked White LED Without Phosphors*

Another way to generate white light without using phosphors is to use several color (individual) LED chips [54]. In this section, we introduce a simple trial for multi-color stacked white LED without phosphors. Figure 9.31 shows a schematic of a multi-color stacked white LED in which a yellow LED is simply stacked on top of a blue LED using silicone as an adhesive. Each LED is connected to different power sources to allow for separate control, hence allowing us to generate either blue, yellow, or white light from a single device. Our LED has a face-up structure using a sapphire substrate as described in Sect. 9.5.1 with no backside electrode in which blue light can be emitted through the yellow LED when both LEDs are emitting.

Figure 9.32 shows optical micrographs during light emission for only the blue LED with 3 mA of injection current, only the yellow LED with 20 mA, and both the blue and yellow LEDs with 3 and 20 mA. Figure 9.33 shows the EL spectra and CIE color chart during emission of white light. When emitting yellow with 20 mA stable and blue with 3, 5, 7 mA, the resulting CIE color chart (Cx, Cy) values were (0.376, 0.387), (0.340, 0.327), and (0.316, 0.287), the color temperatures were 4197 K, 5130 K, and 6742 K, and Ra was approximately 20, 26, and 33, respectively. In this system, it is simple to control the color chart because each LED can be driven separately, although the Ra is quite low due to the narrow FWHM of each LED. Of course, we can use additional color LEDs such as cyan (500 nm), amber (580 nm), or red (630 nm) to improve the Ra as mentioned in Sect. 9.2.1. The maximum LER of approximately 25 lm/W at an injection current of 3 mA for yellow was much higher than the 1 lm/W of the multi-wavelength MQW technique as mentioned in Sect. 9.5.4, probably because the volume of the yellow active region was larger. The multi-color stacked white LED technique is therefore better for high-efficiency phosphor-free white light than the multi-wavelength MQW technique at this point.

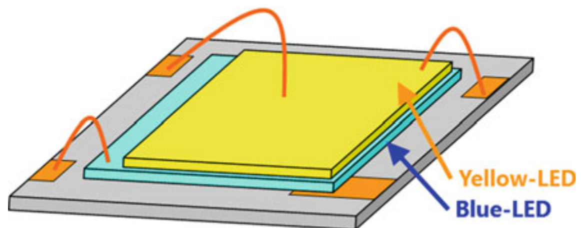

Fig. 9.31 Schematic of a multi-color stacked white LED

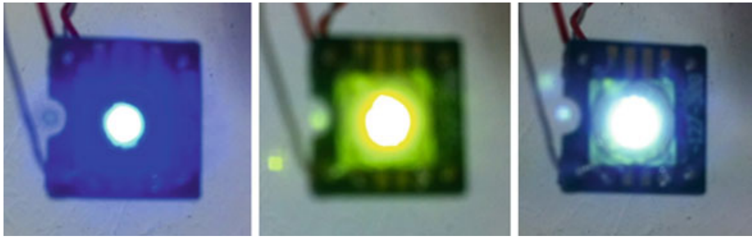

Fig. 9.32 Optical micrographs of during emission of blue, yellow, and white light

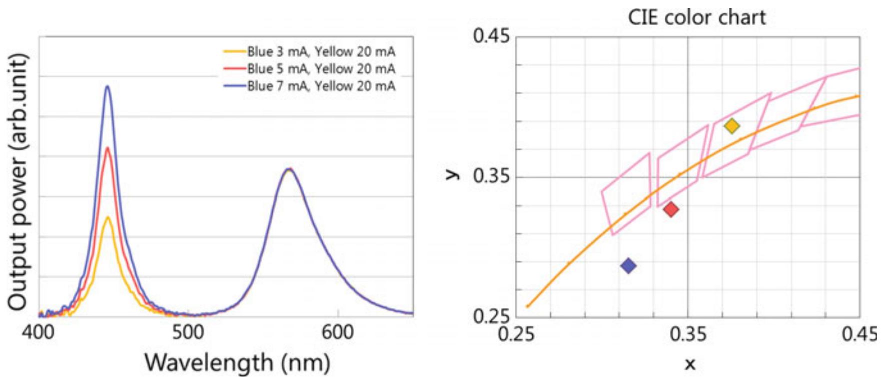

Fig. 9.33 EL spectra and CIE color chart during emission of white light

References

1. Y. Narukawa, M. Ichikawa, D. Sanga, M. Sano, T. Mukai, J. Phys. D **43**, 354002 (2010)
2. Solid-State Lighting R&D plan 2015, Department of Energy, The United States of America
3. M.H. Crawford, IEEE J. Sel. Top. Quantum Electron. **15,** 1028 (2009)
4. Y. Ohba, K. Kaneko, H. Katsuno, M. Kushibe, Appl. Phys. Express **1**, 101101 (2008)
5. Y. Narukawa, M. Sano, M. Ichikawa, S. Minato, T. Sakamoto, T. Yamada, T. Mukai, Jpn. J. Appl. Phys. **46**, L963 (2007)
6. T. Mukai, H. Narimatsu, S. Nakamura, Jpn. J. Appl. Phys. **37**, L479 (1998)
7. S. Yamamoto, Y. Zhao, C.-C. Pan, R.B. Chung, K. Fujito, J. Sonoda, S.P. DenBaars, S. Nakamura, Appl. Phys. Express **3**, 122102 (2010)
8. H. Sato, R.B. Chung, H. Hirasawa1, N. Fellows, H. Masui, F. Wu, M. Saito, K. Fujito, J.S. Speck, S.P. DenBaars, S. Nakamura, Appl. Phys. Lett. **92**, 221110 (2008)
9. S. Chhajed, Y. Xi, Y.-L. Li, Th. Gessmann, E.F. Schubert, J. Appl. Phys. **97**, 054506 (2005)
10. T. Matsuoka, H. Okamoto, M. Nakao, Phys. Status Solidi C **0**, 2806 (2003)
11. A.E. Romanov, T.J. Baker, S. Nakamura, J.S. Speck, J. Appl. Phys. **100**, 023522 (2006)
12. S. Ploch, T. Wernicke, M. Frentrup, M. Pristovsek, M. Weyers, M. Kneissl, Appl. Phys. Lett. **101**, 202102 (2012)
13. Y. Zhao, Q. Yan, C.Y. Huang, S.C. Huang, P.S. Hsu, S. Tanaka, C.C. Pan, Y. Kawaguchi, K. Fujito, C.G. Van de Walle, J.S. Speck, S.P. DenBaars, S. Nakamura, D. Feezell, Appl. Phys. Lett. **100**, 201108 (2012)
14. R. Hashimoto, J.I. Hwang, S. Saito, S. Nunoue, Phys. Status Solidi C **10**, 1529 (2013)

15. R. Hashimoto, J.I. Hwang, S. Saito, S. Nunoue, Phys. Status Solidi C **11**, 628 (2013)
16. J.I. Hwang, R. Hashimoto, S. Saito, S. Nunoue, Proc. SPIE **8625**, 86251G (2013)
17. S. Saito, R. Hashimoto, J.I. Hwang, S. Nunoue, Appl. Phys. Express **6**, 111004 (2013)
18. J.I. Hwang, R. Hashimoto, S. Saito, S. Nunoue, Appl. Phys. Express **7**, 071003 (2014)
19. I.H. Ho, G.B. Stringfellow, Appl. Phys. Lett. **69**, 2701 (1996)
20. S.Y. Karpov, MRS Internet J. Nitride Semicond. Res. **3**, e16 (1998)
21. R. Singh, D. Doppalapudi, T.D. Moustakas, L.T. Romano, Appl. Phys. Lett. **70**, 1089 (1997)
22. N.A. El-Masry, E.L. Piner, S.X. Liu, S.M. Bedair, Appl. Phys. Lett. **72**, 40 (1998)
23. K. Jacobs, B. Van Daele, M.R. Leys, I. Moerman, G. Van Tendeloo, J. Cryst. Growth **248**, 498 (2003)
24. G.T. Thaler, D.D. Koleske, S.R. Lee, K.H.A. Bogart, M.H. Crawford, J. Cryst. Growth **312**, 1817 (2010)
25. C.C. Chuo, C.M. Lee, J.I. Chyi, Appl. Phys. Lett. **78**, 314 (2001)
26. B. Damilano, B. Gil, J. Phys. D: Appl. Phys. **48**, 403001 (2015)
27. C.J. Sun, M. Zubair Anwar, Q. Chen, J.W. Yang, M. Asif Khan, M.S. Shur, A.D. Bykhovski, Z. Liliental-Weber, C. Kisielowski, M. Smith, J.Y. Lin, H.X. Jiang, Appl. Phys. Lett. **70,** 2978 (1997)
28. Y. Chen, T. Takeuchi, H. Amano, I. Akasaki, N. Yamada, Y. Kaneko, S.Y. Wang, Appl. Phys. Lett. **72**, 710 (1998)
29. I.H. Kim, H.S. Park, Y.J. Park, T. Kim, Appl. Phys. Lett. **73**, 1634 (1998)
30. A. Hangleiter, F. Hitzel, C. Netzel, D. Fuhrmann, U. Rossow, G. Ade, P. Hinze, Phys. Rev. Lett. **95**, 127402 (2005)
31. T.L. Song, S.J. Chua, E.A. Fitzgerald, J. Appl. Phys. **98**, 084906 (2005)
32. H.K. Cho, J.Y. Lee, C.S. Kim, G.M. Yang, J. Appl. Phys. **91**, 1166 (2002)
33. H.K. Cho, J.Y. Lee, G.M. Yang, C.S. Kim, Appl. Phys. Lett. **79**, 215 (2001)
34. M. Zhu, S. You, T. Detchprohm, T. Paskova, E.A. Preble, D. Hanser, C. Wetzel, Phys. Rev. B **81**, 125325 (2010)
35. D.I. Florescu, S.M. Ting, J.C. Ramer, D.S. Lee, V.N. Merai, A. Parkeh, D. Lu, E.A. Armour, L. Chernyak, Appl. Phys. Lett. **83**, 33 (2003)
36. T. Langer, A. Kruse, F.A. Ketzer, A. Schwiegel, L. Hoffmann, H. Jönen, H. Bremers, U. Rossow, A. Hangleiter, Phys. Status Solidi C **8,** 2170 (2011)
37. T. Tsuchiya, J. Shimizu, M. Shirai, M. Aoki, J. Cryst. Growth **276**, 439 (2005)
38. J. Smalc-Koziorowska, E. Grzanka, R. Czernecki, D. Schiavon, M. Leszczyński, Appl. Phys. Lett. **106**, 101905 (2015)
39. T. Doi, Y. Honda, M. Yamaguchi, H. Amano, Jpn. J. Appl. Phys **52**, 08JB14 (2013)
40. E. Kuokstis, C.Q. Chen, M.E. Gaevski, W.H. Sun, J.W. Yang, G. Simin, M. Asif Khan, H. P. Maruska, D.W. Hill, M.C. Chou, J.J. Gallagher, B. Chai, Appl. Phys. Lett. **81**, 4130 (2002)
41. R. Cingolani, A. Botchkarev, H. Tang, H. Morkoç, G. Traetta, G. Coli, M. Lomascolo, A. Di Carlo, F. Della Sala, P. Lugli, Phys. Rev. B **61**, 2711 (2000)
42. G. Martin, A. Botchkarev, A. Rockett, H. Morkoç, Appl. Phys. Lett. **68**, 2541 (1996)
43. D.Y. Lee, J.H. Lee, S.H. Han, M.G. Cheong, D.J. Kim, J.S. Park, S.S. Hong, J.Y. Leem, J. Appl. Phys. **108**, 083110 (2010)
44. M. Funato, M. Ueda, Y. Kawakami, Y. Narukawa, T. Kosugi, M. Takahashi, T. Mukai, Jpn. J. Appl. Phys. **45**, L659 (2006)
45. Y.D. Lin, A. Chakraborty, S. Brinkley, H.C. Kuo, T. Melo, K. Fujito, J.S. Speck, S. P. DenBaars, S. Nakamura, Appl. Phys. Lett. **94**, 261108 (2009)
46. M.H. Kim, M.F. Schubert, Q. Dai, J.K. Kim, E.F. Schubert, J. Piprek, Y. Park, Appl. Phys. Lett. **91**, 183507 (2007)
47. M.F. Schubert, S. Chhajed, J.K. Kim, E.F. Schubert, D.D. Koleske, M.H. Crawford, S.R. Lee, A.J. Fischer, G. Thaler, M.A. Banas, Appl. Phys. Lett. **91**, 231114 (2007)
48. T. Mukai, M. Yamada, S. Nakamura, Jpn. J. Appl. Phys. **38**, 3976 (1999)
49. K.G. Belyaev, M.V. Rakhlin, V.N. Jmerik, A.M. Mizerov, Ya.V. Kuznetsova, M.V. Zamoryanskaya, S.V. Ivanov, A.A. Toropov, Phys. Status Solidi C **10**, 527 (2013)

50. I.K. Park, J.Y. Kim, M.K. Kwon, C.Y. Cho, J.H. Lim, S.J. Park, Appl. Phys. Lett. **92**, 091110 (2008)
51. M. Funato, K. Hayashi, M. Ueda, Y. Kawakami, Y. Narukawa, T. Mukai, Appl. Phys. Lett. **93**, 021126 (2008)
52. C.-F. Lu, C.-F. Huang, Y.-S. Chen, W.-Y. Shiao, C.-Y. Chen, Y.-C. Lu, C.C. Yang, IEEE J. Sel. Top. Quantum Electron. **15**, 1210 (2009)
53. S.J. Kowsz, C.D. Pynn, S.H. Oh, R.M. Farrell, J.S. Speck, S.P. DenBaars, S. Nakamura, Appl. Phys. Lett. **107**, 101104 (2015)
54. N.N. Fellow, H. Sato, Y. Lin, R.B. Chung, S.P. DenBaars, S. Nakamura, Appl. Phys. Lett. **93**, 121112 (2008)

Chapter 10
AlGaN-Based Deep-Ultraviolet Light-Emitting Diodes

Hideki Hirayama, Norihiko Kamata and Kenji Tsubaki

Abstract 222–351 nm AlGaN-based deep-ultraviolet (DUV) light-emitting diodes (LEDs) are demonstrated, which have been achieved by the development of crystal growth techniques for wide-bandgap AlN and AlGaN. Significant increases in internal quantum efficiency (IQE) have been achieved for AlGaN quantum well (QW) emissions by introducing low-threading-dislocation density (TDD) AlN grown by an NH_3 pulsed-flow multilayer growth method. Electron Injection efficiency (EIE) of the DUV LED was significantly increased by introducing multi-quantum barrier (MQB). Light extraction efficiency (LEE) was also improved by using a transparent p-AlGaN contact layer. The maximum external quantum efficiency (EQE) was increased up to 10.8% for a 276 nm DUV LED.

10.1 Introduction

Growth techniques of AlN/AlGaN semiconductors and recent advances in AlGaN-based deep-ultraviolet (DUV) light-emitting diodes (LEDs) are demonstrated. 220–350-nm-band DUV LEDs have been realized by developing crystal growth techniques for wide-bandgap AlN and AlGaN semiconductors. Significant increases in internal quantum efficiency (IQE) have been achieved for AlGaN DUV emissions by developing low-threading dislocation density (TDD) AlN buffer layers grown on sapphire substrates. The electron injection efficiency (EIE) of the LEDs was also significantly increased by introducing a multi-quantum barrier (MQB). We also discuss light extraction efficiency (LEE), which is the most important parameter for achieving high-efficiency DUV LEDs. We succeeded in

H. Hirayama (✉)
RIKEN, 2-1 Hirosawa, Wako, Saitama 351-0198, Japan
e-mail: hirayama@riken.jp

N. Kamata
Saitama University, 255 Shimo-Okubo, Sakura-ku, Saitama 338-8570, Japan

K. Tsubaki
Panasonic, 1048, Kadoma, Oaska 571-8686, Japan

© Springer Nature Singapore Pte Ltd. 2017

T.-Y. Seong et al. (eds.), *III-Nitride Based Light Emitting Diodes and Applications*,
Topics in Applied Physics 133, DOI 10.1007/978-981-10-3755-9_10

improving LEE by developing a transparent p-AlGaN contact layer. The maximum external quantum efficiency (EQE) obtained was 7% for a 279 nm DUV LED. EQE could be increased by up to several tens of percent through the improvement of LEE by utilizing transparent contact layers and photonic nanostructures.

In Sect. 10.2, the research background including device applications, history, and the current status of DUV LEDs is described. We will describe the development of crystal growth techniques for obtaining high-quality AlN and AlGaN crystals in Sect. 10.3. We will describe the achievement of high IQE for AlGaN DUV emission and the realization of DUV LEDs in Sects. 10.4 and 10.5, respectively. We will go on to discuss several issues for increasing the efficiencies of DUV LEDs, i.e., EIE and LEE, in Sect. 10.6. Finally, the future prospects of DUV LEDs are discussed in Sect. 10.7.

10.2 Research Background of DUV LEDs

The development of semiconductor light sources operating in the DUV region, such as DUV LEDs and laser diodes (LDs), is quite an important subject because they are required for a wide variety of applications. Figure 10.1 shows the image of application fields of UVA (200–280 nm), UVB (280–315 nm), and UVC (315–400 nm) LEDs and LDs. UV LEDs are expected to be used in applications such as sterilization, water purification, medicine and biochemistry, agriculture, white light illumination, light source of high density optical memory, fluorescence analytical

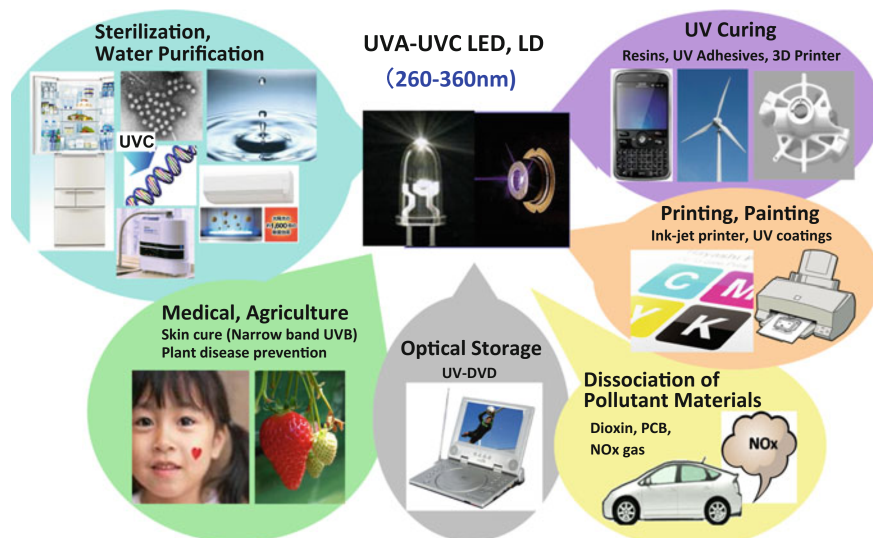

Fig. 10.1 Potential applications of UVA-UVC LEDs and LDs

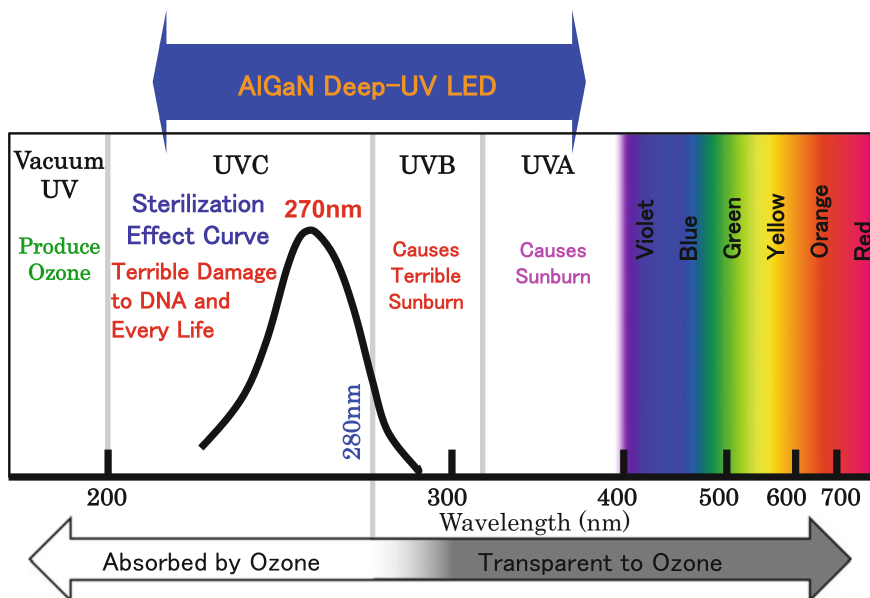

Fig. 10.2 Classification of UV light and the wavelength range achieved by AlGaN DUV LEDs

systems, and related information sensing fields. They are also very important for UV-curing, 3-dimensional (3D) printer, UV adhesives, printing, painting, or courting [1, 2].

Figure 10.2 shows the classification of UV light and the wavelength range achieved by AlGaN DUV LEDs. For applications involving sterilization or water purification with direct UV-light treatment, UVC light with the wavelength range between 260 and 280 nm is most suitable. For the UV purification process using a titanium-oxide (TiO_2) catalyst, the wavelength range between 320 and 380 nm is also useful. For application to white LED illumination produced by a mixture of red-green-blue (RGB) phosphors excited by a UV LED, wavelengths around 340 nm in UVA are considered to be most suitable, taking into account the efficient absorption by phosphors (<350 nm). The wavelength range achieved by AlGaN LED covers from UVA to UVC as shown in Fig. 10.2.

Because of their wide direct transition energy range in the UV, covering the region between 6.2 eV (AlN) and 3.4 eV, AlGaN is attracting considerable attention as candidate materials for the realization of DUV LEDs and LDs [2]. Figure 10.3 shows the relationship between the direct transition bandgap energy and the lattice constant of the wurtzite (WZ) InAlGaN material system and the lasing wavelengths of various gas lasers. The main advantages of using AlGaN for DUV light sources are (1) the possibility of obtaining high-efficiency optical emission from quantum wells (QWs), (2) the possibility of producing both p- and n-type semiconductors in the wide-bandgap spectral region, (3) their physical properties, i.e., nitrides are

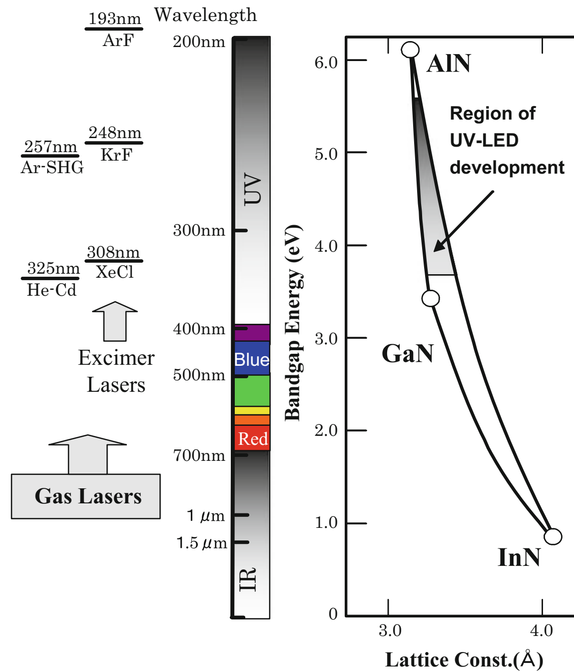

Fig. 10.3 Relationship between the direct transition bandgap energy and the lattice constant of the wurtzite (WZ) InAlGaN material system and the lasing wavelengths of various gas lasers

mechanically hard and the devices have long lifetimes, and (4) the fact that the materials are free from harmful arsenic, mercury, and lead [2].

Research into AlGaN-based UV LEDs for wavelengths shorter than 360 nm was initiated by several research groups between 1996 and 1999 [3–5]. In the US, the effort directed at DUV light sources was driven by DARPA's Semiconductor Ultraviolet Optical Sources (SUVOS) program. A group at the University of South Carolina reported the first 250–280 nm AlGaN-based DUV LEDs between 2002 and 2006 [6–8]. A group at NTT reported the shortest wavelength (210 nm) LED using an AlN emitting layer in 2006 [9]. We started research into AlGaN-based DUV LEDs in 1997, and reported the first efficient DUV (230 nm) photoluminescence (PL) from AlGaN/AlN QWs [10], and a 333 nm AlGaN QW UV LED on SiC in 1999 [4]. We have also developed high-efficiency UV LEDs using In-incorporation effects into AlGaN [2, 11, 12]. We have demonstrated several mW cw operation from 340 to 350 nm InAlGaN QW UV LEDs on both GaN single-crystal substrates [13] and sapphire substrates [14].

The development of 280-nm-band AlGaN DUV LEDs to achieve high-efficiency and high-power operation has become extremely competitive recently, because they are expected to have a huge market for sterilization applications. We developed a growth method for low-threading dislocation density (TDD) AlN templates on sapphire substrates in 2007 [15], and achieved high IQE (>60%) for AlGaN and quaternary InAlGaN QWs in the DUV region [16, 17]. We also achieved high-electron injection efficiency (EIE) by introducing a multi-quantum barrier

(MQB) design as an electron-blocking layer (EBL) [18], and demonstrated AlGaN and quaternary InAlGaN-based UV LEDs with a wide emission range (222–351 nm) [17–21]. We have also improved the light extraction efficiency (LEE) of DUV LED by developing a transparent p-AlGaN contact layer and a highly reflective p-type electrode [22, 23], and have achieved an external quantum efficiency (EQE) of 7% [24]. RIKEN and Panasonic have developed commercially available DUV LED modules for sterilization use in 2014 (270 nm, 10 mW LED module with lifetime longer than 10000 h, EQE of 2–3%) [25, 26].

High-efficiency DUV LEDs with wavelength between 260 and 280 nm have been developed by several companies [27–36]. Sensor electronic technology (SET) has developed commercially valuable UV LEDs with wavelengths ranging between 240 and 360 nm [27–29], and they have reported a maximum EQE of 11% for 278 nm LED [29]. Nikkiso has also reported over 10% EQEs [30]. Crystal IS and Tokuyama have developed efficient DUV LED on single-crystal AlN substrates fabricated by a sublimation method [31, 32] and hydride vapor phase epitaxy (HVPE) [33, 34], respectively. Nitek and Nichia have also developed high-efficiency DUV LEDs [35, 36].

The next targets in UV device research are to develop EQEs of several tens of percent for 220–350 nm LEDs and to achieve 250–330 nm LDs. However, the realization of high-EQE UV LEDs with wavelengths below 360 nm is still challenging owing to some major problems. The sudden drop in efficiency of UV LEDs below 360 nm is mainly due to the following three factors:

1. IQE of AlGaN is more sensitive to TDD than that of InGaN.
2. The hole concentration of p-AlGaN is low, resulting in low injection efficiency (IE).
3. LEE is low because of the absorption of UV light in p-GaN contact layers.

The development of low-TDD AlN templates is most important, because IQE of AlGaN QWs is as low as 1% if we use conventional templates with high TDD. To obtain high IQE of more than 60%, the reduction of TDD to below 5×10^{8} cm^{-2} is required [16, 17]. To fabricate such a low-TDD AlN template on sapphire, it is necessary to introduce some special growth conditions. Low-TDD AlN single-crystal wafers have advantages for high IQE [31–34], although they are expensive for use as commercially available DUV LEDs. We are using the 'ammonia (NH_3) pulsed-flow multilayer (ML) growth' method to fabricate AlN templates on sapphire, and have obtained IQE of over 60% from AlGaN QWs [15–17]. Also, for the realization of high-IQE DUV emission, the use of quaternary InAlGaN with a few percent of indium (In) is effective [2, 17].

The device properties of AlGaN DUV LEDs strongly depend on the properties of the p-AlGaN. The hole concentration of p-AlGaN with high-Al content (Al > 60%) is low (as low as 10^{14} cm^{-3}) owing to its deep acceptor level, i.e., 240 (GaN)–590 meV (AlN). EIE of a DUV LED is reduced owing to the leakage of electrons to the p-side layers. The high-series resistance of p-type layers also becomes a problem for the device properties.

Owing to the lack of high-hole-density p-type AlGaN, we must use p-GaN contact layers. The use of a p-GaN contact layer results in a significant reduction in LEE owing to the strong absorption of DUV light. LEE of a DUV LED is typically below 8%. Transparent p-AlGaN contact layers and highly reflective p-type electrodes are desirable for realizing high-LEE devices.

The current EQE of 270 nm DUV LEDs in our group is approximately 7%, which is determined by 60% IQE, 80% EIE, and 15% LEE. Further improvements in EQE are expected as we start the production of commercially available DUV LEDs. Techniques for increasing each of these efficiencies are described in the following sections.

10.3 Growth of High-Quality AlN on Sapphire Substrate

In order to realize high-efficiency DUV LEDs, it is necessary to develop a low-TDD AlGaN/AlN template. The TDD of a conventional AlN buffer layer on a sapphire substrate, which was fabricated using a low-temperature (LT)-AlN buffer, was greater than 2×10^{10} cm^{-2}. On the other hand, TDD of 10^{8}–10^{9} cm^{-2} is required in order to obtain high IQE values of several tens % from AlGaN QWs. Several fabrication methods have been reported for obtaining high-quality AlN buffers, for example, the use of AlN/AlGaN superlattices (SLs) grown with alternating gas feeds [6], AlGaN buffer layers deposited by epitaxial lateral overgrowth (ELO) [37], and a combination of GaN/AlN SLs and AlGaN produced by alternate source-feeding epitaxy (ASFE) on SiC [38].

In the former experiments, we grew AlN layers directly onto sapphire substrates at high growth temperature (HT) after an initial nitridation treatment using NH_3. The growth temperature was around 1300 °C, and the V/III ratio was a relatively low value. As the nitridation time was increased from 5 to 10 min, the full width at half-maximum (FWHM) of X-ray diffraction (10–12) and (0002) ω-scan rocking curves (XRCs) was reduced to below 600 arcsec. The value of the FWHM of (10–12) XRC corresponds to the edge-type threading-dislocation density. We found that larger AlN nuclei are formed in the initial stages of the growth process by introducing longer nitridation times, and that edge dislocations are reduced by embedding them in a thick AlN layer. However, heavy nitridation on sapphire becomes the cause of a polarity inversion from Al to N polarity, which leads to the generation of abnormal nuclei on the AlN surface. We also found that a long nitridation time leads to cracks on the AlN surface.

It is necessary to satisfy several conditions to achieve high-quality AlGaN/AlN templates that are applicable to DUV emitters, i.e., low-TDD, crack-free, atomically flat surfaces and stable Al (+c) polarity. To obtain all of the conditions mentioned above, we have introduced an ‘ammonia (NH_3) pulsed-flow multilayer (ML) growth’ method for fabricating AlN layers on sapphire [15]. Figure 10.4 shows the typical gas flow sequence and a schematic view of the growth control

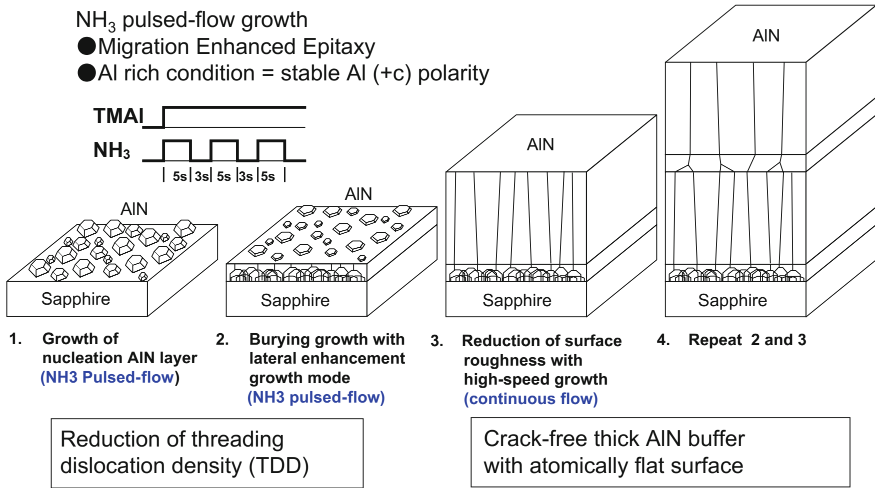

Fig. 10.4 Gas flow sequence and schematic view of the growth control method used for 'an NH_3 pulsed-flow multilayer (ML)-AlN growth technique'

method using pulsed- and continuous-flow gas feeding growth that is used for the NH_3 pulsed-flow ML-AlN growth.

The samples were grown on sapphire (0001) substrates by low-pressure metal-organic chemical vapor deposition (LP-MOCVD). First, an AlN nucleation layer and a 'burying' AlN layer were deposited, both by NH_3 pulsed-flow growth. The trimethylaluminum (TMAl) flow was continuous during the NH_3 pulsed-flow sequence, as shown in Fig. 10.4. Low-TDD AlN can be achieved by promoting the coalescence of the AlN nucleation layer. After the growth of the first AlN layer, the surface is still rough because of the low-growth rate by the pulsed-flow mode growth. We introduced a high-growth rate continuous-flow mode to reduce the surface roughness. By repeating the pulsed- and continuous-flow modes, we can obtain crack-free, thick AlN layers with atomically flat surfaces. NH_3 pulsed-flow growth is effective for obtaining high-quality AlN because of the enhancement of precursor migration. Furthermore, it is effective for obtaining stable Al (+c) polarity, which is necessary for suppressing polarity inversion from Al to N by maintaining Al-rich growth conditions.

As described above, we used three different growth conditions in this method, i.e., the initial deposition in order to fabricate an AlN nucleation layer, migration enhancement epitaxy for decreasing TDD, and a high-growth rate using a conventional continuous-flow mode. The detailed growth conditions were described in [15, 19]. The typical growth rates in the pulsed- and continuous-flow modes were approximately 0.6 and 6 μm/h, respectively. We found recently that a low V/III ratio and higher growth temperature (~1400 °C) are more suitable for obtaining a low-TDD AlN growth on sapphire.

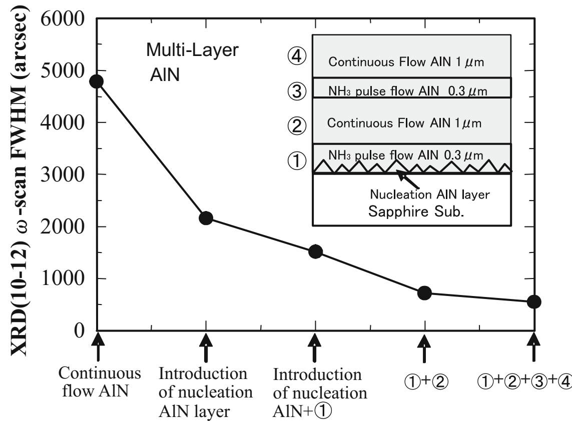

Fig. 10.5 Reduction of FWHM of X-ray diffraction (10–12) ω-scan rocking curve (XRC) for various stages of ML-AlN growth

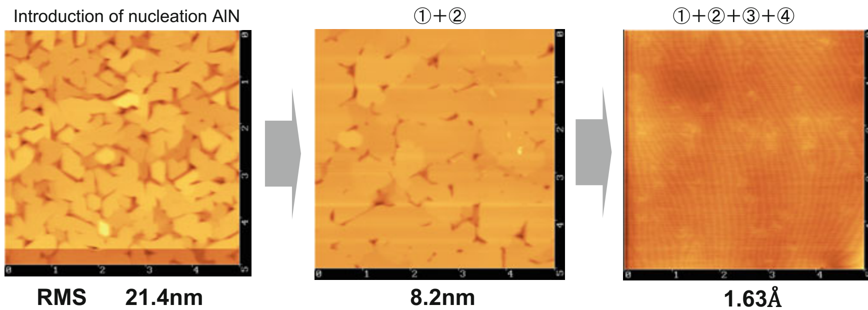

Fig. 10.6 AFM images of the surface of ML-AlN with an area of 5 × 5 μm^2 square for various stages of growth

The advantage of using ML-AlN for the DUV LED is that low-TDD AlN can be obtained without the need for AlGaN layers, yielding a device structure with minimal DUV absorption. An AlGaN-free buffer is believed to be important for realizing sub-250 nm-band high-efficiency LEDs.

Figure 10.5 shows the FWHM of the X-ray diffraction (10–12) ω-scan rocking curves (XRC) for various stages of the ML-AlN growth. The FWHM of XRC (10–12) for AlN was reduced from 2160 to 550 arcsec by introducing 'two-times repetition' of the NH_3 pulsed-flow ML-AlN growth. Figure 10.6 shows atomic-force microscope (AFM) images of the surface of ML-AlN on sapphire at various stages of the ML-AlN growth. We can observe that the surface was improved by growing the multilayers of AlN, and we can finally confirm an atomically flat surface, as demonstrated in Fig. 10.6. The root-mean-square (RMS) value of the surface roughness of the ML-AlN obtained from the AFM image was 0.16 nm.

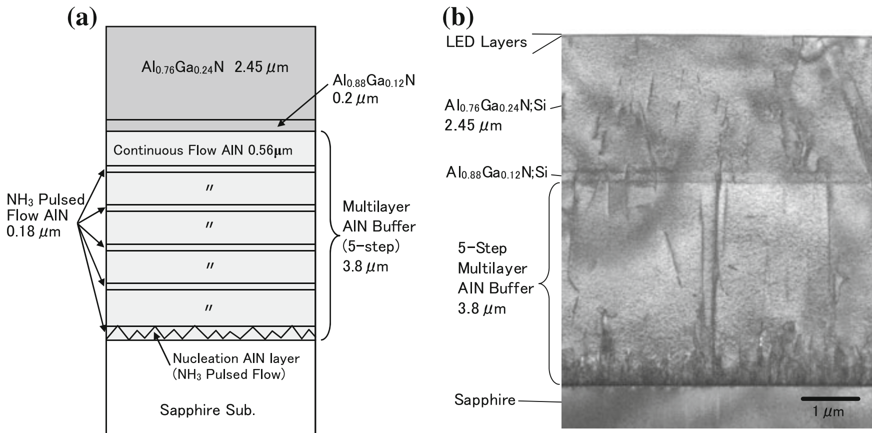

Fig. 10.7 **a** Schematic structure and **b** cross-sectional TEM image of an AlGaN/AlN template including a 5-step ML-AlN buffer layer grown on a sapphire substrate

Figure 10.7 shows (a) a schematic structure and (b) a cross-sectional transmission electron microscope (TEM) image of an AlGaN/AlN template with a 5-step ML-AlN buffer layer grown on a sapphire substrate. The total thickness of the ML-AlN buffer was typically 4 µm. The typical FWHMs of (10–12) and (0002) XRCs of the ML-AlN were approximately 370 and 180 arcsec, respectively, which were achieved by a highly uniform 3 $\times$ 2 in. reactor MOCVD [25]. The minimum FWHMs obtained for a 1 $\times$ 2 in. reactor MOCVD were approximately 290 and 180 arcsec, respectively. The minimum edge- and screw-type dislocation densities of the ML-AlN were below 5×10^8 and 4×10^7 cm^{-2}, respectively, as observed by a cross-sectional TEM image.

For further reduction of TDD of the AlN layer on sapphire, we were introducing AlN epitaxial lateral overgrowth (ELO) on patterned sapphire substrate (PSS). Also recently, we are planning to introduce high-temperature annealing for the reduction of TDD. These methods are effective to reduce TDD to be the order of 10^7 cm^{-2} and will useful to obtain higher IQE.

10.4 Increase in Internal Quantum Efficiency (IQE)

We observed a remarkable enhancement of the DUV emission of AlGaN QWs by fabricating them on low-TDD AlN templates [16, 17]. Figure 10.8 shows a cross-sectional TEM image of an AlGaN multi-(M) QW DUV LED with an emission wavelength of 227 nm fabricated on a ML-AlN buffer. We used a thin quantum well in order to obtain a high IQE by suppressing the effects of the polarization field spontaneously applied in the well. This is believed to be particularly important for obtaining the atomically smooth hetero-interfaces that are

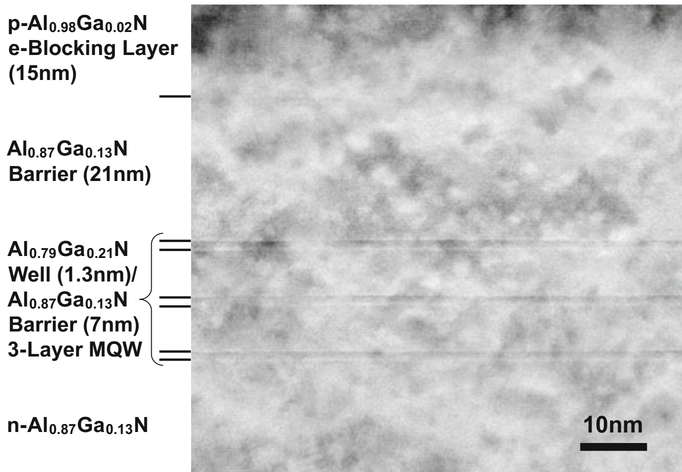

Fig. 10.8 Cross-sectional TEM image of the quantum well region of an AlGaN MQW DUV LED

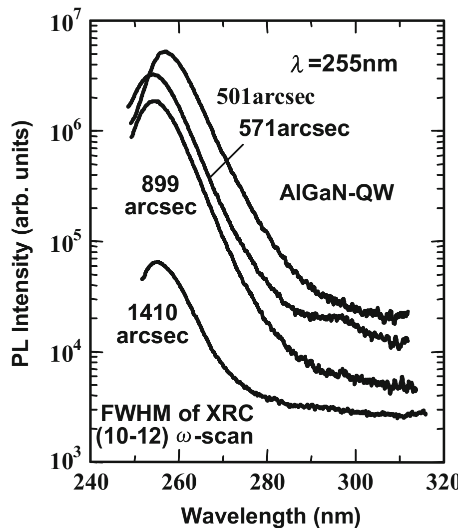

Fig. 10.9 Photoluminescence (PL) spectra of AlGaN QWs on multilayer (ML) AlN templates with various values of XRC (10–12) FWHM measured at room temperature

necessary in order to achieve a high IQE from such a thin QW. The atomically flat hetero-interfaces of the 1.3 nm-thick three-layer QWs are confirmed as observed in the cross-sectional TEM image shown in Fig. 10.8.

Figure 10.9 shows photoluminescence (PL) spectra of AlGaN QWs fabricated on ML-AlN templates with various values of XRC (10–12) FWHM, as measured at room temperature (RT). The peak emission wavelengths of the QWs were around

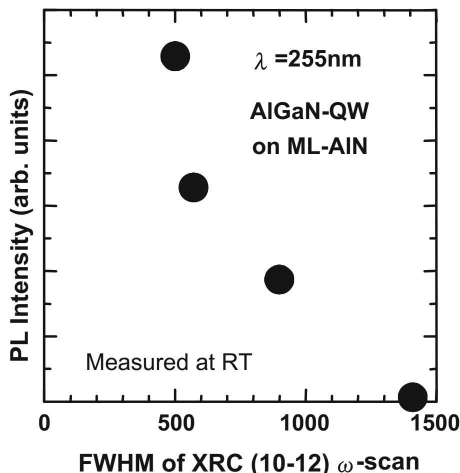

Fig. 10.10 PL intensity of AlGaN QWs as a function of XRC (10–12) FWHM of AlGaN buffers measured at room temperature

255 nm. The QWs were excited with 244 nm Ar-ion second harmonics generation (SHG) laser. The excitation power density was fixed at 200 W/cm^2. The PL emission intensity of the AlGaN QW was significantly increased by improving the XRC (10–12) FWHM, as shown in Fig. 10.9. We can see from Fig. 10.9 that the emission efficiency of AlGaN depends strongly on the edge-type TDD.

Figure 10.10 shows the PL peak intensity as measured at RT for 255-nm-emission AlGaN QWs as a function of XRC (10–12) FWHM. The PL intensity was increased by approximately 80 times by reducing the XRC (10–12) FWHM from 1400 to 500 arcsec. The PL intensity increased rapidly when the FWHM of the XRC was reduced to 500–800 arcsec. The rapid increase in PL intensity can be explained by a reduction of a non-radiative recombination rate as the distance between TDs becomes greater compared with the carrier diffusion length in the QW. We obtained similar enhancement of the emission from AlGaN QWs with various wavelengths QWs. The relationships between IQE and TDD in DUV emission AlGaN QWs were also investigated in [27, 39].

The quaternary alloy InAlGaN is attracting considerable attention as a candidate material for realizing DUV LEDs, since efficient UV emission as well as higher hole concentrations can be realized due to In-incorporation effects. The incorporation of a few percent of In into AlGaN is considered to be quite effective for obtaining high IQE, because an efficient DUV emission can be obtained due to the In-segregation effect, which has already been investigated for the ternary InGaN alloy. We have described the advantages of the use of the quaternary InAlGaN alloy in [2, 11, 12, 17].

Figure 10.11 shows a cathodeluminescence (CL) image obtained from a quaternary InAlGaN layer [2] and a schematic image of carrier recombination in an InAlGaN alloy. Emission fluctuations in the submicron region were clearly observed in the CL image. The emission fluctuation is considered to be due to carrier localization in the In-segregation area. The CL images obtained for

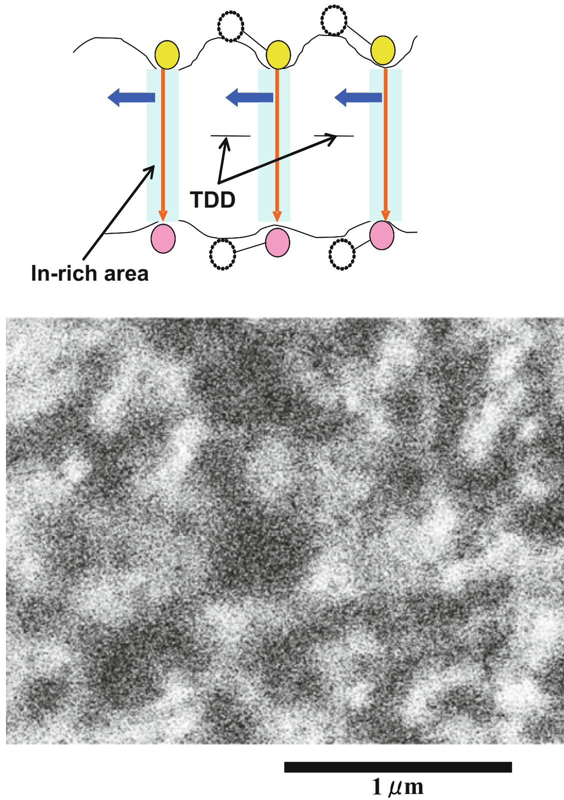

Fig. 10.11 Cathodeluminescence (CL) image obtained from a quaternary InAlGaN layer and a schematic image showing carrier recombination in an InAlGaN alloy

quaternary InAlGaN were very similar to those obtained for InGaN films. Electron–hole pairs localized in the low-potential valley emit before they are trapped in non-radiative centers induced by dislocations. Therefore, the advantage of the In incorporation is that the emission efficiency is less sensitive to TDD.

Figure 10.12 shows the temperature dependence of the integrated PL intensity measured for an InAlGaN/InAlGaN MQW with an emission wavelength of 338 nm fabricated on a high-temperature (HT)-AlN buffer on sapphire. The TDD of the HT-AlN was approximately 2×10^{10} cm^{-2}. The IQE can be roughly estimated from the temperature dependence of the integrated PL intensity, if we assume that the non-radiative recombination rate is quite low at low temperature. The estimated IQE was approximately 47% at RT, from Fig. 10.12. We found that high IQE can be obtained for InAlGaN QWs in the wavelength range between 310 and 380 nm, even when using a high-TDD template [2, 11, 12].

Then, we took up the challenge of developing crystal growth for high-quality InAlGaN alloys emitting at the 'sterilization' wavelength (280 nm) [17].

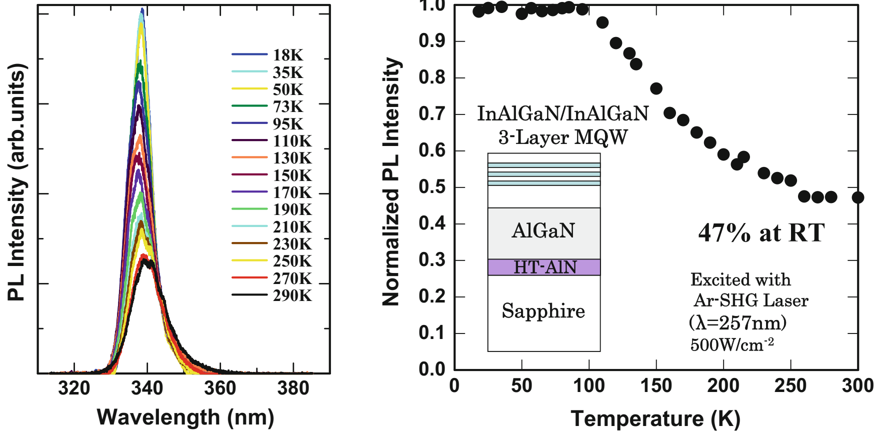

Fig. 10.12 Temperature dependence of integrated PL intensity measured for an InAlGaN/InAlGaN MQW with an emission wavelength of 338 nm fabricated on a high-temperature (HT)-AlN buffer on sapphire

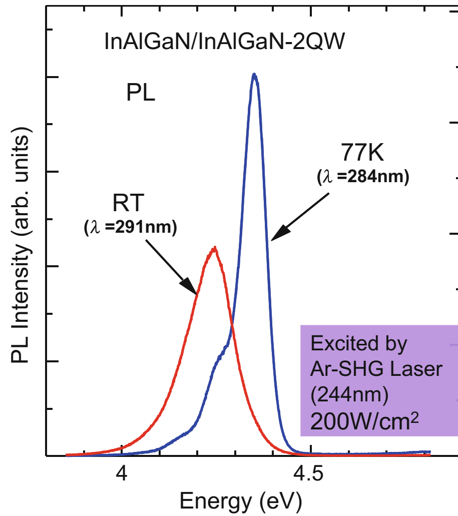

Fig. 10.13 PL spectra of a quaternary InAlGaN/InAlGaN QW emitting at 282 nm measured at 77 K and at RT

The crystal growth of high-Al-composition quaternary InAlGaN is relatively difficult, because In incorporation becomes more difficult with increasing growth temperature, which is required in order to maintain the crystal quality of high-Al content AlGaN. We achieved high-quality quaternary InAlGaN layers with high-Al content (>45%) by using relatively low-growth rate epitaxy, i.e., 0.03 μm/h. The emission intensity of a 280 nm-band quaternary InAlGaN QW at RT was increased by 5 times by reducing the growth rate from 0.05 to 0.03 μm/h. Figure 10.13 shows the PL spectra of a quaternary InAlGaN QW measured at 77 K and at RT.

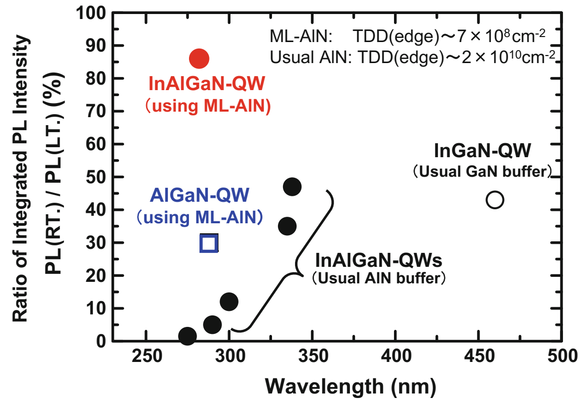

Fig. 10.14 Wavelength dependence of the ratio of the integrated PL intensity (PL measured at RT against PL measured at low temperature) for AlGaN and quaternary InAlGaN QWs fabricated on conventional high-TDD AlN and on low-TDD ML-AlN templates on sapphire substrates

We obtained extremely high intensity PL emission at RT. The ratio of the integrated intensity of the RT-PL against the 77 K-PL was 86%. Thus, high IQE was obtained from the quaternary InAlGaN QW at RT.

Figure 10.14 summarizes the wavelength dependence of the ratio of the integrated PL intensity [PL measured at room temperature (RT) against PL measured at low temperature (usually below 20 K)] investigated in 2008 [17], which is related to IQE. IQE of 340 nm InAlGaN QW was estimated to be 30–50%, even when we using a high-TDD template (TDD ~ 2×10^{10} cm^{-2}). However, IQE was reduced to below 2% for short-wavelength (280 nm) QWs, even we using quaternary InAlGaN QWs. On the other hand, we achieved high IQE by introducing low-TDD ML-AlN templates. The ratios of the integrated PL intensity obtained for 280 nm QWs were approximately 30 and 86% for an AlGaN QW and an InAlGaN QW, respectively, when we use low-TDD ML-AlN templates (TDD ~ 7×10^{8} cm^{-2}). The IQE at RT can also be estimated from the PL intensity observed at RT. We observed higher IQE values (50–60%) for AlGaN QWs by realizing a further reduction of the TDD and by optimizing the AlGaN QW growth conditions.

10.5 222–351 nm AlGaN and InAlGaN DUV LEDs

AlGaN and quaternary InAlGaN MQW DUV LEDs were fabricated on low-TDD ML-AlN templates [15–25]. Figure 10.15 shows a schematic of the structure of an AlGaN-based DUV LED fabricated on a sapphire substrate. Table 10.1 shows the typical design values of the Al compositions (x) in the $Al_xGa_{1-x}N$ wells, the buffer and barrier layers, and the electron-blocking layers (EBLs) that were used for the 222–273 nm AlGaN MQW LEDs. High-Al-composition AlGaN layers were used in order to obtain short-wavelength DUV emissions, as shown in Table 10.1. A typical LED structure consisted of an approximately 4-μm-thick undoped ML-AlN buffer layer grown on sapphire, a 2-μm-thick Si-doped AlGaN buffer

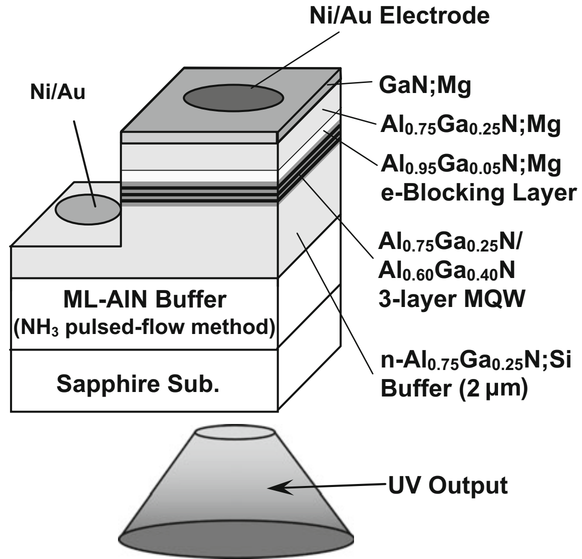

Fig. 10.15 Schematic structure of a typical AlGaN-based DUV LED fabricated on a sapphire substrate

Table 10.1 Typical design values of Al compositions (x) in $Al_xGa_{1-x}N$ wells, buffer and barrier layers, and electron-blocking layers (EBLs) used for 222–273 nm AlGaN MQW LEDs

Wavelength (nm)	Well	Barrier and buffer	Electron-blocking layer
222	0.83	0.89	0.98
227	0.79	0.87	0.98
234	0.74	0.84	0.97
248	0.64	0.78	0.96
255	0.60	0.75	0.95
261	0.55	0.72	0.94
273	0.47	0.67	0.93

layer, followed by a 3-layer undoped MQW region consisting of approximately 1.5-nm-thick AlGaN wells and 7-nm-thick AlGaN barriers, an approximately 20-nm-thick undoped AlGaN barrier, a 15-nm-thick Mg-doped AlGaN electron-blocking layers (EBLs), a 10-nm-thick Mg-doped AlGaN p-layer, and an approximately 20-nm-thick Mg-doped GaN contact layer. The quantum well thickness was varied within the range between 1.3 and 2 nm. Thin quantum wells are preferable for AlGaN QWs in order to suppress the effects of large piezoelectric fields in the well. Ni/Au electrodes were used for both n-type and p-type electrodes. The typical size of the p-type electrode was 300 × 300 μm^2. The output power that radiated into the back of the LED was measured using a Si photodetector located behind the LED sample, which was calibrated to measure the luminous flux so that the output power of a fabricated flip-chip LED device gives an accurate value. The output power of the flip-chip LED was measured precisely using an integrated sphere

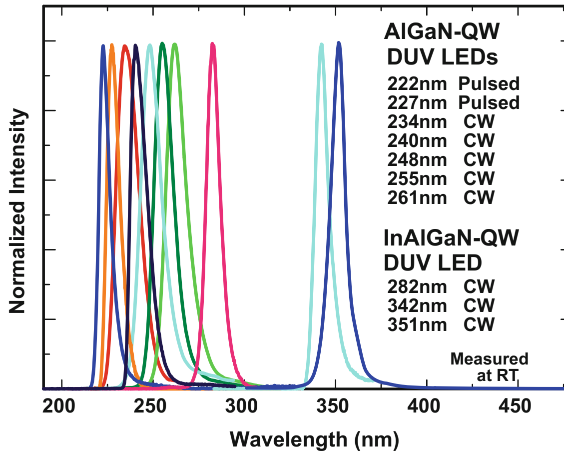

Fig. 10.16 Electroluminescence (EL) spectra of fabricated AlGaN and quaternary InAlGaN MQW LEDs with emission wavelengths between 222 and 351 nm, all measured at room temperature (RT) with injection currents of around 50 mA

system [25]. The LEDs were measured under ‘bare wafer’ or ‘flip-chip’ conditions. The forward voltages (Vf) of the bare wafer and the flip-chip samples with an injection current of 20 mA were approximately 15 and 8.3 V, respectively.

Figure 10.16 shows the electroluminescence (EL) spectra of the fabricated AlGaN and InAlGaN MQW LEDs with emission wavelengths between 222 and 351 nm, all measured at room temperature (RT) with an injection current of approximately 50 mA. As shown in Fig. 10.16, single-peak operation was obtained for every sample. The deep-level emissions were two orders of magnitude smaller than that of the main peak.

Figure 10.17 shows the EL spectra of a 227 nm AlGaN LED on a log scale [19]. We obtained single-peaked EL spectra, even for sub-230 nm wavelength LEDs. The deep-level emissions with wavelengths at around 255 and 330–450 nm were more then two orders of magnitude smaller than the main peak. These peaks may correspond to deep-level emissions associated with Mg-acceptors or other impurities. The output power of the 227 nm LED was 0.15 mW at an injection current of 30 mA, and the maximum EQE was 0.2% under RT pulsed operation. The pulse width and the repetition frequency were 3 μs and 10 kHz, respectively.

Figure 10.18 shows (a) the EL spectra for various injection currents and (b) current versus output power (I–L) and EQE (η_{ext}) characteristics for a 222 nm AlGaN MQW LED measured under RT pulsed operation [20]. Single-peaked operation of a 222 nm DUV AlGaN MQW LED was realized, which is the shortest record wavelength ever reported for a QW LED. The output power of the 222 nm LED was 0.14 μW at an injection current of 80 mA, and the maximum EQE was 0.003% under RT pulsed operation.

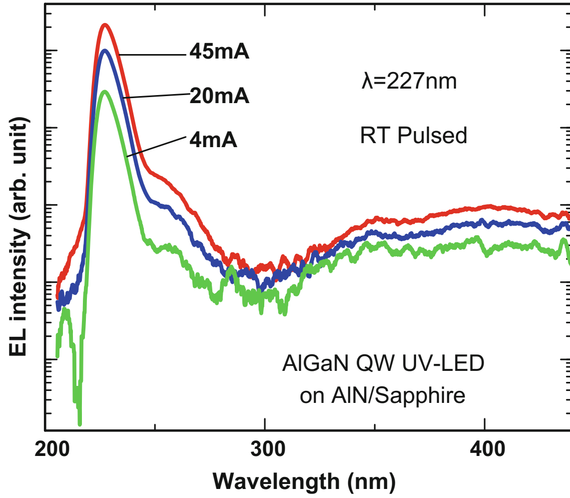

Fig. 10.17 EL spectra on a log scale of a 227 nm AlGaN DUV LED for various injection currents

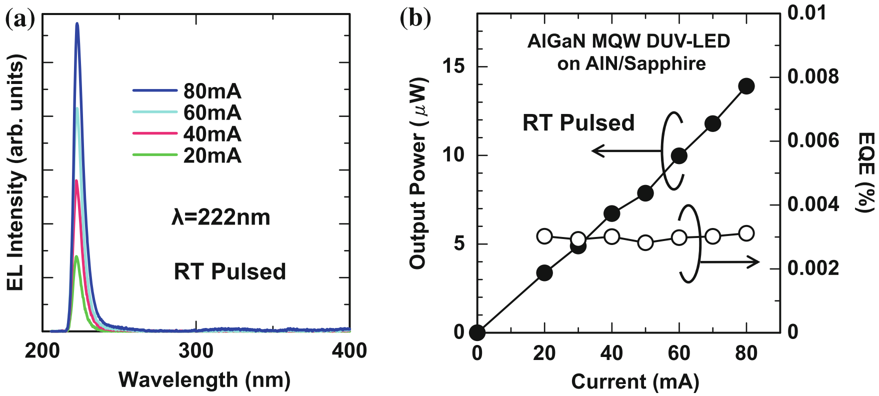

Fig. 10.18 **a** EL spectra for various injection currents and **b** current versus output power (I-L) and EQE (η_{ext}) characteristics for a 222 nm AlGaN MQW LED measured under RT pulsed operation

It has been reported that 'normal' c-axis direction emission (vertical emission) is difficult to obtain from an AlN (0001) or a high-Al content AlGaN surface, because the optical transition between the conduction band and the top of the valence band is mainly only allowed for light that has its electric field parallel to the c-axis direction of AlN (E//c) [9]. The suppression of the vertical emission is a quite severe problem for AlGaN-based DUV LEDs, because it results in a significant reduction in the light extraction efficiency (LEE). Several groups have reported that vertical c-axis emission is suppressed for high-Al content AlGaN QWs [40, 41]. Banal et al. reported that the critical Al composition for 'polarization switching'

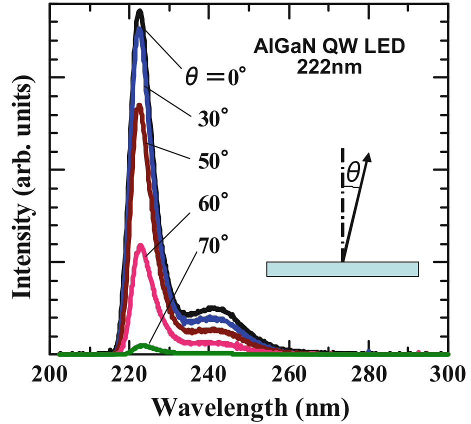

Fig. 10.19 Radiation angle dependence of emission spectra of a 222 nm AlGaN QW DUV LED

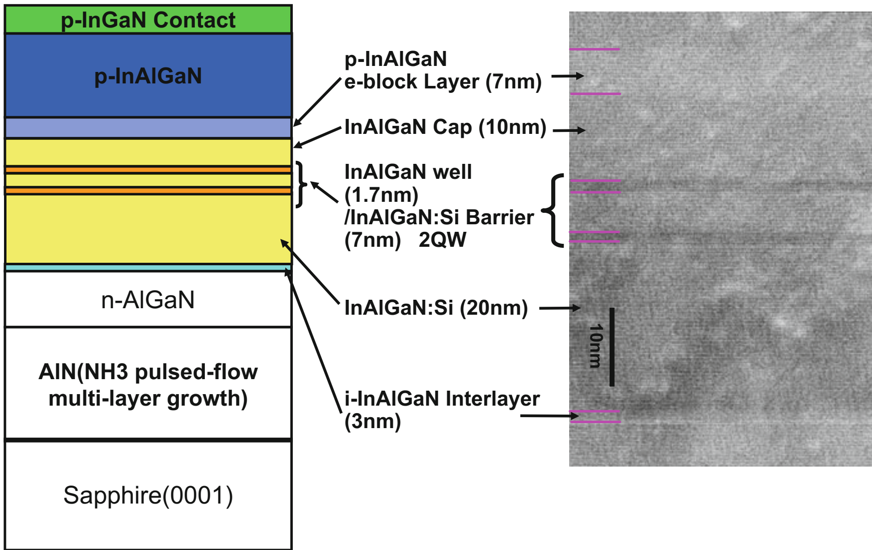

Fig. 10.20 Schematic structure and the cross-sectional TEM image of a quaternary InAlGaN QW DUV LED with emission wavelength at 282 nm

could be expanded to approximately 0.82 by using a very thin (1.3 nm) quantum well, when AlGaN QW was fabricated on an AlN/sapphire template [40].

Figure 10.19 shows the radiation angle dependence of emission spectra of a 222 nm AlGaN QW LED. We demonstrated that 'normal' c-axis-direction emission can be obtained, even for short-wavelength (222 nm) LEDs with a high-Al composition AlGaN QW, as shown in Fig. 10.19 [20]. It was found that vertical c-axis emission can be obtained for an AlGaN QW LED on AlN/sapphire, even when the Al composition range of the AlGaN QW is as high as 83%.

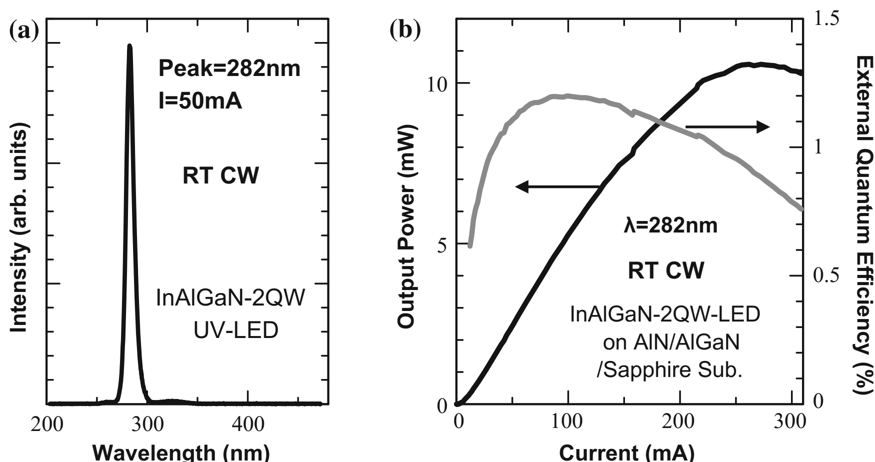

Fig. 10.21 **a** EL spectrum and **b** current versus output power (I-L) and EQE characteristics of the quaternary InAlGaN QW DUV LED with emission wavelength at 282 nm

We fabricated quaternary InAlGaN-based DUV LEDs in order to increase IQE and EIE of the DUV LEDs. Figure 10.20 shows a schematic structure and a cross-sectional TEM image of an InAlGaN QW DUV LED. We confirmed that the surface roughness of the InAlGaN layer was significantly improved by introducing a Si-doped InAlGaN buffer layer. The InAlGaN-based DUV LED is considered to be attractive for achieving high EQE due to the higher IQE and higher hole concentration obtained by In-segregation effects. Figure 10.21 shows (a) an EL spectrum and (b) the current versus output power (I–L) and EQE characteristics of an InAlGaN-based QW DUV LED with an emission wavelength of 282 nm. The maximum output power and EQE were 10.6 mW and 1.2%, respectively, under RT cw operation. From these results, we found that quaternary InAlGaN QWs and p-type InAlGaN are quite useful for achieving high-efficiency DUV LEDs [17].

10.6 Increase in Electron Injection Efficiency (EIE) by MQB

Despite achieving high IQE in DUV as mentioned above, EQE of the LED was still as low as 1–2% [17]. The low EQE figures for AlGaN DUV LEDs compared with those for InGaN blue LEDs are a result of low EIE into the QW due to electron leakage caused by low hole concentrations in the p-type AlGaN layers, as well as inferior light extraction efficiencies (lower than 8%) due to strong UV absorption in the p-GaN contact layer and the p-side electrode. The values of EIE for 250–280 nm-band AlGaN-based DUV LEDs were roughly estimated to be 10–30% [17].

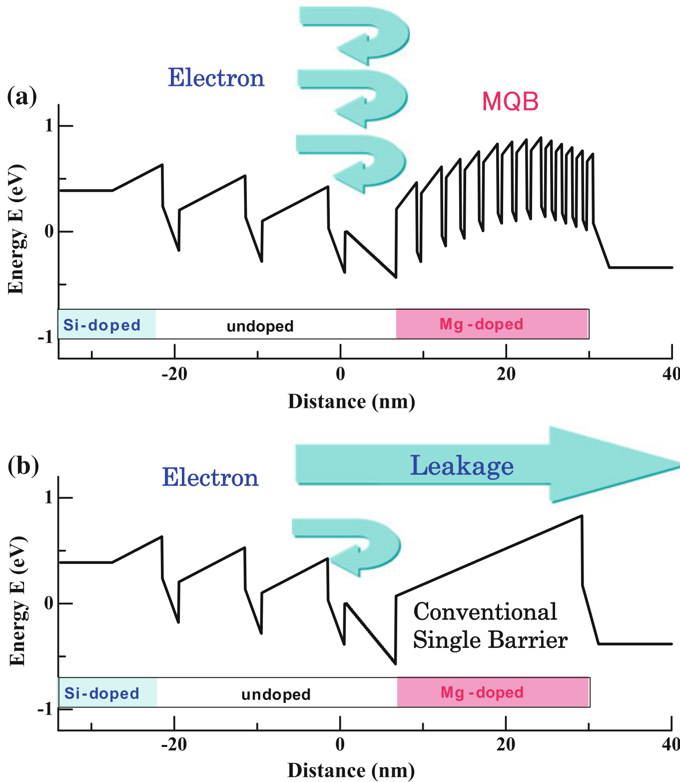

Fig. 10.22 Schematic images of the electron flow for AlGaN DUV LEDs with **a** a MQB EBL and **b** a conventional single-barrier EBL

We have introduced a MQB as an EBL in an AlGaN QW LED, and have consequently achieved a marked increase in EIE [18].

Figure 10.22 shows schematic images of the electron flow for AlGaN DUV LEDs with (a) a MQB EBL and (b) a conventional single-barrier EBL. A large barrier height is required for the EBL to obtain a sufficiently high EIE for the suppression of overflow electrons above the QW into the p-type AlGaN layers. We have tried using AlN or high-Al composition (Al > 0.95) AlGaN layers for the EBL [17, 19, 20], however, the barrier heights of these EBLs were still not sufficient high to obtain the desired high EIE. Indeed, EIE is estimated to be particularly low (<20%) for short-wavelength AlGaN LEDs (<250 nm).

Such a material limitation can be overcome by enhancing the 'effective' barrier height through the introduction of an MQB, which causes multi-reflection effects in the wavefunctions. The MQB was predicted theoretically by K. Iga et al. in 1986 [42], and the effects were demonstrated experimentally in GaInP/AlInP red laser diodes (LDs) [43]. It has been reported that the effective electron barrier height of an MQB in comparison with a bulk potential barrier is increased by as much as 30%

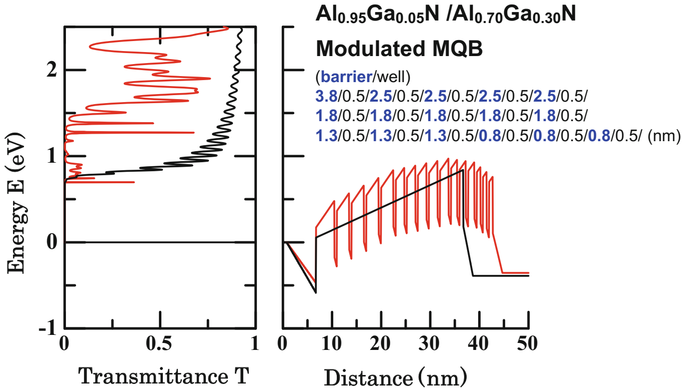

Fig. 10.23 Electron transmittance through AlGaN/AlGaN MQB (*red-line*) and conventional single-barrier EBL (*black-line*) calculated for a 250 nm-band AlGaN QW LED

for GaAs/AlAs and by 50% for GaInAs/InP MQBs. It is believed that the use of AlN/AlGaN or AlGaN/AlGaN MQBs would be quite effective for increasing the 'effective' barrier height of an EBL and, as a result, would contribute to the realization of high-EQE AlGaN DUV LEDs.

Figure 10.23 shows electron transmittance through an AlGaN/AlGaN MQB (red-line) and a conventional single-barrier EBL (black-line) calculated for a 250 nm AlGaN QW LED. The multi-reflection effects in the heterostructures are analyzed by a transfer-matrix method. It was shown that the 'effective' electron barrier height of an MQB in comparison with a conventional single-barrier EBL is increased by maximally 2 times for an AlGaN/AlGaN MQB by using barriers with thickness modulation.

Figure 10.24 shows a schematic structure and a cross-sectional TEM image of a fabricated 250 nm AlGaN QW DUV LED with an MQB EBL. We investigated an appropriate MQB structure experimentally for use with 250 nm DUV LEDs. We found that the insertion of an initial thick barrier is important for obtaining the reflection of lower energy electrons. We also found that thin barriers contribute to the reflection of higher energy electrons. The optimized MQB structure for a 250 nm AlGaN QW LED was a 5-layer $Al_{0.95}Ga_{0.05}N/Al_{0.77}Ga_{0.23}N$ MQB with thicknesses of **7**/4/**5.5**/4/**4**/2.5/**4**/2.5/**4** nm, in which the bold letters are for barriers and the normal letters are for valleys. We should design the total thickness of the MQB to be within 40 nm, because a coherent length exists for obtaining the multi-reflection effect of an MQB.

Figure 10.25 shows (a) a current versus output power (I–L) and (b) a current versus EQE (η_{ext}) characteristics for a 250 nm AlGaN MQW LED with an MQB and with a single-barrier EBL, both measured under RT cw operation. Significant increases in output power and EQE were observed when the single-EBL was replaced by the MQB. The maximum output powers of the 250 nm LED with the MQB and with the single-barrier EBL were 15 mW and 2.2 mW, respectively.

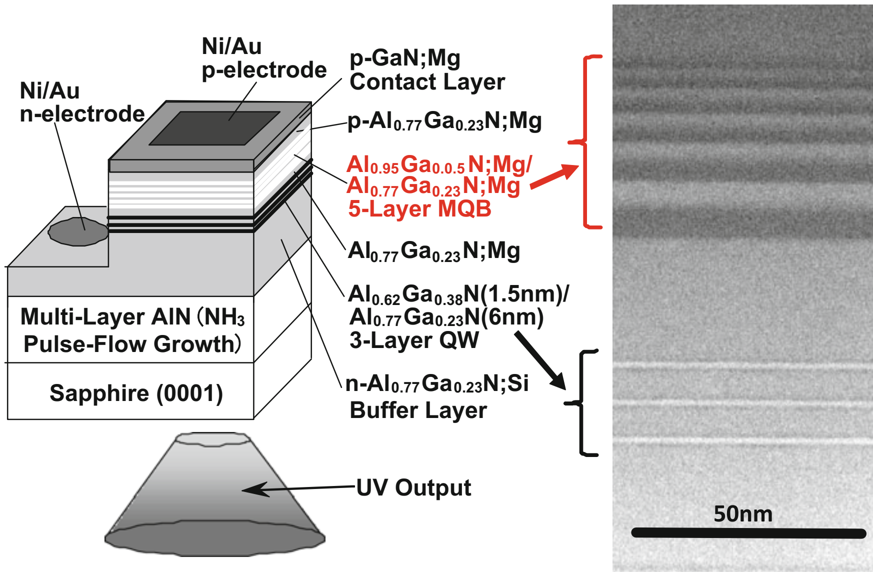

Fig. 10.24 Schematic structure and cross-sectional TEM image of a 250 nm AlGaN QW DUV LED with an MQB

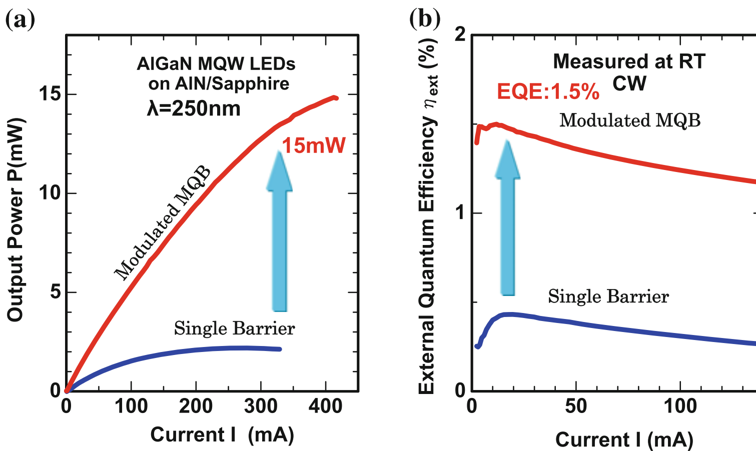

Fig. 10.25 **a** Current versus output power (I-L) and **b** current versus EQE (η_{ext}) characteristics for 250 nm AlGaN MQW LEDs with an MQB and with a single-EBL

The EQE of a 250 nm LED was increased by approximately 4 times by the introduction of the MQB. From Fig. 10.25, we have estimated that the EIE of the 250 nm LED was improved from approximately 25% to more than 80% by introducing the MQB.

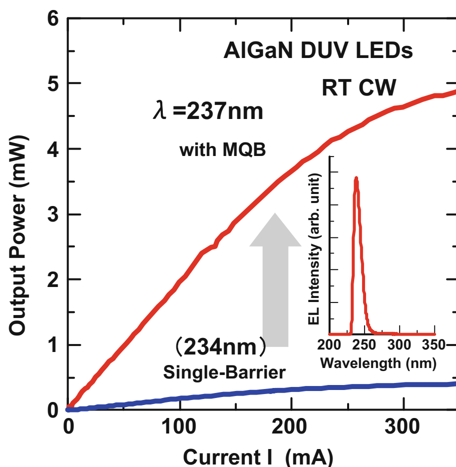

Fig. 10.26 Current versus output power (I-L) characteristic for the 237 nm AlGaN MQW LEDs with an MQB and with a single-EBL

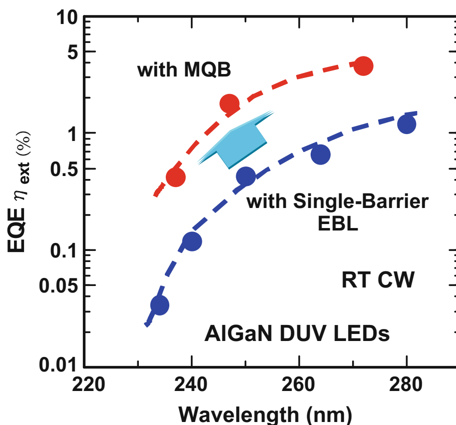

Fig. 10.27 Wavelength dependence of EQE of AlGaN DUV LEDs with MQBs and single-EBLs

Figure 10.26 shows current versus output power (I–L) characteristic for a 237 nm AlGaN MQW LED with an MQB and with a single-barrier EBL, both measured under RT cw operation. The enhancement of EIE when using the MQW was found to be extremely high for short-wavelength DUV LEDs, as shown in Fig. 10.26. The output power of the 234 nm LED was increased by approximately 12 times by replacing a single-barrier EBL by a MQB.

Figure 10.27 summarizes the wavelength dependence of EQE of AlGaN DUV LEDs with MQBs and single-barrier EBLs. The enhancement factors of the value of EQE by introducing the MQB are approximately 10, 4, and 3 times for 235, 250 and 270 nm AlGaN LEDs, respectively. We demonstrated high-output-power 270 nm AlGaN MQW LED with an MQB measured under RT cw operation. A cw output power of 33 mW was obtained for a bare-chip sample. Higher output power may be obtained by performing heat dissipation by using a flip-chip geometry.

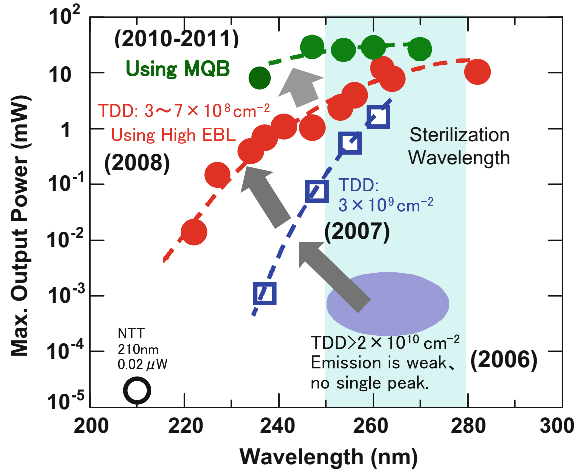

Fig. 10.28 Maximum output powers of AlGaN and InAlGaN-based DUV LEDs fabricated on low-TDD ML-AlN templates that were achieved by RIKEN between 2007 and 2011 [16–22]

The value of the EQE for a 270 nm AlGaN DUV LED with a MQB was 3.8% without using any structures for increasing LEE [21].

Figure 10.28 summarizes the maximum output powers of AlGaN and InAlGaN-based DUV LEDs fabricated on low-TDD ML-AlN templates that were achieved by the RIKEN between 2007 and 2011 [16–22]. We have achieved significant increases in the EQE and output powers of AlGaN-based DUV LEDs by introducing low-TDD AlN templates and MQB electron-blocking layers. The maximum output powers obtained were 15–33 mW for 245–270 nm single-chip LEDs. These achievements will contribute to accelerating the practical application of DUV LED, and to expanding them to a wide range of applications.

RIKEN and Panasonic have developed commercially available DUV LED modules for sterilization use. For developing a commercially available device, the reproducibility and the uniformity of an AlN template and an AlGaN LED layer structure are required for obtaining a constant high EQE and a long device lifetime. To obtain the reproducibility for an AlN and an AlGaN layer is particularly difficult because the growth condition is very sensitive for a vapor reaction between NH_3 and TMAl, which are induced by a high growth temperature (1200–1400 °C). We achieved highly uniform AlN template grown by a NH_3 pulsed flow ML growth method on sapphire using a 3 × 2 in. wafer product type MOCVD. The fluctuation of the FWHM of XRCs in an AlN template on sapphire was within 5%. We also constantly obtain XRC (10–12) FWHM of 340 arcsec for AlN templates on sapphire. Technique to obtain such a highly uniform and low-TDD template wafer is suitable for a product of commercial DUV LEDs. Figure 10.29 shows (a) a bird's eye view and (b) operating properties of a 270 nm 10 mW DUV LED module for an application to sterilization. We integrated 6 chips for the DUV LED module. A lifetime longer than 10000 h has been already achieved for devices with EQE of 2–3% [25, 26].

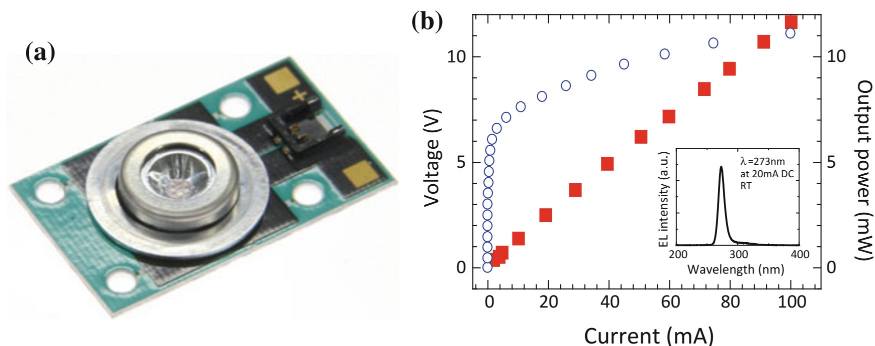

Fig. 10.29 **a** A bird's eye view and **b** operating properties of a commercially available 270 nm 10 mW DUV LED module for an application to sterilization developed by RIKEN and Panasonic

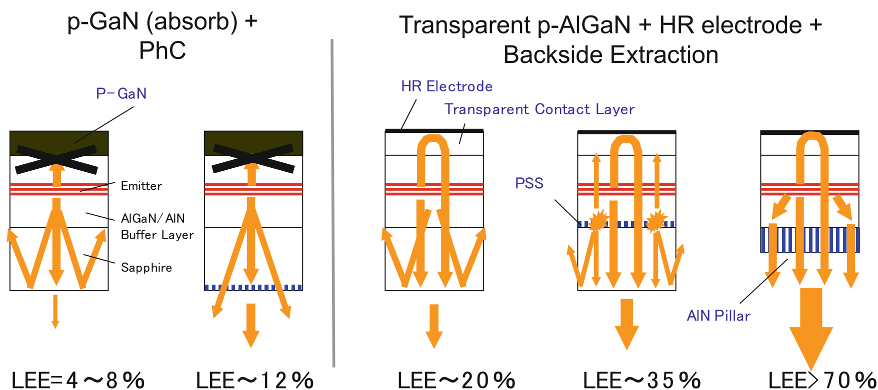

Fig. 10.30 Several schematic structures for improving LEE of a DUV LED and approximate LEE values roughly estimated for each structure

10.7 Future LED Design for High-Light Extraction Efficiency (LEE)

The improvement in LEE is particularly important for the development of an AlGaN DUV LED, because LEE of an AlGaN DUV LED is quite low in comparison with that of an InGaN-based blue LED. The increase in LEE is not so easy because of the lack of suitable transparent and conductive p-type contact layers, transparent p-type electrode, and also the lack of highly reflective p-type electrodes useful in a DUV wavelength range.

Figure 10.30 shows several schematic structures for improving LEE of a DUV LED and approximate LEE values roughly estimated for each structure. In a conventional DUV LED, the QW emission in the upward direction is completely

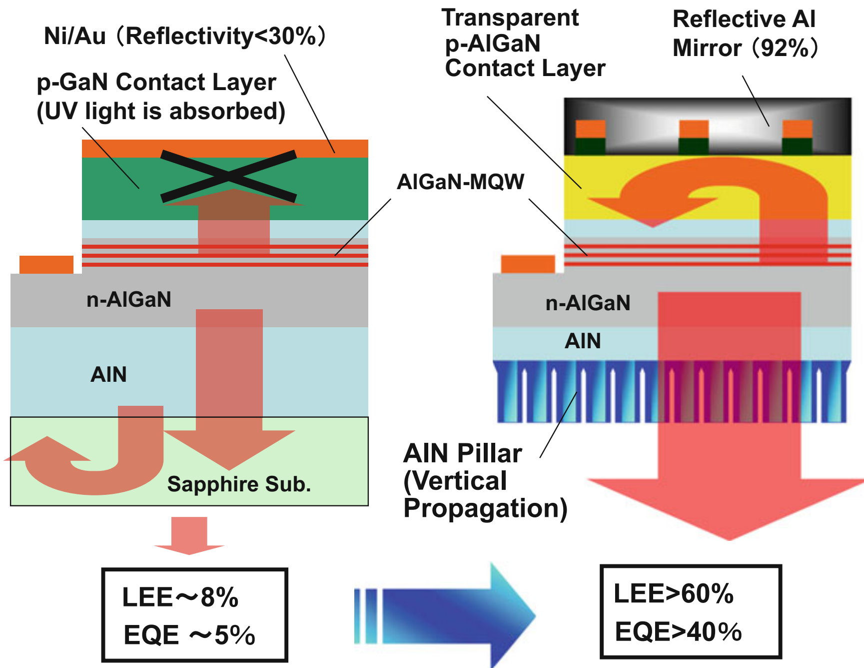

Fig. 10.31 Schematic images of the improvement in LEE of an AlGaN DUV LED by introducing a transparent p-AlGaN contact layer, a highly reflective p-type electrode, and a vertical light-propagation AlN pillar array

absorbed by the p-GaN contact layer. The DUV emission in the downward direction is reflected by the sapphire/air interface (<16% of the downward light is extracted and >84% of the downward light is reflected mainly by a total reflection). As a result, LEE of a conventional DUV LED is reduced to be smaller than 8%. Although we use photonic nanostructures on the surface of sapphire substrates or an encapsulating technique, the LEE improvement is not so high (maximum LEE is expected to around 20%), because of a heavy absorption of a p-GaN contact layer. To realize high LEE, the combination of a transparent contact layer, a highly reflective p-type electrode, and a vertical light-propagation photonic structure is desirable. Figure 10.31 shows schematic images of the improvement in LEE of an AlGaN DUV LED that can be achieved by replacing the conventional p-GaN contact layer structure by the novel LED structure proposed in this work [24].

Recently, we have fabricated a DUV LED with a high-Al content p-AlGaN contact layer. We found that the p-AlGaN can act as a highly transparent p-type contact layer. The reflectance of a conventional Ni/Au p-electrode is low (~25%) and is not suitable as a highly reflective mirror. The reflectance of Al in DUV is 92%, but Ohmic contacts are difficult to obtain. The introduction of a mesh-type electrode with Al mirror windows is one of the solutions for a highly reflective p-type electrode, as shown on the right of Fig. 10.31. If the reflectivity of the p-type

electrode is not sufficiently high (~80%), a photonic structure with a vertical light-propagation property is required to extract the light with the minimum number of reflections. In other words, an efficient light coupling into a photonic structure such as a pillar array is quite useful for obtaining an efficient light extraction.

LEE of an AlGaN DUV LED similar to the proposed was investigated by Ryu et al. [44], based on the analysis by finite-difference time-domain (FDTD) simulations. They also concluded from the calculation that the combination of a vertical LED geometry with a photonic nanostructure and a transparent p-AlGaN contact layer is important for obtaining high LEE in AlGaN DUV LEDs. They demonstrated that LEE of the vertical AlGaN DUV LED is improved by about ten times, when the thickness of the p-GaN contact layer is reduced from 25 nm to zero. They also demonstrated from the simulation that a maximum LEE as high as 72% can be obtained for the transverse electric (TE) mode, if a transparent p-AlGaN contact layer is introduced in the vertical LEDs. Such results match well with our proposal.

We will demonstrate a very simple estimation of LEE for a proposed DUV LED. We assume that the equivalent reflectance for the upward-direction light is 80%, which is determined by the reflectivity of a p-electrode and the absorption through a p-AlGaN contact layer. We also assume that the equivalent coupling coefficient of the downward light into a pillar array is 40%. In other words, 40% of the downward light can be extracted through the pillar array. Of course, they are average values taking into account all propagating light to every direction. At first, 50% light is emitted from the QW toward the downward direction and 40% light is reflected and returned by the p-electrode, then 90% light reaches in front of a pillar array. The amount of the first-time extraction light through the pillar array is calculated to be $90\% \times 0.4 = 36\%$. Then, 54% light is reflected by the pillar array. The amount of the second-time extraction light through the pillar array is obtained as $54\% \times 0.8 \times 0.4 = 17.3\%$. By the same manner, the amounts of the third- and fourth-time extraction light are calculated as 8.3 and 4%, respectively. By integrating the amounts of the first- to the third-time extraction light, we can obtain high LEE of more than 61.6%. The equivalent coupling coefficient of 40% is considered to be reasonable by comparing with FDTD results. Through the above estimations, we can obtain high LEE with the minimum number of reflections.

We demonstrated a DUV LED with a highly transparent p-AlGaN contact layer. Figure 10.32 shows the transparency of a high-Al content Mg-doped p-AlGaN layer, grown on an AlGaN/AlN/sapphire template usually used for a DUV LED. We confirmed that the transparency of a 120-nm-thick p-AlGaN layer with an Al composition of 60% is higher than 94% for 279 nm DUV light, as measured using a spectrophotometer. The transparency of the p-AlGaN contact layer used for an actual DUV LED was estimated to be approximately 97% taking into account the contact layer thickness (70 nm).

As a p-type electrode, we replaced the conventional Ni(25 nm)/Au(150 nm) with a highly reflective Ni(1 nm)/Al(150 nm). Current injection was made possible by inserting a very thin Ni layer (<1 nm) between the Al layer and the p-AlGaN contact layer. Figure 10.33 shows the wavelength dependent of the reflectivity for various type p-type electrodes used for AlGaN DUV LEDs. In the actual 270 nm

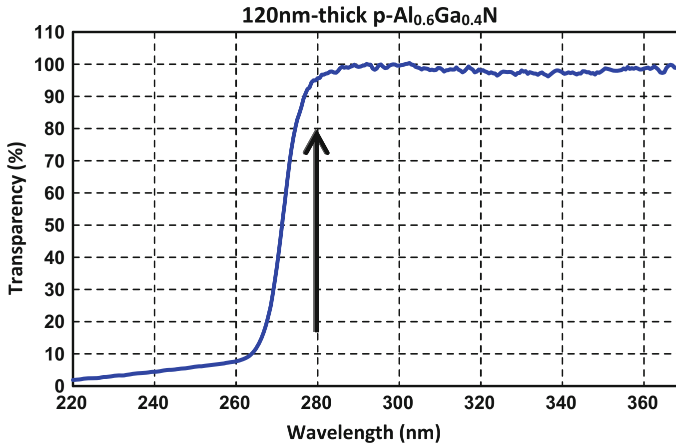

Fig. 10.32 Transparency measured for a Mg-doped p-AlGaN layer with Al composition of 60% grown on an AlGaN/AlN/sapphire template

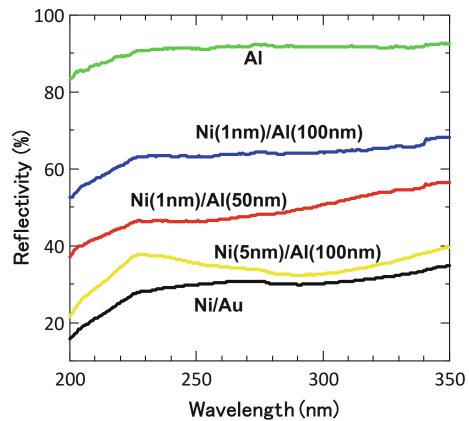

Fig. 10.33 Wavelength dependent of the reflectivity for various type p-type electrodes for AlGaN DUV LEDs

DUV LED devices, the reflectivity of the p-type electrode was increased from 30 to 64% by replacing the conventional Ni(25 nm)/Au(150 nm) electrode with a Ni (1 nm)/Al(150 nm) electrode.

Figure 10.34 shows the current versus EQE (η_{ext}) characteristics of 279 nm AlGaN MQW DUV LEDs with transparent p-AlGaN contact layers, comparing between the different p-electrode structure (conventional Ni(25 nm)/Au(150 nm) and highly reflective Ni(1 nm)/Al(150 nm) p-electrodes), measured under RT cw operation. EQE was significantly increased from 4 to 7% (by 1.7 times) owing to the increase in LEE induced by replacing the conventional Ni/Au p-electrode with a highly reflective Ni/Al electrode. We can estimate that the transparency of the p-AlGaN contact layer is higher than 95% from the enhancement factor of LEE.

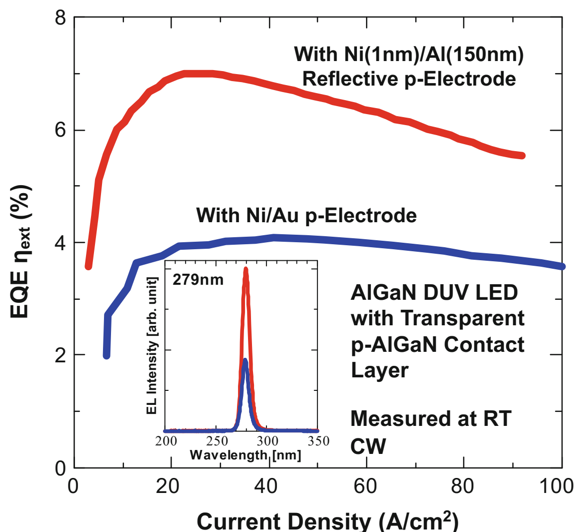

Fig. 10.34 Current versus EQE (η_{ext}) characteristics of 279 nm AlGaN MQW DUV LEDs with transparent p-AlGaN contact layers, comparing between the different p-electrode structures (conventional Ni/Au and highly reflective Ni/Al p-electrodes) measured under RT cw operation

The LEE enhancement factors that were achieved in 265–279 nm DUV LEDs by replacing the Ni/Au p-electrode with the highly reflective Ni/Al electrode were approximately 1.3–1.7.

We also challenged to achieve a shorter wavelength DUV LED with a transparent p-AlGaN contact layer. For obtaining short-wavelength 260 nm LED, high-Al content p-AlGaN contact layer is required. Figure 10.35 shows the transparency of a high-Al content (>70%) Mg-doped p-AlGaN layer, grown on an AlGaN/AlN/sapphire template. We confirmed that the cut-off wavelength was shifted from around 275–245 nm by increasing an Al composition of p-AlGaN. Then, we fabricated DUV LED with a wavelength at 261 nm with a high-Al content (>70%) p-AlGaN contact layer. Figure 10.36 shows (a) the emission spectra and (b) current versus EQE (η_{ext}) characteristics of 261 nm AlGaN MQW DUV LEDs with transparent p-AlGaN contact layers, comparing them with conventional Ni/Au and highly reflective Ni/Al p-electrodes measured under RT cw operation. Maximum EQE was increased from 2 to 3.3% (by 1.6 times) owing to the increase in LEE induced by replacing the conventional Ni/Au p-electrode with a highly reflective Ni/Al electrode.

We observed an increase in the forward voltage (Vf) when p-GaN was replaced with a transparent p-AlGaN contact layer. Vf at an injection current of 5 mA increased from 11 to 17 V for a bare wafer DUV LED when the contact layer was changed from p-GaN to p-AlGaN. Therefore, the high resistivity of p-contacts caused by the low hole concentration is still a problem for the use of p-AlGaN contact layers. The increase in Vf causes a reduction in the wall-plug efficiency (WPE) of the device. We aim to improve Vf by using mesh-type p-electrodes.

Finally, we fabricated a flip-chip (FC)-type DUV LED module with transparent p-AlGaN contact layer and reflective p-type electrode. Figure 10.37 shows

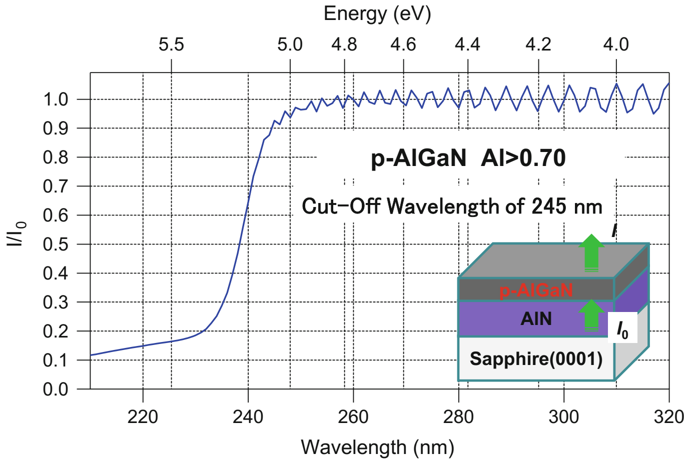

Fig. 10.35 Transparency measured for a Mg-doped p-AlGaN layer with Al composition over 70% grown on an AlGaN/AlN/sapphire template

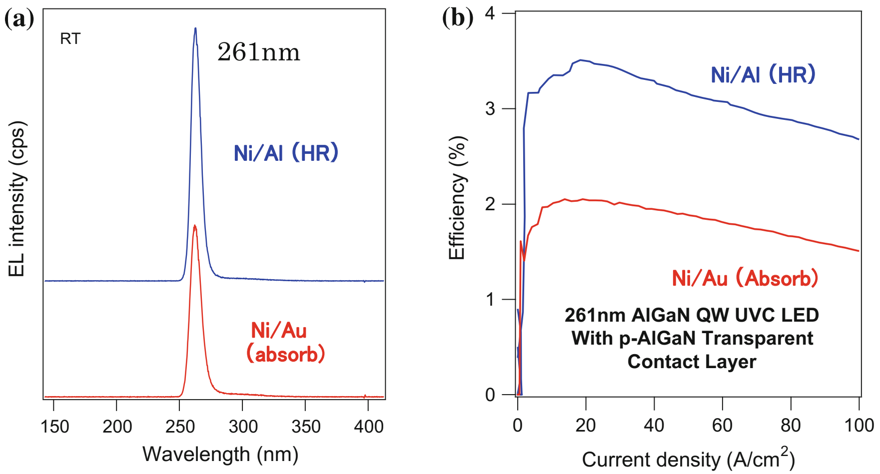

Fig. 10.36 **a** Emission spectra and **b** current versus EQE (η_{ext}) characteristics of 261 nm AlGaN MQW DUV LEDs with transparent p-AlGaN contact layers, comparing between the different p-electrode structures (conventional Ni/Au and highly reflective Ni/Al p-electrodes) measured under RT cw operation

schematic structures of a conventional (left) and a LEE enhancement design (right) FC DUV LED modules. For a conventional structure, we used p-GaN contact layer and Ni/Au p-type electrode, and the LEE value of the LED module was roughly estimated to 8%. For a new structure, we used p-AlGaN transparent contact layer and Ni/Al/Ti/Au reflective p-type electrode. We also adopted encapsulation by resin

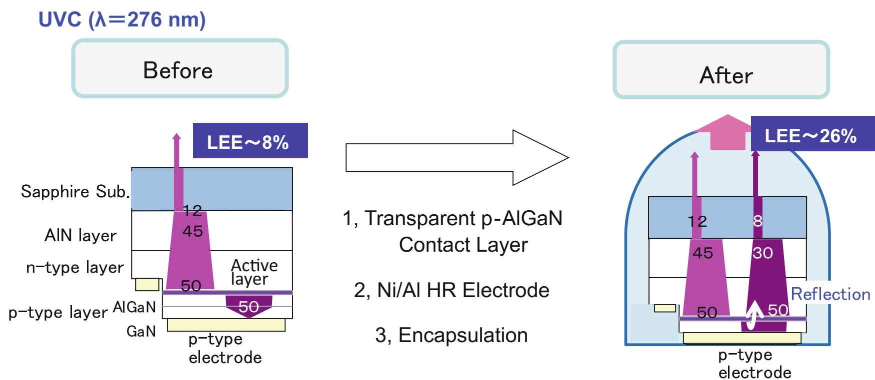

Fig. 10.37 Schematic structures of a conventional (*left*) and a LEE enhancement design (*right*) flip-chip (FC) DUV LED modules

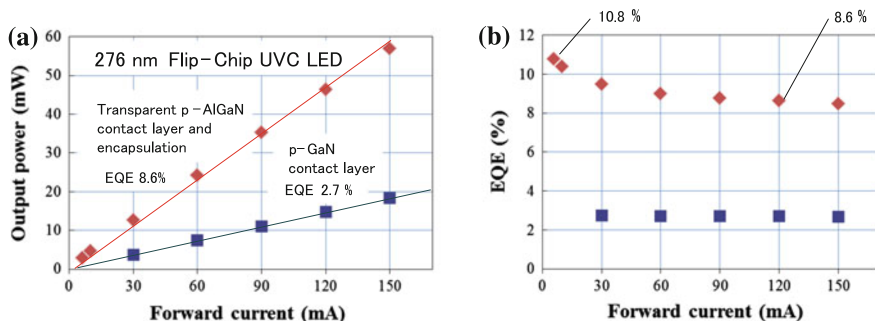

Fig. 10.38 **a** I-L and **b** I-EQE characteristics of fabricated FC DUV LED modules comparing between conventional and LEE enhancement design structures, measured under RT cw operation

only for LEE enhancement structure. The LEE value for new structure LED module was roughly estimated to 26%. Figure 10.38 shows (a) I–L and (b) I–EQE characteristics of fabricated FC DUV LED modules comparing between conventional and LEE enhancement design structures, measured under RT cw operation. The emission peak wavelengths of these LED modules were 276 nm. The EQE under the forward current around 120 mA was dramatically increased from 2.7 to 8.6% by introducing a LEE enhancement structure. The maximum EQE obtained under the forward current of 5 mA was 10.8%. We obtained the output power of 57 mW under the forward current of 150 mA for the LEE enhancement module.

We are planning to realize the proposed structure as shown in Fig. 10.31 by introducing pillar AlN structure grown on patterned sapphire substrate (PSS) and laser lift-off (LLO) techniques, with the aim of achieving a marked improvement in LEE for UVC LEDs. We hope that the application of such devices to fields involving sterilization will be widely expanded through the achievement of high-efficiency UVC LEDs in the near future.

10.8 Summary

We demonstrated the recent progress in AlGaN-based DUV LEDs, which has been achieved by the development of crystal growth techniques for wide-bandgap AlN and AlGaN. Significant increases in IQE have been achieved for AlGaN QW DUV emissions by using low-TDD AlN on sapphire grown by an NH_3 pulsed-flow multilayer growth method. 222–351 nm DUV LEDs have been achieved using the high-IQE emission layers. EIE of the DUV LED was significantly increased by controlling the electron flow using an MQB. We also demonstrated the improvement of LEE by using a transparent p-AlGaN contact layer and a highly reflective p-electrode. The maximum EQE obtained was 10.8% for a 276 nm DUV LED. EQE could be increased up to several tens of percent in the near future by improving LEE by utilizing transparent contact layers and pillar array buffer layers.

References

1. A. Zukauskas, M.S. Shue, R. Gaska, *Introduction to Solid-State Lighting* (Wiley, New York, 2002)
2. H. Hirayama, J. Appl. Phys. **97**, 091101 (2005)
3. J. Han, M.H. Crawford, R.J. Shul, J.J. Figiel, M. Banas, L. Zhang, Y.K. Song, H. Zhou, A.V. Nurmikko, Appl. Phys. Lett. **73**, 1688 (1998)
4. A. Kinoshita, H. Hirayama, M. Ainoya, A. Hirata, Y. Aoyagi, Appl. Phys. Lett. **77**, 175 (2000)
5. T. Nishida, H. Saito, N. Kobayashi, Appl. Phys. Lett. **78**, 711 (2001)
6. W.H. Sun, V. Adivarahan, M. Shatalov, Y. Lee, S. Wu, J.W. Yang, J.P. Zhang, M.A. Khan, Jpn. J. Appl. Phys. **43**, L1419 (2004)
7. V. Adivarahan, S. Wu, J.P. Zhang, A. Chitnis, M. Shatalov, V. Madavilli, R. Gaska, M.A. Khan, Appl. Phys. Lett. **84**, 4762 (2004)
8. V. Adivarahan, W.H. Sun, A. Chitnis, M. Shatalov, S. Wu, H.P. Maruska, M. Asif Khan. Appl. Phys. Lett. **85**, 2175 (2004)
9. Y. Taniyasu, M. Kasu, T. Makimoto, Nature **444**, 325 (2006)
10. H. Hirayama, Y. Enomoto, A. Kinoshita, A. Hirata, Y. Aoyagi, Appl. Phys. Lett. **80**, 37 (2002)
11. H. Hirayama, A. Kinoshita, T. Yamabi, Y. Enomoto, A. Hirata, T. Araki, Y. Nanishi, Y. Aoyagi, Appl. Phys. Lett. **80**, 207 (2002)
12. H. Hirayama, Y. Enomoto, A. Kinoshita, A. Hirata, Y. Aoyagi, Appl. Phys. Lett. **80**, 1589 (2002)
13. H. Hirayama, K. Akita, T. Kyono, T. Nakamura, K. Ishibashi, Jpn. J. Appl. Phys. **43**, L1241 (2004)
14. S. Fujikawa, T. Takano, Y. Kondo, H. Hirayama, Jpn. J. Appl. Phys. **47**, 2941 (2008)
15. H. Hirayama, T. Yatabe, N. Noguchi, T. Ohashi, N. Kamata, Appl. Phys. Lett. **91**, 071901 (2007)
16. H. Hirayama, T. Yatabe, T. Ohashi, N. Kamata, Phys. Status Solidi C **5**, 2283 (2008)
17. H. Hirayama, N. Noguchi, S. Fujikawa, J. Norimatsu, T. Takano, K. Tsubaki, N. Kamata, Phys. Status Solidi A **206**, 1176 (2009)
18. H. Hirayama, Y. Tsukada, T. Maeda, N. Kamata, Appl. Phys. Express **3**, 031002 (2010)
19. H. Hirayama, N. Noguchi, T. Yatabe, N. Kamata, Appl. Phys. Express **1**, 051101 (2008)

20. H. Hirayama, N. Noguchi, N. Kamata, Appl. Phys. Express **3**, 032102 (2010)
21. S. Fujikawa, H. Hirayama, N. Maeda, Phys. Status Solidi C **9**(3–4), 790–793 (2012)
22. N. Maeda, H. Hirayama, Phys. Status Solidi C **10**, 1521 (2014)
23. H. Hirayama, N. Maeda, S. Fujikawa, S. Toyoda, N. Kamata, Optronics **2**, 58 (2014)
24. H. Hirayama, N. Maeda, S. Fujikawa, S. Toyota, N. Kamata, Recent progress and future prospects of AlGaN-based high-efficiency deep-ultraviolet light-emitting diodes. Jpn. J. Appl. Phys. (Sel. Top.) **53**, 100209 1–10 (2014)
25. T. Mino, H. Hirayama, T. Takano, N. Noguchi, K. Tsubaki, Phys. Status Solidi C **9**, 749 (2012)
26. T. Mino, H. Hirayama, T. Takano, K. Tsubaki, M. Sugiyama, Proc. SPIE **8625**, 59 (2013)
27. M. Shatalov, W. Sun, Y. Bilenko, A. Sattu, X. Hu, J. Deng, J. Yang, M. Shur, C. Moe, M. Wraback, R. Gaska, Appl. Phys. Express **3**, 062101 (2010)
28. J. Mickevičius, G. Tamulaitis, M. Shur, M. Shatalov, J. Yang, R. Gaska, Appl. Phys. Lett. **103**, 011906 (2013)
29. M. Shatalov, W. Sun, A. Lunev, X. Hu, A. Dobrinsky, Y. Bilenko, J. Yang, Appl. Phys. Express **5**, 082101 (2012)
30. C. Pernot, M. Kim, S. Fukahori, T. Inazu, T. Fujita, Y. Nagasawa, A. Hirano, M. Ippommatsu, M. Iwaya, S. Kamiyama, I. Akasaki, H. Amano, Appl. Phys. Express **3**, 061004 (2010)
31. J.R. Grandusky, J. Chen, S.R. Gibb, M.C. Mendrick, C.G. Moe, L. Rodak, G.A. Garrett, M. Wraback, L.J. Schowalter, Appl. Phys. Express **6**, 032101 (2013)
32. J.R. Grandusky, S.R. Gibb, M.C. Mendrick, C. Moe, M. Wraback, L.J. Schowalter, Appl. Phys. Express **4**, 082101 (2011)
33. T. Kinoshita, K. Hironaka, T. Obata, T. Nagashima, R. Dalmau, R. Schlesser, B. Moody, J. Xie, S. Inoue, Y. Kumagai, A. Koukitu, Z. Sitar, Appl. Phys. Express **5**, 122101 (2012)
34. T. Kinoshita, T. Obata, T. Nagashima, H. Yanagi, B. Moody, S. Mita, S. Inoue, Y. Kumagai, A. Koukitu, Z. Sitar, Appl. Phys. Express **6**, 092103 (2013)
35. S. Hwang, D. Morgan1, A. Kesler, M. Lachab, B. Zhang, A. Heidari, H. Nazir, I. Ahmad, J. Dion, Q. Fareed, V. Adivarahan, M. Islam, A. Khan, Appl. Phys. Express **4**, 032102 (2011)
36. A. Fujioka, T. Misaki, T. Murayama, Y. Narukawa, T. Mukai, Appl. Phys. Express **3**, 041001 (2010)
37. K. Iida, T. Kawashima, A. Miyazaki, H. Kasugai, A. Mishima, A. Honshio, Y. Miyake, M. Iwaya, S. Kamiyama, H. Amano, I. Akasaki, Jpn. J. Appl. Phys. **43**, L499 (2004)
38. T. Takano, Y. Narita, A. Horiuchi, H. Kawanishi, Appl. Phys. Lett. **84**, 3567 (2004)
39. K. Ban, J. Yamamoto, K. Takeda, K. Ide, M. Iwaya, T. Takeuchi, S. Kamiyama, I. Akasaki, H. Amano, Appl. Phys. Express **4**, 052101 (2011)
40. R.G. Banal, M. Funato, Y. Kawakami, Phys. Rev. B **79**, 121308(R) (2009)
41. H. Kawanishi, M. Senuma, M. Yamamoto, E. Niikura, T. Nukui, Appl. Phys. Lett. **89**, 081121 (2006)
42. K. Iga, H. Uenohara, F. Koyama, Electron. Lett. **22**, 1008 (1986)
43. K. Kishino, A. Kikuchi, Y. Kaneko, I. Nomura, Appl. Phys. Lett. **58**, 1822 (1991)
44. H.Y. Ryu, I.G. Choi, H.S. Choi, J.I. Shim, Appl. Phys. Express **6**, 062101 (2013)

Chapter 11
Ray Tracing for Light Extraction Efficiency (LEE) Modeling in Nitride LEDs

C. Lalau Keraly, L. Kuritzky, M. Cochet and Claude Weisbuch

Abstract We describe simulations of the light extraction efficiency (LEE) as a function of the major materials parameters and geometries in the three main LED structures used today, namely nitride LEDs on GaN substrates, on patterned sapphire substrates and flip chip nitride LEDs. We use ray tracing simulations of LEDs to show how the various extraction schemes operate. The simulations of this chapter show that both surface roughening and PSS lead to high efficiencies, although based on somewhat different mechanisms. The results appear here for the same device parameters (most of them with conservative values), which allow meaningful comparisons. Some industry results may be higher, either due to better materials quality (lower absorption in particular for ITO and metals) or more aggressive designs (smaller lossy contact areas). For LEDs on GaN substrates, the LEE is determined by residual substrate absorption. A desirable feature is the ability to scale the extraction efficiency for large chips in order to reduce costs. In almost all cases, the use of large surface LEDs is detrimental due to the long ray paths to reach the sidewalls except for those extraction schemes where light is continuously extracted or when substrates have very low absorption.

A chapter for "III-nitride-based light-emitting diodes and applications."

Prof. T.-Y. Seong (Korea University), Prof. H. Amano (Nagoya University), Prof. J. Han (Yale University), Prof. H. Morkoç (Virginia Commonwealth University) eds.

C. Lalau Keraly · L. Kuritzky · M. Cochet · C. Weisbuch (✉)
Materials Department, University of California, Santa Barbara 93106-5050, USA
e-mail: claude.weisbuch@polytechnique.fr; weisbuch@engineering.ucsb.edu

C. Weisbuch
Laboratoire de Physique de la Matière Condensée, CNRS,
Ecole Polytechnique, 91128 Palaiseau Cedex, France

Present Address:
C. Lalau Keraly
Department of Electrical Engineering, University of California at Berkeley,
Berkeley, USA

© Springer Nature Singapore Pte Ltd. 2017

T.-Y. Seong et al. (eds.), *III-Nitride Based Light Emitting Diodes and Applications*,
Topics in Applied Physics 133, DOI 10.1007/978-981-10-3755-9_11

11.1 Introduction

The development and commercialization of high efficiency light emitters is a major technical challenge that will have a huge impact on efficient energy use, as worldwide 15–20% of the electricity consumption is due to lighting. Today, lighting is performed mostly with incandescent light bulbs with efficiencies below 5%, compact fluorescent lamps with efficiencies in the 20%+ range, or fluorescent tubes with efficiencies in the 30%+ range.

The direct conversion of electricity into light in semiconductor light-emitting diodes (LEDs) could, in principle, occur with 100% efficiency. The total efficiency of electricity to light conversion is given by the product of three terms:

$$Total\,Efficiency = IQE \times LEE \times \eta_{elec} \tag{11.1}$$

where IQE is the internal quantum efficiency, describing the conversion of electrical current into photons inside the material, LEE is the light extraction efficiency of photons generated in the active region that are emitted to free space, and η_{elec} is the electrical efficiency, mainly related to ohmic losses in the electrical contacts and to the carrier injection efficiency into the active layers for radiative recombination, η_{inj}.

This chapter focuses on LEE, which is adversely impacted by the high indices of refraction of semiconductors ($n > 2$). The index mismatch between semiconductor and air leads to a large fraction of light being trapped within the material by total internal reflection (TIR), which occurs when light rays impinge on the semiconductor–air interface at an incident angle larger than the critical angle for refraction. The problem of total internal reflection is often addressed using chip shaping or textured interfaces, which cause light rays to impinge on the semiconductor–air interface at different angles as they make multiple escape attempts. Chip shaping and surface texturing features in LEDs have relatively large dimensions compared to the wavelength of light in the device, such that they can be described by geometrical or ray optics.

High light extraction and greater beam control is also achieved in LEDs through the use of optical mode quantization using microcavities of varied photonic dimensionalities [1, 2] and photonic crystals [7, 19, 23, 27]. Such solutions are still at the research level today and require more complex analysis incorporating wave optical physics. We mainly discuss here simulations of structures based on ray optics. This chapter aims to clarify the origin of improvements in LEE, identify the main loss mechanisms in given structures, and provide a method for designing LEDs with high LEE. We provide, in particular, simulations of the variation in LEE as a function of the major materials parameters and geometries associated with the three main structures used today, namely nitride LEDs on GaN substrates, on patterned sapphire substrates and flip chip nitride LEDs.

11.2 Background on Ray Optics

11.2.1 Snell-Descartes Law

The central issue in light extraction comes from the nature of light interaction at the surface between two dielectric materials. When a propagating light ray hits an interface between two different materials, part of it will be reflected, and part of it will be transmitted (or equivalently, refracted) into the new material. The angle of reflection will be the same as the angle of incidence, while the angle of refraction follows a more complicated law named the Snell-Descartes law, (11.2), where n_1 and n_2 are the refractive indices of the different materials and θ_1 and θ_2 are the angles of incidence and refraction, as shown in Fig. 11.1.

$$n_1 \sin(\theta_1) = n_2 \sin(\theta_2) \tag{11.2}$$

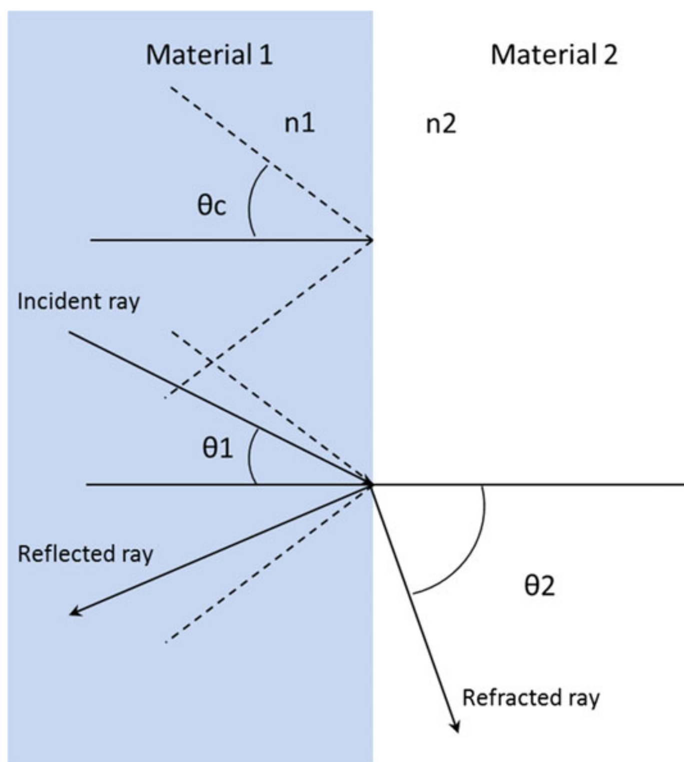

Fig. 11.1 Schematic of the interaction of a light ray at a dielectric interface, displaying the critical angle θ_c beyond which rays are fully reflected by total internal reflection

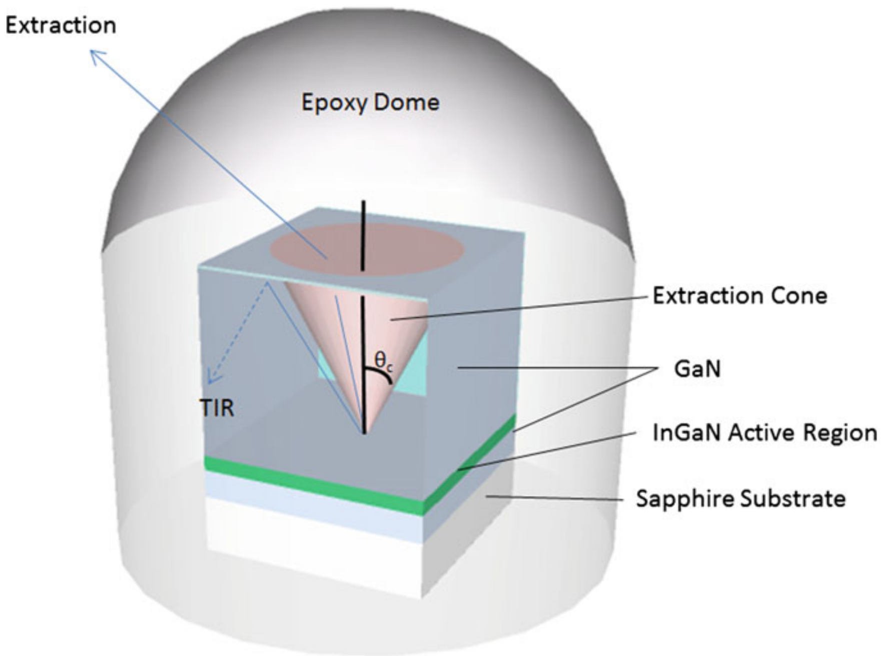

Fig. 11.2 Light emitted from the active region may be extracted via the epoxy extraction cone or internally reflected in the device. Most light that reaches the edge of the epoxy/air interface will be extracted due to the dome shape of the epoxy

As shown in (11.2), if the refractive index n_1 of the original material is higher than that of the second material n_2, there can be some incidence angles that lead to unphysical solutions for the refracted angle when the term $\frac{n_1}{n_2}\sin(\theta_1)$ is greater than 1. This leads to an effect referred to as total internal reflection (TIR): beyond a certain critical angle, defining an “extraction cone” (also called a light cone), the light is entirely reflected at the interface, and no light is transmitted. Only light situated within the “extraction cone” may then be transmitted (Fig. 11.2).

11.2.2 Fresnel Coefficients

While the Snell-Descartes law describes the angles at which the light is refracted, it does not deal with the intensity of light in the reflected and refracted portions. This is described by the Fresnel coefficients and depends on the polarization of the light. For s-polarized incident light (the electric field is parallel to the interface) the reflection coefficient (for power) is

$$R_s = \left| \frac{n_1 \cos(\theta_1) - n_2 \cos(\theta_2)}{n_1 \cos(\theta_1) + n_2 \cos(\theta_2)} \right|^2 \tag{11.3}$$

For p-polarized incident light (the magnetic field is parallel to the interface), it is

$$R_p = \left| \frac{n_1 \cos(\theta_2) - n_2 \cos(\theta_1)}{n_1 \cos(\theta_2) + n_2 \cos(\theta_1)} \right|^2 \tag{11.4}$$

Therefore, the total reflection including both polarizations is $R_t = \frac{(R_s + R_p)}{2}$ and the transmission is $T_t = 1 - R_t$. Materials that absorb light can also be defined by their complex index of refraction; these formulas still hold and can be used to calculate the reflection on lossy metals for instance. In that case, the angle (θ_2) is not defined as a real number, and the complex value of $\cos(\theta_2)$ must be directly deduced from Snell-Descartes law.

11.2.3 Modeling with a Ray Optics Approach

The behavior and propagation of light is thoroughly described by Maxwell's equations, but their resolution requires tremendous calculation power in finite, heterogeneous structures, and therefore cannot be used to calculate light propagation in complex and large geometries such as those used for LEDs. The laws of geometrical optics constitute a very good approximation in the limit of dimensions larger than that of the wavelength of the light traveling in the material (for GaN blue LEDs, the wavelength is typically of 460 nm in air and 187 nm in GaN). Ray tracing is a Monte Carlo-based method that uses the laws of geometrical optics to statistically simulate the behavior of a great number of light rays in a given system. Throughout this chapter, we will report results from the Lightools® ray tracing software. Ray tracing requires a detailed knowledge of the geometry and of the optical properties of all the different materials present in the system.

During a ray tracing simulation, many light rays are shot in random directions (or following a probability distribution corresponding to the characteristics of emission when emission is not random) from defined light-emitting sources. The rays follow the rules of geometrical optics until they are either absorbed or exit the system. For example, during propagation in materials, rays will follow Beer–Lambert's absorption laws using the absorption coefficient of the given material or, equivalently, the complex refractive index of the material. Then upon arrival at an interface between two materials, rays of light can be reflected or refracted according to Fresnel's laws, which also require knowledge of the refractive indices of the materials in play. Surfaces can be defined as reflectors, absorbers, scatterers, or smooth optical surfaces.

Once a large number of rays have been traced, the extraction efficiency and breakdown of the absorption mechanisms can be calculated from the fate of all the rays to give an overall picture of light behavior in the chip. Of course, because the ray tracing method relies on the rules of geometrical optics, it is unable to describe and calculate phenomena such as interference or diffraction, which can only be described by optical wave theory, but these effects are of minor importance for the chips with large-scale features.

11.3 The Issue of LEE in GaN-Based LEDs

GaN-based LEDs tend to have low LEE, largely because of the high index of refraction of GaN (n = 2.5). This high value leads to a low critical angle (23.6°) and a small extraction cone. The total transmission versus angle for both interfaces is plotted in Fig. 11.3, using n = 1 for air and n = 1.5 for epoxy.

The integrated values over all solid angles of a half sphere is 6.5% for the GaN/air interface. Extraction into dome-shaped silicone or epoxy encapsulant (n ~ 1.5) typically doubles the extraction value to ~17.4% by increasing the escape angle to ~36.9°. Most light escapes the encapsulant material into free space because a dome shape ensures that most rays impinge at the encapsulant–air interface at near-normal angles, and thus within the critical angle (Fig. 11.2). Further increasing the index of the encapsulant material could lead to unity extraction efficiency, but this requires higher indices than are typically available for most epoxies and resins [18].

In a simple first pass light extraction analysis, it is assumed that the light that is not directly extracted is lost. This actually depends on the internal losses of the device structure and on its geometry: if there were no internal losses, one might expect that the light will eventually escape after many rebounds in the device.

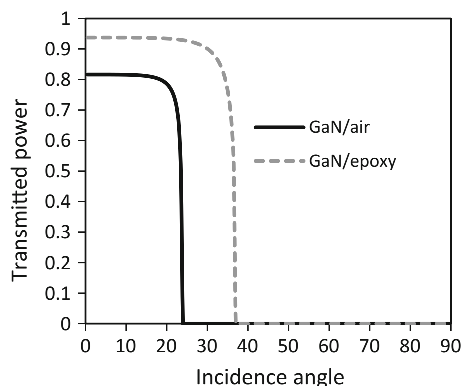

Fig. 11.3 Transmitted power versus incidence angle at a GaN/air and GaN/epoxy interface

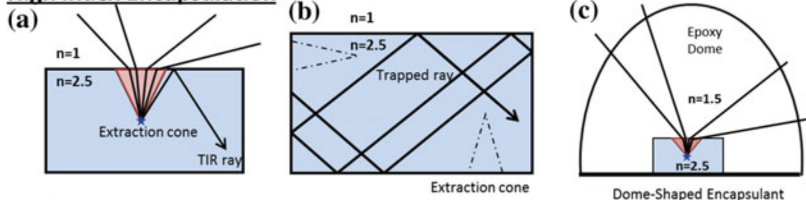

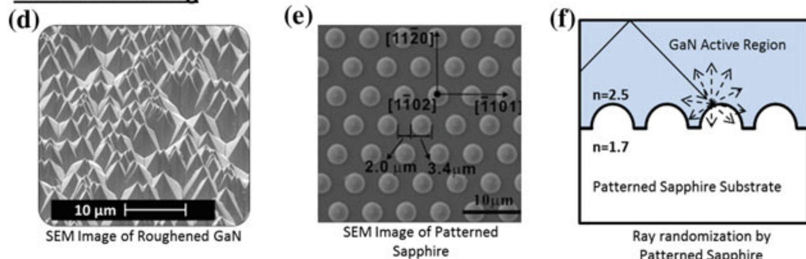

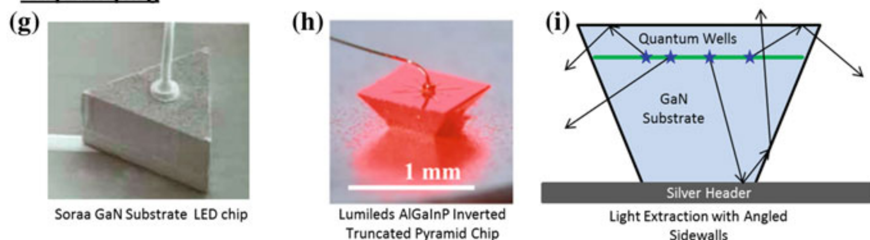

Fig. 11.4 Summary of techniques used to enhance light extraction in LED chips. These include (A) high index encapsulation to increase the critical angle for extraction, (B) surface texturing such as roughening or patterning to randomize light, and (C) chip shaping to redirect rays at each bounce and increase the probability of extraction on the next attempt

However, if the geometry of the chip is very regular, such as cubic, multiple reflections on the various interfaces may occur without change of angle, such that the rays propagate indefinitely under TIR (Fig. 11.4b). In this situation, even the tiniest loss mechanisms will destroy the optical power carried by such rays. Thus, even with a very transparent substrate, extraction is limited to ~30% [10, 11] if no other extraction techniques are employed.

Some efficient schemes are based on roughened surfaces or interfaces that change the direction of light at each rebound [8, 25, 29, 30]. Another option is the use of chip shaping, such as pyramidal [12, 13] or cone [24, 28] shaping, which breaks the symmetry of the optical cavity and randomizes the light rays which can then escape after a few trips within the device (Fig. 11.4h–i). This can increase efficiency up to 60% in transparent substrate LEDs.

11.4 Ray Propagation and Absorption in Layered Structures

It is useful to understand the modal distribution of emission in layered structures in order to understand better the issues for conventional LEDs grown on sapphire, which has a heterogeneous set of optical properties. Light is emitted into extracted photon modes or into a variety of guided modes. The emission distribution actually depends very little on the specific layer thicknesses or on the active layer structure [19, 20].

A ray tracing simulation can determine the intensities of the various modes in a semi-infinite planar structure. Assuming a two-layer structure of GaN (n = 2.5) on sapphire (n = 1.7) with light emission radiating from inside the GaN (as in Fig. 11.5) and no sources of light absorption, 8.6% of light is directly extracted into the air cones, 23.3% enters the sapphire mode and the remaining 68.4% is guided in the GaN mode.

As rays propagate in various modes within the device, many absorption sources in the structure can contribute to reduction in LEE (Fig. 11.6) which includes the following:

1. Absorption in the substrate
2. Absorption (complete or partial) on the contact pads
3. Absorption upon reflection on an imperfect backside mirror
4. Absorption in the active region (doped regions, current spreading layer, and quantum wells)

Depending upon the structure of the chip and on the extraction method used, the different sources of loss will not have the same importance and will not have to be optimized in the same way.

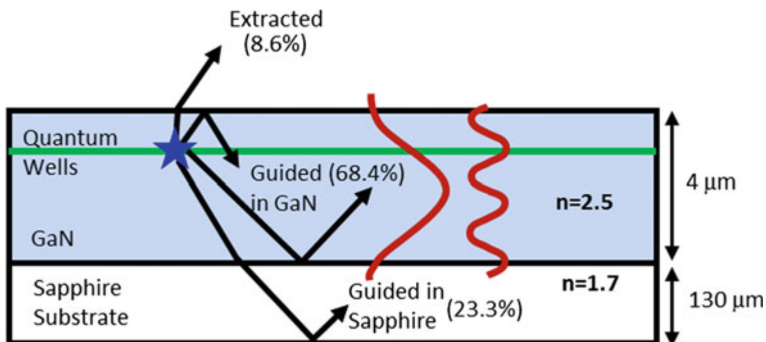

Fig. 11.5 Schematic of the various modes existing in a standard GaN on sapphire LED

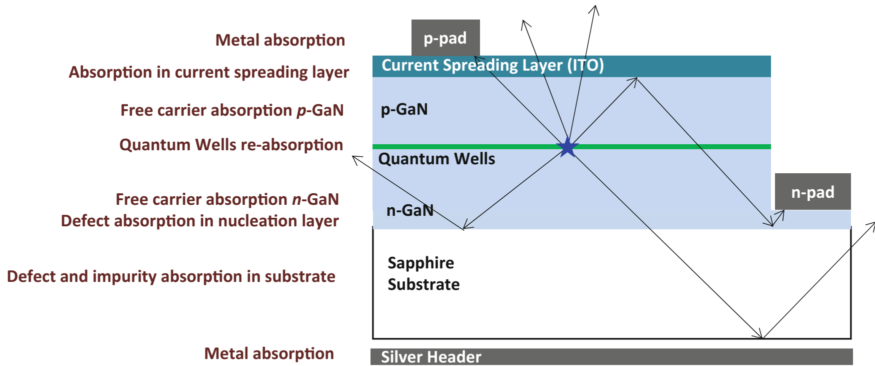

Fig. 11.6 Schematic of the various absorption phenomena within an LED

11.4.1 Localized Versus Distributed Loss Sources

Losses accumulate due to materials absorption when light propagates through the layers (losses are then distributed and connected to propagating rays) or can occur at selected areas of the device (localized losses), such as at contacts or mirrors. These will have different impacts on LEE, depending on the extraction mechanisms; one of the most common methods for light extraction in LEDs uses surface roughness or substrate patterning to break the guided modes and randomize light in the structure. Light then bounces in the LED until it ends in an extraction cone at a surface of the chip and is effectively extracted. After each unsuccessful extraction attempt, a light ray must travel through the LED, and thus propagate through a certain path length of absorbing material. In such cases, these distributed losses must be kept to a minimum to ensure high extraction. Hence, the goal will be to minimize the roundtrips of light in the device by enhancing the extraction probability at each incidence at the semiconductor–air (or encapsulant) interface. For localized losses, the goal is to diminish the interaction of rays with lossy regions, for example, by minimizing contact area, insulating lossy mirrors from the device material by a low index dielectric gap, or using current apertures away from the contact regions. Such strategies will be discussed in the section on real-world LED structures.

11.4.2 Material Absorption

Optical losses due to propagation in absorbing materials are described by the Beer–Lambert law. To the first order, they are directly proportional to the absorption coefficient and the thickness of the materials. This type of loss will occur in the substrate material and more importantly in the active region, which is often more

lossy and interacts more with the rays. It is therefore important to keep these regions as thin as possible is while enabling satisfactory electrical properties, especially for very lossy materials such as the current spreading layer or p-doped GaN layer. Trade-offs for the substrate thickness can occur when the chip geometry is such that sidewall extraction is important. This will be explained in more detail for a GaN chip on a bulk GaN substrate.

11.4.3 Quantum Well Absorption and Photon Recycling

Absorption of light in the quantum wells will generate electron-hole pairs, which may be recycled by radiative recombination to form a new photon. In this case, the effective loss every time a ray of light goes through the quantum wells is only (1-IQE) × (absorption probability), which can, however, lead to a large decrease in EQE when repeated multiple times [25, 26]. A favorable effect of photon recycling is that the photons absorbed and reemitted from the quantum well will effectively loose directional information and will be reemitted in random directions. We will neglect this phenomenon because (i) the randomization effect is small compared to that induced by the roughened surface or substrate; (ii) absorption is rather low for the typical few tens of nm total QW thickness due to the Stokes shift between emission and absorption peaks. This is even more pronounced for c-plane LEDs where the Quantum Confined Stark Effect (QCSE) leads to a very large Stokes shift (for measurements of the Stokes shifted emission and absorption, see, e.g., [6]). This is compounded with the very high IQE so that the net contribution to losses per pass, (1-IQE) × (absorption probability) would be quite small.

11.4.4 Metal Losses: Mirrors and Contacts

The metallic contacts in the LED are a potential source of loss by absorption. The typical absorption length of these metals is in the order of 20 nm, much thinner than the thickness of the contacts (typically 300 nm), so all the incoming light is either reflected or absorbed as the contacts can be considered optically thick (i.e., infinite).

Metal reflectivity can be accurately described for all angles of incidence using Fresnel's laws. The metal is then characterized by its real and imaginary indices, and the reflectivity is given by (11.3) and (11.4) where the complex value of the metal index for n_2 is used. The result of the calculation for silver and titanium in air at a wavelength of 450 nm is given in Fig. 11.7 using 1.69 + 2.27i for titanium's refractive index and 0.15 + 2.46i for silver's refractive index.

As can be observed, the reflectivity significantly varies with the incidence angle, especially for titanium, so the angular dependant reflectivity is used in the

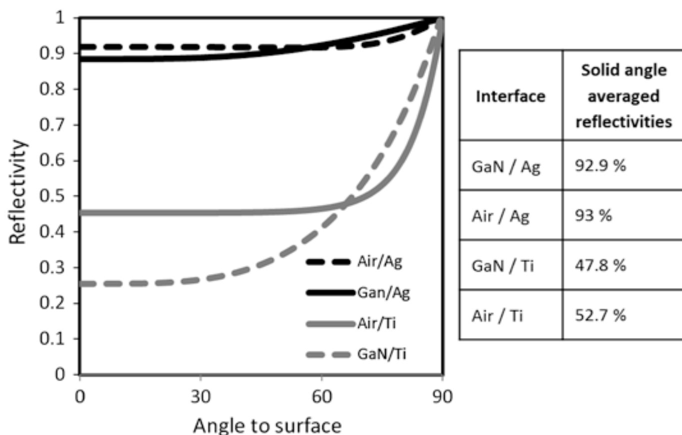

Interface	Solid angle averaged reflectivities
GaN / Ag	92.9 %
Air / Ag	93 %
GaN / Ti	47.8 %
Air / Ti	52.7 %

Fig. 11.7 Angular dependence of reflectivity and average reflectivity for silver and titanium at either GaN or air interfaces

simulations through the complete Fresnel law for the Ti contacts rather than the normal or average reflectivity. One should also note that these metals are usually used in combination with other materials to ensure better electrical and optical properties, so this is a first-order approximation.

The contact regions are a major source of loss, which will be shown in the precise modeling of LED structures. This is due, in particular, to the emission of light directly below the contacts, a fraction of which is promptly absorbed when it strikes the contacts. Strategies to diminish their impact include reducing the surface area of the top contacts, using current blocking layers below the contacts [5], or using current apertures away from the contacts.

11.5 Extraction Strategies and Considerations

11.5.1 Index Matching and Guided Modes

In addition to roughening and chip shaping techniques that modify the geometry of the substrate, packaging schemes that utilize high index, transparent encapsulant materials may also be used to increase light extraction [18]. In this scenario, instead of attempting to break the guided modes in the material, the rays are simply given a larger extraction cone. If the encapsulant is large compared to the chip and dome-shaped, then the rays propagating to the edge of the encapsulant would likely strike the surface at angles near perpendicular, and thus be extracted to free space (the normal incidence reflected intensity for an epoxy (n = 1.5)/air is only 4%).

Semiconductor materials in LEDs have high refractive indices, exceeding n = 2. The rays incident on infinite-area flat surface between the semiconductor and the encapsulant will only have a complete extraction cone when the encapsulant index equals the semiconductor index. In a real cuboid-shaped chip with finite surface area, however, full extraction can be achieved when the encapsulant index is somewhat lower than that of the semiconductor. This is because the extraction cones from different faces of the chip will begin to overlap, enabling all of the rays to escape. For a semiconductor with an index of n = 2.5, like GaN, overlap of the cones occurs around n = 2. As shall be demonstrated later, in chips with roughening or advanced geometries, extraction saturates at as low as n = 1.8.

11.5.2 The Effect of Surface or Interface Texturing

A very common method used to break the guided modes in LED structures is to introduce surface roughness on one of the interfaces to randomize the propagation direction of light rays as they strike the surface (for a review, see, e.g., [33]; see also [9, 16, 17, 31]. This enables all the optical modes in the LED to be radiative after some impacts on the interface, i.e., to have an in plane wave vector smaller than the wave vector in air. Anisotropic wet etching of the N-face of GaN that forms hexagonal pyramids at the surface is a common way of achieving this surface roughness [8]. Interface roughness can be produced by using a patterned sapphire substrate before growth [30].

While the main effect of surface roughness is randomization of light rays, another very important effect is often overlooked: the single path escape probability is increased [14]. We define single pass escape probability as the probability for a random ray of light propagating from the high index material to be transmitted to the lower index material. This value will be modified by surface roughness since light, at the second escape attempt, will not be intersecting the material interface with the same angle, giving the ray a greater chance to be in the extraction cone. Figure 11.8 shows a ray bouncing twice against the surface, increasing its probability of being extracted by roughly a factor of two.

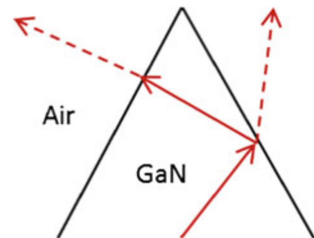

Fig. 11.8 A double reflection inside a pyramid leads to approximately double the escape probability because the successive angles of incidence are different

The two important effects of surface roughness are therefore, the randomizing efficiency and the single pass escape probability enhancement. We discuss in the appendix the randomization effect of surface roughness and sapphire substrate patterning, and give a brief description of the enhancement of single pass extraction by surface roughness.

The first pass extraction probability was calculated by ray tracing for a surface of randomly roughened pyramids, such as would result from a wet chemical etching. As is shown in Appendix C, randomly distributed pyramids or regularly patterned pyramids give similar results for ray tracing purposes, so that regular patterns are used in the rest of the simulations for simplicity.

The extraction probability for a roughened surface is completely changed compared to a flat surface: less light is transmitted at angles below the critical angle, but light transmission is increased in the range of 40°–70°, outside of the flat surface extraction cone. Once averaged over all solid angles, it leads to a 13.4% average first attempt transmission, twice better than for a flat surface (6.5%).

Detailed simulations (see Appendix A) show that due to randomization of reflected rays, the transmission probabilities of second and further attempts are nearly constant around 13%. So even if the rays are not extracted on the first try, they have a large probability of being extracted later. This is very different from a flat surface: if the ray is not in the extraction cone, it will never be extracted, so in that case, the transmission probability of further attempts drops to zero.

Increasing the index of the surrounding medium has a similar effect for roughened surfaces as for flat surfaces; for a given ray hitting the interface, the reflection angle will not be changed, but the fraction of the extracted light will be improved as more incident rays fall in the increased extraction cone. Comparing the angular transmission of the hexagonal pattern in air and epoxy (Fig. 11.9), one can see that the peak of extraction is around 50° for both, but is more widely spread for the epoxy case. The total transmission goes from 13.4% to 26.9% (compared to 6.5% for flat GaN/air and 17.5% for flat GaN/epoxy interfaces). However, we can note that in both cases the transmission at high incidence angle is low.

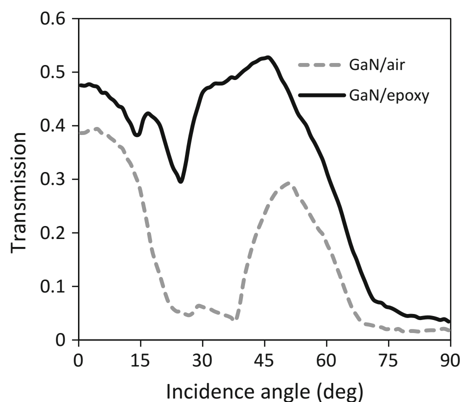

Fig. 11.9 GaN roughened surface transmission in air (n = 1) and in an epoxy encapsulant (n = 1.5)

11.5.3 Limit to the Ray Tracing Method

When dealing with devices where the feature size of the texture is close to or smaller than the wavelength of light considered, the ray optics method is no longer suitable. The only wave optics results on texturing to our knowledge are found in [7]. We find that the effects of roughness described here and in Appendix A (namely, randomization and increased single pass transmission) are similar in both ray optical and wave optical treatments. The single pass extraction found by David is larger than for our large features (31% for the single pass extraction instead of 13.4% here), which should improve the competition between extraction and internal losses within the chip. The same trend at high incidence angles on the interface is observed, however, in both the ray optics and the wave optics approaches: the transmission efficiency tends to zero, meaning that the roughness does not improve light extraction. Thus, the trends reported here *between* structures are valid, at least semi-quantitatively.

11.5.4 Sidewall Extraction and Chip Shaping

While surface roughening strongly improves light extraction, it can also induce some fabrication difficulties. For example, photoelectrochemical etching mainly works on the N-face of GaN, which is only accessible in flip chip geometries by removal of the substrate. Some LED geometries work around this problem and rely on different extraction mechanisms that do not require surface roughening or patterned substrates.

High extraction in LEDs may rely strongly on the extra extraction cones on the sides of the chip [10, 11]. Extraction from these cones is referred to as sidewall extraction. Two features are crucial for sidewall extraction to contribute to optimized efficiency. First, the light must be able to reach the sidewalls without being significantly absorbed, and second, the geometry must be adapted to not have any indefinitely propagating guided modes.

For the first requirement, LEDs with GaN substrates are the most naturally adapted, since light can propagate easily in the substrate which is naturally index-matched to the active region. However, GaN substrate LEDs are limited by a maximum size that allows light to reach the side without undergoing substantial absorption losses in the substrate material.

The second requirement can be fulfilled by shaping the chip in a way that nonextracted light impinging on an interface is reflected in the structure at a different angle, directing it into an extraction cone. This can be achieved by either in plane or out of plane chip shaping. In plane shaping means that the sidewalls remain vertical, and that the top view of the LED is a nonrectangular shape, such as a

triangle or parallelogram (Fig. 11.4g). The triangular shape meets the above requirements, and has the benefit of allowing cleaving along the natural planes of the crystal. Additionally, this geometry allows close packing of a larger number of die on the wafer [4].

A ray tracing simulation of different chip shaping schemes shows that out of plane chip shaping such as the truncated inverted pyramid (TIP) are most effective at breaking the guided modes (Fig. 11.10). The in plane shaping (triangle) provides a benefit over the perfect cuboid, but is not as effective at breaking all guided modes.

Introducing just a single angled sidewall to a nonroughened GaN-based device can increase extraction dramatically (~15%) by breaking the initial symmetry of the chip. In an idealized model of a point source emission at the center of a nonabsorbing cube with refractive index n = 2.5, only two sidewalls need to be angled to achieve 100% light extraction into air, provided that those sidewalls are adjacent and not opposite. Further, the angle can be as small as 3° or 4° to achieve this.

It is also useful to note that even for the geometry with no chip shaping, the system does not need to be index-matched to the encapsulant to get 100% extraction. The cube-shaped nonabsorbing semiconductor (n = 2.5) in Fig. 11.10 reaches 100% extraction with an encapsulant index of just n ~ 2.

In a real chip with lossy materials, it is advantageous to angle all four sidewalls and to have a greater degree of angle in order to minimize the number of bounces, and thus the path length the material. An example of this situation will be described further in a later section.

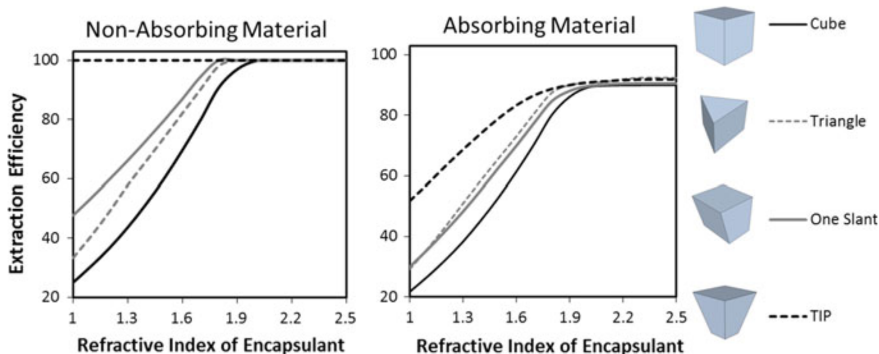

Fig. 11.10 Four different chip geometries (n = 2.5) with smooth surfaces and central isotropic point sources were compared using ray tracing to determine how efficiently they break the guided modes as a function of increasing ambient refractive index. Trends are shown for two cases: for nonabsorbing materials (where LEE goes to 100%) and for absorbing materials where the LEE reaches a maximum ~90% LEE at high ambient refractive indices. The absorption value for the latter was set to yield a typical amount of loss that is representative of a full LED structure (including contacts, etc.)

11.6 Simulation of Real LEDs

In order to quantify all these loss mechanisms and to compare different extraction strategies, several representative chips of the state of the art in industry were compared using ray tracing simulations. While this does not aim to be an exhaustive comparison of all chips being manufactured today, it helps to understand the crucial parameters for different chip geometries. Different parameters are swept independently to understand their effect on LEE. Material properties were chosen based on the most commonly accepted values in the literature, but would differ from one growth method to another. Therefore, the calculated values of absorption in the layers, while providing much insight on the extraction mechanisms of the chip, should not be considered as universal values.

All simulated chips are GaN-based chips with the same active region, described in Figs. 11.11, 11.12, and 11.13. The first two chips are similar but the first one is grown on a GaN substrate with a roughened backside (Fig. 11.11) while the second is grown on a patterned sapphire substrate (Fig. 11.12). Both of them have a back mirror separated from the chip by an air or dielectric spacer. The third is a simplified version of a flip chip configuration that outlines the important effects, in particular that of the lossy back mirror acting as the p-side contact of the chip (see below Fig. 11.21). All chips are simulated in an infinite environment of refractive index 1.5 to model encapsulation. All rays entering the encapsulant are considered

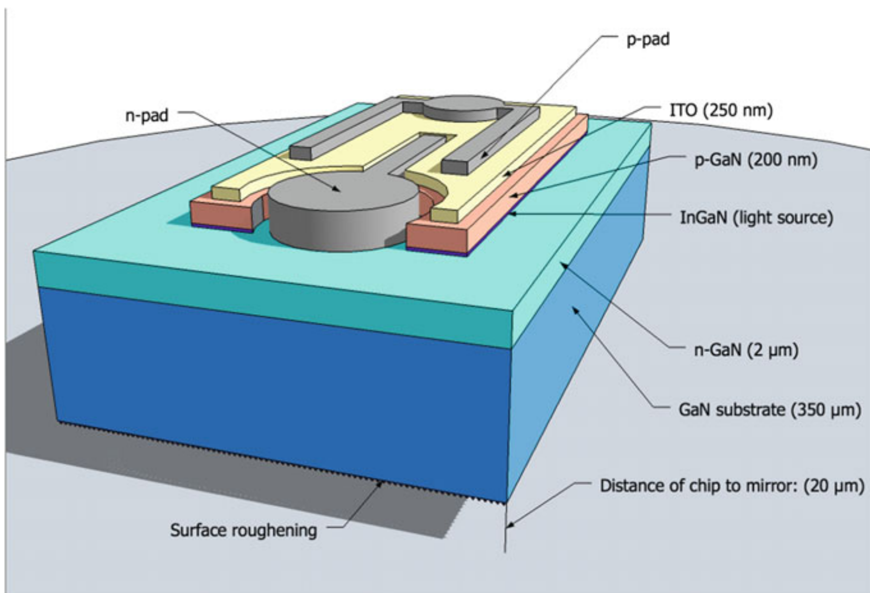

Fig. 11.11 Schematic of GaN substrate chip geometry as used in simulations (not to scale)

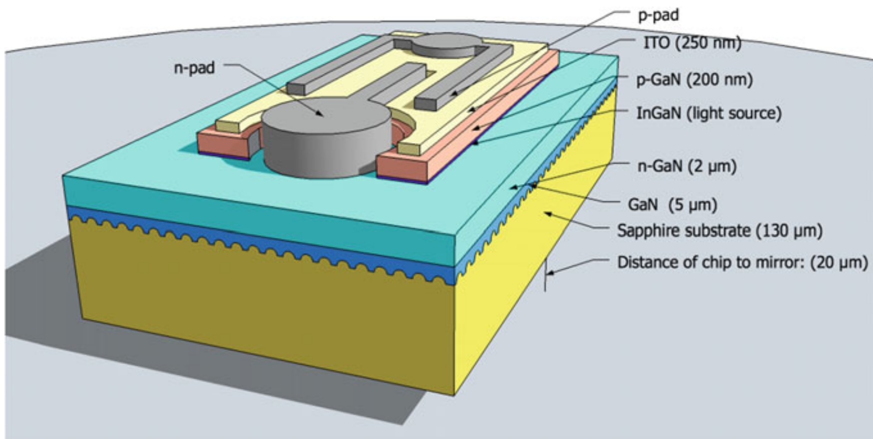

Fig. 11.12 Schematic of PSS chip geometry used for simulations (not to scale)

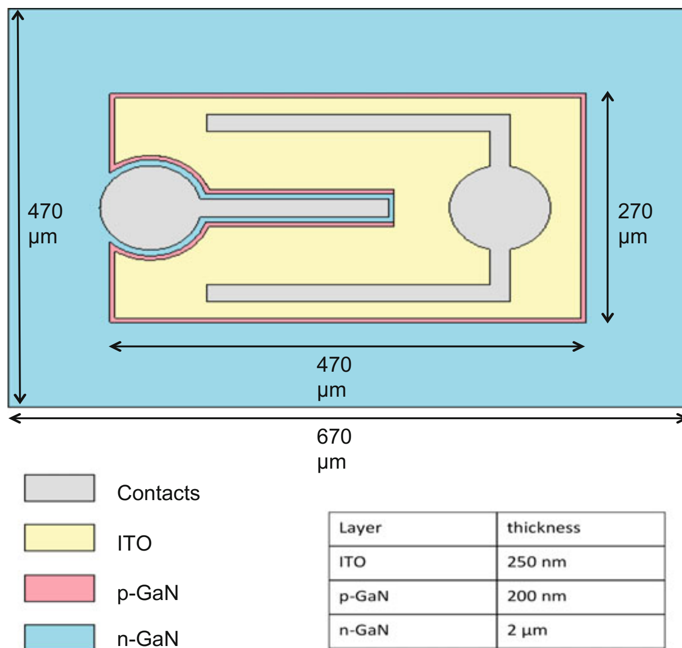

Layer	thickness
ITO	250 nm
p-GaN	200 nm
n-GaN	2 µm

Fig. 11.13 Schematic of the top geometry of GaN and PSS reference chips used for the simulations and table of the layer thicknesses in the active region

Table 11.1 Relevant intrinsic materials properties for ray tracing simulations for reference chips: absorption coefficient and refractive index

	Refractive index	Absorption coefficient
Bulk GaN	2.5	1 cm^{-1}
Sapphire	1.7	0.1 cm^{-1}
p-GaN	2.5	100 cm^{-1}
n-GaN	2.5	7 cm^{-1}
ITO	2.1	500 cm^{-1}
Epoxy	1.5	0
Silver header	/	92% isotropic reflectivity
Contacts	1.69 + 2.27i	Reflectivity given by Fresnel law (Ti on GaN, 47.8% average)

as extracted, as is the case to a good approximation for low loss, dome-shaped, large encapsulants where light back-reflected at the encapsulant–air interface represents only a very small portion, and has only a very small probability to hit a highly absorptive region of the LED. The exact geometries of the simulated chips are given in Fig. 11.13, and the material properties used are described in Table 11.1. In first simulations of the structures, we used the geometries and parameters of Fig. 11.13 and Table 11.1. We later report structures with varying geometries and parameters.

11.6.1 GaN-on-GaN Chip Simulations

The GaN substrate chip presented in Fig. 11.11 is simulated with the material properties described previously. Three scenarios are chosen: one when the encapsulant is air, and two where the encapsulant is epoxy. The source of light is situated at the interface of the p-GaN and the n-GaN layers. In one case though, the emission is removed from under the p contact, so as to simulate a current blocking layer. The different losses are extracted from the simulation results and are tabulated in Table 11.2. Various simulations were then run while varying only one parameter to evaluate the sensitivity of the LEE to the value of that parameter for the GaN substrate chip LED, and for the PSS substrate chip.

11.6.2 Effects of Propagation in the GaN Substrate

The losses are dominated by the absorption in the chip's GaN substrate, the contacts, and the backside mirror. The modeling indicates that rays hit the top surface once and a half on average. This is consistent with the loss observed in the

Table 11.2 Extraction efficiency of the reference GaN chip simulation in different encapsulation environments and the breakdown of loss mechanisms by material layer

Encapsulant	Epoxy		Air
Current blocking under P contact	No	Yes	No
Percent extracted	72.6%	75.1%	51.9%
Loss on P contact	4.4%	2.2%	5.1%
Loss on N contact	1.6%	1.6%	3.7%
Loss in N doped GaN	0.6%	0.6%	1.5%
Loss in ITO	2.5%	2.5%	4.4%
Loss in undoped GaN substrate	12.1%	12.1%	28.8%
Loss on backside mirror	5.5%	5.5%	3.8%

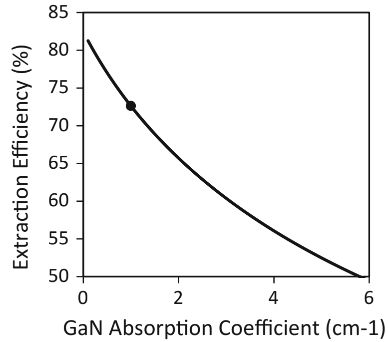

Fig. 11.14 Influence of absorption coefficient of the undoped GaN substrate on the LEE for a GaN substrate chip (the *dot* indicates the reference chip for 1 cm^{-1})

substrate, which corresponds to approximately one millimeter of distance traveled in the substrate per ray before extraction. This illustrates the fact that the light propagates in the entire chip and is quickly extracted from one of the sidewalls or from the top surface with very few reflections, and that the material quality of the GaN is of crucial importance for the LEE in these chips. This is shown in Fig. 11.14 where the absorption coefficient of the GaN substrate has been varied while keeping all other parameters constant.

The transparency of bulk GaN substrates has seen improvements as defect concentrations in the growth have been reduced. As a result, absorption coefficients in the literature range over two orders of magnitude, as high as 125 cm^{-1} [3]. Modern substrates from industry suppliers typically have absorption coefficients between 1 and 2 cm^{-1} and are grown by hydride vapor phase epitaxy. Ammonothermal growth is another technique that is attracting research attention for high efficiency, high transparency bulk GaN growth.

Because light propagates extensively in the substrate, its thickness has an optimal value: a thinner substrate will induce less absorption by the GaN but will also make it harder for rays to reach the sidewalls and will therefore rely more on top surface extraction, which is inherently more lossy due to the contacts and the active region (Fig. 11.15).

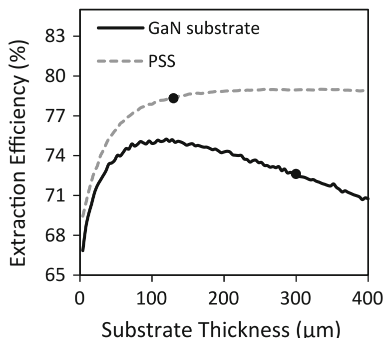

Fig. 11.15 Influence of substrate thickness on LEE for PSS or GaN substrate LED chips (the *dot* indicates the reference chip for 130 mm and 300 mm respectively)

11.6.3 Roughening Interaction with Backside Mirror

The roughening pattern in the GaN-on-GaN chip design is situated on the backside of the chip, which limits its benefits to its randomization effects. As previously discussed, roughening patterns at an interface help to both randomize rays and to increase the single path extraction. In the case of the GaN-on-GaN chip with backside roughening, the rays extracted from the backside will bounce off the mirror and back into the LED, canceling the benefit of improved single path extraction on that side. Increasing the distance between the chip and the mirror improves this, such as shown in Fig. 11.16 because it will enable a larger fraction of rays extracted from the backside to escape the structure without reentering in the LED. This design causes other problems, however, such as poorer thermal management due to a larger thermal resistance of the dielectric or air gap. Various

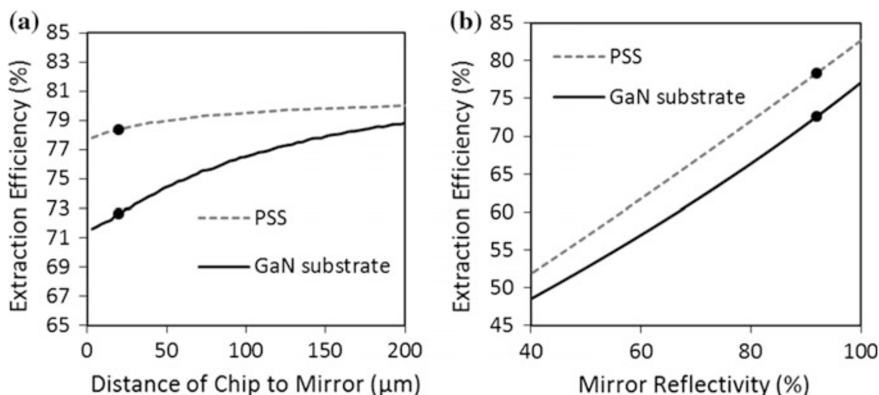

Fig. 11.16 Influence of **a** the backside mirror distance to the chip (the chip and mirror are separated by a transparent dielectric or air), and **b** the backside mirror reflectivity on LEE (the dot indicates the reference chip at 20 mm and 92% respectively)

strategies have been explored to solve this problem, but have not proven practical [22]. Finally, the backside mirror reflectance is also of high importance, justifying the use of silver that has a very high reflectivity as the backside mirror.

11.6.4 Angled Sidewalls

The GaN substrate LED is an interesting design because the naturally index-matched substrate enables light not to be trapped in the thin, lossy active region (which is one of the drawbacks of a patterned sapphire substrate, which will be discussed next). The challenge is that the GaN substrate must be of superior quality (low absorption) to ensure low enough losses, since light propagates extensively in it, and requires an extraction strategy such as surface roughening or angled sidewalls to break the guided modes.

Angled sidewalls are effective options for increasing light extraction in GaN chips because of both the high refractive index and high absorption of GaN substrates. This section demonstrates the extraction improvements achieved by shaping the chip into a truncated pyramid structure created by angling all four sidewalls (Craford, Krames, Krames US Patent 2001). This shape breaks all of the guided modes propagating to the sidewalls, while reducing the path length of the light in the lossy substrate. The large improvements based on such techniques were first demonstrated in the GaAlInP materials system for red-orange LEDs where the initial GaAs absorbing substrate is substituted by a shaped, transparent GaP substrate leading to extraction efficiencies up to 60% [12, 13] (Fig. 11.4h).

In Fig. 11.17, extraction efficiencies are shown for increasing sidewall angle for a GaN-on-GaN chip in an epoxy environment. It is apparent that nonroughened GaN substrates experience a greater increase in extraction by angled sidewalls than roughened GaN substrates. When angles of ~15° or greater are employed, the

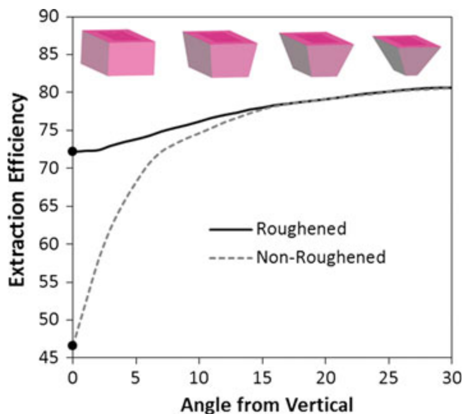

Fig. 11.17 A truncated inverted pyramid chip shaping design is applied to the roughened and nonroughened GaN-on-GaN chip simulation. The LEE is viewed as a function of sidewall angle. Simulations were performed using an epoxy ambient environment

distinction between roughened and nonroughened chips vanishes. Furthermore, 15° is an attainable angle in device processing.

In this simulation, all four sidewalls of the chip were angled to increase extraction, but it should be noted that ~50% of the improvement in extraction is obtained by angling just the first sidewall (at 15° angle from vertical). Furthermore, ~96% of the extraction improvement is achieved by angling just two of the four sidewalls, provided that they are adjacent sidewalls, which will break all guided modes in the chip.

The effect of combining angling and roughening methods are discussed in Appendix B.

11.6.5 Impact of Current Spreading Layers

Current spreading in the LED is a necessity because p-GaN is such a poor conductor. Without current spreading, there is significant current crowding under the p contact to the p type material, which lowers IQE. This is done in "epi up" structures (p-side of active layer is always grown last because p layers introduce defects and roughness detrimental to active layer growth) by using transparent current spreading layers (thin metal, e.g., Ni/Au, transparent conducting oxides, e.g., ITO or ZnO), or by having a p contact covering the p type material in flip chip device structures. In such cases, one can assume in the simulations that the light is uniformly generated throughout the active region. If no spreading layer were used, current crowding would occur under the p contact leading to a localization of emission under the contact, which would reduce light extraction efficiency, in addition to diminishing IQE.

When a current spreading layer is used, the p contact absorption can be mitigated through the use of a current blocking layer under the p contact, forcing hole current and emission away from the p contact [5]. The effect of this is shown for the GaN and patterned sapphire substrate chips: the result of a simulation where light emission has been suppressed under the p contact region is given alongside the other results above in Table 11.2. Quite naturally, it displays that the improvement in extraction efficiency comes from lower absorption in the p contacts.

11.6.6 Patterned Sapphire Substrate (PSS)

Sapphire substrates are the most common substrates for industry GaN LED growth because they are low cost, very transparent (0.1 cm^{-1}) and can also lead to high IQE devices. Patterns can be formed on top of the sapphire in order to create the same effect as a rough surface, i.e., randomizing light ray trajectories. Ray tracing results of a PSS chip, described in Fig. 11.12, are given in Table 11.3.

Table 11.3 Extraction efficiency of the PSS chip simulation in different encapsulation environments, and the breakdown of loss mechanisms by materials

Encapsulant	Epoxy		Air
Current blocking under P contact	No	Yes	No
Propagated	78.3%	82.3%	66.4%
Losses			
P contact	6.8%	2.6%	7.9%
N contact	1.5%	1.7%	4.5%
P-GaN	1.3%	1.3%	2.1%
N-GaN	1.3%	1.3%	2.9%
ITO	5.6%	5.7%	9.5%
Undoped GaN	0.2%	0.2%	0.5%
Sapphire	0.3%	0.3%	1.7%
Mirror	4.5%	4.5%	4.3%

11.6.7 Propagation of Light in the Substrate and Active Region for PSS Chips

The low refractive index of PSS leads to much of the light staying confined in the active region layer: it hits the top surface of the chip on average three times before being extracted, which is twice as often as for the GaN substrate chip and thus leads to a much higher absorption in the doped regions. The light that does make it into the substrate is almost all directly extracted into the surrounding epoxy because the indices of sapphire and epoxy are close. This requires only that the sapphire is thick enough that light can easily reach the sidewalls and does not bounce back into the active region. In fact, the simulations show that light rays only travel on average a distance on the order of 150 μm in the substrate, compared to 1 mm for a GaN substrate. Because the sapphire is also very transparent, there is very little loss in the substrate.

The two exit paths for light are therefore the top surface and the sapphire substrate sidewalls. In this regime, there is therefore no need for any modification of the substrate shape to enhance extraction. The most important region to optimize in a PSS chip is the active region. As can be seen from the single parameter sweeps, the PSS chip is shown to be much more sensitive to the parameters of the active region (such as ITO absorption coefficient, Fig. 11.18) than the GaN chip. Optimization of these layers can be achieved in two ways: ensuring that the active region is as transparent as possible (which depends mostly on material quality, contact geometry and current spreading), and making sure the light spends as little time as possible in it (which is the motivation for patterning the sapphire surface on which the GaN is grown). The LEE is also much less sensitive to the distance between the substrate and the mirror (Fig. 11.16a) because light extracted into the sapphire will very likely be extracted by the sidewalls or the top side if it is not extracted by the backside, since the index of sapphire and epoxy are almost matched, which is not the case for GaN.

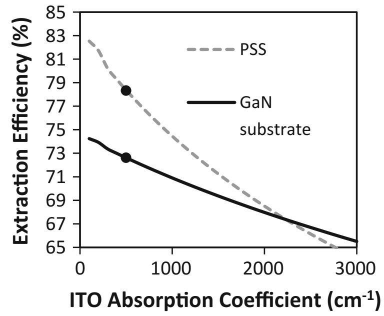

Fig. 11.18 ITO absorption impact on LEE for GaN substrate and PSS chips (the *dot* indicates the reference chip at 500 cm^{-1})

11.6.8 Effect of the Patterning the Sapphire Substrate

The patterned sapphire surface is what is responsible for randomizing the direction of the light rays trapped in the active region and ensuring that light can be extracted quickly from the active region. Increasing the pattern density increases the randomization efficiency, and the light therefore propagates less in the active region, improving extraction efficiency. Patterns that enable more light to refract into the sapphire are also beneficial, as subsequently, this light will be easily extracted from the substrate to air. If no patterning is done, only rays emitted within the extraction cone of the top air surface and bottom epoxy surface may be extracted quickly. The rest must propagate all the way to the sidewall in the lossy active region, and will only be extracted if they lie in one of the sidewall extraction cones. This results in high losses and underlines the importance of the substrate patterning (Fig. 11.19).

In summary, the PSS chip and the GaN substrate chip both rely on extraction from the sidewalls of the substrates, although the two mechanisms differ slightly. GaN substrates are of the same material as the active region (and are therefore index-matched) so that light penetrates easily into them, but suffer from losses due to a higher absorption coefficient of the substrate. PSS chips on the other hand have an almost lossless substrate, but are not index-matched to the active region. Light

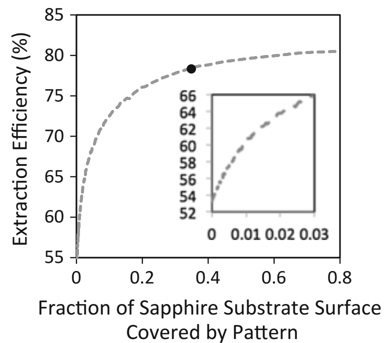

Fig. 11.19 Influence of pattern density on LEE for a PSS chip (the *dot* indicates the reference chip at 34.9%)

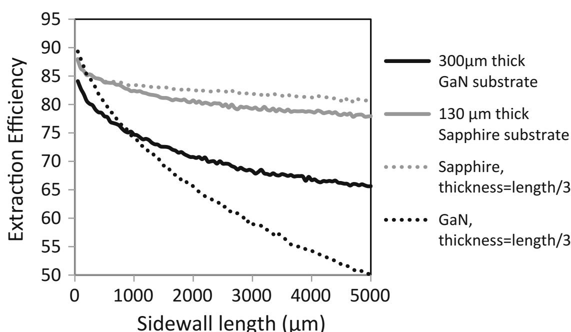

Fig. 11.20 Influence of chip size on LEE for simplified GaN-on-GaN and PSS chip simulations that have no top contacts and for which the active region covers the entire top area of the chip. The simulations are performed using an ambient epoxy environment

thus takes a longer time in the lossy active materials before getting into the substrate, but can then propagate with very low loss and quick extraction. The crucial levers for high LEE are therefore substrate absorption for a GaN chip, and active region absorption for a PSS chip.

This results in a fundamental limitation for the dimensions of GaN chips that rely strongly on sidewall extraction. The light must be able to propagate to the sidewalls without undergoing large losses, so their size is limited by the absorption coefficient of the GaN. PSS substrate chips, however, can be made quite large because the absorption coefficient of sapphire is low, as long as the aspect ratio of the substrate is kept constant. Light can then propagate enough horizontally to reach the sidewalls, as shown in Fig. 11.20, where both types of chips are increased in size. In one scenario, the substrates are kept the original thickness, in the other they are also scaled up to allow more sidewall extraction. The GaN chip suffers strongly in both schemes but the PSS extraction remains satisfactory when the aspect ratio is kept constant. For simplicity, contacts were omitted and the active region covered the chip entirely in these simulations. It is also evident from the large chip limits that the GaN substrate chips are the most dependent on sidewall extraction.

11.6.9 Flip Chip LEDs

While standard LEDs have historically been top p layer emitters that use current spreading layers and back side substrate texturing, the flip chip design is a more recent commercialized design with several benefits.

In flip chip designs, the backside mirror covers the whole p-side of the chip and serves as the p contact, enabling excellent current spreading. The sapphire substrate is removed and the exposed n doped GaN surface is roughened [8]. The resulting extraction mechanism is for the light to bounce several times between the backside mirror/contact and the GaN surface until it is extracted. The two benefits associated with surface roughness are therefore fully utilized, since the high single path extraction probability leads to better extraction at each attempt. Every extraction

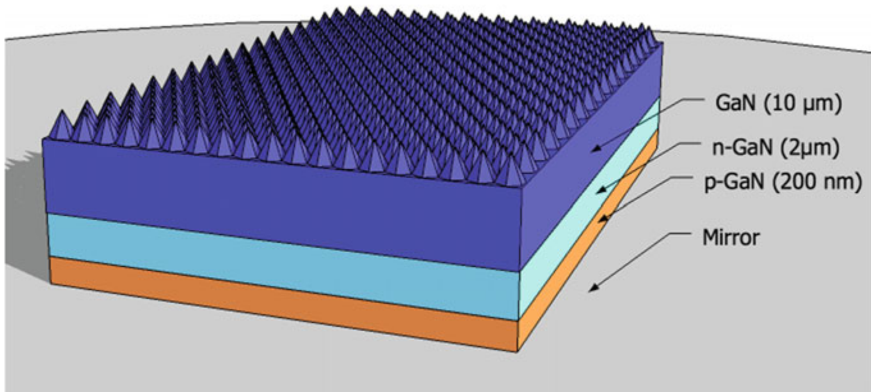

Fig. 11.21 Schematic of a flip chip used in simulations (not to scale, chip is approximately infinite in lateral dimensions)

attempt comes with its associated losses, such as on the mirror or in the active region of the device. A simplified structure without top electrode shown in Fig. 11.21 simulated through ray tracing gives the following loss sources (a n-side electrode would only introduce a small loss, see Table 11.2).

The mirror's nonperfect reflectivity is responsible for the bulk of the losses, and is the crucial element for this configuration, since a ray of light will, on average, need approximately six bounces before being extracted. Even a slight absorption in the mirror will lead to large losses, as seen in Fig. 11.22. Losses in the active region each time a photon passes through will play a similar role, but will only dominate as a loss mechanism in the event that the loss per pass is higher than the loss per interaction with the mirror. In the case of the modern materials properties and chip geometry studied here, the mirror is a much greater source of loss than the active region. The flip chip structure is the one most sensitive to mirror losses, and high performance can only be obtained, besides using highest possible reflecting contacts, by reducing the surface in contact with the mirror.

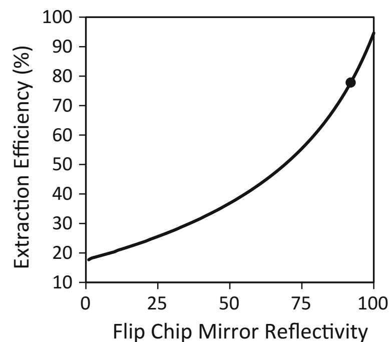

Fig. 11.22 Influence of mirror reflectivity on LEE for a flip chip LED in epoxy (the *dot* indicates the reference chip at 92%)

11.6.10 Index Effects

It is also of interest to compare the effect of the encapsulant index on all of the LED case studies discussed in this chapter. As shown in Fig. 11.23, the GaN-based chips, which experience greater internal reflection due to their high refractive index (n = 2.5), will see a much greater enhancement in their light extraction as the refractive index of the transparent encapsulant is increased.

High index encapsulation may allow GaN substrate chips to compete with PSS chips for high light extraction efficiency. Use of native GaN substrates for nitride LEDs is well known to improve other aspects of LED optical performance due to the low dislocation densities and high thermal conductivity relative to sapphire substrates. Thus, the use of encapsulation and other techniques may allow GaN substrates to achieve high extraction efficiency while capturing the benefits of GaN substrates for high IQE. Additionally, at high refractive indices, the distinction between roughened and nonroughened GaN vanishes, so there would be no need to roughen the device if sufficiently high index, transparent encapsulants are used.

The extraction efficiencies in these various chips all exceed 80% at a relatively low index of n = 1.8–1.9. Refractive indices of this magnitude are readily available in commercial glasses and some epoxies and polymers. In practice, however, most of these materials are somewhat absorbing, so there will need to be a balance of the index, absorption coefficient, and thickness of the encapsulant to maximize light extraction.

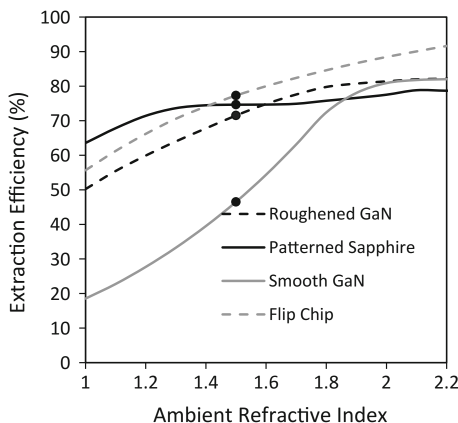

Fig. 11.23 Extraction efficiencies with increasing ambient refractive index for four chip simulations (the *dot* indicates the reference chip at 1.5)

11.7 Conclusions

This chapter on ray tracing simulations of LEDs shows how the various extraction schemes operate. Besides the simple use of a high index, dome-shaped encapsulant, the use of index-matched transparent substrates, such as GaN substrates, is very efficient, provided the substrate is very transparent, which reduces absorption resulting from long propagation path lengths in the substrate.

The most advanced techniques today yield extraction efficiencies in the 80% range, and rely mostly on texturing of the LED surfaces (surface roughening or surface photonic crystals) or interfaces (patterned sapphire substrate or embedded photonic crystal). Such values are indeed obtained in industry [13, 15, 21].

Surface roughening and PSS operate differently: the former relies on both ray randomization and increased single pass extraction while the latter only relies on ray randomization. Surface roughening is not well adapted to p-side up LEDs on sapphire substrates because it is difficult to etch the p materials, and it requires a current spreading layer on top of the p-GaN, usually ITO or a semi transparent metal because of the poor p conductivity. Attempts have been made to structure the ITO spreading layer, by roughening or etching a PhC but the index difference between the GaN and ITO limits the efficiency of that solution because a large fraction of light will be guided in the GaN layer and will only weakly interact with the surface texturing [9]. One can both etch the ITO and the p layer, but this comes at the expense of some degradation of the p contact [9]. The high performance surface roughened LEDs are therefore obtained either using a p-side up LED on GaN substrate with back roughened n-type surface or in flip chip geometries using a substrate lift off.

Although based on somewhat different mechanisms, the simulations of this chapter show that both surface roughening and PSS lead to high efficiencies (Tables 11.2, 11.3, and 11.4). The results appear here for the same device parameters (most of them with conservative values), which allow meaningful comparisons. Some industry results may be higher, either due to better materials quality (lower absorption in particular for ITO and metals) or more aggressive designs (smaller lossy contact areas).

A desirable feature is the ability to scale of the extraction efficiency for large chips in order to reduce costs. In almost all cases, the use of large surface LEDs is detrimental due to the long ray paths to reach the sidewalls (see Fig. 11.20) except

Table 11.4 Extraction efficiency for simple flip chip simulation and breakdown of losses in material layers

Encapsulant	Epoxy	Air (%)
Propagated	**78.7%**	**58**
Mirror losses	16.8%	34.2
p-Gan	1.9	3.2
n-Gan	1.4	2.4
GaN	1.2%	2

for those extraction schemes where light is continuously extracted or when substrates have very low absorption.

Acknowledgements CLK and MC acknowledge support from the Solid State lighting and Energy Center at UCSB. The work of LK and CW is supported by the Center for Energy Efficient Materials at UCSB, an Energy Frontier Research Center funded by the U.S. Department of Energy, Office of Science, Office of Basic Energy Sciences under Award Number DE-SC0001009 and by the Department of Energy (DOE) under project No. DE-FC26-06NT42857.

Appendix A

Discussion of the Origins of the Effects of Surface Roughness and of Sapphire Patterning

The Effect of GaN Surface Roughening: Randomization

We discussed above the increased single pass extraction due to surface roughness. A second essential effect is the randomization of light. Even if a ray is not extracted on first try, it will be reflected at a random angle, and may escape on the next attempt. We can quantify this using ray tracing by considering the fate of a random collection of rays and their angular distribution for each incident angle. Figure 11.24 shows the angular distribution of reflected rays as a function of incidence angle and Fig. 11.25 gives some examples of reflected rays distributions for a given incidence angle.

It is shown that for a given angle of incidence from an isotropic source, the reflected light pattern is complicated and very different from a specular reflection pattern. The angular distribution of reflected light is obtained by summing over all incidence angles (Fig. 11.26).

These reflected rays will hit the header and will be specularly reflected back to the roughened surface for a second attempt. As we know their angular distribution, the second attempt extraction can be computed using the transmission coefficient as a function of the incidence angle of Fig. 11.26a. It is 15.3%, slightly more than the first attempt probability (13.4%). We can iterate this process and compute the *n*th attempt extraction probability (Fig. 11.27). Due to randomization of the rays, nearly the same fraction of the light is extracted after each attempt (around 12.9% after a few bounces). These values were computed for a GaN/air interface; adding a high index encapsulating epoxy would significantly increase them.

In contrast, a flat surface with no randomization effect exhibits specular reflection and the second attempt rays are mostly outside of the transmission window of the surface. Thus, the extraction probability drops to zero after two to three successive attempts (Fig. 11.27).

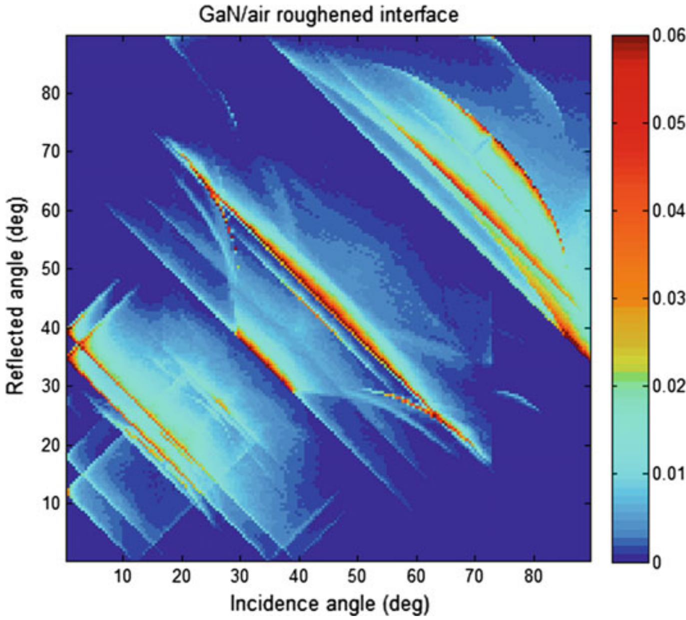

Fig. 11.24 Angular distribution of reflected rays as a function of incidence angle for a roughened surface (hexagonal nonrandom pyramids, with a top angle of 28°, for a GaN/air interface)

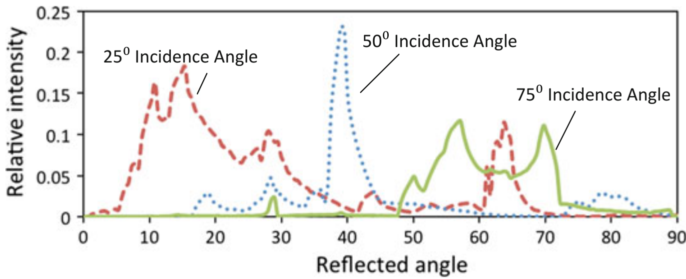

Fig. 11.25 Example of reflected light angular distribution pattern on a roughened surface (hexagonal nonrandom pyramids, with a top angle of 28°) for 25°, 50° and 75° incidence angles

The Effect of Patterned Sapphire Substrate (PSS)

We can also study PSS interface the same way. We will consider a cone shaped pattern in a square packing arrangement. The exact geometry is given in Fig. 11.28. This results in a filling factor of 34.9%.

The angular reflection pattern of the PSS is given in Fig. 11.29. We can see that, compared to the GaN surface, the pattern is overall simpler because of the cylindrical symmetry of the cone compared to the hexagonal pyramid. We can also see

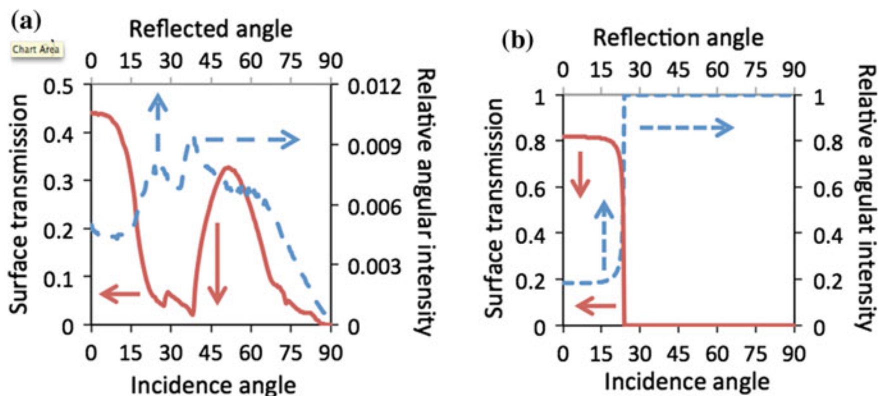

Fig. 11.26 **a** Surface transmission as a function of incident angle (*solid*) and angular distribution of the reflected rays integrated on all incidence angles (*dashed*) from a rough surface. **b** Similar results for a flat GaN/air surface

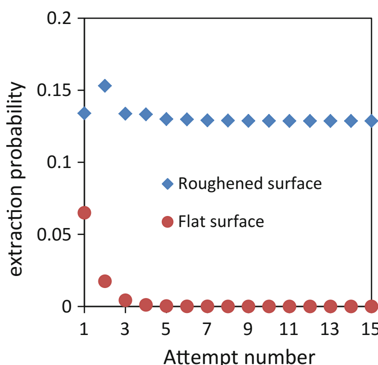

Fig. 11.27 Successive *n*th attempt extraction probability for a roughened (*diamonds*) and flat surface (*circles*)

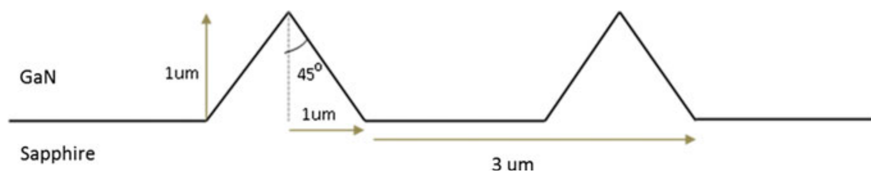

Fig. 11.28 Cone patterning of the GaN/sapphire interface

that there is high intensity along the main diagonal; this is specular light that is reflected exactly at the incidence angle. It comes from the fact that contrary to GaN roughening, the filling factor is not 100%; some of the interface is still flat.

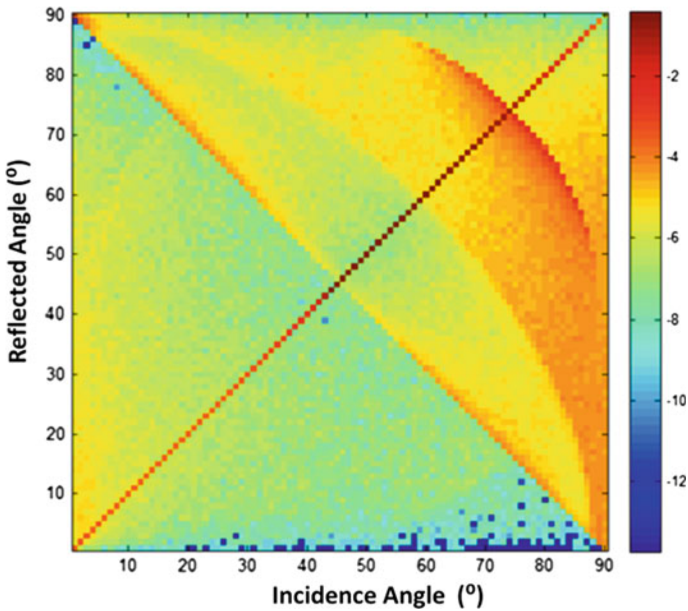

Fig. 11.29 Angular distribution of reflected rays as a function of incidence angle (intensity is on a log scale)

We can quantify the intensity of specular reflection, randomized reflection and transmission as a function of incidence angle by averaging over the reflected and transmitted solid angles (Fig. 11.30).

This figure is the result of the superposition of two effects: the specular reflection by the flat part of the GaN–sapphire interface and the randomization by the cones. Below the critical angle (42.6°), the cones transmit part of the light and reflect the rest at random angles. The flat surface transmits all of the light that strikes it (modulo the Fresnel transmission coefficient). For higher angles, the flat surface

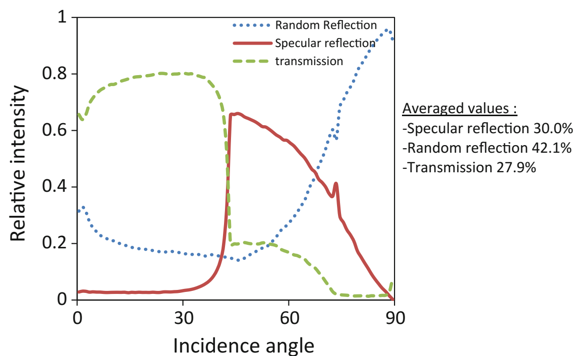

Fig. 11.30 Fate of the incident rays for a PSS surface

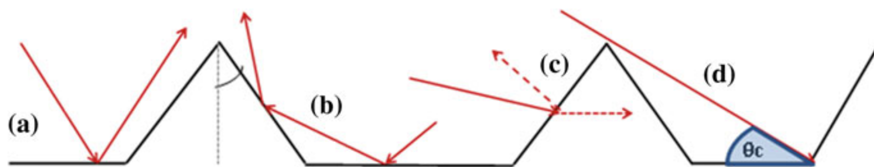

Fig. 11.31 **a** 44° specularly reflected ray, **b** high angle ray undergoing specular and random reflection, **c** high angle ray that is directly randomized by a pattern that "shades" the flat surface, and **d** a ray impinging at the critical angle beyond which there is no specular reflection

reflects all the rays striking it, and because the filling factor is ~35%, this explains the 65% specular reflection for incidence angle around 43° (Fig. 11.31a). However, for angles larger than 45°, some of the specularly reflected light can immediately hit another cone and be randomized (Fig. 11.31b). This explains the decrease in specular reflection. This also corresponds to the "shading" of the flat surface by the cones (Fig. 11.31c, d).

The purpose of patterning the sapphire differs subtly from that of roughening the surface of GaN. The GaN roughening is used both for its randomization effect and improvement of first pass extraction. However, in the case of GaN/sapphire patterned interface, the situation is different: extracting the rays from GaN to the sapphire substrate is not the final purpose of the texture. Like for the GaN-on-GaN chip with roughened backside, it is the randomization effect that is the most beneficial.

Indeed, getting the light into the sapphire has two opposite effects: due to the sapphire's lower index and absorption, sidewall extraction is facilitated, but on the other hand, light in the substrate will most likely hit the lossy mirror. So, contrary to flip chip roughening, we cannot simply compute the *n*th pass extraction in sapphire to determine the efficacy of the structure. We have to study in more detail the extraction process.

As seen in Fig. 11.32, the PSS interface will extract a downwards traveling ray in two ways: (a) it can reflect the ray into the GaN extraction cone or (b) it can refract the ray into the sapphire extraction cone, which leads to the ray being extracted after it bounces back on the LED rear reflector [1]. For (a), rays reflected

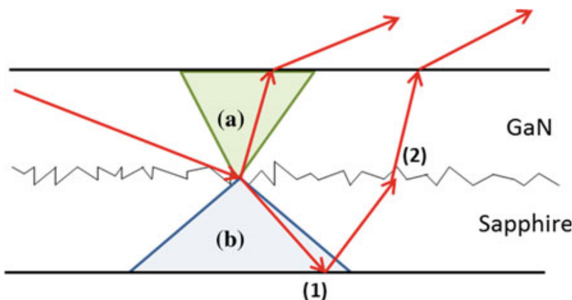

Fig. 11.32 First attempt extraction rays: **a** reflected at low angles in GaN and **b** transmitted at low angles in sapphire

into GaN must be below 23.6° (GaN/air TIR angle), and for (b), transmitted rays must be in the sapphire/air extraction cone (36.0°).

The fraction of incident rays reflected into the GaN light cone will be referred to as the "GaN efficacy." The smaller number of rays that are transmitted into the sapphire light cone can be extracted, too. For a simplified first pass calculation, we will not take into account the effect of the second randomization of rays going back through the sapphire/GaN interface (Fig. 11.32(2)). The "sapphire efficacy" is then defined as the fraction of rays inside the sapphire light cone (Fig. 11.32b). The total first pass efficacy is then defined as the sum of the GaN efficacy and of the sapphire efficacy. It estimates the fraction of the incident rays that will be extracted on first attempt via scattering by the patterned interface into the air cone directly into GaN, or through the sapphire and back through the GaN into the air cone.

One should note that this model does not take into account the reflectivity of the GaN/air interface inside the light cone (some of the low angle incident rays will still be reflected according to Fresnel laws), the losses on the bottom mirror (taken as zero), and the effect of the sidewall extraction. However, all these effects are mostly independent of the pattern choice, so the total first pass efficacy is a good relative indicator to compare different patterns.

To find the optimal pattern to achieve maximal first pass efficacy, we first find the optimal shape, comparing a flat surface, half sphere, and cone. The cone pattern is still according to Fig. 11.28, and the half sphere has the same filling factor as the cone (34.9%). The total efficacy, for different incidence angles is given in Fig. 11.33.

We can compute the average efficacy over all incidence angles for the three surfaces. We find 8.6% for the flat surface, 13.0% for the half sphere and 14.8% for the cone pattern. The higher performance of the cone can be explained by the high efficacy at high angles.

In more detail, we can see that this high angle efficacy comes from GaN efficacy: the cone pattern reflects some of the light incident at high angles into GaN extraction cone (Fig. 11.34a). Qualitatively, we can understand it from simple ray tracing (Fig. 11.34b).

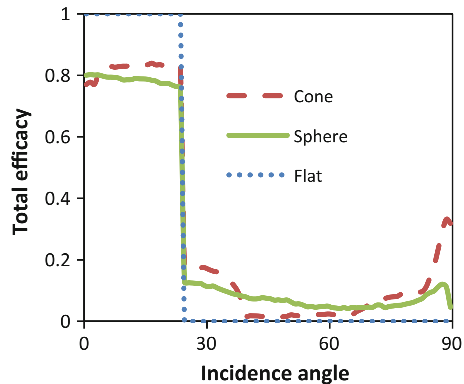

Fig. 11.33 Comparison of total efficacy (sapphire efficacy + GaN efficacy) for different pattern geometries (cone, half sphere with 34.9% filling factor, and flat surface)

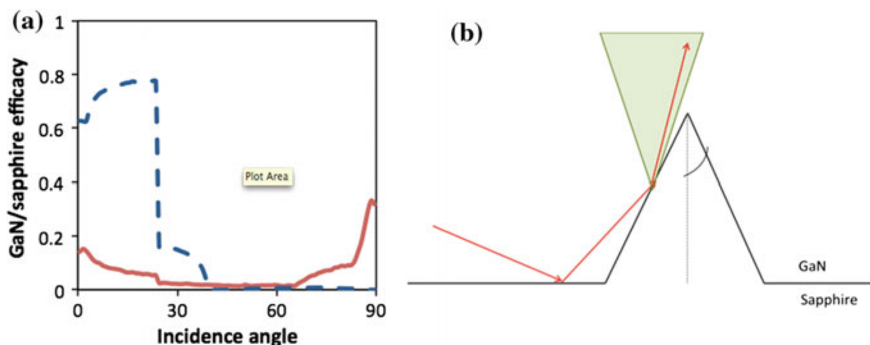

Fig. 11.34 **a** Breakdown of the efficacy of the cone pattern between the sapphire efficacy (*dashed blue*) and GaN efficacy (*solid red*), **b** Simple 2D model of the high angle GaN efficacy

Once the cone pattern was identified as the optimal pattern, simulations were performed to determine the cone apex angle that maximizes the efficacy. This was done by varying the height of the cones (while keeping the fill factor and all other parameters the same) from 0.15 to 7 µm. These cone heights correspond to cone apex angles from 85.7° to 17.7°. For each geometry, the average low angle transmission and reflection were computed. The results are given in Fig. 11.36 (Fig. 11.35).

We can see that the fraction of light transmitted to the sapphire extraction cone does not change much with the cone shape. On the contrary, the reflection in GaN is very sensitive to the cone angle. It reaches a maximum for a cone apex of 66°. We can understand why if we compare the GaN efficacy as a function of incidence angle for four geometries (Fig. 11.36).

For very flat cones (high apex angle), the result is close to that of a flat surface, with little reflection at low angles and diminishing to nearly zero for angles beyond the GaN/air critical angle (23.6°). An angle of 67° is approximately optimal, with good reflection at high angles (as explained in Fig. 11.34b). For more peaked cones,

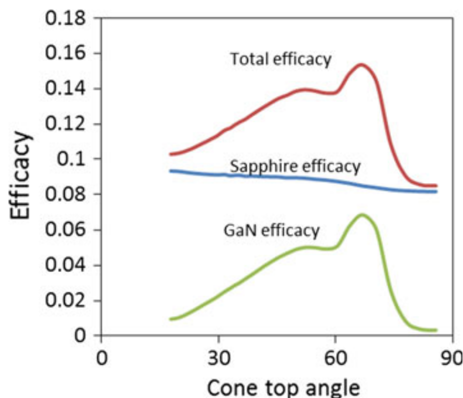

Fig. 11.35 Effect of cone apex angle on PSS single pass efficacy

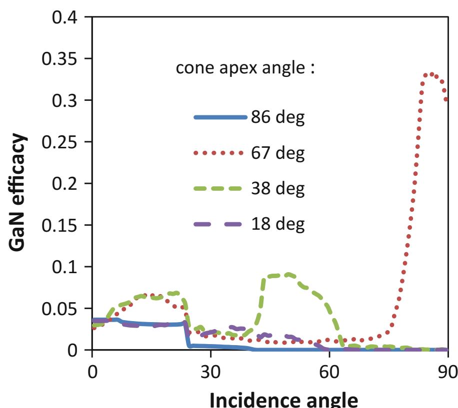

Fig. 11.36 Comparing the GaN efficacy for different cone geometries

we lose this high angle extraction, but this is partly balanced by an increase in reflection for angles around 40°–60°. Then for an even more peaked cone, this reflection diminishes.

Finally, the optimal filling factor for these 66° cones was determined by varying the distances between cones (2–20 μm) in the simulations (Fig. 11.37). As the patterns are in square packing, this results in filling factors from 3.1% to 79%. We can see that the part of light reflected in GaN increases with the filling factor. The light extracted in sapphire is almost constant (8.2%–8.5%).

These results can qualitatively predict the LEE, for example [32], showed that increasing the filling factor leads to better extraction. However, both the full chip modeling and the experimental results show that the incremental improvement in LEE with increasing filling factor tends to diminish for high filling factors. This is because only the first pass efficacy was computed. In reality, if the light is not extracted on first attempt, it can reach the patterned interface again, where it would be more likely to be extracted after fewer attempts for a high filling factor.

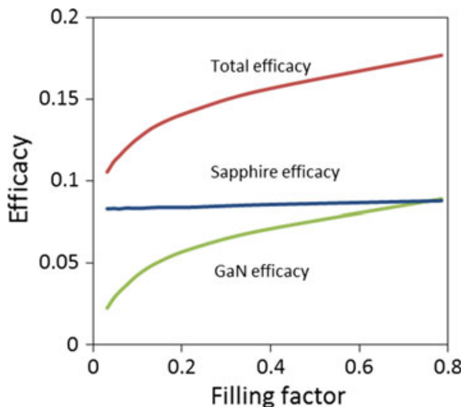

Fig. 11.37 Effect of varying the filling factor for a given cone shape on the pattern first pass efficacy. To obtain an even better filling factor, a hexagonal packing can be used, resulting in about 91% filling factor. For this filling factor, the resulting efficacy is 18.1% compared to just 8.4% for a flat GaN/sapphire interface

Appendix B

Comparison of Roughening and Angled Sidewalls for GaN Substrate LEDs

A comparison was done to demonstrate the hierarchy of techniques of roughening, out of plane angled sidewalls (truncated inverted pyramid structure) and high refractive index encapsulation. An angle of 15° was used for the sidewalls (Fig. 11.38). The most effective extraction techniques have high extraction values at low index that saturate earlier with increasing index. The combination of roughening and the sidewall angling gives the highest extraction for low- index encapsulants and the benefit of increasing encapsulant index saturates at ~n = 1.8.

The advantage of combining both roughening and sidewall angling over sidewall angling alone, however, is small, differing at most by less than 2%. Roughening without sidewall angling follows after that, indicating that at least for the chip dimensions modeled here, sidewall angling into a truncated pyramid structure is a more effective extraction method. It should be noted, however, that for larger chip sizes, backside roughening may gain an advantage over chip shaping. This is because the improvement from angled sidewalls diminishes with increasing chip area as the rays must travel further through the device to reach a wall where they may be extracted or redirected.

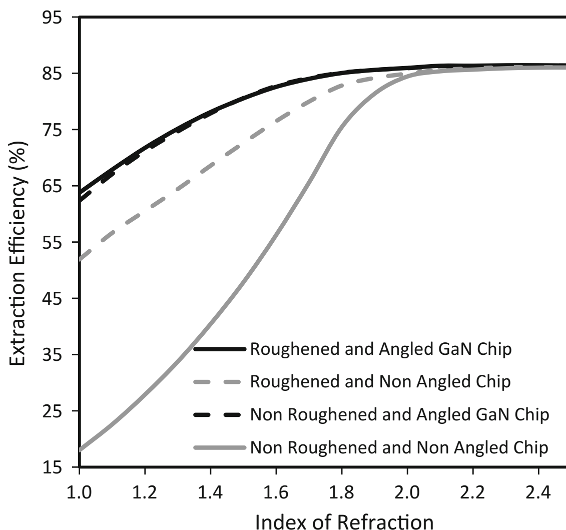

Fig. 11.38 Comparison of roughening and chip shaping techniques for light extraction

Appendix C

Simulations of Periodic "Rough" Surfaces Versus Random Rough Surfaces

The first pass extraction probability can be quantified by analyzing the intensity of light emission through a roughened surface as a function of incidence angle. In real systems, the surface texturing is not of constant size or regularly distributed on the surface, as for GaN roughening from a chemical etching. Generating random patterns in ray tracing considerably increases the complexity of the simulations, so a simpler model was considered, which uses a periodic pattern rather than a random one (Fig. 11.39). For comparison, the transmission function was computed in the two cases of random and periodic surfaces (Fig. 11.40). Little difference was found between the two, not surprisingly as ray tracing is a geometric optics approach, so the size of the pyramids does not affect the results. Randomizing the position of the pyramids can only modify the trajectory of those already extracted rays that hit a

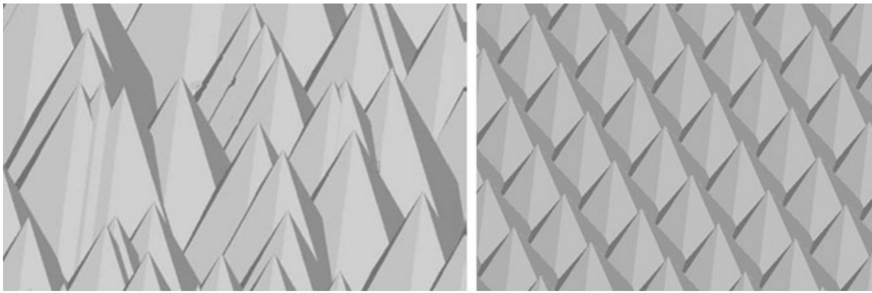

Fig. 11.39 Random simulated pyramids (*left*) and evenly spaced pyramids (*right*)

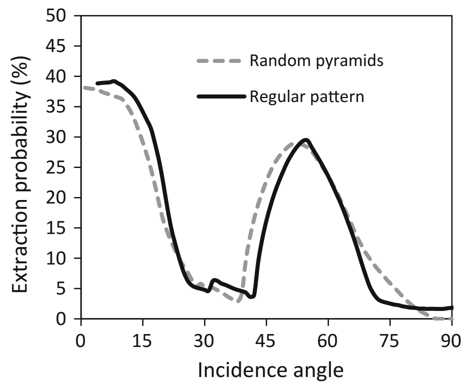

Fig. 11.40 Transmission function of GaN/air interface with random or periodic rough patterns

second pyramid, which is very rare. Therefore, the periodic pattern will be further used to simplify the simulations without losing accuracy compared to the actual random patterns.

References

1. H. Benisty, H. De Neve, C. Weisbuch, Impact of planar microcavity effects on light extraction: I. basic concepts and analytical trends. IEEE J. Quantum Electron. **34**, 1612–1631 (1998)
2. H. Benisty, H. De Neve, C. Weisbuch, Impact of planar microcavity effects on light extraction: II. Selected exact simulations and role of photon recycling. IEEE J. Quantum Electron. **34**, 1632–1643 (1998)
3. A. Borbely, S.G. Johnson, Prediction of light extraction efficiency of LEDs by ray trace simulation. Proc. SPIE **5187**, 301–308
4. S.E. Brinkley, C.L. Keraly, J. Sonoda, C. Weisbuch, J.S. Speck, S. Nakamura, S.P. DenBaars, Chip shaping for light extraction enhancement of bulk c-plane light-emitting diodes. Appl. Phys. Express **5**, 032104 (2012)
5. S.J. Chang, C.F. Shen, W.S. Chen, T.K. Ko, C.T. Kuo, K.H. Yu, S.C. Shei, Y.Z. Chiou, Nitride-based LEDs with an insulating SiO_2 layer underneath p-pad electrodes. Electrochem. Solid-State Lett. **10**, H175–H177 (2007)
6. S.F. Chichibu, A.C. Abare, M.S. Minsky, S. Keller, S.B. Fleischer, J.E. Bowers, E. Hu, U.K. Mishra, L.A. Coldren, S.P. DenBaars, Effective band gap inhomogeneity and piezoelectric field in InGaN/GaN multiquantum well structures. Appl. Phys. Lett. **73**, 2006 (1998)
7. A. David, H. Benisty, C. Weisbuch, Photonic crystal light-emitting sources. Reports on Progress in Physics, 2012 (to be published)
8. T. Fujii, Y. Gao, R. Sharma, E.L. Hu, S.P. DenBaars, S. Nakamura, Increase in the extraction efficiency of GaN-based light-emitting diodes via surface roughening. Appl. Phys. Lett. **84**, 855–857 (2004)
9. J.H. Kang, J.H. Ryu, H.K. Kim, H.Y. Kim, N. Han, Y.J. Park, P. Uthirakumar, C.-H. Hong, Comparison of various surface textured layer in InGaN LEDs for high light extraction efficiency. Opt. Express **19**, 3637–3647 (2011)
10. F.A. Kish, F.M. Steranka, D.C. DeFevere, D.A. Vanderwater, K.G. Park, C.P. Kuo, T.D. Osentowski, M.J. Peanasky, J.G. Yu, R.M. Fletcher, D.A. Steigerwald, M.G. Craford, V.M. Robbins, Very-high efficiency semiconductor wafer-bonded transparent-substrate (AlGa) InP/GaP light-emitting diodes. Appl. Phys. Lett. **64**, 2839–2841 (1994)
11. F.A. Kish, R.M. Fletcher, AlGaInP light-emitting diodes, in *Semiconductors and Semimetals*, vol. 48, ed. by GB stringfellow, M. George Craford (Academic, San Diego, 1997), p. 149
12. M.R. Krames, M.R. Krames, M. Ochiai-Holcomb, G.E. Hofler, C. Carter-Coman, E.I. Chen, I.-H. Tan, P. Grillot, N.F. Gardner, H.C. Chui, J.-W. Huang, S.A. Stockman, F.A. Kish, M.G. Craford, High-power truncated-inverted-pyramid (AlxGa1-x)0.5In0.5P/GaP light-emitting diodes exhibiting >50% external quantum efficiency. Appl. Phys. Lett. **75**, 2365–2367 (1999)
13. M.R. Krames, O.B. Shchekin, R. Mueller-Mach, G.O. Mueller, L. Zhou, G. Harbers, M. George Craford, Status and future of high-power light-emitting diodes for solid-state lighting. J. Display Technol. **3**, 2 (2007)
14. P. Kumar, S.Y. Son, R. Singh, K. Balasundaram, J. Lee, R. Singh, Analytical treatment of light extraction from textured surfaces using classical ray optics. Opt. Comm. **284**, 4874–4878 (2011)
15. A. Laubsch, M. Sabathil, J. Baur, M. Peter, B. Hahn, High-power and high-efficiency InGaN-based light emitters. IEEE Trans. Electron Dev. **57**, 79 (2010)

16. S.J. Lee, Study of photon extraction efficiency in InGaN light-emitting diodes depending on chip structures and chip-mount schemes. Opt. Eng. **45**, 1–14 (2006)
17. T.-X. Lee, K.-F. Gao, W.-T. Chien, C.-C. Sun, Light extraction analysis of GaN-based light-emitting diodes with surface texture and/or patterned substrate. Opt. Express **15**, 6670–6676 (2007)
18. M. Ma, F.W. Mont, X. Yan, J. Cho, E.F. Schubert, G.B. Kim, C. Sone, Effects of the refractive index of the encapsulant on the light-extraction efficiency of light-emitting diodes. Opt. Express **19**, A1135 (2011)
19. E. Matioli, C. Weisbuch, Impact of photonic crystals on LED light extraction efficiency: approaches and limits to vertical structure designs. J. Phys. D **43**, 354005 (2010)
20. E. Matioli, C. Weisbuch, Direct measurement of internal quantum efficiency in light emitting diodes under electrical injection I: Modeling. J. Appl. Phys. **109**, 073114 (2011)
21. Y. Narukawa, M. Ichikawa, D. Sanga, M. Sano, T. Mukai, White light emitting diodes with super-high luminous efficacy. J. Phys. D Appl. Phys. **43**, 354002 (2010)
22. C.-C. Pan, I. Koslow, J. Sonoda, H. Ohta, J.-S. Ha, S. Nakamura, S.P. DenBaars, Vertical stand transparent light-emitting diode architecture for high-efficiency and high-power light-emitting diodes. Jpn. J. Appl. Phys. **49**, 080210 (2010)
23. M. Rattier, H. Benisty, R. Stanley, J.-F. Carlin, R. Houdré, U. Oesterle, C.J.M. Smith, C. Weisbuch, T.F. Krauss, Towards ultra-high efficiency aluminum oxide microcavity light-emitting diodes: guided mode extraction by photonic crystals. J. Sel. Top. Quantum Electron. **8**, 238–247 (2002)
24. W. Schmid, R. Jager, F. Eberhard, R. King, M. Miller, M. Joos, K.J. Ebeling, 45% quantum efficiency light-emitting-diodes with radial outcoupling taper, in *Light-Emiting Diodes IV*, ed. by H. Walter Yao, I.T. Ferguson, F. Fred Schubert. Proc. SPIE **3938**, 90 (2000)
25. I. Schnitzer, E. Yablonovitch, C. Caneau, T.J. Gmitter, Ultrahigh spontaneous emission quantum efficiency, 99.7% internally and 72% externally, from AlGaAs/GaAs/AlGaAs double heterostructures. Appl. Phys. Lett. **62**, 131 (1993)
26. I. Schnitzer, E. Yablonovitch, C. Caneau, T.J. Gmitter, A. Scherer, 30% external quantum efficiency from surface textured, thin-film light-emitting-diodes. Appl. Phys. Lett. **63**, 2174–2176 (1993)
27. C. Wiesmann, K. Bergenek, N. Linder, U.T. Schwarz, Photonic crystal LEDs—designing light extraction. Laser Photon. Rev. **3**, 262–286 (2009)
28. W.R. Windish, P. Heremans, A. Knobloch, P. Kiesel, G.H. Döhler, B. Dutta, G. Borghs, Light-emitting diodes with 31% quantum efficiency by outcoupling of lateral waveguide modes. Appl. Phys. Lett. **74**, 2256–2258 (1999)
29. E. Yablonovitch, Statistical ray optics. J. Opt. Soc. Am. **72**, 899–907 (1982)
30. M. Yamada, T. Mitani, Y. Narukawa, S. Shioji, I. Niki, S. Sonobe, K. Deguchi, M. Sano, T. Mukai, InGaN-based near-ultraviolet and blue-light-emitting diodes with high external quantum efficiency using a patterned sapphire substrate and a mesh electrode. Jpn. J. Appl. Phys. **41**, L 1431–L 1433 (2002)
31. V. Zabelin, D.A. Zakheim, S.A. Gurevich, Efficiency improvement of AlGaInN LEDs advanced by ray-tracing analysis. IEEE J. Quantum Electron. **40**, 1675–1686 (2004)
32. Y. Zhao, J. Sonoda, C. Pan, S. Brinkley, I. Koslow, K. Fujito, H. Ohta, S.P. DenBaars, S. Nakamura, 30-mW-Class high-power and high-efficiency blue semipolar (1011) InGaN/GaN light-emitting diodes obtained by backside roughening technique. Appl. Phys. Express **3**, 102101 (2010)
33. A.I. Zhmakin, Enhancement of light extraction from light emitting diodes. Phys. Rep. **498**, 189–241 (2011)

Chapter 12
Light Extraction of High-Efficient Light-Emitting Diodes

Ja-Yeon Kim, Tak Jeong, Sang Hern Lee, Hwa Sub Oh, Hyung Jo Park, Sang-Mook Kim and Jong Hyeob Baek

Abstract This chapter deals with methods for fabricating high-efficient light-emitting diodes (LEDs) with higher light extraction efficiency (LEE). Some LED prototypes are then reviewed to investigate how their performance was enhanced by utilizing a variety of chip processes. The most efficient devices were found to be produced with unique fabrication processes, having at least one patterned sapphire substrate, chip shaping, vertical configuration, and/or flip-chip packaging, among others.

12.1 High Extraction Efficiency Structures

12.1.1 Enhanced Light Extraction for GaN LEDs Using Surface Shaping

In order to improve the external quantum efficiency (EQE) in LED structures, it is essential to enhance both the light extraction efficiency (LEE) as well as the internal quantum efficiency (IQE) [1, 2]. In particular, improving the LEE is considered to be crucial for fabricating high-efficiency LEDs. To date, methods such as chip shaping [3–8], surface texturing [9–12], flip-chip packaging [13–15], use of a patterned sapphire substrate (PSS) [16–23], and use of photonic crystals [24–28] have been proposed in attempts to enhance the light extraction.

The descriptions of some of these proposals are outlined as follows. Kao et al. [6] reported that ~22° etching undercut sidewalls in a nitride-based LED (LED II) could be achieved using controllable inductively coupled plasma etching, which was comparable to results obtained using a conventional LED (LED I). Note that an undercut angle could be definitely observed when the ~22° oblique sidewall profile was compared to the initial unetched mesa (Fig. 12.1a). In the figure, the angle is very close to the critical angle (~23°) between GaN and air. It was also found that

J.-Y. Kim · T. Jeong · S.H. Lee · H.S. Oh · H.J. Park · S.-M. Kim · J.H. Baek (✉)
Korea Photonics Technology Institute, Gwangju, Republic of Korea
e-mail: jhbaek@kopti.re.kr

© Springer Nature Singapore Pte Ltd. 2017

T.-Y. Seong et al. (eds.), *III-Nitride Based Light Emitting Diodes and Applications*,
Topics in Applied Physics 133, DOI 10.1007/978-981-10-3755-9_12

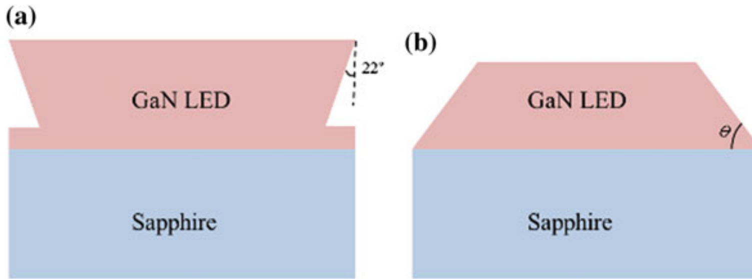

Fig. 12.1 **a** Schematic of the fabricated LED device having a 22° undercut angle and **b** SDI-LED structure

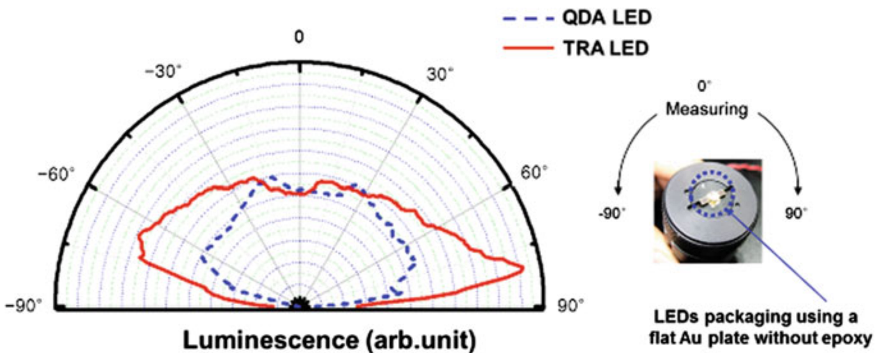

Fig. 12.2 Angle-dependent scan of the far-field beam distribution of the TRA and QDA LED at a current injection of 20 mA (*left*). Photo shows the angle dependent measurement of the emitted light (*right*)

the current–voltage (I–V) curves shown at around 3.5 V at 20 mA for an LED with undercut sidewalls were almost identical to the LED with normal sidewalls. This observation indicates that undercutting the sidewalls should not result in any degradation in the electrical properties of nitride-based LEDs. In the electroluminescence (EL) measurement, the current was continuously injected into the device at room temperature.

Lee et al. [7] also reported LEDs with modified mesa sidewalls, referred to as sidewall-deflector-integrated (SDI)-LEDs, in which smooth mesa sidewalls were prepared at an oblique angle (Fig. 12.2b) all over the GaN epilayer; in this case, the air-GaN-sapphire waveguide structure terminates at the angle between the GaN LED and sapphire substrate.

Kim et al. [8] investigated the characteristics of a triangular (TRA) LED and compared it to a standard quadrangular (QDA) LED having the same surface area and contact area. The range of the incident angle for the total internal reflection (TIR) for photons kept inside the QDA LED is given by

$$23.5^\circ < \theta_{i(\mathrm{QDA})} < 66.5^\circ. \quad (1)$$

For an equilateral TRA LED, the range of incident angles for TIR inside the LED can be estimated by

$$23.5^\circ < \theta_{i(\mathrm{TRA})} < 36.5^\circ. \quad (2)$$

As such, this simple calculation shows that the range of the incident angle for TIR of the TRA LED is much smaller than that of the QDA LED. Therefore, the LEE of the TRA LED can be greatly enhanced when using the increased probability of the emitting photon from the LED chip compared to that of the QDA LED. These considerations indicate that the light extraction from the packaged TRA LED is substantially enhanced compared to that of the packaged QDA LED.

This theoretical analysis can be proven by comparing properties of the TRA LED to the standard QDA LED. Here, the optical output power of the TRA LED is higher than that of the QDA LED over the entire input current range. The total radiant fluxes of the QDA and TRA LEDs measured in the integrating sphere were 8.9 and 13.2 mW at an input currents of 20 mA and 38 mW and 47.2 mW at 100 mW, respectively [8a]. The enhancement of the total radiant flux of the TRA LED compared to that of the QDA LED was 48% at 20 mA and 24% at 100 mA. These improvements in the optical power enhancement of the TRA LED can be attributed to a significant reduction in TIR.

Figure 12.2 shows the angular dependence of the light far-field beam distribution of TRA and QDA LEDs at an injection current of 20 mA. In the figure, it can be clearly seen that the emission intensities of QDA and TRA LEDs after packaging were almost identical in the vertical direction, but the emission intensity of the TRA LED in the horizontal direction was greater than that of the QDA LED. This enhancement of the light emission from the TRA LED in the horizontal direction can be attributed to the significant reduction of TIR at the sidewalls of the TRA LED. According to this study, the light extraction efficiency (LEE) can be greatly enhanced in the TRA LED, with increasing the probability of photon escape, by significantly reducing TIR at the sidewalls of the TRA LED, compared to the QDA LED.

Kim et al. [8b] compared QDA LEDs to various polygonal LEDs in an attempt to determine an optimum structure for improving the extraction and current injection efficiencies. Figure 12.3 presents the EL intensity mapping images of

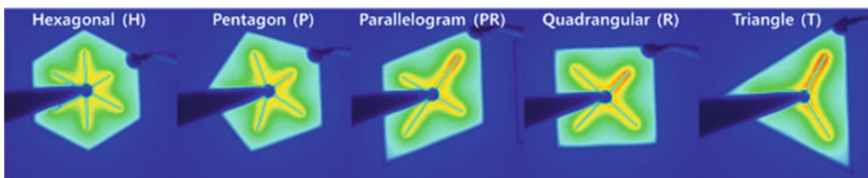

Fig. 12.3 EL intensity of polygonal LEDs at an injection current of 120 mA

Fig. 12.4 Emission images of scribed polygonal LEDs with TO-can package at an injection current of 120 mA

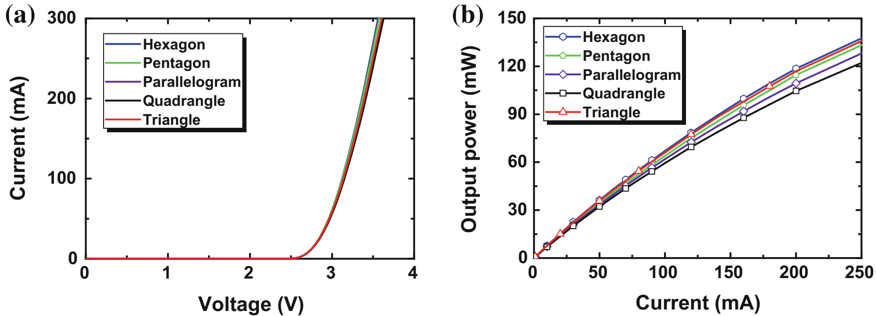

Fig. 12.5 **a** *I-V* and **b** *L-I* curves of polygonal LEDs over the entire input current range

LEDs at an input current injection of 120 mA. The hexagonal LED shows good current spreading characteristics, compared to the pentagon, parallelogram, quadrangular, and triangular LED shapes. To measure their electrical and optical properties, LEDs were packaged onto a TO can after scribing with a diamond tip; the total radiant flux was then measured using an integrating sphere measurement system (Fig. 12.4). This study revealed similar *I-V* characteristics, though the polygonal LED showed an increase in the total radiant flux, compared to that of the quadrangular LED. Specifically, the hexagonal LED had the highest value, resulting from an increase in its extraction and injection efficiency. These results indicate that the fabrication of LEDs with polygonal shapes is a very promising way to develop high-efficiency LEDs (Fig. 12.5).

12.1.2 Textured Surfaces for High Extraction

Roughening the top surface of an LED is one method for improving its light extraction [9–12], as the roughened top surface reduces the internal light reflection and scatters the light outward. Huh et al. [9] reported the fabrication of an InGaN-based LED with a top *p*-GaN surface microroughened using metal clusters as a wet etching mask. The light output power of LED chips having

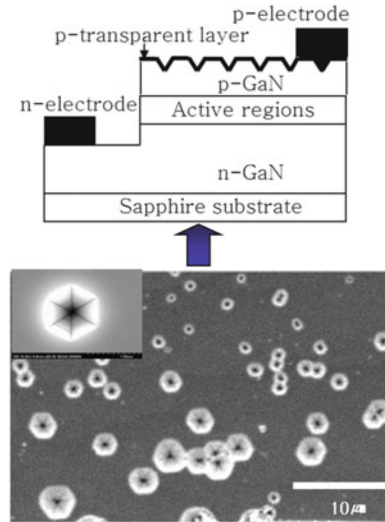

Fig. 12.6 Scanning electron microscopy (SEM) images of top *p*-GaN surfaces of LEDs etched using KE solution

microroughening was increased compared to LED chips with no roughening; by employing this structure, the power conversion efficiency was increased. Compared to conventional LED chips, the light output power for the LED chip with a microroughened top surface increased by 52.4% for the front side and 30% for the backside.

In another study, Na et al. [10] reported the selective wet etching of a *p*-GaN layer by using a solution of KOH in ethylene glycol (KE), in an attempt to enhance the optical and electrical performances of GaN-based LEDs. The selectively etched *p*-GaN surface showed hexagonal-shaped etch pits (Fig. 12.6), and the light output power of the LEDs was improved by 29.4% compared to that of non-etched LEDs.

12.1.3 Patterned Sapphire Substrate

LEDs grown on a patterned sapphire substrate (PSS) have also shown higher performances than those grown on an *a*-plane sapphire substrate. Several groups have demonstrated the direct epitaxial growth onto various PSS shapes, in attempts to enhance both the epitaxial quality and LEE. For instance, Tadatomo et al. [16, 17] adopted models of parallel grooves along the (11–20) sapphire to fabricate nitride LEDs, Bell et al. [18] used the trenches of sapphire (11–20) direction to growth Mg-doped AlGaN epilayers, and a hexagon pattern parallel with the axis of the sapphire was reported by Yamada et al. [19]. In addition, Chang et al. [20] described the use of parallel stripes along the sapphire (100) direction for blue LED growth [16–23], and Wuu and Wang et al. [21, 22] proposed an approach for growing a high-quality GaN film using a PSS; this technique eliminated dislocations and increased the probability of light extraction (Fig. 12.7).

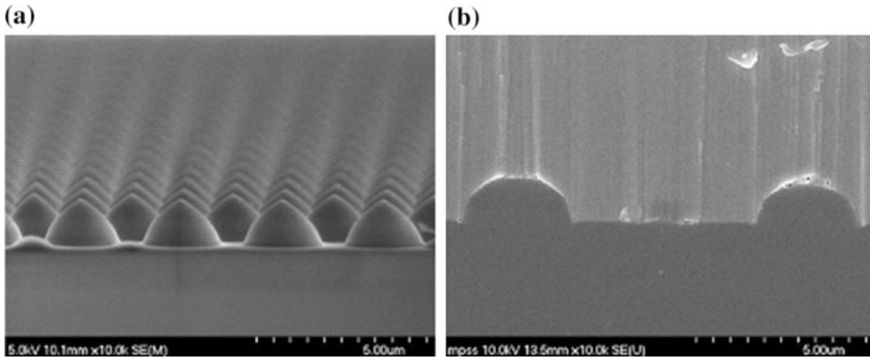

Fig. 12.7 **a** Tilted SEM images of PSS and **b** cross-sectional SEM images of GaN epilayer grown on a PSS

Another type of PSS was prepared using periodic hole patterns, in which the etching depths ranged from 0.5 to 1.5 µm [22]. For the PSS LED, the GaN epilayer grew laterally from the top of the sapphire substrate and covered the holes. The enhanced output power (~21%) can be attributed to the combination of improved LEE and the crystalline quality by the reduction of threading dislocations (TDs) density with the PSS structure. Lee et al. [23] reported a chemical wet-etched PSS, used to eliminate the sapphire surface damage induced by dry etching. The crystallography-etched pattern of a (0001)-oriented sapphire substrate has a flat-surface {0001} *C*-plane that is triangle-shaped in the center. Surrounding this plane are three facets: an {1-102} *R*-plane with an angle of 57° against the [0001] *C*-axis; this inclined facet with a steep slope is useful for light extraction. It was also found that the sapphire etching rate depends on the crystal orientation and decreases in the order of *C*-plane > *R*-plane > *M*-plane > *A*-plane. They reported that the output power of the PSS LED increased by approximately 15% relative to conventional LEDs at an injection current of 20 mA. This improvement was attributed to not only the geometrical shape of the {1-102} crystallography-etched facets that efficiently redirected the trapped light to escape, but also to the reduction of the dislocation density by adopting the PSS growth scheme.

Recently, nanosized PSSs (NPSSs) were fabricated using nanotechnologies such as laser holographic lithography, e-beam lithography, and nanoimprint technology to enhance the LEE of LEDs. Relaxation of the residual strain in GaN layers on the PSS was found to reduce the resultant piezoelectric field in the quantum wells (QWs) [29] (Fig. 12.8).

12.1.4 High-Power Vertical-Type LEDs

Sapphires are one of the most commonly used materials for substrates in GaN-based LEDs. However, the relatively poor thermal conductivity of the

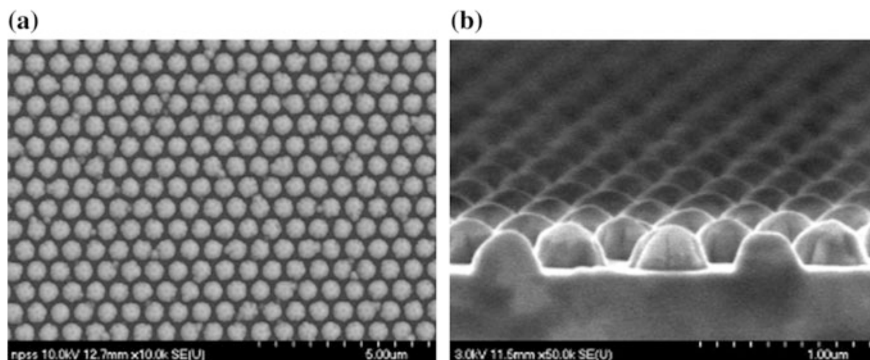

Fig. 12.8 **a** Top and **b** tilted SEM images of NPSSs fabricated using nanoimprint technology

sapphire substrate has been recognized as a major limitation to its further application in high-brightness LEDs. In addition, sapphire substrates impose constraints on attempts to improve the quality of GaN films due to the lattice and thermal-expansion coefficient mismatch between these two materials. To resolve these problems, an LED structure with GaN epilayers can be transferred to another substrate with good thermal conductivity using wafer-bonding and laser lift-off (LLO) techniques [30–32]. LLO processes were first demonstrated by Kelly et al. [33]; these types of LED structures have been extensively investigated [34–38] since. Compared to the conventional lateral structures, these vertical-type LEDs (VLEDs) have advantages such as better current injection, good heat dissipation (due to wafer bonding or electroplating with highly conductive materials), and enhanced reliability against electrostatic discharge. For example, Huang et al. [32] used high-power GaN-based VLEDs to improve light extraction and heat dissipation. They showed that VLEDs having a textured surface produced a 65% higher extraction efficiency compared to conventional GaN-based LEDs at an injection current of 20 mA. Indeed, compared to conventional LEDs, VLEDs are known to have better performance, in particular, at high current injection due to their excellent heat dissipation capability. Figure 12.9 presents the schematic for vertical-type GaN LED device fabrication processes using wafer-bonding technology. First, metal reflectors are deposited on the top side of the epitaxial wafer using an electron-beam evaporator or sputter system. Then, rapid thermal annealing (RTA) is performed to make an Ohmic contact. The process is normally performed within a temperature range of 400–650 °C in air or N_2 ambient conditions for 1 min to 5 min in order to minimize the thermal damage. Then, a bonding metal is deposited onto the reflector for the wafer-bonding process. To facilitate a good bonding scheme for GaN, different approaches have been reported in the literature [39–42]. In order to prevent diffusion of the bonding metal into the epitaxial layer, multiple barrier layers consisting of Ni, Ti, W, and Pt can be applied onto the reflectors prior to depositing the bonding metal. After the bonding process, the sapphire substrate is detached using a 248 nm-KrF excimer laser during the LLO

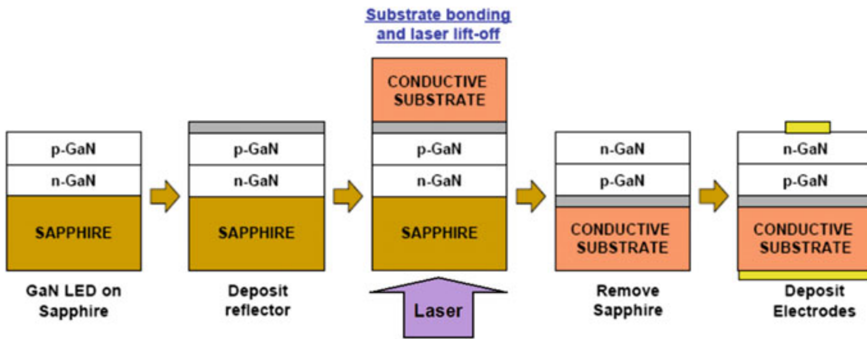

Fig. 12.9 Schematic of vertical-type GaN LED device fabrication process

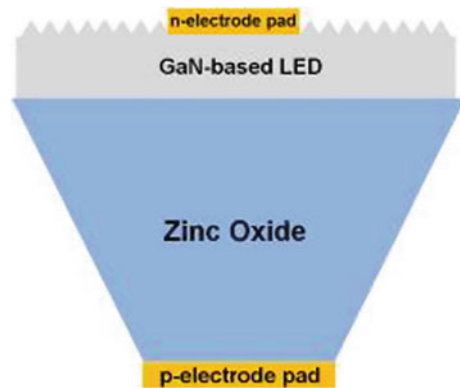

Fig. 12.10 Schematic cross-sectional image of the hexagonal pyramidal LED structure

process, and the undoped GaN layer is etched off using an inductively coupled plasma (ICP) etching system to expose the *n*-GaN layer. Finally, Cr/Au, or Ti/Al layers are deposited in sequence on the exposed *n*-GaN layer to serve as the *n*-type electrode.

12.1.5 Wafer-Bonding and Electroplating Techniques

To fabricate GaN-based VLEDs, the formation of a receptor, diffusion barrier, and soldering (seeding) layer is critical. Recently, a great deal of effort has been made to fabricate a receptor using Si, Cu, Ni, etc., for wafer-bonding and electroplating techniques. For example, Peng et al. [43] reported the fabrication of VLEDs on a 50 mm diameter Si wafer using wafer-bonding and LLO technologies. The light output power of the VLEDs was 20% higher than for conventional sapphire-based LEDs, and the VLED chip had a relatively smaller viewing angle. In addition, the performance of the vertical InGaN LEDs did not degrade during a 1000 h aging

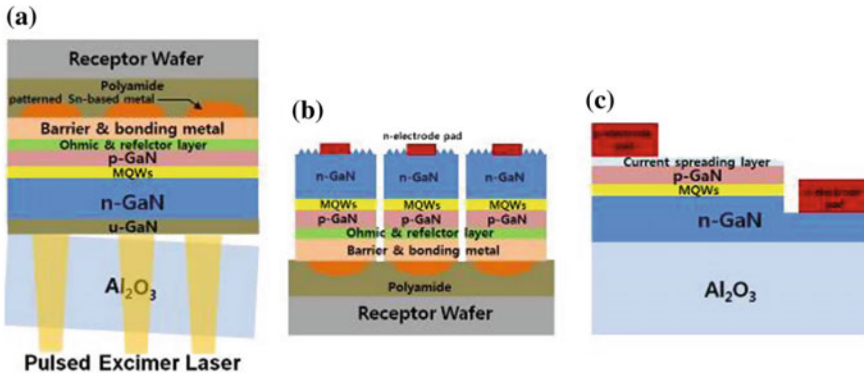

Fig. 12.11 Schematics of VM-LED processing stages using the proposed Sn-based metal substrate technology: **a** sample at the patterned LLO processing stage, **b** sample at the *n*-GaN Ohmic contact processing stage, and **c** cross-sectional schematic of a regular GaN-based LED

test. Uang et al. [44] used a thick electroplated Ni layer as the conductive supporter to realize large-area VLEDs using a similar LLO technique. They showed that the VLEDs (compared to conventional LEDs having the same size as the proposed VLEDs) produced a significantly improved operating voltage drop and light output power. Figure 12.10 shows the hexagonal pyramidal LEDs fabricated through a process including the wafer bonding of ZnO to GaN, LLO, and photochemical etching. ZnO contacts allow for the creation of a vertical current path; selective etching was then used to form truncated hexagonal ZnO pyramids. At a current of 20 mA, the output power of the hexagonal pyramidal structure LED was 23.6 mW, with an EQE of 43.6% [45].

Kuo et al. [46] also proposed a metal substrate technology using Sn-based solder balls and a patterned LLO technique to fabricate vertical-structured metal substrate GaN-based light-emitting diodes (VM-LEDs). Figure 12.11 schematically illustrates the layer structure and key fabrication processes of VM-LEDs using the proposed metal substrate engineering process. As compared to regular LEDs, the proposed VM-LEDs improve the optical power by about 145.36%, with a voltage drop of 1.05 V at 350 mA.

12.1.6 Chemical Lift-Off

It has been reported that the high-energy laser treatment of the LLO process leads to local heating of the GaN layer and causes its destruction [38]. An alternative method to detach the GaN epilayer from the sapphire substrate is the chemical lift-off (CLO) technique [47, 48]. Figure 12.12a presents VLEDs fabricated by CLO in which a CrN buffer layer was placed between the epilayer and the sapphire substrate, and this CrN buffer was selectively etched laterally resulting in lift-off of

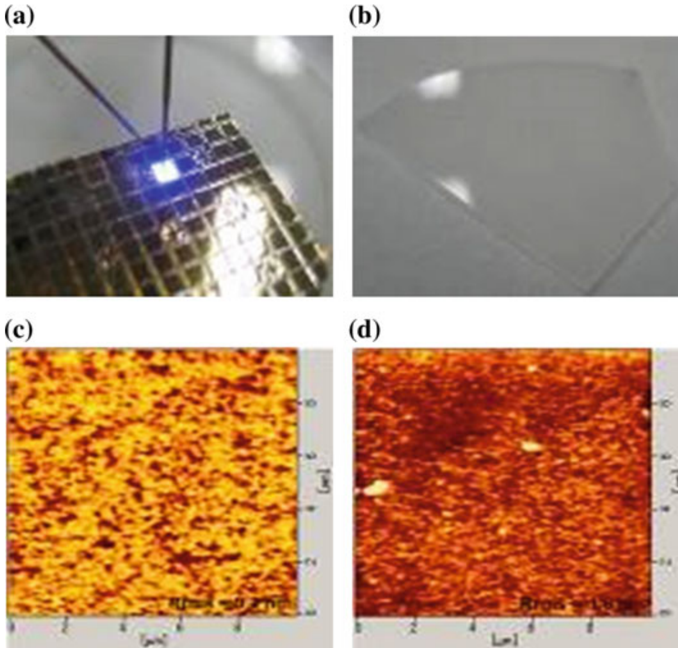

Fig. 12.12 **a** CLO GaN vertical LED, **b** CLO sapphire substrate, **c** atomic force microscopy surface images of chemical lift-off GaN, and **d** that of sapphire substrate

the epilayer grown over it. Park et al. [48] also reported an electrochemical etching method based on the use of oxalic acid. However, although the CLO method has several advantages over LLO such as low stress and low cost, there is still a need to improve the epitaxial quality of the layer grown.

12.1.7 n-*Type Contacts*

The GaN substrate has two faces with different crystal polarities, the Ga-face and N-face polarities (Fig. 12.13), which greatly influence the electrical properties at the metal/GaN interface [49]. During VLED fabrication, the exposed *n*-type GaN layer is formed to have an N-face polarity after LLO. Note that *n*-Ohmic contacts for the Ga-face GaN could easily be formed using either Ti/Al or Cr/Au schemes; however, the N-face surface of GaN has displayed somewhat different Ohmic contact properties compared to the Ga-face surface. For instance, Kwak et al. [50] investigated the dependence of the Ohmic contact property on both the Ga- and N-face surfaces of an *n*-type GaN layer. They showed that it was difficult for the Ti/Al contacts to the N-face *n*-GaN to have Ohmic properties. Jang et al. [51] then introduced a thin Pd layer at the interface between a typical Ti/Al scheme and an

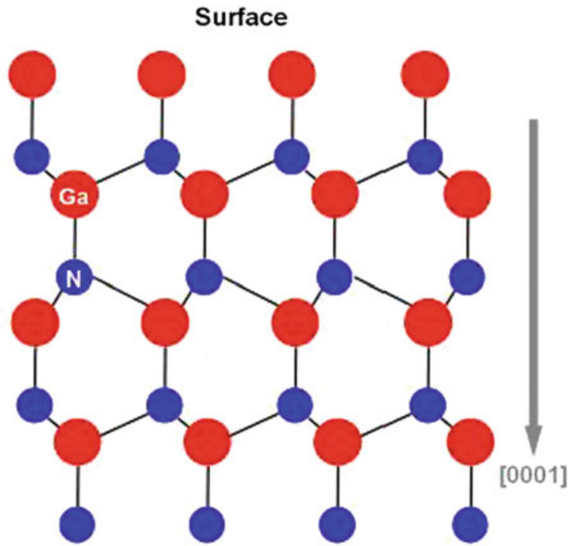

Fig. 12.13 Atomic structure of N-polarity GaN crystal

N-face *n*-GaN layer. The Pd interlayer resulted in a reduction of the specific contact resistance by about one order of magnitude as compared to the Ti/Al scheme when annealed at temperatures in excess of 400 °C. After annealing at 450 °C, the contact resistivity reached $9.08 \times 10^{-6}\ \Omega\ \mathrm{cm}^2$ and remained stable up to an annealing temperature 600 °C.

In addition, Jeon et al. [52] reported the fabrication of TiN/Al contacts for N-face *n*-GaN layers for high-performance VLEDs. The electrical characteristics of the TiN/Al contacts before annealing were similar to those of Ti/Al contacts; however, annealing the samples at 300 °C caused a degradation of their electrical properties. Jeong et al. [53] then demonstrated high-performance VLEDs having non-alloyed reflective Cr/Al/Pt/Au *n*-type electrodes; the Cr/Al/Pt/Au contacts for *n*-GaN exhibited good Ohmic properties.

12.1.8 Randomly Roughened Structure for VLEDs

One method for increasing the LEE in GaN-based VLEDs is to form a roughened structure on the surface of VLEDs. Using the LLO technique, followed by a wet etching process to roughen the VLED surface, an *n*-type side-up GaN-based LED with hexagonal cone-like features was achieved [12]. Another method to improve the LEE is to form a corrugated pyramid-shaped (CPS) structure on the VLED surface [54]. A technique to further enhance the number of photons that escaped from VLED slab forming randomly roughened CPS structure was then developed (Fig. 12.11b). The CPS structure increased the surface areas having angular randomization allowing more scattering of photons (Fig. 12.14).

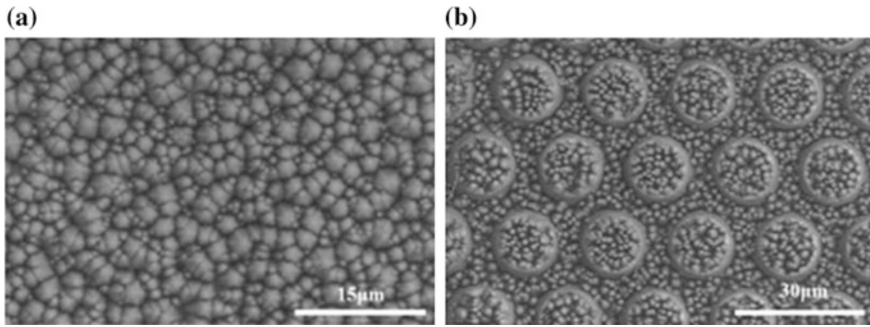

Fig. 12.14 SEM micrographs of VLED surface covered with **a** randomly roughened surface **b** corrugated pyramid-shaped (CPS) surface

12.1.9 Photonic Crystal Structure

A photonic crystal in general is the one-, two-, or three-dimensional periodic arrangement of materials with different refractive indices, in which the characteristic length scale is of the order of the wavelength [55]. Using photonic crystals in VLEDs is a possible next step to improve performance, as they can be used to increase the LEE and also enhance the IQE by means of the Purcell effect [56]. Coupling a photon into guided modes is allowed, though these modes are subsequently out-coupled by the diffractive properties of the photonic crystal. Several research groups have demonstrated GaN-based VLEDs having photonic-crystal diffractive layers on the surfaces, which display an improvement of light extraction and control of the radiation pattern [25, 56, 57]. In photonic crystal LEDs, various parameters contribute to the overall LED performance, such as the thickness of the epitaxial layers, as well as the type, depth, filling factor, and pitch of the photonic crystal. Within the parameter range investigated, the best photonic-crystal LED shows a very high. In randomly roughened LEDs, all waveguide modes inside the VLED have an average probability of being extracted into an outer medium; the extraction solely depends on the reabsorption occurring along this path length. In a photonic crystal LED, the discrete diffraction of the modes according to Bragg's Law means that not all waveguide modes can be extracted into an outer medium with high-efficiency. However, the diffraction of certain modes is very efficient and leads to a fast extraction of that mode, thereby reducing the effect of absorption, and the design of a photonic crystal LED can be optimized for improved directionality [56, 57].

In VLED structures having a several microns thickness, a large fraction of the photon is not extracted even with an optimized photonic crystal, such that the overall light output of a roughened LED is superior even in a forward direction. A higher light output in the forward direction can also be obtained using ultra-thin (>1 μm) LED structures; however, such ultra-thin structures require additional challenges in terms of homogeneous current injection [58] (Fig. 12.15).

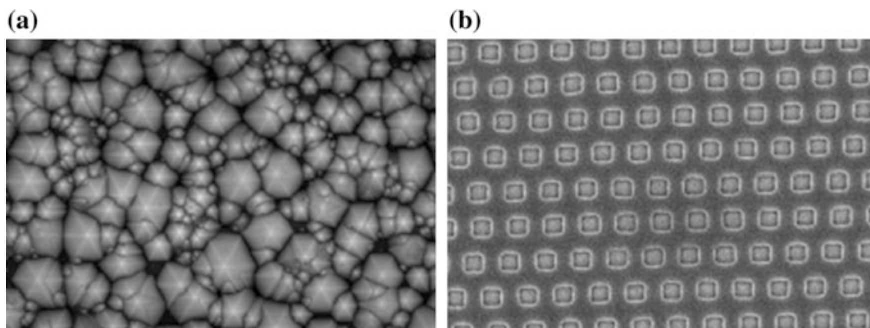

Fig. 12.15 Schematic of VLEDs with a **a** roughened structure and **b** photonic crystal structure

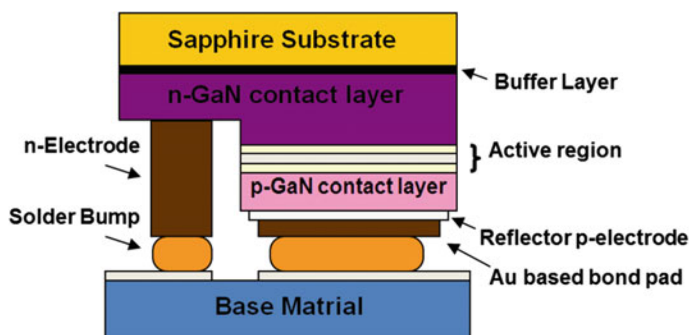

Fig. 12.16 Structure of flip-chip LEDs having a reflector electrode

12.1.10 High-Power Flip-Chip LEDs

The basic structure of a GaN flip-chip LED (FCLED) is shown in Fig. 12.16. In light extraction, flip-chip type LEDs have advantages over top-emitting LEDs because the thick reflective mirror on the *p*-GaN layer is quite effective in enhancing the LEE, thus enabling the structure to be used extensively in high-power and high-efficiency LEDs [59–61].

In order to develop high-performance FCLEDs, a key technique might be to realize high-quality *p*-Ohmic contacts that have characteristics of high reflectivity, low contact resistance, and good thermal stability. To this end, Ag is considered the most attractive candidate for *p*-type reflectors for fabricating GaN-based LEDs having flip-chip or vertical-structure configurations because of its high reflectance in the visible wavelength range and reasonable Ohmic behavior [62, 63]. However, Ag shows poor adhesion to *p*-GaN due to agglomeration during the annealing process [64–67], leading to deterioration in its electrical and optical properties [66, 67]. Therefore, thin transparent layers such as nickel oxide and transparent conducting oxides are typically inserted between Ag and *p*-GaN in order to improve the

adhesion of Ag to *p*-GaN and to decrease agglomeration [62, 63, 67–73]. However, these thin interlayers can absorb light generated from the InGaN/GaN multiple quantum well (MQW), resulting in a decrease in the optical power of LEDs [74, 75].

To resolve these problems, Kim et al. [76] reported that an Ag-based alloy reflector for the FCLED should first be made. In other studies, AgCu was also applied to alloy *p*-type reflectors for GaN FC LEDs [77], and an AgAl reflector showed a specific constant resistance of $5.3 \times 10^{-4}\ \Omega\ \text{cm}^2$ and reflectance of 86.7% at a 450 nm wavelength after annealing at 500 °C (Fig. 12.17b).

Figure 12.18 shows the light output-current (*L-I*) characteristics of FCLEDs having Ag and AgAl layers that were annealed at 300 and 500 °C for 1 min in air. Figure 12.18b shows that the optical output power of an LED with the Ag layer decreases with increasing annealing temperature. This result can be attributed to the decrease in reflectance, which is largely due to the formation of holes and

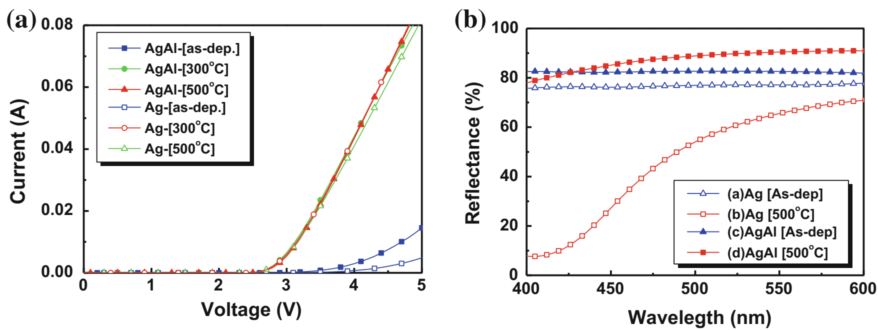

Fig. 12.17 **a** Typical *I-V* characteristics of LEDs with Ag and AgAl layers on *p*-GaN annealed at different temperatures. **b** Reflectance of Ag and AgAl layer before and after annealing at 500 °C for 1 min in air

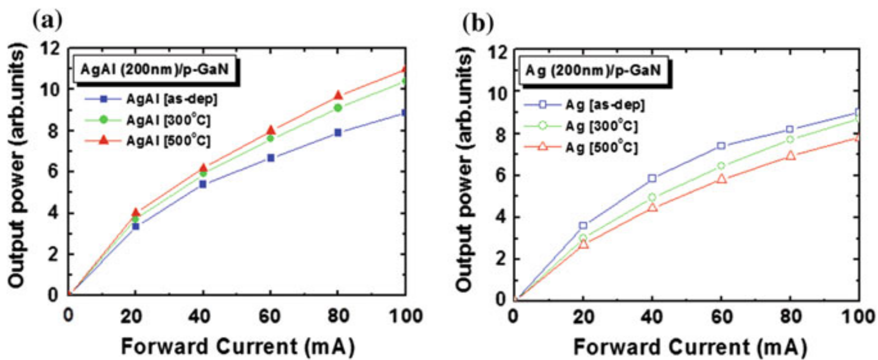

Fig. 12.18 *L-I* characteristics of LEDs having an **a** AgAl layer before and after annealing at 500 °C for 1 min in air and **b** Ag layer before and after annealing at 500 °C for 1 min in air

agglomeration after the thermal annealing of the Ag layer. Figure 12.18a, however, shows that the light output power of LEDs having AgAl layers is enhanced with increasing annealing temperature due to the higher thermal stability of the AgAl layer compared to the Ag layer [76].

Kim et al. [77] reported the specific contact resistance of $7.5 \times 10^{-5}\ \Omega\ \text{cm}^2$ of AgCu after annealing at 400 °C. Furthermore, compared to the Ag contacts, the AgCu contacts remain reasonably stable at higher temperatures of 500 and 600 °C, and their contact resistivity is comparable to that of Ag contacts. The AgCu alloy reflector also has a high reflectance of 89.5% at a 400 nm wavelength after annealing. Note that despite the absence of interfacial voids, the AgCu sample shows a lower reflectance compared to the as-deposited sample, possibly attributed to the presence of an interfacial Cu-oxide phase. Compared to the LED having an Ag reflector, the LED with the AgCu reflector shows better *L-I-V* characteristics. For example, the forward bias voltage and output power measured at 20 mA were 3.56 V and 1.21 mW for the LED with the Ag reflector, and 3.26 V and 1.31 mW for the LED with the AgCu reflector, respectively.

Conductive omnidirectional reflectors (ODRs) consisting of GaN, an ITO nanorod low-refractive-index layer, and an Ag layer have been demonstrated in GaInN LEDs [71]. GaInN LEDs with GaN/low-*n* ITO/Ag ODR showed a lower forward voltage and a 31.6% higher LEE than LEDs having an Ag reflector. This increase in efficiency could be attributed to the enhanced reflectivity of an ODR employing a low-*n* ITO layer, which has a refractive index of 1.34 at 461 nm (Fig. 12.19).

The LEE in LEDs is limited by TIR due to the high index of the GaN relative to the surrounding medium, air, or epoxy. Therefore, LEE enhancement is typically attributed to an escape cone that is produced by the change in propagation direction of light rays. Subsequently, a pyramid reflector consisting of an array of three-dimensional SiO_2 pyramids and an Ag layer was developed [72], and a diffused reflector with Ag on nanotextured ITO was proposed (Fig. 12.20) [73].

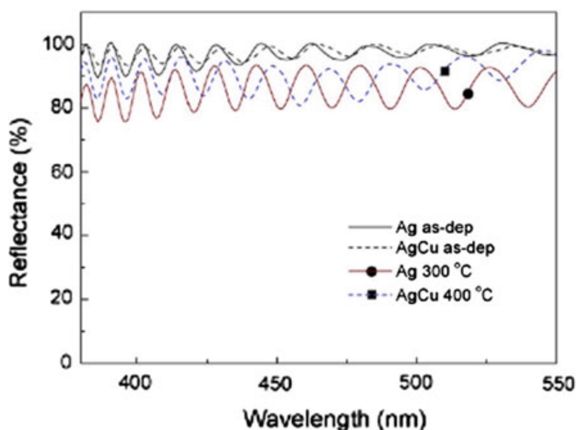

Fig. 12.19 Light reflectance of Ag and AgCu samples before and after annealing

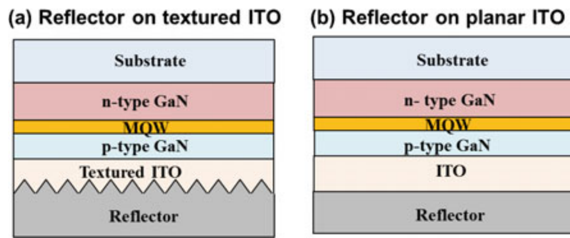

Fig. 12.20 Schematic cross-sectional views of FCLEDs with **a** Ag reflector on nanotextured ITO layer, and **b** Ag reflector on planar ITO layer

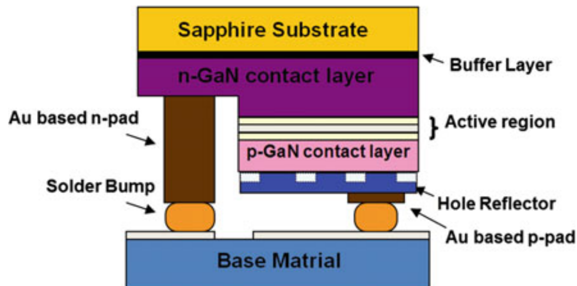

Fig. 12.21 Structure of GaN filp-chip LEDs with AgIn reflector on ITO hole-shape pattern

Experimental results showed that the pyramid and reflector improved the LED extraction efficiency by 13.9% and output power by 153.9% compared to a conventional GaInN LED with a planar Ag reflector.

Lee et al. [13] reported the LEE enhancement obtained by adopting a hole-shape patterned ITO Ohmic contact layer (HITO) and AgIn reflector in GaN-based FCLEDs (Fig. 12.21).

Figure 12.22 shows the *L-I-V* curves of GaN-based FCLEDs with hole-shaped patterned ITO (HITO) and AgIn reflector with microsized hole-shaped patterned ITO layers. In this configuration, the optical output power of FCLEDs was improved by approximately 30%, which can be attributed to the good adhesion and low resistance, high reflection, and transmission of the patterned ITO/Ag layer.

Shen et al. [14] investigated an FCLED having a double-sided PSS. For comparison, a conventional FCLED with no PSS patterning and an FCLED prepared on a PSS were prepared at the same time using exactly the same epitaxial layers [14] (Fig. 12.23).

Under a 350 mA current injection, the forward voltages were 3.24 V, 3.26 V, and 3.25 V for the conventional FCLED, FCLED prepared on a PSS, and an FCLED having a double-sided PSS, respectively. Compared to the conventional FCLED with no PSS patterning, the 24% EL intensity enhancement observed for the FCLED on the PSS should be attributed to the decreased dislocation density in the epitaxial layer and to enhanced light scattering at the GaN-sapphire interface [14]. However, it is expected that the LED output intensity can be further improved by texturing the sapphire bottom surface, thereby enabling photons to undergo multiple scattering and easily escape from the roughened sapphire surface.

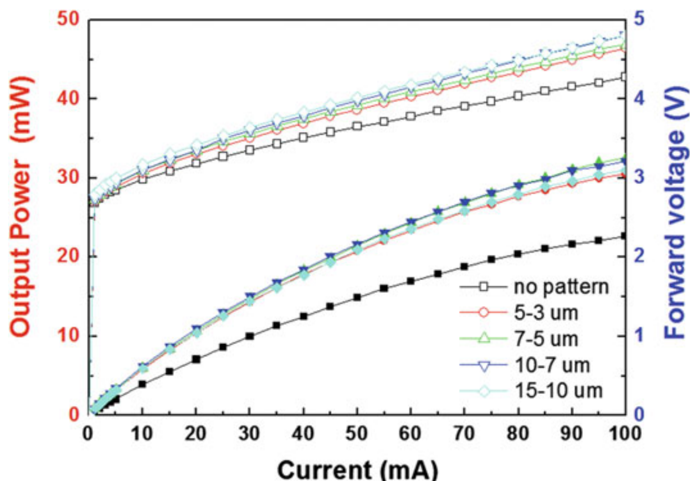

Fig. 12.22 Light-current-voltage (*L*-*I*-*V*) curves of GaN-based filp-chip LEDs with hole-shaped patterned ITO Ohmic contact layer and AgIn reflector as a function of hole radius and spacing between holes

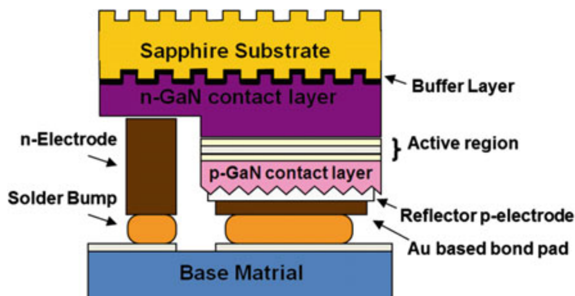

Fig. 12.23 Schematic of fabricated FCLED with double-side PSS

Shchekin et al. [15] compared the performances of standard FCLEDs to vertical injection thin-film (VTF) and thin-film flip-chip (TFFC) LEDs by performing a split-wafer experiment, in which the three types of devices were processed from the same epi-structure. Figure 12.24 presents a cross-sectional schematic of the InGaN/GaN TFFC-LED structure. The radiance of the blue TFFC-LED was 168 mW/mm^2 sr, and is 1.2 times and 2.3 times that of the VTF- and FCLEDs, respectively. Standard deviations for all measured radiances in the group were less than 5%. The optical power output of the encapsulated TFFC-LED was 750 mW, which is 51% and 15% higher than for the encapsulated FC- and VTF-LEDs, respectively. The superior performances of the VTF- and TFFC-LEDs compared to the FCLED are due to the enhanced extraction efficiency of the roughened GaN thin film. In LEDs, the roughened surface disrupts the guiding of light in the high refractive index layers and enhances the out-coupling of light, resulting in a

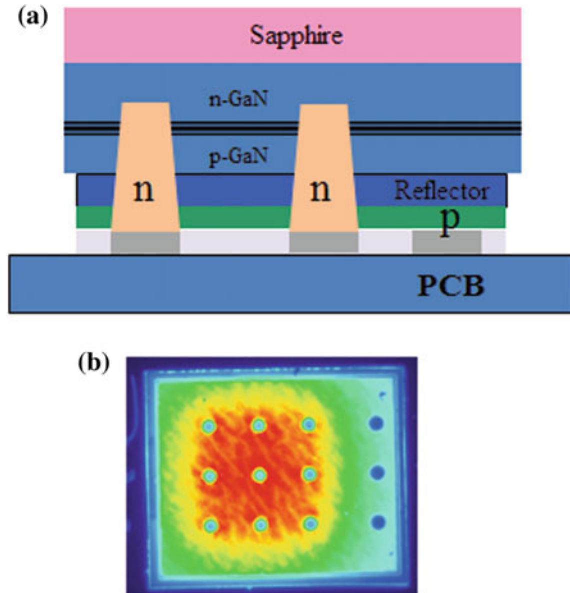

Fig. 12.24 **a** Cross-sectional schematic of InGaN/GaN thin-film flip-chip LED structure. **b** Plane view photomicrograph of the device during operation

dramatically increased EQE. The higher radiance and output power of the TFFC-LEDs compared to VTF-LEDs are the result of adopting a superior flip-chip device structure that eliminates occlusion caused by the top-contact and wire bond pads. However, even though patterning of the top metal contact in VTF-LEDs can be further optimized, there is a trade-off between the extraction efficiency and high current operation. The top-contact area has to be minimized to maximize the LEE, whereas the higher the electrical input power applied, the greater the contact area required to minimize current crowding effects [15].

References

1. J.K. Sheu, C.J. Pen, G.C. Chi, C.H. Kuo, L.W. Wu, C. Chen, H. Chang, Y.K. Su, IEEE Photon. Technol. Lett. **14**, 450 (2002)
2. I. Schnitzer, E. Yablonovitch, C. Caneau, T.J. Gmitter, A. Scherer, Appl. Phys. Lett. **63**, 2174 (1993)
3. A.R. Franklin, R. Newman, J. Appl. Phys. **35**, 1153 (1964)
4. E.E. Loebner, Proc. IEEE **61**, 837 (1973)
5. M.R. Krames, M. Ochiai-Holcomb, G.E. Hofler, C. Carter-Coman, E.I. Chen, I.-H. Tan, P. Grillot, N.F. Gardner, H.C. Chui, J.-W. Huang, S.A. Stockman, F.A. Kish, M.G. Craford, T.S. Tan, C.P. Kocot, M. Hueschen, J. Posselt, B. Loh, G. Sasser, D. Collins, Appl. Phys. Lett. **75**, 2365 (1999)
6. C.C. Kao, H.-C. Kuo, H.W. Huang, J.T. Chu, Y.C. Peng, Y.L. Hsieh, C.Y. Luo, S.C. Wang, C.C. Yu, C.F. Lin, IEEE Photon. Technol. Lett. **17**, 19 (2005)
7. J.S. Lee, J. Lee, J. Kim, J. Jeon, IEEE Photon. Technol. Lett. **18**, 1588 (2006)

8. (a) J.Y. Kim, M.K. Kwon, J.P. Kim, S.J. Park, IEEE Photon. Technol. Lett. **19**, 1865 (2007). (b) J.Y. Kim, S.B. Yang, Y.J. Kang, M.K. Kwon, J.H. Baek, J.K. Lee, *International Workshop on Nitride Semiconductors*, TuP-OD-13 (2012)
9. C. Huh, K.S. Lee, E.J. Kang, S.J. Park, J. Appl. Phys. **93**, 9383 (2003)
10. S.I. Na, G.Y. Ha, D.-S. Han, S.S. Kim, J.Y. Kim, J.H. Lim, D.-J. Kim, K.I. Min, S.J. Park, IEEE Photon. Technol. Lett. **18**, 1512 (2006)
11. D.S. Han, J.Y. Kim, S.I. Na, S.H. Kim, K.D. Lee, B. Kim, S.J. Park, IEEE Photon. Technol. Lett. **18**, 1406 (2006)
12. T. Fujii, Y. Gao, R. Sharma, E.L. Hu, S.P. DenBaars, S. Nakamura, Appl. Phys. Lett. **84**, 855 (2004)
13. S.H. Lee, J.H. Baek, T.H. Kim, L.S. Park, J. Nanosci. Nanotechnol. **11**, 1 (2011)
14. C.F. Shen, S.J. Chang, W.S. Chen, T.K. Ko, C.T. Kuo, S.C. Shei, IEEE Photon. Technol. Lett. **19**, 780 (2007)
15. O.B. Shchekin, J.E. Epler, T.A. Trottier, T. Margalith, D.A. Steigerwald, M.O. Holcomb, P.S. Martin, M.R. Krames, Appl. Phys. Lett. **89**, 071109 (2006)
16. K. Tadatomo, H. Okagawa, T. Tsunekawa, T. Jyouichi, Y. Imada, M. Kato, H. Kudo, T. Taguchi, Phys. Status Solidi (A) **188**, 121–125 (2001)
17. H. Kudo, K. Murakami, R. Zheng, Y. Yamada, T. Taguchi, K. Tadatomo, H. Okagawa, Y. Ohuchi, T. Tsunekawa, Y. Imada, K. Kata, Jpn. J. Appl. Phys. **41**, 2484–2488 (2002)
18. A. Bell, R. Liu, F.A. Ponce, H. Amano, I. Akasaki, D. Cherns, Appl. Phys. Lett. **82**, 349–351 (2003)
19. M. Yamada, T. Mitani, Y. Narukawa, S. Shioji, I. Niki, S. Sonobe, K. Deguchi, M. Sano, T. Mukai, Jpn. J. Appl. Phys. **41**, L1431–L1433 (2002)
20. S.J. Chang, Y.C. Lin, Y.K. Su, C.S. Chang, T.C. Wen, S.C. Shei, J.C. Ke, C.W. Kuo, S.C. Chen, C.H. Liu, Solid-State Electron. **47**, 1539–1542 (2003)
21. D.S. Wuu, W.K. Wang, W.C. Shih, R.H. Horng, C.E. Lee, W.Y. Lin, J.S. Fang, IEEE Photon. Technol. Lett. **17**, 288–290 (2005)
22. W.K. Wang, D.S. Wuu, S.H. Lin, P. Han, R.H. Horng, T.C. Hsu, D.T.C. Huo, M.J. Jou, Y.H. Yu, A. Lin, IEEE. J. Quan. Electron. **41(**11) (2005)
23. Y.J. Lee, J.M. Hwang, T.C. Hsu, M.H. Hsieh, M.J. Jou, B.J. Lee, T.C. Lu, H.C. Kuo, S.C. Wang, IEEE Photon. Technol. Lett. **18**, 1152–1154 (2006)
24. A. David, T. Fujii, B. Moran, S. Nakamura, S.P. Denbaars, C. Weisbuch, H. Benisty, Appl. Phys. Lett. **88**, 133514 (2006)
25. T.N. Oder, J. Shakya, J.Y. Lin, H.X. Jiang, Appl. Phys. Lett. **83**, 1231 (2003)
26. D. Ho Kim, C.O. Cho, Y.G. Roh, H. Jeon, Y.S. Park, J. Cho, J.S. Im, C. Sone, Y. Park, W. J. Choi, Q.H. Park, Appl. Phys. Lett. **87**, 203508 (2005)
27. J.Y. Kim, M.K. Kwon, K.S. Lee, S.H. Kim, K.D. Lee, S.J. Park, Appl. Phys. Lett. **91**, 181109 (2007)
28. S.H. Kim, K.D. Lee, J.Y. Kim, M.K. Kwon, S.J. Park, Nanotechnology **18**, 055306 (2007)
29. S.M. Kim, H.S. Oh, J.H. Baek, K.H. Lee, G.Y. Jung, J.H. Song, H.J. Kim, B.J. Ahn, D. Yanqun, J.H. Song, IEEE Electron Dev. Lett. **31**, 842–844 (2010)
30. W.S. Wong, T. Sands, N.W. Cheung, M. Kneissl, D.P. Bour, P. Mei, L.T. Romano, N.M. Johnson, Appl. Phys. Lett. **75**, 1360 (1999)
31. D.S. Wuu, S.C. Hsu, S.H. Huang, C.C. Wu, C.E. Lee, R.H. Horng, Jpn. J. Appl. Phys. **43**, 5239 (2004)
32. S.H. Huang, R.H. Horng, S.C. Hsu, T.Y. Chen, D.S. Wuu, Jpn. J. Appl. Phys. **44**, 3028 (2005)
33. M.K Kelly, O. Ambacher, R. Dimitriv, R. Handschuh, M. Stutzmann, Phys. Status Solidi (A) **159** (1997)
34. H.S. Kim, K.K. Kim, K.K. Choi, H.K. Kim, J.O. Song, J.H. Cho, K.H. Baik, C.S. Sone, Y. J. Park, T.Y. Seong, Appl. Phys. Lett. **91**, 023510 (2007)
35. C.C. Kao, H.C. Kuo, K.F. Yeh, J.T. Chu, W.L. Peng, H.W. Huang, T.C. Lu, S.C. Wang, IEEE Photon. Technol. Lett. **19**, 849 (2007)

36. S.H. Su, C.C. Hou, M.H. Lin, M. Yokoyama, S.M. Chen, H. Kuan, Jpn. J. Appl. Phys. **46**, 965 (2007)
37. S.L. Chen, S.J. Wang, K.M. Uang, T.M. Chen, B.W. Liou, IEEE Photon. Technol. Lett. **19**, 351 (2007)
38. Y.S. Wu, J.H. Cheng, W.C. Peng, Appl. Phys. Lett. **90**, 251110 (2007)
39. W.S. Wong, T. Sands, N.W. Cheung, M. Kneissl, D.P. Bour, P. Mei, L.T. Romano, N.M. Johnson, Appl. Phys. Lett. **77**, 2822 (2000)
40. J. Arokiaraj, C.K. Leong, V. Lixian, A.M. Yong, W. Xincai, Appl. Phys. Lett. **92**, 124105 (2008)
41. S.C. Hsu, C.Y. Liu, Electrochem. Solid-State Lett. **9**(5), G171 (2006)
42. T. Jeong, K.H. Kim, H.H. Lee, S.J. Lee, S.H. Lee, J.H. Baek, J.K. Lee, IEEE Photon. Technol. Lett. **20**, 1932 (2008)
43. W.C. Peng, Y.C.S. Wu, IEEE Photon. Technol. Lett. **18**, 613 (2006)
44. K.M. Uang, S.J. Wang, S.L. Chen, Y.C. Yang, T.M. Chen, B.W. Liou, Jpn. J. Appl. Phys. **45**, 3436 (2006)
45. D.B. Thompson, A. Murai, M. IZA, S. Brinkley, S.P. Denbaars, U.K. Mishra, S. Nakamura, Jpn. J. Appl. Phys. **47**, 3447 (2008)
46. H.Y. Kuo, S.J. Wang, P.R. Wang, K.M. Uang, T.M. Chen, H. Kuan, Appl. Phys. Lett. **92**, 021105 (2008)
47. J.S. Ha, S.W. Lee, H.J. Lee, H.J. Lee, S.H. Lee, H. Goto, T. Kato, K. Fujii, M.W. Cho, T. Yao, IEEE Photon. Technol. Lett. **20**, 175 (2008)
48. J.M. Park, K.M. Song, S.R. Jeon, J.H. Baek, S.W. Ryu, Appl. Phys. Lett. **94**, 221907 (2009)
49. E. Monroy, E. Sarigiannidou, F. Fossard, N. Gogneau, E. Bellet-Amalric, J.L. Rouviere, S. Monnoye, H. Mank, B. Daudin, Appl. Phys. Lett. **84**, 3684 (2004)
50. J.S. Kwak, K.Y. Lee, J.Y. Han, J. Cho, S. Chae, O.H. Nam, Y. Park, Appl. Phys. Lett. **79**, 3254 (2001)
51. T. Jang, S.N. Lee, O.H. Nam, Y. Park, Appl. Phys. Lett. **88**, 193505 (2006)
52. J.W. Jeon, T.Y. Seong, H.S. Kim, K.K. Kim, Appl. Phys. Lett. **94**, 042102 (2009)
53. T. Jeong, S.W. Kim, S.H. Lee, J.W. Ju, S.J. Lee, J.H. Baek, J.K. Lee, J. Electrochem. Soc. **158** (9), H908 (2011)
54. J.Y. Chu, C.F. Chu, C.C. Cheng. W.H. Liu, H.C. Cheng, F.H. Fan, J.K. Yen, Proc. SPIE **6894**, 68940X-1 (2008)
55. E.F. Schubert, *Light Emitting Diode*s, 2nd edn. (Cambridge University Press, 2006)
56. J.J. Wierer, A. David, M.M. Megens, Nat. Photonics **3**, 163 (2009)
57. A. David, H. Benisty, C. Weisbuch, J. Display Tech. **3**, 133 (2007)
58. R. Windisch, N. Linder, C. Wiesmann, K. Streubel, *IEEE/LEOS Winter Topical Meeting* (2009), p. 10
59. J.J. Wierer, D.A. Steigerwald, M.R. Krames, J.J. O'Shea, M.J. Ludowise, G. Christenson, Y. C. Shen, C. Lowery, P.S. Martin, S. Subramanya, W. Gotz, N.F. Gardner, R.S. Kern, S.A. Stockman, Appl. Phys. Lett. **78**, 3379 (2001)
60. D.L. Hibbard, S.P. Jung, C. Wang, D. Ullery, Y.S. Zhao, W. So, H. Liu, H.P. Lee, Appl. Phys. Lett. **83**, 311 (2003)
61. S.J. Chang, W.S. Chen, Y.C. Lin, C.S. Chang, T.K. Ko, Y.P. Hsu, C.F. Shen, J.M. Tsai, S.C. Shei, IEEE Trans. Adv. Packag. **29**, 403 (2006)
62. J.O. Song, D.S. Leem, J.S. Kwak, O.H. Nam, Y. Park, T.Y. Seong, Appl. Phys. Lett. **83**, 4990 (2003)
63. J.O. Song, J.S. Kwak, Y. Park, T.Y. Seong, Appl. Phys. Lett. **86**, 062104 (2005)
64. S.K. Sharma, J. Spitz, Thin Solid Films **65**, 339 (1980)
65. D.J. Srolovitz, M.G. Goldiner, JOM **47**, 31 (1995)
66. H.C. Kim, N.D. Theodore, T.L. Alford, J. Appl. Phys. **95**, 5180 (2004)
67. H.S. Venugopalan, A. DiCarlo, X. Cao, S. Libon, B.S. Shelton, E. Stefanov, T. Zhang, I. Eliashevich, S.E. Weaver, M. Hsing, B. Kolodin, T. Soules, D. Florescu, S. Guo, M. Pophristic, B. Peres, Proc. SPIE **4996**, 195 (2003)

68. D.A. Steigerwald, J.C. Bhat, D. Collins, R.M. Fletcher, M.O. Holcomb, M.J. Ludowise, P.S. Martine, S.L. Rudaz, IEEE J. Sel. Top. Quan. Electron. **8**, 310 (2002)
69. H.W. Jang, J.L. Lee, Appl. Phys. Lett. **85**, 5920 (2004)
70. J.H. Son, Y.H. Song, H.K. Yu, J.L. Lee, Appl. Phys. Lett. **95**, 062108 (2009)
71. J.K. Kim, T. Gessmann, E.F. Schubert, J.Q. Xi, H. Luo, J.H. Cho, C.S. Sone, Y.J. Park, Appl. Phys. Lett. **88**, 013501 (2006)
72. J.Q. Xi, H. Luo, A.J. Pasquale, J.K. Kim, E.F. Schubert, IEEE Photon. Technol. Lett. **18**, 2347 (2006)
73. J.Y. Kim, M.K. Kwon, I.K. Park, C.Y. Cho, S.J. Park, D.M. Jeon, J.W. Kim, Y.C. Kim, Appl. Phy. Lett. **93**, 021121 (2008)
74. J.H. Lim, D.K. Hwang, H.S. KIM, J.Y. Oh, J.H. Yang, R. Navamathavan, S.J. Park, Appl. Phys. Lett. **85**, 6191 (2004)
75. J.K. Ho, C.S. Jong, C.N. Huang, C.Y. Chen, C.C. Chiu, K.K. Shih, Appl. Phys. Lett. **74**, 1275 (1999)
76. J.Y. Kim, S. In Na, G.Y. Ha, M.K. Kwon, I.K. Park, J.H. Lim, S.J. Park, M.H. Kim, D. Choi, K. Min, Appl. Phys. Lett. **88**, 043507 (2006)
77. H. Kim, K.H. Baik, J. Cho, J.W. Lee, S. Yoon, H. Kim, S.N. Lee, C. Sone, Y. Park, T.Y. Seong, IEEE Photon. Technol. Lett. **19**, 336 (2007)

Chapter 13
Electrical Properties, Reliability Issues, and ESD Robustness of InGaN-Based LEDs

M. Meneghini, G. Meneghesso and E. Zanoni

This chapter describes the physical mechanisms that may induce the degradation of InGaN-based LEDs. Before going into a detailed description of the main degradation processes, we will give a brief overview on the electrical (current–voltage) characteristics of LEDs, to provide the basic information which is useful to understand the electrical characterization data reported in the subsequent part of the chapter. On the basis of literature data, we will analyze the main mechanisms responsible for current conduction, with focus on tunneling mechanisms, reverse-current conduction, and on the origin of the high ideality factors, always present in InGaN LEDs.

After this introductory section, we will discuss the main physical mechanisms that may limit the lifetime of GaN-based LEDs submitted to short- and long-term operation. More specifically, we will focus on the following mechanisms: *(i)* the degradation of the blue semiconductor chip, due to the generation of non-radiative recombination centers, and to the degradation of the p-type semiconductor and contacts; *(ii)* the degradation mechanisms that affect the performance of the package and phosphors, which are typically activated at high-temperature levels; and *(iii)* the failure of LEDs submitted to Electrostatic Discharges (ESD).

13.1 Current–Voltage Characteristics

The electrical characteristics of LEDs based on nitrides are different from those of conventional diodes, such as pn or Schottky diodes. Several factors can influence the main parameters of the devices, and in particular the operating voltage, the reverse current, the ideality factor, and their dependence on temperature. In this

M. Meneghini · G. Meneghesso · E. Zanoni (✉)
University of Padova, Padua, Italy
e-mail: zanoni@dei.unipd.it

© Springer Nature Singapore Pte Ltd. 2017

T.-Y. Seong et al. (eds.), *III-Nitride Based Light Emitting Diodes and Applications*,
Topics in Applied Physics 133, DOI 10.1007/978-981-10-3755-9_13

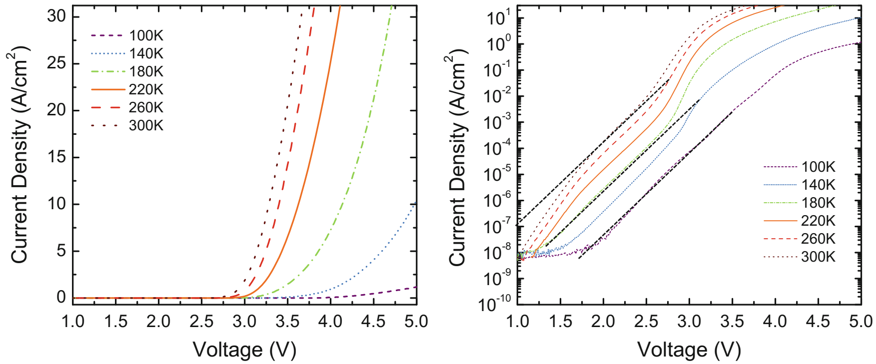

Fig. 13.1 Current–voltage characteristics of a multiple-quantum-well LED measured at different temperature levels. Curves are plotted in (*left*) linear scale and in (*right*) semi-logarithmic scale

section we briefly summarize the main features of the electrical characteristics of GaN-based LEDs: we focus on the origin of reverse-current conduction, tunneling-related components, and high ideality factors, since this information is of fundamental importance for understanding the degradation processes that limit the reliability of LEDs, which are described in the next section.

In Fig. 13.1 we report the typical current–voltage (I–V) characteristics of a multiple-quantum-well (MQW) LED, measured at different temperature levels between 100 K and room temperature (RT). The curves are plotted both in linear (left) and semi-logarithmic (right) scale. With increasing temperature from 100 K to RT, the forward voltage of the LEDs shows a remarkable decrease, due to the following factors: (i) a decrease in the resistivity of the p-type and n-type layers; (ii) an increase in the injection of holes from the p-side of the diodes to the active layer; and (iii) a decrease in the resistivity of the ohmic contacts. An accurate analysis of the I–V curves in semi-logarithmic scale reveals the presence of different conduction mechanisms.

For low voltage levels (here below 2.5 V), the semi-logarithmic I–V curves indicate that current has a nearly exponential dependence on voltage: the slope of the semi-logarithmic IV curves does not significantly depend on temperature, thus suggesting that in this voltage region the main mechanism responsible for current conduction is a field-dependent process—such as tunneling—rather than a thermally activated one. For GaN-based LEDs, forward-bias tunneling components are usually represented in the form

$$I \sim I_0 \exp\left(\frac{qV}{E}\right), \tag{13.1}$$

where E represents an energy parameter, which reflects the transparency of the energy barriers to tunneling carriers, and has a negligible temperature dependence [1, 2]. According to [3, 4], for a p^+-n junction, parameter E can be expressed as

$$E = \frac{4\hbar q\sqrt{N_D}}{\pi\sqrt{m^*\epsilon}}, \tag{13.2}$$

where q is the electron charge, $\hbar$ is the Planck's constant divided by 2π, m* is the effective mass of the electrons, and N_D represents the doping concentration. Typical reported values for E range between 72 and 220 meV for GaN-based LEDs [1]. As deeply discussed in [1, 5, 6], several models have been proposed to explain the tunneling processes that occur in GaN-based LEDs: (i) tunneling of holes to the active region, (ii) tunneling of electrons to deep levels located within the barriers [5] or the p-GaN region [1], with subsequent recombination; (iii) tunneling recombination via multiple-step processes [1]; and (iv) diagonal tunneling [6]. Several defects may enhance carrier tunneling in GaN-based MQW LEDs, including point defects located within the quantum-well region, clusters of defects close to dislocations, nitrogen vacancies or oxygen impurities [1], Mg-related defective structures, and defects related to indium segregation [5].

Recent studies demonstrated that strong tunneling between the quantum wells and the barriers can be detected by means of spatially and spectrally resolved electroluminescence measurements. Analyses on blue [7] and green [5] LEDs operated at low forward-bias levels reveal the presence of localized dots, with emission wavelength significantly longer than the peak wavelength of the devices. In Fig. 13.2 we report the false-color micro-electroluminescence images taken at two different wavelengths on a green LED, with a peak wavelength close to 540 nm: as can be noticed, this device emits a weak luminescence signal also in the yellow-red spectral region (see the image taken with the monochromator set to 600 nm). The presence of yellow localized luminescence dots was found to be strongly correlated to the existence of high tunneling components in the I–V characteristics of the devices (see [5]): dot-like luminescence was ascribed to the injection/tunneling of electrons from the quantum wells to the barriers, with subsequent recombination via the defective states that are commonly considered to be responsible of yellow luminescence in GaN [8].

In Fig. 13.1, it is clearly noticeable that while current conduction is dominated by tunneling for $V < 2.5$ V, for higher voltage levels the slope of the semi-logarithmic I–V curves shows a significant increase, indicating that current diffusion and recombination is starting to dominate. As a consequence, the relation between current and voltage can be expressed as

$$I = I_0\left(e^{qV/nkT} - 1\right), \tag{13.3}$$

where I_0 is the saturation current, q is the electron charge, k is the Boltzmann constant, and n is the ideality factor. In agreement with [3], in the region between 2.5 and 3 V the slope of the I–V curves is significantly temperature dependent. For high current densities (in Fig. 13.1), the presence of the series resistance results in a significant decrease in the slope of the I–V curves: series resistance originates from the nonideal conductivity of the ohmic contacts and of the quasi-neutral regions,

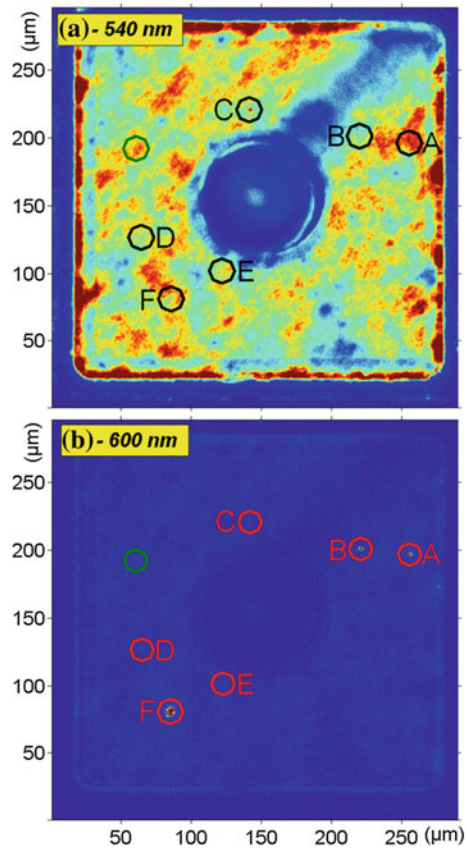

Fig. 13.2 False-color emission images showing the intensity of the EL of *green* LED, measured through a monochromator set at **a** 540 nm and **b** 600 nm (monochromator spectral width is 10 nm)

and may significantly impact the operating voltage of the devices. High resistive components may also result in the so-called current crowding phenomenon: due to the nonideal conductivity of the semiconductor layers, current crowds in proximity of the mesa edge (see a schematic representation of this mechanism in Fig. 13.3), for LEDs with horizontal structure. This mechanism has been investigated by several research groups (see for instance [9–15]), who provided information on the role of current crowding in limiting the optical performance of LEDs, and complete

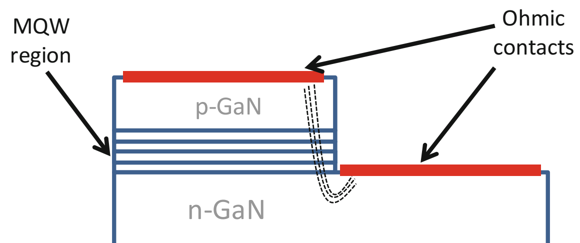

Fig. 13.3 Schematic representation of the current crowding phenomenon. *Dashed lines* represent the existence of preferential current paths

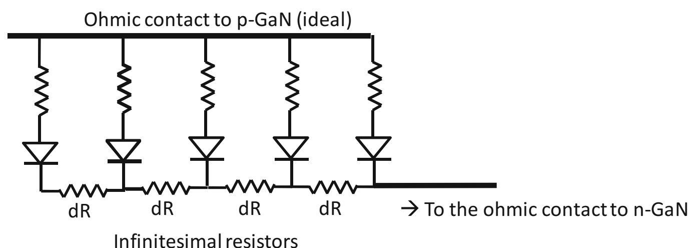

Fig. 13.4 Schematic representation of a model used for the study of current crowding in LEDs with horizontal structure (see [12] for a detailed description of this model)

analytical models for the description of this phenomenon. Distributed models are commonly used for the description of current crowding in horizontal LEDs: as widely discussed in [12], both the resistance of the n-type and p-type materials must be considered for the definition of an accurate model for current crowding. In Fig. 13.4 we report a typical schematic circuit used for the study of current crowding: the vertical resistors are used to take into account the resistance of the ohmic contact on p-GaN, and of the p-type material, while the horizontal resistors represent the ohmic losses in the n-type region. The uniformity of current distribution in a horizontal LED can be evaluated by calculating the *current spreading length* (see [12]), according to the formula

$$L_s = \sqrt{\left(\rho_c + \rho_p t_p\right) t_n / \rho_n}, \tag{13.4}$$

where ρ_p, ρ_n, and ρ_c represent the resistivities of the p-type material, n-type material, and ohmic contact to p-GaN, while t_p and t_n are the thicknesses of the p- and n-type regions. In a first-order approximation, the *current spreading length* represents the distance (from the mesa edge) for a 1/e decrease in current density. As shown in [4], L_s depends only on the geometry of the samples (thickness of the p- and n-side regions) and on the specific resistivity of the materials adopted for the realization of the LEDs. Current crowding can be significantly limited by decreasing the resistivity of the n-GaN layer, and by increasing the thickness of the n-type material.

Current crowding can have detrimental effects in terms of performance, thermal management, and reliability. In fact, when current is focused on a limited region, this results in a reduction of the effective area of the LED. Furthermore, in the region characterized by crowding, current density is significantly higher than in other regions. This determines a decrease in LED efficiency since (i) due to the efficiency droop, IQE decreases monotonically with current density; and (ii) a stronger self-heating of the junction in proximity of the most effective conductive paths induces a further efficiency decrease.

A significant current crowding can be present even when the current spreading length has been carefully optimized: an example is shown in Fig. 13.5, which

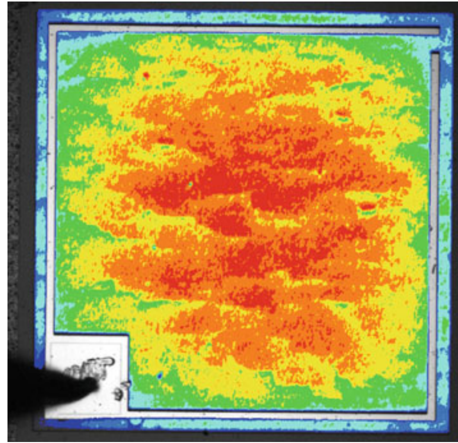

Fig. 13.5 False-color emission microscopy image showing the distribution of light intensity on a 500 × 500 μm^2 LED chip with horizontal structure

reports the false-color electroluminescence map measured on a 500 × 500 μm^2 LED chip with horizontal structure. As can be noticed, the device does not show any crowding related to the resistivity of the n- or p-type material (i.e., current does not flow only in proximity of the mesa edge as schematically shown in Fig. 13.3). On the other hand, current focuses to the center of the LEDs: this mechanism can be partly explained by considering that the center of the LED is the region from which heat extraction is most difficult. During LED operation, junction temperature can be higher at the center of the LED, with respect to the borders. This may result in an increased current density at the center, and therefore in a higher emission intensity, as shown in Fig. 13.5.

13.2 The Ideality Factor of GaN-Based LEDs

The I–V curves of diodes are commonly modeled by means of the first-order equation

$$I = I_0\left(e^{qV/nkT} - 1\right), \tag{13.5}$$

where I_0 is the saturation current, q is the electron charge, k is the Boltzmann constant, and n is the so-called ideality factor, which is a measure of how much the I curve of the diode is close to the theoretical one. For conventional diodes (e.g., Schottky and pn diodes based on silicon), this parameter ranges between 1 and 2. Based on the theory proposed by Sah-Noyce-Shockley [16], values of n close to 1 indicate that current conduction is dominated by diffusion processes, while on the other hand ideality factors equal to 2 indicate that current is strongly influenced by

carrier generation and recombination. The ideality factor n can be easily estimated through the fitting of the semi-logarithmic I–V curves of the diodes.

Several reports [17–23] indicate that the ideality factor of GaN-based diodes and LEDs can be significantly higher than 2. Many theories were proposed to explain such anomalously high ideality factors: to provide a more detailed view on this particular aspect, in the following we give a brief description of the most common theories.

In [4], Franssen et al. explained the high ideality factors by considering that in a MQW-based LED, electrons and holes do not simply diffuse toward the neutral regions, where they eventually recombine (as in a pn junction), but they are injected into the quantum wells where they undergo radiative recombination. In a first-order approximation, i.e., by assuming similar carrier concentrations in the neutral regions, recombination rate is supposed to be maximum at the center of the active layer, i.e., in the region where the concentrations of both electrons and holes are high. Under this hypothesis, described in [4], carriers must overcome an energy barrier which is half the intrinsic barrier of the junction, before undergoing radiative recombination. The authors of [4] suggest that an ideality factor close to 2 can be obtained by considering the presence of this (halved) barrier into the Shockley equation.

A different model was proposed by Shah et al. in [23]: in this study, the authors demonstrated that high ideality factors can be present even without the presence of a multi-quantum-well structure. The devices analyzed in [23] were pn junction diodes with/without AlGaN/GaN heterostructure, with ideality factors in the range between 4 and 6.9. The presence of such high ideality factors was explained by considering that the structure of a diode based on GaN consists in the series connection of several heterojunctions, with nonlinear characteristics (see Fig. 13.6 for a schematic representation of a typical diode): (i) the metal–semiconductor junctions of the ohmic contacts, which have the following (nonlinear) I–V equation:

$$I_{ms} \approx I_{s,ms} e^{\frac{qV_{ms}}{n_{ms}kT}}, \tag{13.6}$$

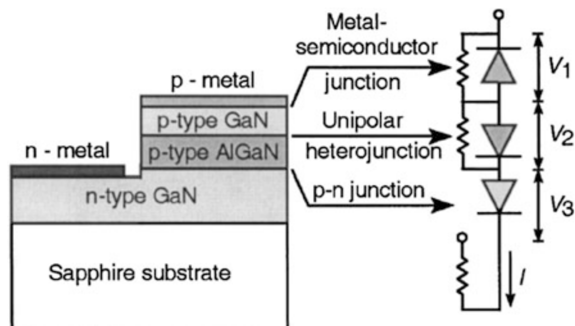

Fig. 13.6 Structure of one of the diodes studied in [23]. Reprinted with permission from [23]. Copyright [2003], American Institute of Physics

and (ii) the AlGaN/GaN or InGaN/GaN heterojunctions, for which the following equation holds:

$$I_h \approx I_{s,h} e^{\frac{qV_h}{n_h kT}}. \tag{13.7}$$

In (13.6) and (13.7) $I_{s,ms}$ and $I_{s,h}$ (n_{ms} and n_h) represent the saturation current (ideality factor) of a generic metal–semiconductor junction and of a heterostructure, k is the Boltzmann constant, q is the electron charge, and T is the temperature.

These heterojunctions are placed in series to the main pn junction of the diode, with equation

$$I_{pn} \approx I_{s,pn} e^{\frac{qV_{pn}}{n_{pn} kT}}. \tag{13.8}$$

According to [23], the current–voltage relation of a diode results from the series connection of the different heterojunctions, and can be expressed as

$$\ln(I) = \frac{q/kT}{\sum_i n_i} V + \frac{\sum_i n_i \ln(I_{si})}{\sum_i n_i}, \tag{13.9}$$

where the index i is used to take into account that several heterojunctions are contributing to the I–V relation, according to (13.6–13.8).

Equation (13.9) clearly indicates that the ideality factor of a GaN-based diode is the sum of the ideality factors of each of the heterojunctions which constitute the diode ($n = \sum_i n_i$, see [23] for details). This result explains the high ideality factors recorded in GaN-based diodes and LEDs.

This interesting theory is partly in contrast with more recent data published on AlGaN-based quantum-well LEDs: in [17], the I–V curves of ultraviolet LEDs with identical structures, but different EBL (electron blocking layer) thicknesses were compared. Results indicated that the ideality factor strongly depends on the thickness of the EBL: LEDs without EBL showed an ideality factor of 7.2, while LEDs with an EBL thickness of 4 (10) nm were found to have ideality factor of 6.9 (5.5). This result indicates that the overall ideality factor cannot be directly determined as the sum of the contributions of the several heterojunctions which constitute an LED device. On the other hand, the authors of [17] indicate that the ideality factor of a LED can be strongly temperature dependent, while the slope of the semi-logarithmic I–V curves does not depend on temperature, thus suggesting that tunneling dominates current conduction below the turn-on voltage of the diodes.

Results reported in the literature therefore suggest that the large ideality factors reported for LEDs cannot be explained by a simple, first-order, model: to accurately explain the I–V characteristics of the LEDs, and the high values of the ideality factor, several factors must be considered, including the existence of significant tunneling components, the presence of several nonlinear junctions, and the existence of efficient recombination paths within the active layer.

13.3 Current Conduction in Reverse-Bias

LEDs are not ideal blocking devices, and for this reason they can have a significant current conduction even when they are biased with a negative voltage. The existence of reverse-current components has been analyzed by several authors [1, 2, 4, 5, 24–26]. In Fig. 13.7 we report typical current–voltage characteristics measured, at different temperature levels, on a GaN-based LED: data are plotted in log–log scale. As can be noticed, current has a power-law dependence on voltage ($I \sim V^n$), where the exponent n ranges between 5 and 6 [26, 27]. Other reports [2] indicated that reverse current can have an exponential dependence on voltage, according to $I = I_0 e^{\frac{qV}{E}}$, where E is a characteristic energy parameter, ranging between 1 and 2. Previous reports [25] indicated that reverse current is directly proportional to junction area, and this suggests that leakage is dominated by bulk components, rather than by the conduction through the mesa/surface. Interestingly, the shape of the reverse-bias I–V curve does not significantly change with temperature. This result suggests that, under reverse-bias, current conduction is dominated by a field-dependent mechanism, rather than by a thermally activated one. Results reported in the literature therefore suggest that reverse-current conduction is dominated by tunneling.

Leakage current strongly depends on the density of structural defects. In Fig. 13.8 we report the current–voltage characteristics measured on two LEDs with identical structure, grown on two templates with different Threading Dislocation Densities (TDD), namely 3×10^8 cm^{-2} and 8×10^9 cm^{-2}: the existence of high reverse-current components is strongly correlated to the density of threading dislocations, thus indicating that TDDs act as efficient channels for reverse-current conduction. Dislocations with screw component are supposed to give the stronger

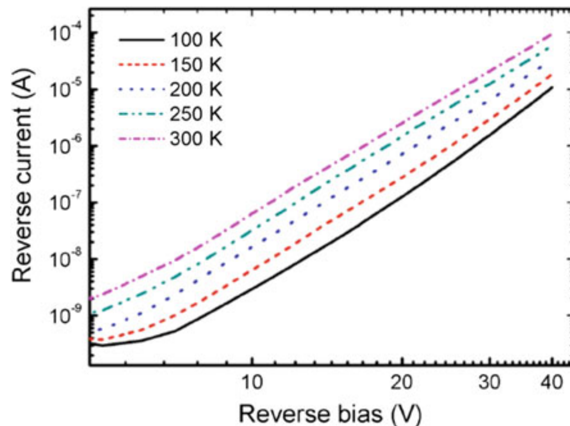

Fig. 13.7 Current–voltage characteristics of a GaN-based light emitted diode measured at different temperature levels in the reverse-bias region. Reprinted with permission from [27]. Copyright [2009], American Institute of Physics [27]

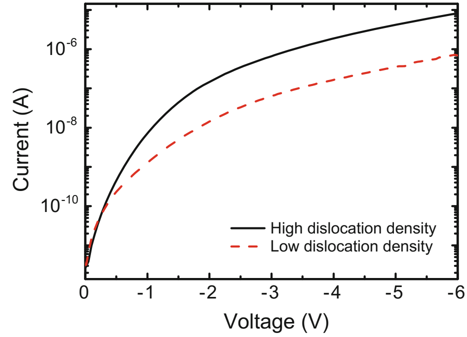

Fig. 13.8 Current–voltage characteristics measured on two LEDs with identical structure grown on templates with different threading dislocation densities

contribution to reverse-current conduction [2]: in many cases, dislocations can be connected to V-shaped defects, which are quite common in InGaN/GaN-based structures, and can act as preferential tunneling paths [28].

A further confirmation on the role of structural defects in governing reverse-bias current conduction was obtained by means of electroluminescence measurements. As described in [5, 27], LEDs can emit a weak electroluminescence signal even when they are under reverse-bias conditions. The intensity of reverse-bias luminescence (RBL) is directly proportional to the injected reverse-current level [27]: RBL occurs at localized spots (see the false-color image in Fig. 13.9), which correspond to the presence of preferential paths for leakage current conduction. The density of luminescence dots recorded by EL measurements is strongly correlated to the density of threading dislocations (Fig. 13.9), and to the level of the reverse current. The origin of reverse-bias luminescence can be understood through EL

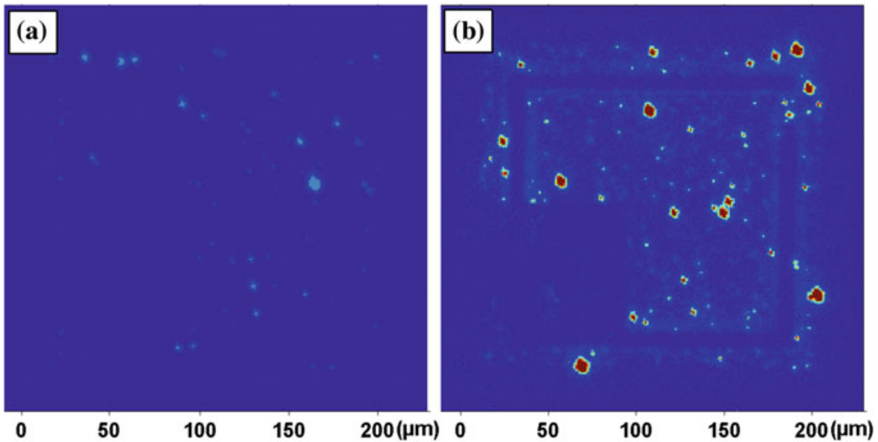

Fig. 13.9 False-color electroluminescence images measured in reverse-bias conditions on two LEDs with **a** low and **b** high threading dislocation densities. Measurements were taken at the same voltage level of −11 V

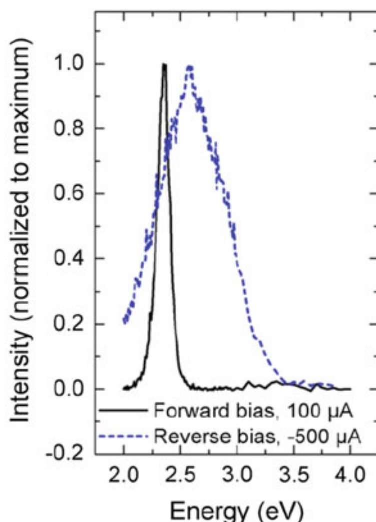

Fig. 13.10 Electroluminescence spectra taken in reverse and forward-bias conditions on a *green* LED. Reprinted with permission from [27]. Copyright [2009], American Institute of Physics [27]

spectral investigation. In Fig. 13.10 we report the comparison between the EL spectra measured under forward and reverse-bias conditions on a green LED: as can be noticed, reverse-bias luminescence has a broad spectrum, which is slightly blue-shifted with respect to the EL peak recorded under forward-bias. Results reported in the literature suggest that RBL originates from the recombination of electrons and holes injected, by tunneling, to the quantum wells. The slight blue shift measured between forward- and reverse-bias luminescence can be explained by considering that, under reverse-bias, the internal fields are partly compensated [29], and this leads to a change in the peak emission wavelength. Another, concurrent, mechanism can be the following: the localized emission paths, which are responsible for reverse-bias current conduction and luminescence, correspond to the presence of structural defects, such as V-pits. In correspondence of V-pits, the thickness of the quantum wells can be significantly smaller than in non-defective regions [30]. This leads to a higher tunneling probability (and this may explain the fact that reverse current preferentially flows in proximity of defects), and to a higher transition energy [27].

13.4 Degradation of LEDs

Over the last few years, important efforts have been done in order to improve the performance and the reliability of GaN-based LEDs. As a result, it is now possible to fabricate LEDs with a luminous flux of several hundreds or thousands of lumen.

Thanks to these achievements, LEDs are expected to replace conventional light sources in the next future. To be used in the lighting field, LEDs must have a very high luminous output (in the range 100–1000 lm): as a consequence, devices can be operated at current densities around 100 A/cm^2, junction temperatures greater than 85 °C, and power densities around 2–300 W/cm^2. Operation at high current densities or high-temperature levels may determine an acceleration of the degradation processes: the reliability of LEDs must be therefore carefully optimized, in order to guarantee that the LEDs, mounted in their final application, are capable of the long lifetime (typically 30,000–50,000 h) which is expected from the LED technology. This requires an accurate knowledge of the physical mechanisms responsible for the degradation of the LEDs.

A white light-emitting diode is a complex system, which is typically constituted by several elements: the core of a white LED structure is a blue-emitting semiconductor chip (see Fig. 13.11), based on gallium nitride. In most of the cases, this chip has a dimension of approximately 1 mm^2, a typical operating current of 700 mA, and a voltage around 3 V. The conversion of blue light into white light is obtained by the use of a phosphor layer, which can be deposited directly on the chip (chip-level conversion, CLC), or placed some centimeters away from the light-emitting device (remote phosphor approach), in order to reduce the effects related to heating. The LED–phosphor system is then integrated within a package, which must maximize the light extraction efficiency, and guarantee a good thermal dissipation. A lens is placed over the chip, in order to shape the output beam, and to improve the extraction efficiency. Bonding wires are used to bring current to the

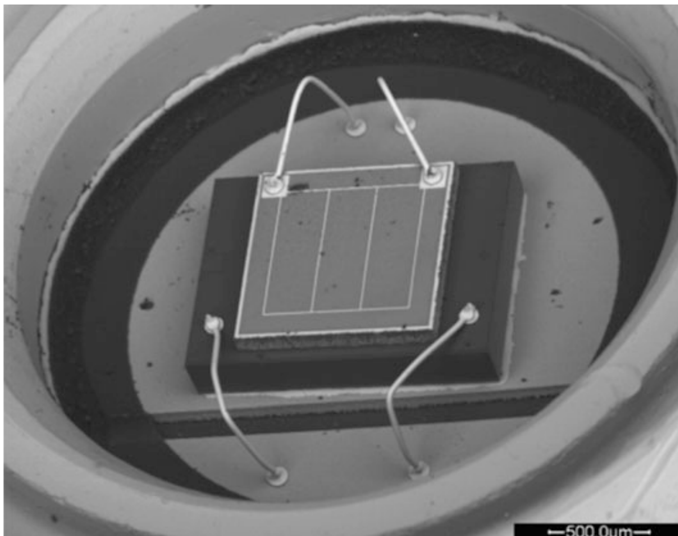

Fig. 13.11 SEM micrograph of a *blue* LED chip mounted in its package. To take this picture, the lens was removed from the *top* of the package. This image is reproduced, with permission, from [61], IOP Publishing, doi:10.1088/0022-3727/43/35/354007

device, from metallic pads located on the package. All the components of an LED structure can degrade, when the device is operated at high current and/or temperature levels: the blue semiconductor chip, based on a InGaN/GaN Multi-Quantum-Well (MQW) structure, may show an efficiency decrease due to the generation of lattice defects within the active layer, or to the degradation of the ohmic contact and semiconductor material at the p-side of the diode. On the other hand, the package/phosphor system may degrade due to the high temperatures reached by the device during operation, and this may significantly modify the output power emitted by the devices, and induce an important worsening in the chromatic properties (CCT, CRI) of the LEDs. Finally, bonding wires, metallization lines, and the whole LED junction can fail as a consequence of Electrostatic Discharges (ESD), or hot-plugging of the LEDs. Due to the intrinsic complexity of an LED system, studying how each individual component of a LED structure degrades over time can be complicated: to this aim, it is important to design appropriate test strategies, capable of analyzing specific degradation mechanisms, and of separately evaluating the role of the different driving forces (current, temperature) in determining the measured degradation process. In the following, we describe the main degradation mechanisms of GaN-based LEDs, and the experimental strategies that have been adopted in order to accurately study their origin.

13.5 Degradation of the Blue Semiconductor Chip Activated by Current

Several authors (see for example [26, 31–48]) have demonstrated that during constant current stress, LEDs can show a remarkable degradation of their optical and electrical characteristics. In Fig. 13.12 we report typical degradation kinetics measured on a GaN-based LED chip submitted to constant current stress, with a

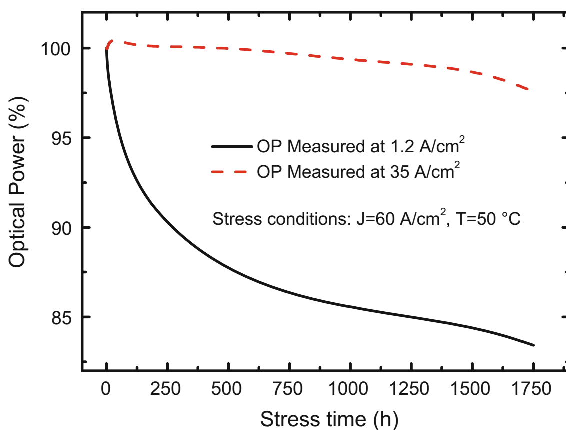

Fig. 13.12 Optical power degradation measured on a GaN-based LED submitted to stress at 60 A/cm^2, with a case temperature of 50 °C

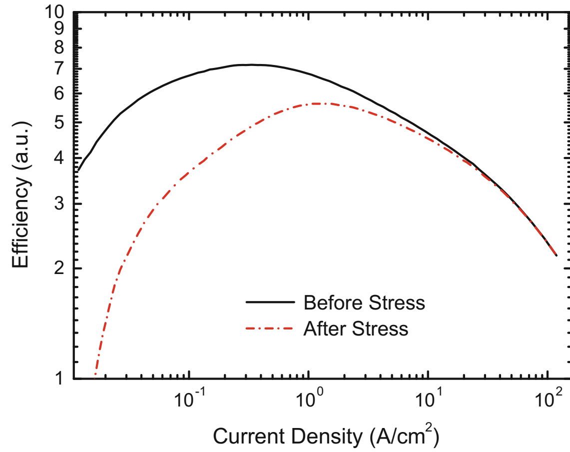

Fig. 13.13 Degradation of the efficiency versus current characteristics of a GaN-based LED submitted to stress at 60 A/cm^2, with a case temperature of 50 °C

current density of 60 A/cm^2, and a case temperature of 50 °C. During stress time, junction temperature was smaller than 100 °C, in order to be able to evaluate stress mechanisms activated by the flow of current, without any strong thermally induced degradation. For the execution of this stress experiment, device was mounted on a metallic TO package, without any phosphors and lens: in this way, it was possible to analyze the failure mechanisms related to the degradation of the blue semiconductor chip, without involving other elements of a conventional LED structure. As shown in Fig. 13.12, stress can induce a significant decrease in the optical power emitted by GaN-based LEDs. The decrease in optical power is more prominent at low measuring current levels, while on the other hand, at high measuring current levels no significant degradation is revealed. This is better explained in Fig. 13.13, which shows the efficiency versus current (η–I) characteristics measured before/after stress on a GaN-based LED. The η–I curves can be ideally divided into two parts: in the high current region, the efficiency is mainly limited by the efficiency droop, while in the low current region, the efficiency of the LEDs is determined by the balance between the radiative and non-radiative recombination rates within the active layer of the devices. The fact that after stress the devices show a remarkable efficiency decrease in the low current region is a clear signature that stress is inducing an increase in the non-radiative recombination rate, due to the generation of lattice defects within the active region [35, 36, 41, 45, 49]. At low measuring current levels, defect-related centers can effectively act as alternative recombination paths, thus limiting device efficiency. On the other hand, at high current densities, defective recombination paths can be saturated by the high number of injected carriers, and device efficiency only depends on radiative recombination processes, and—for extremely high current levels—by the physical mechanisms responsible for droop.

The fact that stress induces an increase in the non-radiative recombination rate is usually explained by considering a defect generation process activated by the flow of electrons through the active layer [34]: even at low current densities, and at

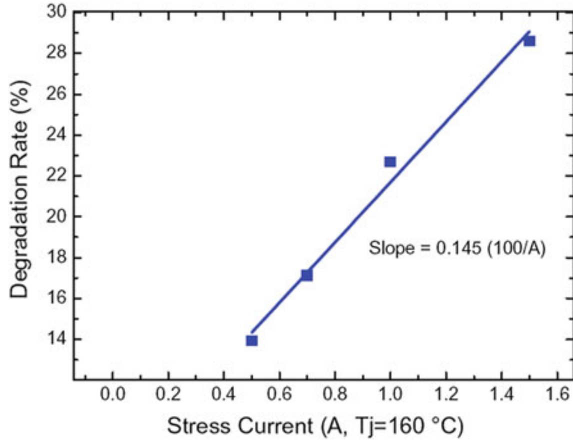

Fig. 13.14 Degradation rate (degradation after 1000 h) for high-power LEDs stressed at different current levels, same junction temperature (160 °C). *Solid line* represents a linear fit of the experimental data. This image is reproduced, with permission, from [50]

moderate temperatures, some of the carriers injected toward the active region may have enough energy to induce a damage in the lattice, thus limiting the performance of the devices. In this view, the degradation rate is strongly dependent on the stress current density, and current acts as a major driving force for the degradation process. Many studies (see for instance [50] and [42]) analyzed the role of current in determining the degradation of MQW-based diodes: results effectively indicated that the degradation rate of LEDs can have a linear dependence on the stress current density (see Fig. 13.14), thus confirming the important role of current as a major driving force for device degradation.

In order to achieve a better description of the physical mechanisms responsible for the degradation of the blue semiconductor chip, current–voltage (I–V), capacitance–voltage (C–V), and Deep Level Transient Spectroscopy (DLTS) can be used in combination. Results of electrical (I–V) measurements usually indicate that stress induces an increase in the reverse-bias leakage components (Fig. 13.15): this result is consistent with the hypothesis that stress induces the generation of point defects within the active layer of the devices, and suggests that, by suitable analytical techniques, it is possible to extrapolate the properties of the defects involved in the degradation process. Capacitance–voltage measurements represent a powerful tool for the analysis of the modification of the heterostructure of GaN-based LEDs arising as a consequence of stress. Stress may induce severe modifications in the C–V curves of GaN-based LEDs (see typical results in Fig. 13.16), namely an increase in device capacitance, which occurs in a specific voltage region (here between −6 and 2 V). In the hypothesis that the p-side of the diodes is more heavily doped with respect to the n-side, using the well-known formulas

$$N(W) = \frac{2}{q\varepsilon}\frac{1}{d\left(\frac{1}{C^2}\right)/dV} \tag{13.10}$$

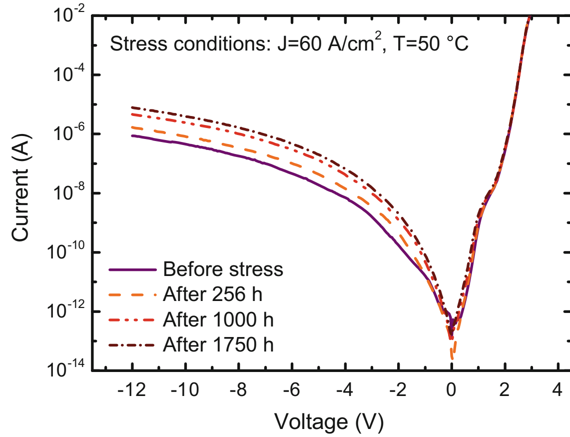

Fig. 13.15 Current–voltage characteristics measured during stress of a LED

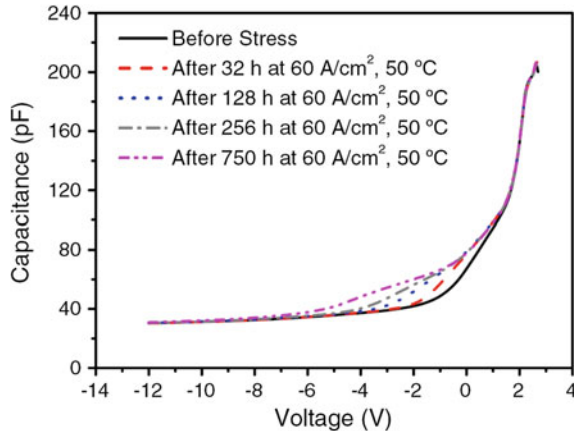

Fig. 13.16 Capacitance–voltage characteristics measured on a GaN-based LED submitted to stress at 60 A/cm^2, with a case temperature of 50 °C. This image is reproduced, with permission, from [61], IOP Publishing, doi:10.1088/0022-3727/43/35/354007

$$W = \frac{\varepsilon}{C}, \tag{13.11}$$

it is possible to extrapolate the Apparent Charge Distribution (ACD) profile of the analyzed devices. In [9] and [10], N(W) represents the charge profile as a function of the depth W, while q and ε are the electron charge and the permittivity of the semiconductor material.

Results of this analysis (see an example in Fig. 13.17) provide information on the distribution of free charge within an LED structure: an ACD profile of a MQW structure usually has one or more peaks, corresponding to regions where charge is accumulated (the quantum wells), one or more valleys, representing depleted regions (usually the barriers), and a region where the charge concentration is almost constant (the n-type material). From the comparison of the diagrams in Figs. 13.16 and 13.17, it can be easily understood that the semiconductor region interested by

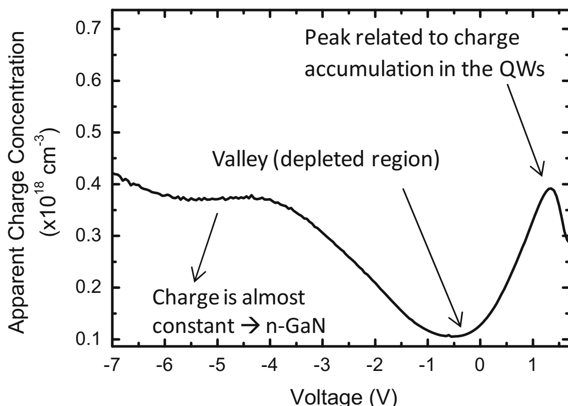

Fig. 13.17 Apparent charge distribution profile measured on a GaN-based LED starting from C–V measurements

the increase in charge concentration detected after stress is the region close to the active layer (here between −6 and 2 V). Results therefore suggest that constant current stress may induce a significant increase in the charge close to the quantum-well region, due to the generation of electrically active defects. This strong correlation between the increase in defect-related charge and the optical degradation is confirmed by Fig. 13.18, which shows that the two parameters (integrated junction charge and optical power) vary with similar kinetics. A powerful technique for the identification of the defects which are generated as a consequence of electrical stress within an LED structure is Deep Level Transient Spectroscopy (DLTS) [51]: this technique is based on the analysis of the capacitance transients generated by a sudden change in junction voltage from a filling voltage level (used to charge trap levels in a specific semiconductor region) to a reverse-voltage level, at which the capacitance variation is recorded. DLTS provides—as a result—the extrapolation of the activation energy and of the capture cross section of the defective levels that are present in a semiconductor-based device. DLTS investigation is usually carried out by selecting filling and

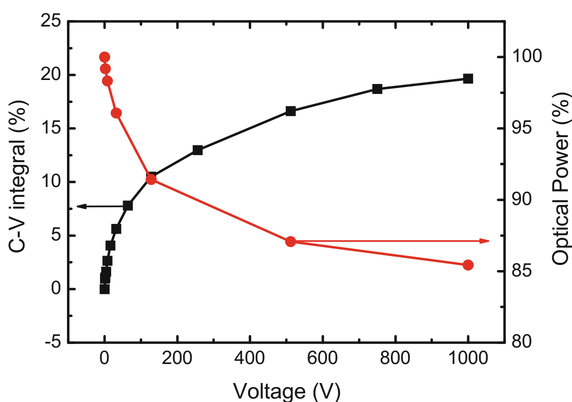

Fig. 13.18 Variation of the integral of the C–V curves and of the optical power measured on a GaN–based LED submitted to stress at 60 A/cm^2, with a case temperature of 50 °C

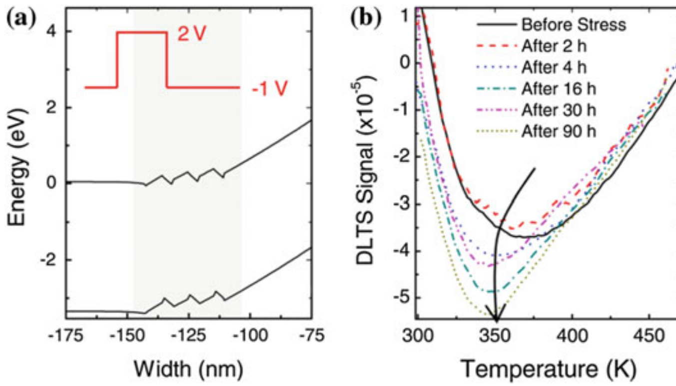

Fig. 13.19 **a** Simulated band diagram of a MQW LED structure; **b** change in the DLTS spectrum of a LED device submitted to stress at high current densities. Reprinted with permission from [52]. Copyright [2011], American Institute of Physics [52]

reverse-voltage pulses that allow to explore a specific semiconductor region: for the analysis of MQW structures, voltage levels are chosen on the basis of 2D simulation. A typical example is reported in Fig. 13.19a: 2D simulation reveals that, in order to explore the active region of these specific devices, voltage must be swept between −1 and +2 V during the DLTS measurement. Using this voltage range, DLTS analysis reveals, as a consequence of stress, the increase in the peak amplitude (see Fig. 13.19b), which corresponds to a majority trap level, located within the active region of the devices (see [52] and [36] for details on this kind of investigation). To achieve more detailed information on the origin of this deep level, its Arrhenius plot must be compared with the Arrhenius plot of other deep levels reported in the literature for GaN: typical results of this analysis are summarized in Fig. 13.20, which shows the Arrhenius plots of several deep levels

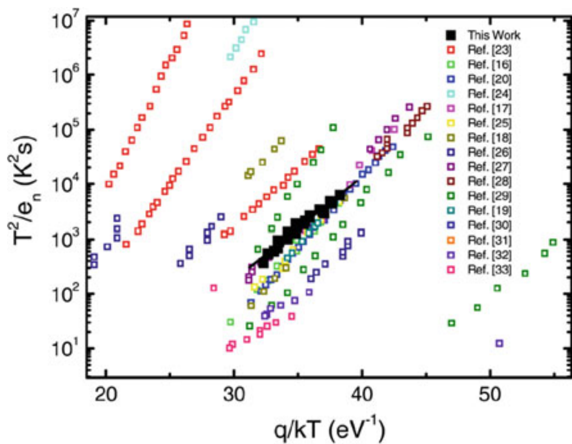

Fig. 13.20 Arrhenius plot of the deep level in Fig. 13.19b, plotted together with several Arrhenius plots that have been reported in the literature for deep levels in GaN-based materials. The numbers of the references in the legend correspond to the references of [52]. Reprinted with permission from [52]. Copyright [2011], American Institute of Physics [52]

identified by DLTS in GaN-based materials and devices, together with the Arrhenius plot of the deep level in Fig. 13.19b. By an accurate analysis of the deep levels reported in the literature, several types of point defects have been proposed as responsible for the degradation of GaN-based LEDs [52]: (i) nitrogen–antisite defects, whose properties have been described in [52–54], that have very high formation energy [55], and therefore are supposed not to be easily generated during stress time; (ii) defects related to foreign impurities, such as carbon, whose properties have been described in [56]; (iii) point defects related to gallium vacancies, such as those described in [57], that have a high probability of being generated near the dislocations. Further investigations are still in progress, with the aim of understanding if and how these deep levels can influence the degradation kinetics of high-power LED chips.

13.6 Degradation of the Blue Semiconductor Chip Activated by Temperature

In the previous section, we have described how the electrical and optical properties of a blue LED chip can significantly degrade as a consequence of the flow of current through the active region of the devices: most of the results described above were obtained by stressing the devices at constant current, with a moderate junction temperature, smaller than 100 °C. In this section we demonstrate that the blue LED chip can significantly degrade also when it is submitted to stress at high-temperature levels, usually greater than 140 °C.

In the inset of Fig. 13.21 we report the optical degradation of a high-power LED that was submitted to stress at 1 A, with an ambient temperature Ta = 100 °C, corresponding to a junction temperature of 160 °C. As can be noticed, stress induces a significant decrease in the optical power emitted by the device.

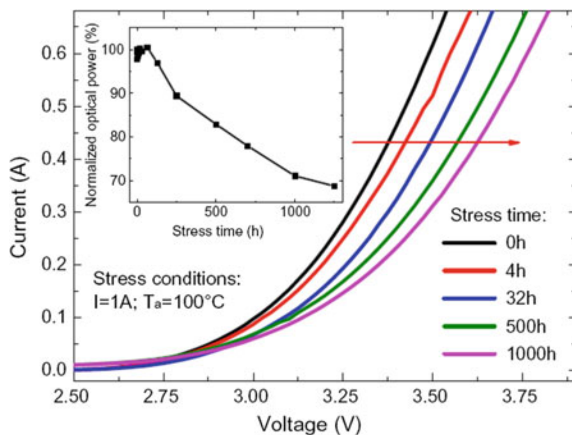

Fig. 13.21 Modifications in the electrical characteristics of a high-power LED submitted to stress at 1 A, with an ambient temperature of 100 °C (junction temperature equal to 160 °C). *Inset* degradation of the optical power measured (At 700 mA) on the same LED device. Reprinted with permission from [60]

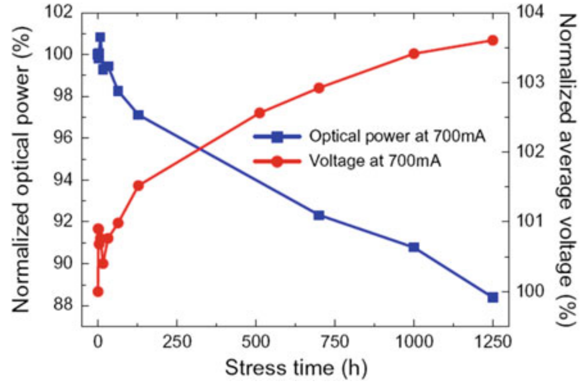

Fig. 13.22 Correlation between the optical degradation and the increase in operating voltage of a high-power LED submitted to stress at 1 A, with an ambient temperature of 100 °C (junction temperature equal to 160 °C). Reprinted with permission from [60]

High-temperature degradation may correspond to important modifications in the electrical characteristics of the devices, namely in an increase in the series resistance, and/or in the increase in the operating voltage (see Fig. 13.21). An accurate analysis reveals that kinetics of the increase in the operating voltage and of the optical power degradation can be strongly correlated (Fig. 13.22). The high-temperature degradation of blue LED chips can be explained according to the following interpretation [58, 59]: at high-temperature levels the resistivity of the ohmic contact and of the semiconductor at the p-side of the diodes can significantly increase, due to the interaction between hydrogen, which is normally present within the semiconductor and passivation layer, and the acceptor dopant (Mg). As a consequence, magnesium can be passivated by hydrogen, and this may result in a significant decrease in the effective acceptor concentration and, therefore, in a worsening of the conductivity of the ohmic contact and of the p-type GaN layer. This results in an increase in the operating voltage, and therefore in a remarkable decrease in device efficiency. In extreme cases, as a result of the increase in the resistivity of the p-type material, stressed devices can show an increase current and emission crowding: an example is reported in Fig. 13.23, reporting the false-color emission pattern of a blue semiconductor chip, measured after a 20 min stress at 250 °C. As can be noticed, stress induced a significant emission crowding that can be attributed to the increase in the resistivity of the p-type material. This degradation mechanism occurs only at relatively high-temperature levels: for clarity, in Fig. 13.24 we report the results obtained by aging several high-power LEDs at 1 A, with different temperature levels: results clearly show that an increase in the operating voltage is generated only when the LEDs are stressed with junction temperatures greater than 140 °C (413 K). Typical activation energies for this degradation process are in the range of 1.1–1.3 eV, as demonstrated by recent reports [58, 60].

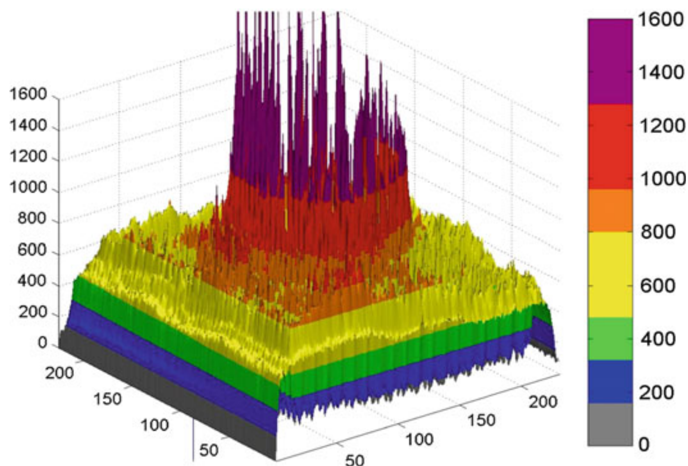

Fig. 13.23 False-color emission pattern measured on a LED submitted to high-temperature stress (250 °C, 20 min)

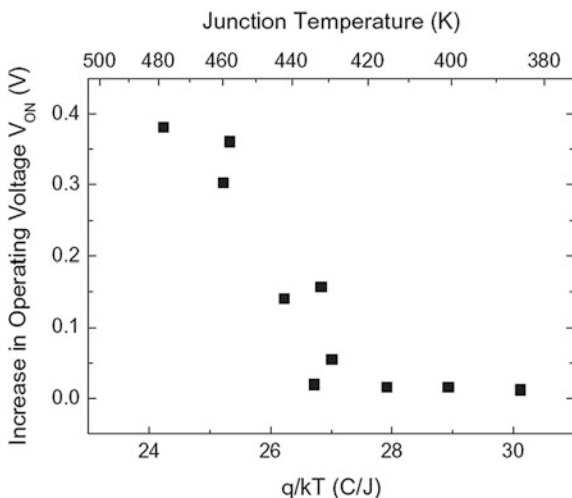

Fig. 13.24 Variation of the forward voltage measured, on several devices aged with a stress current of 1 A, different junction temperature levels. Reprinted with permission from [60]

13.7 Degradation of the Package/Phosphor System

So far, we have discussed the degradation mechanisms of the blue semiconductor chip, activated by temperature and current. The semiconductor chip is only one of the components of a power LED structure: the package and the phosphor layer play an important role in determining the overall efficiency and chromatic properties of the device. For this reason, it is of fundamental importance to understand how package and phosphors degrade when they are submitted to high-temperature

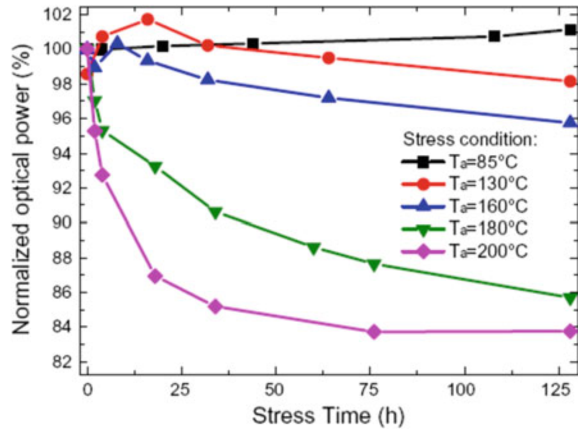

Fig. 13.25 Degradation of the optical power measured on a set of LEDs submitted to purely thermal stress at different temperature levels, without applied bias. Reprinted with permission from [60]

levels. Typically, these two components degrade at temperatures greater than 100 °C: the best methodology to study the thermally activated degradation of high-power LEDs is to carry out "purely-thermal" stress tests, in which the devices are exposed to relatively high-temperature levels, with no applied current. In this way, all the degradation mechanisms can be ascribed to the high temperatures, without mixing the effects of temperature and current in the analysis.

Typically, exposure to stress temperatures greater than 100 °C may result in a remarkable decrease in the efficiency of the LEDs: in Fig. 13.25 we report typical degradation curves, measured on commercially available LEDs submitted to thermal storage. Most the analyses on package and phosphor degradation are usually carried out on LEDs with a very stable p-type material: as a result, the degradation mechanisms described in the previous section do not take place on these LEDs, and the electrical and optical characteristics of the blue chips are stable over stress time (for instance see [60] and references therein). Degradation can therefore be unambiguously attributed to the worsening of the package/phosphor system.

Package degradation can be particularly severe in the case of LEDs with a white, reflective, package. In this case the package has the important role of maximizing the extraction efficiency of the LEDs, by guaranteeing a high reflectivity. As a consequence of the high temperatures reached during stress, or (when devices are operated with high current levels) due to the short wavelength of blue and white LEDs, the plastic material used for the realization of the package can show a remarkable browning. As an example, in Fig. 13.26 we report a micrograph of the section of a LED package which was submitted to stress at high-temperature levels: in this case stress does not affect the quality of the phosphor material, but induces a severe darkening of the surface of the package [60], and this can significantly limit its ability of reflecting light out of the device. In Fig. 13.27 we show a front picture of the same kind of package, taken after the removal of the lens and phosphors. The browning of the surface of the package may determine a modification in the chromatic properties of the LEDs: as shown in Fig. 13.28, the angular distribution

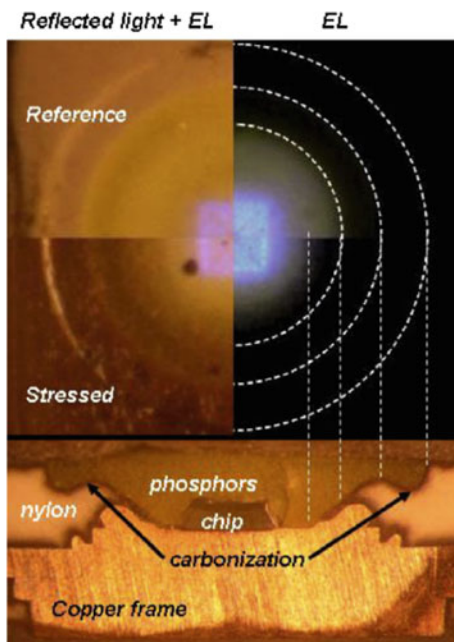

Fig. 13.26 (*top*) Electroluminescence image taken before and after stress on a high-power LED. (*bottom*) Micrograph of a section of the same LED, showing the carbonization of the package. Reprinted with permission from [61]

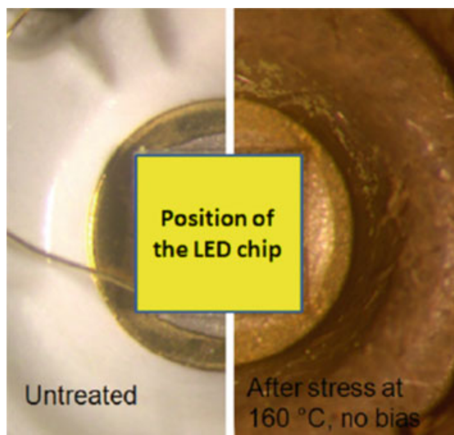

Fig. 13.27 Micrograph of the package of a power LED that was submitted to stress at high temperature. The image was taken after the chemical removal of the lens, and of the phosphors. Reprinted with permission from [60]

of light can be significantly affected by stress, especially for high emission angles. Degradation is also correlated to important modification in the spectral power distribution of the devices, as representatively shown in Fig. 13.29. Similar degradation processes are more prominent in devices with a white plastic package, rather than in LEDs with a ceramic package. However, since plastic package is widely used both for lighting, outdoor applications, backlighting, and automotive, it is very important to study and optimize the degradation of LEDs with a plastic reflector, and to carefully optimize the lighting systems in order to avoid exposure

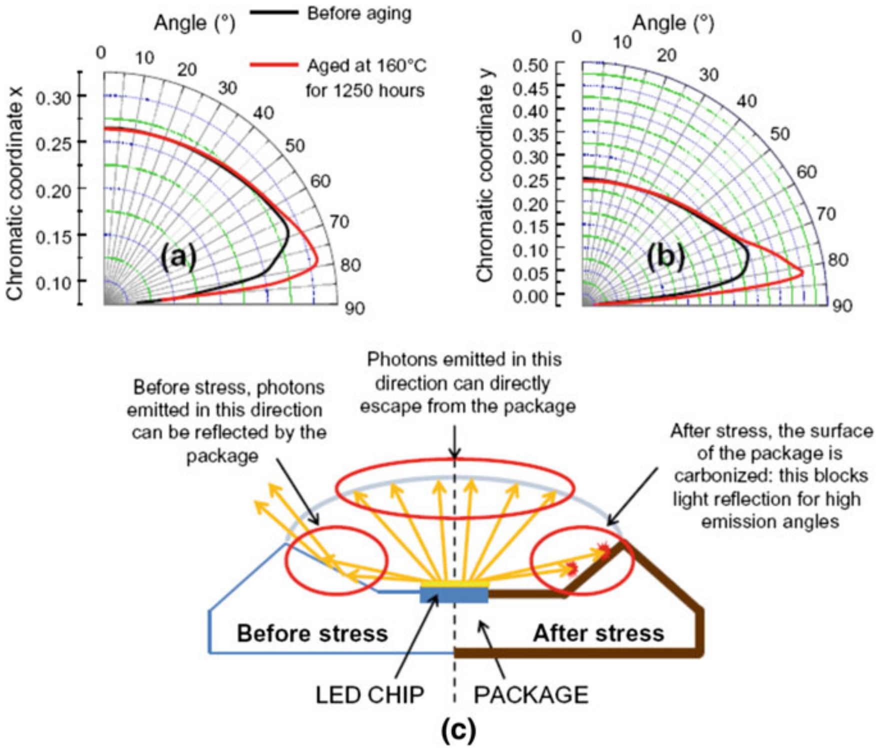

Fig. 13.28 **a** and **b** Variation of the chromatic coordinates x and y measured after high-temperature stress on high-power LEDs. **c** Schematic picture of the effect of the darkening of the package on the light extraction efficiency. Reprinted with permission from [60]

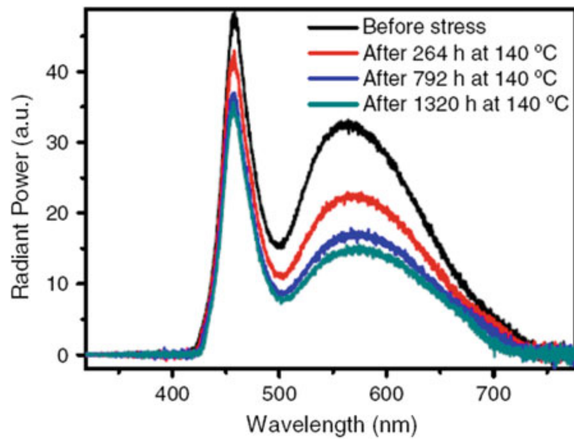

Fig. 13.29 Spectral power distribution measured at different stress times on a power LED submitted to high-temperature stress. This image is reproduced, with permission, from [61], IOP Publishing, doi:10.1088/0022-3727/43/35/354007

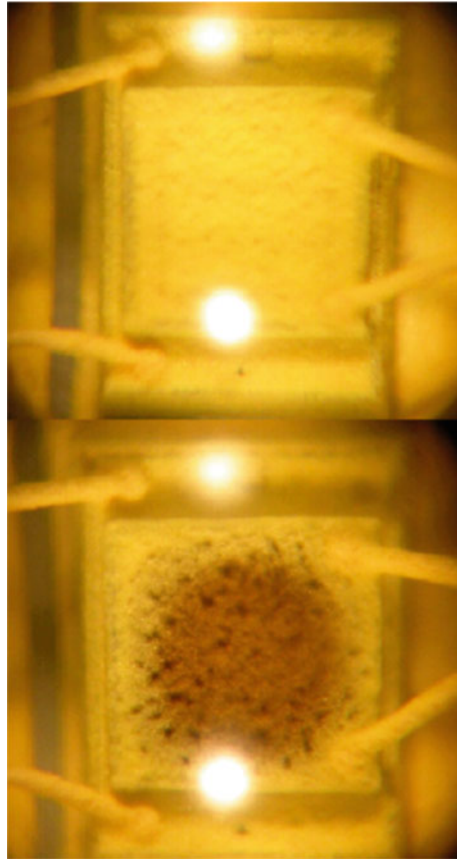

Fig. 13.30 Micrograph of a power LED taken before and after stress at 100 A/cm^2, 120 °C. This image is reproduced, with permission, from [61], IOP Publishing, doi:10.1088/0022-3727/43/35/354007

to high-temperature levels. As described above, the degradation of the package is strongly thermally activated, with activation energies in the range between 0.5 and 1.8 eV, depending on the specific analyzed technology (see for instance [60, 62] and references therein).

Another part of a white LED that may be prone to thermally activated degradation is the phosphor layer, used to convert the blue radiation of the LED chips into white light. In most of the cases, phosphors are dispersed in a matrix, which can become dark as a consequence of high-temperature treatment [62]. An example is reported in Fig. 13.30, which clearly shows that, as a consequence of high temperature, high current stress, the power LED shows a remarkable darkening of the phosphor layer. Interestingly, degradation is mostly focused at the center of the LED, since this is the region which is more prone to self-heating. Recently, ceramic phosphor layers have been proposed as an interesting solution for the realization of highly reliable phosphors (see for instance [62, 63] and references therein): ceramic

phosphors are good candidates for adoption in all those fields in which LEDs can be exposed to high-power levels and high temperatures, including automotive head-lamps, and indoor and outdoor lighting.

13.8 ESD Failure of GaN-Based LEDs

Electrostatic Discharges (ESD) may be present during the whole life of a LED-based system. During the fabrication of the wafer, improper handling by a charged operator, or the contact with a charged machine, may result in the ESD failure of the LEDs. On the other hand, when the LEDs are mounted in the final system, they can receive voltage/current spikes through the electrical contacts of the whole luminaire, and this can, if there are specific technological weaknesses, damage the devices. For this reason, several research groups have investigated the origin of the ESD failures, and proposed methods for improving the robustness of the LEDs (see for instance [64–67]).

As a consequence of ESD events, LEDs can show either a catastrophic failure, or a latent damage. In the first case, after the ESD event, the impedance of the device shows a sudden decrease and, in most of the cases, devices behave as short circuits. In other cases, it may happen that the ESD event is not completely destructive: after the discharge, devices may still be able to be operated, but they can show an unstable behavior, due to the fact that an unstable leakage path is generated in parallel to the junction. As a consequence, luminous power may dim, or show a variable intensity over time, due to the intrinsic instabilities of the shunt path generated after the ESD event. A similar behavior is the signature of a latent damage, which can significantly limit the stability of the LEDs.

Several models can be efficiently adopted to evaluate the ESD robustness of LEDs: the most important include the Human Body Model (HBM), the Machine Model (MM), the Charged Device Model (CDM) [68], and the Transmission Line Pulse (TLP) method [69]. Among these methods, the TLP analysis allows to achieve a detailed description of the damages introduced during ESD testing. The operating principle of a TLP system is the following: a transmission line of appropriate length is charged by means of a high-voltage generator, and then, by suitable switches, is discharged on the LED sample, thus obtaining very short pulses (duration around 100 ns). During the discharge, the voltage and the current that flow on the sample are measured by oscilloscope probes. After the electrical discharge, several device parameters—including leakage current, optical power, emission pattern—are measured in order to characterize the effects of a ESD pulse on the properties of the devices. This procedure is repeated for increasing voltage levels, until the failure is reached. The typical output of a ESD analysis is twofold: on one hand, a complete pulsed I–V characterization of the characteristics of the devices up to the failure limit; on the other hand, a description of how some device parameters (for instance the leakage current) vary as a consequence of the application of voltage pulses with increasing amplitude. In Fig. 13.31 we report a

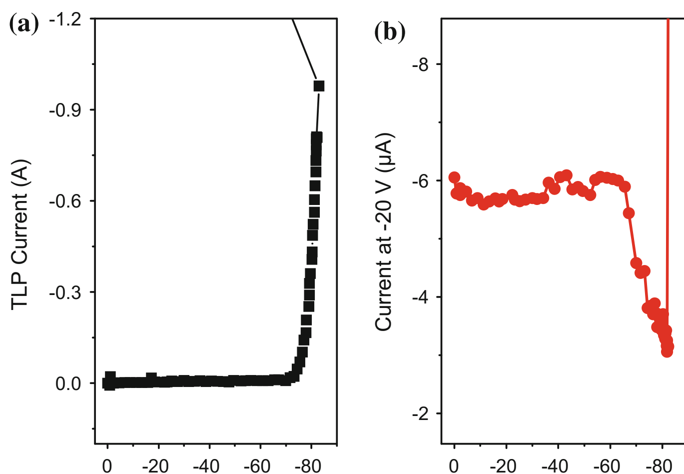

Fig. 13.31 Typical output of a TLP test carried out on a GaN-based LED with an area of 290 × 290 μm^2. **a** Current–voltage characteristic measured during a TLP test, until the failure is reached. **b** Leakage current measured after each of the TLP pulses on the analyzed LED. Failure can be recognized as a sudden increase in device leakage current

representative output of a TLP test carried out on a GaN-based LED with an area of 290 × 290 μm^2. This test was carried out by applying pulses with increasing (negative) amplitude to the devices. As can be noticed, during a TLP test the device could withstand a negative current of 1 A (corresponding to a current density around −1.2 kA/cm^2) before reaching the failure, which can be clearly identified as a sudden decrease in device impedance. In most of the cases, device failure can be ascribed to the generation of a short-circuit path, which can be identified by SEM investigation (see an example in Fig. 13.32). The failure under reverse-bias ESD events is related to the fact that, under reverse-bias, conduction mostly occurs

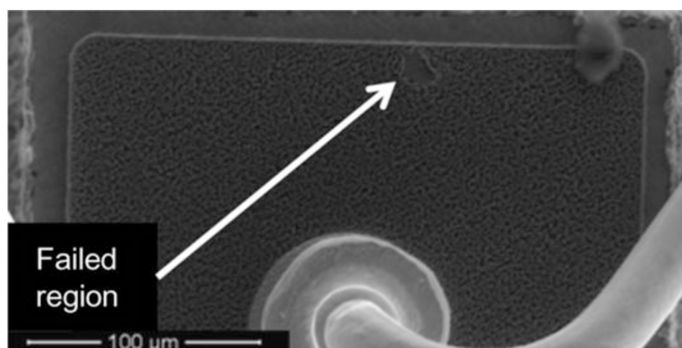

Fig. 13.32 SEM micrograph taken on a LED after the execution of a ESD failure test. This image is reproduced, with permission, from [61], IOP Publishing, doi:10.1088/0022-3727/43/35/354007

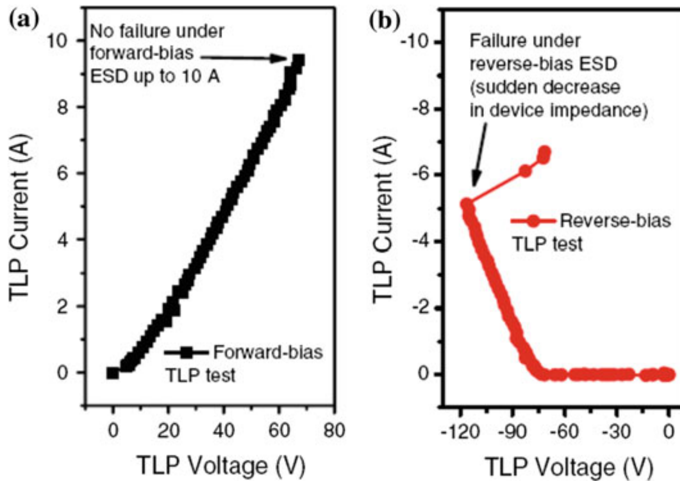

Fig. 13.33 Results of ESD test carried out under **a** forward- and **b** reverse-bias on LED chips. This image is reproduced, with permission, from [61], IOP Publishing, doi:10.1088/0022-3727/43/35/354007

through preferential leaky paths, related to the presence of structural defects, such as dislocations and/or V-shaped defects (see Fig. 13.9). These defects have a nanometer size, and for this reason, they can be crossed by very high current densities during the ESD event [61, 64]. When a critical current/energy level is reached on one of these defects, a localized failure may occur, and this determines the sudden shortening of the device. This kind of failure only occurs under reverse-bias ESD tests: when TLP robustness tests are carried out in forward-bias, since the whole device contributes to current conduction, devices can reach current densities in excess of 10 kA/cm^2 without showing any failure (see an example in Fig. 13.33a). Results presented in the literature indicate that, while the robustness to forward-bias ESD pulses does not represent a serious issue for state-of-the-art LEDs, the robustness of current LED technologies to reverse-voltage pulses still has to be optimized, through a careful improvement of the epitaxial quality of the devices aiming at a significant reduction of the defects responsible for reverse-current conduction.

Besides catastrophic (or hard) failures, GaN-based LEDs can show also a soft (or non-destructive) degradation when they are submitted to ESD-like events with negative voltage [67]. As shown in Fig. 13.31, during the execution of a TLP test, pulses with increasing amplitude are applied to the LED. Beyond a certain voltage (here for $V < -70$ V), the reverse current of the ESD pulses significantly increases. As a result, the leakage current measured after each of the ESD-like pulses shows a remarkable decrease (see Fig. 13.31b). This effect has been attributed to the partial annihilation of the defective paths responsible for reverse-current conduction, which are related to the presence of structural defects (see Fig. 13.9 and its

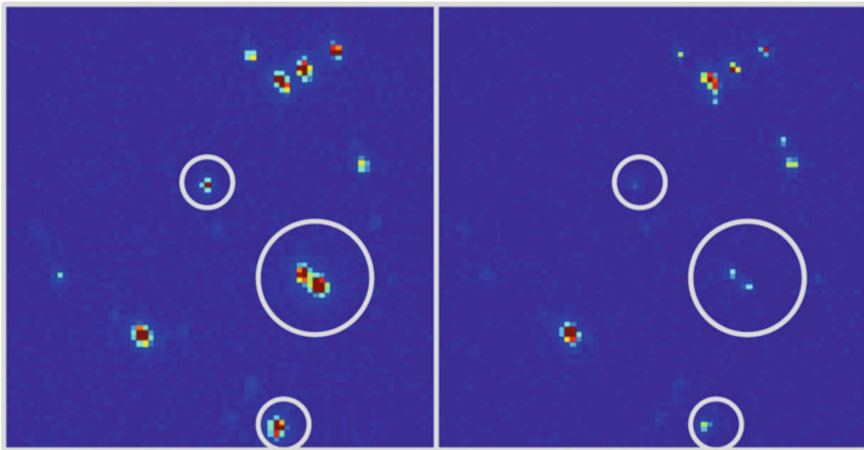

Fig. 13.34 Spatially resolved electroluminescence profiles measured, under reverse-bias conditions, on a LED before and after a non-destructive ESD-like event

explanation). This mechanism is supposed to be related to the high energy released, during a negative-bias ESD pulse, in correspondence of the nanometer-size regions that carry most of the reverse current that flows through the device. The annihilation of the reverse-leakage paths can be detected by spatially resolved electroluminescence measurements, carried out under reverse-bias [67]. An example is reported in Fig. 13.34, which shows the false-color electroluminescence profile measured before and after a series of non-destructive ESD-like events that have determined a remarkable decrease in leakage current. As can be noticed, after the execution of the non-destructive ESD tests, some of the luminescent dots detected before stress almost disappear. Since these dots indicate the presence of leaky regions, related to defects, results strongly support the hypothesis that ESD-like events induce the partial annihilation of the preferential paths responsible for leakage current conduction. This effect, which is still under investigation, indicates that ESD events may significantly affect the characteristics of GaN-based LEDs, even when they are not destructive. To improve the stability of the devices, it is therefore necessary to minimize the density of epitaxial defects, through the improvement of the growth conditions, the adoption of optimized interlayers, and the selection of suitable substrates.

13.9 Conclusions

Thanks to their high performance and potential reliability, LEDs based on gallium nitride are expected to widely penetrate the lighting market in the next years. However, the efficiency and the lifetime of these devices can be significantly

limited by a number of factors that have been extensively studied by several research groups. Within this chapter, we have discussed the main processes that limit the reliability of LEDs submitted to short- and long-term stress experiments, by critically comparing the results with the data present in the literature.

Results described within this chapter provide information on the most common degradation modes and mechanisms, and on the role of the main driving forces (current and temperature) in determining device degradation. Furthermore, we have described specific methodologies that can be adopted to study the individual degradation mechanisms that limit the lifetime of LEDs. The experimental data discussed within this chapter indicate that the robustness of the different components of an LED structure must be carefully optimized, in order to fabricate devices with intrinsically high reliability. On the other hand, since degradation mechanisms and kinetics are significantly dependent by the operating conditions, the designers of LED-based systems must carefully optimize the thermal management, the driving conditions, and the lamp layout in order to minimize the risk of early degradation.

References

1. X.A. Cao, E.B. Stokes, P.M. Sandvik, S.F. LeBoeuf, J. Kretchmer, D. Walker, Diffusion and tunneling currents in GaN/InGaN multiple quantum well light-emitting diodes. IEEE Trans. Electron Devices **23**, 535 (2002)
2. D.S. Li, H. Chen, H.B. Yu, H.Q. Jia, Q. Huang, J.M. Zhou, Dependence of leakage current on dislocations in GaN-based light-emitting diodes. J. Appl. Phys. **96**, 1111 (2004)
3. D.J. Dumin, G.J. Pearson, Properties of gallium arsenide diodes between 4.2° and 300 °K. J. Appl. Phys. **36**, 11 (1965)
4. G. Franssen, E. Litwin-Staszewska, R. Piotrzkowski, T. Suski, P. Perlin, Optical and electrical properties of homoepitaxially grown multiquantum well InGaNÕGaN light-emitting diodes. J. Appl. Phys. **94**, 6122 (2003)
5. M. Meneghini, S. Vaccari, N. Trivellin, D. Zhu, C. Humphreys, R. Butendheich, C. Leirer, B. hahn, E. Zanoni, G. Meneghesso, Analysis of defect-related localized emission processes in InGaN/GaN-based LEDs. IEEE Trans. Electron Devices **59**, 1416, 2012
6. D. Yan, H. Lu, D. Chen, R. Zhang, Y. Zheng, Forward tunneling current in GaN-based blue light-emitting diodes. Appl. Phys. Lett. **96**, 083504 (2010)
7. A. Mao, J. Cho, Q. Dai, E.F. Schubert, J.K. Son, Y. Park, Characteristics of dotlike green satellite emission in GaInN light emitting diodes. Appl. Phys. Lett. **98**, 1–023503 (2011)
8. E. Calleja, F.J. Sánchez, D. Basak, M.A. Sánchez-García, E. Muñoz, I. Izpura, F. Calle, J.M. G. Tijero, J.L. Sánchez-Rojas, B. Beaumont, P. Lorenzini, Yellow luminescence and related deep states in undoped GaN. Phys. Rev. B **55**, 4689 (1997)
9. A.V. Zinovchuk, O.Yu. Malyutenko, V.K. Malyutenko, A.D. Podoltsev, A.A. Vilisov, The effect of current crowding on the heat and light pattern in high-power AlGaAs light emitting diodes. J. Appl. Phys. **104**, 033115 (2008)
10. Y.Y. Kudryk, A.K. Tkachenko, A.V. Zinovchuk, Temperature-dependent efficiency droop in InGaN-based light-emitting diodes induced by current crowding. Semicond. Sci. Technol. **27**, 055013 (2012)
11. I.Yu. Evstratov, V.F. Mymrin, S.Yu. Karpov, Yu.N. Makarov, Current crowding effects on blue LED operation. Phys. Stat. Sol. (C) **3**(6), 1645–1648 (2006)

12. X. Guo, E.F. Schubert, Current crowding and optical saturation effects in GaInN/GaN light-emitting diodes grown on insulating substrates. Appl. Phys. Lett. **78**, 3337 (2001)
13. M. Meneghini, L.-R. Trevisanello, U. Zehnder, T. Zahner, U. Strauss, G. Meneghesso, E. Zanoni, High-temperature degradation of GaN LEDs related to passivation. IEEE Trans. Electron Devices **53**, 2981 (2006)
14. K.A. Bulashevich, I.Yu. Evstratov, V.F. Mymrin, S.Yu. Karpov, Current spreading and thermal effects in blue LED dice. Phys. Stat. Sol. (C) **4**(1), 45–48 (2007)
15. M.V. Bogdanov, K.A. Bulashevich, I.Yu. Evstratov, A.I. Zhmakin, S.Yu. Karpov, Coupled modeling of current spreading, thermal effects and light extraction in III-nitride light-emitting diodes. Semicond. Sci. Technol. **23**, 125023 (2008)
16. C. Sah, R.N. Noyce, W. Shockley, Carrier Generation and Recombination in pn junctions and pn junction characteristics. Proc. IRE **45**, 1228 (1957)
17. K.B. Lee, P.J. Parbrooky, T. Wang, J. Bai, F. Ranalli, R.J. Airey, G. Hill, The origin of the high ideality factor in AlGaN-based quantum well ultraviolet light emitting diodes. Phys. Status Solidi B **247**(7), 1761–1763 (2010)
18. Y.-J. Lin, Origins of the temperature dependence of the series resistance, ideality factor and barrier height based on the thermionic emission model for n-type GaN Schottky diodes. Thin Solid Films **519**, 829–832 (2010)
19. H. Masui, Diode ideality factor in modern light-emitting diodes. Semicond. Sci. Technol. **26**, 075011 (2011)
20. H. Masui, S. Nakamura, S.P. DenBaars, Technique to evaluate the diode ideality factor of light-emitting diodes. Appl. Phys. Lett. **96**, 073509 (2010)
21. K. Mayes, A. Yasan, R. McClintock, D. Shiell, S.R. Darvish et al., High-power 280 nm AlGaN light-emitting diodes based on an asymmetric single-quantum well. Appl. Phys. Lett. **84**, 1046 (2004)
22. D. Zhu, J. Xu, A.N. Noemaun, J.K. Kim, E. Fred Schubert et al., The origin of the high diode-ideality factors in GaInN/GaN multiple quantum well light-emitting diodes. Appl. Phys. Lett. **94**, 081113 (2009)
23. J.M. Shah, Y.-L. Li, Th. Gessmann, E.F. Schubert, Experimental analysis and theoretical model for anomalously high ideality factors n > 2.0 in AlGaN/GaN p-n junction diodes. J. Appl. Phys. **94**, 2627 (2003)
24. X.A. Cao, J.M. Teetsov, M.P. D'Evelyn, D.W. Merfeld, Electrical characteristics of InGaN/GaN light-emitting diodes grown on GaN and sapphire substrates. Appl. Phys. Lett. **85**, 7 (2004)
25. X.A. Cao, J.A. Teetsov, F. Shahedipour-Sandvik, S.D. Arthu, Microstructural origin of leakage current in GaN/InGaN light-emitting diodes. J. Cryst. Growth **264**, 172–177 (2004)
26. Z.-Q. Fang, D.C. Reynolds, D.C. Look, Changes in electrical characteristics associated with degradation of InGaN blue light-emitting diodes. J. Electron. Mater. **29**(4) (2000)
27. M. Meneghini, N. Trivellin, M. Pavesi, M. Manfredi, U. Zehnder, B. Hahn, G. Meneghesso, E. Zanoni, Leakage current and reverse-bias luminescence in InGaN-based light-emitting diodes. Appl. Phys. Lett. **95**, 173507 (2009)
28. S. Mahanty, M. Hao, T. Sugahara, R.S.Q. Fareed, Y. Morishima, Y. Naoi, T. Wang, S. Sakai, V-shaped defects in InGaNrGaN multiquantum wells. Mater. Lett. **41**, 67–71 (1999)
29. Y.D. Jho, J.S. Yahng, E. Oh, D.S. Kim, Field-dependent carrier decay dynamics in strained InxGa1-xN/GaN quantum wells. Phys. Rev. B **66**, 035334 (2002)
30. A. Hangleiter et al., Suppression of nonradiative recombination by V-shaped pits in GaInN/GaN quantum wells produces a large increase in the light emission efficiency. Phys. Rev. Lett. **95**, 127402 (2005)
31. S. Buso, G. Spiazzi, M. Meneghini, G. Meneghesso, Performance degradation of high brightness light emitting diodes under DC and pulsed bias. IEEE Trans. Device Mater. Reliab. **8**, 312 (2008)
32. S. Bychikhin, D. Pogany, L.K.K. Vandamme, G. Meneghesso, E. Zanoni, Low-frequency noise sources in as-prepared and aged GaN-based light-emitting diodes. J. Appl. Phys. **97**, 12371 (2005)

33. Z.Z. Chen et al., Study on the stability of the high-brightness white LED. Phys. Status Solidi B **241**, 2664 (2004)
34. F. Manyakhin, A. Kovalev, A.E. Yunovich, Aging mechanisms of InGaN/AlGaN/GaN light-emitting diodes operating at high currents. MRS Internet J. Nitride Semicond. Res. **3** (1998)
35. P.N. Grillot, M.R. Krames, H. Zhao, S.H. Teoh, Sixty thousand hour light output reliability of AlGaInP light emitting diodes. IEEE Trans. Device Mater. Rel. **6**(4), 564–574 (2006)
36. F. Rossi, M. Pavesi, M. Meneghini et al., Influence of short-term low current dc aging on the electrical and optical properties of InGaN blue light-emitting diodes. J. Appl. Phys. **99**, 053104 (2006)
37. J. Hu, L. Yang, M.W. Shin, Electrical, optical and thermal degradation of high power GaN/InGaN light-emitting diodes. J. Phys. D Appl. Phys. **41**, 035107 (2008)
38. S. Ishizaki, H. Kimura, M. Sugimoto, Lifetime estimation of high power LEDs. J. Light Vis. Environ. **31**, 11 (2007)
39. S. Levada, M. Meneghini, G. Meneghesso, E. Zanoni, Analysis of DC current accelerated life tests of GaN LEDs using a Weibull-based statistical model. IEEE Trans. Device Mater. Reliab. **5**, 688 (2005)
40. M. Meneghini, L.-R. Trevisanello, F. de Zuani, N. Trivellin, G. Meneghesso, E. Zanoni, Extensive analysis of the degradation of phosphor-converted LEDs. Proc. SPIE **7422**, 74220H (2009)
41. M. Meneghini, N. Trivellin, K. Orita, S. Takigawa, M. Yuri, T. Tanaka, D. Ueda, E. Zanoni, G. Meneghesso, Degradation of InGaN-based laser diodes related to nonradiative recombination. IEEE Electron Device Lett. **30**(4), 356–358 (2009)
42. M. Meneghini, N. Trivellin, E. Zanoni, G. Meneghesso, K. Orita, M. Yuri, D. Ueda, Analysis of the role of current, temperature, and optical power in the degradation of InGaN-based laser diodes. IEEE Trans. Electron Devices **56**(2)
43. N. Narendran, Y. Gu, J.P. Freyssinier, Y. Yu, L. Deng, Solid-state lighting: failure analysis of white LEDs. J. Cryst. Growth **268**, 448 (2004)
44. A.Y. Polyakov et al., Enhanced tunneling in GaN/InGaN multi-quantum-well heterojunction diodes after short-term injection annealing. J. Appl. Phys. **91**, 5203 (2002)
45. O. Pursiainen, N. Linder, A. Jaeger, R. Oberschmid, K. Streubel, Identification of aging mechanisms in the optical and electrical characteristics of light-emitting diodes. Appl. Phys. Lett. **79**(18), 2895–2897 (2001)
46. L. Rigutti, L. Basirico, A. Cavallini, M. Meneghini, G. Meneghesso, E. Zanoni, Redistribution of multi-quantum well states induced by current stress in InGaN/GaN light-emitting diodes. Semicond. Sci. Technol. **24**, 055015 (2009)
47. L. Trevisanello, M. Meneghini, G. Mura, M. Vanzi, M. Pavesi, G. Meneghesso, E. Zanoni, Accelerated life test of high brightness light emitting diodes. IEEE Trans. Device Mater. Reliab. **8**, 304 (2008)
48. A. Uddin, A.C. Wei, T.C. Andersson, Study of degradation mechanism of blue light emitting diodes. Thin Solid Films **483**, 378 (2005)
49. M. Meneghini, A. Tazzoli, G. Mura, G. Meneghesso, E. Zanoni, A review on the physical mechanisms that limit the reliability of GaN-based LEDs. IEEE Trans. Electron Devices **57** (1), 108–118 (2010)
50. M. Meneghini, M. dal Lago, N. Trivellin, G. Mura, M. Vanzi, G. Meneghesso, E. Zanoni, Chip and package-related degradation of high power white LEDs. Microelectron. Reliab. **52**, 804–812 (2012)
51. D.V. Lang, Deep Level transient spectroscopy: a new method to characterized traps in semiconductors. J. Appl. Phys. **45**, 3023 (1974)
52. M. Meneghini, C. de Santi, N. Trivellin, K. Orita, S. Takigawa, T. Tanaka, D. Ueda, G. Meneghesso, E. Zanoni, Investigation of the deep level involved in InGaN laser degradation by deep level transient spectroscopy. Appl. Phys. Lett. **99**, 093506 (2011)
53. H.M. Chung, W.C. Chuang, Y.C. Pan, C.C. Tsai, M.C. Lee, W.H. Chen, W.K. Chen, C.I. Chiang, C.H. Lin, H. Chang, Appl. Phys. Lett. **76**, 897 (2000)

54. H.K. Cho, C.S. Kim, C.-H. Hong, Electron capture behaviors of deep level traps in unintentionally doped and intentionally doped n-type GaN. J. Appl. Phys. **94**, 1485 (2003)
55. M.A. Reshchikov, H. Morkoç, Luminescence properties of defects in GaN. J. Appl. Phys. **97**, 061301 (2005)
56. D.C. Look, Z.-Q. Fang, B. Claflin, Identification of donors, acceptors, and traps in bulk-like HVPE GaN. J. Cryst. Growth **281**, 143–150 (2005)
57. H.K. Cho, F.A. Khan, I. Adesida, Z.-Q. Fang, D.C. Look, Deep level characteristics in n-GaN with inductively coupled plasma damage. J. Phys. D Appl. Phys. **41**, 155314 (2008)
58. M. Meneghini, L.-R. Trevisanello, U. Zehnder, T. Zahner, U. Strauss, G. Meneghesso, Enrico Zanoni, High-temperature degradation of GaN LEDs related to passivation. IEEE Trans. Electron Devices **53**(12), 2981–2987 (2006)
59. M. Meneghini, L.-R. Trevisanello, U. Zehnder, G. Meneghesso, E. Zanoni, Reversible degradation of ohmic contacts on p-GaN for application in high brightness LEDs. IEEE Trans. Electron Devices **54**, 3245 (2007)
60. M. Meneghini, L. Trevisanello, C. Sanna, G. Mura, M. Vanzi, G. Meneghesso, E. Zanoni, High temperature electro-optical degradation of InGaN/GaN HBLEDs. Microelectron. Reliab. **47**, 1625–1629 (2007)
61. G. Meneghesso, M. Meneghini, E. Zanoni, Recent results on the degradation of white LEDs for lighting. J. Phys. D Appl. Phys. **43**, 354007 (2010)
62. S. Fujita, A. Sakamoto, S. Tanabe, Luminescence characteristics of YAG glass–ceramic phosphor for white LED. IEEE J. Sel. Top. Quantum Electron. **14**(5), 1387 (2008)
63. S. Nishiura, S. Tanabe, K. Fujioka, Y. Fujimoto, Properties of transparent Ce:YAG ceramic phosphors for white LED. Opt. Mater. **33**, 688–691 (2011)
64. G. Meneghesso, A. Chini, A. Maschietto, E. Zanoni, P. Malberti, M. Ciappa, Electrostatic discharge and electrical overstress on GaN/InGaN light emitting diodes, in *23rd Electrical Overstress/Electrostatic Discharge Symposium Proceedings*, Portland (OR) (2001)
65. S.K. Jeon, J.G. Lee, E.H. Park, J.H. Jang, J.G. Lim, S.K. Kim, J.S. Park, The effect of the internal capacitance of InGaN-light emitting diode on the electrostatic discharge properties. Appl. Phys. Lett. **94**, 131106 (2009)
66. S.-C. Shei, J.-K. Sheu, C.-F. Shen, Improved reliability and ESD characteristics of flip-chip GaN-based LEDs with internal inverse-parallel protection diodes. IEEE Electron Device Lett. **28**(5), 346–349 (2007)
67. M. Meneghini, A. Tazzoli, R. Butendeich, B. Hahn, G. Meneghesso, E. Zanoni, Soft and hard failures of InGaN-based LEDs submitted to electrostatic discharge testing. IEEE Electron Device Lett. **31**(6), 579–581 (2010)
68. http://www.esda.org/documents/FundamentalsPart5.pdf
69. A. Amerasekera, C. Duvvury, *ESD in Silicon Integrated Circuits*, 2nd edn. (Wiley, New York, 2002)

Chapter 14
Phosphors and White LED Packaging

Rong-Jun Xie and Naoto Hirosaki

Abstract Both phosphors and the LED packaging play a crucial role in optical properties of white LEDs. The selection criteria of the host lattice, activator ions as well as phosphors utilized in white LEDs are firstly discussed, followed by the overview of the technologically important phosphors, including yttrium aluminum garnets, alkaline earth orthosilicates, alkaline earth sulfides/thiogallets, and (oxo) nitridosilicates (i.e., nitrides). Typically, (oxo)nitridosilicate phosphors are highlighted and introduced in this chapter as they have significantly red-shifted photoluminescence spectra, abundant emission colors and high reliability. Then, the LED packaging configurations, such as "phosphor-in-cup," "remote-phosphor," and quantum dot (QD) white LEDs, are discussed in terms of their luminous efficacy, color rendering index, and color temperature. Finally, some issues on phosphors (materials searching, color tuning, particle size, and geometry) and white LEDs (packaging configurations and reliability assessments) are addressed.

14.1 Introduction

Although there are lots of issues needed to be addressed in white LEDs, such as chip processing, light extraction efficiency, heat sink structures, resin materials, reliability, and life test this chapter focuses on phosphors materials and their applications in white LED packaging.

White light-emitting diodes are attracting considerable attention from both academic and industrial communities, because they are generally accepted as the next-generation energy saving and green solid-state lighting sources. A world record of 130 lm/W at 1A drive current for white LEDs with the color temperature

R.-J. Xie (✉) · N. Hirosaki
National Institute for Materials Science (NIMS), Tsukuba, Japan
e-mail: XIE.Rong-Jun@nims.go.jp

© Springer Nature Singapore Pte Ltd. 2017

T.-Y. Seong et al. (eds.), *III-Nitride Based Light Emitting Diodes and Applications*,
Topics in Applied Physics 133, DOI 10.1007/978-981-10-3755-9_14

of 4700 K was announced recently by Nichia [1], and Cree also claimed a R&D record of 254 lm/W at a drive current of 350 mA [2]. Nevertheless, such performance levels greatly surpass that of fluorescent tubes (~80–100 lm/W), and far exceed that of incandescent (~17 lm/W) and halogen (~25 lm/W) lamps. Thanks to the great progress in optical qualities (luminous efficacy, color temperature, color rendition, lifetime, etc.), white LEDs are now penetrating into the lighting market very rapidly, which are steadily replacing incandescent lamps and fluorescent tubes for general lighting, cold cathode fluorescent lamps (CCFL) for liquid crystal display TVs for backlighting, or substitute Xeon lamps for automotive headlights. The use of white LEDs will significantly save huge electrical energy, and reduce carbon emissions [3]. For example, the worldwide energy saving would reach ~1000 TW · h/year if all traditional lighting sources were replaced by white LEDs. This corresponds to a budget savings of ~ US$ 100 billion/year, and a carbon emission reduction of 200 M/year [4]. For improving the energy savings and reducing the greenhouse effect, lots of governments around the world have banned or will ban the use of incandescent bulbs for general lighting, encouraging peoples to use more energy efficient lighting alternatives, such as LED lamps.

There are basically three options to create white lighting using LED chips, and each of them has their own advantages and disadvantages. The first option is called multi-chip white LED, which combines individual R (red), G (green), and B (blue) monochromatic LED chips. The multi-chip white LEDs, however, have the problem of that three different LEDs age over time and temperature at different rates, causing the white light to take on colored hues. Moreover, the luminous efficacy is not high because the green LEDs are not bright enough (this is called green window). To solve those problems, a green phosphor instead of a green LED is combined with RB LEDs. The second option is to pump a yellow phosphor (usually the Ce^{3+}-doped yttrium aluminum garnet, YAG:Ce) with a blue LED chip. This bichromatic (blue LED + YAG) white LED is the simplest one and produces very efficient light with a medium color rendering index (CRI) of ~70–80. To achieve a higher CRI, green/red (RG) or green/red/yellow (RGY) phosphor blends are used instead of a single yellow phosphor. The third option is to down-convert an ultraviolet (UV) or near-UV LED by using a red/green/blue (RGB) phosphor blend. Among the last two approaches, phosphors are often utilized as the down-conversion luminescent material, which absorb the emitted light from the LED chip and convert it into visible light (green, yellow, or red). LEDs using phosphor materials are also named phosphor-converted white LEDs (pc-wLEDs).

In the following, the development and photoluminescence properties of phosphor materials used in white LEDs will be overviewed. Furthermore, the status of white LED lamps utilizing phosphors will be discussed, and the optical properties of these lamps will be demonstrated.

14.2 Phosphor Materials for White LEDs

14.2.1 Selection Criteria of Phosphors

In pc-wLEDs, phosphor materials play a crucial role in the color quality of LED lamps, such as luminous efficacy, color rendering index, color temperature, and lifetime. Therefore, to realize highly efficient and reliable white LEDs, it is of quite importance to choose appropriate phosphors. Although the history of luminescent materials dates back to one century ago, and there are numerous phosphors that have been developed for cathode-ray tube displays and fluorescent lighting tubes, only a limited number of phosphors are known to be suitable for use as wavelength-conversion materials in wLEDs [5]. wLED phosphors are excited by lower energy irradiations, i.e., 440–470 nm of blue light, compared to those phosphors for displays and traditional lightings. This makes most traditional phosphors impossible for use in wLEDs, and novel phosphors are to be developed to meet new requirements.

The selection rules of phosphor materials for wLEDs, in terms of spectral features, quantum efficiency, stability as well as particle characteristics, are summarized as below [6, 7].

(i) An **excitation spectrum** is determined by monitoring fluorescence emission at the wavelength of maximum intensity while the phosphor is excited through a group of consecutive wavelengths. To convert the emitted light of LED chips more efficiently, the excitation spectrum should be broad enough to cover the emission spectrum, and to endure variations of the emission spectrum of LED chips. This requires the phosphor to absorb strongly the light of LEDs, and to have a flat excitation spectrum near the maximum emission wavelength of LEDs.

(ii) An **emission spectrum** records a set of fluorescence intensity of light given off by a phosphor when it is excited by a certain wavelength of light. The emission spectrum of a phosphor is required to be useful (i.e., aiming at a certain color) and broad sufficiently to realize high color rendering white light, when it is combined with that of a LED chip. On the other hand, the emission spectrum is required to be as narrow as possible (typically for green or red phosphors) to achieve wide color gamut LED backlights and high efficiency white LEDs. Furthermore, to minimize the reabsorption of light, the overlap between the excitation and emission spectra should be as small as possible.

(iii) The **quantum efficiency** of a phosphor is subdivided in *internal quantum efficiency* and *external quantum efficiency*. The internal quantum efficiency is defined as the ratio of the number of emitted photons to the number of absorbed photons, and the external quantum efficiency is defined as the ratio between the number of emitted photons and the number of incident photons. Higher quantum efficiency of phosphors leads to higher luminous efficiency of white LEDs. It is required to reduce the concentration of lattice defects

that absorb the incident photons and to decrease the probability of the nonradiative energy transfer. In addition, the light scattering by phosphor particles is also required to be minimized.

(iv) The **stability** of a phosphor requires that the shape of luminescence spectra, luminescence intensity, and quantum efficiency do not change over the entire operating temperature range and the lifespan of wLEDs. The thermal quenching of the phosphor should be as small as possible. In addition, the phosphor is required to be stable against chemical attacks (including moisture, O_2, CO_2, etc.) and irradiation attacks (including UV or laser light). Moreover, there should be no saturation effects in phosphors when the excitation flux increases, typically in high-power wLEDs.

(v) The **particle size and morphology** of phosphor particles affects the quantum efficiency of phosphors as well as the luminous efficiency of wLEDs greatly. Generally, to reduce the light scattering and improve the quantum efficiency of the phosphor, the particle size is required to be as uniform as possible, and the distribution as narrow as possible. Spherical particle morphology is highly desired. In addition, phosphors should be easily mixed with and well dispersed in silicones and epoxy resins, which again requires the homogeneous particle size, narrow size distribution and spherical morphology.

(vi) The **production cost** of the phosphor should be as low as possible. The phosphor is required to be synthesized cost-effectively.

14.2.2 Selection of Host Crystals and Activators

Phosphors are inorganic luminescent materials that usually consist of a host lattice and a small concentration of optically active metal ions (dopant). To obtain the phosphor with desired luminescence spectra (shape, emission color) and high quantum efficiency, both host lattice and activators should be carefully selected.

For the **host crystal**, the following requirements will be fulfilled [6].

- *It has a very large crystal-field strength* that splits the 5d energy levels to a great extent and thus reduces the electronic transition energy (see Fig. 14.1). The crystal field is the electric field of the surrounding ions at the site of activator using the approximation of point charges. It increases with increasing the coordination number and the charge of neighboring ions.
- *It has strong covalent chemical bonding* that lowers the excited state of the activations ions through the nephelauxetic effect (see Fig. 14.1).
- *It has a wide band gap* that enables it to be optically transparent. In addition, this also enables the excited state of the activator ions to be located at a right place in between the conduction band and the valence band of the host crystal.
- *It is chemically and thermally stable*. Air-, moisture-, or temperature-sensitive materials are not suitable for use as host crystals unless they are well protected by the surface coating or other treatments.

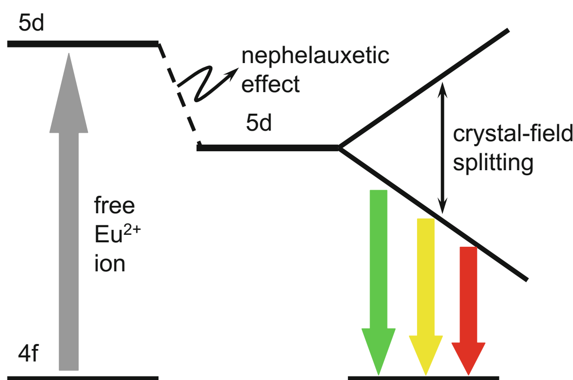

Fig. 14.1 Schematic of lowering the 5d energy levels of Eu^{2+} by the nephelauxetic effect and the crystal-field splitting

- *It is easily to be synthesized* to reduce the production cost.

Shifting to the **activator ion**, the following suggestions should be considered while they are selected [6].

- *It has a small coordination number when bonded to the nearest ligands*. This will lead to a large crystal-field splitting of the dopant ion.
- *It is covalently bonded to the nearest ligands at relatively short distance*, so that the crystal-field splitting and nephelauxetic effect will be enhanced.
- *It has the spin-allowed electronic transitions* to realize intense luminescence. The 4f → 5d electronic transitions of Eu^{2+} or Ce^{3+} are spin-allowed, yielding intense emission of Eu^{2+} or Ce^{3+}. So these ions are popularly used as activators in rare earth phosphor. Whereas the d-d electronic transitions of Mn^{2+} in some cases are spin-forbidden, resulting in weak Mn^{2+} emission due to the low oscillator strength.
- *It shows the desired emission color and spectrum*. Some ions having the f–f electronic transitions (e.g., Tb^{3+}, Eu^{3+}) usually show their characteristic narrow emission spectra and colors which are not sensitive to the local environment. Their emission wavelengths are not tunable, so that they are not commonly used in LED phosphors.

With these in mind, numerous compounds have been investigated as phosphor host lattices, and a number of phosphors have thus been developed and suggested for use in wLEDs. In the next section, an overview of some technologically important phosphors will be given.

14.2.3 Type of Phosphors

Phosphors can be divided into many groups, depending on their chemical composition, crystal structure, emission color, as well as the dopant type. Here, the

phosphors are classified into garnets, orthosilicates, sulfides, nitrides, and so on [6]. In this part, the discussion will be concentrated on the phosphors that are mostly popular in the market, including garnets, alkaline earth orthosilicates, alkaline earth sulifes, and (oxo)nitridosilicates.

14.2.3.1 Garnets

Garnet phosphors refer to a family of Ce^{3+}-doped luminescent materials that have a general chemical formula of $X_3Y_2Z_3O_{12}:Ce^{3+}$ (X = Ca, Mg, Y, Lu; Y = Al, and Z = Si, Ge) [8, 9]. The three different cations X, Y, and Z are coordinated to the nearest oxygen with the coordination number of 8, 6, and 4, respectively, which forms a very stiff cubic structure with the space group of Ia -3d.

The yellow-emitting Ce^{3+}-acvtivated yttrium aluminum garnet ($Y_3Al_5O_{12}:Ce^{3+}$, simply YAG:Ce) is the first phosphor that was used to combine with a blue LED to generate white light by Nakamura in 1995 [10]. Although it was reported as a phosphor for flying spot cathode-ray tubes by Blasse in 1967 [11], YAG:Ce is now the most popular yellow phosphor in wLEDs because of its excitation spectrum matching perfectly with the blue LED, very intense yellow emission color, high quantum efficiency, composition-tunable emission wavelength, high thermal quenching temperature, and ease of synthesis.

Figure 14.2 shows the typical excitation and emission spectra of YAG:Ce. The excitation spectrum is significantly split into several bands due to a very large Ce^{3+} crystal-field splitting ε_{CFS} of ~26,050 cm^{-1} [12], so that the lowest-energy excitation band covering the spectral range of 380–550 nm has the peak wavelength (450–470 nm) equivalent to the emission maxima of blue LEDs. The emission spectrum shows an asymmetric broadband peaking at 560 nm as a result of the electronic transitions from the ^5D excited states to the $^2F_{5/2}$ and $^2F_{7/2}$ doublet ground states. The full-width at half maximum (FWHM) of YAG:Ce is as large as ~120 nm, enabling to achieve an acceptable color rendering index (Ra ~ 70–80) of wLEDs for general illumination.

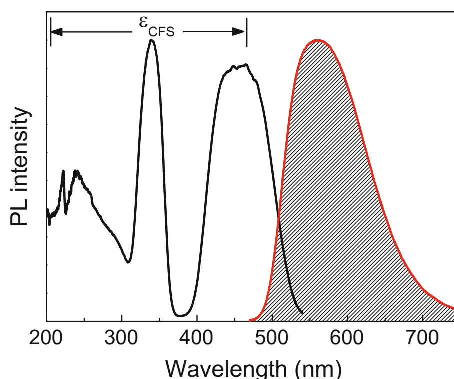

Fig. 14.2 Excitation and emission (*shadow*) spectra of $Y_3Al_5O_{12}:Ce^{3+}$, showing the crystal-field splitting ε_{CFS}

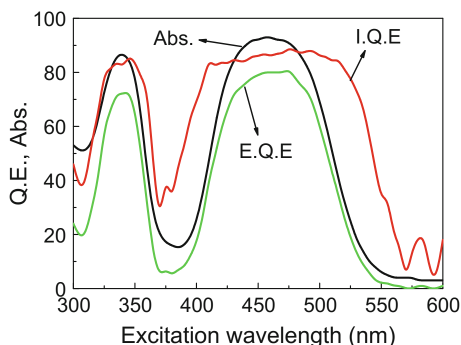

Fig. 14.3 Plot of absorption (Abs.), internal quantum efficiency (I.Q.E.) and external quantum efficiency (E.Q.E.) of YAG:Ce versus excitation wavelength

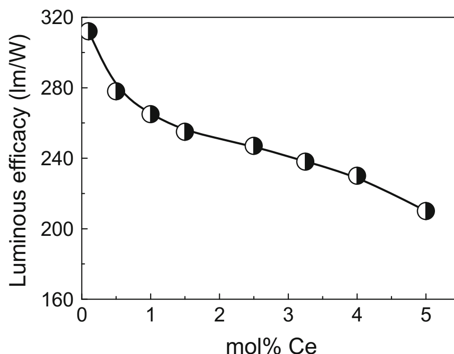

Fig. 14.4 Luminous efficiency of the YAG:Ce phosphor as a function of the Ce concentration (excitation wavelength = 470 nm) (Reproduced from [13], with permission)

As shown in Fig. 14.3, the yellow-emitting YAG:Ce phosphor (1 mol% Ce) has a very good luminescence efficiency, the internal quantum efficiency, and external quantum efficiency being 86 and 80% under the 460 nm excitation, respectively. The absorption at 460 nm is 93%, only 7% incident light being reflected.

The Ce concentration affects the luminescence properties (i.e., efficiency, emission color, absorption) and thermal quenching temperature greatly. Silver et al. [13] reported that the luminous efficacy of YAG:Ce decreased continuously as the Ce concentration increased, as shown in Fig. 14.4. Although the diluted phosphor has the luminous efficacy approaching the theoretic value, it is not recommended for the practical use because of its high reflectance at the emission wavelength of blue LEDs. A redshift in emission spectrum is often observed when the Ce concentration increases, which is due to the reabsorption and the enhanced Stokes shift. Bachmann [14] conducted a comprehensive investigation on thermal quenching of YAG:Ce. He addressed that the thermal quenching temperature is intrinsically high ($\gg$680 K), and YAG:Ce with the lower Ce concentration had the higher thermal quenching temperature. Ueda et al. [15] did a temperature dependence of photoconductivity measurement, and reported that the threshold of photoionization from the 4f level of Ce^{3+} to the conduction band in YAG:Ce was 3.8 eV, and the main quenching process was caused by the thermally stimulated ionization process from the $5d_1$ to the conduction band.

Table 14.1 Peak excitation wavelength (λ_{exc}), peak emission wavelength (λ_{em}), and thermal quenching temperature (T_{tq}) of some garnet phosphors

	λ_{exc} (nm)	λ_{em} (nm)	T_{tq}	References
$Ca_3Sc_2Si_3O_{12}$	455	505/560	High	[21]
$Lu_2CaMg_2(Si,Ge)_3O_{12}$ (6 mol%)	470	605	Medium	[22]
$Mg_3Gd_2Ge_3O_{12}$ (2 mol%)	464	600	–	[23]

The $Y_3Al_5O_{12}$:Ce composition is usually modified to achieve green or orange–yellow-emitting colors [14, 16–19]. Substitutions on the Y dodecahedral site with a smaller Lu ion or on the Al octahedral site with a larger Ga ion will lead to the blue shift. On the contrary, considerable red-shifts can be realized by substituting Y by larger La, Gd, Tb ions, Al by a Mg–Si pair, or Al–O bonds by Si–N ones. The modified YAG:Ce phosphors compensate the loss of thermal stability and visual efficiency by achieving lower color temperature (red-shift) or higher color rendering index (blue shift). A yellow $Tb_3Al_5O_{12}$:Ce phosphor was used by Osram, which has no intelligence property (IP) problems with Niichia's YAG-based phosphors. However, Jang et al. [20] indicated that the luminous efficacy of wLEDs using TAG:Ce was lower than that of YAG-based wLEDs, which was due to the significant sedimentation of TAG:Ce particles in the epoxy resin caused by the higher density of TAG:Ce (6.085 vs. 4.657 g/cm^3 of YAG:Ce).

Other Ce^{3+}-activated garnet phosphors are listed in Table 14.1. These garnet phosphors show red-shifted emission spectra compared to YAG:Ce, which enables them to create warm white light when combined with blue LEDs.

14.2.3.2 Alkaline Earth Orthosilicates

Alkaline earth metal orthosilicates, such as Sr_2SiO_4 and Sr_3SiO_5, are interesting host lattices for wLED phosphors. The highly polarisable Si–O bonds in these orthosilicates yield strongly covalent binding between alkaline earth metals and oxygen, thus resulting in a large nephelauxetci effect. This strong nephelauxetic effect considerably reduces the transition energy of Eu^{2+}, leading to red-shifted excitation spectrum of alkaline earth metal orthosilicate phosphors and thus a significant overlap with the emission spectrum of blue LEDs.

Barry [24] did a comprehensive survey on the photoluminescence of Eu^{2+}-doped Sr_2SiO_4–Ba_2SiO_4 solid solutions. A continuous color shift from green (λ_{em} = 505 nm, Ba_2SiO_4:Eu) to yellow (λ_{em} = 575 nm, Sr_2SiO_4:Eu) was observed, indicative of the composition-tunable emission wavelength that is very important for practical applications. Typical photoluminescence spectra of green and yellow $(Sr,Ba)_2SiO_4$:Eu phosphors are given in Fig. 14.5. The emission spectrum shows a broadband, which is due to the 4f → 5d electronic transition of Eu^{2+}. This Eu^{2+} emission band is slimmer than the Ce^{3+} one because of the single electronic transition of Eu^{2+}. The excitation spectrum extends from UV to the visible spectral range (~500 nm), but the excitation maxima does not perfectly match with the peak

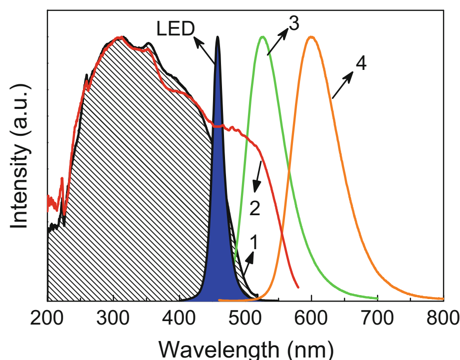

Fig. 14.5 Photoluminescence spectra of the green- and yellow-emitting (Sr, Ba)$_2$SiO$_4$:Eu phosphor (*1*, *3* excitation and emission spectra for the green phosphor, and *2*, *4* excitation, and emission spectra for the yellow phosphor). The emission spectrum of a blue LED (λ_{em} = 460 nm) is also plotted

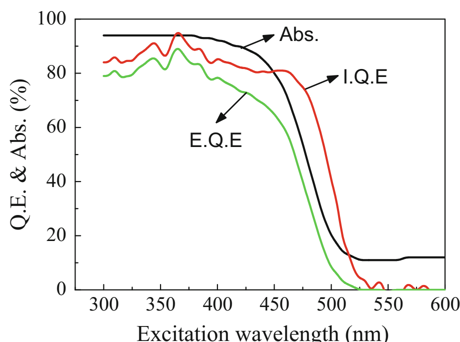

Fig. 14.6 Plot of the absorption (Abs.), internal quantum efficiency (I.Q.E) and external quantum efficiency (E.Q.E) of the (Sr, Ba)$_2$SiO$_4$:Eu green phosphors versus excitation wavelength

emission wavelength of blue LEDs. It indicates that (Sr,Ba)$_2$SiO$_4$-based phosphors are more suitable for use in combination with short-wavelength blue LEDs (i.e., λ_{em} = 430–450 nm). On the other hand, the blue light absorption can be enhanced by the compositional tailoring (See curve 2 in Fig. 14.5). In addition, the low absorption of the blue light is compensated by higher visual efficiency of orthosilicate phosphors. As seen in Fig. 14.6, under the 450 nm excitation the internal quantum efficiency and external quantum efficiency of a green orthosilicate phosphor are 81% and 65%, respectively. The absorption at 450 nm is around 80%, much lower than that of YAG:Ce (93%).

Compared to YAG:Ce, Sr$_2$SiO$_4$:Eu-based phosphors show stronger temperature-dependent efficiency and a larger shift of chromatic coordinates, typically the end members of the Ba$_2$SiO$_4$–Sr$_2$SiO$_4$ system (see Fig. 14.7). Besides this, another disadvantage is the lower CRI of the wLEDs utilizing a single Sr$_2$SiO$_4$:Eu-based yellow phosphor. These shortcomings prevent it from their use in high-power LEDs.

Both of the excitation spectrum and the emission spectrum are considerably red-shifted in Eu^{2+}-doped Sr$_3$SiO$_5$ phosphors, leading to orange–yellow or orange emission colors (See Fig. 14.8) [25–27]. The peak emission wavelength varies in the range of 570–610 nm, depending on the Sr/Ba ratio [27]. Therefore, the

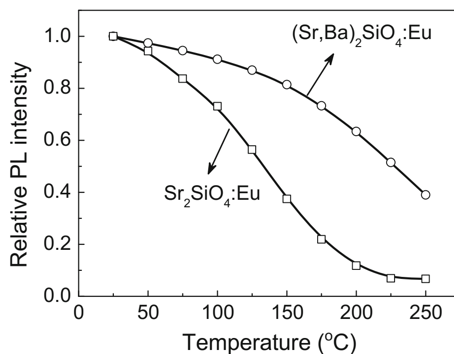

Fig. 14.7 Thermal quenching of Sr_2SiO_4:Eu-based green phosphors

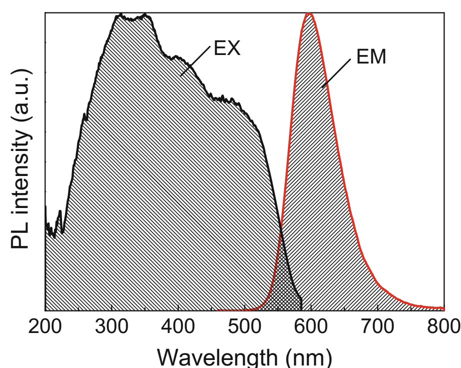

Fig. 14.8 Excitation and emission spectra of the (Sr,Ba)$_3$SiO$_5$:Eu orange–yellow phosphor

Sr_3SiO_5:Eu-based phosphors are one of the best choices to compensate for the red component in wLEDs to realize warm white when it is blended with a green phosphor. In addition, a much broader emission band (FWHM = 121.8 nm) can be obtained in the Ce^{3+}-doped Sr_3SiO_5 yellow phosphor, thus enabling to achieve a color rendering index comparable to YAG:Ce [28].

The orange–yellow/orange (Sr,Ba)$_3$SiO$_5$:Eu phosphors have higher thermal quenching temperatures than the green/yellow (Sr,Ba)$_2$SiO$_4$:Eu ones. Moreover, (Sr,Ba)$_3$SiO$_5$:Eu absorbs the blue light (λ_{em} = 450–470 nm) more efficiently than (Sr,Ba)$_2$SiO$_4$:Eu. For example, the absorption at 450 nm is about 91% for (Sr,Ba)$_3$SiO$_5$:Eu, and a higher external quantum efficiency of 70% is thus achieved (See Fig. 14.9).

Other interesting orthosilicate phosphors reported so far include Eu^{2+}-doped $MMg_2Si_2O_7$ (M = Ca, Sr, Ba) [29], $CaAl_2Si_2O_8$ [30], $M_3MgSi_2O_8$ (M = Ca, Sr, Ba) [31], Li_2SrSiO_4 [32], etc. These phosphors show intense blue-to-yellow emission colors under the excitation of the UV light. However, most of these orthosilicates (except Li_2SrSiO_4) show a very low absorption of the blue light, making them impossible to be combined with blue LEDs.

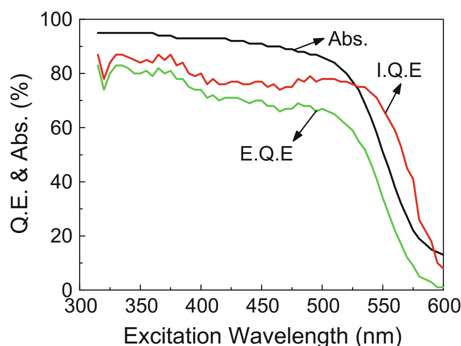

Fig. 14.9 Plot of absorption (Abs.), internal quantum efficiency (I.Q.E.) and external quantum efficiency (E.Q.E) of Sr_3SiO_5:Eu versus excitation wavelength

14.2.3.3 Alkaline Earth Sulfides/Thiogallates

Inorganic sulfides are also covalent compounds that become interesting host lattices for phosphors. The most notable materials are Eu^{2+}-doped alkaline earth metal sulfides (MS:Eu, M = Ca, Sr, Ba) [32, 33] and alkaline earth metal thiogallates (MGa_2S_4:Eu, M = Ca, Sr, Ba) [34–37].

(Sr,Ca)S:Eu phosphors show very broad excitation bands covering the UV-to-green spectral range, and absorb the blue and green light very efficiently. The phosphors emit red colors in the spectral range of 600–655 nm, depending on the Sr/Ca ratio. These features indicate that the (Sr,Ca)S:Eu phosphors are suitable for white LEDs. However, the strong moisture-sensitivity and large thermal quenching of these red phosphors make them impossible for practical applications. The surface coating of Al_2O_3 and SiO_2 is an effective way to protect (Sr,Ca)S:Eu phosphors against moisture and thermal attacks.

The $SrGa_2S_4$:Eu phosphor has a broad excitation band maximum at 470 nm, and it emits a green light with the peak wavelength of 535 nm. The emission color is further red-shifted when Sr is partially substituted by Ca or Ba [36]. This phosphor has already been considered as a green conversion luminescent material in high color rendering wLEDs due to its promising luminescent properties [36]. On the other hand, the poor thermal and chemical stabilities again will not enable it to be used in wLEDs widely.

14.2.3.4 (Oxo)nitridosilicates

(Oxo)nitridosilicate phosphors or nitride phosphors are newly developed luminescent materials that are very suitable for wLED applications [6, 38]. (Oxo)nitridosilicates have stiff structures built up on highly dense three-dimensional SiN4 tetrahedral networks, and have covalent chemical binding characters and strong crystal-field strength [6, 39, 40]. Therefore, (oxo)nitridosilicate phosphors show red-shifted photoluminescence spectra, high thermal/chemical stability, high quantum efficiency, abundant emission colors, etc. Extensive investigations on

Table 14.2 Photoluminescence properties of (oxo)nitridosilicate phosphors

Phosphors	λ_{exc}	λ_{em}	I.Q.E/E.Q.E	References
$LaAl(Si_{6-z}Al_z)N_{10-z}O_z$ (2.75%Ce)	380	496	–/48%*	[61]
$LaSi_3N_5$ (10%Ce)	360	440	–/67%	[62]
AlN (0.28%Eu)	290	465	76/46%**	[63]
β-sialon (0.3%Eu)	450	535	49/33%	[51]
$BaSi_2O_2N_2$ (2%Eu)	458	492	–/41%	[64]
$SrSi_2O_2N_2$ (2%Eu)	456	544	–/69%	[64]
$Ba_3Si_6O_{12}N_2$	–	525	–	[65]
$Sr_5Al_{5+x}Si_{21-x}N_{35-x}O_{2+x}$ (10%Eu)	400	510	–	[66]
$Sr_{14}Si_{68-s}Al_{6+s}O_sN_{106-s}$(s ~ 7) (6%Eu)	376	508	–	[67]
$Sr_3Si_{13}Al_3O_2N_{21}$ (8%Eu)	365	515	75/67%	[68]
Ca-α-sialon (7%Eu)	450	580	61/49%	[6]
$La_3Si_6N_{11}$ (10%Ce)	460	595	–/42%	[69]
$CaAlSiN_3$ (10%Ce)	483	570	71/50%	[70]
$CaAlSiN_3$ (1.0%Eu)	450	660	83/70%	[6]
$Sr_2Si_5N_8$ (2%Eu)	450	627	87/71%	[71]
$SrAlSi_4N_7$ (5%Eu)	450	639	76/53%	[72]

* The measurements were done under 365 nm excitation

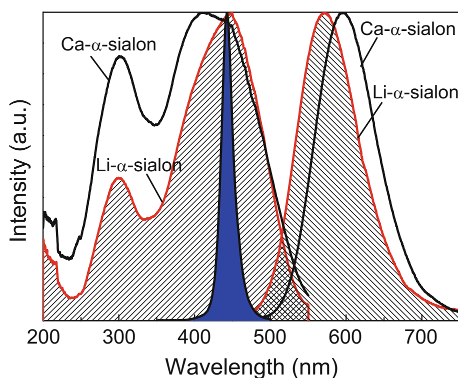

Fig. 14.10 Excitation (*left*) and emission (*right*) spectra of Ca-α-sialon:Eu and Li-α-sialon:Eu (hatched) phosphors. The emission spectrum of a blue LED (λ_{em} = 450 nm) is also plotted

(oxo)nitridosilicate phosphors have been done in recent years, but the number of phosphors reaching the sufficient level of practical applications is limited. In this section, only three (oxo)nitridosilicate phosphors will be discussed, and others are summarized in Table 14.2.

α-sialon has a chemical formula of $M_xSi_{12-m-n}Al_{m+n}O_nN_{16-n}$ ($x = m/\nu$, ν is the valence of metal M), which is limited solid solutions in the system α-Si_3N_4-Al_2O_3-AlN-$MO_{\nu/2}$ [41]. The α-sialon:Eu is a yellow-emitting phosphor [42–45]. As seen in Fig. 14.10, the excitation band centered at 400–450 nm matches well with the emission spectrum of blue LEDs. The excitation spectrum changes in the shape with accommodating different metal ions, the low-energy band being enhanced by substituting Li for Ca [46]. The emission spectrum shows a broadband peaked at

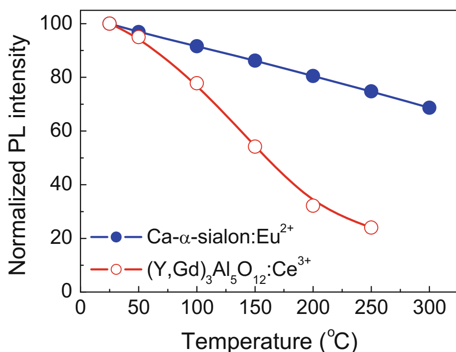

Fig. 14.11 Temperature-dependent luminescence intensity of Ca-α-sialon:Eu (m = 2, n = 1, 7 mol% Eu) and the red emission enhanced $(Y,Gd)_3Al_5O_{12}$:Ce phosphors

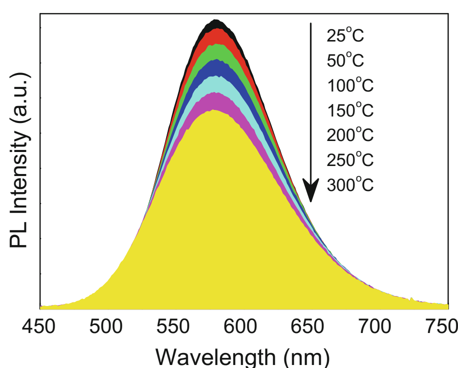

Fig. 14.12 Temperature-dependent emission spectrum of Ca-α-sialon:Eu (m = 2, n = 1, 7 mol% Eu)

585 nm for Ca-α-sialon and 570 nm for Li-α-sialon [47]. The full-width at half maximum for both sialons is about 94 nm, which is narrower than that of YAG:Ce. α-sialon:Eu is the first nitridosilicate phosphor that is suggested for use in warm wLEDs [44, 48].

Compared to YAG:Ce, α-sialon:Eu has a much higher thermal quenching temperature due to its extremely rigid structure. As shown in Fig. 14.11, The luminescence of $(Y,Gd)_3Al_5O_{12}$:Ce is significantly quenched at temperatures above 100 °C, whereas that of α-sialon:Eu slightly decreases. In addition, with increasing temperature the shape of the emission spectrum of α-sialon:Eu remains unchanged (See Fig. 14.12), indicating that its chromaticity coordinates are quite stable against temperature. This is of importance when it is applied in high-power wLEDs.

Although it is superior to YAG:Ce in thermal stability, enhanced red emission, and color point stability, α-sialon:Eu has a lower quantum efficiency than YAG:Ce. The external quantum efficiency is 49% when Li-α-sialon:Eu is excited at 450 nm

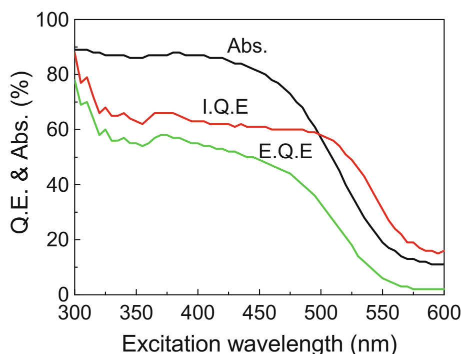

Fig. 14.13 Plot of absorption (Abs.), internal quantum efficiency (I.Q.E) and external quantum efficiency (E.Q.E) of Li-α-sialon:Eu (m = 1, n = 1.8, 7 mol% Eu) versus excitation wavelength

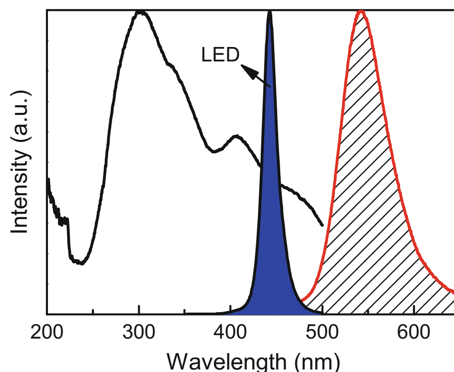

Fig. 14.14 Excitation and emission (hatched) spectra of β-sialon:Eu. The emission spectrum of a blue LED (λ_{em} = 450 nm) is also plotted

(See Fig. 14.13). It is increased up to 60% by modifying the processing conditions. The lower efficiency is ascribed to the low absorption and lattice defects.

Thanks to the wide range of the solid solution forming area, the emission color of α-sialon:Eu can be tuned in a wide range by changing the *m* and *n* values and the type of accommodating metal ions [6]. The composition-tunable emission of α-sialon:Eu enables it to fabricate wLEDs with varying color temperatures.

β-sialon ($Si_{6-z}Al_zO_zN_{8-z}$) is a limited solid solution between β-Si_3N_4 and Al_2O_3 with $0 \leq z < 4.2$ [49, 50]. The Eu^{2+}-doped β-sialon shows an intense emission band centered at 530–550 nm, depending on the z value and the Eu concentration [51, 52]. The emission band is abnormally narrow and the FWHM value is only 55 nm. The narrow band results in a higher color purity of β-sialon:Eu in comparison with green-emitting $Y_3(Al,Ga)_5O_{12}$:Ce and $(Sr,Ba)_2SiO_4$:Eu phosphors. On the other hand, β-sialon:Eu does not absorb the blue light strongly (See Fig. 14.14), leading to the external quantum efficiency less than 50%.

The z value and the Eu concentration in β-sialon are optimized as 1.0 mol% and 0.3 mol%, respectively [51, 52]. The absorption is inevitably low because of the low Eu concentration. It is reported that Eu ions are accommodated in the large channel parallel to the c-axis, and are coordinated by six (N,O) anions at equal distances [53, 54].

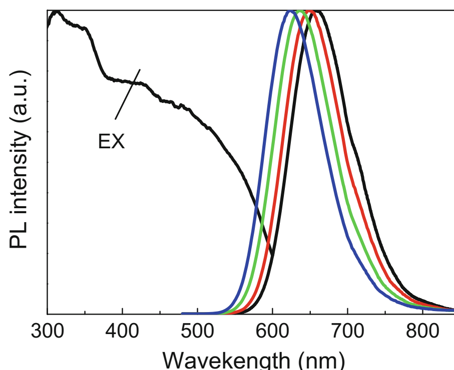

Fig. 14.15 Excitation and emission spectra of (Ca,Sr)$AlSiN_3$:Eu. Emission spectrum from right to left: $CaAlSiN_3$, $(Ca_{0.6}Sr_{0.4})AlSiN_3$, $(Ca_{0.4}Sr_{0.6})AlSiN_3$, and $(Ca_{0.1}Sr_{0.9})AlSiN_3$

Under the 450 nm excitation, the internal quantum efficiency and external quantum efficiency of β-sialon:Eu are 49% and 33%, respectively. The external quantum efficiency is greatly enhanced (~50%) by the compositional tailoring and the processing control. Like α-sialon:Eu, β-sialon:Eu is also very stable against thermal and chemical attacks. The luminous efficiency of β-sialon:Eu basically does not change over time and temperature, making it more suitable for use in wLED backlights [55]. Due to its narrow emission band, β-sialon:Eu is not the best choice for use in general lighting.

Eu^{2+}-doped nitridosilicates $CaAlSiN_3$, $M_2Si_5N_8$ (M = Ca, Sr, Ba), and $CaSiN_2$ are red-emitting phosphors that have the similar excitation and emission spectra [56–59]. As presented in Fig. 14.15, $CaAlSiN_3$:Eu considerably extends its excitation spectrum from UV to the red spectral region. The emission band is centered at 660 nm for $CaAlSiN_3$:Eu (0.8 mol%), and can be blue-shifted to 620 nm when Sr substitutes for Ca [60]. Besides these excellent photoluminescence properties, $CaAlSiN_3$:Eu shows higher thermal quenching temperature than the $Ca_2Si_5N_8$:Eu counterpart. In addition, $CaAlSiN_3$:Eu is more stable than the $Sr_2Si_5N_8$:Eu red phosphor.

The luminous efficiency $CaAlSiN_3$:Eu is much higher than most (oxo)nitridosilicate phosphors. The absorption and external quantum efficiency of $CaAlSiN_3$ (1.0%Eu) are 86% and 70% under the blue light excitation (λ_{em} = 450 nm), respectively. On the other hand, $CaAlSiN_3$:Eu has an excitation spectrum tail largely covering the green spectral region, therefore it will also absorb the emission from the combined green phosphor and reduce the total green light of wLEDs. To solve this problem, a larger quantity of the green phosphor should be used.

Photoluminescence properties of other interesting (oxo)nitridosilicate phosphors are summarized in Table 14.2.

14.3 Color Issues and Luminous Efficacy of White LEDs

For all types of white LEDs, color rendering and luminous efficacy are two most important criteria for general lighting, which determine the optical quality and the application purpose of wLEDs. There is a trade-off between these two important criteria because color rendering and luminous efficacy are best achieved by different shapes and broadness of the emission spectra of wLEDs.

The color rendering of wLEDs will be discussed in detail in Chap. 9.

14.3.1 Color Rendering

Color rendering of a light source is determined by comparing the appearance of varying object colors illuminated by the given light source with that illuminated by reference illuminant. The reference illuminant is the Planckian radiation for test sources with a correlated color temperature (CCT) of <5000 K, or a phase of daylight for test sources with CCT > 5000 K. In the standardized method, the C*olor Rendering Index* (CRI), fourteen Munsell samples of various different colors were carefully chosen [73]. The color differences, denoted as ΔE_i, of these color samples under a given illumination and under the reference illumination are calculated on the 1964 W*U*V* uniform color space. The *Special Color Rendering Index*, R_i, for each sample is then given by [74]

$$R_i = 100 - 4.6\Delta E_i (i = 1, \ldots, 14) \tag{14.1}$$

The R_i value is an indication of color rendering for each particular color. The *General Color Rendering Index, Ra*, is often used to evaluate the color rendering of a light source. Ra is calculated by averaging the values of R_i for the first eight color samples that have the medium color saturation.

$$\mathrm{Ra} = 1/8 \times (\mathrm{R}_1 + \mathrm{R}_2 + \cdots + \mathrm{R}_8) \tag{14.2}$$

The low Ra value means that some colors (e.g., red and green) may appear unnatural when illuminated by the light. So, high values of CRI or Ra are always pursued for general lighting. Basically, Ra > 70 is considered acceptable for illumination purposes, values greater than 80 are regarded as high quality and suitable for interior lighting, and *Ra* > 95 is suitable for visual inspection purposes. High color rendering is realized by broadband spectra covering the whole visible region. Therefore, the spectral distribution of wLEDs should be designed or modified to achieve the *Ra* value required for the application in mind.

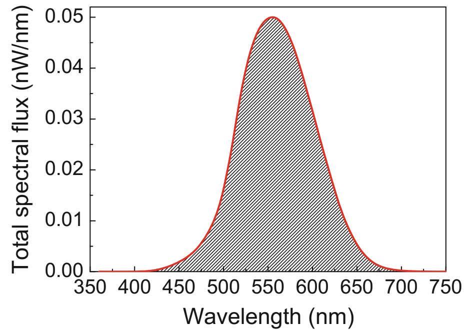

Fig. 14.16 Eye sensitivity spectral curve for photopic vision V(λ)

14.3.2 Luminous Efficacy

Luminous efficacy of a light source, or *luminous efficacy of radiation*, is the efficiency of energy conversion from electrical power to optical power, or from radiant flux to luminous flux. The *luminous efficacy of radiation*, in lm/W (lumen per watt), describes the brightness of the radiation perceived by the average human eye, and is calculated by the eye sensitivity over the entire spectral distribution of light through the following equation [75]:

$$LER(lm/W) = 683\,\mathrm{lm/W} \times \frac{\int_{380}^{780} V(\lambda)S(\lambda)d\lambda}{\int_{0}^{\infty} S(\lambda)d\lambda} \tag{14.3}$$

$V(\lambda)$ is the spectral luminous efficiency of photopic vision (eye sensitivity curve) defined by CIE which is defined in the visible range of 380–780 nm, as shown in Fig. 14.16. $S(\lambda)$ is the *spectral power distribution* (SPD), which describes the power per unit area per unit wavelength of wLEDs. The theoretical limit of the luminous efficacy of monochromatic green radiation (555 nm) is 683 lm/W, whereas it is only 26 lm/W for a blue monochromatic light at 450 nm, since the eye sensitivity peaks at 555 nm. For creating white light, blue, and red components in the emission spectrum of wLEDs are essential, so the luminous efficiency of wLEDs is always considerably lower than the theoretical limit.

14.3.3 Chromaticity Coordinates and Color Temperature

White light generated by wLEDs is required to show all the colors of illuminated objects appropriately, so that the white color should be reasonable and acceptable. To quantitatively describe the color of the white light, chromaticity coordinates, and color temperature are utilized.

For a given light the spectrum $S(\lambda)$ can be weighted by the *XYZ color matching functions* as seen in Fig. 14.17. The resultant three weighted integral values X, Y,

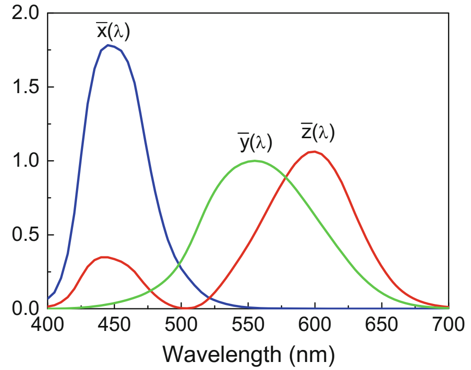

Fig. 14.17 CIE 1931 XYZ color matching functions

Z, also called triastimulus values, are obtained by using the following equations [76].

$$X = \int \bar{x}(\lambda)S(\lambda)d\lambda \tag{14.4a}$$

$$Y = \int \bar{y}(\lambda)S(\lambda)d\lambda \tag{14.4b}$$

$$Z = \int \bar{z}(\lambda)S(\lambda)d\lambda \tag{14.4c}$$

The *chromaticity coordinate x, y* of the given light is thus calculated by

$$x = \frac{X}{X + Y + Z} \tag{14.5a}$$

$$y = \frac{Y}{X + Y + Z} \tag{14.5b}$$

Any color of light can be expressed by the chromaticity coordinate (x, y) on the CIE 1931 chromaticity diagram, as shown in Fig. 14.18. In the horseshoe-shaped diagram, the boundaries are called *spectrum locus*, representing the monochromatic light. *Planckian locus* or *blackbody locus* is plotted near the center of the diagram, which represents the chromaticity coordinates of a blackbody having various temperatures.

The colors on the planckian locus can be specified by *color temperature* in Kelvin [77]. The colors around the Planckian locus from the color temperature of ~2500–20,000 K are recognized as *white*. For most of traditional lamps their colors fall in the region between 2850 and 6500 K. The color of white light can be purposely shifted along the Planckian locus (i.e., from warm to cool) for desired mood. However, the color shifted away from the Planckian locus is not regarded as

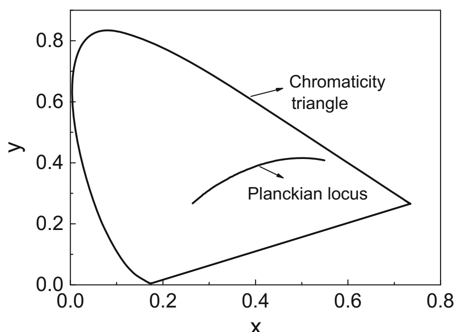

Fig. 14.18 1931 CIE chromaticity diagram

white, and hence is hardly accepted for general lighting. Strictly speaking, color temperature cannot be used for the colors whose chromaticity coordinates are beyond the Planckian locus. In this case, correlated color temperature (CCT) is used instead. The CCT for any white light can be determined by drawing a perpendicular line from the measured 1931 CIE chromaticity coordinates to the Planckian locus to obtain the (x, y) intercept. Then the CCT of the white light would correspond to the surface temperature of a blackbody radiator with the same (x, y) chromaticity coordinates.

The chromaticity coordinate and color temperature of four standard white points are shown as below.

$$\begin{aligned}
&\textit{Tungsten lamp}: 2865\,\text{K}, \text{x} = 0.448,\ \text{y} = 0.408\\
&\textit{Direct sunlight}: 4870\,\text{K},\ \text{x} = 0.348,\ \text{y} = 0.352\\
&\textit{Overcast sunlight}: 6770\,\text{K},\ \text{x} = 0.310,\ \text{y} = 0.316\\
&D65(\textit{daylight}): 6504\,\text{K},\ \text{x} = 0.313,\ \text{y} = 0.329
\end{aligned}$$

14.4 White LED Packaging

As mentioned previously, white light can be generated by multi-chip or phosphor-converted white LEDs. The multi-chip white LEDs have advantages of high luminous efficacy and high color rendering index, but they are costly. In addition, the choice of monochromatic LED chips is strictly limited. On the other hand, pc-wLEDs are cheaper and allow a much more flexible design in spectra as phosphors are easily selected and combined. Furthermore, they are getting more efficient and reliable, making them to be the mainstream products of the market.

Besides the above two packaging methods, white light generated by using nanotechnology such as quantum dots (QDs) and quantum wells (QWs) is also extensively investigated. It is well known that the size-tunable emission wavelength is usually observed in low-dimensional structures (i.e., QDs or QWs), which is

ascribed to the quantum confined Stark effect which is induced by the presence of large piezoelectric field [78]. The generation of white light by stacking the GaN/AlGaN QDs with different sizes, as well as the incorporation of InGaN/GaN QWs with different thicknesses in the active region has been intensively investigated [79–83].

The manufacturing of wLEDs consists of several steps, but not limited to: die attach, wire bonding, wavelength-conversion materials application, encapsulation, curing, optic lens attach, singualtion, testing, binning, and taping. The wLED products can be divided into various groups depending on the *chip type* (i.e., ultraviolet, near-ultraviolet, or blue), *wavelength-conversion materials (phosphors or QDs) and their locations*, the *input power* (low or high-power), and the *construction*. From the viewpoint of conversion materials and configurations, we will group the wLEDs into "phosphor-in-cup" white LEDs, "remote-phosphor" white LEDs and QDs white LEDs, and discuss them in the following sections.

14.4.1 Phosphor-in-Cup White LEDs

Usually, phosphor(s) is dispersed in the transparent epoxy resin, and then mounted on the LED chip. In the case of phosphor(s) dispersed epoxy resin is uniformly distributed in the reflector cup (See Fig. 14.19), such a LED configuration is called "*phosphor-in-cup*" [84]. In an extreme case, a "*conformal*" configuration is recognized when the phosphor(s) is not homogenously distributed in the epoxy resin but conformally coated on the LED chip (phosphor replicating the contour of the chip) [84].

The most popular way to fabricate "phosphor-in-cup" wLED is using a blue LED chip in conjunction with a yellow-emitting phosphor. Such a LED type is also known as "bichromatic" or "one-phosphor-converted (1-pc)" wLEDs. The

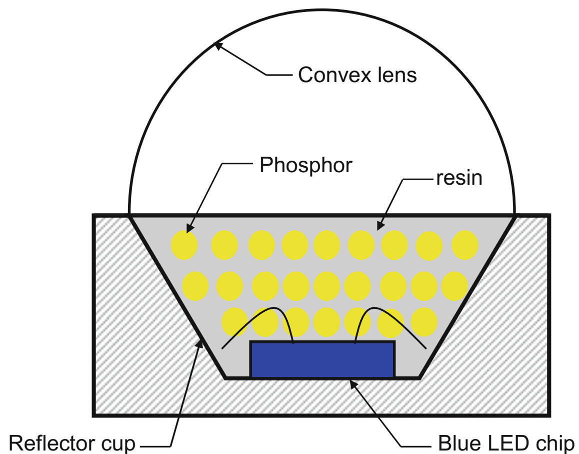

Fig. 14.19 Schematic of white LEDs with the phosphor-in-cup configuration

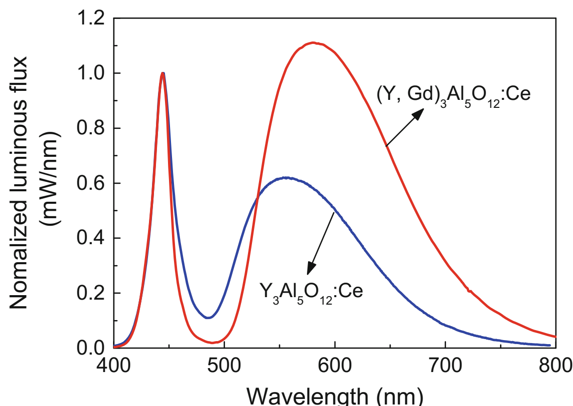

Fig. 14.20 Emission spectra of white LEDs using $Y_3Al_5O_{12}$:Ce and $(Y, Gd)_3Al_5O_{12}$:Ce, respectively. The bias current is 20 mA

Table 14.3 Color rendering indices of white LEDs using $Y_3Al_5O_{12}$:Ce

Ra	R1	R2	R3	R4	R5	R6	R7	R8	R9
71	67	74	80	71	68	65	82	57	−39

commonly used yellow phosphor is cerium-doped yttrium aluminum garnet ($Y_3Al_5O_{12}$:Ce). As this method is patented by the Niichia company, to avoid the IP problems, alternative yellow phosphors, such as orthosilicates and (oxo)nitridosilicates, have been developed.

Figure 14.20 shows a typical emission spectrum of wLEDs using a single YAG: Ce phosphor. It consists of two bands: the narrow blue band is the emission spectrum of the LED chip, and the broad yellow band is from the YAG phosphor. For the $Y_3Al_5O_{12}$:Ce phosphor, the wLED has a correlated color temperature of 5200 K, the color rendering index Ra of 71, and the chromaticity coordinates of x = 0.340, y = 0.354. Krames et al. [4] reported a similar YAG-based wLED with CCT = 5600 K. The first nine special color rendering indices of the wLED are shown in Table 14.3. To obtain warm white light, the emission wavelength of $Y_3Al_5O_{12}$:Ce needs to be red-shifted by partial substitution of Gd for Y. So the use of the modified $(Y,Gd)_3Al_5O_{12}$:Ce phosphor leads to a lower color temperature of 2960 K. At the same time, the color rendering index is reduced to 63 due to the larger gap in between the blue band and the yellow band. As the thermal quenching of $(Y,Gd)_3Al_5O_{12}$:Ce is higher than that of $Y_3Al_5O_{12}$:Ce, the $(Y,Gd)_3Al_5O_{12}$:Ce-based LED achieves warm white by sacrificing reliability or lifetime.

Warm white can also be realized by using orange-yellow phosphors, such as $Sr_3SiO_5:Ce^{3+}$ [28], Eu^{2+}-doped Ca-α-sialon [38, 44, 48], and Ce^{3+}-doped $CaAlSiN_3$ [70], and $La_3Si_6N_{11}$ [69]. As these (oxo)nitridosilicate or orthosilicate phosphors have higher thermal quenching temperature than $(Y,Gd)_3Al_5O_{12}$:Ce, the warm white LEDs using them have stabilized luminous efficacy and chromaticity coordinates when the temperature changes. Sakuma et al. [48] addressed that the chromaticity coordinates of Ca-α-sialon:Eu-based wLEDs were only 1/3–1/4 of

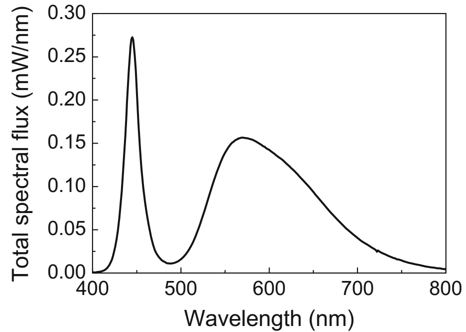

Fig. 14.21 Emission spectra of white LEDs using $CaAlSiN_3$:Ce. The bias current is 20 mA

Table 14.4 Color rendering indices of white LEDs using $CaAlSiN_3$:Ce

Ra	R1	R2	R3	R4	R5	R6	R7	R8	R9
70	71	78	77	65	67	63	79	63	8

those of YAG-based ones when the temperature increases. In Fig. 14.21 is shown the white emission spectrum for blue (~450 nm) pumped LED based on orange–yellow $CaAlSiN_3$:Ce. The wLED has the color temperature of 3700 K, the color rendering index of 70, and the luminous efficacy of 51 lm/W, respectively [70]. As given in Table 14.4, the color rendering index R9 is significantly improved (compared to YAG-based wLED), since the red spectral part of the emission spectrum is enhanced.

Although the use of a single yellow phosphor in combination with a blue LED results in high luminous efficacy, the color rendering index is less than 80. To enhance the color rendering, it is necessary to utilize red and green phosphors, i.e., the mutli-phosphor approach (See Fig. 14.22). In this approach, green and red phosphors, or green, yellow, and red phosphors are blended with the epoxy resin, and then mounted on the LED chip. In addition to realizing high color rendering index, the color temperature of white light could also be varied by controlling the phosphor blend ratio.

In Fig. 14.23 are shown the luminescence spectra of warm white LEDs using multi-phosphors. High color rendering index is then expected (See Table 14.5). Typically, the deep red color rendering for the multi-phosphor-converted white LEDs is excellent [85, 86]. The emission spectrum of the 4-pc white LED nearly mimics the spectrum of the CIE standard illuminant A, leading to a super-high color rendering index of 98 [85]. The color temperature is 2840 and 2900 K for the 3-pc and 4-pc white LEDs, respectively. Compared to the 1-pc white LEDs, the multi-phosphor-converted white LEDs have lower luminous efficacy. For example, the luminous efficacy of the 4-pc warm white LED is 30 lm/W, but it far exceeds the incandescent lamps (~15 lm/W). The lower luminous efficacy for the multi-phosphor-converted white LEDs is due to increased reabsorption and optical losses, and lower lumen equivalent.

The “hallo effect” or bleed-through effect occurs in the architecture using the blue LED chip because the light from the blue LED is directional while the light

Fig. 14.22 Schematic of white LEDs with the phosphor-in-cup configuration

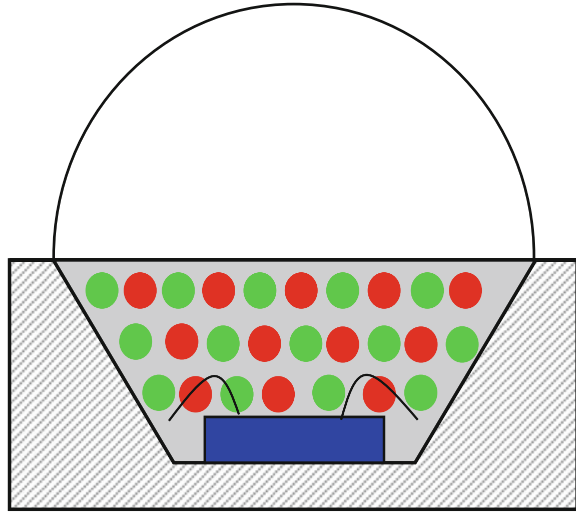

Fig. 14.23 Emission spectra of the 3-pc warm white LED usingβ-sialon:Eu, Ca-α-sialon:Eu and $CaAlSiN_3$:Ce, as well as the 4-pc warm white LED using $BaSi_2O_2N_2$:Eu, β-sialon:Eu, Ca-α-sialon:Eu, and $CaAlSiN_3$:Ce. The bias current is 20 mA

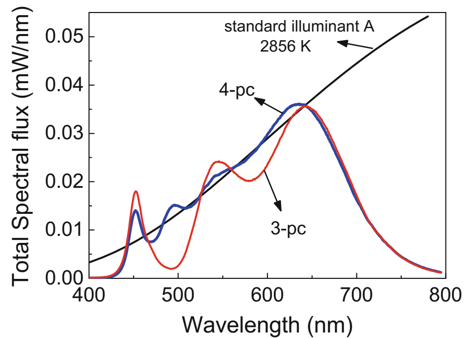

Table 14.5 Color rendering indices of 3-pc and 4-pc warm white LEDs

	Ra	R1	R2	R3	R4	R5	R6	R7	R8	R9
3-pc	88	97	90	73	92	91	80	89	91	96
4-pc	98	99	99	98	97	98	99	96	94	88

from the phosphor radiates over a 2p solid angle. In addition, much higher color rendering index (Ra > 95) is usually not realized by using the blue LED chip because there is a large gap in between the blue and green emission spectra (i.e., the number of green phosphors with λ_{em} < 525 nm is extremely limited). To avoid the hallo effect and further improve the color rendering index, it is required to use the UV or near UV LED chips [61].

Table 14.6 lists some examples of white LEDs by using difference phosphor combinations.

Table 14.6 Examples of phosphor-converted white LEDs

λ_{LED} (nm)	Phosphor(s)	η (lm/W)	CRI	CCT (K)	References
385	$La_{0.827}Al_{11.9}O_{19.09}$:Eu,Mn	–	–	3100–3600	[87]
395	$Sr_6B_5O_{20}:Eu^{2+}$ + (Sr, Ca)$_5(PO_4)_3Cl:Eu^{2+},Mn^{2+}$	–	87.3	5686	[88]
405	α-$Ca_2P_2O_7$:Eu,Mn + Ba_2SiO_4:Eu	9	78	10,465	[89]
405	Sr_3SiO_5:Ce,Li	25.0	69	–	[28]
405	JEM:Ce + β-sialon + α-sialon + $CaAlSiN_3$:Eu	19–20	95–96	2830–4300	[61]
450	Ca-α-sialon:Eu	25.9	61	2750	[48]
450	Li-α-sialon:Eu	46–55	60–65	3000–5200	[47]
450	(La,Ca)$_3Si_6N_{11}$:Ce	34.8	65	2911	[69]
450	$CaAlSiN_3$:Ce	50	70	3722	[70]
450	$Sr_{1.95-x}Eu_{0.05}Bi_xSiO_4$	10–25	65–68	8000–10,000	[90]
450	$Sr_3Si_{13}Al_3O_2N_{21}$:Eu + (Sr,Ca)$_2SiO_4$:Eu	56–62	82–88	3230–6450	[68]
450	Ca-α-sialon:Yb + $Sr_2Si_5N_8$:Eu	17–23	82–83	2744–6508	[91]
450	$Sr_2Si_5N_8$:Eu + YAG	94	72	3791	[92]
450	$Sr_2Si_5N_8$ + $SrSi_2O_2N_2$:Eu	25	>90	3200	[93]
450	$Ca_3Sc_2Si_3O_{12}$:Ce + (Sr,Ca)$AlSiN_3$:Eu	–	90	–	[94]
450	(Sr,Ca)$_3$(Al,Si)O_4(F,O):Ce +$K_2TiF_6:Mn^{4+}$	82	90	3088	[95]
450	β-sialon + α-sialon + $CaAlSiN_3$:Eu	24–28	81–88	2840–6580	[86]
450	$BaSi_2O_2N_2$ + β-sialon + α-sialon + $CaAlSiN_3$:Eu	25	95–98	–	[85]
455	$SrSi_2O_2N_2$:Eu + $CaSiN_2$:Ce	30	90.5	5206	[96]
460	Sr_3SiO_5:Ce,Li	31.7	81	–	[28]
460	$La_{1-x}CeSr_2AlO_5$	10–17	80–82	4340–5122	[97]
460	YAG:Ce + Sr_2SiO_4:Eu	40.9	76	5716	[98]
460	$Tb_3Al_3O_{12}$:Ce	34.1	79	5026	[98]
460	Sr_3SiO_5:Eu	41.3	57	3387	[98]
460	YAG	38.9	75	7756	[98]

14.4.2 *Remote-Phosphor White LEDs*

The "phosphor-in-cup" configuration has the advantages of compactness and ease of mass production. On the other hand, the disadvantages of this configuration include the photodegradation of the epoxy resin (yellowing) and low phosphor extraction efficiency. The yellowing of the epoxy resin is caused by the circulation of the emitted light from the phosphor and the unconverted blue light between the phosphor-distributed epoxy and the LED reflector. Moreover, the heat generated by the LED junction accelerates the degradation of the epoxy. The efficiency loss of phosphor is attributable to the reflection of the blue light back into the LED chip and the large fraction of reemitting light directed into the LED chip. It has been reported that ~60% of the reemitted light backscatters to the LED chip, which significantly decreases the luminous flux. Therefore, separating of the phosphor-dispersed resin from the LED chip by a certain distance is one of the approaches to alleviate the yellowing of the resin and the reduction of the absorption of the reemitting light by the LED chip. This packaging mode is named the "remote-phosphor" configuration [84], as shown in Fig. 14.24.

Kim et al. [99] addressed that the conversion efficiency of the blue-pumped YAG:Ce yellow phosphor was enhanced by 15.4% by using the remote-phosphor configuration and diffuse reflector cup. Zhu et al. [100] suggested that for remote-phosphor white LEDs with multi-phosphor layers the highest light output was realized by placing the red phosphor as the second layer. And he also pointed out that the performance of the white LEDs was controlled by several factor, such as mixture or stacked layers, specific layer order, phosphor density, phosphor external quantum efficiency, overall spectral power distribution, phosphor photo-luminescence spectra. A lighting system based on the white LEDs using a

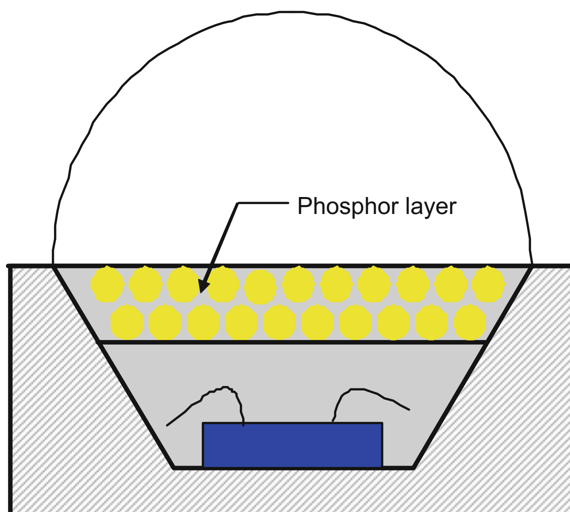

Fig. 14.24 Schematic of the remote-phosphor white LED configuration

remote-phosphor film (YAG:Ce) was investigated by Huang et al. [101] Compared with the lighting system using the traditional white LED with the phosphor-in-cup configuration, the novel system yielded higher lumen efficiency (73 vs. 64.7 lm/W), less angular color deviation, and more uniform luminous distribution (Uniformity = 82 vs. 12%).

In addition to the use of the mixture of phosphor powders and the organic resins, some other forms of the remote luminescence layer are also applied, such as transparent YAG:Ce ceramics, glass-ceramic phosphors and phosphor(s)/glass composites. Nishiura et al. [102] prepared a transparent yellow YAG:Ce ceramic which has the emission peak at 530 nm and transmittance of 70–87% at 800 nm. The white light was achieved by packing the ceramic with a blue LED (λ_{em} = 465 nm), and the emission color could be adjusted by controlling the thickness of the transparent ceramic. The luminous efficacy of 73.5 lm/W was obtained for the ceramic with the thickness of 0.632 nm. Tanabe et al. [103] suggested that the YAG glass-ceramic phosphors (Ce^{3+}-doped glasses in SiO_2–Al_2O_3–Y_2O_3 and SiO_2–Al_2O_3–Y_2O_3–Gd_2O_3 systems) could be used in high-power white LEDs. The quantum efficiency of the glass-ceramic phosphor is around 30%. Moreover, the glass-ceramic phosphor has the high thermal conductivity of 2.2 $Wm^{-1}K^{-1}$ (compared to 0.19 $Wm^{-1}K^{-1}$ of the resin) as well as a high bending strength of 125 MPa (compared to 93 MPa of the resin). Fujita et al. [104] reported that the luminous efficacy of the white LED using the glass-ceramic phosphor achieved 80% of that using the phosphor powder. Furthermore, the white LED using the glass-ceramic phosphor exhibited higher thermal resistance than the commercial white LEDs using the YAG phosphor powder (See Fig. 14.25). Cheng et al. [105] prepared the YAG-doped low-temperature glass (with the glass transition temperature of 400 °C) by distributing the YAG:Ce phosphor powder in a SiO_2–Na_2O–Al_2O_3–Li_2O glass, and firing it at 650 °C. The YAG-doped glass has the luminous efficacy of 51% with the YAG:Ce concentration of 4 wt%. Wang et al. [106] addressed that white LEDs employing the YAG:Ce-doped glass demonstrated better performances than the conventional ones using the YAG:Ce-distributed silicone resin (See Fig. 14.26), in terms of lumen loss, chromaticity shift,

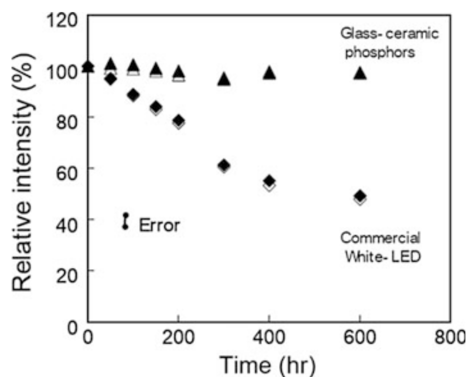

Fig. 14.25 Emission intensity change in the heat-resistant test of the YAG glass-ceramic phosphor and commercial white LEDs (Reprinted from [104], with permission)

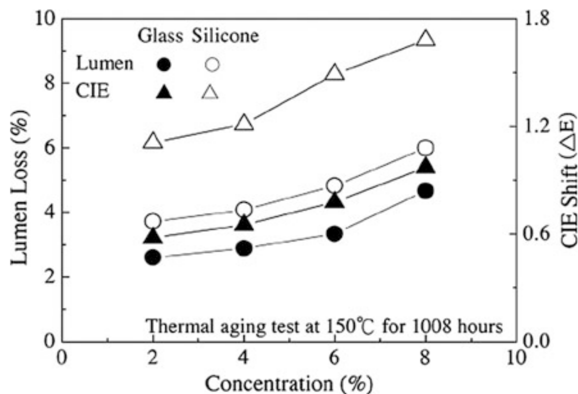

Fig. 14.26 Lumen loss and CIE shift as a function of the YAG:Ce concentration in the thermal aging test for white LEDs using the YAG-doped glass and the YAG-distributed silicone resin (Reprinted from [106], with permission)

transmittance loss as well as peak emission intensity undergoing three industry-standard reliability tests (i.e., 150 °C thermal aging for 1008 h, 85% RH/85 °C damp heat for 1008 h, and −40 to 125 °C thermal shock for 200 cycles).

14.4.3 Quantum Dots White LEDs

Semiconductor nanocrystals, i.e., quantum dots (QDs), have been also proposed to be alternative color-conversion materials in wLEDs, because they exhibit high photon conversion efficiency (~80%), high photostability, and wide absorption spectrum. Their optical properties can be conveniently tuned by controlling size and shape, and using different material systems [107]. Moreover, the narrow emission linewidths (FWHM ~ 30 nm) enable the custom-design of a desired emission spectrum by using proper combinations of differently sized QDs.

CdSe QDs are one of the extensively investigated nanocrystals with high quantum efficiencies, and their emission colors can be readily adjusted in the range of 500–650 nm by manipulating the particle size [108–111]. The use of CdSe QDs in wLEDs has been reported in the literature recently. Chen et al. [112] synthesized core-shell CdSe–ZnSe QDs which exhibited a high quantum yield of ~40% and size-tunable emission colors (510–620 nm). A three band white LED with the color rendering index Ra of 91 was attempted by combining CdSe–ZnSe QDs with the InGaN blue chip (See Fig. 14.27). Jang et al. [109] prepared a high color rendering white LED by using Sr_3SiO_5:Ce^{3+}, Li^+ (yellow) and CdSe QDs (red), the color rendering index Ra, and the luminous efficacy being 90.1 lm/W and 14 lm/W, respectively. Lita et al. [113] synthesized a CdSe-silica nanocomposite phosphor, and packed it with the blue GaN chip to obtain stable and efficient wLEDs.

As the Cd-based compounds are not green materials, Cd-free QDs with high quantum yields are thus required. Zhang et al. [114] reported white LEDs using heavy metal-free quantum dots. White light was obtained by mixing the red emission of ZnCuInS/ZnS core/shell QDs and the blue–green emission of

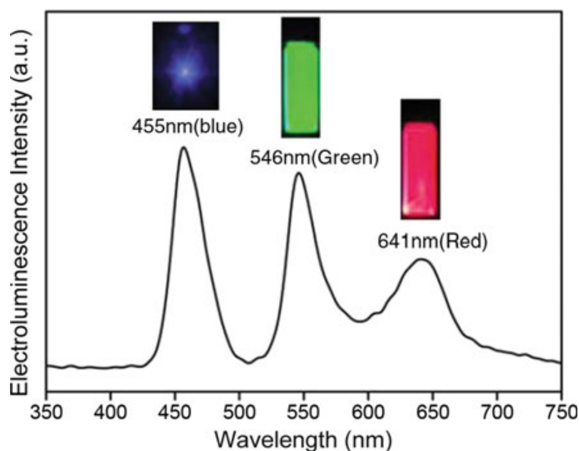

Fig. 14.27 Emission spectrum of the InGaN-CdSe-ZnSe QDs white LEDs (Reprinted from [112], with permission)

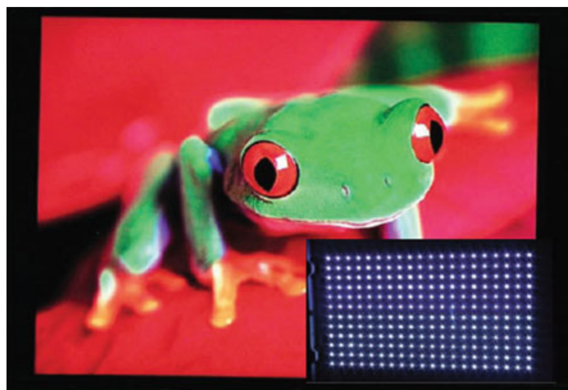

Fig. 14.28 A 46-in. LCD TV panel using the white QD-LED backlight (Reprinted from [111], with permission)

poly(N,N″-bis(4-butylphenyl)-N,N″-bis(phenyl)benzidine) with blue LED chips. A high color rendering index of 92 was achieved as compared to a 5310 K blackbody reference.

White QD-LEDs are very suitable for use in the display applications because of their high color rendering properties. Jang et al. [111] prepared highly luminescent core-shell CdSe/ZnS/CdSZnS (green) and CdSe/CdS/ZnS/CdSZnS (red) QDs with external quantum efficiency of 72% and 34%, respectively. A white QD-LED backlight with the color gamut of 100% of the NTSC standard and a luminous efficacy of 41 lm/W was achieved, which was then applied in a 46 inch LCD TV panel (See Fig. 14.28). By using the white QD-LEDs, Nanosays also announced a LCD backlight product which produced a triangular color gamut exceeding 100% of Adobe RGB and provided an improvement of 20% in power efficiency compared to existing backlight solutions [115].

14.5 Summary and Perspective

Recent trends and developments in LED phosphor materials and white LED packaging are overviewed in this chapter. Although a large quantity of phosphors have been investigated as down-conversion luminescent materials for white LEDs, only a very limited number of them can be used practically. To judge whether the phosphors are valuable for wLEDs or not depends mainly on their photoluminescence spectra, quantum efficiency, thermal quenching/degradation, chemical stability, etc. According to these requirements, the selection rules of host crystals and activator ions have been proposed.

The rare-earth phosphors that are commercially available now include yttrium aluminum garnets, alkaline earth orthosilicates, and (oxo)nitrido(alumino)silicates. Among these, (oxo)nitrido(alumino)silicates demonstrate their superior suitability in producing highly reliable and efficient wLEDs with high color rendition and tunable color temperatures. Luminescent quantum dots with very slim emission spectra and high efficiencies have been shown as promising alternative color-conversion materials in lighting and displays, but the production cost, stability/reliability, and the limited host crystals are the major problems for QDs.

Novel phosphor materials with excellent photoluminescence properties are continuously pursued by material scientists and chemists, with focus on understanding the crystal structure, photoluminescence spectra, and the relationship between them. In addition to the searching for new materials, the modifications of the existing phosphors are also the interesting topics, such as the enhancement of photoluminescence properties, tuning of the emission colors, particle size and morphology control, optimization of processing conditions, and so on.

Considering their use in the LED packaging, phosphors are also required to have the refractive index close to that of epoxy resin to enhance the luminous efficacy of wLEDs. However, the refractive index is not available for most phosphors. In addition, the phosphors including (oxo)nitridosilicates have the thermal quenching/degradation problems when they are combined with LED chips. It is thus necessary to understand the quenching/degradation mechanisms through the reliability test (for example, high temperature and high humidity test, thermal attack test, etc.) and finally to solve the problems.

The optical quality of wLEDs (i.e., luminous efficacy, chromaticity, and lifetime) is significantly dependent on chip processing, packaging configuration, heat sink material/structure, phosphor materials, and the epoxy resin. The "remote-phosphor" wLEDs reduce the reabsorbed light by the LED chip as well as the thermal attacks on phosphors and the epoxy resin, and show higher luminous efficacy than traditional "phosphor-in-cup" wLEDs. By using heat sink materials and structures, the thermal effect on the packaging materials, such as the yellowing of the epoxy resin, will be significantly reduced. In addition, to achieve high performance of wLEDs, the phosphor concentration, geometry, and particle size/morphology should be carefully considered [116–119]. The low concentration phosphor mixture employed in LED packaging usually leads to flux enhancement and stable color point, due to the

reduced reabsorption of the phosphor mixture and the absorption saturation. Further, the LED chip/green/red phosphors geometry is superior to the chip/phosphors (mixed randomly) geometry in reducing the reabsorption of green light by the red phosphor.

Much attention is now paid to the reliability assessments of wLEDs. Degradations induced by external stresses (i.e., temperature and moisture) dramatically affect the long lumen maintenance of wLEDs, leading to the lumen loss of LED chips, the transparency reduction and refractive index change of the resin, and the compositional change and lumen loss of phosphors as well [120]. Therefore, to truly understand the factors determining the reliability and use them to set an appropriate warranty period can reduce the risks of a higher than expected rate of claim against the warranty and the end users' dissatisfaction with the products. The reliability of wLEDs is thus becoming an urgent topic that needs to be strengthened.

References

1. Y. Narukawa, M. Ichikawa, D. Sanga, M. Sano, T. Mukai, White light emitting diodes with super-high luminous efficacy. J. Phys. D Appl. Phys. **43**(35), 354002 (2010)
2. http://www.cree.com/news-and-events/cree-news/press-releases/2012/april/120412-254-lumen-per-watt
3. J.K. Kim, E.F. Schubert, Transcending the replacement paradigm of solid-state lighting. Opt. Express **16**, 21835–21842 (2008)
4. M.R. Krames, O.B. Shckekin, R. Mueller-Mach, G.O. Mueller, L. Zhou, G. Harbers, M.G. Craford, Status and future of high-power light-emitting diodes for solid state lighting. J. Displ. Technol. **3**, 160–175 (2007)
5. W.M. Yen, S. Shionoya, H. Yamamoto, *Phosphor Handbook*, 2nd edn. (CRC Press, Boca Raton, 2006)
6. R.J. Xie, Y.Q. Li, N. Hirosaki, H. Yamamoto, *Nitride Phosphors and Solid State Lighting* (CRC Press, Boca Raton, 2010)
7. P.F. Smet, A.B. Parmentier, D. Poelman, Selecting coversion phosphors for white light-emitting diodes. J. Electrochem. Soc. **158**, R37–R54 (2011)
8. A. Pavese, G. Artioli, M. Prencipe, X-ray single-crystal diffraction study of pyrope in the temperature 30-973 K. Am. Mineral. **80**, 457–464 (1995)
9. E.P. Meagher, The crystal structures of pyrope and grossularite at elevated temperatures. Am. Mineral. **60**, 218–228 (1975)
10. S. Nakamura, S.F. Chichibu, *Introduction to Nitride Semiconductor Blue Lasers and Light Emitting Diodes* (Taylor & Francis, London, 2000)
11. G. Blasse, A. Bril, A new phosphor for flying spot cathode-ray tubes for color television: yellow emitting $Y_3Al_5O_{12}:Ce^{3+}$. Appl. Phys. Lett. **11**, 53–55 (1967)
12. A.A. Setlur, W.J. Heward, Y. Gao, A.M. Srivastava, R.G. Chandran, M.V. Shankar, Crystal chemistry and luminescence of Ce^{3+}-doped $Lu_2CaMg_2(Si, Ge)_3O_{12}$ and its use in LED based lighting. Chem. Mater. **18**, 3314–3322 (2006)
13. J. Silver, R. Withnall, Color conversion phosphors for LEDs, in *Luminescent Materials and Applications*, ed. by A. Kitai (Wiley, 2008)
14. V. Banchmann, C. Ronda, A. Meijerink, Temperature quenching of yellow Ce^{3+} luminescence in YAG:Ce. Chem. Mater. **21**, 2077–2084 (2009)

15. J. Ueda, S. Tanabe, T. Nakanishi, Analysis of Ce^{3+} luminescence quenching in solid solutions between $Y_3Al_5O_{12}$ and $Y_3Ga_5O_{12}$ by temperature dependence of photoconductivity measurement. J. Appl. Phys. **110**, 053102 (2011)
16. W.W. Holloway, M. Kestigian, Optical properties of cerium-activated garnet crystals. J. Opt. Soc. Am. **59**, 60–63 (1969)
17. H.S. Jang, W.B. Im, D.C. Lee, D.Y. Jeon, S.S. Kim, Enhancement of red spectral emission intensity of $Y_3Al_5O_{12}$:Ce^{3+} phosphor via Pr co-doping and Tb substitution for the application to white LEDs. J. Lumin. **126**, 371–377 (2007)
18. Y.S. Lin, R.S. Liu, B.M. Cheng, Investigation of the luminescent properties of Tb^{3+}-substituted YAG:Ce,Gd phosphors. J. Electrochem. Soc. **152**(6), J41–J45 (2005)
19. A.A. Setlur, W.J. Heward, M.E. Hannah, U. Happek, Incorporation of Si^{4+}-N^{3-} into Ce^{3+}-doped garnets for warm white LED phosphors. Chem. Mater. **20**, 6277–6283 (2008)
20. H.S. Jang, J.H. Kang, Y.H. Won, K.M. Chu, D.Y. Jeon, Origin of the discrepancy between photoluminescence brightness of TAG: Ce and electroluminescence brightness of TAG: Ce-based white LED expected from phosphor brightness. Opt. Lett. **33**(18), 2140–2142 (2008)
21. Y. Shimomura, T. Honma, M. Shigeiwa, T. Akai, K. Okamoto, N. Kijima, Photoluminescence and crystal structure of green-emitting $Ca_3Sc_2Si_3O_{12}$:Ce^{3+} phosphors for white light emitting diodes. J. Electrochem. Soc. **154**, J35–J38 (2007)
22. A.A. Setlur, W.J. Heward, Y. Gao, A.M. Srivastava, R.G. Chandran, M.V. Shankar, Crystal chemistry and luminescence of Ce^{3+} -doped $Lu_2CaMg_2(Si, Ge)_3O_{12}$ and its use in LED based lighting. Chem. Mater. **18**, 3314–3322 (2006)
23. J.L. Wu, G. Gundiah, A.K. Cheetham, Structure-property correlations in Ce-doped garnet phosphors for use in solid state lighting. Chem. Phy. Lett. **441**, 250–254 (2007)
24. T.L. Barry, Fluorescence of Eu^{2+} activated phase in binary alkaline earth orthosilicate system. J. Electrochem. Soc. **115**, 1181–1183 (1968)
25. G. Blasse, W.L. Wanmaker, J.W. Vrugt, A. Bril, Fluorescence of Eu^{2+}-activated silicates. Philips Res. Repts. **23**, 189–200 (1968)
26. J.K. Park, C.H. Kim, S.H. Park, H.D. Park, S.Y. Chois, Application of strontium silicate yellow phosphor for white light-emitting diodes. Appl. Phys. Lett. **84**, 1647–1649 (2004)
27. J.K. Park, K.J. Choi, J.H. Yeon, S.J. Lee, C.H. Kim, Embodiment of the warm white-light-emitting diodes by using a Ba^{2+} codoped Sr_3SiO_5: Eu phosphor. Appl. Phys. Lett. **88**, 043511 (2006)
28. H.S. Jang, D.Y. Yeon, Yellow-emitting Sr_3SiO_5:Ce^{3+}, Li^+ phosphor for white-light-emitting diodes and yellow-light-emitting diodes. Appl. Phys. Lett. **90**, 041906 (2007)
29. T.L. Barry, Luminescent properties of Eu^{2+} and Eu^{2+}+Mn^{2+} activated $BaMg_2Si_2O_7$. J. Electrochem. Soc. **117**, 381–385 (1968)
30. W.J. Yang, L.Y. Luo, T.M. Chen, Luminescence and energy transfer of Eu- and Mn-coactivated $CaAl_2Si_2O_8$ as a potential phosphor for white-light UVLED. Chem. Mater. **17**, 3883–3888 (2005)
31. J.S. Kim, P. Jeon, J.C. Choi, Warm-white-light emitting diode utilizing a single-phase full-color $Ba_3MgSi_2O_8$:Eu^{2+}, Mn^{2+} phosphor. Appl. Phys. Lett. **84**, 2931–2933 (2004)
32. M.P. Saradi, U.V. Varadaraju, Photoluminescence studies on Eu^{2+}-activated Li_2SrSiO_4—a potential orange-yellow phosphor for solid-state lighting. Chem. Mater. **18**, 5267–5272 (2006)
33. Y. Hu, W. Zhuang, H. Ye, S. Zhang, Y. Fang, X. Huang, Preparation and luminescent properties of $(Ca_{1-x}Sr_x)S$:Eu^{2+} red-emitting phosphor for white LED. J. Lumin. **111**, 139–145 (2005)
34. D. Poelman, J.E. Haecke, P.F. Smet, Advances in sulfide phosphors for displays and lighting. J. Mater. Sci.: Mater. Electron. **20**, S134–S138 (2009)
35. T.E. Peter, J.A. Baglio, Luminescence and structural properties of thiogallate phosphors Ce^{3+} and Eu^{2+} activated phosphors. Part I. J. Electrochem. Soc. **119**, 230–236 (1972)

36. R. Mueller-March, G.O. Mueller, M.R. Krames, T. Trottier, High-power phosphor-converted light-emitting diodes based on III-nitrides. IEEE J. Sel. Topics Quantum Electron **8**, 339–345 (2002)
37. Y.R. Do, K.Y. Ko, S.H. Na, Y.D. Huh, Luminescence properties of potential $Sr_{1-}xCa_xGa_2S_4$: Eu green and greenish-yellow-emitting phosphors for white LED. J. Electrochem. Soc. **153**, H142–H146 (2006)
38. R.-J. Xie, N. Hirosaki, Silicon-based oxynitride and nitride phosphors for white LEDs—a review. Sci. Tech. Adv. Mater. **8**, 588–600 (2007)
39. W. Schnick, Nitridosilicates, oxonitridosilicates (sions), and oxonitridoaluminosilicates (sialons)—new materials with promising properties. Int. J. Inorg. Mater. **3**, 1267–1272 (2001)
40. M. Zeuner, S. Pagano, W. Schnick, Nitridosilicates and oxonitridosilicates: from ceramic materials to structural and functional diversity. Angew. Chem. Int. Ed. **50**, 7754–7775 (2011)
41. G.Z. Cao, R. Metselaar, α'-sialon ceramics, a review. Chem Mater. **3**, 242–252 (1991)
42. J.W.H. van Krevel, J.W.T. van Rutten, H. Mandal, H.T. Hintzen, R. Metselaar, Luminescence properties of terbium-, cerium-, or europium-doped α-sialon materials. J. Solid State Chem. **165**, 19–24 (2002)
43. R.-J. Xie, M. Mitomo, K. Uheda, F.F. Xu, Y. Akimune, Preparation and luminescence spectra of calcium- and rare-earth (R = Eu, Tb, and Pr)-codoped α-SiAlON ceramics. J. Am. Ceram. Soc. **85**, 1229–1234 (2002)
44. R.-J. Xie, N. Hirosaki, K. Sakuma, Y. Yamamoto, M. Mitomo, Eu^{2+}-doped Ca-alpha-SiAlON: a yellow phosphor for white light-emitting diodes. Appl. Phys. Lett. **84**, 5404–5406 (2004)
45. R.-J. Xie, N. Hirosaki, M. Mitomo, Y. Yamamoto, T. Suehiro, Optical properties of Eu^{2+} in α-SiAlON. J. Phys. Chem. B **108**, 12027–12031 (2004)
46. R.-J. Xie, N. Hirosaki, M. Mitomo, K. Takahashi, K. Sakuma, Highly efficient white-light-emitting diodes fabricated with short-wavelength yellow oxynitride phosphors. Appl. Phys. Lett. **88**, 101104 (2006)
47. R.-J. Xie, N. Hirosaki, M. Mitomo, K. Sakuma, N. Kimura, Wavelength-tunable and thermally stable Li-α-SiAlON: Eu^{2+} oxynitride phosphors for white light-emitting diodes. Appl. Phys. Lett. **89**, 241103 (2006)
48. K. Sakuma, K. Omichi, N. Kimura, M. Ohashi, D. Tanaka, N. Hirosaki, Y. Yamamoto, R.-J. Xie, T. Suehiro, Warm-white light-emitting diode with yellowish orange SiAlON ceramic phosphor. Opt. Lett. **29**, 2001–2003 (2004)
49. T. Ekstrom, M. Nygen, SiAlON ceramics. J. Am. Ceram. Soc. **75**, 259–276 (1992)
50. K.H. Jack, Review—sialons and related nitrogen ceramics. J. Mater. Sci. **11**, 1135–1158 (1976)
51. H. Hirosaki, R.-J. Xie, K. Kimoto, T. Sekiguchi, Y. Yamamoto, T. Suehiro, M. Mitomo, Characterization and properties of green-emitting β-SiAlON:Eu^{2+} powder phosphors for white light-emitting diodes. Appl. Phys. Lett. **86**, 211905-1–211905-3 (2005)
52. R.-J. Xie, N. Hirosaki, H.L. Li, Y.Q. Li, M. Mitomo, Synthesis and photoluminescence properties of α-sialon:Eu^{2+} ($Si_{6-z}Al_zO_zN_{8-z}$:Eu^{2+})—a promising green oxynitride phosphor for white light-emitting diodes. J. Electrochem. Soc. **154**, J314–J319 (2007)
53. Y.Q. Li, N. Hirosaki, R.-J. Xie, T. Takeda, M. Mitomo, Crystal and electronic structures, luminescence properties of Eu^{2+}-doped $Si_{6-z}Al_zO_zN_{8-z}$ and $M_ySi_{6-z}Al_{z-y}O_{z+y}N_{8-z-y}$ (M = 2Li, Mg, Ca, Sr, Ba). J. Solid State Chem. **181**, 3200–3210 (2008)
54. K. Kimoto, R.-J. Xie, Y. Matsui, K. Ishizuka, N. Hirosaki, Direct observation of single dopant atom in light-emitting phosphor of β-SiAlON:Eu^{2+}. Appl. Phys. Lett. **94**, 041908 (2009)
55. R.-J. Xie, N. Hirosaki, T. Takeda, Wide color gamut backlight for liquid crystal displays using three-band phosphor-converted white light-emitting diodes. Appl. Phys. Express **2**, 022401 (2009)

56. K. Uheda, N. Hirosaki, Y. Yamamoto, A. Naoto, T. Nakajima, H. Yamamoto, Luminescence properties of a red phosphor, $CaAlSiN_3:Eu^{2+}$, for white light-emitting diodes. Electrochem. Solid State Lett. **9**, H22–H25 (2006)
57. X.Q. Piao, T. Horikawa, H. Hanzawa, K. Machida, Characterization and luminescence properties of $Sr_2Si_5N_8:Eu^{2+}$ phosphor for white light-emitting-diode illumination. Appl. Phys. Lett. **88**, 161908 (2006)
58. Y.Q. Li, J.E.J. van Steen, J.W.H. van Krevel, G. Botty, A.C.A. Delsing, F.J. DiSalvo, G. de With, H.T. Hintzen, Luminescence properties of red-emitting $M_2Si_5N_8:Eu^{2+}$ (M = Ca, Sr, Ba) LED conversion phosphors. J. Solid State Compd. **417**, 273–279 (2006)
59. C.J. Duan, X.J. Wang, W.M. Otten, A.C.A. Delsing, J.T. Zhao, H.T. Hintzen, Preparation, electronic structure, and photoluminescence properties of Eu^{2+}- and Ce^{3+}/Li^{+}-activated alkaline earth silicon nitride $MSiN_2$ (M = Sr, Ba). Chem. Mater. **20**, 1597–1605 (2008)
60. H. Watanabe, H. Wada, K. Seki, M. Itou, N. Kijima, Synthetic method and luminescence properties of $Sr_xCa_{1-x}AlSiN_3:Eu^{2+}$ mixed nitride phosphors. J. Electrochem. Soc. **155**, F31–F36 (2008)
61. K. Takahashi, N. Hirosaki, R.-J. Xie, M. Harada, K. Yoshimura, Y. Tomomura, Luminescence properties of blue $La_{1-x}Ce_xAl(Si_{6-z}Al_z)(N_{10-z}O_z)(z \sim 1)$ oxynitrides phosphors and their application in white light-emitting diode. Appl. Phys. Lett. **91**, 091923 (2007)
62. T. Suehiro, N. Hirosaki, R.-J. Xie, T. Sato, Blue-emitting $LaSi_3N_5:Ce^{3+}$ fine powder phosphor for UV-converting white light diodes. Appl. Phys. Lett. **95**, 051903 (2009)
63. K. Inoue, N. Hirosaki, R.-J. Xie, T. Takeda, Highly efficient and thermally stable blue-emitting $AlN:Eu^{2+}$ phosphor for ultraviolet white light-emitting diodes. J. Phys. Chem. C **133**, 9392–9397 (2009)
64. V. Bachmann, C. Ronda, O. Oeckler, W. Schnick, Meijerink., Color point tuning for (Sr, Ca, Ba)SiON: Eu for white light LEDs. Chem. Mater. **21**, 316–325 (2009)
65. C. Braun, M. Seibald, S.L. Börger, O. Oeckler, T.D. Boyko, A. Moewes, G. Miehe, A. Tuckes, W. Schnick, Material properties and structural characterization of $M_3Si_6O_{12}N_2:Eu^{2+}$ (M = Ba, Sr)—a comprehensive study on a promising green phosphor for pc-LEDs. Chem. Euro. J. **16**, 9646–9657 (2010)
66. O. Oeckler, J.A. Kechele, H. Koss, P.J. Schmidt, W. Schnick, $Sr5Al_{5+x}Si_{21-x}N_{35-x}O_{2+x}:Eu^{2+}$ ($x \approx 0$)—a novel green phosphor for white light pcLEDs with disordered intergrowth structure. Chem. Eur. J. **15**, 5311–5319 (2009)
67. K. Shioi, Y. Michiue, N. Hirosaki, R.-J. Xie, T. Takeda, Y. Matsushita, M. Tanaka, Y.Q. Li, Synthesis and photoluminescence of a novel $Sr\text{-}SiAlON:Eu^{2+}$ blue-green phosphor ($Sr_{14}Si_{68}\text{-}sAl_{6+s}O_sN_{106-s}:Eu^{2+}$ ($s \approx 7$)). J. Alloy Compds. **509**, 332–337 (2011)
68. Y. Fukuda, K. Ishida, I. Mitsuishi, S. Nunoue, Luminescence properties of Eu^{2+}-doped green-emitting Sr-Sialon phosphor and its application to white light-emitting diodes. Appl. Phys. Express. **2**, 012401 (2009)
69. T. Suerhiro, N. Hirosaki, R.-J. Xie, Synthesis and photoluminescent properties of $(La, Ca)_3Si_6N_{11}:Ce^{3+}$ fine powder phosphors for solid-state lighting. ACS Appl. Mater. Interf. **3** (3), 811–816 (2011)
70. Y.Q. Li, N. Hirosaki, R.-J. Xie, T. Takeda, M. Mitomo, Yellow-orange-emitting $CaAlSiN_3:Ce^{3+}$ phosphor: structure, photoluminescence, and application in white LEDs. Chem. Mater. **20**, 6704–6714 (2008)
71. R.-J. Xie, N. Hirosaki, T. Suehiro, F.-F. Xu, M. Mitomo, A simple, efficient synthetic route to $Sr_2Si_5N_8:Eu^{2+}$-based red phosphors for white lighting-emitting diodes. Chem. Mater. **18**, 5578–5583 (2006)
72. J. Ruan, R.-J. Xie, N. Hirosaki, T. Takeda, Nitrogen gas pressure sintering and photoluminescence properties of orange-red $SrAlSi_4N_7:Eu^{2+}$ phosphors for white light-emitting diode. J. Am. Ceram. Soc. **94**(2), 536–542 (2011)
73. A.H. Munsell, *A Color Notation*, 1st edn. (Munsell Color Company, Baltimore, MD, 1905); A.H. Munsell, *Atlas of the Munsell Color System* (Wadsorth-Howland & Company, Malden, MA, 1915)

74. Y. Ohno, Color rendering and luminous efficacy of white LED spectra, in *Proceedings of SPIE*, vol. 5530, ed. by I.T. Ferguson, N. Narendran, S.P. DenBaars, J.C. Carrano (SPIE, Bellingham, 2004), pp. 88–98
75. A. Zukauskas, R. Vaicekauskas, F. Ivanauskas, R. Gaska, M.S. Shur, Optimization of white polychromatic semiconductor lamps. Appl. Phys. Lett. **80**, 234–236 (2002)
76. A. Zukauskas, M.S. Shur, R. Gaska, *Introduction to Solid State Lighting* (Wiley, New York, 2002)
77. R.W.G. Hunt, M.R. Pointer, *Measuring Colour* (Wiley, New York, 2011)
78. V.L. Colvin, M.C. Schlamp, A.P. Alivisatos, Light-emitting diodes made from cadmium selenide nanocrystals and a semiconducting polymer. Nature **370**, 354–357 (1994)
79. B. Damilano, N. Grandjean, F. Semond, J. Massies, M. Leroux, From visible to white light emission by GaN quantum dots on Si(111) substrate. Appl. Phys. Lett. **75**, 962–964 (1999)
80. B. Damilano, N. Grandjean, F. Semond, J. Massies, M. Leroux, Violet to orange room temperature luminescence from GaN quantum dots on Si(111) substrates. Phys. Status Solidi B **216**, 451–455 (1999)
81. Y. Li, A. Rizzo, R. Cingolani, G. Gigli, White-light-emitting diodes using semiconductor nanocrystals. Microchim. Acta **159**, 207–215 (2007)
82. A.J. Shields, Semiconductor quantum light sources. Nat. Photonics **1**(215), 1–18 (2007)
83. I.K. Park, J.Y. Kim, M.K. Kwon, C.Y. Cho, J.H. Lim, S.J. Park, Phosphor-free white light-emitting diode with laterally distributed multiple quantum wells. Appl. Phys. Lett. **92**, 091110-1 (2008)
84. J.K. Kim, H. Luo, E.F. Schubert, J. Cho, C. Sone, Y. Park, Strongly enhanced phosphor efficiency in GaInN white light-emitting diodes using remote phosphor configuration and diffuse reflector cup. Jpn. J. Appl. Phys. **44**(21), L649–L651 (2005)
85. N. Kimura, K. Sakuma, S. Hirafune, K. Asano, N. Hirosaki, R.-J. Xie, Extrahigh color rendering white light-emitting diode lamps using oxynitride and nitride phosphors excited by blue light-emitting diode. Appl. Phys. Lett. **90**, 051109 (2007)
86. K. Sakuma, N. Hirosaki, N. Kimura, M. Ohashi, R.-J. Xie, Y. Yamamoto, T. Suehiro, K. Asano, D. Tanaka, White light-emitting diode lamps using oxynitride and nitride phosphor materials. IEICE Trans. Electron. **E88-C**, 2057–2064 (2005)
87. H.S. Jang, W.B. Im, D.Y. Jeon, J.S. Lee, Tunable full-color-emitting $La_{0.827}Al_{11.9}O_{19.09}$: Eu^{2+}, Mn^{2+} phosphor for application to warm white-light-emitting diodes. Appl. Phys. Lett. **89**, 231909 (2006)
88. M. Zhang, J. Wang, W. Ding, Q. Zhang, Q. Su, A novel white light-emitting diode (w-LED) fabricated with $Sr_6BP_5O_{20}:Eu^{2+}$ phosphors. Appl. Phys. B **86**, 647–651 (2007)
89. J.H. Zhang, X. Zhang, X. Sun, Y. Luo, S. Lu, X.J. Wang, White light emitting diode by using α-$Ca_2P_2O_7:Eu^{2+}$, Mn^{2+} phosphor. Appl. Phys. Lett. **90**, 261113 (2007)
90. S.H. Park, H.S. Yoon, H.M. Boo, H.G. Jang, K.H. Lee, W.B. Im, Efficiency and thermal stability enhancement of $Sr_2SiO_4:Eu^{2+}$ phosphor via Bi^{3+} codoping for solid state white lighting. J. Jpn. Appl. Phys. **51**, 022602 (2012)
91. R.-J. Xie, N. Hirosaki, N. Kimura, K. Sakuma, M. Mitomo, 2-phosphor-converted white light-emitting diodes using oxynitride/nitride phosphors. Appl. Phys. Lett. **90**, 191101 (2007)
92. S.E. Brinkley, N. Pfaff, K.A. Denault, Z.J. Zhang, H.T. Hintzen, R. Seshadri, S. Nakamura, S.P. DenBaars, Robust thermal performance of $Sr_2Si_5N_8:Eu^{2+}$: an efficient red emitting phosphor for light emitting diode based white lighting. Appl. Phys. Lett. **99**, 241106 (2011)
93. R. Mueller-Mach, G. Mueller, M.R. Krames, H.A. Hoppe, F. Stadler, W. Schnick, T. Juestel, P. Schmidt, Highly efficient all-nitride phosphor-converted white light emitting diode. Phy. Status Solidi (A) **202**, 1727–1732 (2005)
94. H. Watanabe, H. Wada, K. Seki, M. Itou, N. Kijima, Synthetic method and luminescence properties of $Sr_xCa_{1-x}AlSiN_3:Eu^{2+}$ mixed nitride phosphors. J. Electrochem. Soc. **155**, F31–F36 (2008)
95. A.A. Setlur, E.V. Radkov, C.S. Henderson, J.H. Her, A.M. Srivastava, N. Karkada, M.S. Kishore, N.P. Kumar, D. Aesram, A. Deshpande, B. Kolodin, L.S. Grigorov, U. Happek,

Energy-efficient, high-color-rendering LED lamps using oxyfluoride and fluorite phosphors. Chem. Mater. **22**, 4076–4082 (2010)

96. C.C. Yang, C.M. Lin, Y.J. Chen, Y.T. Wu, S.R. Chuang, R.S. Liu, S.F. Hu, Highly stable three-band white light from an InGaN-based blue light-emitting diode chip precoated with (oxy)nitride green/red phosphors. Appl. Phys. Lett. **90**, 123503 (2007)
97. W.B. Im, N.N. Fellows, S.P. DenBaars, R. Seshadri, Y.I. Kim, $LaSr_2AlO_5$, a versatile host compound for Ce^{3+}-based yellow phosphors: structural tuning of optical properties and use in solids state white lighting. Chem. Mater. **21**, 2957–2966 (2009)
98. H.S. Jang, Y.H. Won, D.Y. Jeon, Improvement of electroluminescent properties of blue LED coated with highly luminescent yellow-emitting phosphors. Appl. Phys. B **95**, 715–720 (2009)
99. J.K. Kim, H. Luo, E.F. Schubert, J. Cho, C. Sone, Y. Park, Strongly enhanced phosphor efficiency in GaInN white light-emitting diodes using remote phosphor configuration and diffuse reflector cup. Jpn. J. Appl. Phys. **44**(21), L649–L651 (2005)
100. H.T. Huang, Y.P. Huang, C.C. Tsai, Planar lighting system using array of blue LEDs to excite yellow remote phosphor film. J. Display Technol. **7**(1), 44–51 (2011)
101. Y. Zhu, N. Narendran, Investigation of remote-phosphor white light-emitting diodes with multi-phosphor layers. Jpn. J. App. Phys. **49**, 100203 (2010)
102. S. Nishiura, S. Tanabe, K. Fujioka, Y. Fujimoto, Properties of transparent Ce:YAG ceramic phosphors for white LED. Opt. Mater. **33**, 688–691 (2011)
103. S. Tanabe, S. Fujita, S. Yoshihara, A. Sakamoto, S. Yamamoto, YAG glass-ceramic phosphor for white LED (II): luminescence characteristics. Proc. SPIE **5941**, 594112-1 (2005)
104. S. Fujita, S. Yoshihara, A. Sakamoto, S. Yamamoto, S. Tanabe, YAG glass-ceramic phosphor for white LED (I): background and development. Proc. SPIE **5941**, 594111-1 (2005)
105. W.C. Cheng, S.Y. Huang, C.C. Tsai, J.S. Liou, J.H. Chang, J. Wang, W.H. Cheng, The efficacy study of Ce:YAG doped low-temperature glass for white LED modules, in *Proceedings of the 16th Opto-electronics and Communication Conference,* 2011, pp. 481–482
106. J. Wang, C.C. Tsai, W.C. Cheng, M.H. Chen, C.H. Chung, W.H. Cheng, High thermal stability of phosphor-converted white light-emitting diodes employing Ce:YAG-doped glass, IEEE. J. Sel. Topics Quantum Electron. **17**(3), 741–746 (2011)
107. A.P. Alivisators, Perspectives on the physical chemistry of semiconductor nanocrystals. J. Phys. Chem. **100**, 13226–13239 (1996)
108. M.J. Bowers, J.R. McBridge, S.J. Rosenthal, White-light emission from magic-sized cadmium selenide nanocrystals. J. Am. Chem. Soc. **127**, 378 (2005)
109. H.S. Jang, H. Yang, S.W. Kim, J.Y. Han, S.G. Lee, D.Y. Jeon, White light-emitting diodes with excellent color rendering based on organically caped CdSe quantum dots and Sr_3SiO_5: Ce^{3+},Li^+ phosphors. Adv. Mater. **20**, 2696–2702 (2008)
110. W. Chung, K. Park, H.J. Yu, J. Kim, B.Y. Chun, S.H. Kim, White emission using mixtures of CdSe quantum dots and PMMA as a phosphor. Opt. Mater. **32**, 515–521 (2010)
111. E. Jang, S. Jun, H. Jang, J. Lim, B. Kim, Y. Kim, White-light-emitting diodes with quantum dot color converters for display backlights. Adv. Mater. **22**(28), 3076–3080 (2010)
112. H.S. Chen, C.K. Hus, H.Y. Hong, InGaN-CdSe-ZnSe quantum dots white LEDs. Photon. Technol. Lett. **18**, 193–195 (2006)
113. A. Lita, A.L. Washington II, L. Van de Burgt, G.F. Strouse, A.E. Stiegman, Stable efficient solid-state white-light-emitting phosphors with a high scotopic/photopic ratio fabricated from fused CdSe-silica nanocomposites. Adv. Mater. **22**, 3987–3991 (2010)
114. Y. Zhang, C. Xie, H. Su, J. Liu, S. Pickering, Y. Wang, W.W. Yu, J. Wang, Y. Wang, J. Hahm, N. Dellas, S.E. Mohney, J. Xu, Employing heavy metal-free colloidal quantum dots in solution-processed white light-emitting diodes. Nano Lett. **11**, 329–332 (2011)
115. http://www.qled-info.com/nanosys-qdef-led-backlight-technology-at-sid-2011/
116. N.T. Tran, J.P. You, F.G. Shi, Effect of phosphor particle size on luminous efficacy of phosphor-converted white LEDs. J. Lightwave Technol. **27**, 5145–5150 (2009)

117. Y.C. Lin, J.P. You, N.T. Tran, Y. He, F.G. Shi, Packaging of phosphor based high power white LEDs: effects of phosphor concentration and packaging configuration. J. Electron Packing. **133**, 011009 (2011)
118. J.P. You, N.T. Tran, F.G. Shi, Light extraction enhanced white light-emitting diodes with multi-layered phosphor configuration. Opt. Express **18**, 5055–5060 (2010)
119. Y.H. Won, H.S. Jang, K.W. Cho, Y.S. Song, D.Y. Jeon, H.K. Kwon, Effect of phosphor geometry on the luminous efficiency of high-power white light-emitting diodes with excellent color rendering property. Opt. Lett. **34**, 1–3 (2009)
120. M. Meneghini, A. Tazzoli, G. Mura, G. Meneghesso, E. Zanoni, A review on the physical mechanisms that limit the reliability of GaN-based LEDs. IEEE Trans. Electron Dev. **57**, 108–118 (2010)

Chapter 15
High-Voltage LEDs

Wen-Yung Yeh, Hsi-Hsuan Yen, Kuang-Yu Tai and Pei-Ting Chou

Abstract In this chapter, the basic mechanisms, opto-electrical characteristics, variety designs, and development process of the high-voltage light-emitting diode (HVLED) and alternating current light-emitting diode (ACLED) were extensively discussed. Some important issues, such as the efficiency drooping, flickering illumination, harmonic distortion limitation, and lifetime result of the HV/ACLED were also studied. Furthermore, packaging methods, safety considerations, and measurement techniques of the HV/ACLED were mentioned to assist readers in applying the HV/ACLED safely and properly.

15.1 Introduction of Assembled HVLED Modules and Single-Chip HVLEDs

With the phasing out of incandescent light bulbs, the development of high efficiency, low pollution alternative light sources has become a common objective of the world's leading manufacturers and research institutes. In particular, light-emitting diodes (LEDs), with their high efficiency, lengthy lifetime, compact size, absence of mercury, etc., are widely considered to be the most promising candidates for becoming the mainstream light sources of the future. Nonetheless, for end users, the decision on the kind of new lighting products to purchase hinges not only on factors such as efficiency and environmental friendliness but also on prices and compatibility with existing equipment. In view of this, researchers, while continuing their works on improving LED luminous efficacy, should at the same time ponder how end users can more conveniently utilize LED lighting products in their everyday lives.

Due to the inherent limitations imposed by the physical mechanism underpinning the operation of a LED, the typical operating voltage of a single LED die, depending on the materials utilized in the fabrication process, falls between 1.8–3.3 V.

W.-Y. Yeh (✉) · H.-H. Yen · K.-Y. Tai · P.-T. Chou
Industrial Technology Research Institute, Hsinchu, Taiwan, ROC
e-mail: WenYungYeh@itri.org.tw

© Springer Nature Singapore Pte Ltd. 2017

T.-Y. Seong et al. (eds.), *III-Nitride Based Light Emitting Diodes and Applications*,
Topics in Applied Physics 133, DOI 10.1007/978-981-10-3755-9_15

The mains voltages worldwide range from 100–220 V AC, and the use of a single LED die for lighting purposes at such mains voltages will require the coupling of the single LED die with rectifier and transformer elements. However, the addition of rectifier and transformer elements will inevitably increase the cost and scale of the LED lighting module. Additionally, the shorter lifetimes of the rectifier and transformer elements compared to those of the LEDs, as well as the waste heat generated during the operation, will further lower the efficiency and shorten the lifetime of the entire LED lighting module. In view of these shortcomings, researchers and manufacturers alike have attempted to develop LED lighting modules operating at mains voltages and with less reliance on electronic devices.

Figure 15.1 shows the schematic diagrams of fluorescent lamp type and light bulb type high-voltage LED (HVLED), or also so-called alternating current LED (ACLED), lighting modules obtained by assembling several encapsulated LED dies on a circuit board. By connecting the LED dies in series via a circuit board, one enables their use in a high-voltage AC environment with only rectifier elements. In comparison with traditional high power LED dies which easily consume hundreds of mA of drive current, assembled HVLED modules not only do not require the use of transformers for operations but also can reduce transmission line losses due to their low drive currents, thereby further enhancing the luminous efficacy of the LED modules. On the other hand, assembled HVLED modules also suffer from several shortcomings; for example, they are difficult to reduce in size and their light emission mode is similar to that of flat light sources and thus limits the scope and flexibility for application.

To resolve the aforementioned issues, the concept of single-chip HVLED die (henceforth referred to as HVLED) was proposed. Compared to assembled HVLED modules, HVLEDs not only retain the advantage of LED operation at high voltage, but also are compact and possess a concentrated emission area, rendering them eminently suitable for use as light source elements in such standard lightings as the

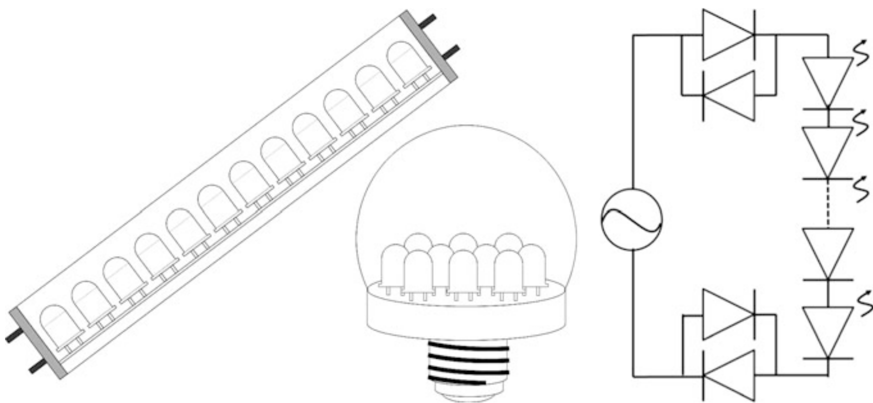

Fig. 15.1 Schematic diagrams for a HVLED lighting modules

E12, E27, and MR16. In this chapter, we shall discuss in detail the development processes as well as operating characteristics of HVLEDs, and compare the differences in the opto-electrical properties of HVLED and traditional low voltage DCLED dies during practical use.

15.2 Fabrication, Development, and Characteristics of HVLEDs

HVLEDs are fabricated with semiconductor manufacturing processes, through which several micro-chips are formed on the same substrate and electrically connected with metal wires. The fabrication technology is very similar to that utilized in the fabrication of traditional LEDs. However, the distinct drive modes, especially under AC driving conditions, necessarily mean that HVLEDs will exhibit distinct characteristics from traditional LEDs and thus require significantly different design considerations. In this section, we shall describe the fabrication flow of HVLEDs as well as the unique opto-electrical properties of the LED devices under AC, and discuss the development processes and differences of the disparate types of HVLEDs.

15.2.1 Structure and Fabrication of HVLED Micro-Chip

Figure 15.2 shows the structural diagram for a HVLED die. The micro-chips were fabricated on the same substrate and connected via metal wires, while the high-voltage drive current is injected into the micro-chip array via the two wire pads at the opposite ends. From the side view of the micro-chip structure in Fig. 15.3, one can see that the structure of a single micro-chip differs from that of a traditional LED only in size, while other features such as the transparent conductive layer, surface roughness, and patterned sapphire substrate, all employed extensively to enhance the efficiency of traditional LEDs, are readily transferrable to HVLEDs. The key differences in the fabrication of HVLED and traditional LED dies are the use of the insulating substrate, the etching of the insulation trench, as well as the fabrication of the metal wire.

The core concept of HVLED is to fabricate and connect several micro-chips in series on the same substrate. Therefore, the use of the insulating substrate to ensure electrical insulation between the micro-chips is a fundamental condition for the normal operation of HVLEDs. For LEDs grown with GaN materials, the sapphire substrates used already possess excellent insulating properties, and one can achieve excellent electrical insulation simply by etching trenches among the micro-chips until the substrate is exposed. However, most red LEDs grown with AlGaInP materials employ electrically conducting GaAs as the substrate, and one must

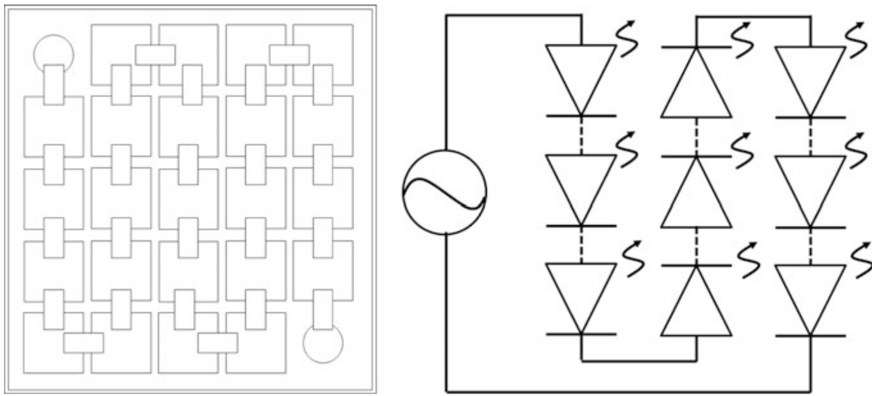

Fig. 15.2 The *top view* of a HVLED structure

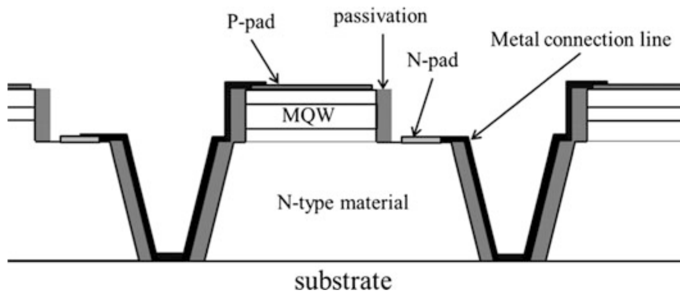

Fig. 15.3 The *side view* of the structure of a GaN micro-chip grown on a sapphire substrate

necessarily resolve the issue of the conductivity of the substrate before the mass production of high-voltage AlGaInP LEDs is even possible. The feasible approaches include the use of insulating GaAs materials as the substrate, the transfer of the AlGaInP epitaxial structure to the insulating substrate, or the use of insulating materials to effect the transfer of the AlGaInP epitaxial structure to any arbitrary substrate, etc., all of which will serve the purpose of ensuring electrical insulation among the micro-chips. Figure 15.4 shows the side-view structural diagram and actual operating conditions of an AlGaInP HVLED device where the original substrate was replaced with an insulating substrate.

In addition, from Fig. 15.5, one can see that although the insulation trenches amongst the micro-chips are critical for the normal operation of the HVLED, they also reduce the overall light emission area of the HVLED die. Although increasingly thin insulation trenches will theoretically increase the light emission area of the HVLED die, the complexity of the fabrication process will also increase accordingly. The sidewalls of the insulation trenches need to be coated with a layer of dielectric materials to avoid a short circuit between the PN materials where the metal wires are deposited across the surface. However, when the insulation trenches

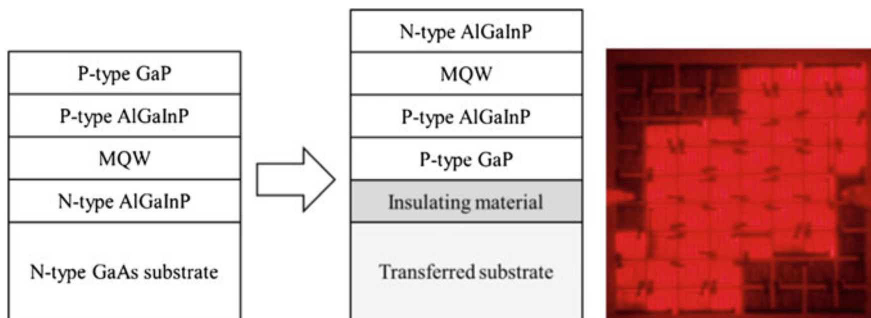

Fig. 15.4 Structural diagram and actual operating conditions of a device where the AlGaInP substrate was replaced with an insulating substrate

Fig. 15.5 SEM photographs of a HVLED die

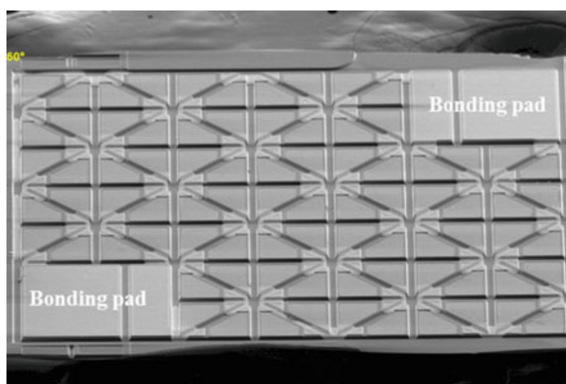

are overly thin, incomplete coating is likely to occur, regardless of whether one employs chemical vapor deposition or evaporation for the fabrication of the dielectric films, leading to the short circuit of the PN materials and thus failure of the micro-chip. Likewise, insulation trenches that are overly thin are not easily accessible to the metal vapor, resulting in an overly thin or even discontinuous metal wire film, and subsequently an increase in the series resistance of the HVLED die or even open circuit failure. In order to enhance the process yield of the dielectric coating and conducting metal film, one feasible approach is to employ an inverted trapezoidal structure for the fabrication of the insulation trench, with the opening facing upward.

The sloped sidewall structure shown in Fig. 15.6 can improve the manufacturing yield of the micro-chips and the HVLED, and the nonrectangular geometrical structure will also help enhance the light extraction efficiency of the micro-chip. In addition, to prevent the metal shielding from reducing the luminous efficacy of the HVLED, the metal wires amongst the micro-chips must also simultaneously possess low impedance and low light obscuration. The fabrication of narrow yet thick metal wire is one feasible approach for achieving the aforementioned objective.

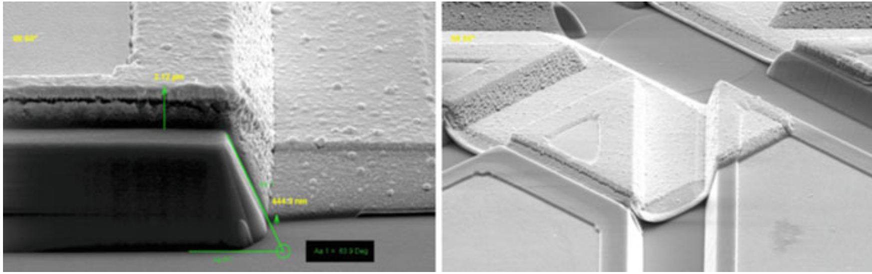

Fig. 15.6 Micro-chip structure with sloped sidewalls and inverted trapezoidal opening

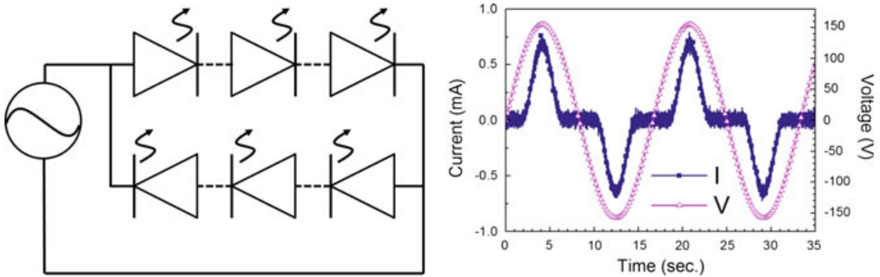

Fig. 15.7 Equivalent circuit and the time-dependent relationship between the voltage and current for a HVLED

Another viable possibility is the use of transparent metal oxides (such as ITO or ZnO) as the wire material. Both approaches will help to enhance the luminous efficacy of the HVLED.

15.2.2 Basic Characteristics and Methods of Measurement for HVLEDs Under AC Operation

In addition to the chip structure and a number of the fabrication steps, the key differences between traditional DCLEDs and HVLEDs are the low voltage DC and high-voltage AC drive modes employed, respectively. The different drive modes result in drastically different opto-electrical properties of the devices, meaning that the measurement techniques must also be modified accordingly. A traditional DCLED is driven by a constant direct current and one can simply integrate over time at any instance after the device characteristics have stabilized to obtain accurate measurements of its operating power and luminous intensity. However, this is not the case for AC-driven HVLEDs. Figure 15.7 shows the equivalent circuit of a HVLED device, as well as the time-dependent relationship between the voltage and current. When a HVLED is driven by a sine wave type AC voltage, it

will only start emitting light when the input voltage is higher than the threshold voltage. Therefore, when driven under AC, HVLEDs often exhibit a flashing phenomenon also known as pulsed emission.

From Fig. 15.7, one can see that for this HVLED operating under AC, the frequency of the light output will be identical to the frequency of the current, both twice the frequency of the input AC voltage. In addition, under AC operation, the current and light output intensity of a HVLED at any instance will vary continually with the time-dependent input voltage, and it is difficult to extrapolate the full characteristics of the HVLED from data accrued from an arbitrary instance in time. The current consensus is that a better measurement approach is to set the integration time of the measurement to an integer multiple of the period of the input AC voltage. Take a HVLED operating under a 60 Hz AC voltage as an example; the integration time for the measurement can be set to 50 ms, which covers three full AC cycles, whereas the integration time for the measurement for a HVLED operating under a 50 Hz AC voltage can be set to 60 ms.

15.2.3 Light Emission Characteristics of HVLEDs Under AC Operation

Being driven by AC voltage not only transforms the light emission of HVLEDs from the steady mode under DC to the flashing mode under AC, but also significantly impacts the luminous efficacy. In Fig. 15.8, we compared the current characteristics of the same HVLED operating under DC and AC. When the operating power was 0.45 W in both cases, the operating voltage of the HVLED under DC and AC were 125 V and 100 $V_{rms,}$ respectively. Since the threshold voltage of the HVLED was about 90 V, an input voltage between 90–140 V ($100\,V * \sqrt{2}$) was required to induce a response current under AC operation and thus light emission. This duration accounted for about 60% of the AC voltage cycle. In addition, under

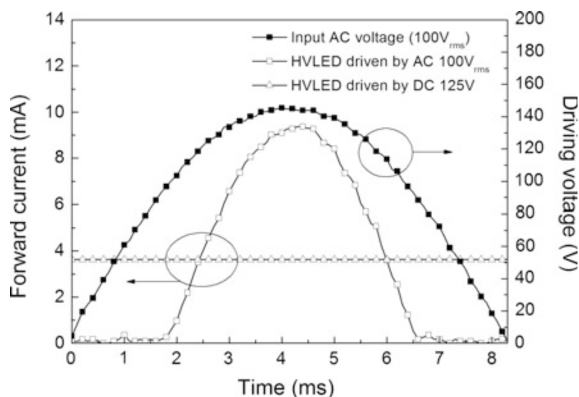

Fig. 15.8 Time-dependent relationship of the forward current and driving voltage in the HVLED, when driven under DC and AC

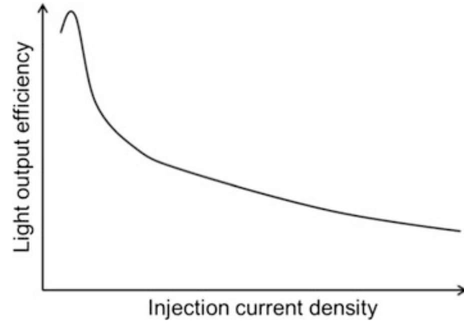

Fig. 15.9 Relationship between the injection current density and luminous efficacy of a LED

DC operation, the current in the HVLED was constant at 3.6 mA. Under AC operation, the current in the HVLED ranged from 0 to 9.5 mA and varied with changes in the input voltage. If one compares only the duration in which a response current could be observed in the HVLED under AC operation, for more than 70% of the time, the response current in the HVLED under AC operation is higher (or much higher than) than that under DC operation.

Figure 15.9 shows the relationship between the injection current density and the LED luminous efficacy. Due to the efficiency drooping effect, the internal quantum efficiency of the LED will decrease with increasing current density passing through the LED, thereby lowering the overall luminous intensity and efficacy of the LED. Since the current or current density in a HVLED driven by AC is higher during most of the light emission cycle, a HVLED operating under AC exhibits lower luminous intensity or efficacy than when operating under DC, provided that the operating power and light emission area are identical. From the above discussions, one can see that although operating a HVLED under AC sidesteps the drawbacks of the rectifier and transformer elements, the luminous efficacy is limited by the physical mechanism and will necessarily be lower than that of a traditional DCLED with the same light emission area and operating power. To rectify the aforementioned issue, different designs for HVLEDs have been proposed. We shall introduce, in chronological order of their development, the designs and characteristics of HVLEDs that are representative of their respective generations.

15.2.4 Design and Characteristics of HVLED Devices

15.2.4.1 Anti-parallel HVLED

The equivalent circuit of the first single-chip HVLED is shown in Fig. 15.10. The core concept is to connect two chains of micro-chips fabricated on the same insulating substrate in an anti-parallel configuration, enabling at least one chain of micro-chips to be under forward bias and thus light emitting, regardless of the bias of the input AC voltage. However, clearly, in such an anti-parallel type HVLED

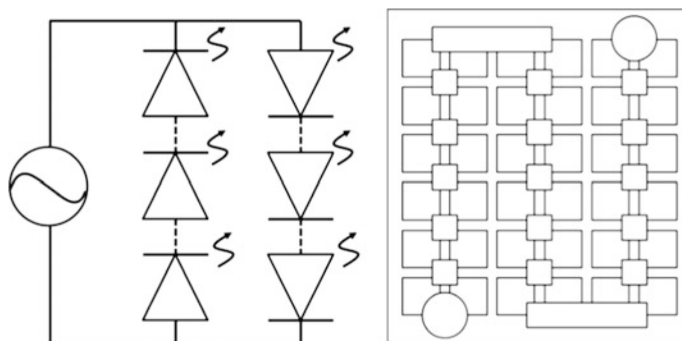

Fig. 15.10 Equivalent circuit for an anti-parallel HVLED die

(AP-HVLED), only half of the micro-chips will be luminescent at any instance under AC operation, with the remaining half of the micro-chips not illuminated since they are under reverse bias. Therefore, when calculating the ratio of the light emission area of a HVLED at any instance, one obtains chip area utilization efficiency (CAUE) of only 50% for the AP-HVLED. Although the two chains of micro-chips in the AP-HVLED design will be alternatively luminescent, the CAUE is a paltry 50%. As such, under AC operation, the current density passing through the micro-chips within the AP-HVLED is still about 2 times that in a traditional DCLED with identical chip area and effective operating power. In other words, if one wishes to operate an AP-HVLED under AC with similar luminous efficacy to that of a traditional DCLED with the same effective operating power, even without taking into account the efficiency drooping effect on the luminous efficacy, the chip area of the AP-HVLED must still be at least two times that of the traditional DCLED.

Although the AP-HVLED successfully realizes the concept of a single-chip HVLED, the low CAUE necessarily implies that its operating current density will be higher than that of a traditional DCLED with the same area and operating power. While boosting the area of the AP-HVLED die is a feasible approach for solving the aforementioned problem, an excessively large chip area will result in increased production costs. Therefore, developing a HVLED die with a higher CAUE became a primary goal of researchers.

15.2.4.2 Wheatstone Bridge HVLED

The equivalent circuit of a Wheatstone bridge type HVLED (WB-HVLED) with greater than 50% CAUE is shown in Fig. 15.11. In the standard design of a WB-HVLED, the micro-chips on the insulating substrate are arranged into an array that assumes the form of a Wheatstone bridge and placed in four rectifier branches and an output branch. Regardless of the bias direction of the input AC, the micro-chips in two of the rectifier branches and the output branch of the

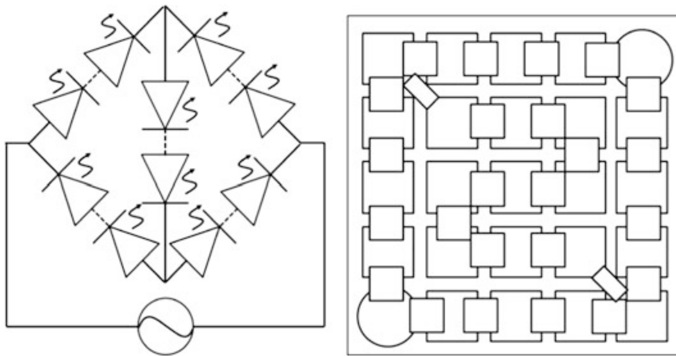

Fig. 15.11 Equivalent circuit of a Wheatstone bridge type HVLED die

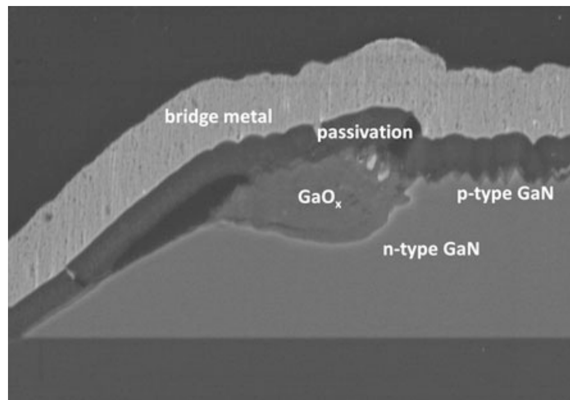

Fig. 15.12 Side-view SEM images of the destruction to the micro-grain structure caused by the GaO_x oxide

WB-HVLED will be under forward bias and thus luminescent, thereby enabling the WB-HVLED to exhibit a higher CAUE than the AP-HVLED does. For example, suppose the number of micro-chips (with identical area) in the rectifier branches and output branch of the WB-HVLED is 5 and 10 respectively. Under AC operation, there will be 20 micro-chips illuminated at any instance in the WB-HVLED, accounting for 67% of the 30 micro-chips. If one decreases the number of micro-chips in the rectifier branches while simultaneously increasing the number of micro-chips in the output branch, one can further enhance the CAUE of the WB-HVLED without altering the total number of uni-directional light-emitting micro-chips. For example, when the number of micro-chips in the rectifier and output branches of the WB-HVLED is 3 and 14 respectively, the number of uni-directional light-emitting micro-chips remains the same at 20. However, the total number of micro-chips is reduced to 26, enabling the CAUE of this type of WB-HVLED to soar to 77%. However, there are limitations on the use of such a mechanism to enhance the CAUE of the WB-HVLED. Figure 15.12 shows GaN micro-chips placed under excessively high reverse bias for a prolonged duration.

Lumps of GaO_x oxide can arise in the n-type GaN, leading to the destruction of the epitaxial structure of the micro-grain and thus device failure [1]. Although this phenomenon can be alleviated by fabricating a denser coating layer to block out water vapor, when the number of micro-chips in the rectifier branches is too low, the micro-chips in the rectifier branches may still suffer from reverse breakdown due to the excessively high reverse bias electric field, leading to short circuit failure of the WB-HVLED. In view of the above two factors, a more appropriate ratio of the number of micro-chips in the rectifier and the output branches of a GaN WB-HVLED is 1:3, with a CAUE of about 70%.

For HVLEDs, a chip design with a higher CAUE implies a higher luminous efficacy (for identical total chip area and operating power) or lower manufacturing costs (for identical light emission area under uni-directional bias). WB-HVLEDs that incorporate the concept of the Wheatstone bridge exhibit an increase in the CAUE to 70%, which represents an increase of 40% on the 50% CAUE exhibited in AP-HVLEDs, but the improvement still falls far short of the nearly 100% CAUE exhibited by traditional LEDs. Further attempts to enhance the CAUE of the WB-HVLEDs have floundered due to the fact that the LED micro-chips in the rectifier branches are unable to withstand too large a reverse bias. Extended operation at high reverse bias will lead to the formation of GaO_x oxide in the rectifier micro-chips and thus device failures. As such, it is not feasible to drastically enhance the CAUE without compromising on the reliability and longevity of the WB-HVLEDs. One possible solution is to employ selective area regrowing techniques in combination with the epitaxial structures of the LED and Schottky Barrier Diode (SBD) for the fabrication of WB-HVLEDs with SBD rectifier elements. The equivalent circuit is shown in Fig. 15.13. Since the capacity of the SBD

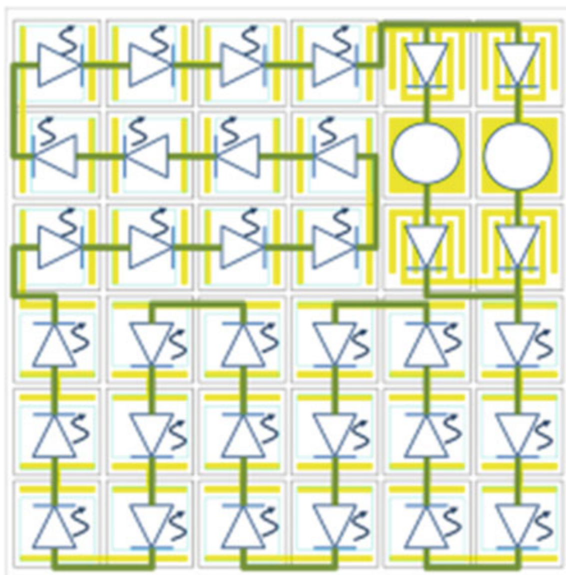

Fig. 15.13 A WB-HVLED utilizing four SBDs as the rectifier elements

to withstand reverse bias is far superior to those of the LED micro-chips, the use of merely four SBDs as rectifier elements in a WB-HVLED will enable normal operation under 110–220 V AC and an increase in the CAUE to more than 90%. However, at this point in time (early 2012), technologies enabling the epitaxial stacking of SBD and LED structures is still under research. Further, simultaneously optimizing the characteristics of the two devices is fraught with complications, and numerous issues will need to be clarified and resolved before the use of SBD as a rectifier element in a WB-HVLED and the subsequent mass production can be realized.

15.2.4.3 Hybrid HVLED

In view of the technical bottlenecks encountered in the continuing attempts to improve the CAUE of single-chip high HVLEDs, LED manufacturers and researchers begun attempts to redefine the mode of operation of the single-chip HVLED. In assembled HVLED modules, numerous encapsulated LEDs are typically connected in series to withstand high voltages, and then coupled with an external bridge component to enable the LED arrays to be illuminated regardless of the bias of the input AC. The same concept also applies to single-chip HVLEDs. The use of the external bridge component does away with the need for rectifier elements within the single-chip HVLED, and one needs only to configure the number of micro-chips capable of withstanding the uni-directional AC voltage in the array. Figure 15.14 shows the equivalent circuit of such a hybrid type HVLED (H-HVLED) chip coupled with external bridge components and operating under AC. Since all the micro-chips in the H-HVLED can be illuminated under bi-directional AC bias, its CAUE can be enhanced to the 100% exhibited by traditional DCLEDs, if one does not take into consideration the insulation trenches. Although the external bridge components increase the size and cost of a lighting

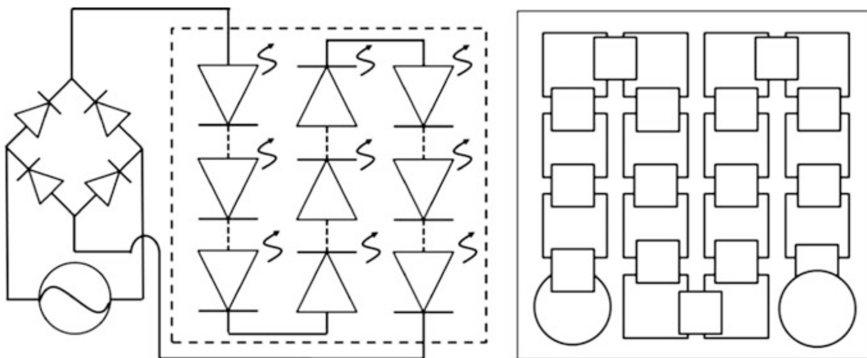

Fig. 15.14 Schematic diagram of the entire module consisting of a single-chip H-HVLED coupled with external bridge components

module employing the H-HVLED as the light source to levels slightly exceeding those of modules employing the AP-HVLED or WB-HVLED, when one considers the die by itself, the H-HVLED actually exhibits superior CAUE to both the AP-HVLED and WB-HVLED, and thus a higher luminous efficacy (for identical chip area) and lower manufacturing costs (for identical uni-directional light emission area). This is the main reason why the H-HVLED has become widely adopted by numerous LED die manufacturers at this point in time (early 2012).

15.2.5 Characteristics of Various HVLEDs and Traditional DCLED

Figure 15.15 shows the external views of a traditional DCLED as well as three different HVLED dies. All four dies were fabricated with the same GaN wafer and the same die area. We compared the opto-electrical properties of the four LEDs at the same operating power. In particular, the AP-HVLED, WB-HVLED and H-HVLED consisted of 54, 45, and 27 micro-chips respectively, and in all three designs, 27 micro-chips were illuminated under uni-directional bias. The areas of the micro-chips in the AP-HVLED and H-HVLED were identical, whereas the areas of micro-chips in the output branch of the WB-HVLED was twice that in the rectifier branches.

From Fig. 15.16, one can see that when all four LEDs were operated under DC, the order of the luminous intensity and efficacy of the dies was H-HVLED > DCLED > WB-HVLED > AP-HVLED. At the same operating power, an LED die with a smaller light emission area will exhibit higher operating power and current density, and the efficiency drooping effect will result in the internal quantum effectiveness of the LED die and the overall luminous efficacy becoming lower than that of the LED die with a larger light emission area. Since the CAUEs of the WB-HVLED and AP-HVLED were significantly lower than those of the H-HVLED and DCLED, the luminous efficacy of the former two must be less than those of the latter two. A comparison of the H-HVLED and DCLED revealed

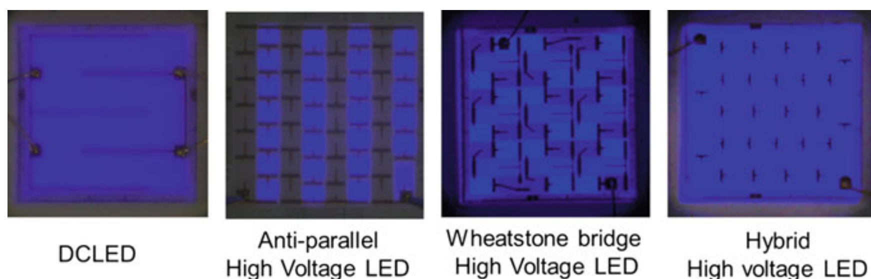

Fig. 15.15 Photos of a traditional DCLED and three different HVLED dies under DC operation

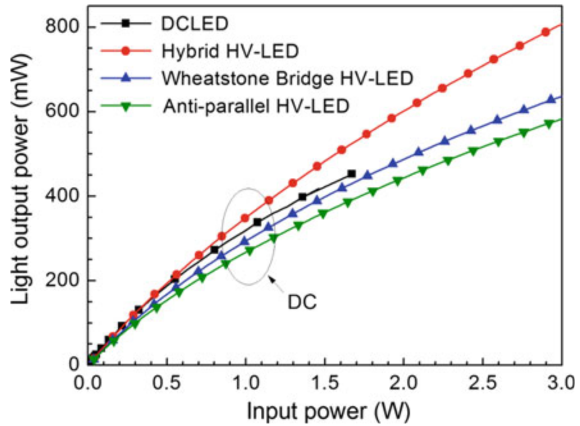

Fig. 15.16 Relationship between the input power and light output power for the four different LEDs under DC operation

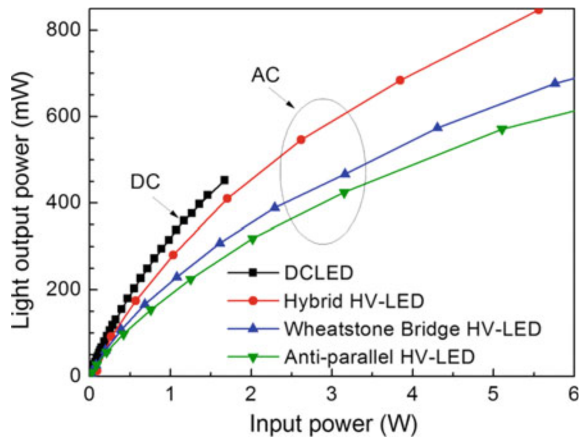

Fig. 15.17 Comparison of the input power and light output power of the four LEDs under different operating conditions

that although the CAUE of the H-HVLED was slightly lower than that of the DCLED after taking into consideration the losses due to the insulating trenches, the current diffusion uniformity of the H-HVLED was actually superior to that of the single-chip DCLED with greater area, since the H-HVLED was composed of numerous micro-chips with small area. Therefore, in comparison to the DCLED, in which the current tends to be concentrated near the electrodes, the H-HVLED exhibited better current diffusion properties. As such, the efficiency drooping effect was less pronounced. Further, the side wall structure of the micro-chips further increased the light extraction area and efficiency of the H-HVLED, enabling the H-HVLED to exhibit a higher luminous efficacy under DC operation than the DCLED did.

Figure 15.17 shows the comparison of the light-emitting efficacy of the AP-HVLED, WB-HVLED, and H-HVLED under AC operation with that of the DCLED under DC operation. By comparing with the characteristics measured

under DC operation, one can see that the luminous efficacy of three HVLEDs under AC operation all suffered significant declines. As discussed in Sects. 15.2.3 and 15.2.4, when the operating wattage or voltage is identical, the response current in a HVLED will be significantly higher than the response current under DC operation most of the time, resulting in the HVLED exhibiting lower luminous efficacy when operating under AC than when operating under DC because of the pronounced efficiency drooping effect. Thus, although the H-HVLED still exhibited higher luminous efficacy under AC operation compared to the WB-HVLED and AP-HVLED, it lagged slightly behind the performance of the DCLED.

In sum, our findings imply that, under DC operation, the H-HVLED exhibited higher luminous efficacy, lower circuit losses, and higher module efficiency than the DCLED did. However, under AC operation, the H-HVLED, due to the impact of efficiency drooping effect, exhibited luminous efficacy that was slightly lower than that of the DCLED under DC operation. Since the WB-HVLED and AP-HVLED had CAUEs that were both significantly lower than those of the H-HVLED and DCLED, their luminous efficiencies lagged rather far behind those of the H-HVLED and DCLED both under DC and AC operations. Under the premise that the chip area was identical, all three of the HVLEDs, namely H-HVLED, WB-HVLED, and AP-HVLED, exhibited inferior luminous efficacy under AC operation to the traditional DCLED. Nonetheless, the elimination of some of the electronic devices offers tangible competitive advantages for the HVLED modules in terms of cost, space, and lifetime. Should technological breakthroughs allow one to reduce or even completely avert the negative impacts of the efficiency drooping effect on the internal quantum efficiency of the LED through modifying the epitaxial structure, the luminous efficacy of HVLEDs operating under AC can be further brought closer to the level of DCLEDs, thereby allowing one to make the former even more competitive in comparison.

15.3 Important Issues on the Applications of HVLEDs

The applications for HVLEDs can be classified into two categories, namely high DC voltage drive mode and high AC voltage drive mode. The former is characterized by stable optical output characteristics, and particular attention needs to be paid to the flammability and pressure withstanding capability of the encapsulation materials. For the latter, the optical output characteristics of the devices will vary according to changes in the AC input. Therefore, on top of the aforementioned encapsulation material properties, one must also further explore issues such as light flickering, harmonic distortion and optical–electrical measurements. In addition, since the opto-electrical characteristics vary significantly from those of traditional DCLEDs, the evaluation and estimation of the lifetime will also be one of the most important issues.

15.3.1 Characteristics of and Possible Solutions for Light Flickering

HVLEDs typically operate at a frequency of 60 Hz. Due to the AC driving mode of the devices, the brightness as perceived by the human eye will vary dynamically at the rate of 120 Hz. The perception threshold of the human eye to flickering is about 100 Hz. Therefore, the 120 Hz variation in the HVLED light source can result in the perception of flickering for some people. In order to overcome, the potential problems associated with the flickering phenomenon of the HVLED light source as well as to enhance the luminous performance, thereby enabling HVLEDs to gain wider acceptance in the lighting application markets, numerous studies are currently in progress to identify possible solutions, one of which is the development of high thermal stability, long afterglow phosphor materials for encapsulating HVLEDs and thus eradicating the flickering phenomenon. When a HVLED is driven by an AC voltage, the latter assumes the form of an alternating sine wave. The HVLED light source will exhibit cycles of bright and dark light emission states, and the development of the new long afterglow phosphors will alter the luminescence decay time after excitation of the fluorescent powder, enabling the decay time to 50% brightness to exceed the period of the bright and dark cycles. This will reduce the differences in the luminous intensity of the bright and dark states and thus vastly stabilize the light source output of the HVLEDs, as shown in Fig. 15.18.

An alternative approach is to employ an external combinational circuit to sidestep the light flickering of the HVLEDs. Both the industry and academia have successfully developed simple integrated circuits for overcoming the flickering, and these circuits, on top of alleviating the flickering, can also boost the power factor of the HVLED light source system. However, the issues of effectively reducing the

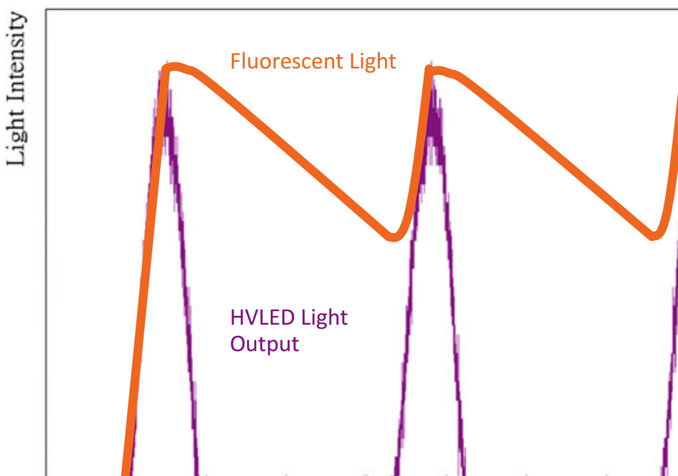

Fig. 15.18 Variation in the intensity of the HVLED output light and fluorescent light

size of the combinational circuit and its subsequent integration into the light source system, as well as considerations on the operating lifetime of the applications, are all challenges to be overcome.

15.3.2 Total Harmonic Distortion Limits

In addition to the impacts of the input operating voltage on the optical properties of the HVLEDs, one must also consider the issue of Total Harmonic Distortion (THD) for applications in lighting. The limits on the harmonic distortion for lighting fixtures consuming 25 W and above are clearly spelled out under the International Standards on Lighting Equipment IEC/EN 61000-3-2 (Harmonic Standards) Class C. The limits for lighting fixtures consuming less than 25 W are not specified [2]; however, under the U.S. ANSI C82.77 Standards (Harmonic Emission Limits—Related Power Quality Requirements for Lighting Equipment), it is expressly stipulated that the total harmonic distortion of light sources slated for illumination purposes must be less than 32% [3].

Although current HVLED devices typically consume less than 25 W of operating power by themselves, they will necessarily need to be integrated into light source modules in order to break into the field for lighting applications, in view of current LED device light radiation flux. In that case, the operating power will likely exceed 25 W. In other words, the total harmonic distortion for HVLEDs must also be in compliance with the IEC/EN 61000-3-2 Class C specifications and the ANSI C82.77 standards, as shown in Tables 15.1 and 15.2.

For compliance with the IEC/EN 61000-3-2 Class C and ANSI C82.77 total harmonic distortion specifications, one can alter the number of micro-chips on a single-chip HVLED to lower the threshold voltage and control the conduction angle

Table 15.1 IEC/EN 61000-3-2, class C, harmonic current limits (input power $\geqq$ 25 W)

Harmonic order (n)	Maximum permissible harmonic current expressed as a percentage of the input current at the fundamental frequency
2	2
3	30 * power factor
5	10
7	7
9	5
$11 \leqq n \leqq 39$	3

Table 15.2 ANSI C82.77 harmonic emission limits (commercial indoor hard wired ballasts or luminaries)

Input power (P)	Minimum PF	Maximum line current THD (fundamental)
All	0.9	32% and the requirements of ANNEX I

of the current, but this method will also test the high current density tolerance of the HVLED die itself. A more plausible solution is perhaps to employ simple combinations of electronic devices and highly efficient driver circuit designs to improve the total harmonic distortion of the light source system and at the same time improve the power factor of the entire lighting system.

15.3.3 The Effect of Floating Driving Voltage

The floating range of most mains voltages is about ±10%, and light sources that directly utilize AC will also exhibit cycles of brightness and darkness in their light outputs during operation in accordance with the floating voltage. The impacts on the human vision caused by the variations in the brightness of the light source are known as "stroboscopic effects," and they are characterized by a tendency to visually perceive fast-moving objects as slow-moving or stationary ones, which constitute obvious safety hazards. The unit for evaluating the light flux is known as the strobe depth, where a strobe depth of less than 5% may be regarded as the absence of stroboscopic effects.

The threshold of the human eye for perceiving strobe depth is 100 Hz. In HVLED applications, when the power supply exhibit fluctuations of ±10% for frequency of 100 Hz or less, the HVLEDs will exhibit strobe effects synchronized with the floating frequency, with a strobe depth of up to 50%. In such cases, prolonged use of said applications will result in discomforts to the human body.

Therefore, in order to overcome the strobe effects of the light source brought about by the variations in mains voltages, the development of a simple driving circuit to stabilize the driving voltage of the light source and hence reduce the strobe depth of the HVLED light output will also be a critical research thrust.

15.3.4 Safety Considerations of HVLED Encapsulation Structural Design

There is essentially little difference in the encapsulation mode of HVLEDs and that of DCLEDs. In both cases, the operating power of the LED will determine the design for the thermal dissipation structure, and the encapsulation modes can roughly be categorized into Surface Mounted Device (SMD), Chip-on-Board (COB), etc. In addition to continually developing and improving upon such traditional encapsulation approaches, LED manufacturers have begun contemplating other possible uses of LED components, and gradually devised a LED encapsulation device that can be plugged and unplugged and thus installed and replaced easily, as shown in Fig. 15.19. In other words, no welding is required, and one needs only plug the pins into a connector assembly. Especially for HVLED

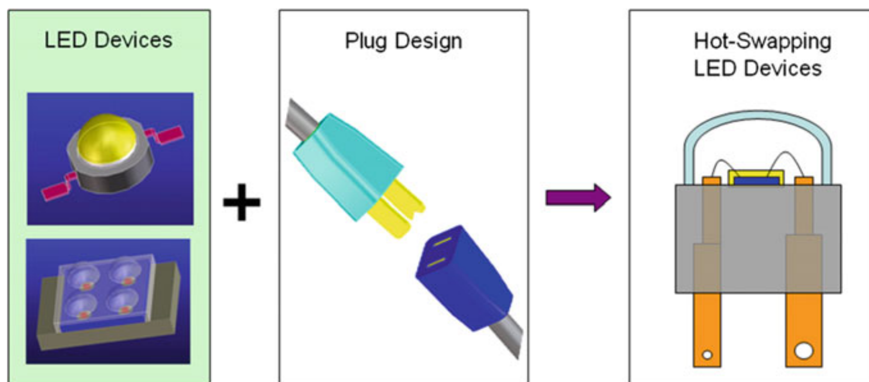

Fig. 15.19 Possible uses of HVLED encapsulation device

applications, the direct use of AC mains has made it more expedient for users to upgrade and replace HVLED light sources, thereby dramatically improving the ease of operation.

There are more restrictions on the structural design of HVLED encapsulation, the most important of which is the pin specifications of the encapsulated device. HVLED encapsulation devices still employ the traditional two-pin approach for electrical connection, and special attention needs to be paid to the pin spacing design.

In the official ANSI/UL 8750 (Standard for Light-Emitting Diode (LEDs) Equipment for Use in Lighting Product) safety specifications [4] released by the product safety testing and certification organization Underwriters Laboratories (UL) for LED lighting products and related devices, it was specifically pointed out that the two inputs must comply with the insulation requirements for meeting the highest operating voltage conditions of the entire circuit. Otherwise, the designer must do an excellent job of separating the pins. It is further stipulated that the minimum insulation spacing should be no less than 6.44 mm, in order to prevent electrical hazards arising from the two inputs coming into contacts.

The commonly used insulating materials in LED encapsulation, such as the LED bracket coating materials, encapsulation materials, substrate support materials, must all be moisture-proof materials whose structural strength will not be altered under real world operating temperatures. It is also stipulated in ANSI/UL 8750 that the evaluation of these insulation materials should be performed in accordance with the specifications of the ANSI/UL 746C, using criteria such as the mechanical strength, fire resistance, dielectric strength, electrical insulation, thermal resistance before and after aging, degree of coating, anti-moisture capacity in a nondry environment, and other characteristics that will affect the risk of fire and electric shock. When it comes to the choice of the encapsulation materials, such as the plastic colloid for the bracket, the encapsulating epoxy, silicone, aluminum substrates, the fire-resistance rating cannot be less than that specified by the ANSI/UL 94 V-1 safety limits.

Table 15.3 Dielectric Voltage Withstand Potential (UL8750 Table 8.3)

Applied potential	Circuit location
2 V + 1000	Between primary circuits or secondary circuits operating at greater than 70 V peak and accessible dead conductive parts
	Between the primary and secondary of a transformer
	Between PWB traces or other parts operating at different potentials
500	Between a secondary circuit operating at no more than 70 V peak and accessible dead conductive parts

Since HVLED encapsulation components operate in a high-voltage system, special consideration must also be taken for safety concerns such as the combustivity of the material, anti-electrical sparks characteristics, anti-moisture resistance when it comes to the choice of the aforementioned polymer materials.

The stipulated moisture and insulation tests for HVLED encapsulation devices involve placing said devices (or modules) under normal operations in a test environment with a relative humidity of 91–95%, with the temperature maintained in the room temperature range, for up to 48 h. Thereafter, the insulation devices are subjected to a 500 V DC voltage, followed one minute later with an insulation resistance measurement. Under normal conditions, the insulation resistance must be greater than 2 MΩ, to ensure the anti-moisture and insulation capacity of the encapsulation materials.

The test conditions for the Dielectric Voltage Withstand Test referred to in ANSI/UL 8750 are shown in Table 15.3. A potential of 1000 V plus twice the maximum rated AC operating voltage is applied between a line and a conductor that carries no charge and can be placed in contact (i.e., the input end of the HVLED and a neighboring conductor) for 1 min, during which the HVLED encapsulation devices must not suffer dielectric breakdown. The test voltage needs to be applied to the power supply, LED modules, and control circuit modules that are directly connected to the circuit branch. Double or reinforced insulation test conditions are also described under the IEC/EN 60598-1:2008 (General Requirements and Tests for Lightings) specifications, whereby a voltage of 2000 V plus four times the maximum rated AC operating voltage is applied for advanced electrical insulation test [5].

15.3.5 Measurement Techniques for the Optical, Electrical, and Thermal Properties of HVLED Modules

During the operation of a HVLED under AC, its opto-electrical characteristics as well as temperature will exhibit cyclical changes with the input AC frequency. Therefore, one cannot simply use the “input of a small instantaneous current for

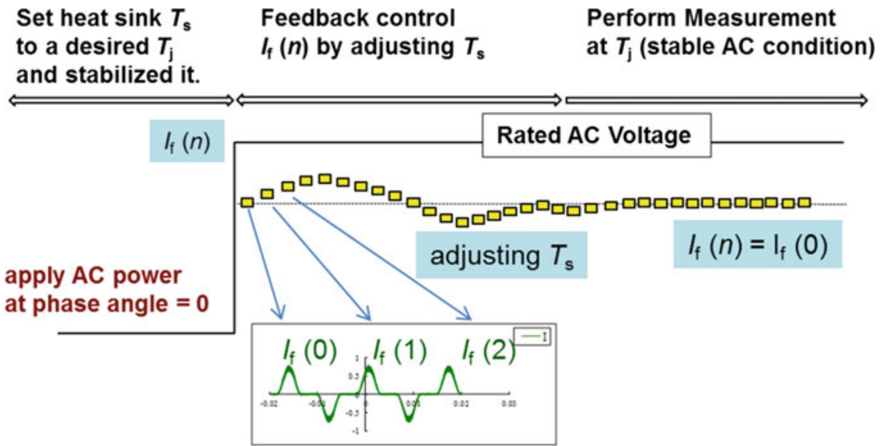

Fig. 15.20 A viable HVLED measurement approach

eliciting and measuring the response voltage" approach for DCLEDs to deduce the T_j of HVLED.

In 2008, the NIST (National Institute of Standards and Technology) and the Taiwan Industrial Technology Research Institute (ITRI) jointly proposed a reference HVLED opto-electrical measurement approach based on extending the measurement time and which borrows from and modifies the aforementioned traditional measurement approach for high-power DCLEDs. The scheme is outlined step-by-step in Fig. 15.20 and described in detail as follows: (1) Install the HVLED to be tested onto a metal core printed circuit board (MCPCB), where the heat sink with temperature control function is located. (2) Turn on the temperature controls to maintain the measurement point temperature (T_s, typically a specified point on the MCPCB) of the HVLED (yet to be turned on and tested) at the specified $T_{j(0)}$. (3) Turn on the AC power for measurement with zero phase, and simultaneously commence measurements. (4) Adjust the temperature T_s such that during any half-cycle, the root-mean-square current value If (n) is equal to the If (0) of the first half-cycle, i.e., $T_{j(n)} = T_{j(0)}$. (5) Perform opto-electrical measurements of the HVLED at $T_{j(n)} = T_{j(0)}$. It should be noted that the measurement time should be integer multiples of the driving cycle of the HVLED to be tested, so as to ensure the accuracy of the data.

The aforementioned measurement approach can be integrated with existing measurement equipment for lighting, e.g., integrating sphere for discharge lamp, goniophotometer, array or scanning spectrometer. Utilizing this approach, one can also precisely calculate the thermal resistance of a HVLED by computing the difference between the default T_j and the actual measured T_s.

15.3.6 Operating Lifetime

The output intensity of the LED light source will gradually decline over time, and one can typically calculate the lumen maintenance rate of a LED light source by comparing its initial light output intensity and its light output intensity after use. In the LM-80-08 testing standards developed by the North American Illuminating Engineering Society (IESNA), the standard measurement procedures [6] for the lumen maintenance rate of a LED light source, including the measurement equipment, environmental settings, definition of testing conditions, are all clearly defined. Further, the actual operating time of the LED light source will be symbolically denoted as a percentage of the initial output light intensity, e.g., L_{70} (hours) indicates that after said hours have elapsed, the lumen of the light source is maintained at 70% of its initial value, while L_{50} (hours) indicates that after said hours have elapsed, the lumen of the light source is maintained at 50% of its initial value. The U.S. ENERGY STAR standards stipulate that for indoor lightings, the lumen maintenance rate after 25,000 h must be no lower than 70%. For outdoor lightings, the lumen maintenance rate after 35,000 h must be no lower than 70%. The lumen maintenance rate is further used as a criterion for gauging the operating lifetime of a LED light source. The above criterion is based on calculating the decay of the light intensity from the variations in the light intensity of the DCLED, whose optical output is more stable. The operation of a HVLED differs from the stable current drive mode of a traditional DCLED in that it utilizes a constant AC voltage. Therefore, it is recommended that the decay of the light output intensity under AC driving is used as the basis for calculating the lumen maintenance rate.

In addition, due to prolonged operations, the operating power of a HVLED device or module may vary. Therefore, another possibility is to utilize the decay in the luminous efficacy as the basis for gauging the operating lifetime of a HVLED.

In sum, the relevant lifetime testing, failure criteria, and lifetime testing standards for HVLED are still undergoing discussions. Before lifetime testing procedures are standardized, there still remain several related or corresponding opto-electrical characteristics worthy of further research, discussions, and analysis.

15.4 Summary

HVLED utilizes semiconductor fabrication techniques to grow and connect in series several micro-chips on the same substrate, enabling a single-chip LED to operate directly under AC. By avoiding (or partially circumventing) the use of rectifier and transformer elements, HVLED modules perform lower manufacturing costs and smaller module volumes than traditional DCLED modules. As opposed to traditional DCLEDs driven by a constant current, HVLEDs are designed to operate under AC voltage. Therefore, issues such as the luminous intensity varying with the input voltage, limitations due to total harmonic distortion can arise. All the

aforementioned issues have been discussed in great detail in this chapter, along with the feasible solutions.

In addition, due to the fact that the characteristics of HVLEDs under AC operation are very different from those exhibited by traditional DCLEDs, the relevant safety and measurement standards will also need to be modified in accordance with the actual operating conditions of HVLEDs. In this chapter, the relevant standards and recommendations have also been discussed, enabling the users to more safely and properly operate HVLEDs and measure the characteristics exhibited under AC operation.

The purpose of HVLEDs is to provide a single-chip solution capable of operation under AC. Although the efficiency drooping effect means that for identical operating power and chip area, the luminous efficacy of a HVLED operating under AC will be lower than that of a traditional DCLED, the compactness, low cost, and possibly longer operating lifetime of the overall module are all vast improvements on traditional DCLEDs with regard to application.

References

1. H.H. Yen, H.C. Kuo, W.Y. Yeh, Particular failure mechanism of GaN-based alternating current light-emitting diode induced by GaOx oxidation. IEEE Photonics. Technol. Lett. **22**(15), 1168–1170 (2009)
2. IEC/EN 6 1000-3-2, Harmonic Standards, Class C: Lighting Equipment
3. ANSI C82.77:2002, Harmonic Emission Limits—Related Power Quality Requirements for Lighting Equipment
4. ANSI/UL 8750:2009, Light Emitting Diode (LED) equipment for use in lighting products
5. IEC/EN 60598-1:2008, Luminaries, Part 1: General requirements and test
6. IES LM-80-08, Approved method: Measuring Lumen Maintenance of LED Light Sources

Chapter 16
Color Quality of White LEDs

Yoshi Ohno

Abstract This chapter provides an overview of the fundamentals of chromaticity and color rendering, the two important aspects of color quality of light sources for general illumination. There is a special focus on the use of solid-state light sources. The section on chromaticity discusses chromaticity coordinates and diagrams, correlated color temperature (CCT), Duv, and specifications for color differences. The section on color rendering discusses object color evaluation, the color rendering index (CRI) and the shortcomings thereof, and color quality beyond CRI, introducing the color quality scale (CQS) as a design tool. The chapter also discusses luminous efficacy of radiation and the color characteristics used for single-color LEDs. Finally, future considerations on color quality for white LED developments are given.

16.1 Introduction

It is critical for LED sources for general illumination to have acceptable color quality suitable for intended applications. There are two aspects to the color quality of lighting sources: chromaticity and color rendering. These two aspects are interrelated. Both of these characteristics are critical for general lighting sources.

The chromaticity of a light source is the color of light emitted from the light source, and is normally expressed in chromaticity coordinates, (x, y) or (u', v') [1], and is often plotted in two-dimensional chromaticity diagrams using these coordinates. The chromaticities of illumination sources are normally chosen to be around the Planckian locus or the daylight locus, which are generally considered as the center curves for white light. Shifts of chromaticity along these center curves result in warmer or cooler color appearance, and are specified by correlated color temperature (CCT) [1]. Shifts of chromaticity across these center curves make the lights appear yellowish, greenish, or pinkish and are specified by the term, Duv [2].

Y. Ohno (✉)
National Institute of Standards and Technology, Gaithersburg, USA
e-mail: ohno@nist.gov

© Springer Nature Singapore Pte Ltd. 2017

T.-Y. Seong et al. (eds.), *III-Nitride Based Light Emitting Diodes and Applications*,
Topics in Applied Physics 133, DOI 10.1007/978-981-10-3755-9_16

While a wide range of CCT is suitable depending on application, the range of acceptable Duv is much narrower on the color space. Duv is important especially for indoor applications. There have been standards for chromaticity of fluorescent lamps for many years [3]. A standard for chromaticity specifications for solid-state lighting products [2] was recently developed and widely used. However, there are still some questions about whether these Planckian or the daylight loci represents optimal white light for lighting [4]. Chromaticity coordinates and CCT are fundamental terms defined by International Commission on Illumination (CIE) and their official definitions are available in [5]. The details of these chromaticity terms and formulae are presented in Sect. 16.2.

Another important aspect of color quality is color rendering. Even if the light has perfect white chromaticity, color rendering can be very poor. Color rendering is a property of a light source that quantifies how natural the colors of objects look under the given illumination. If color rendering is poor, the light source will not be useful for general lighting. The term color rendering is defined by CIE [5] with a rather narrow meaning, but this term is often used with a broader meaning including the aspects of color fidelity and color preference. The current international standard to evaluate color rendering is the Color Rendering Index (CRI) [6] defined by CIE. The CRI has been used very widely for a number of years. The formulae used in CRI are old, and recently problems related to the CRI when used for LED sources have been identified [e.g., 7] and are being addressed by CIE (TC1-90 and TC1-91). Several new metrics to replace or supplement CRI have been recently proposed [8–12], and many other old research results and metric proposals are available [e.g., 13–15]. The details and issues related to color rendering are presented and discussed in Sect. 16.3.

Color rendering depends on the spectrum of the light source, which also affects the energy efficiency of light source. Color rendering is generally more superior if the spectrum is broadly distributed over the visible region. However, such broadband spectra are generally less energy-efficient. The theoretical energy efficiency of a spectrum is defined by CIE [5] as *luminous efficacy of radiation* (LER). The formula to calculate the LER is introduced, and some examples of white LED spectra are analyzed for LER and discussed in Sect. 16.4. Section 16.5 introduces the definitions of the color-related terms used for single-color LEDs including dominant wavelength, centroid wavelength, and peak wavelength.

In Sect. 16.6, the color rendering of typical phosphor white LEDs is examined and the improvements of color rendering are discussed. To analyze the color rendering characteristics of white LEDs and also the problems of the CRI, a color simulation program was developed [16]. Various white LED spectra, multi-chip type, and phosphor type were modeled and analyzed in comparison to conventional lamps. Some results of the past studies [17] are presented, and the problems and necessary improvements of the CRI are discussed in Sect. 16.5.

16.2 Chromaticity

16.2.1 Chromaticity Coordinates and Diagrams

The CIE 1931 (x, y) and CIE 1976 (u', v') chromaticity coordinates and corresponding diagrams are defined by the CIE [5]. Both are widely used to specify chromaticity of light sources for illumination. The (x, y) diagram is very spatially nonuniform in terms of color differences. Figures 16.1 and 16.2 show the plots of MacAdam Ellipses (just noticeable color differences) [18] on these diagrams, with the ellipses' sizes magnified by ten. For the same difference values in x or y, the perceived color differences of a green LED would be much smaller than blue LEDs. The (u', v') diagram is more spatially uniform and is preferred, especially to specify chromaticity of colored sources including single-color LEDs.

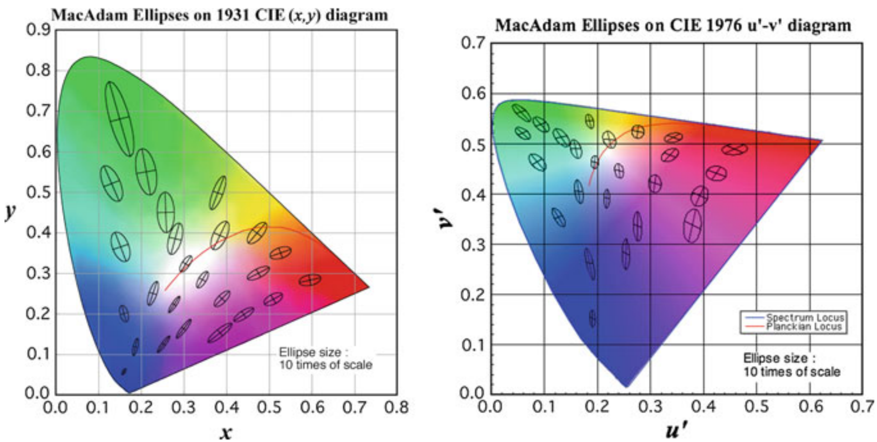

Fig. 16.1 CIE 1931 (x, y) chromaticity diagram and CIE 1976 (u', v') chromaticity diagram with MacAdam Ellipses plotted

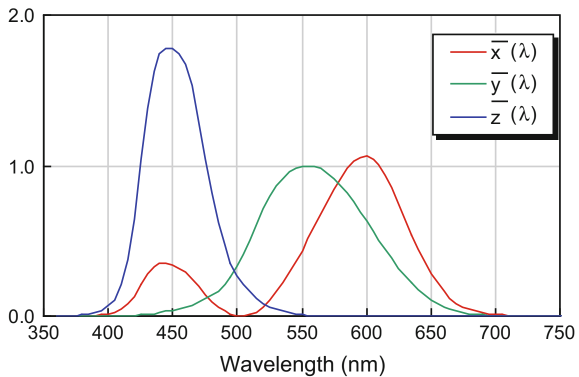

Fig. 16.2 CIE 1931 color matching functions

The chromaticity coordinates of a light source are calculated from its spectral power distribution $\phi(\lambda)$. The tristimulus values X, Y, Z are first calculated as

$$X = k \int_{\lambda} \phi(\lambda)\bar{x}(\lambda)\,\mathrm{d}\lambda$$
$$Y = k \int_{\lambda} \phi(\lambda)\,\bar{y}(\lambda)\,\mathrm{d}\lambda \qquad (16.1)$$
$$Z = k \int_{\lambda} \phi(\lambda)\,\bar{z}(\lambda)\,\mathrm{d}\lambda,$$

where $\bar{x}(\lambda)$, $\bar{y}(\lambda)$, $\bar{z}(\lambda)$ are the CIE 1931 color matching functions (Fig. 16.2).

The values of these functions at 5 nm interval and 1 nm interval are available in [1, 19]. The chromaticity coordinates (x, y) and (u', v') are calculated by

$$x = \frac{X}{X+Y+Z},\; y = \frac{Y}{X+Y+Z} \qquad (16.2)$$

$$u' = \frac{4X}{X+15Y+3Z},\; v' = \frac{9Y}{X+15Y+3Z} \qquad (16.3)$$

The (u', v') coordinate can also be calculated from (x, y):

$$u' = \frac{4x}{(-2x+12y+3)},\; v' = \frac{9y}{(-2x+12y+3)} \qquad (16.4)$$

Likewise, (x, y) coordinate can be converted from (u', v') by

$$x = \frac{9u'}{(6u'-16v'+12)},\; y = \frac{2v'}{(3u'-8v'+6)} \qquad (16.5)$$

The CIE 1960 (u, v) coordinates (now obsolete) is introduced here only for the purpose of calculating CCT and Duv, and is obtained by,

$$u = u',\; v = \frac{2}{3}v' \qquad (16.6)$$

The (u, v) coordinates should not be used for calculations other than CCT and Duv. The curve formed by the plots of the chromaticity coordinates of monochromatic radiation at various wavelengths is called the *spectrum locus* (this forms the horseshoe shape of the diagram), and the curve formed by the plots of Planckian radiation at various blackbody temperatures is called the *Planckian locus*, as depicted in Fig. 16.3 on the (x, y) diagram. The straight line connecting both ends of the spectrum locus is called the *purple line*.

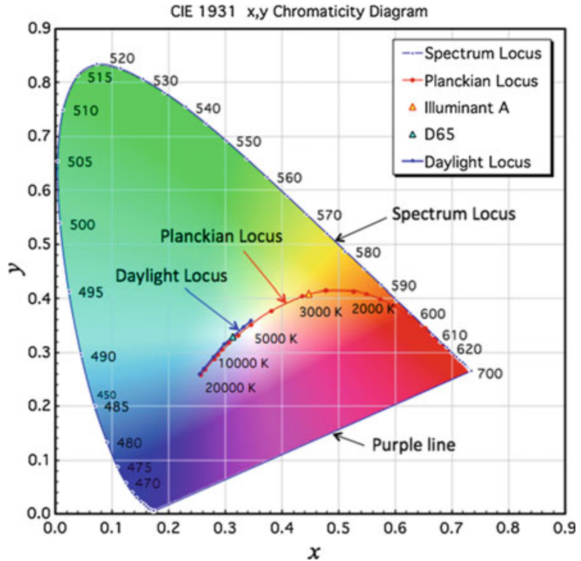

Fig. 16.3 The spectrum locus and the Planckian locus on the (x, y) diagram

The Planckian locus is generally considered as the center curve of white light for low CCT sources (CCT < 5000 K). For higher CCT sources (CCT $\geq$ 5000 K), the different phases of daylight (called the *daylight locus*), also plotted in Fig. 16.3, is generally considered as the center curve of white light for lighting. The formula to calculate the daylight locus is available in [1]. Several specific points on this locus, at 5000, 5500, 6500, and 7500 K are defined as standard illuminants D50, D55, D65, and D75 [1, 20]. The boundary between the two curves is not definite, and the 5000 K is used, e.g., in [6], for standardization purpose only. Also, if such a curve for center white exists, there should be a smooth transition between the two curves. The traditional chromaticity specifications of fluorescent lamps [3, 4] somewhat follow such a smooth transition between the Planckian and the daylight locus, though not exactly.

The CIE also specifies the color matching functions $\bar{x}_{10}(\lambda), \bar{y}_{10}(\lambda), \bar{z}_{10}(\lambda)$ for the 10 degree field of view [5], and the corresponding chromaticity coordinates are also available but these are mainly used for object color specification and generally not used for specification of light sources.

Light sources for general lighting must have acceptable white light chromaticity. ANSI C78.377 [2] specifies the ranges of chromaticity for solid-state lighting products as illustrated in Fig. 16.4, and is often used as the basis for color binning of white LED products. There are eight nominal CCTs in this standard, and also the Flexible CCT specification is provided as an option, in which nominal CCTs at every 100 K can be selected, and the formulae to calculate each quadrangle are provided.

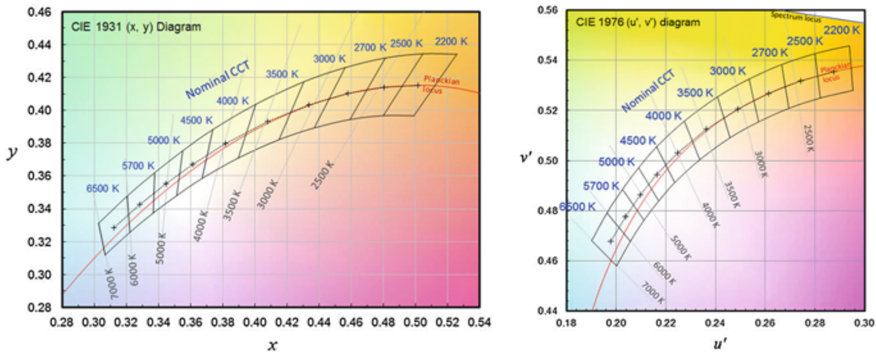

Fig. 16.4 The chromaticity specifications for solid-state lighting products by ANSI C78.377 [2] on the CIE (x, y) diagram (*left*) and on the (u', v') diagram (*right*)

16.2.2 CCT and Duv

Correlated Color Temperature (CCT, Symbol: T_{cp}) is defined as the temperature of the Planckian radiator having the chromaticity that is closest to the chromaticity of the given light source, on the CIE (u', 2/3 v') coordinate, as illustrated in Fig. 16.5. A more official definition is available elsewhere [1, 5].

The (u', 2/3v') coordinate is the same as now-obsolete CIE 1960 (u, v) coordinate. The Planck's equation generally used in photometry and radiometry is given in the form:

$$L_{e,\lambda}(\lambda, T) = \frac{c_1 n^{-2} \lambda^{-5}}{\pi} \left[\exp\left(\frac{c_2}{n \lambda T} \right) - 1 \right]^{-1}, \qquad (16.6)$$

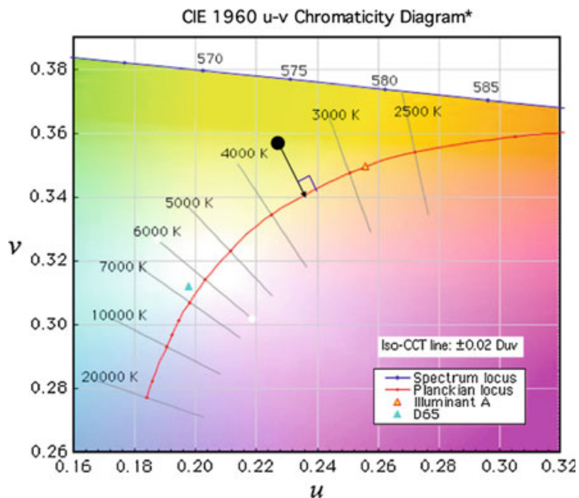

Fig. 16.5 Illustration of the definition of CCT on the 1960 (u, v) diagram (now obsolete)

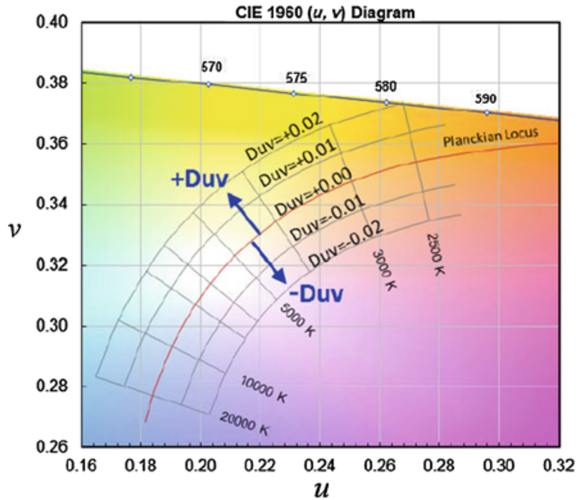

Fig. 16.6 The scales of Duv shown on the 1960 (u, v) diagram

where L is the spectral radiance, T is the temperature [K], n is the refraction index of the medium. For historical reasons, $n = 1$ (exactly 1) has been used and must be used for calculation of CCT. The parameters c_1, c_2 are the radiation constants; but only c_2 is relevant the value of CCT, and the value of c_2 used in the calculation of CCT must follow the value adopted in the current International Temperature Scale (ITS-90), namely $c_2 = 1.4388 \times 10^{-2}$ m K. See Appendix E of CIE 15:2004 [1] for the details of these constants used for calculation of CCT.

Duv (symbol: D_{uv}) is defined as the closest distance from the Planckian locus on the CIE $(u', 2/3v')$ coordinates, with + sign for above and − sign for below the Planckian locus [2]. The distance is measured on the CIE 1960 (u, v) diagram. A positive value of Duv indicates a shift in yellowish/greenish direction, and a negative value indicates a shift in pinkish direction. Figure 16.6 shows the scales of Duv depicted on the (u, v) diagram.

While the ANSI specification [2] is widely accepted, it is still a question whether the Planckian locus and Daylight locus truly represent most preferred white light for lighting [4]. Some lighting engineers experience that light with slight shift of Duv to negative side provides better color quality perception. Such an effect was studied with the NIST spectrally tunable lighting facility [34]. This is a subject that needs thorough study in the future.

Duv can normally be calculated in the process of calculating CCT, which requires determination of the closest point on the Planckian locus to the (u, v) chromaticity coordinates of the light source being tested.

If it needs to be calculated separately, and if the CCT of the light source is known, Duv can be obtained by calculating the spectral distribution of Planckian radiation at the CCT of the source using the Planck's equation (16.6), then calculate $(u_0', 2/3v_0')$ of that Planckian spectral distribution, then Duv is given by

$$D_{uv} = \left[(u' - u_0')^2 + \left(\frac{2}{3} v_0' - \frac{2}{3} v_0' \right)^2 \right]^{\frac{1}{2}} \cdot SIGN(v' - v_0'), \qquad (16.7)$$

where $SIGN(z) = 1$ for $z \geq 0$ and $SIGN(z) = -1$ for $z < 0$.

16.2.3 Color Differences for Light Source

Color difference of light sources need to be specified in many cases, for example, for angular color uniformity, shift of color during lifetime (color maintenance), and individual color variation of products. The color difference of light stimuli, in general, is expressed by the distance on CIE (u', v') diagram, which is the uniform color space for light stimuli officially recommended by the CIE. The term "color difference" should not be confused by that for object colors, which are measured as the Euclidian distance in a three-dimensional object color space such as CIE $L^*a^*b^*$ (also called CIELAB). Color difference of object color is briefly discussed in Sect. 16.3.3.

The color difference of light sources for illumination is often expressed by the size of MacAdam ellipses [18] as introduced in Sect. 16.2.1. For example, the ellipses included in Fig. 16.4 are seven times the size of MacAdam ellipses, so-called seven-step MacAdam ellipses, used for specification of compact fluorescent lamps in USA [21]. The chromaticity specification for linear fluorescent lamps in USA [3] uses four-step MacAdam ellipses. Similar expressions occasionally used are SDCM (standard deviation of color matching) or JND (just noticeable difference), meaning the color difference corresponding to one-step MacAdam ellipses. However, these are not internationally defined standard metrics. While these served many years for fluorescent lamps, which have only six nominal CCTs (in the specifications in the USA [3]), this method does not work for new lighting technologies, which are more versatile. Note that the shape and size of the seven-step MacAdam ellipses in Fig. 16.4 are all slightly different. Their shape and size change depending on the chromaticity coordinates and they have to be interpolated between the original 25 chromaticity points measured by MacAdam (Fig. 16.1). Such interpolation formulae are not defined in any international standard. This is a problem for LED light sources that do not follow the traditional nominal CCTs of fluorescent lamps. For example, the 4500 K and 5700 K nominal CCTs or any of the flexible CCTs in the ANSI specification [2] do not have corresponding MacAdam ellipses defined. Even if interpolation of ellipses can be specified, it would be complicated for practical use.

As described in Sect. 16.2.1, the CIE (u', v') diagram is the uniform color space for light sources. Figure 16.7 shows the white part of the CIE (u', v') diagram, on which seven-step MacAdam ellipses (blue) [21] and circles with radius of 0.008 (red) are plotted on top of each other. As shown, these ellipses and the circles are

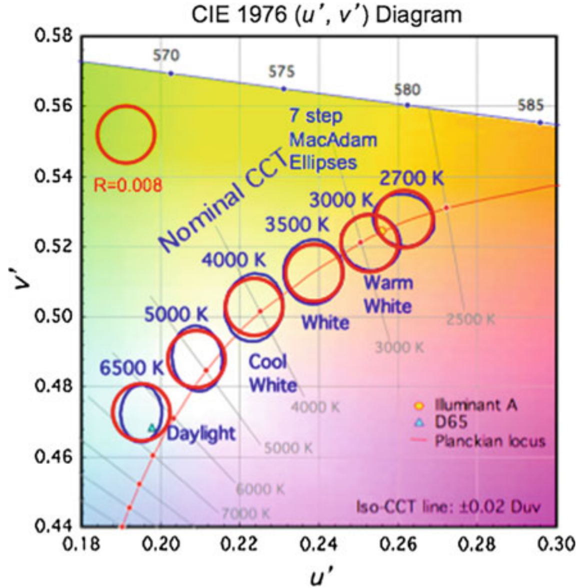

Fig. 16.7 7-step MacAdam *ellipses* and *circles* (radius 0.008) on the CIE (u', v') diagram

closely overlapped, which means that circles can be used to replace MacAdam ellipses in this white region on (u', v') diagram. There is such a recommendation by CIE [22]. Seven-step MacAdam ellipses are roughly equivalent to the circles with radius 0.008. The n step corresponds to $0.0011 \times n$ in radius on the (u', v') diagram. There are small differences between the circles and the ellipses, but it is considered insignificant in practical applications. Especially, the experimental uncertainty of MacAdam ellipses measured 70 years ago with only one experimental subject is not well known. Rather than MacAdam ellipses, it is recommended that simply the distance in (u', v'), e.g., expressed as $\Delta u'v'$, be used to specify the color uniformity, color maintenance, and color variation of SSL products.

16.3 Color Rendering Characteristics

16.3.1 Object Color Evaluation

Color rendering is a phenomenon in which colors of objects appear differently under illumination by different spectra. Thus, in discussing color rendering, it is important to understand how object colors and their differences are evaluated, so a short introduction is given in this section. The essential component of evaluating color rendering is to measure or calculate color differences of objects under given illumination, and this approach is used in CRI and other new proposed metrics.

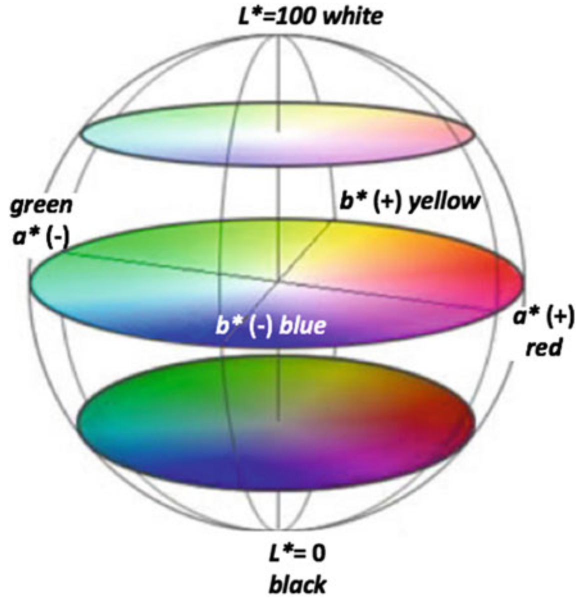

Fig. 16.8 Illustration of CIELAB object color space

Unlike light source color, which has two dimensions, object color requires another dimension, lightness—a scale from black, gray, to white. For example, there is no brown or black in the (x, y) diagram. Brown color has the same chromaticity as red but has a different lightness. Therefore, a three-dimensional color space is needed for object color.

There are two standardized object color spaces defined by CIE, which are $L^*a^*b^*$ (CIELAB) [1, 23], and $L^*u^*v^*$ (CIELUV) [1, 24]. CIELAB is commonly used in lighting research as well as imaging applications, and is illustrated in Fig. 16.8. The horizontal two axes, a^* and b^*, determine *hue* and *chroma*, and the vertical axis L^* gives *lightness*. The center is gray, and the further a point is shifted outside horizontally, the more colorful the object is. The three coordinates L^*, a^*, b^* of an object surface are calculated by

$$\begin{aligned} L^* &= 116(Y/Y_n)^{1/3} - 16 \\ a^* &= 500\left[(X/X_n)^{1/3} - (Y/Y_n)^{1/3}\right] \\ b^* &= 200\left[(Y/Y_n)^{1/3} - (Z/Z_n)^{1/3}\right] \\ &(\text{when}\, X/X_n, Y/Y_n, Z/Z_n > 0.008856), \end{aligned} \tag{16.8}$$

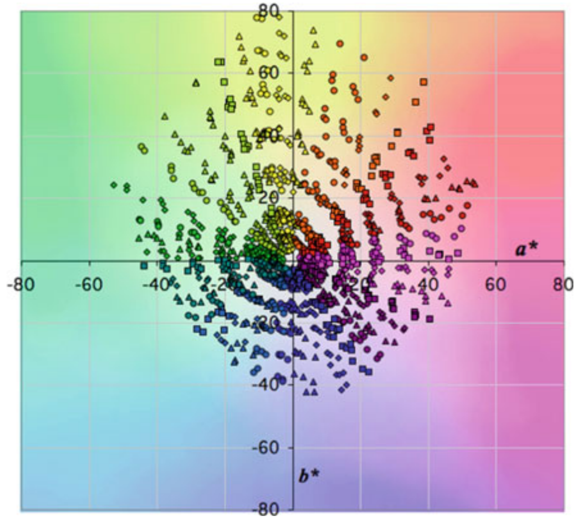

Fig. 16.9 The CIELAB (a^*, b^*) plots of 1200 Munsell color samples under D65

where X, Y, Z are the tristimulus values of the object surface, and X_n, Y_n, Z_n are the tristimulus values of the white reference (perfect diffuser) under a given source of illumination. Note that there are further formulae for samples with very low reflectance, but these are practically not needed. To specify object colors, one of standard illuminants such as CIE D65 [20] is used to calculate the tristimulus values. The color difference between two objects are calculated by

$$\Delta E^*_{ab} = \left[(\Delta L^*)^2 + (\Delta a^*)^2 + (\Delta b^*)^2 \right]^{1/2} \tag{16.9}$$

For evaluation of color rendering of light sources, object colors are calculated with the reference source and given light source, and the difference ΔE^*_{ab} between them are evaluated. Since it is not convenient to draw three-dimensional diagram, only (a^*, b^*) is often plotted as a two-dimensional graph. As an example, Fig. 16.9 shows (a^*, b^*) plots of 1269 Munsell color samples [25] under D65.

The 1964 $W^*U^*V^*$ object color space used in the CRI [6] is the same concept as CIELAB but is very outdated and nonuniform. Figure 16.10 shows the comparison of the two-dimensional plots of 15 saturated color samples (from Munsell) under standard Illuminant A (2856 K blackbody) on $W^*U^*V^*$ and CIELAB. It shows that the red area on $W^*U^*V^*$ is extremely stretched compared to the yellow and blue region.

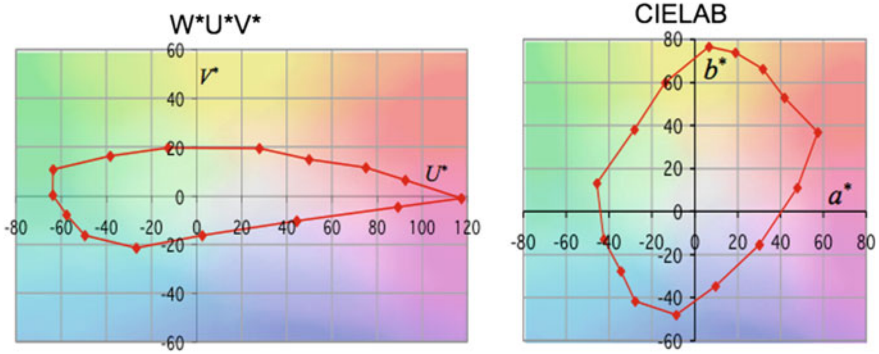

Fig. 16.10 Two-dimensional plots of 15 saturated color samples under Illuminant A in $W^*U^*V^*$ and CIELAB object color space

16.3.2 Color Rendering Index

Color rendering is defined by the CIE [5] as "effect of an illuminant on the color appearance of objects by conscious or subconscious comparison with their color appearance under a reference illuminant." The CIE color rendering index (CRI) [6] is widely used and the only internationally accepted metric for assessing the color rendering performance of light sources.

The details of procedure for the calculation are available in [6], but a brief introduction is provided in this section. The first step of the calculation is to calculate the color differences ΔE_i (in the 1964 $W^*U^*V^*$ uniform color space—now obsolete) of 14 selected Munsell samples when illuminated by a reference illuminant and when illuminated by a given light source (spectrum). The first eight samples are medium saturated colors, and the last six include four highly saturated colors (red, yellow, green, and blue), skin complexion, and leaf green. These samples are shown in Fig. 16.11. The reference illuminant is Planckian radiation for test light sources having a correlated color temperature (CCT) < 5000 K, or a phase of daylight (one of daylight spectra at varied CCT; the formula is available in [1]) for test sources with CCT $\geq$ 5000 K. The chromaticities of the test samples

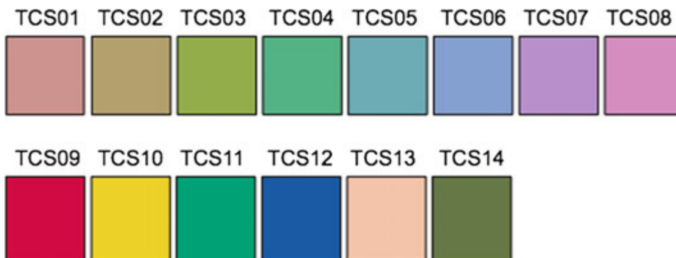

Fig. 16.11 The 14 test color samples used in the calculation of CRI

are adjusted by the von Kries chromatic adaptation transformation. The *Special Color Rendering Indices* R_i for each color sample are obtained by

$$R_i = 100 - 4.6\Delta E_i;\ (i = 1, \ldots, 14) \tag{16.10}$$

This gives the evaluation of color rendering for each particular object sample color. The *General Color Rendering Index* R_a is calculated as the average of R_i for the first eight color samples

$$R_\mathrm{a} = \sum_{i=1}^{8} R_i/8 \tag{16.11}$$

The score for perfect color rendering (zero color differences) is 100, and the values of R_i or even R_a can be below zero (negative) if color differences are extremely large. Note that the term CRI is often used referring to R_a, but the CRI actually consists of 15 numbers; R_a and R_i (i = 1–14).

The values of $R_\mathrm{a} \geq 80$ are generally considered acceptable for indoor lighting and Ra $\geq$ 90 is generally considered excellent color rendering. The special color rendering indices R_i are not often used except R_9 (index for the saturated red sample), which is often examined as red is critical for overall color rendering and also to supplement R_a to address some of its problems. Note that color rendering is often not critical for outdoor lighting and $R_\mathrm{a} < 80$ can be well used for such applications.

16.3.3 Shortcomings of CRI

The CRI was first developed in the 1960s to evaluate the color rendering performance of then-new fluorescent lamps. The formulae used in the current version of CRI date back to 1974 (CRI 2nd edition) using $W^*U^*V^*$ object color space and von Kries chromatic adaptation transform formula, which are now outdated and known to be very inaccurate. The number of test color samples (eight) used in the CRI R_a has been considered to be too few. In spite of these known shortcomings, the CRI served well for traditional light sources (discharge lamps) for over 35 years, and the lighting industry did not find serious problems with the CRI, rejecting a recent revision attempt [26]. However, some serious problems of the CRI when applied to LED sources have been identified and needs for improvements are addressed [27–31] and also by CIE [7]. The CRI R_a score often does not correlate well with visual evaluation, particularly with RGB(A) LED sources, and such problems can occur for other types of narrowband source such as narrowband phosphor LEDs and quantum dots. Several aspects of problems of the CRI are explained below. These problems of the CRI should be noted when it is used.

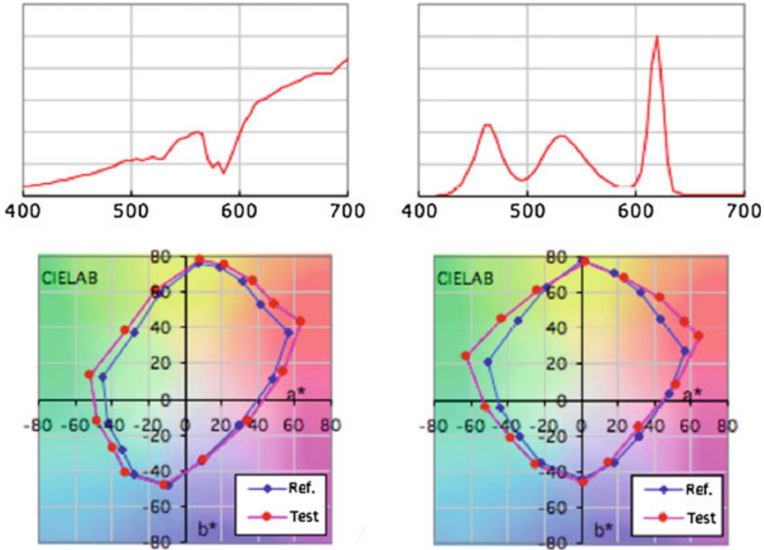

Fig. 16.12 Examples of color enhancement by a neodymium lamp and an RGB LED source

16.3.3.1 CRI Penalizes Preferred Color-Enhancing Lights

The CRI R_a score does not correlate well with visual evaluation when the chroma (color saturation) of objects is increased by the light source. This is well demonstrated by the case of a neodymium lamp,[1] as shown in Fig. 16.12 (left). This lamp produces a slight increase of color gamut in the red and green region, and the color contrast of objects is slightly enhanced. Object colors under this light look more vivid, and this lamp is often preferred over normal incandescent lamps (R_a = 100). But this lamp is given a CRI score of only R_a = 77. Neodymium lamps are popularly sold in USA and this evidence suggests that this lamp deserves a much higher score. Figure 16.12 (right) shows an example made by a real RGB source, under which is highly rated by visual evaluation but is given a CRI score of R_a = 71. The red-green contrast is said to be very important for overall color rendering of a light source [32], and enhancement of red and green is considered to be good trait of lighting source as long as it is not excessive. The R_a score tends to be much reduced for enhanced red due to very nonuniform $W^*U^*V^*$, which is extraordinarily stretched in the red region.

[1]Incandescent lamp with its glass envelope doped with neodymium, which absorbs much of the yellow portion of the lamp spectrum. This type of lamp is popularly sold in the USA and some other countries.

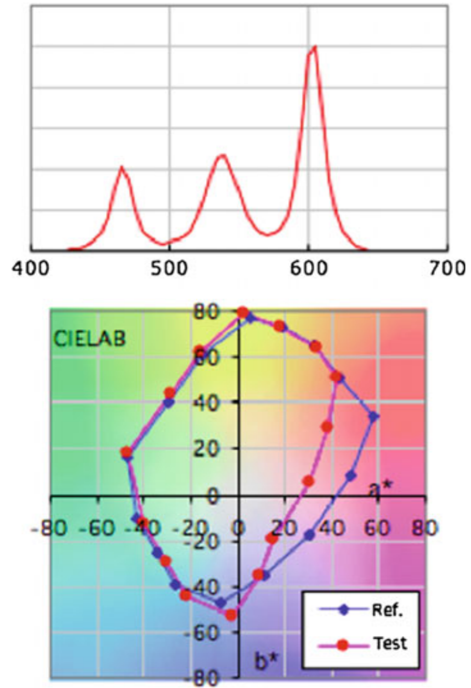

Fig. 16.13 An example of RGB spectrum (simulation) with very poor *red* rendering

16.3.3.2 A High CRI Score Does not Guarantee Good Color Quality

There are some cases where the CRI gives fairly high scores though some saturated object colors appear very poorly. An example in Fig. 16.13 shows a case of RGB white LED simulation optimized for highest luminous efficacy of radiation at CRI $R_a = 80$. This light would qualify for ENERGY STAR [33] and achieve high luminous efficacy, but the actual color rendering is very poor with $R_9 = -114$. Skin tones under this light look pale and very unhealthy. This problem occurs due to the use of medium saturated test color samples in CRI, which fail to detect problems with saturated color samples under such narrowband sources.

16.3.3.3 Problem with Duv Shifts

There are some cases where the CRI R_a score does not reflect the effects of Duv shifts correctly. The example below shows the case of an RGBA spectrum with a CCT of 2700 K with shifts of Duv from −0.02 to +0.02 (by only changing the ratios of four peaks). These spectra were created in the National Institute of Standards and Technology (NIST) Spectrally Tunable Lighting Facility [43]. NIST conducted vision experiments on Duv shifts, and the results show yellowish shifts are disliked especially at low CCT ranges and slight shifts toward negative Duv are

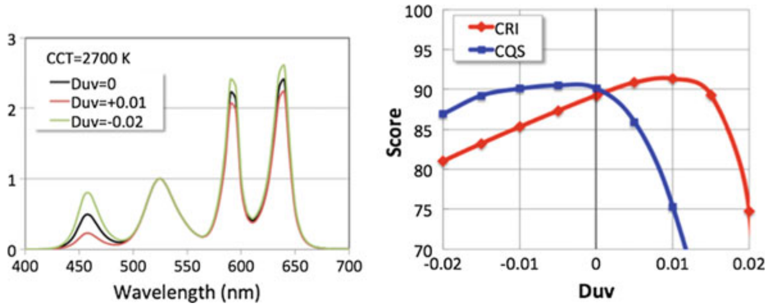

Fig. 16.14 Change of CRI R_a score with shifts of Duv on an RGBA spectrum

preferred [34]. Figure 16.14 (right) shows that the CRI R_a score (red curve) increases at positive Duv up to +0.01. This is the opposite of the visual preference. Color quality scale (CQS) scores (see next section), on the other hand, penalize the yellow shifts. In this example, the CRI encourages yellowish shifts, which does not reflect user perception and preference. This difference between the CRI and CQS comes from the chromatic adaptation transform. The von Kries formula used in the CRI is very outdated and considered not working accurately. The CQS uses one of the latest chromatic adaptation transforms, CMCCAT 2000[2] [35, 36].

16.3.4 Color Quality Beyond CRI

The CRI assesses the fidelity of color rendition (color fidelity) with respect to a reference illuminant. It has long been known that color fidelity cannot serve as the sole indicator of color quality for lighting. There are other aspects of color quality, such as general color preference as well explained in [37, 38] and color discrimination [14], which influence the visual experience of color rendering. In particular, object color shifts that increase color saturation enhances visual clarity and color discrimination ability, and improves the subjective rating of color appearance of the illuminated scene. It is also known that perceived chroma (color saturation or colorfulness) of objects is reduced at lower light levels (Hunt Effect) [39]. Therefore, it seems that sources that enhance color slightly in indoor lighting conditions may achieve higher color fidelity to real daylight (which has much higher illuminance than indoor lighting). An attempt was made to measure this effect [40]. In the past, there have been attempts to account for these effects beyond color fidelity by various proposed metrics such as the Flattery Index [13], the Color Discrimination Index [14], the Color Preference Index [15], and more recently, the Feeling of

[2]CMCCAT represents Color Measurement Committee (of the Society of Dyers and Colourists for predicting the degree of color inconsistency of surface colors) Chromatic Adaptation Transform.

Contrast Index [41], and the Gamut Area Index [12]. None of them, however, has been accepted as a standard, probably due to the fact that the CRI has been so widely used (in spite of its problems) and that the lighting industry does not want to use more than one number to rate color rendering of products.

Recently, the Color Quality Scale [8] has been developed to address such needs providing a one-number output. The CQS was developed especially to solve the problems of the CRI for LED sources described in the previous section. The CQS is designed to provide a score that correlates well with visual evaluation of color rendering. While this evaluation procedure is not adopted as a standard, this metric and its associated analyses can be used as design tool for color quality of SSL products. The CQS is basically a fidelity metric producing one number like R_a with a maximum score of 100, but the CQS has improvements including the ability to account for the direction of object color shifts, which deviate from a pure fidelity metric. The CQS score, therefore, agrees well with visual ratings for color-enhancing sources, while it works as an accurate fidelity metric for non-color-enhancing sources. The CQS is designed to evaluate the overall color quality of products for all types of light sources including narrowband LED sources and traditional lamps.

The detailed formulae of the CQS are available [8] but important features are explained below. The CQS has the same calculation structure as the CRI, with many improvements of components as below.

(1) 15 highly saturated test color samples selected from the 1200 Munsell color samples. They are: 5R4-14, 10R6-12, 7.5YR7-12, 5Y8-12, 2.5GY8-10, 7.5GY7-10, 2.5G6-12, 2.5BG6-10, 10BG6-8, 7.5B5-10, 2.5PB4-10, 7.5PB4-12, 5P5-10, 2.5RP6-12, 7.5RP5-12. This allows the metric to detect problems with rendering of saturated color objects as discussed in Sect. 16.3.3 (*A high CRI score does not guarantee good color quality*.) Doubling the number of samples also improves for the problem of the CRI, that allows gaming of the metric in spectral design (Fig. 16.15).
(2) CIELAB object color space (see Sect. 16.3.1). This replaces the obsolete $W^*U^*V^*$ color space and mitigates the problem discussed in Sect. 16.3.3 (*CRI penalizes preferred color-enhancing light*). The plots of the 15 test color samples of the CQS on the CIELAB (a^*, b^*) graph provide intuitive information of color rendering. Examples have already been shown in Figs. 16.12 and 16.13.
(3) CMCCAT2000 chromatic adaptation transform [36]. This provides more accurate prediction of effects of Duv shifts on color rendering and ameliorates the problem discussed in the previous section (*Problem with Duv shifts*).

Fig. 16.15 The 15 saturated test color samples used in the CQS

(4) The *saturation factor*, with which the increase of chroma is not penalized for a limited range of chroma increases $\left(\Delta C^{*}_{ab} < 10\right)$. This overcomes the problem of the CRI unduly penalizing chroma-enhancing sources as discussed in Sect. 16.3.3. The CQS starts penalizing excessive chroma increases $\left(\Delta C^{*}_{ab} > 10\right)$ when perceived color rendering starts appearing unnatural.
(5) Root-mean-square (RMS) averaging. This lowers the score if one or two of the 15 samples have very poor color rendering (example in Fig. 16.13), compared to simple averaging. This further addresses the issue discussed in Sect. 16.3.3 (*A high CRI score does not guarantee good color quality*.)
(6) The score is on a 0–100 scale, so that there can be no negative scores.

Note that the information above is on the current version of the CQS (version 9.0), which includes a few small improvements from the contents of publication [8]. Several of the 15 test samples in (1) were reselected for more uniform spacing in hue angle (listed above are the current sample sets). The ΔC^{*}_{ab} limit in (4) above was introduced based on the later experiments done at NIST. The CCT factor was dropped, as it has not been verified experimentally. The CQS calculation program is available from the author.

16.4 Luminous Efficacy of Radiation

The spectrum of light source affects not only color rendering but also energy efficiency (luminous efficacy) of light source. Thus color rendering is closely related to energy issues. A brief introduction on luminous efficacy is provided here.

The energy efficiency of a light source or a lighting product is evaluated by *luminous efficacy of a source* (often called simply *luminous efficacy*), which is the ratio of *luminous flux* (lumen) emitted by the source to the input electrical power (watt). The luminous efficacy of a source, η_v [lm/W], is determined by two factors

$$\eta_v = \eta_e \cdot K, \tag{16.12}$$

where η_e is the *radiant efficiency* of the source (ratio of radiant flux output to input electrical power; "external quantum efficiency" is often used with the same meaning). K is the *luminous efficacy of radiation* (ratio of luminous flux to radiant flux, denoted as LER in this chapter), and is determined by the spectral distribution $S(\lambda)$ of the source as given by,

$$K = \frac{K_m \int_{\lambda} V(\lambda) S(\lambda) \mathrm{d}\lambda}{\int_{\lambda} S(\lambda) \mathrm{d}\lambda}, \text{ where } K_m = 683 \text{ [lm/W]}. \tag{16.13}$$

K_m is *the maximum luminous efficacy of radiation*, and its value, 683 lm/W (for monochromatic radiation at 555 nm) comes from the international definition of the candela. While various other terms are used in the LED industry, the terms

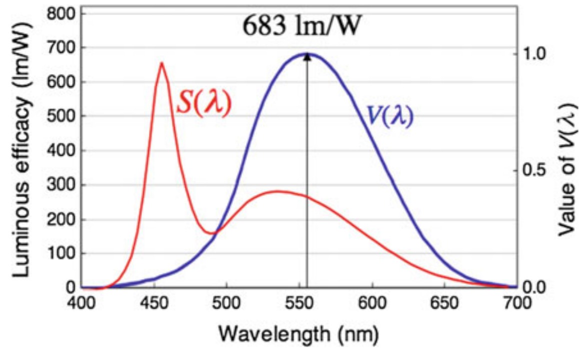

Fig. 16.16 Luminous efficacy of monochromatic radiation (*blue*), plotted with an example of LED spectrum (*red*)

introduced above are the ones officially defined internationally [5]. Figure 16.16 illustrates the calculation of the LER. This LED spectra have an LER value of $K = 294$ (lm/W). The LER of common discharge lamps range from ~250 to ~380 lm/W. The maximum LER for white light with acceptable color rendering is considered to be around 400 lm/W. The LER is entirely dependent on the SPD of the light source and represents the luminous efficacy that would be possible if the conversion of electricity to light could happen without any losses.

16.5 Color Characteristics for Single-Color LEDs

Chromaticity, as described in Sect. 16.2.1, is used for all LED devices including white and single-color LEDs. In addition to chromaticity, the characteristics below are used for single-color LEDs.

16.5.1 Dominant Wavelength λ_d

The dominant wavelength is commonly used to specify the color of single-color LEDs. It is defined in [42] as follows:

The wavelength of a monochromatic stimulus that, when additively mixed in suitable proportions with the specified achromatic stimulus, matches the color stimulus considered.

This is illustrated in Fig. 16.17. For characterizing LEDs, the reference achromatic stimulus should be an equal-energy spectrum (sometimes called Illuminant E), which has the chromaticity coordinates $x_E = 0.3333$, $y_E = 0.3333$. It should be noted that dominant wavelengths of red LEDs are shorter than their peak wavelengths as shown in Fig. 16.18, and longer for blue LEDs. This is due to the slope of the color matching functions in the red and blue region, where deeper red and blue contribute less to color perception. The difference can be greater than 10 nm for deep red and deep blue LEDs.

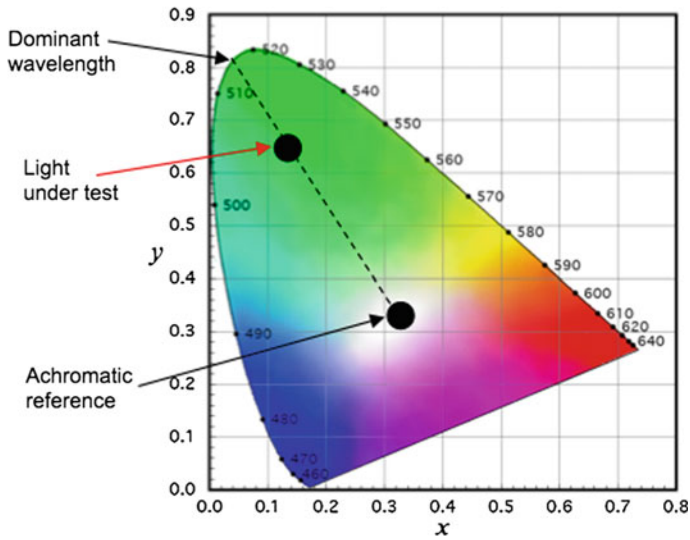

Fig. 16.17 Illustration of dominant wavelength

Fig. 16.18 An example of dominant wavelength and peak wavelength

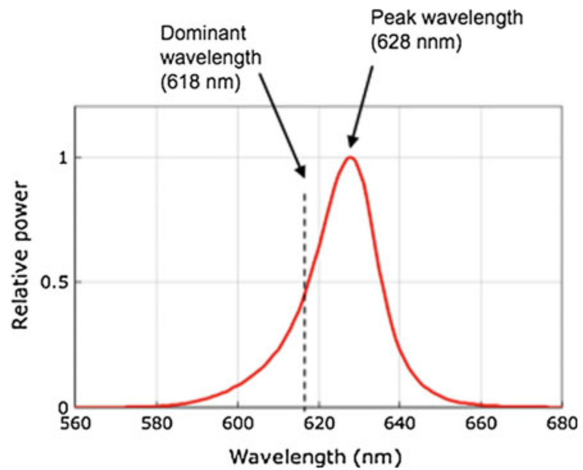

16.5.2 Centroid Wavelength λ_c

The centroid wavelength λ_c is defined in [42] and is calculated as the "center of gravity wavelength" by

$$\lambda_c = \int_{\lambda_1}^{\lambda_2} \lambda \cdot S(\lambda) \mathrm{d}\lambda \Big/ \int_{\lambda_1}^{\lambda_2} S(\lambda) \mathrm{d}\lambda \quad (16.14)$$

The diminishing tails of LED spectrum (including noise and stray light) may affect the value of centroid wavelength significantly, which should be considered as an uncertainty in a given measurement.

16.5.3 Peak Wavelength λ_p

As defined in [42], as the wavelength at the maximum of the spectral power distribution is known as the peak wavelength λ_p. The (absolute) spectral distribution is usually normalized at this wavelength rather than at an arbitrary wavelength, to give a relative spectral distribution with a maximum value of unity. See an example in Fig. 16.18.

16.6 Future Considerations on Color Quality for White LED Developments

By studying the CRI, people may be led to believe that white LED spectra should mimic the spectrum of the sun or a blackbody for best color rendering. While such spectra would certainly give high CRI values and provide excellent color rendering, they would not be very energy efficient. The main driving force for solid-state lighting is for huge energy savings on a national or global scale. The challenge in developing LEDs for use as illumination sources is to provide the highest possible energy efficiency while achieving the best color rendering possible for intended applications. These two factors tend to be in a trade-off relationship, and the balance between the two is often a compromise. However, there are some ways to design light sources for which both merits are high.

Phosphor white LEDs are currently dominant in the market and play important roles in introducing solid-state lighting with competitive energy efficiency and affordable cost that meet current needs. However, there is the potential of achieving much higher energy efficiency and excellent color rendering using other technologies such as RGB, RGBA, and narrowband phosphors, quantum dots, even though these technologies still have technical challenges and cost issues. Narrowband combinations, having deep valleys in the spectrum, may not be considered as good color rendering sources, but if the peaks are selected properly, they can provide excellent color rendering, which has been well demonstrated at the NIST facility [43].

Figure 16.19 shows the spectra and color analyses of examples of various types of white LEDs currently available. From the left, (1) is an example of a typical warm white phosphor LED lamp found in the market. This example has an LER of 305 lm/W, and the LER of other similar products range from 300 to 320 lm/W. While these products are meeting current needs, higher color rendering is desired.

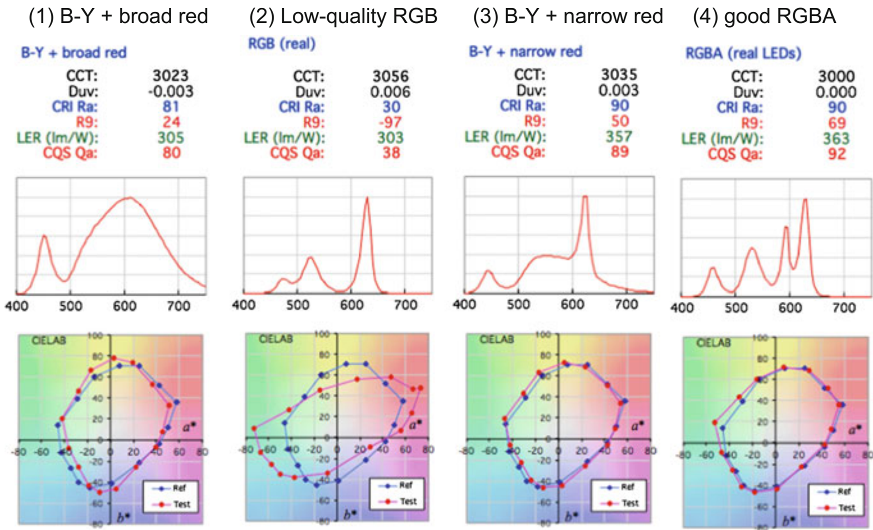

Fig. 16.19 Color rendering analyses of examples of real white LED products

The main issue is that the red object rendering of these products is not adequate, as can be seen on the CIELAB chart. To improve this, a deeper red phosphor would be needed, but the LER will then drop further. (2) is an example of a typical low-quality RGB product found in the market, exhibiting very poor color rendering and low LER of ~300 lm/W. (3) is a hybrid product using phosphor and a red LED peak, having much increased LER of 357 lm/W and high CRI of $R_a = 90$, and is considered one of solutions that overcome the limitations of broadband phosphor technology. (4) is an RGBA spectrum with selected single-color LED packages commercially available, showing LER of 363 lm/W and $R_a = 90$ and $Q_a = 92$. Examples (3) and (4) show ~15% higher LER (lm/W) than the phosphor warm white LED, while achieving much higher scores of the CRI and CQS.

Further analyses not limited to currently available LEDs show results of some RGB model (3000 K) with LER of 378 lm/W with $R_a = 86$, $R_9 = 90$, and an RGBA model (3000 K) with LER 382 lm/W and $R_a = 91$, $Q_a = 90$. Such LED sources can realize very high luminous efficacy as well as excellent color rendering. These models use LED peaks such as 547 nm or 576 nm. High power LEDs with such peak wavelengths are currently not available. Development of efficient high power LEDs in such deep green and yellow regions will make such high performance RGB or RGBA systems possible.

Fluorescent lamps evolved from broadband to narrowband throughout their long history to better achieve both high efficacy and good color rending. As discussed above, RGB or RGBA technologies, though they still have technical challenges, have theoretically higher luminous efficacies. As well as having no Stokes loss, they have a potential of reaching 20–30% higher luminous efficacy than the limit of the broadband phosphor LED technology. Narrowband phosphors replacing broadband

phosphors would also enable significant improvements in this respect. Narrowband components may play important roles in the future developments of SSL, especially when broadband phosphor technology matures.

LED sources with slightly increased color gamut as discussed in Sect. 16.3.3 are known to have a merit of general preference. Such color-enhancement effects can be easily created with narrowband sources and may facilitate important new applications of SSL. The effects of negative Duv as discussed in Sect. 16.2.2 need to be studied further, and such light sources may also find popularity in the future.

The author thanks Dr. Wendy Davis at the University of Sydney for her valuable inputs and discussions to some of the sections in this chapter.

References

1. CIE 15:2004 Colorimetry, 3rd ed.
2. ANSI_NEMA_ANSLG C78.377-2015 Specifications for the Chromaticity of Solid State Lighting Products (2008), and its revision C78.377-2011
3. ANSI C78.376 Specifications for the Chromaticity of Fluorescent Lamps (2001)
4. M.S. Rea, J.P. Freyssinier, White lighting. Color Res. Appl. (2011). doi:10.1002/col.20738
5. CIE S 017/E:2011, ILV: International Lighting Vocabulary, and its on-line version at http://eilv.cie.co.at
6. CIE 13.3-1995, Method of Measuring and Specifying Colour Rendering of Light Sources, 3rd ed.
7. CIE 177: 2007, Colour Rendering of White LED Light Sources
8. W. Davis, Y. Ohno, Color quality scale, Opt. Eng. **49**(3), 033602-1–033602-15 (2010)
9. C. Li, M.R. Luo, C. Li, G. Cui, The CRI-CAM02UCS colour rendering index. Color Res. Appl. **37–3**, 160–167 (2012)
10. K. Smet, S. Jost-Boissard, W.R. Ryckaert, G. Deconinck, P. Hanselaer, Validation of a colour rendering index based on memory colours, CIE x035:2010, in *Proceedings of CIE 2010* "*Lighting Quality and Energy Efficiency*," (2010), pp. 136–142
11. K. Smet, L. Whitehead, Meta-standards for color rendering metrics and implications for sample spectral sets, in *Proceedings of 19th Color Imaging Conference*, San Jose (2011), pp. 76–81
12. Lighting Research Center, Guide to Light and Color in Retail Merchandising, ASSIST Recommends, vol. 8, Issue 1, March 2010
13. D.B. Judd, A flattery index for artificial illuminants. Illum. Eng. (N.Y.) **62**, 593–598 (1967)
14. W.A. Thornton, Color-discrimination index. J. Opt. Soc. Am. **62**, 191–194 (1972)
15. W.A. Thornton, A validation of the color preference index. J. Illum. Eng. **4**, 48–52 (1974)
16. Y. Ohno, Simulation Analysis of white LED spectra and color rendering, in *Proceedings of CIE Symposium '04, LED Light Sources: Physical Measurement and Visual and Photobiological Assessment*, 7–8 June 2004, Tokyo Japan (2004), pp. 28–32
17. Y. Ohno, Spectral design considerations for color rendering of white LED light sources. Opt. Eng. **44**, 111302 (2005)
18. D.L. MacAdam, Visual sensitivities to colour differences in daylight. J. Opt. Soc. Am. **32**, 247 (1942)
19. ISO 11664-1:2007(E)/CIE S 014-1/E:2006: Joint ISO/CIE Standard: Colorimetry—Part 1: CIE Standard Colorimetric Observers
20. ISO 11664-2:2007(E)/CIE S 014-2/E:2006: Joint ISO/CIE Standard: Colorimetry—Part 2: CIE Standard Illuminants for Colorimetry

21. ENERGY STAR® Program Requirements for CFLs ENERGY STAR Eligibility Criteria Energy-Efficiency Criteria—Version 4.1, Department of Energy (2008)
22. CIE TN 001:2014, Chromaticity difference specification for light sources
23. ISO 11664-4:2008(E)/CIE S 014-4/E:2007: Joint ISO/CIE Standard: Colorimetry—Part 4: CIE 1976 L*a*b* Colour Space
24. ISO 11664-5:2009(E)/CIE S 014-5/E:2009: Joint ISO/CIE Standard: Colorimetry—Part 5: CIE 1976 L*u*v* Colour Space and u′, v′ Uniform Chromaticity Scale Diagram
25. http://en.wikipedia.org/wiki/Munsell_color_system
26. CIE 135/2, Colour rendering, TC 1-33 closing remarks (1999)
27. N. Narendran, L. Deng, Color rendering properties of LED sources. Proc. SPIE **4776**, 61–67 (2002)
28. P. Bodrogi, P. Csuti, P. Horváth, J. Schanda, Why does the CIE color rendering index fail for white RGB LED light sources?, in *Proceedings of CIE Expert Symposium LED Light Sources: Physical Measurement and Visual and Photobiological Assessment* (2004), pp. 24–27
29. Y. Ohno, Spectral design considerations for white LED color rendering. Opt. Eng. **44**(11), 111302-1–111302-9 (2005)
30. M.S. Rea, J.P. Freyssinier-Nova, Color rendering: a tale of two metrics. Color Res. Appl. **33** (3), 192–202 (2008)
31. W. Davis, Y. Ohno, Approaches to color rendering measurement. J. Modern Opt. **56**(13), 1412–1419 (2009)
32. J.A. Worthey, Color rendering: asking the question. Color Res. Appl. **28**, 403–412 (2003)
33. EPA, ENERGY STAR® Program Requirements for Integral LED Lamps, Eligibility Criteria —Version 1.4, 13 May 2011
34. Y. Ohno, M. Fein, Vision experiment on acceptable and preferred white light chromaticity for lighting, CIE x039:2014, pp. 192–199 (2014)
35. CIE 160:2004. A review of chromatic adaptation transforms (2004)
36. C. Li, M.R. Luo, B. Rigg, R.W.G. Hunt, CMC 2000 chromatic adaptation transform: CMCCAT2000. Color Res. Appl. **27**(1) (2002)
37. D.B. Judd, A flattery index for artificial illuminants. Illum. Eng. **62**, 593–598 (1967)
38. W.A. Thornton, A validation of the color-preference index. J. Illum. Eng. Soc. **4**, 48–52 (1974)
39. R.W.G. Hunt, Light and dark adaptation and the perception of color. J. Opt. Soc. Am. **42**, 190–199 (1952)
40. W. Davis, Y. Ohno, Studies on the effect of illuminance on color rendering, in *Proceedings of CIE 2009: Light and Lighting Conference*, Budapest, Hungary (2009)
41. K. Hashimoto, T. Yano, M. Shimizu, Y. Nayatani, New method for specifying color-rendering properties of light sources based on feeling of contrast. Color Res. Appl. **32**, 361–371 (2007)
42. CIE 127:2007 (2nd ed.): Measurement of LEDs
43. C. Miller, Y. Ohno, W. Davis, Y. Zong, K. Dowling, NIST spectrally tunable lighting facility for color rendering and lighting experiments, in *Proceedings CIE 2009: Light and Lighting Conference* (2009)

Chapter 17
Emerging System Level Applications for LED Technology

Robert F. Karlicek Jr.

Abstract This chapter describes possible future system level applications of LED technology from the viewpoint of emerging trends in lighting related human health, communications, and display technologies. Currently, almost every aspect of LED technology from substrates to systems applications is undergoing rapid technical evolution, so projections about future system level applications is highly speculative, and this assessment presumes that solutions to long standing LED issues like droop and poor green/yellow performance will ultimately be found. Future system level applications will also be tightly convolved with the system level incorporation of new types of light sensors and embedded processing capabilities so that feedback loops between the light source, the environment, and the control system can be closed. Future systems level applications will also be tightly convolved. The development of new features and services needed to extend business revenue models of lighting companies as the progress in LED system reliability drives future applications in lighting to the point that bulb/socket commodity business models begin to fail, and business models based on the offering of new lighting features and services are developed.

17.1 Introduction

The development of highly efficient LED technology, particularly for the generation of visible light has progressed rapidly, especially since the development of high brightness GaN-based LEDs in the early 1990s [1]. Even as LED-based lighting systems are now beginning to penetrate conventional lighting markets at commercially significant levels [2], there is still considerable, basic and developmental research focused on almost every fundamental aspect of the LED technology supply chain, from substrate type and device design to fixture level packaging and control systems architectures. While the main driver for this research is the substantial

R.F. Karlicek Jr. (✉)
Rensselaer Polytechnic Institute, New York, USA
e-mail: karlir@rpi.edu

© Springer Nature Singapore Pte Ltd. 2017

T.-Y. Seong et al. (eds.), *III-Nitride Based Light Emitting Diodes and Applications*,
Topics in Applied Physics 133, DOI 10.1007/978-981-10-3755-9_17

global lighting market and the realization of improved energy efficiency possible with LED-based solid state lighting (SSL) relative to the widely used incandescent bulb, the high efficiency and lower cost of some conventional lighting systems (i.e., fluorescent-based technologies) will continue to limit adoption of SSL technologies for illumination until the cost of SSL technology decreases significantly. Beyond cost, the current widespread cultural acceptance of existing illumination system designs and technology specific capabilities (e.g., CCT decrease with dimming for incandescent) will continue to represent a challenge for SSL penetration in some applications. Finally, the very high reliability of LEDs (in properly designed systems) is approaching the point where the long life of LED-based illumination systems may ultimately lead to the demise of well established bulb/socket-based lighting systems.

These challenges in the lighting space can be contrasted with the incredibly rapid penetration of LED technology in mobile video displays where the basic LED capabilities of efficiency, size, and robustness are essential to the performance of these sophisticated devices. Coupled with what seems to be an insatiable desire for people everywhere to network, remain connected, access video information, and function in an increasingly untethered world, LEDs have become a basic part of a complex engineered system that provides a valuable service that was never before possible. In spite of their critical role in mobile communications in this market, LEDs simply provide white light, and the wider fundamental capabilities (i.e., spectral control properties and digital signaling capabilities) of LED technology are largely unused. As in the case of mobile video, the future value of new markets enabled by LEDs will largely be driven by system level capabilities that provide unique, value added solutions for overcoming challenges in energy efficiency, human health and wellbeing, and productivity. This chapter examines some of the system considerations and applications, some now emerging, where broader advantages of LED system level technology can play a unique, enabling role in developing new illumination applications.

17.2 Advanced Lighting Systems

Solid state lighting is at its core, a transition from electric to electronic lighting, much as the transistor was a transition from electric to electronic switching. At the semiconductor technology level, comparisons are even being made between the well-known Moore's Law [3] for transistor technology and Haitz's Law [4] for LED/IC roadmapping efforts [5]. While visible LEDs were first demonstrated in 1962 [6], the real breakthrough in LED technology required the demonstration of high brightness GaN-based LEDs about 30 years later. Chronologically, one might say that the {transistor–systems–market} ecosystem is running about four to five decades ahead of its {semiconductor diode SSL} sibling, so one can consider the evolution of advanced lighting systems to still be in a rather early developmental phase.

While terms like “Smart” or “Intelligent” are increasingly being applied to SSL technologies, most of these technologies focus on a merger of basic communications technology (wireless or wired) to effect rather rudimentary control of lighting functions like dimming and remote controlled on/off switching. While elaborate lighting control systems exist today, they are rarely selected by lighting designers because they cannot easily adapt to post installation interior design changes without recalibration or programming changes. The US Department of Energy’s (DOE) recent data on lighting installations suggests that fewer most US lighting installations lack even simple dimming controls in spite of the potential energy savings that automatic controls could bring to lighting systems [7].

Perhaps one of the most important drivers for advanced LED-based lighting systems development stems from the long lifetime of properly designed LED systems. In spite of current limitations of some LED driver lifetimes and photothermal degradation of certain types of encapsulation and secondary optics in LED fixtures (both are addressable issues with continued research), future LED system lifetimes will be measured in decades and will outlive the design life of both commercial and residential interior spaces [8]. In such a scenario, LED systems may be sold more as durable goods or as an integral part of construction systems, with revenue models for LED systems manufacturers depending increasingly upon providing new features and services derived from perceived or real market needs and consumer benefits. This vision is already emerging as companies seek to gain a competitive advantage in the nascent SSL market space by offering lighting with embedded operating systems [9] and simple video functions [10, 11] and may mirror the development of the evolving smart TV market space.

Presuming that continued research on the materials and device designs used to manufacture LEDs will ultimately address common LED maladies like droop (non-thermal) and green (and yellow) gap issues, then efficient lighting systems with embedded intelligence that can control color dynamically and be modulated at high speed at any wavelength will open a wide range of new system level capabilities that offer new functions and services that go well beyond the simple mapping of legacy communications and control technologies to LED replacement bulb and fixture technology. Identification of possible future lighting system applications outlined here involve the integration of LED lighting systems with impact on human health and well-being, improved and expanded access to wireless data, and the integration with video systems. These services will be constrained, to some degree, by the ability to provide these services at a reasonable energy cost relative to the benefit provided. This view is captured schematically in Fig. 17.1, and three of the non-energy related future system level applications are briefly described here.

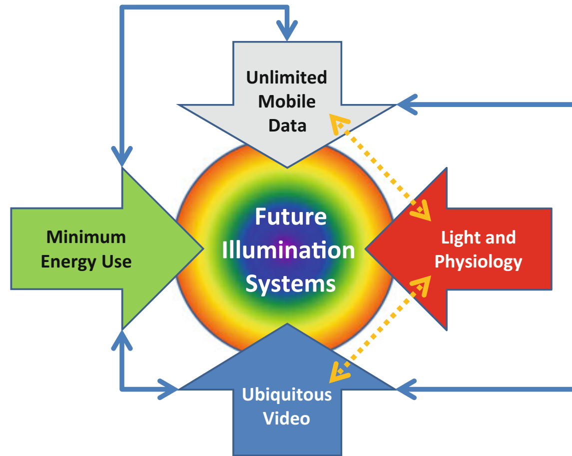

Fig. 17.1 Future illumination system will balance energy efficiency with new features and services in areas of human health and well-being, communications, and integrated video/illumination capabilities

17.2.1 New Applications in the Field of Human Health and Well-being

Throughout the history of lighting, illumination has been inextricably involved with human well-being and productivity [12], with extensive research on electric lighting design's impact on human performance starting shortly after the introduction of the incandescent light bulb [13]. The Lighting Handbook published by Illumination Engineering Society of North America (IESNA) [14], provides basic guidelines on lighting design and human factors illumination considerations, including some discussion of lighting applications using LED technology. Most of this guidance pertains to how humans respond to nominally conventional white lighting sources in terms of safety, comfort, and satisfaction with the quality of light. The first wave of SSL products now available seek to replicate or marginally improve on the performance of existing white light incandescent or fluorescent sources, with the control of spectral output limited to what can be achieved at a reasonably high efficacy with phosphor-converted blue or near UV LED sources. SSL spectral output is typically static (except during the initial warm-up period), though lighting systems with dynamic tuning between cool white and warm white LEDs have been available for several years, and color tunable bulbs that are wirelessly programmable for a wide variety of color functions have become available recently [15]. Ideally, LED systems should offer better spectral control of illumination and can enable a much wider range of color and gamut tuning capabilities, but it is not clear that these features will lead to broader or more rapid adoption of solid state lighting. Studies of artificial lighting and human satisfaction can be difficult to perform and outcomes can be impacted by notions that artificial light (perhaps regardless of the source) is of lower quality or less desirable than natural daylight [16].

In spite of issues with quantifying customer acceptance of different types of lighting sources, the spectral flexibility available with more advanced SSL systems

will offer new capabilities with regard to improving human health and well-being, with the benefits being in the area of circadian regulation, education, and improved worker productivity. Research has shown that exposure to sunlight can have an impact on hospitalized patient health and well-being [17]. Tailoring the circadian color temperature of solid state illumination systems is now being explored in a hospital setting to study the impact on patient sleep [18]. It will be interesting to see just how much impact spectral control of lighting in healthcare environments will impact patient recovery, and how these findings would migrate to improved worker health and on-the-job performance, where lighting quality is already a major factor in worker productivity and job satisfaction [19].

Research on light and sleep has a long history, but the discovery of non-visual light receptors in the human retina [20] and their role in setting and altering human circadian rhythm and sleeping patterns, coupled with the relationship with sleep problems on disease [21], suggest that future lighting systems could play an important role in human sleep management and health. Correlations of lighting and shift work has been linked to serious health issues like cancer [22] and heart disease [23], the possible impact lighting on shift worker health (and by extension to the general population) represents an important area of research. Several lighting products that use blue LEDs for personalized circadian rhythm management are already available on the market and undergoing serious evaluation [24]. These systems run "open loop", since circadian function is part of a closed loop control system where one of the elements of the control loop involves internal circadian regulation mechanisms. Ideally, the use of light to manage circadian entrainment would use some form of sensors to provide information on light dose and the human circadian status, and these sensors are under development [25]. It is probably unlikely to expect that most people would try to actively manage their circadian entrainment, but applications in relatively controlled healthcare environments (hospitals and eldercare facilities) are quite feasible.

Beyond impacting circadian rhythm and sleep, the timing, wavelength, and magnitude of the lighting dose can impact the alertness and performance of humans for some time after the light exposure has occurred [26]. Also, new studies are emerging that suggest new approaches for control of light spectral content may be helpful for circadian management in shift workers. Recent studies on subtracting a narrow band of blue wavelengths from conventional lighting systems suggest that subtractive spectral methods may be useful for circadian rhythm management may have an impact on the health and alertness of shift workers [27]. Lighting spectral content is also being studied with regard to impact on education and learning [28, 29]. Beyond simple illumination, studies on health related impacts of near UV radiation (common in sunlight) suggest that, while there are health concerns at much shorter UV wavelengths, certain health benefits may result from exposure to portions of the longer wavelength UVA region [30] and these considerations could be important in the design of solid state lighting systems with optimized UV output.

Human factors studies based on the new spectral tuning capabilities of solid state lighting systems are in their very early stages and much more work remains to be done. Initial studies, however, already indicate that systems capable of dynamically

adjusting spectral content will be an important part of advanced lighting systems for optimizing human health and well-being. Given the globally soaring costs of health care, well designed lighting systems with dynamic spectral tuning capabilities may open lucrative new markets for solid state lighting systems.

17.2.2 Illumination with Communication

Communicating with light is commonplace (i.e., fiber optic communications), but lighting that communicates with visible light represents a new application uniquely enabled by solid state lighting, as LEDs can be modulated at relatively high speed. Referred to as Visible Light Communication (VLC) or more recently LiFi (like the RF-based WiFi), this sort of functionality has been under development for some time [31]. Most VLC efforts focus on the wireless transmission of data at high bit rates as a means to augment or even replace radio frequency (RF) based wireless communications due to rapidly increasing demand for bandwidth and the limited regulated RF spectrum available to meet demand [32]. It should be possible to significantly expand RF-based wireless capacity by moving to RF systems operating at 60 GHz, but communications at this radio frequency are line of sight (just as is VLC) and 60 GHz signals are more strongly absorbed by a wider range of common materials (similar to light). These limitations require special considerations for the design and implementation of 60 GHz wireless technology [33], many of which are similar to challenges faced by proponents of VLC systems. Lighting systems designed to supply high speed wireless data and illumination simultaneously could relax demand for more sophisticated high frequency wireless systems and provide wireless connectivity in RF restricted locations and provide a somewhat higher level of security than is possible with RF wireless services. The concept is shown in Fig. 17.2.

Dual use (illumination with communication) lighting systems being explored with current phosphor-converted white LED systems typically use filtered detections systems to receive only the modulated blue LED emission because the radiative lifetimes of efficient phosphors are too long to permit high speed data transmission. Recently, relatively high bit rate data transmission with white LEDs and without the use of a blue filter using special modulation and digital filtering has been demonstrated [34]. When efficient color tunable lighting systems using RGBY LEDs become available, VLC applications can be partitioned by color (coarse wavelength division multiplexing). Using these sorts of multi-wavelength experimental systems, high speed data links using LED systems have been demonstrated [35]. Advantages of VLC over RF-based wireless systems include security and unrestricted allocation of bandwidth, though many challenges need to be worked out on topics of mobility, integration with fixture designs (combinations of spot and diffuse lighting), and integration with RF uplink channels. Preliminary standards for VLC applications are under development [36]. Ultimately, integrated combinations of VLC and RF wireless communications will mostly likely be needed to meet the seemingly endless growth in demand for wireless data and mobile connectivity [37].

Fig. 17.2 Dual use (illumination and communications) will enable new lighting services as well as sensing technologies enabling autonomous, dynamic optimization illumination patterns

Solid state lighting systems that can illuminate an area and simultaneously transmit and receive data will enable other new and interesting functionality. For example, the use of modulated lighting for indoor localization (indoor GPS) is now being commercialized [38]. Drawing on concepts of time-of-flight sensing and the use of structured light for coarse 3D mapping of surfaces [39], it will be possible to design illumination systems equipped with embedded light detector networks to perform light-only based occupancy sensing and localization of occupants. When sources in an illumination system simply transmit identification codes and setting information (dimming, color point, etc.), networked receivers in the illumination system could monitor scattered light to characterize the rough geometry of the illuminated space and determine the when, where, and type of illumination required based on the environment [40]. The ultimate goal of such systems is the development of autonomous, adaptive lighting control capability that will enable much more intuitive, self calibrating, and self commissioning illumination systems. In some sense these types of applications are similar to earlier work where simple camera networks have been applied to issues of lighting control [41], but have seen very limited application, possibly for privacy concerns.

More broadly, equipping illumination systems with specialized sensors to enable low resolution light field mapping will create lighting systems which, for the first time, will “see” where the emitted light is going, coarsely image the surfaces that scatter or reflect it, and localize the illuminated objects in its field of view. Reflected light without a digital signature would suggest daylight and color tunable systems could adjust the spectral output for circadian matching (or not, depending on the illumination requirements of the occupants detected by the lighting system), assuming the digital light detection system can adequately resolve color and directionality. Lighting systems could also autonomously interact with other light emitting systems with their own digital light signature (e.g., projection or video systems), adapting the illumination as required. As lighting continues its migration to the electronic age, even more novel applications of communicative illumination systems will emerge.

17.2.3 Illumination with Display Capability

As mentioned earlier, LED technology has had a significant impact on display technology, enabling technologies like tablet computers and thin form factor LCD displays. Evolving development of gaming, immersive digital environments, and new lighting technologies is already leading to the fusion of illumination and display technology. Like the integration of illumination and communications, this trend has been under development for some time, and includes the use of LCD display technology for virtual windows and skylights [42], and the use of color tunable LED lighting panel technology for illumination from an “open sky” source [43, 44]. An early design of this concept is shown in Fig. 17.3. The integration of display and illumination technology, if accomplished with inorganic LEDs in an emissive display format, will require significant improvements in the operating efficiency of green and yellow LED devices, and this has proven difficult for the LED die developers, though these wavelengths might start to receive more research attention as blue LED performance gains saturate. Significant technical development of both display and LED technology will be needed to fully develop this fusion, but it is likely that future lighting systems will more closely approximate natural lighting (and can display the scenery that accompanies it). Display manufacturer Sony has recently described an experimental inorganic LED display format (no OLED, no LCD) [45], and as both lighting and display technologies are under pressure to be more energy efficient, it is expected that more illumination capable video systems will be developed. This trend will be analogous to trends observed in telephony, where what was once known as “plain old telephone service” (or POTS) transitioned to smart mobile communications systems with a fusion of communications, computation, and display technology.

Fig. 17.3 Moving Sky Panel using dynamically controlled RGB LEDs to simulate a skylight (courtesy of SHENZHEN NEONNY TECHNOLOGIES CO., LTD.). Continued improvements in LED efficiency and packaging technology will enable the creation of energy efficient, high resolution video—illumination dual function systems

17.3 Summary

The rapid development of LED technology, largely driven by the need for efficient illumination, is a truly disruptive technology that will have wide technological, commercial, and social applications beyond simple illumination. Increasingly, lighting suppliers will need to explore systems that deliver new services from lighting if only to maintain a viable business strategy as simple replacement bulb/socket technologies gradually become increasingly anachronistic (if not extinct) and the long service life of properly designed SSL systems drive new models for revenue generation. This is already occurring in the marketplace as lighting suppliers seek to leverage the capabilities of solid state lighting, offering dynamic lighting concepts tied to warm/cool color tuning capabilities simply to differentiate SSL offerings relative to highly efficient but spectrally static fluorescent lighting systems where the differential energy efficiency savings are small.

As developers explore the new spectral, spatial, and temporal properties afforded by advanced LED-based illumination systems it is likely that a very wide range of advanced system features and services will be developed and some of those possibilities are described in this chapter. Industry is already testing some of these concepts by developing dynamic lighting systems that offer applications-based illumination recipes, tunable lighting on or off the black body curve, indoor localization services with digital lighting, and even fixtures that can dynamically

alter the fixture beam pattern electronically. Increasingly, the effective use of advanced solid state lighting systems will require advanced sensor capabilities and standardized control and communications protocols which will take some time to develop. The evolving Internet of Things (IoT) concepts already connecting consumer products to a growing network will enable lighting systems to seamlessly interface with building and grid systems while providing illumination of vastly improved quality relative to that available with incumbent incandescent and tube technologies. Ultimately, SSL will enable unforeseen systems capabilities and services much as the introduction of the transistor did over half a century ago.

Acknowledgements The author would like to thank colleagues at Rensselaer Polytechnic Institute, Boston University and the University of New Mexico participating in the Smart Lighting Engineering Research Center (ERC) for extensive discussions relating to the future development of solid state lighting systems and applications. This work has also been shaped by extensive discussions with many of the solid state lighting industry members of the Smart Lighting ERC who are actively involved in developing new systems level solutions based on advanced LED technology. This work was supported primarily by the Engineering Research Centers Program (ERC) of the National Science Foundation under NSF Cooperative Agreement No. EEC-0812056 and in part by New York State under NYSTAR contract C090145.

References

1. S. Nakamura, M. Senoh, T. Mukai, High-power InGaN/GaN double-heterostructure violet light-emitting diodes. Appl. Phys. Lett. **62**(19), 2390 (1993)
2. L. Peters, M. Wright, LED lighting market to grow while LED component market goes flat. LEDs Mag. **50**, 21 (2012)
3. G.E. Moore, Cramming more components onto integrated circuits. Electronics **38**(8), 4 (1965)
4. Haitz’s Law was first mentioned in at LED conferences 2000. A more detailed description can be viewed at Nature Photonics 1, p. 23 (2007)
5. http://www.bbc.com/future/story/20120314-the-end-of-the-lightbulb/2. Accessed 15 Sept 2012
6. N. Holonyak, S.F. Bevacqua, Coherent (visible) light emission from $GaAs_{1-x}P_x$ junctions. Appl. Phys. Letts. **1**, 82 (1962)
7. U.S. Department of Energy, Building Technologies Program. 2010 U.S. Lighting Market Characterization (2012), pp. 58–62
8. Based on numerous conversations with lighting designers, the estimated average interior lighting design lifetime for retail and commercial spaces is between 7 and 10 years, approximately equal to or less than the lifetime of well designed SSL systems
9. http://www.forbes.com/sites/eco-nomics/2011/05/12/googles-bright-new-idea-android-controlled-light-bulbs/. Accessed 10 Oct 2012
10. Neonny Press Release, Neonny Unveils Amazing Moving Sky LED Panels (2012), http://www.ledinside.com/products/2012/9/neonny_led_panel_20120904. Accessed 20 Oct 2012
11. Fraunhofer Press Release, Sky Light Sky Bright—In the Office (2012), http://www.fraunhofer.de/en/press/research-news/2012/january/sky-light-sky-bright.html. Accessed 5 Jan 2012
12. P.R. Boyce, *Human Factors in Lighting*, 2nd edn. (Taylor and Francis Inc., London, 2003)
13. D. Burnett, Distributed lighting. Trans. Am. Inst. Electr. Eng. 71–76 (1902)
14. D. DiLaura, K. Houser, R. Mistrick, G. Steffy, *The Lighting Handbook*, 10th edn. (Illumination Engineering Society, 2011). ISBN 978-0-97995-241-9

15. New color tunable bulb from Philips permits the interface of smart devices and the bulb through a wireless connection, http://www.meethue.com/en-US. Accessed 29 Oct 2012
16. J.A. Veitch, R. Gifford, Assessing beliefs about lighting effects on health, performance, mood, and social behavior. Environ. Behav. **28**(4), 446–470 (1996)
17. J.M. Walch, B.S. Rabin, R. Day, J.N. Williams, K. Choi, J.D. Kang, Psychosom. Med. **67**, 156–163 (2005)
18. Philips Study, http://www.newscenter.philips.com/main/standard/news/press/2011/20111122-healwell.wpd. Accessed 3 Apr 2012
19. L. Edwards, P. Torcelli, *A literature review of the effects of natural light on building occupants*. National Renewable Energy Laboratory (NREL TP-550-30769) (2002)
20. D.M. Berson, F.A. Dunn, M. Takao, Phototransduction by retinal ganglion cells that set the circadian clock. Science **295**, 1070 (2002)
21. R.G. Stevens, D.E. Blask, G.C. Brainard, J. Hansen, S.W. Lockley, I. Provencio, M.S. Rea, L. Reinlib, Meeting report: the role of environmental lighting and circadian disruption in cancer and other diseases. Environ. Health Perspect. **115**(9), 1357 (2007)
22. S. Davis, D.K. Mirick, R.G. Stevens, Night shift work, light at night and risk of breast cancer. J. Natl. Cancer Inst. **93**(20), 1557–1562 (2001)
23. C. Sabanayagam, A. Shankar, Sleep duration and cardiovascular disease: results from the national health interview survey. Sleep **33**(8), 1037–1042 (2010). and references therein
24. V.L. Revell, T.A. Molina, C.I. Eastman, Human phase response curve to intermittent blue light using a commercially available device. J. Psychol. **590**(19), 4859–4868
25. A research tool developed at Rensselaer's Lighting Research Center, http://www.lrc.rpi.edu/programs/lightHealth/projects/Dimesimeter.asp. Accessed 17 Nov 2012
26. M. Munch, F. Linhart, A. Borisuit, S.M. Jaeggi, J.-L. Scartezzini, Effects of prior light exposure on early evening performance, subjective sleepiness, and hormonal secretion. Behav. Neurosci. **126**(1), 196–203 (2012)
27. S.A. Rahman, S. Marcu, C.M. Shapiro, T.J. Brown, R.F. Casper, Spectral modulation attenuates molecular, endocrine and neurobehavioral disruption induced by nocturnal light exposure. J. Physiol. Endocrinol. Metab. **300**, E518 (2011)
28. T. Goven, T. Laike, P. Raynham, E. Sansal, Influence of ambient light on the performance, mood, endocrine systems and other factors of school children, in *CIE 27th Session* (Sun City, South Africa, 2011), p. 112
29. M.S. Mott, D.H. Robinson, A. Walden, J. Burnette, A.S. Rutherford, Illuminating effects of dynamic lighting on student learning. Sage Open **2012**, 2 (2012). doi:10.1177/2158244012445585
30. A. Juzeniene, J. Moan, Beneficial effects of UV radiation other than via vitamin D production. Dermato-Endocrinol. **4**(2), 109–117 (2012). and references therein
31. S. Arnon, J. Barry, G. Karagiannidis, R. Schober, M. Uysal (eds.), *Advanced Optical Wireless Communication Systems* (Cambridge University Press, New York, 2012)
32. M. Kavehrad, Sustainable energy-efficient wireless communications using light. IEEE Commun. Mag. **48**(12), 66 (2010)
33. B.V. Quang, V. Prasad, I. Niemegeers, A survey on handoffs—lessons for 60 GHz based wireless systems. IEEE Commun. Surv. Tutor. **14**(1), 64–85 (2012)
34. C.H. Yeh, Y.F. Liu, C.W. Chow, Y. Liu, P.Y. Huang, H.K. Tsang, Investigation of 4-ASK modulation with digital filtering to increase 20 times of direct modulation speed of white-light LED visible light communication system. Opt. Express **20**(15), 16218 (2012)
35. W.Y. Lin, C.Y. Chen, H.H. Lu, C.H. Chang, Y.P. Lin, H.C. Lin, H.W. Wu, 10 m/500 Mbps visible light communications systems. Opt. Express **20**(9), 9919–9924 (2012)
36. See the IEEE 802.15.7 draft standard for visible light communications
37. M.B. Rahaim, A.M. Vegni, T.D.C. Little, Hybrid radio frequency and broadcast system, in *Proceedings of the 2nd IEEE Globecom 2011 Workshop on Optical Wireless Communications* (2011)
38. A new company has developed indoor light-based communications services for a variety of uses, http://www.bytelight.com

39. J. Geng, Structured light 3D surface imaging: a tutorial. Adv. Opt. Photonics **3**, 128 (2011)
40. F. Chiabrando, R. Chiabrando, D. Piatt, F. Rinaudo, Sensors for 3D imaging: metric evaluation and calibration of a CCD/CMOS time-of-flight camera. Sensors **9**(12), 10080 (2009). An IR camera technology highlights the concept
41. G.R. Newsham, C.D. Arsenault, A camera as a sensor for lighting and shading control, NRCC-50453 national research council Canada (a version of this report is published). Light. Res. Technol. **41**(2), 143 (2009)
42. B. Witherspoon, M. Petrick, Scientific research and sky image ceilings. Sky Factory White Paper (2008), http://www.skyfactory.com/files/SkyFactory_White_Paper_032408.pdf. Accessed 5 Jan 2012
43. Fraunhofer Press Release (2012) Sky Light Sky Bright—In the Office, http://www.fraunhofer.de/en/press/research-news/2012/january/sky-light-sky-bright.html. Accessed 5 Jan 2012
44. http://www.ledinside.com/products/2012/9/neonny_led_panel_20120904. Accessed 15 Oct 2012
45. See http://www.sony.net/SonyInfo/News/Press/201201/12-005E/index.html. Accessed 10 Jan 2012

Index

A
Absorption, 403, 405–407, 410, 411, 421, 423, 426
AlGaN, 267–272, 274–277, 279–297
AlN, 267–276, 278, 280, 283, 284–288, 290, 292–297
Alternating current, 433, 434
Alternating Current Light-Emitting Diode (ACLED), 433, 434
Anti-parallel, 440, 441
Auger recombination, 168–171, 183–185, 187

C
Catastrophic failure, 388
Chip shaping, 341
Chromaticity, 457–464, 466, 475
Chromaticity coordinates, 409, 413–415, 417
Color-mixing LED, 240, 241
Color quality, 457, 458, 463, 471–474, 477
Color quality scale, 457, 472, 473
Color rendering, 14–17, 26, 397–399, 402, 404, 406, 407, 412, 415, 417–419, 423, 424, 457, 458, 465, 467–478
Color rendering index (CRI), 397–399, 402, 406, 412, 415, 417–419, 424, 458, 468, 469
Color temperature, 263, 397–399, 404, 410, 413–415, 417, 418, 425, 485
Conduction mechanism, 364
Constant ABC model, 163, 170, 183, 185, 203
Consumption of light, 17–20
Correlated color temperature (CCT), 412, 415, 417
Current crowding, 366, 367
Current spreading length, 367

D
Deep-UV LEDs, 267–272, 274–277, 280–297
Dislocation Density, 69–75, 77, 84, 88
Distributed Bragg reflector, 31, 39

E
Efficiency droop, 163, 166–170, 172–174, 176, 177, 180, 185, 187, 203
Electroluminescence, 12, 26, 129, 131–133, 146
Electrostatic discharge (ESD), 363, 388
Energy economics, 17
Escape cone, 78–82
External efficiency, 341
External Quantum Efficiency (EQE), 117, 120, 117, 120, 121

F
Factor of production, 17–20
Flip chip, 341, 353, 357, 358

G
GaAsP laser diode, 2
GaInN, 223, 229
GaN-based LED, 4
GaN on Si, 29, 33, 34, 36, 39, 41, 42, 60
Green gap, 120, 121, 240–243, 256, 257, 260

H
Heteroepitaxial growth, 31
Highly luminescent InGaN, 4
High voltage, 433–436, 438, 444, 452
History of nitride research, 2
Human centric lighting, 484
High-Voltage Light-Emitting Diode(HVLED), 433–454

I
InGaN, 239, 241–254, 261
InGaN alloy, 3
Injection efficiency, 164–166, 171, 182, 183, 187, 203
Integrated Lighting/Display Technology, 483, 488

© Springer Nature Singapore Pte Ltd. 2017

T.-Y. Seong et al. (eds.), *III-Nitride Based Light Emitting Diodes and Applications*,
Topics in Applied Physics 133, DOI 10.1007/978-981-10-3755-9

Intensity-dependent photoluminescence, 183, 191, 193, 204
Internal quantum efficiency (IQE), 95, 129–133, 135, 138–140, 142, 144–146, 267, 275

L
Lasers, 11, 14, 15, 21, 23–26
Lateral epitaxial overgrowth (ELOG), 102, 103
Lattice constant, 30, 40
LED losses, 309, 310, 314
LED modeling, 138, 156, 158, 311
LED optimization, 243, 254, 425
LEDs, 69–72, 75, 78–87, 89, 129, 130, 132–135, 137–139, 141, 142, 144–147, 152, 157–159
LiFi, 486
Light-emitting diode (LED), 1–5, 8
Light extraction, 341, 343, 345–347, 352, 353
Light extraction efficiency, 69, 70, 72, 78–82, 84, 267, 271, 283, 301, 302, 322, 327
Light extraction,GaN, 136, 139, 146
Lighting market disruption, 481, 482
Low-temperature-deposited buffer layer, 1, 3, 4, 6
Luminous efficacy, 3, 69, 187, 398, 399, 403, 404, 412, 413, 415, 417, 418, 422, 423, 425, 433, 434, 437, 439–441, 445–447, 454, 455, 457, 471, 474, 475, 478
Luminous efficacy of radiation, 14, 16, 17, 24, 26, 239

M
Meltback etching, 33, 41, 42, 45
Metal organic chemical vapor deposition, 31, 39
Mg-doped GaN, 7
Micro-chip, 435–438, 440–446, 449, 454
Miscibility gap, 242
MOCVD, 211–213, 215–220, 222, 224, 227, 229, 234, 273, 275, 290
Molecular Beam Epitaxy (MBE), 211–213, 215-218, 222, 227, 229, 234
Multi-phosphor converted white LEDs, 418
Multiple active region LED, 211, 214, 235

N
Nanostructure, 293
III-Nitride Tunnel Junctions, 212, 213, 219, 222, 227, 234, 235
Nonpolar, 93, 94, 96, 98, 101–106, 108–110, 112–121
Nonpolar GaN, 87

O
Optical losses, 309

P
Package degradation, 384
Patterned sapphire, 341, 345
Patterned Sapphire Substrate (PSS), 69–78, 80, 81–89
Phosphor-free white LED, 261, 262
Phosphors, 397–409, 411, 415–423, 425, 426
Photoluminescence, 245
Photonic crystal (PhC), 118
Photon recycling, 129, 133, 144, 145
Photovoltaic cell, 2
Piezoelectric, 242, 248, 252, 258
Polarization discontinuity, 97, 98
Polarization switching, 98, 111–114
p-type GaN, 2, 7, 8

Q
Quantum confined Stark effect (QCSE), 95, 115, 117, 242
Quantum dots (QDs), 415, 423, 425
Quantum well LED, 309

R
Radiative efficiency, 164–166, 187, 203
Ray tracing, 301, 305, 306, 308, 313–316, 318, 322, 326, 328, 338
Reabsorption, 000
Reverse-current conduction, 363, 364, 371, 372, 390

S
Saturated radiative recombination rate, 173
Selective re-growth/selective growth, 102, 103, 119
Semiconductor nanocrystals, 423
Semipolar, 93, 94, 96–106, 109, 110, 112–121
Semipolar GaN, 69, 70, 86, 87
Series resistance, 365
Short-circuit path, 389
Smart lighting, 490
Solid-state lighting, 11, 12, 14, 17, 20–24, 26, 461, 462, 477
Spectral power distribution, 386, 413, 421, 475
Stokes loss, 240
Strained-layer superlattice, 29
Surface orientation, 94, 98, 99, 100, 102, 104
Surface roughness, 129, 142–144, 146, 158, 159

T
Temperature-dependent photoluminescence, 182, 187, 203
Tensile stress, 30
Texturing, 341, 356
Thermal aging, 423
Thermal expansion coefficient, 30, 32, 48
Thermal quenching, 403, 404, 406, 409, 411, 417, 425
Thermal stress test, 384
Threading dislocation, 30, 43, 46, 57
Threading-dislocation density, 267, 272
Time-resolved photoluminescence, 182, 203
Two-dimensional electron-gas (2DEG), 94

V
Vertical chip, 341
Visible Light Communications, 486

W
Wavelength down conversion, 12, 17
Wheatstone Bridge, 441–443
White LED, 457, 458, 461, 471, 478